Puffer circuit breaker diagnostics using novel optical fibre sensors

Thesis submitted in accordance with the requirements of the University
of Liverpool for the degree of Doctor in Philosophy by
Leslie Thomas Isaac

May 1997

ABSTRACT

Novel optical fibre sensors have been developed and employed on a commercial 145kV / 40kA (rms) sulphur hexafluoride puffer circuit breaker, to investigate its behaviour during interruption of short-circuit fault currents. The sensors were used to monitor a wide range of parameters within the circuit breaker: contact travel; gas pressure; gas dielectric strength; optical radiation emitted from the circuit breaker; and the production of arc-induced degradation particles in the interrupter enclosure. A significant database of results has been compiled, to characterise the circuit breaker during fault current interruption, which have been further employed in the validation of a mathematical model of the breaker. In addition to this, the suitability of the sensors for inclusion in a circuit breaker condition monitoring system, for which this work is a precursor, has been assessed.

ACKNOWLEDGEMENTS

I would like thank Prof. G.R. Jones for supervising this project and for his continuous encouragement.

I owe particular thanks to my colleagues Dr. J.A. Chaaraoui, Dr. M.G. Ennis and Dr. J.A. Cosgrave for their assistance and good advice during difficult periods. I am also grateful to Dr. S.U Ahmed, Mr. Gongde Li, Mr. D. Messent, Mr. P.T. Singh, Dr. C. Yakum and Mr. S. Furlong for their help.

I would like to thank experimental officers, Dr. J.K. Wood and Mr. J.E. Humphries, for their assistance during the assembly of experiments and Dr. C. Gerrard for his photographic work.

Throughout the project I have received invaluable assistance and advice from members of the Department of Electrical Engineering Mechanical Workshop; Mr. J. Roberts, Mr. P. Storey, Mr. T. Heywood, Mr. I. Kelly, Mr. K. Graham and Mr. R. Downward, and from members of the Electronics Workshop; Mr. A. Edwards, Mr. R. Smith, Mr. G. King and Mr. M. Owen.

I am grateful to Reyrolle Switchgear and Rolls-Royce Applied Sciences Laboratories for financing this PhD and owe particular thanks to Dr. W.B. Hall and Dr. M. Christodoulou for their help and advice during the work.

Finally, I am sincerely grateful to my family and my fiancee, Cathy, for their support and encouragement, which helped me to complete the work.

CONTENTS

Page

Part I - Background

Part II - Development of optical fibre sensors

Part III - Main circuit breaker experiments

CHAPTER 1 - INTRODUCTION

During this century significant, continual improvements have been made in circuit breaker technology. The discovery of sulphur hexafluoride gas (SF_6) as being an excellent arc quenching medium in the 1950s transformed the development of circuit breakers, particularly at transmission voltage levels, where oil and airblast breakers were traditionally employed. Two-pressure SF_6 gas-blast breakers were developed during the 1960s, but this type has been superseded by single-pressure "puffer" circuit breakers, which offer several advantages. One of the main disadvantages of puffer circuit breakers, however, is the requirement for a powerful (and hence expensive) driving mechanism. Therefore, substantial research has been performed in the last two decades into methods of reducing the mechanism requirement (autoexpansion hybrid puffers), or even eliminating the pressurising mechanism (rotary arc electromagnetic breakers). Commercial rotary arc breakers are currently limited in their switching capacity to distribution service. Therefore, it is likely that puffer circuit breakers, and their autoexpansion hybrids, will continue to be extensively used at transmission levels for the foreseeable future.

Circuit breaker advancements have been made possible by improvements in diagnostic equipment. Early diagnostics consisted of simple measurements of current through and voltage across a circuit breaker terminals, to indicate a successful interruption, and have evolved to the present level where a wide range of electrical, aerodynamic, radiative, mechanical and chemical parameters can be monitored on a circuit breaker to investigate performance characteristics. Traditional diagnostics were often difficult to employ on circuit breakers in service due to their size and, since many were electrical devices, there existed problems of shielding transducer signals from electromagnetic interference during switching and also of potentially compromising the insulation requirements of the circuit breaker to ground. However, the advent of optical fibre sensing has made it possible to produce small, non-invasive diagnostics with inherent insulation and freedom from electromagnetic interference (via optical fibres), which are, therefore, suitable for on-site circuit breaker monitoring.

As a consequence of the widespread popularity of SF_6 puffer circuit breakers at transmission voltage levels, significant commercially-driven research is being undertaken to attempt to mathematically model the current interruption process (often incorporating experimental results), in order to provide an effective design tool for manufacturers. Further research is being conducted into circuit breaker condition monitoring, which employs sensors to monitor the internal "health" of breakers in service, with the aim that potential malfunctions can be predicted and unnecessary periodic maintenance can be avoided. This leads to the objectives of the work reported in this thesis, which were:

- To design and develop optical sensors, which can withstand the harsh environment within a transmission puffer circuit breaker.
- To test the optical sensors on a full size commercial 145kV / 40kA (rms) puffer circuit breaker, which was modified for research purposes (although these modifications did not alter the internal layout of the device).
- To use the sensors, pending successful trials, to improve the understanding of the processes occurring during short-circuit fault current interruption within the circuit breaker.
- To use the results obtained from the sensors to validate a mathematical model for the test circuit breaker, which was developed by colleagues as a parallel project to this experimental work.
- To identify the suitability of the sensors for inclusion into a circuit breaker condition monitoring system, which is a subsequent project to this work.

This thesis, which describes the achievements in realising the above objectives, is divided into three main parts. **Part I** sets the background to the project. This begins with a review of circuit breaker evolution and the development of circuit breaker diagnostics, highlighting the work of previous authors (**chapter 2**). The advantages of optical fibre sensing are introduced, revealing why their use is often preferable to traditional methods for circuit breaker diagnostics. The final part of this chapter discusses the two major applications of circuit breaker diagnostics, mathematical modelling and condition monitoring, to which the work described later can be applied.

Chapter 3 considers the relevant aspects of circuit breaking, beginning with the principles of current interruption. A brief discussion of the theory of high pressure arcs is included to illustrate the difficulties involved in arc modelling, showing why many models require empirical input. The chapter concludes with a review of radiation emission from circuit breaker arcs, so that these results can be compared with other authors to explain the features of radiation measurements taken during this project.

In **part II** development of the optical sensors is addressed. This begins with **chapter 4**, which discusses the principles of optical fibre sensing and the modulation techniques that have traditionally been employed. A recently developed method of light modulation, chromatic modulation, is introduced. This method offers several advantages and was, therefore, used for the optical sensors developed in the project.

Chapter 5 describes the development of an optical fibre linear travel recorder (OFLTR), for measuring the opening stroke of the moving contact and piston assembly of the test interrupter. Traditionally, these devices were electrical potentiometers, which, because of their size, required a relatively remote location from the interrupter unit. This caused errors on the travel record produced for the interrupter. The optical fibre device, described in **chapter 5**, was sufficiently compact to install within the interrupter unit itself, to provide an accurate record of the interrupter motion. The results from this device provide an important base for the mathematical circuit breaker model, and the device itself is regarded as an important member of the future condition monitoring system.

An optical fibre particle concentration monitor (OFPCM) is described in **chapter 6**. This device was used to monitor the concentration of arc-induced degradation particles in suspension in the SF_6 gas, after current interruption, since these particles contain metallic elements, which may compromise the dielectric strength of the gas. The OFPCM was used to indicate the time taken for the particles to settle out of the gas (a time scale of many minutes), and thus for dielectric recovery to be complete.

A hybrid sensor is introduced in **chapter 7**. The definition of hybrid, used here, is to make an electrical measurement, but to use appropriate electro-optic and opto-electronic conversions, such that the signal links between the circuit breaker and control room instrumentation can be made entirely with optical fibres. This provides the required insulation between the circuit breaker and control room and improves the electromagnetic interference independence of the signals. The sensor discussed is a gas dielectric strength probe, which monitored the breakdown voltage of the SF_6 gas in a test-gap. The device may be used to indicate regions of dielectric weakness immediately after arcing (up to ~100ms), which may cause late breakdown leading to arc reignition, and it is shown that, provided certain assumptions are acknowledged, estimates of gas temperature may be made from its breakdown voltage.

A recent collaborative project between the University of Liverpool and Lucas Control Systems Products has produced novel micromachined silicon optical fibre pressure sensors. As part of this work, the suitability of the sensors for circuit breaker application was assessed (**chapter 8**). This involved designing housings for the sensors with appropriate optical fibre inputs. It was subsequently proved that this type of sensor may be successfully used within the harsh environment of a transmission puffer circuit breaker. The results are used later, in conjunction with the travel record, to validate the mathematical model produced for the test circuit breaker. This chapter concludes **part II** of the thesis.

Part III of the thesis presents and discusses the results obtained from the range of optical sensors, whose development is described in **part II**, during the main series of experiments on the test circuit breaker. Firstly, **chapter 9** describes the test circuit breaker, with the modifications made for research use. This is followed by a description of the power circuit used, in order to replicate short-circuit fault conditions at the circuit breaker. The instrumentation used and their locations within the circuit breaker are discussed, together with the appropriate signal processing equipment. The chapter then concludes with a global test strategy, devised to gain maximum benefit from the sensors employed.

Chapter 10 presents the results obtained from the main series of tests. Firstly, coldflow results are shown, i.e. in the absence of arcing, for the gas pressure (near the top-plate and in the piston chamber of the circuit breaker) and interrupter travel. A relationship is deduced between peak piston pressure and interrupter velocity. For the arcing tests, results are presented for the following: current through and voltage across the circuit breaker terminals; gas pressure near the top-plate and in the piston chamber; optical radiation from the circuit breaker; particle concentrations within the circuit breaker; and post-arc gas dielectric strength. The implications of each of the results is discussed in turn.

The gas pressure and circuit breaker radiation results require further analysis, which is provided in **chapter 11**. One of the most important sections of the analysis is the use of the piston chamber pressure results, with the travel record for the interrupter, to compare with the results predicted by the mathematical model, developed by colleagues, for the test circuit breaker. The radiation results are compared with results obtained from previous authors (discussed in **chapter 3**), to identify the dominant processes affecting the radiation emission from the circuit breaker. Furthermore, the energy transfer mechanisms occurring during fault current interruption are analysed with the aid of the electrical, gas pressure and particle concentration results obtained.

The thesis is completed by **chapter 12**, which presents conclusions and recommendations for further development of the sensors, including an assessment of their usefulness within the condition monitoring system to be developed.

Part I - Background

CHAPTER 2 - REVIEW

2.1 EVOLUTION OF THE CIRCUIT BREAKER

2.1.1 Introduction

The required functions of a circuit breaker are (Lythall, 1972):

1. It must be capable of closing on to, and carrying, full load currents for long periods of time.
2. Under prescribed conditions, it must open automatically to disconnect the load or some small overload.
3. It must successfully and rapidly interrupt the heavy currents which flow when a short-circuit has to be cleared from the system.
4. With its contacts open, the gap must withstand the circuit voltage.
5. It must be capable of closing on to a circuit in which a fault exists and of immediately re-opening to clear the fault from the system.
6. It must be capable of carrying current of short-circuit magnitude until, and for such time as, the fault is cleared by another breaker (or fuse) nearer to the point of fault.
7. It must be capable of successfully interrupting quite small currents, such as transformer magnetising currents (inductive) or line and cable charging currents (capacitive).
8. It must be capable of withstanding the effects of arcing at its contacts and the electromagnetic forces and thermal conditions which arise due to the passage of currents of short-circuit magnitude.

Of the various duties required of circuit breakers, the interruption of short circuit fault currents is one of the most arduous. The increasing demand for electricity since the turn of the century, combined with the rise in network transmission voltages, has caused a substantial increase in short-circuit levels which circuit breakers need to successfully interrupt (Shimmin, 1986). It has also been necessary, for system stability, to reduce the total interruption time from 10-20 cycles of 50Hz AC, associated with the early plain break oil circuit breakers, to the 2 cycles or less that can be achieved with modern SF_6 breakers (Flurscheim, 1982). At transmission voltage levels (≥132kV) circuit breakers have traditionally consisted of a number of interrupters (breaks) in series, in order that the circuit voltage could be shared between them. The first 420kV breakers in the UK employed 12 series airblast interrupters per phase (Ali and Headley, 1984); the ensuing development has meant that the same function can now be performed with a single break in SF_6 (Suzuki *et al*, 1993 and Toda *et al*, 1993). This reduction in the number of breaks has occurred due to the advances in circuit breaker technology, which has been driven by competing manufacturers seeking to produce more cost-effective and reliable equipment.

This section reviews the development of circuit breakers from inception in the late nineteenth century to the present date. Initially, the significant breakthroughs are dealt with regarding oil, air and SF_6 breakers, with emphasis on the increase in short circuit current interruption capability. Although the development is discussed with reference to short circuit interruption, it is recognised that circuit breakers are required to perform other duties, as described above, which can cause problems of a different nature. Such circuit breaker duties are not directly relevant to the research presented in this thesis and are, therefore, acknowledged rather than discussed. The work described later was performed on a 145kV / 40kA transmission puffer circuit breaker; hence, this review is biased towards the development of circuit breakers for transmission rather than distribution service.

2.1.2 The early years

The quick-break knife switch (Holmes, 1984) has been described as probably the first circuit breaker. Flurscheim (1965) records that such switches were "without any formal arc control other than that provided by the switch attendant who, armed with an insulated hatchet, was invited to chop the arc in two". The limitations of the knife switch prompted an “unknown inventor” to take the surprising step of immersing the device in flammable transformer oil. However, this proved to be an effective move, resulting in the inception of the oil circuit breaker and the beginning of circuit breaker development.

2.1.3 Oil circuit breakers

The first oil circuit breaker was a plain break type i.e. there were no methods employed for controlling the arc (Flurscheim, 1982). As the arc was extended between two electrodes the energy released caused the dissociation of oil molecules to generate gas, principally hydrogen, which cooled and compressed the arc to extinction.

A significant feature of this type of oil circuit breaker was the relatively large post-arc leakage current. This characteristic contributed to the early success of the oil circuit breaker, since the leakage resistance damped the restrike voltage, reducing the severity of duty placed upon the breaker (Flurscheim, 1982). It also provided resistance grading, which helped to equalise the distribution of the restrike voltage across each break of a multi-break system. However, the leakage current was unstable and could sometimes cause a full arc reignition. The need for a more controlled system of interruption within the oil circuit breaker was recognised and several designs followed.

2.1.3.1 Bulk oil and small oil volume circuit breakers

The development of the oil circuit breaker followed two schools of thought. One method was the bulk oil circuit breaker (BOCB). In the BOCB the oil-containing tank is dead i.e. it is at earth potential and the necessary clearances for the system voltage must be obtained in oil between the live contacting elements within the tank and also between the contacts and the tank itself (Lythall, 1972).

The alternative design was the small oil volume circuit breaker (SOVCB). As the name suggests the amount of oil in which the contacts are immersed is much less than in the BOCB. In the SOVCB the tank is a tube of insulating material held between metal end caps and, as these caps are the terminal points for the external circuit, the tank is live at line potential. This assembly, designated the interrupter head, has to be supported on one or more insulators to isolate it from the earth.

2.1.3.2 Developments in oil circuit breakers

One of the earliest designs for controlling the arc was the H-type SOVCB (fig.2.1) designed by General Electric Company, USA (GE-USA) in the 1920s (Coates and Pearce, 1938). This design, which was reproduced in Britain by the British Thomson-Houston Co. Ltd. employed two metal explosion pots per phase, oil filled, and with insulating nozzles, through which the moving contacts were withdrawn vertically upwards, the explosion pots being mounted on ceramic insulators within an air insulated cubicle.

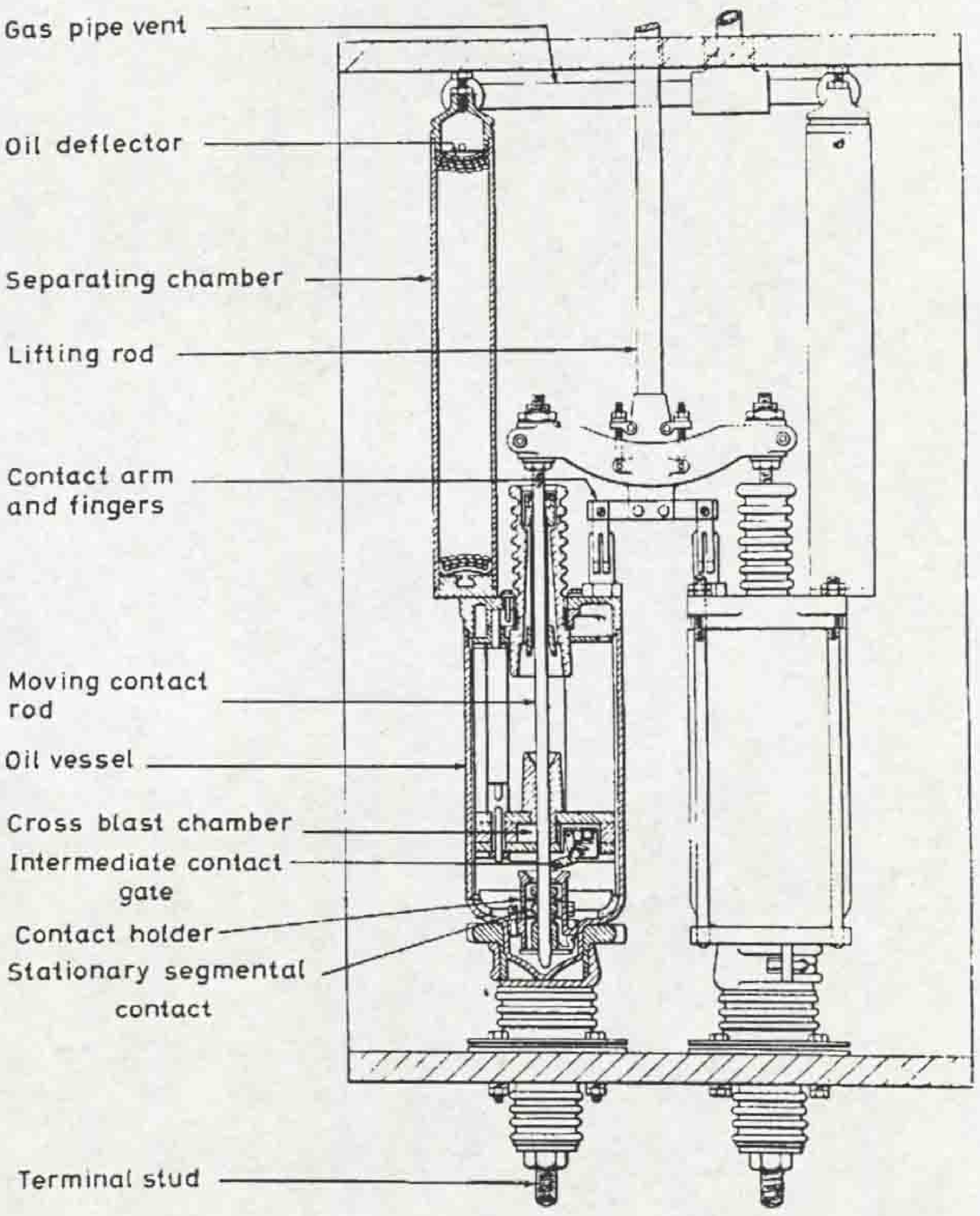

Figure 2.1 - “H” type oil circuit breaker (British Thomson-Houston Co. Ltd.)

The de-ion circuit breaker, produced by Westinghouse Electric Corporation (Slepian, 1929), used a novel technique to electromagnetically force the arc into a narrow insulation slot within an assembly of fibre plates submerged in the BOCB tank, thus "increasing the effectiveness of the means for preventing the escape of gases generated in the vicinity of the arc without passing through the arc stream" (Baker and Wilcox, 1930).

The axial flow oil blast BOCB, developed at GE-USA (Prince and Skeats, 1931), is shown on fig.2.2. This design utilises an explosion chamber to produce an axial "scavenging blast of oil" surrounding the arc to achieve extinction.

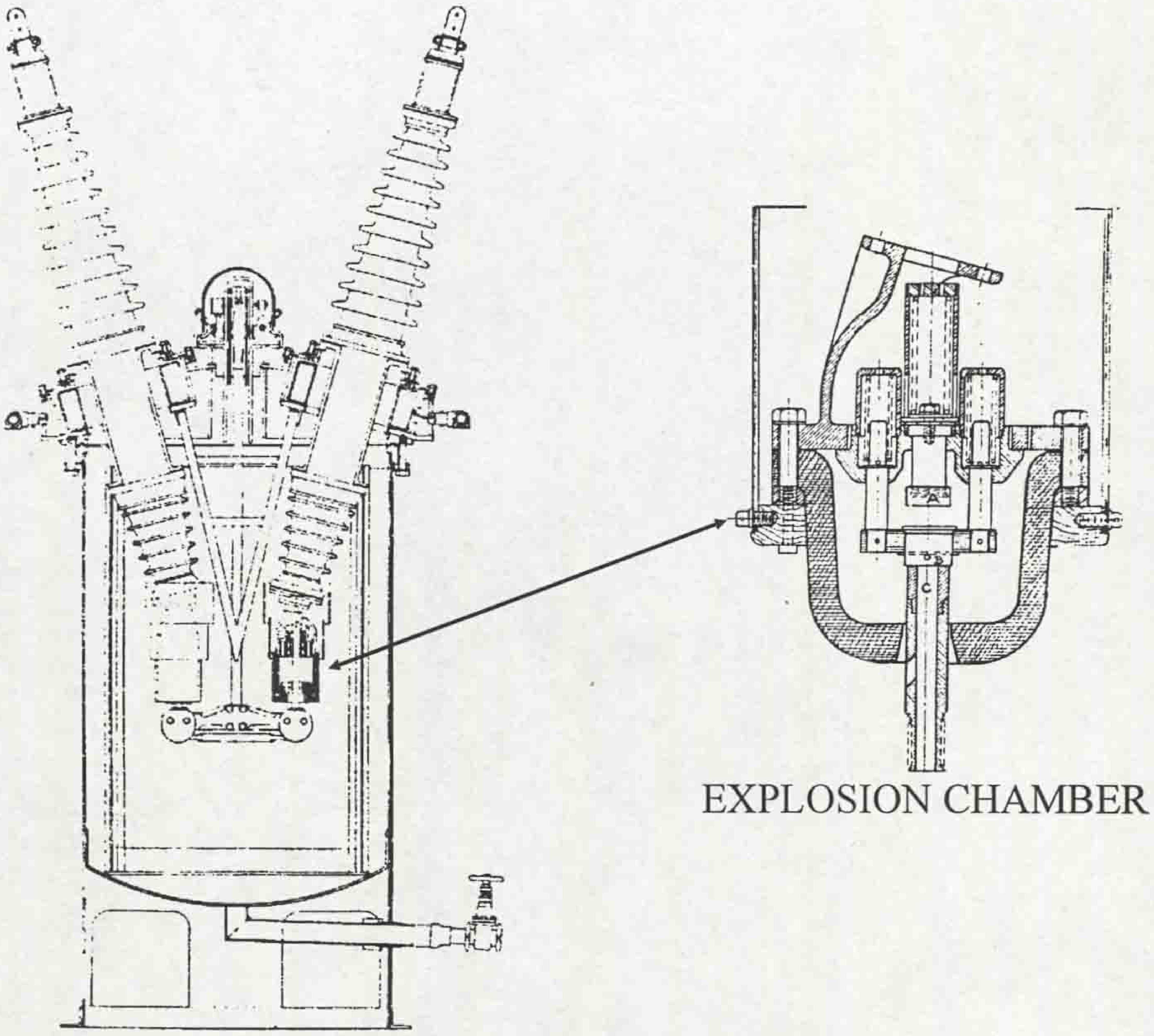

Figure 2.2 - Axial flow oil blast BOCB (Prince and Skeats, 1931)

At the British Electrical and Allied Industries Research Association (ERA) the side-blast arc control device was developed (Whitney and Wedmore, 1930). The operation of this device is shown on fig.2.3a. When the arc produces gas from the oil the increased pressure forces the gas bubble across the arc, through side vents, thus displacing and lengthening the arc to cause extinction. Fig.2.3b shows an engineered crossblast interrupter. The side-blast arc control device was a major breakthrough for

BOCB development in Britain. It was also later adopted by other European countries for use within their favoured SOVCBs.

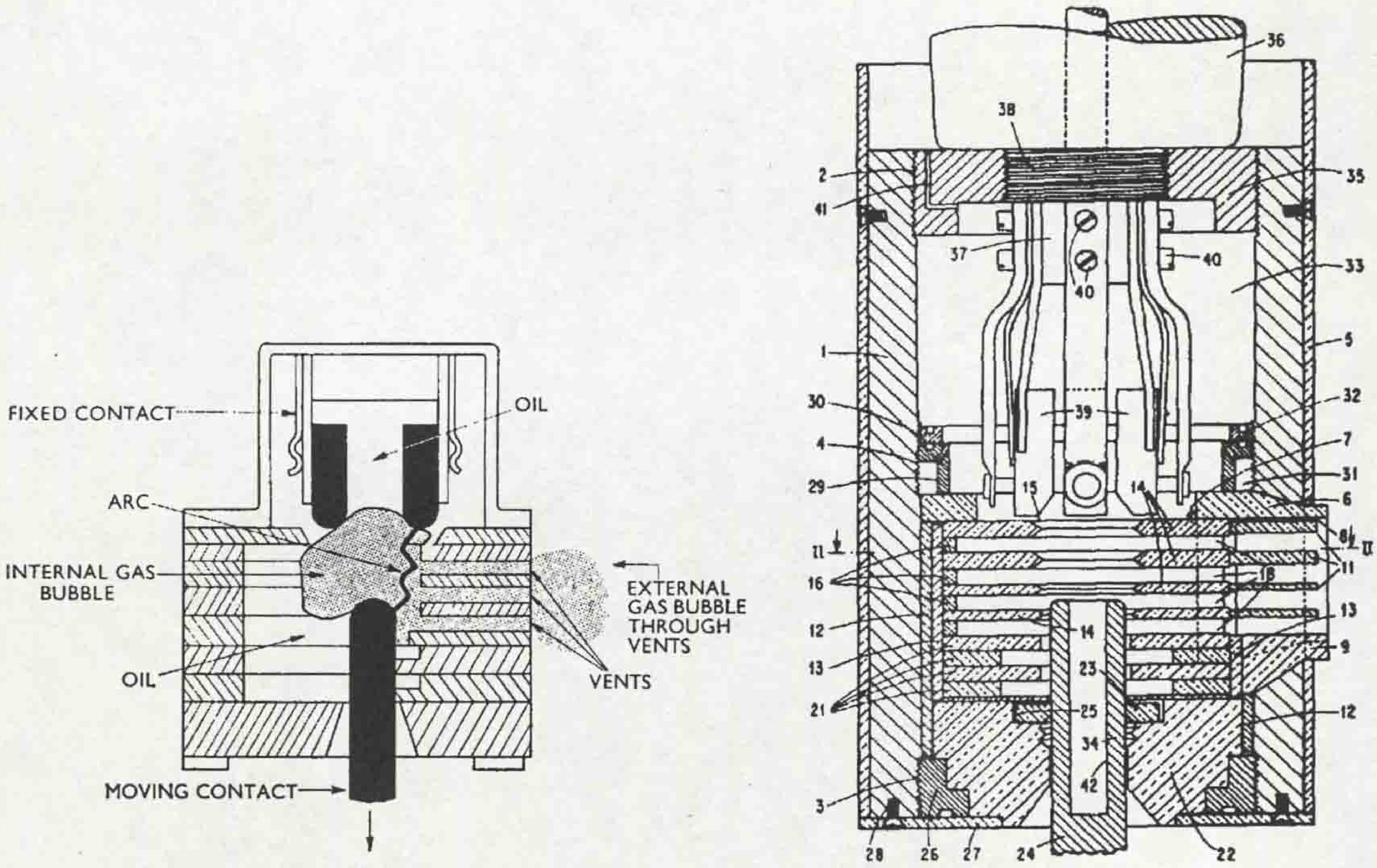

(a) (b)

Figure 2.3 - The side blast arc circuit breaker (Whitney and Wedmore, 1930)

These designs of oil circuit breakers achieved their aim of providing more control over the arc and eliminating the unstable post-arc leakage current. Unfortunately, in eliminating the leakage current, the restrike voltage damping and distribution in multi-break systems was also lost. Several designs were produced to maintain parity of voltage division in multi-break systems.

One successful design was the multi-break impulse oil circuit breaker (fig.2.4), developed at GE-USA (Prince, 1935). In this SOVCB the combination of the livetank construction, together with external capacitance shielding, ensured that the voltage duty was shared reasonably equally across each of the breaks. An 8-break 287kV 2500MVA breaker was commissioned on the Boulder Dam to Los Angeles 275kV transmission line in 1935, providing consistently successful interruption within 3 cycles. The same circuit breakers were reported to be still operating successfully some four decades later on a network with 7000MVA fault capacity (Flurscheim, 1982). The main drawback of this breaker was the high cost of the powerful mechanism to drive the oil. Combined with the trend towards airblast circuit breakers, this discouraged further development of this design at that time.

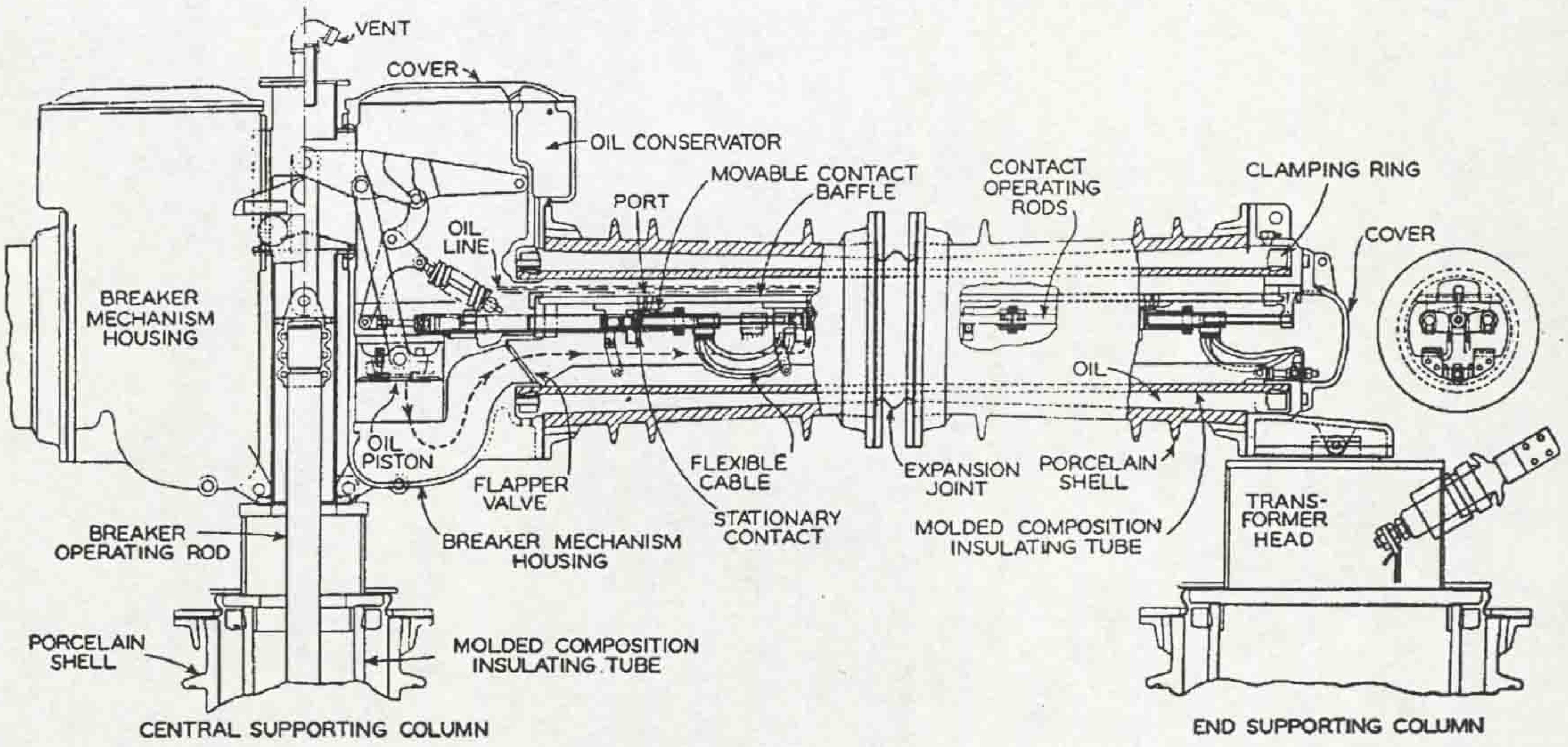

Figure 2.4 - The multi-break impulse oil circuit breaker (Prince, 1935)

2.1.4 Emergence of test facilities

The improvements to bulk oil circuit breakers in Britain during the 1920s meant that the hitherto testing of circuit breakers, with facilities made available by power stations, was becoming increasingly unfeasible. Clothier (A. Reyrolle & Co. Ltd.) had campaigned with the ERA for a separate testing facility. Indeed, in Germany AEG had reportedly built a test laboratory as early as 1917. Since support was not forthcoming, Reyrolle independently built the first short circuit testing station in Britain, commissioned in 1929. Other large manufacturers followed in building their own test stations. The availability of these test facilities and the emergence of new technologies, such as the cathode ray oscillograph, to provide accurate performance measurement, led to a rapid acceleration of circuit breaker development.

2.1.5 Airblast circuit breakers

Although in the late 1920s work at the ERA gave preference to the side-blast arc control device for oil circuit breakers, research on using air for the interrupting medium had already been investigated. The airblast circuit breaker was invented at the ERA (Whitney and Wedmore, 1926) and put into production in Germany by AEG (Biermanns, 1929) and in Switzerland by Brown Boveri (Walty, 1935).

From 1935-1945 the development of high voltage airblast circuit breakers followed two routes. The German AEG design (Biermanns, 1938) operated at up to 110kV per break using insulated Ruppel nozzles. Most other manufacturers, for example Brown Boveri (Thomen, 1941), adopted the use of metal nozzles operating at 35kV per break.

Early designs of airblast circuit breakers employed an automatic external isolating switch to provide insulation strength in the open position. Developments ensued (Thomen, 1950) which eliminated the series isolator by increasing the internal pressure to provide the required dielectric strength in the open position. Another advantage of internal pressurisation was the ability to obtain higher breaking capacities (Flurscheim, 1982).

2.1.6 SF_6 circuit breakers

The emergence of sulphur hexafluoride (SF_6) in the 1950s as being an excellent arc quenching medium totally transformed the development of switchgear. Although other interrupting media, such as oil, air and vacuum can compete with SF_6 at distribution levels, for transmission voltages (≥132kV) SF_6 is by far the most popular.

2.1.6.1 The pioneering experiments

The dielectric properties of SF_6 were known at around 1940 (Cooper, 1940 and Nonken, 1941). It is a little surprising that results of the arc quenching capability of SF_6 were not published until more than ten years later (Lingal *et al*, 1953). Fig.2.5 shows an example of the results obtained from this study. Using a simple plain break system housed in a porcelain enclosure, it was found that SF_6 at a given pressure could interrupt an arc current of roughly 100 times the value that air could. This is due to the effectiveness of SF_6 properties during the two phases of arc interruption, thermal recovery and dielectric recovery.

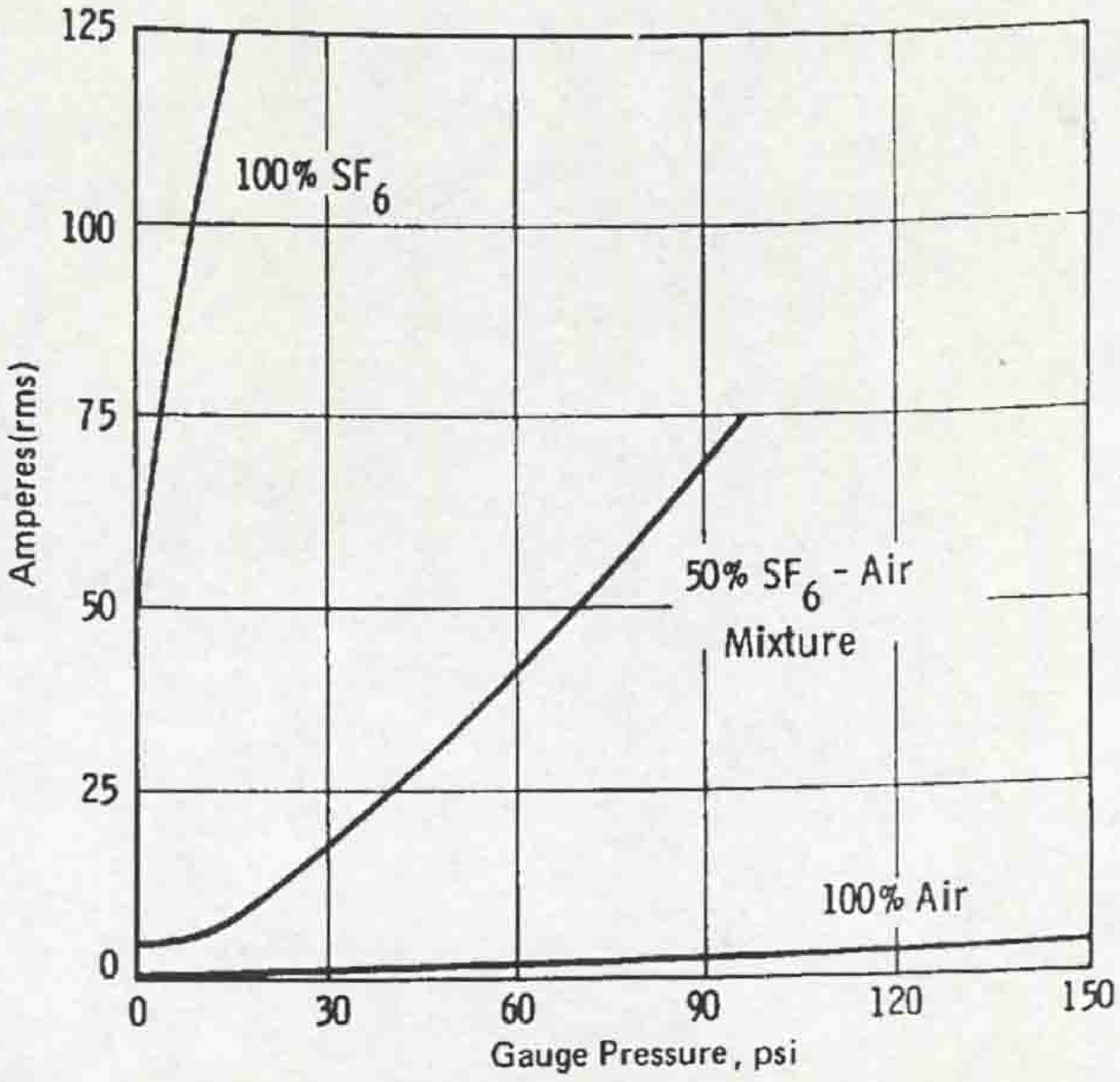

Figure 2.5 - Interrupting performance of a 3-in. plain-break gap in SF_6 at 2300V compared with that of air (Lingal *et al*, 1953)

2.1.6.2 Methods of interruption in SF_6

Traditionally, there have been four methods of effecting arc interruption in SF_6. Each of these is shown on fig.2.6 (Browne, 1984). Fig.2.6a shows the simplest method, a simple plain break system with no arc control device. Separation of the contacts draws a free burning arc to a sufficient length to cause extinction. It was found that by imposing even a moderate gas flow through the arc, as on fig.2.6b, significant improvements on arc interruption capability could be made (Lingal *et al*, 1953). If the nozzle is attached to the moving contact and the two are moved together then the principle of modern puffer circuit breakers is replicated.

Another method of imposing gas flow on the arc is by using the self-generation / self-pressurisation / auto-expansion principle (fig.2.6c), where the flow is produced by using expansion chambers powered by arc heating (Suzuki *et al*, 1984). However, the most successful method, in terms of current interruption capability, during the early development of SF_6 circuit breakers was the two-pressure (or double-pressure) system. Shown on fig.2.6d, SF_6 is held at high pressure (usually around 15bar) in a chamber separated from the main tank held at low pressure (around 3bar). When the arc is drawn the blast valve is released to cause the high pressure SF_6 to flow through the arc region (Leeds *et al*, (1957).

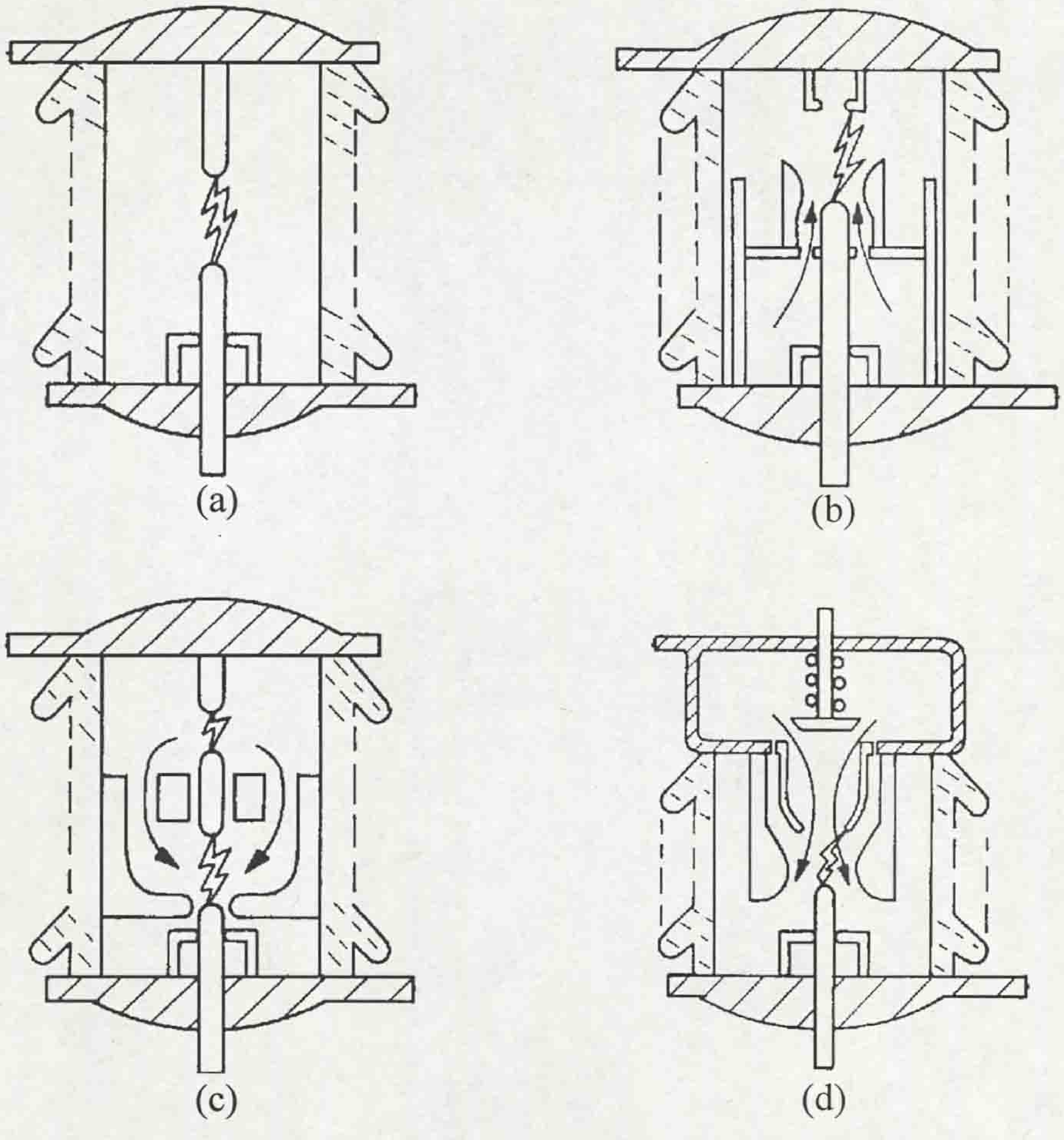
(a) (b) (c) (d)

Figure 2.6 - Traditional methods of arc interruption in SF_6 (Browne, 1984)

2.1.6.3 SF_6 Circuit breaker development

The development of SF_6 switchgear was initiated at Westinghouse. The first application was to a HV load break switch. Using the puffer principle the switches were designed for voltage ratings from 15 to 161kV, opening load circuits with currents up to 600A. The first SF_6 power circuit breaker was put into service in 1956. This was a 115kV breaker with 1000MVA interrupting capability (Cromer and Friedrich, 1956), based on the self-generation principle.

In 1959, the appearance of high power, high voltage SF_6 circuit breakers, rated in excess of 10000MVA at 230kV showed the first serious threat to the well established oil and compressed air HV breakers (Friedrich and Yeckley, 1959). These were based on the two-pressure principle. Further development of such circuit breakers continued (Einsele, 1964).

In the early 1960s, puffer circuit breaker development led to puffer breakers being produced with voltage ratings of up to 69kV and interrupting capacities up to 30kA (Easly and Telford, 1964). However, in the early development years of SF_6 circuit breakers the highest interruption capability was achieved using the two-pressure principle. In the late 1960s EHV circuit breakers (up to 800kV) were developed with interrupting capabilities which have since reached in excess of 63kA (Yeckley and Cromer, 1970).

2.1.6.3.1 Direction towards puffer circuit breakers

With the increasing ratings achieved by puffer circuit breakers, manufacturers saw the possibility of superseding the transmission voltage two-pressure SF_6 circuit breakers with puffers. Puffer breakers have the following advantages:

- Increased reliability due to fewer parts and a simpler layout.
- No requirement for the complicated high pressure systems associated with two pressure breakers.

- In two pressure breakers heaters are required to avoid liquefaction of the SF_6 stored at high pressure. These are not necessary with puffer circuit breakers, as there is no requirement for high pressure gas storage.

Fig.2.7 shows the operation of a partial duo-blast puffer circuit breaker, typical of the type used in this work. (Other types are discussed below).

1. Fig.2.7a shows the puffer interrupter in the closed position. Load current flows through the fixed contact (1), through the moving contact (2), the puffer cylinder (3) and the stationary puffer casing.
2. In fig.2.7b contact separation has occurred and an arc is struck between the fixed (1) and moving contact (2). As the moving contact and piston cylinder move away from the fixed electrode, the piston chamber volume is reduced. The fixed electrode is still inside the nozzle, restricting the downstream cross-section and causing the piston gas to increase in pressure. The piston pressure increases further due to the heat produced by the arc, the extent of the heating being determined by the arc current.
3. The fixed contact continues to be withdrawn from the nozzle, thus extending the arc length through the nozzle. When the contact leaves the nozzle (fig.2.7c) the piston gas at elevated pressure escapes axially past the arc, causing cooling by forced convection and, hence, arc control and eventual extinction. This process is further enhanced by turbulence effects induced in the arcing region.
4. The circuit breaker is designed so that the factors causing arc extinction are enhanced at a current zero on the AC current cycle. The fully open position of the puffer interrupter, following arc extinction, is shown on fig.2.7d.

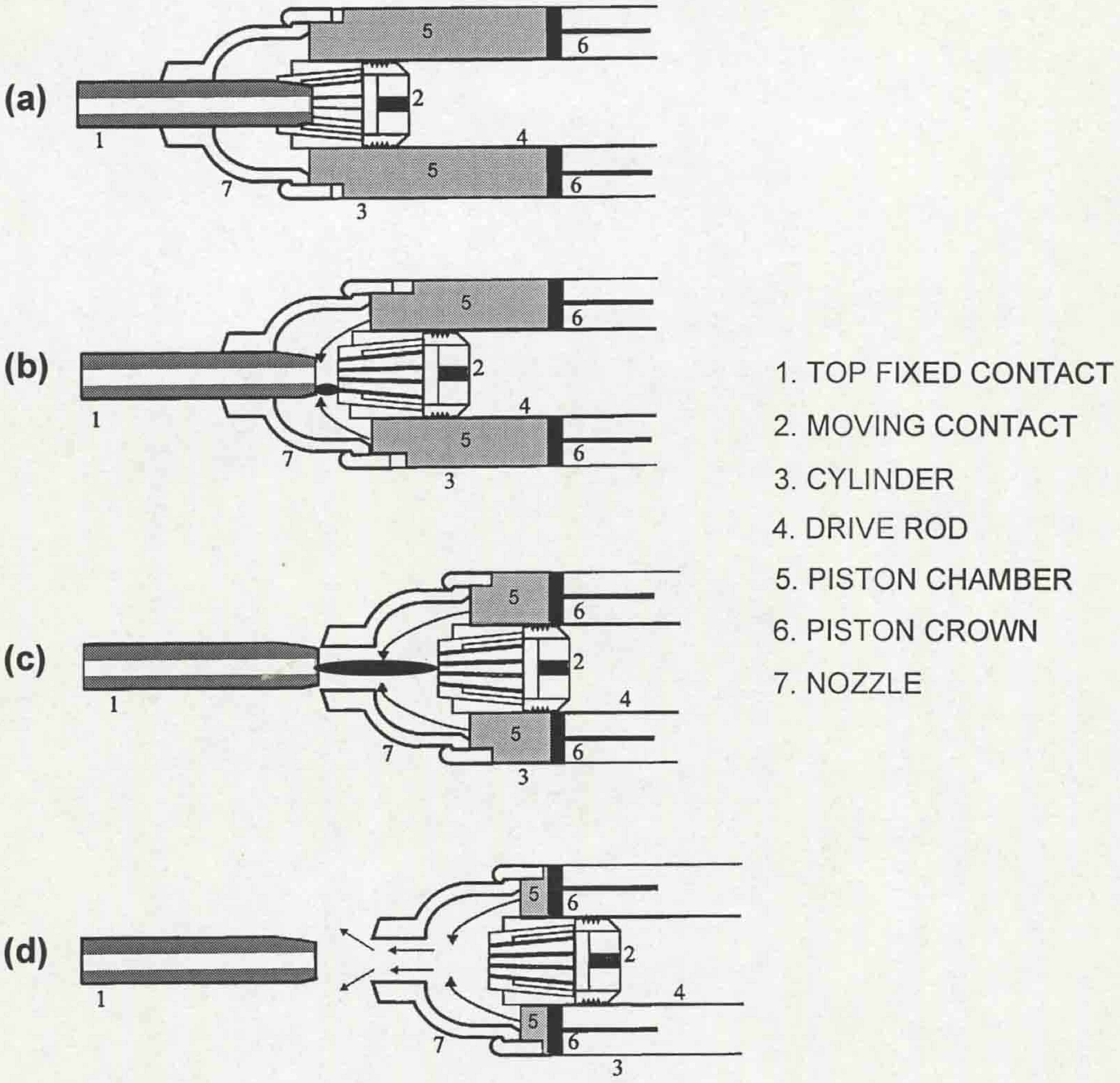

Figure 2.7 - Operation of a partial duo-blast puffer circuit breaker

The physical properties of the arc plasma column need to be incorporated into interrupter design considerations to provide proper control over the gas flow. For instance, when load currents are to be interrupted (typically less than a few kA) then a powerful gas blast could interrupt the arc prior to current zero, leading to a phenomenon known as current chopping. In such circumstances dangerously high overvoltages (Ldi/dt), due to the inductive nature of power systems, may be generated. However, in a puffer circuit breaker, when a low current is being interrupted the arc cross-section is small and its blocking effect on the nozzle of the interrupter is also small; thus, the pressure build-up in the piston chamber is limited. The ensuing gas blast is weak enough to avoid current chopping, but strong enough to extinguish the arc at current zero. On the other hand the interruption of very high short-circuit currents (possibly up to 100kA) requires a substantial gas blast. Since a short-circuit current arc will have a large cross-section and effectively fill the nozzle throat, the pressure build-up will be high to provide the required blast. This current-controlled pressure rise is a major inherent advantage of puffer circuit breakers.

Fig.2.8 shows the various types of puffer interrupters (Ryan and Jones, 1989). The simplest type is the mono-flow system (2.8a), utilising a unidirectional flow from the piston chamber. This type has been superseded by other types to improve performance by, amongst other things, reducing contact vapour in the arcing region. The partial duo-blast in fig.2.8b, whose operation is detailed above (fig.2.7), has a main flow through the centre of the insulating (PTFE) nozzle, with subsidiary flows through both of the hollow electrodes. The subsidiary flows limit the entrainment of contact material into the main nozzle. The full duo-blast puffer utilises two conducting nozzles, which act as the main contacts also. Again, this system reduces metal vapour entrainment. The fourth type is the full duo-blast puffer incorporating insulating nozzles, so that full advantage can be taken of optimised down-stream flow produced by detailed profiling of the nozzle and without interference by arc root movement (Ryan and Jones, 1989).

The main drawback of puffer circuit breakers is the requirement for a powerful mechanism to overcome nozzle blocking and arc-induced pressurisation. Indeed, a single break 300kV 50kA puffer breaker produced in 1982 (Yanabu *et al*) could not be economically developed for this reason. Manufacturers therefore sought means by which the mechanism power specification could be reduced by utilising the arc's energy (electromagnetic or thermal) to assist in the interruption process. This resulted in the production of "hybrid puffer circuit breakers". Initial studies (Yanabu *et al*, 1989) were further developed to produce a 550kV, 63kA single break hybrid interrupter (Suzuki *et al*,1993 and Toda *et al*, 1993). The redirection of the arc's thermal energy into the puffer cylinder to act in conjunction with the external mechanism provided a piston pressure up to 1.5 times that obtained from the mechanism alone.

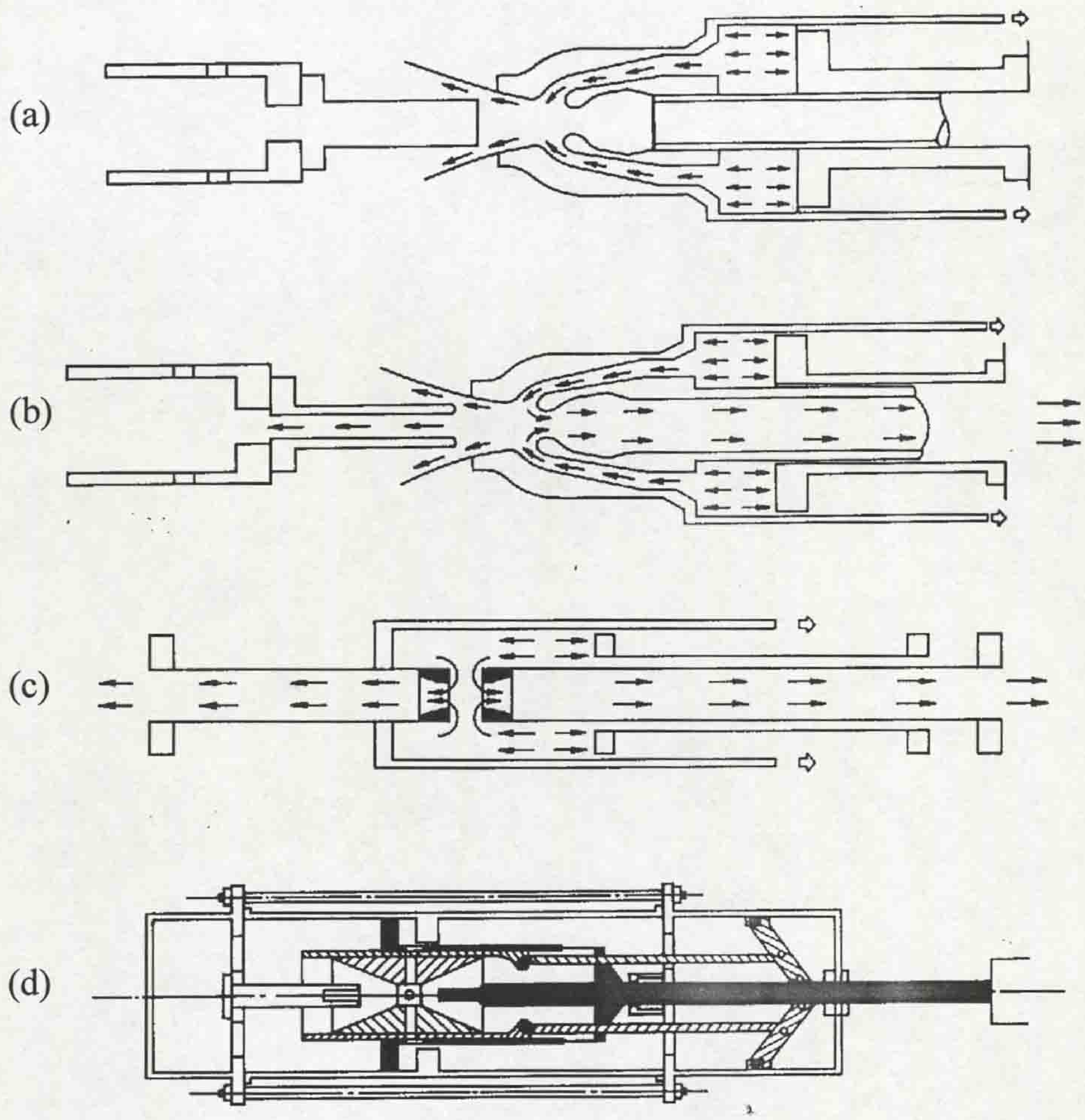

Figure 2.8 - Types of puffer interrupters (Ryan and Jones, 1989)

2.1.6.3.2 Development of rotating arc interrupters

In order to avoid the expensive mechanisms required with puffer circuit breakers, significant recent research (eg. Spencer, 1985) has been undertaken to evaluate rotating arc interrupters. Here the driving Lorentz force is usually produced by the fault current through the arc and by the magnetic field produced by the fault current through a solenoid. Thus, unlike the puffer interrupters which utilise superimposed axisymmetric flows, the rotary arc interrupters are non-axisymmetric and the arc, rather than the surrounding gas, suffers most movement to generate an effective cross-flow (Ryan and Jones, 1989).

Rotating arc interrupters have found increasing use at distribution levels with two commercially available types (Parry, 1984 and Duplay and Hennebert, 1983).

However, research is currently underway to advance the rotating arc circuit breaker to transmission levels (Ennis *et al*, 1996).

2.1.7 Vacuum circuit breakers

Arc interruption studies in vacuum originated in the 1920s (Sorenson and Mendenhall, 1926). However, due to a wide range of problems to overcome in their development, the first interrupters capable of heavy short circuit duty were not produced until 1960 (Lee *et al*, 1962). There are some significant advantages gained with vacuum interrupters, such as freedom from maintenance and consistent interruption at the first current zero after contact separation. However, vacuum interrupters have only been successfully employed at distribution levels up to 38kV. The economic problems in producing multi-break systems for transmission voltages mean that, at least for the foreseeable future, vacuum cannot compete with SF_6 in this voltage range (Flurscheim, 1982).

2.2 REVIEW OF CIRCUIT BREAKER DIAGNOSTICS

2.2.1 Requirement for diagnostic schemes

In an industrial test environment two parameters are sufficient to indicate whether a circuit breaker has successfully interrupted a short circuit fault. They are the overall voltage across the breaker contacts and the current flowing through the breaker. However, at laboratory research level much more detailed and localised information concerning the arc and its interaction with the surrounding medium can be obtained. This information is essential for the effective development of interrupters with greater arc control and interruption capabilities.

In the laboratory, measurements have usually been taken on small scale circuit breaker models and the extrapolation of such results to commercial interrupters is often difficult. Therefore, it is preferable to use the diagnostics on practical circuit breakers. This has traditionally been difficult owing to the size of much conventional instrumentation, and the problems of isolation from live equipment. However, the advent of optical fibre sensing techniques with inherent isolation has allowed a wide range of parameters to be measured on commercial breakers, using small, non-invasive or non-obstructive optical devices which can be easily incorporated (eg. Noeske *et al*, 1983, Ali *et al*, 1985 and Henderson *et al*, 1993). Such devices can be used on circuit breakers in service to provide information for a condition monitoring system (**2.2.4.2**).

The parameters, which can be measured using conventional methods or optical fibre sensing techniques, can be conveniently divided into five groups; electrical, aerodynamic, radiative, mechanical and chemical (Jones, 1988). This section discusses the specific parameters, which belong to these groups, and examples of how each has been measured, firstly using traditional techniques and then using optical fibre sensors. The review is completed by discussing the advantages of optical fibre sensors, revealing why their use is often preferred.

2.2.2 Classification of measurable parameters

2.2.2.1 Electrical

Electrical parameters can be further classified as either overall parameters or localised parameters (Jones, 1988). The overall parameters are those which can readily be measured in an industrial environment to give an immediate performance assessment. They are the overall voltage across the arc gap and the total current flowing through the gap. From these parameters it is easy to calculate the total power dissipated by the arc and the effective resistance of the arc. Resistive current shunts have been used effectively to measure the total arc current (Chapman *et al*, 1975). Overall arc voltages can be measured by using a tailored R-C voltage divider system, though for many applications a commercial high voltage probe (eg. Tektronix model P6015, 1000:1) will suffice (Jones *et al*, 1973).

Localised parameters provide a convenient intermediary between fundamental plasma research, eg. determining species temperatures and concentrations, and the overall parameters. Measurement of localised parameters can yield very useful information about the arc behaviour to assist in interrupter development. Examples of such measurements include spatial voltage variation (Chapman, 1977), current density distribution (Barrault and Jones, 1974) and the electrical cross-section of the arc column (Dhar *et al*, 1977).

Localised parameters are measured by using the electromagnetic interaction of the arc with search coils or similar pick-up devices and, therefore, optical fibres are unsuitable for direct measurement, although it is possible that they could be used in "hybrid" systems to relay electro-optically encoded signals and so provide electrical isolation from the circuit breaker. Care has to be taken with conventional measurement of overall electrical parameters to avoid electromagnetic distortion from the discharge and insulation failure problems. Hence, recent research has been undertaken to measure the current and voltage using optical techniques (eg. Pilling, 1992, and Moghisi, 1989). Such techniques offer distinct advantages over conventional methods, including reduced size, electrical isolation for the processing instrumentation and freedom from electromagnetic interference.

2.2.2.2 Aerodynamic

Parameters which fall into the aerodynamic category are those that provide information regarding the flow conditions within the circuit breaker. Pressure measurements, using piezoelectric or piezoresistive transducers, have been made on puffer circuit breakers to determine piston pressures and axial pressure distributions (Shimmin, 1986 and Tominaga *et al*, 1980). Fig.2.9 describes how the piston pressure would typically change from coldflow to an arcing situation, as measured using such transducers.

The problem with using electrical transducers is the requirement to provide electromagnetic shielding from the arc. In addition, thermal protection is required for measurements close to the arc and is usually achieved with interconnecting tubes. Distortion can be minimised in such systems by acoustic correction (Jones, 1984). Localised measurements of plasma and gas velocities have been achieved using laser Doppler velocimetry (Todorovic and Jones, 1985).

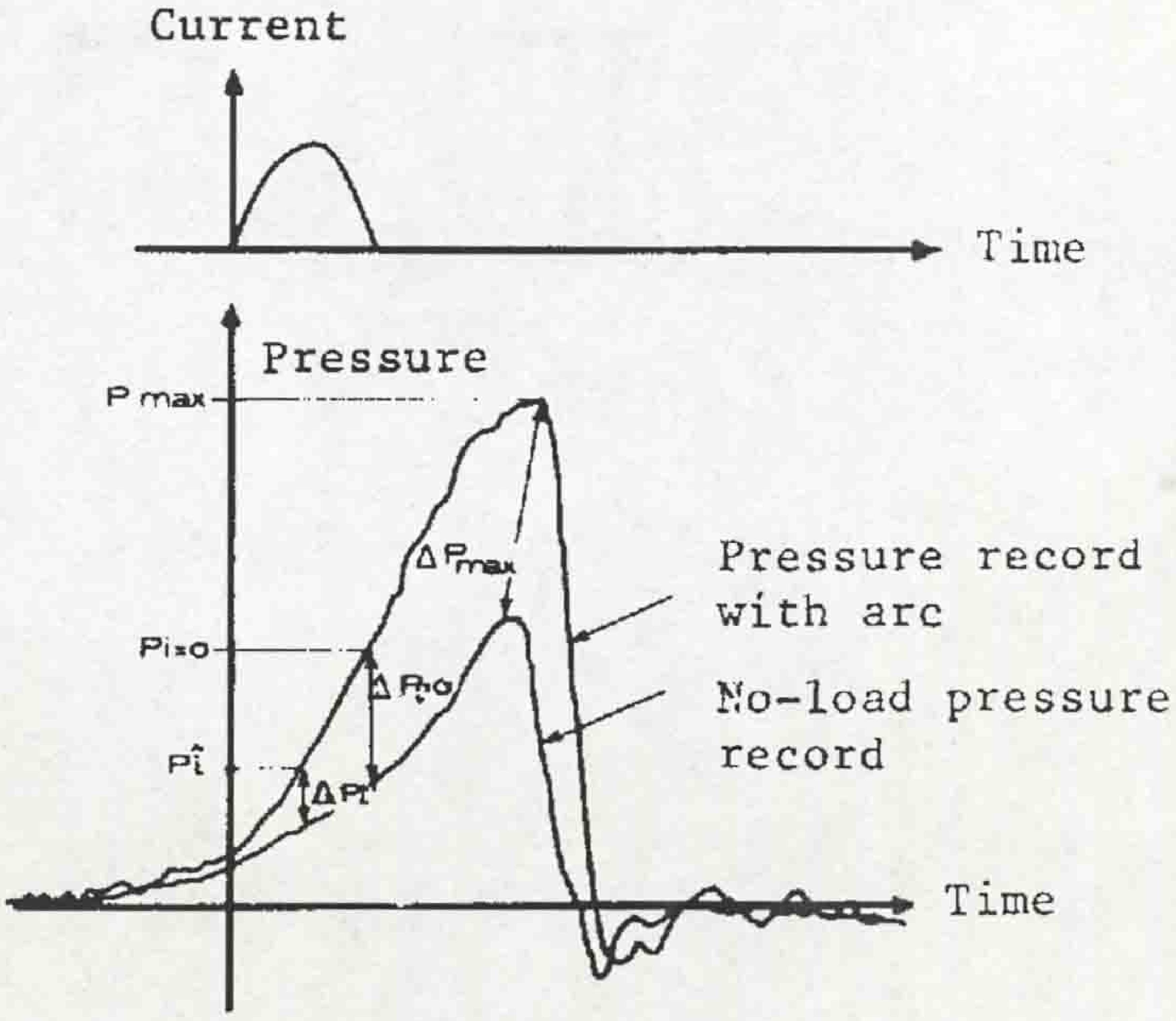

Figure 2.9 - Measurements of puffer piston pressure (Shimmin, 1986)

Pressure is the most applicable aerodynamic parameter for optical fibre sensing. Noeske *et al* (1983) monitored pressure in the nozzle of a gas blast circuit breaker using a technique called intensity modulation (section **4.1.4** discusses optical modulation methods). The problems associated with using an intensity based system are that the light intensity can be affected by many factors other than the measurand, such as contamination, disturbance of fibres and source variations caused by ageing. These problems can be minimised by using the novel chromatic modulation technique for pressure sensing (Henderson *et al*, 1993). The principle has been extended in the research reported in this thesis to produce small robust units which were successfully tested on the commercial 145kV transmission puffer circuit breaker.

2.2.2.3 Radiative

The simplest form of radiation measurement is using high speed photography to determine the plasma boundaries. Such techniques can provide information which is useful for nozzle blocking investigations and also identify the location of arc rupture at current zero (Lewis *et al*, 1985). Another radiation monitoring technique involves the use of high speed photomultipliers and optical filters to measure the total radiation reaching the nozzle wall and also the temperature of the ablated nozzle material (Jones *et al*, 1986). Recent developments in high speed optical spectrum analysers and data acquisition systems mean that a more detailed spectral analysis is possible. Spectroscopic methods have been widely used to determine temperature profiles of arc plasmas (eg. Airey, 1977) and electron densities. Spectroscopy also provides a means for investigating the effects of material entrainment from contacts and nozzles into the arc plasma and vapour jetting (Ryan and Jones, 1989).

The problem with most of these techniques is the requirement for optical access to the arc. This is inconvenient in commercial systems and has thus been restricted to research laboratories. However, developments in optical fibre technology have meant that radiation monitoring systems incorporating optical fibres can be designed with minimal intrusion so that their use on commercial breakers is acceptable. One such system was used in conjunction with the development of a commercial 420kV, 63kA SF_6 puffer circuit breaker (Ali *et al*, 1985). Fibres were installed in the nozzle (fig.2.10) to provide both axial and radial radiation measurement of total radiation, and also radiation levels at chosen wavelengths by using narrowband optical filters.

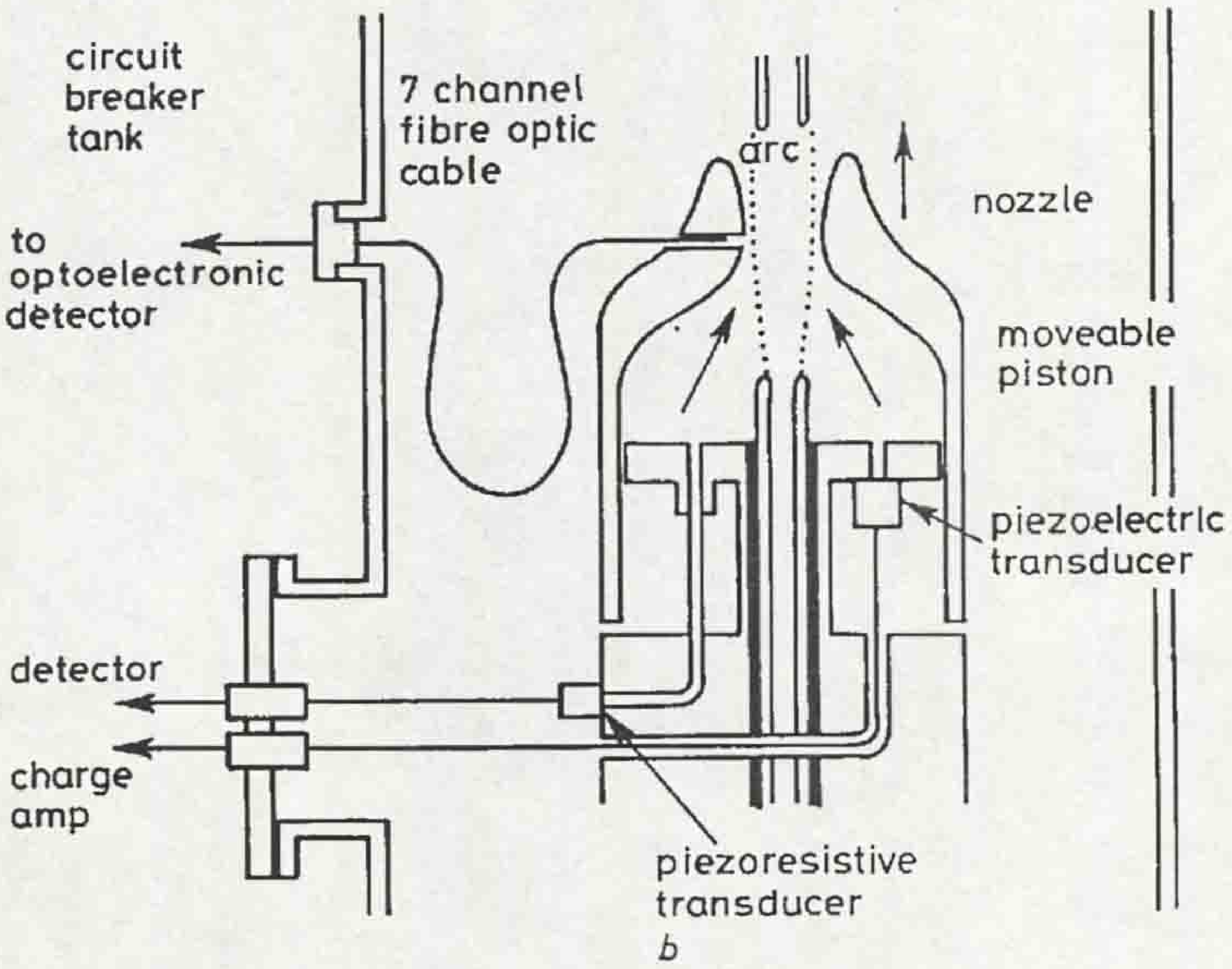

Figure 2.10 - Location of fibres in commercial 420kA 63kA puffer circuit breaker tests (Ali *et al*, 1985)

2.2.2.4 Mechanical

In order to assess the mechanical condition of a puffer interrupter, displacement sensors have extensively been used to monitor the travel of the moving contact (Hall, 1992). The main disadvantage of conventional potentiometric devices is that their size necessitates a location which is remote from the interrupter, at the other end of a drive rod and separated by linkages. Such devices therefore provide a travel record of the mechanism rather than the interrupter, with the possibility that a defective link might go undetected.

Recent developments in optical fibre travel recorders have permitted the measurement of the contact movement directly, due to their small size. One such arrangement (Shimmin, 1986) used a wheel which was rotated by the linear movement of the drive rod (fig.2.11). The digital encoding of the wheel allowed travel records to be produced by a summing method, with a typical result as shown in fig.2.11. The potential drawbacks of this system are the possibility of slippage between the wheel and drive rod and also the inability to provide absolute position in the event of a mechanical linkage failure. An optical fibre linear travel recorder, which overcomes these difficulties, is reported later in this thesis (**chapter 5**).

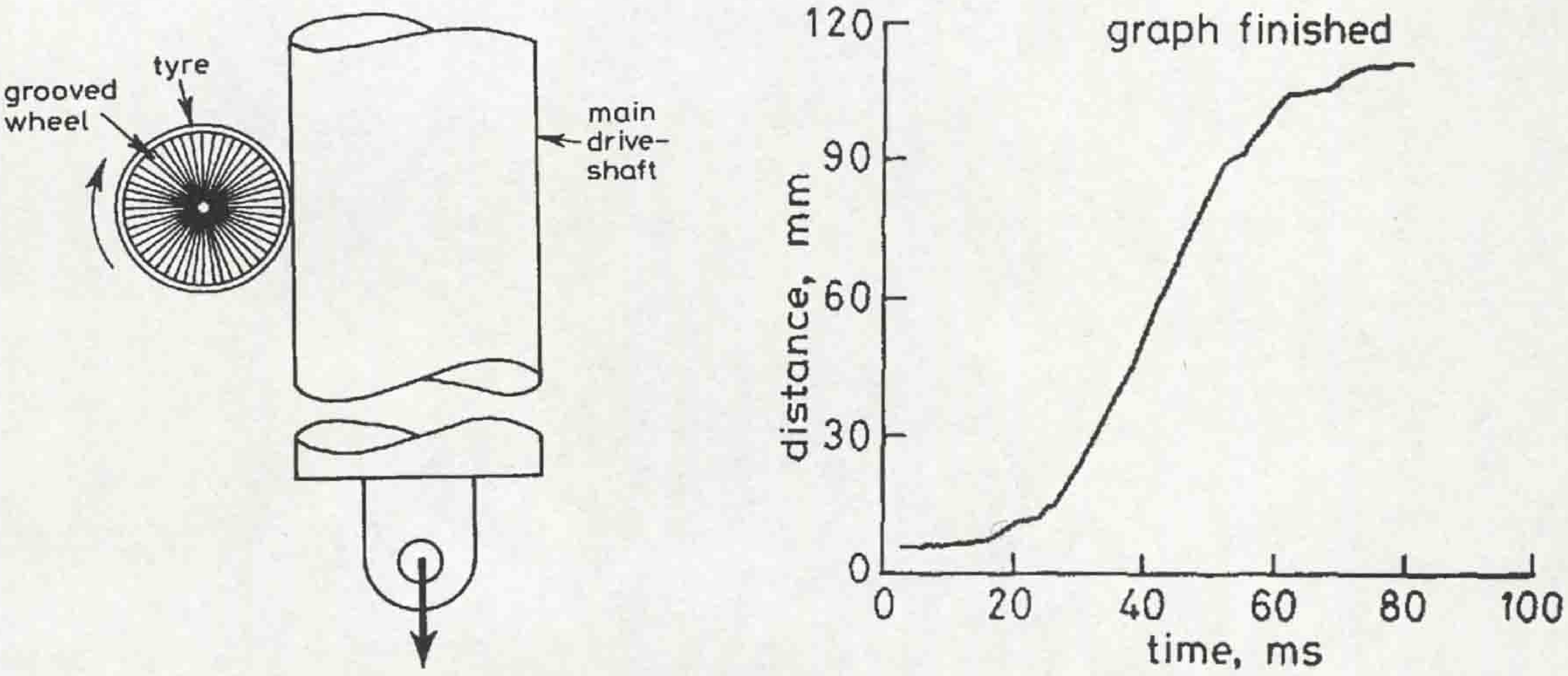

Figure 2.11 - Optical fibre digital rotary travel recorder (Shimmin, 1986)

2.2.2.5 Chemical

The decomposition products of SF_6, caused by a circuit breaker arc, can be monitored off-line by gas chromatography (Sauers, 1984). In particular the quantification of CF_4 (the carbon being produced by the thermal degradation of the polymeric nozzle) can indicate the cumulative arc energy dissipated in a circuit breaker and hence the extent of nozzle wear (Belmadini *et al*, 1991, Chu, 1986 and Ruegsegger *et al*, 1985). The major drawback with this technique is the difficulty of on-site analysis. Simpler sensors for use on site (Tominaga *et al*, 1981 and Ryan *et al*, 1985) have monitored contamination product concentrations using colour changing indicators which are sensitive to certain contaminant species.

Due to their general chemical inertness, optical fibres do not lend themselves to direct measurements of individual species concentrations. However, since simple optical fibre systems do exist which can accurately quantify colour, or more correctly "chromaticity" (Jones *et al*, 1987), the possibility of using fibre systems to analyse the colour indicators mentioned above does exist. Optical fibre systems, which are currently being researched, have the potential of monitoring decomposition products from SF_6 but as yet few results have been reported in the literature. The use of chromaticity monitoring is described in this thesis to indicate decomposition particle levels produced during arcing in SF_6 (**chapter 6**).

2.2.3 Advantages of optical fibre sensing

Optical fibre sensors are gradually becoming accepted for use in electrical power environments. Apart from the ability to make optical transducers much smaller than their conventional counterparts the following advantages can be achieved:

- Freedom from electromagnetic interference.
- Electrical isolation between instrumentation and test point.
- High dielectric strength.

- Wide bandwidth capabilities.
- Low attenuation compared with electrical wires.
- Light weight.

The reason why optical fibre sensing has only slowly been considered for power engineering instrumentation is due to the reluctance of the power industry to replace tried and trusted methods and also the cost of initial development. However, the reasons outlined above have been responsible for the continuing interest in optical fibre sensors for such environments.

2.2.4 Applications of circuit breaker diagnostics

2.2.4.1 Arc modelling

The fundamental aim of arc modelling is to predict the electrical response of the arc, through either an explicit or implicit knowledge of temporal thermal changes in the arc column (Ryan and Jones, 1989). A complete analytical solution would involve the simultaneous solution of the governing equations - mass, momentum and energy conservation, Ohm's law and Maxwell's equations - in three dimensions (axial, radial and time) for an axi-symmetric arc. In order to achieve this an immense amount of computation would be required; furthermore, the problem is complicated by other effects such as electrode melting, nozzle ablation, radiation transport and turbulence, all of which are difficult to define mathematically (Fang, 1995). It is often necessary to simplify the problem by producing semi-empirical models, which can incorporate accurately measured parameters; hence the need for reliable diagnostics.

Early arc models (Cassie, 1939, Mayr, 1943 and Browne, 1948) reduced the problem to a single ordinary differential equation. These models required test results for parameters such as the arc time constant, steady state electric field and power loss per unit length, which cannot easily be related to fundamental physical processes (Park, 1993). Since the models do not account for physical processes occurring within the arc, they cannot give an accurate prediction of circuit breaker performance.

In order to produce a model which can be used as an analytical design tool, it is necessary to numerically solve the governing arc equations. A recent popular approach is the boundary layer integral method (Cowley, 1974), which has been developed in further studies (eg. Fang, 1983 and Tuma, 1980). This method describes arc behaviour on the assumption of similarities between the radially integrated properties of various arc types. Thus a detailed knowledge of the radial arc structure becomes redundant, once the scaling laws relating the various radial integrals have been established (Ryan and Jones, 1989). This approach can account for axial variations caused by, for example, flow straining (Jones, 1977). It expresses the various radial integrals as characteristic areas, such as conductance area θ_c and thermal area, θ_δ. The defining equations are closed by using shape factors Λ, which relate each of the various characteristic areas to the thermal area. The advantage of the integral method is its ability to incorporate empirical data, so that discharge conditions which are difficult to define mathematically may be accommodated quantitatively (eg. radiation results - Strachan *et al*, 1977). Furthermore, turbulence effects are inherently incorporated in the radial integrations (Ryan and Jones, 1989).

Experimental data are important to arc modelling. Apart from the requirement to validate models with experimental data, all present models require empirical information for accurate calculation and, in many cases, the control parameters are chosen for a "best fit" to experimental results (Shimmin, 1986). The problem, with respect to circuit breaker design, is compounded by the shortage of measurements taken on actual circuit breakers, rather than scaled models. The work reported in this thesis involves the development of novel diagnostics, which can be used on practical circuit breakers, so that their results may be useful to the development of mathematical modelling.

The governing equations, which are used in arc modelling, are discussed in **3.2**. These equations contain parameters, which may be measured experimentally (eg. gas pressure, velocity and temperature, current density, electric field strength and radiation loss), in order to facilitate solution of the equations. For modelling of a puffer circuit breaker the stroke of the piston is an additional important parameter, since it indicates the piston chamber volume and arc length. In this project measurements of gas pressure and piston stroke were taken, among other parameters, and used to validate a mathematical model developed for the circuit breaker under test.

2.2.4.2 Circuit breaker condition monitoring

Since circuit breakers are used to control and protect electrical power networks by switching circuits on, carrying loads and switching circuits off, their reliability is of extreme importance. To maintain a high level of reliability, the traditional approach is to carry out regular routine maintenance, which is costly. Chen (1992) reports that a 245kV circuit breaker in Australia incurs maintenance costs amounting to A$2000/year. The study deduced an overall maintenance cost for Australia running into millions of dollars. The drawback of routine maintenance is the frequent withdrawal of "healthy" circuit breakers from service to carry out the necessary checks.

In the last decade, significant research has been undertaken in the field of predictive maintenance by circuit breaker condition monitoring (eg. Hoff *et al*, 1992, Chen *et al*, 1992 and Hallgren *et al*, 1988). Such an approach has the advantages of achieving reduced maintenance cost (by eliminating unnecessary maintenance), higher reliability and potentially increased circuit breaker lifetime. The essence of circuit breaker condition monitoring is to monitor several parameters in the circuit breaker during operation. Resistances, contact travel and opening times have traditionally been monitored (Hoff *et al*, 1992). However, these parameters do not provide any information regarding the internal condition of the interrupter.

With the advent of optical fibre sensing and its associated advantages for use in power environments (**2.2.3**) it has become possible to monitor internal parameters such as puffer piston chamber pressure, gas dielectric strength, arc radiation and contact temperatures. An internal condition monitoring system will monitor several of these parameters simultaneously. A "healthy" circuit breaker will have a characteristic parameter signature; then, if a parameter deviates from this healthy base, the condition monitoring system should act in identifying the problem and indicating the most appropriate corrective action.

In the condition monitoring system of a transmission circuit breaker some sensors will monitor continuously (eg. tank gas pressure), while others will require operation of the circuit breaker (eg. contact travel). However, each sensor must operate successfully over the wide range of duties that similar circuit breakers perform at different locations in the transmission circuit. Some breakers may be used simply to switch load currents (eg. 4000A @ 400kV at St. John's Wood) several times daily and may never be required to interrupt a short-circuit fault. Other breakers of the same type may be located in parts of the circuit, which are susceptible to short-circuit faults (eg. part of the transmission network close to Glasgow is vulnerable to lightning strikes, which can lead to short-circuit faults requiring 63000A @ 400kV to be interrupted). Although the wear on these two sets of circuit breakers is caused by different means, the condition monitoring sensors can still be used to monitor the internal health of both sets.

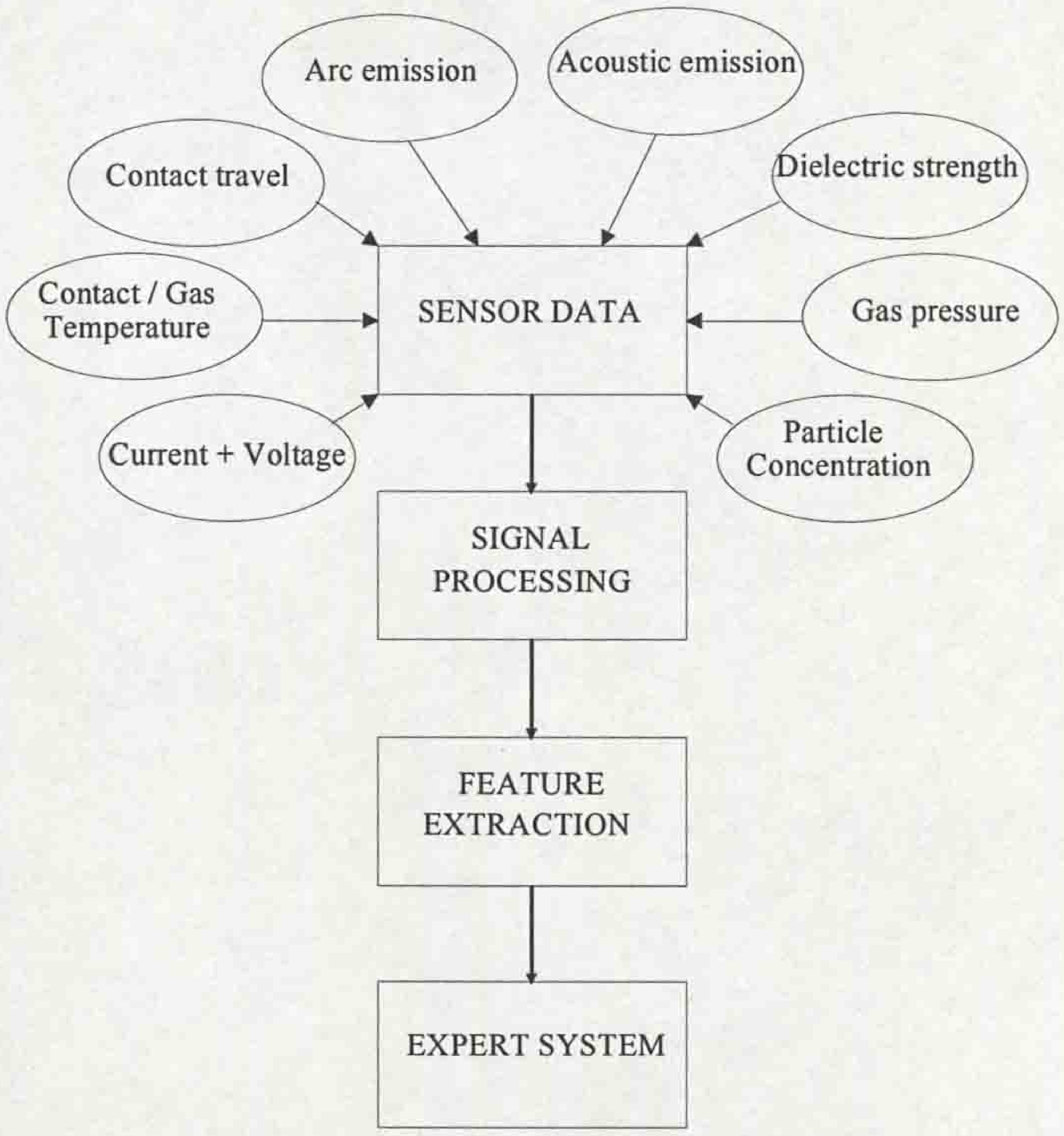

Figure 2.12 - Condition monitoring system

An example of a simple condition monitoring approach (Messent, 1995) is shown in fig.2.12. The data from each of several (mainly optical fibre) sensors is assimilated and processed for each circuit breaker operation, in order to extract the relevant features. This parameter signature can then be compared to the healthy signature in an expert system in order to evaluate the internal condition of the circuit breaker. In addition to using previous test data in the expert system, a neural network can be incorporated to improve the accuracy of prediction with time (Chen, 1992).

Fig.2.13 (Pilling, 1995) shows some of the circuit breaker interrupter failure mechanisms, which a suitable condition monitoring system should be able to predict. The work reported in this thesis involves the development of several novel sensors, highlighted in fig.2.13 - contact travel, piston pressure, tank pressure, particle deposition, gas dielectric strength and arc emission. The remaining sensors are being developed in parallel projects at Liverpool University. Therefore, this work represents the first major step in the development of a circuit breaker condition monitoring system.

2.3 CONCLUSIONS

The increasing demand for electricity since the turn of the century, combined with the rise in network transmission voltages, has caused a substantial increase in short-circuit levels, which circuit breakers need to successfully interrupt. Short-circuit level is the electrical power that a circuit breaker can interrupt, when a short-circuit fault occurs on the power system (eg. a circuit breaker rated at 145kV/40kA has a power rating of 5800MVA). The developments in circuit breaker technology have produced single break circuit breakers which can interrupt 63kA at 550kV within 2 cycles of A.C. (Suzuki *et al*, 1993 and Toda *et al*, 1993).

The discovery of the arc quenching capability of SF_6 (Lingal *et al*, 1953) has seen this gas become the accepted interruption medium at transmission level. Puffer circuit breakers offer several advantages over other types (**2.1.6.3.1**) and are thus the most prominent type at transmission level. More recently, rotary arc interrupters have effectively eliminated the powerful mechanism associated with puffer breakers; however, their interrupting capability is still limited, at present, to distribution service. Therefore, puffer circuit breakers (and their auto-expansion hybrids) are likely to remain the mainstay of transmission circuit breaking in the near future.

COMPONENT	FAILURE MODE(S)	SENSOR(S)	MEASUREMENT TREND
ARCING CONTACTS	Contact wear out	ARC SPECTRA CURRENT	*As contact wears different metals are vapourised leading to a change in chromaticity for a given current.*
		VIBRATION	*Change in vibration signature may indicate wear or failure.*
TRANSFER CONTACTS	Contact wear out	ARC SPECTRA	*Optical emissions from arc should increase with wear.*
		VIBRATION	*Change in vibration signature may indicate wear.*
		CONTACT TEMPERATURE	*Contact temperature may increase for a given current.*
	Contact spring failure	CURRENT VOLTAGE	*Resistance may increase.*
MECHANISM	Sliding interface wear including ageing of grease Gas valve spring failure	ACOUSTIC	*Change in acoustic signature reveal mechanism wear or defects. Travel may be used to synchronize measurements.*
	Loose fixings	TRAVEL	*Travel also for velocity.*
		ARC EMISSION TRAVEL	*Time to arc emission may change.*
PUFFER AND NOZZLE	Piston ring failure or wear	PISTON PRESSURE	*Pressure drop.*
	Nozzle loosening		
	Nozzle blockage	TRAVEL	*Change in velocity.*
	Nozzle wear	ARC EMISSION	*Viewed through nozzle, arc emission may indicate wear.*
GAS	Dielectric deterioration	PARTICLE CONCENTRATION	*Indicated by accumulating deposits.*
		DIELECTRIC STRENGTH	*Reduced breakdown strength.*
	Leak	TANK PRESSURE TEMPERATURE	*Pressure drop (temperature compensated).*

Figure 2.13 - Potential failure schemes for a circuit breaker (Pilling, 1995)

Circuit breakers have been continually improved throughout the century as a result of the advancements made in diagnostics. This began with the development of the cathode ray oscillograph to record circuit breaker currents and voltages and has progressed to the stage where a wide range of electrical, aerodynamic, radiative, mechanical and chemical properties can be measured. It was often necessary to use the diagnostics on scaled circuit breaker models due to the bulky nature of conventional instrumentation and the problems of isolation from live equipment. However, the advent of optical fibre sensing techniques with inherent isolation has allowed a wide range of parameters to be measured on commercial breakers, using small, non-invasive optical devices which can be easily incorporated (Noeske *et al*, 1983, Ali *et al*, 1985 and Henderson *et al*, 1993).

The work reported in this thesis involved the development of novel optical fibre and hybrid (combined electrical and optical) sensors and their use on a commercial 145kV puffer circuit breaker to gain an insight into the internal behaviour of the circuit breaker. The results obtained will be useful in two areas of circuit breaker research; modelling and condition monitoring. The sensors themselves are intended to be the first step in the development of a generic condition monitoring system, which will be based on the chromatic modulation method (Jones *et al*, 1987) for optical sensing (**4.3**).

CHAPTER 3 - CIRCUIT BREAKER MODELLING AND MEASUREMENTS

3.1 PHILOSOPHY OF CIRCUIT BREAKING

3.1.1 Fundamental philosophy of interruption

A circuit breaker is a device comprising a pair of mating metallic contacts, which are closed under normal conditions and carry a load current. These contacts open on the command of a tripping signal when, for example, a short-circuit occurs on the power system and an excessive fault current flows, which needs to be interrupted. At contact separation an electric arc is formed (**3.2**), which consists of a volume of highly ionised gas (a plasma).

During current interruption the circuit breaker must switch from a state of near zero to extremely high resistance, in a controlled manner. The electric arc can satisfy this requirement, its resistance change being automatically and synchronously controlled by the changing value of the alternating current, which it is interrupting (Flurscheim, 1982). One of the extremely useful features of the arc, particularly with respect to transmission circuit breakers, is that it has no practical upper limit in current carrying capacity.

In order to maintain system stability and reduce public danger, the arc must be extinguished in the shortest possible time after contact separation. This is usually achieved at a "current zero" on the current waveform, which occur every 10ms at 50Hz. Reducing the current interruption time also reduces wear on critical circuit breaker components (eg. electrodes and nozzle), thus prolonging their lifetime.

Extinction of the arc at a current zero usually involves a combination of one or more of the following: a high gas pressure; forced convection; turbulence and arc lengthening. All of these interruption aids are incorporated into a puffer circuit breaker (**2.1.6.3.1**). This type of circuit breaker was used to test the optical and hybrid sensors developed in this project and is described later (**9.2**).

3.1.2 Voltage behaviour during interruption

It is the voltage imposed across the open electrodes of a circuit breaker, after an arc has been extinguished, which will determine, in conjunction with the gas dielectric recovery, whether there will be an arc restrike to threaten the interruption process. Typical voltage waveforms existing prior to, during and after a short-circuit fault are shown in fig.3.1. The normal system voltage, existing prior to the short-circuit, falls to near zero when the fault occurs and remains at that level during the pre-arcing period (until the contacts separate). At this point an arc is stuck, with a voltage reappearing which is low and fairly constant (although it increases with arc length). This voltage is known as the arc burning voltage.

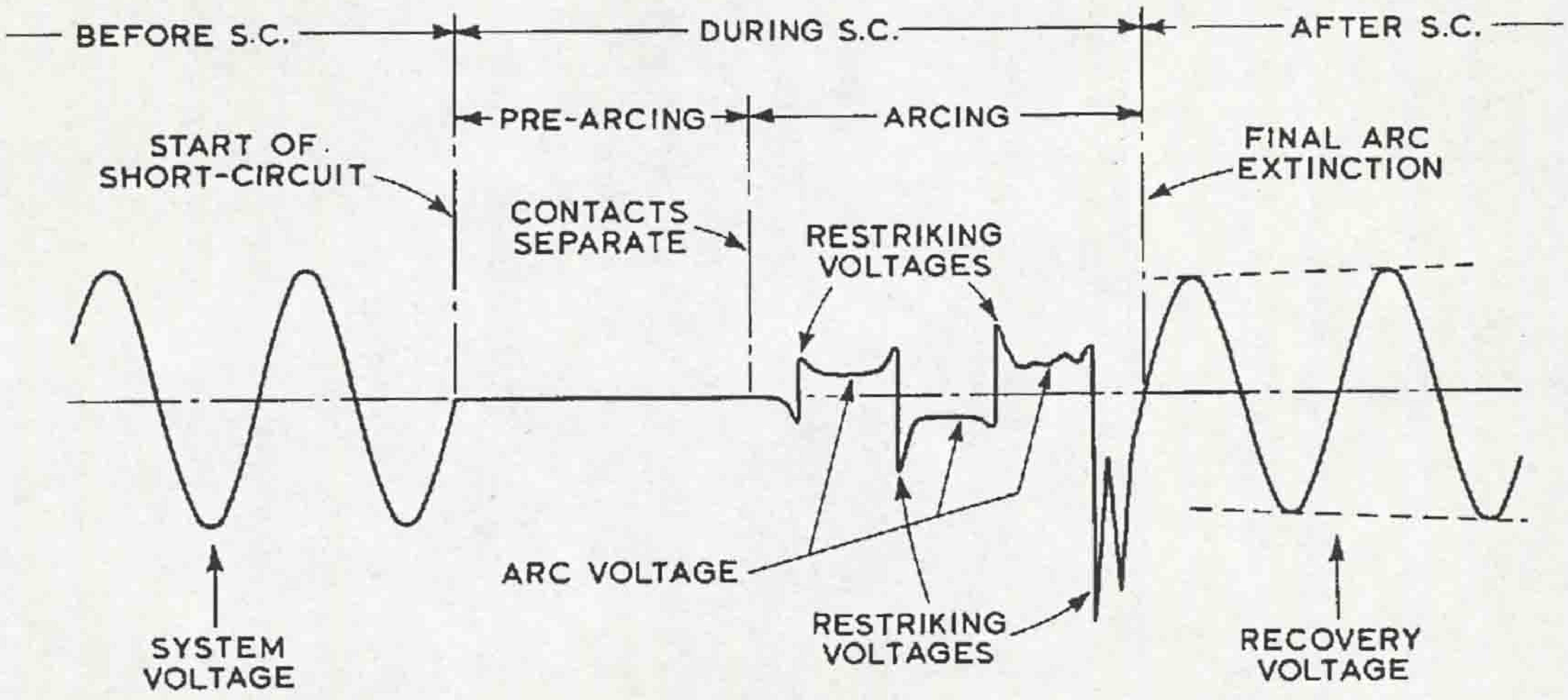

Figure 3.1 - Voltage waveforms before, during and after a short-circuit fault

Just prior to the current reaching its natural zero, the effects of the deionisation and cooling of the arc gap predominate, causing the arc voltage to rise to a peak above its average (Flurscheim, 1982). If at this point de-ionisation has not advanced sufficiently, the restriking voltage, rising rapidly to a higher peak in the opposite sense, will reignite the arc and fault current will flow again until the next natural zero, a process which may be repeated several times. It can be seen that, for the particular example of fig.3.1, successful interruption occurs at the fourth current zero following contact separation. The restrike voltage now appears as a high frequency transient, which oscillates about the normal recovery voltage base at power frequency (Lythall, 1972).

3.1.3 Influence of power factor and fault type on the restrike voltage

The magnitude of the restrike voltage peaks, which are imposed across the arc gap at each current zero, depend on the power factor of the circuit and the type of fault. Under short circuit conditions, the power factor will be low. Hence, at current zero the instantaneous recovery voltage, about which the restrike voltage transient oscillates, will be close to its maximum. Thus, a low power factor increases the magnitude of the restrike voltage and the difficulty of successful interruption. The current and voltage waveforms (assuming zero power factor) are shown in fig.3.2 (Lythall, 1972).

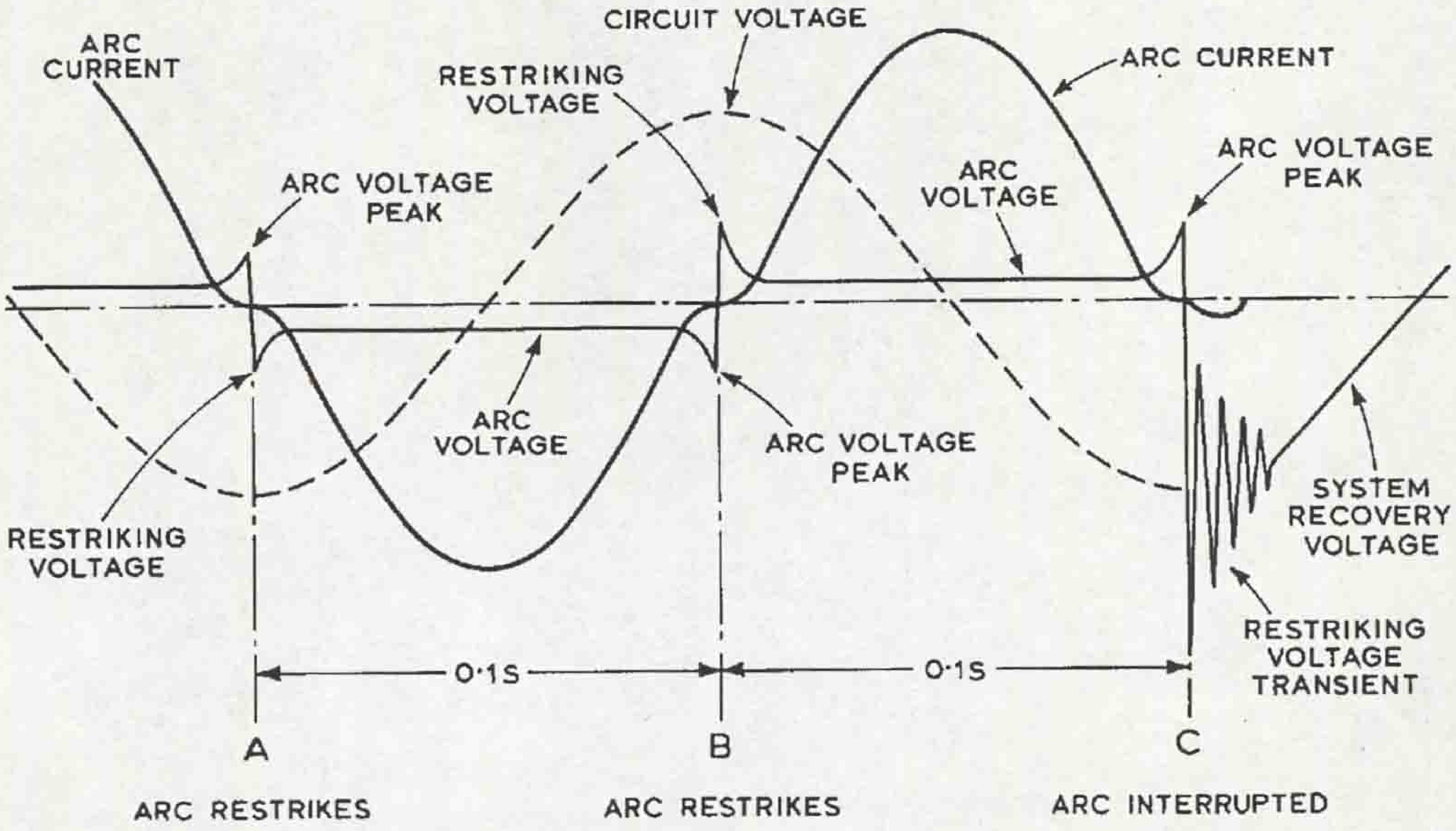

Figure 3.2 - Current and voltage waveforms during zero power factor fault

The amplitude of the restrike voltages is further affected by the nature of the fault. For example, a fault to earth on a system, which is earthed at the supply neutral, can cause the peak voltage to reach 2√2 times the phase voltage. Further, on a 3-phase fault, with the supply neutral earthed, one phase will clear before the other two and this phase will experience a peak voltage which is 1.5 x 2√2 times the phase voltage.

The frequency of the transient recovery voltage depends upon the inductance and capacitance on the supply and load sides of the circuit breaker. The natural frequency of oscillation would be given by (Flurscheim, 1982)

$$F_n = \frac{1}{2\pi\sqrt{LC}} \tag{3.1}$$

where L is the inductance, largely determined by the plant, and C is the capacitance, determined by the system length up to the point of the fault. In practice the electrical resistance of the connecting cables will dampen the oscillations to a certain extent.

3.1.4 Rate of rise of recovery voltage (RRRV)

The higher the frequency of the transient voltage, the steeper will be the average slope of the voltage rise from zero to its first peak. This is defined as the rate of rise of recovery voltage (RRRV) and is shown on fig.3.3 by the straight line. The RRRV is a measure of the severity of duty imposed on a circuit breaker.

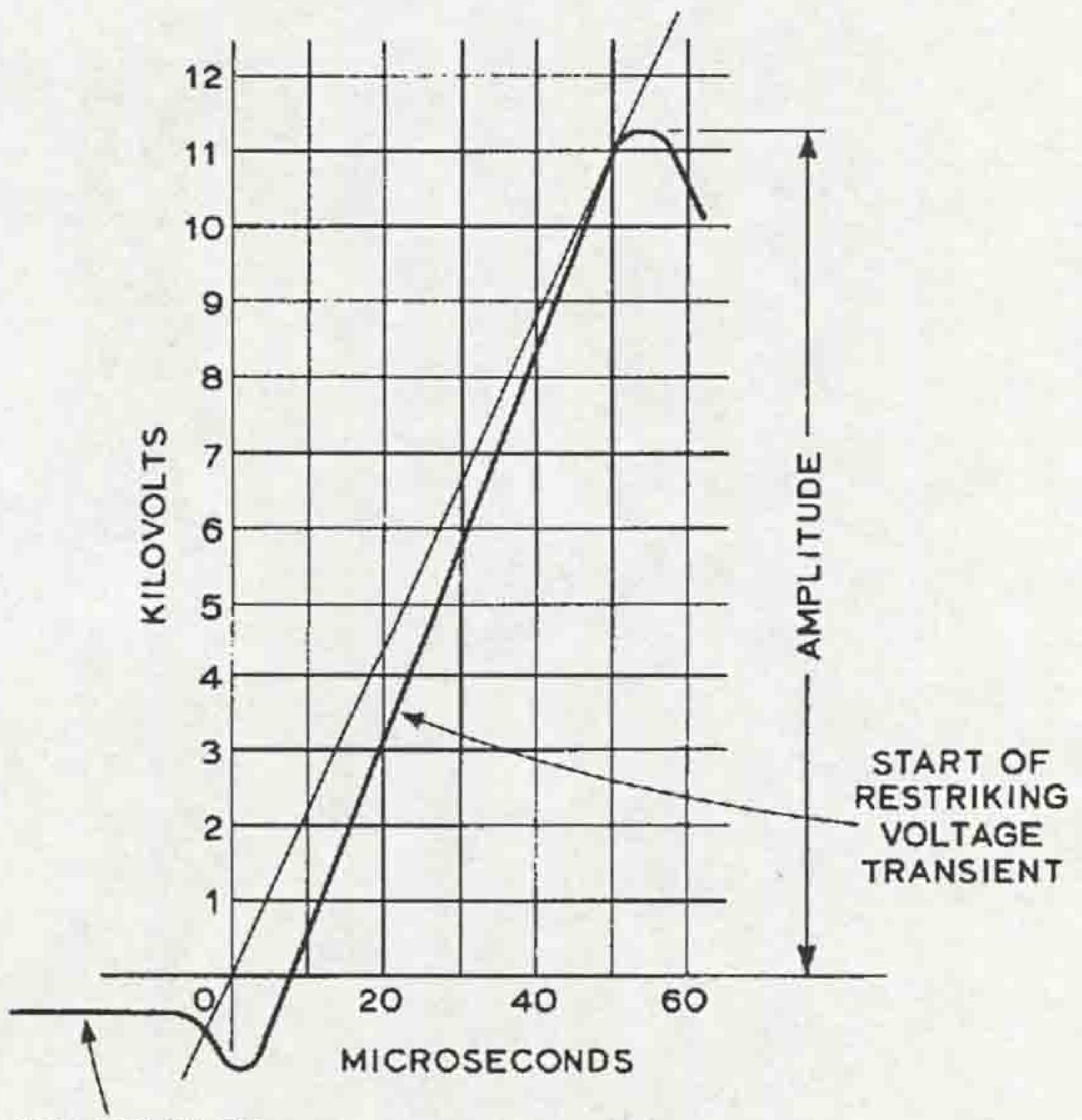

Figure 3.3 - Definition of rate of rise of recovery voltage (RRRV - Lythall, 1972)

3.1.5 The dielectric race theory

The dielectric race theory (Slepian, 1929) is one of the earliest examples of circuit breaker modelling. Although it is an over-simplification of the complex processes occurring during the current zero period, the idea is useful to visualise the point of successful interruption. It is based upon the premise that, if the rate of dielectric recovery in the electrode gap is higher than the RRRV, then successful interruption will occur. If not then the arc will restrike. Fig.3.4a shows an example of the current and voltage waveforms for the arc and the rate of dielectric recovery. The rate of dielectric recovery is lower than the RRRV so the arc restrikes at the intersection between the two. Conversely, fig.3.4b shows the case when the rate of dielectric recovery is higher than the RRRV. There is thus no intersection point and the arc is successfully extinguished.

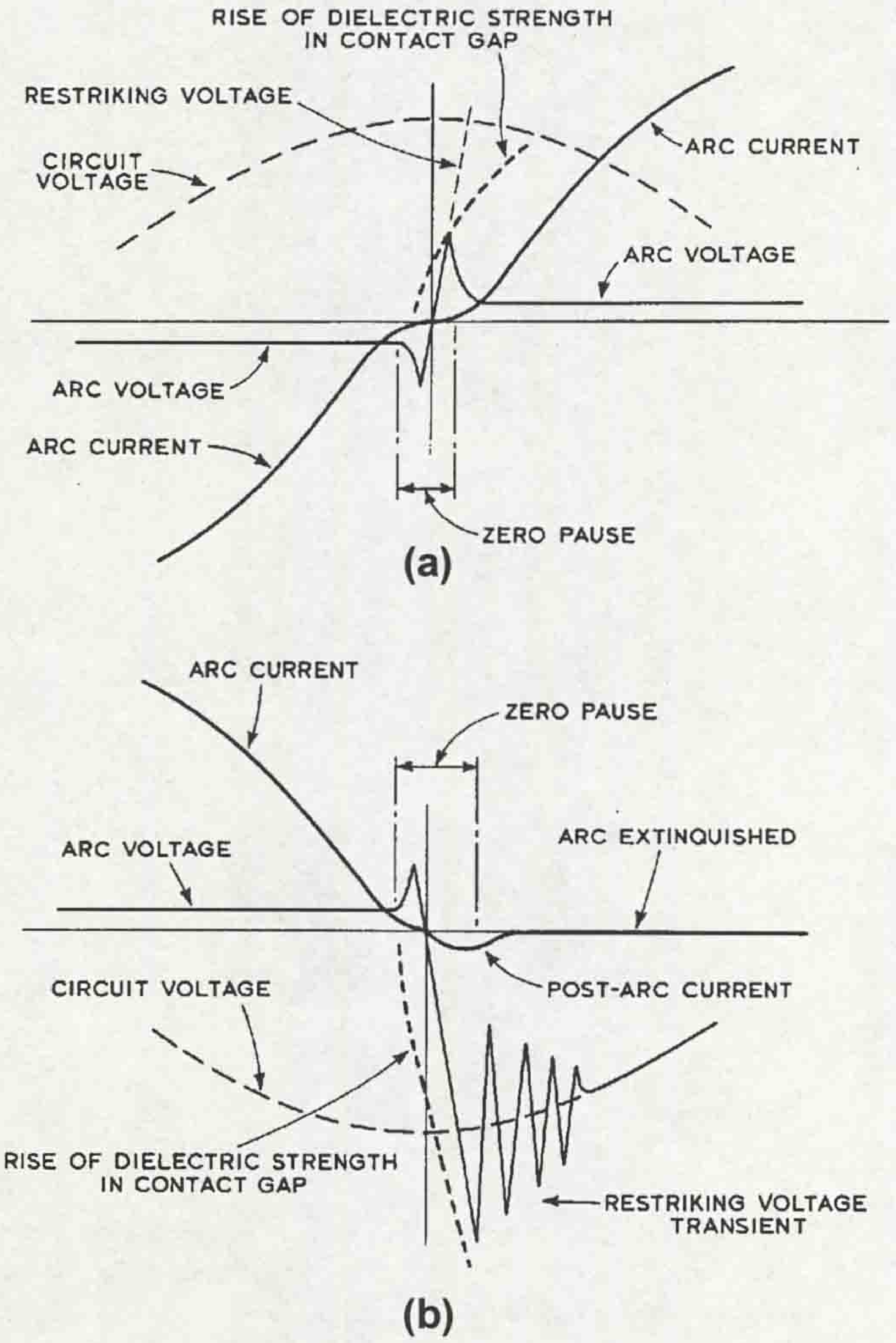

Figure 3.4 - Diagrammatic representation of the dielectric race theory

3.2 GENERAL THEORY OF HIGH PRESSURE ARCS

The arc is an electric discharge which consists of a plasma, whose component species possess temperatures typically ranging from 4000K to 25000K (Jones, 1988). The arc is distinguishable from other electrical discharges by its ability to conduct very high currents, whilst being sustained by a relatively low electric field strength. Further, an arc burning between two electrodes will have a high current density and low voltage drop at the cathode (Jones and Fang, 1980).

Circuit breaker arcs consist of three regions, the cathode region, anode region and the arc plasma column (fig.3.5). The typical form of the potential distribution along the arc axis is shown on fig.3.6. The column cross-section tends to adjust itself so that the potential gradient assumes the lowest value compatible with the imposed operating conditions.

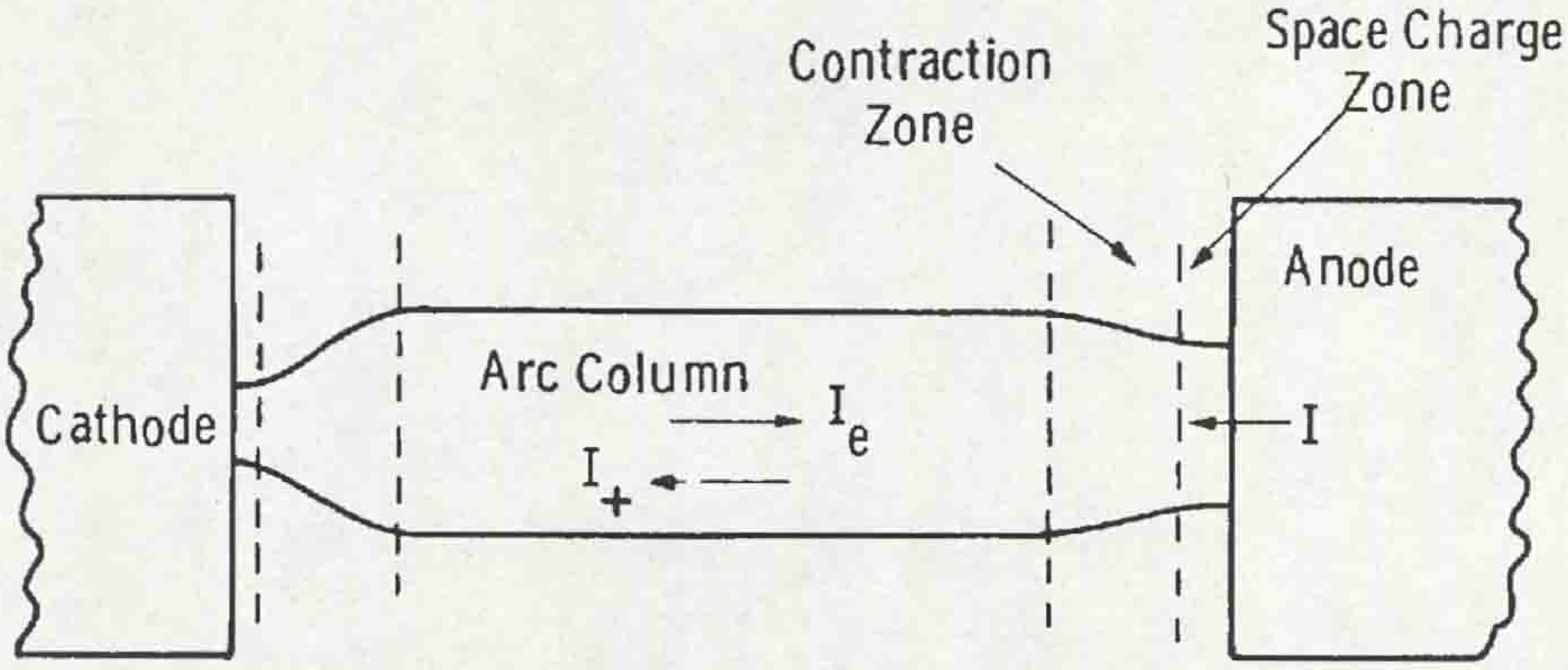

Figure 3.5 - Regions of a circuit breaker arc

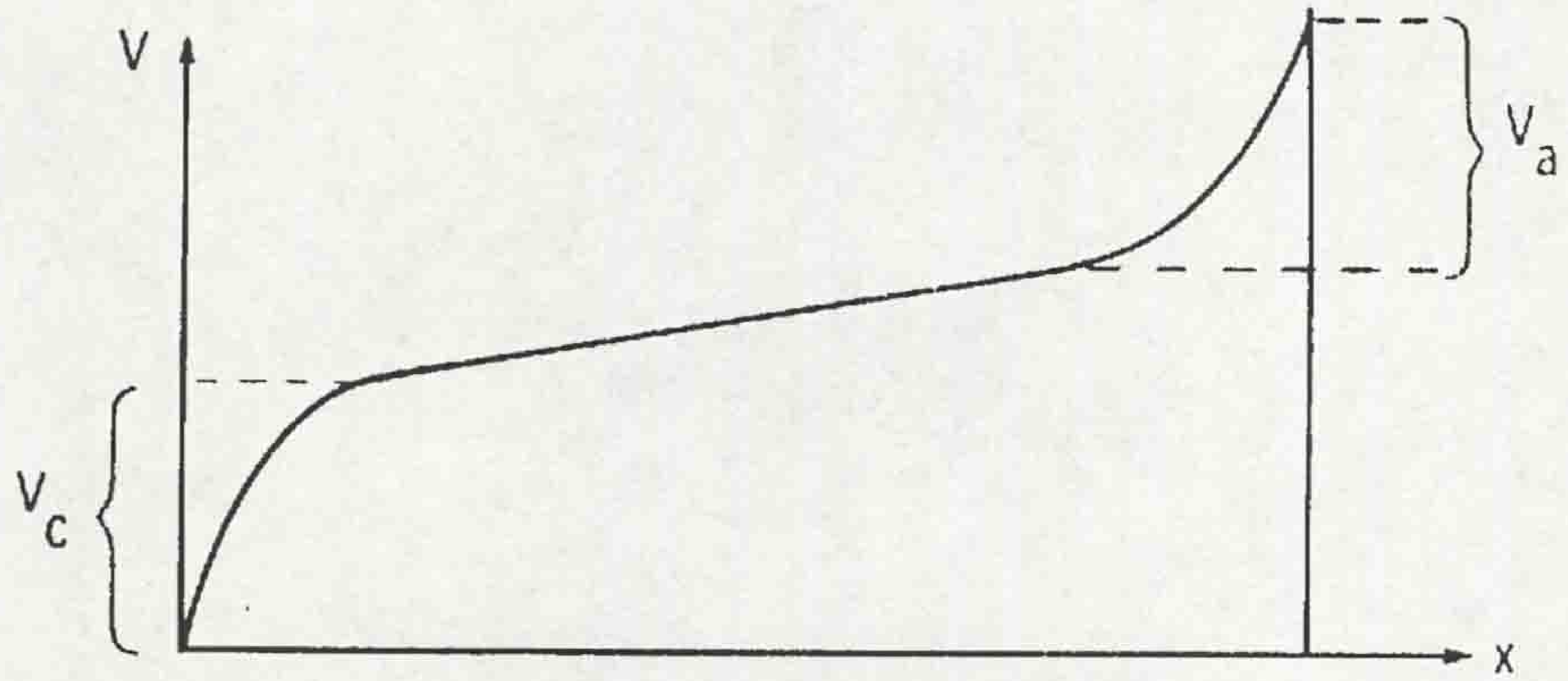

Figure 3.6 - Potential distribution along arc axis

3.2.1 Types of electric arc

Fig.3.7 indicates the various types of electric arc, which are known to exist.

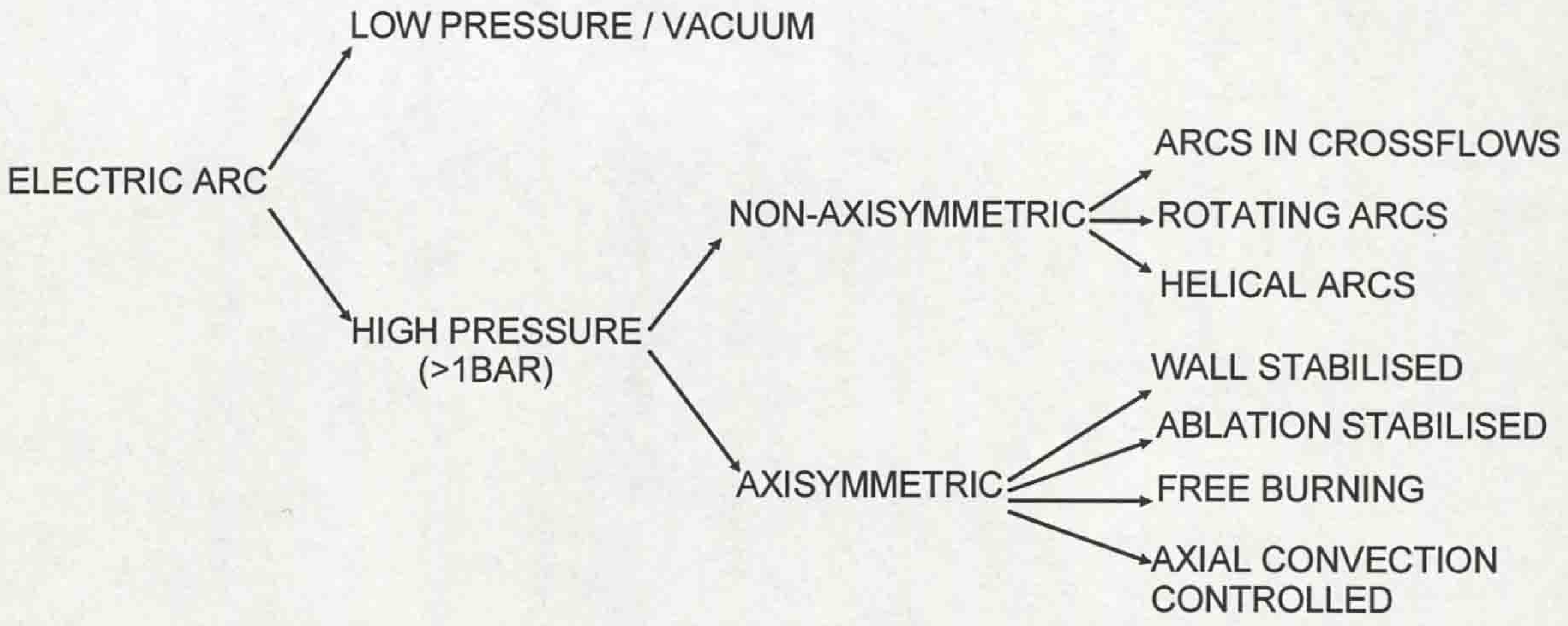

Figure 3.7 - Various types of electric arc (Jones, 1988)

The fundamental classification is between vacuum (or low pressure) arcs and high pressure (>1bar). It was indicated (**2.1.7**) that arcs in a vacuum have only been successfully utilised at distribution level. Hence, all transmission level circuit breakers involve interruption of a high pressure arc. Such arcs can be further classified as axisymmetric or non-axisymmetric. The axial convection-controlled axisymmetric arc, which prevails in puffer circuit breakers, has found the most widespread use in circuit breaker technology and has received much theoretical investigation. This type of arc burns within a co-axial flow of high speed gas (fig.3.8), which constricts the arc boundary to an extent which is controlled by the flow convection. It is discussed further in **3.2.2.1**.

3.2.2 The governing equations of high pressure arcs

High pressure arcs are generally collision dominated (Heberlein *et al*, 1984), where the particle species attain a common temperature, so that local thermal equilibrium is usually a valid assumption. Thermal ionisation is the main provider of charge carriers and is strongly dependent on the plasma pressure.

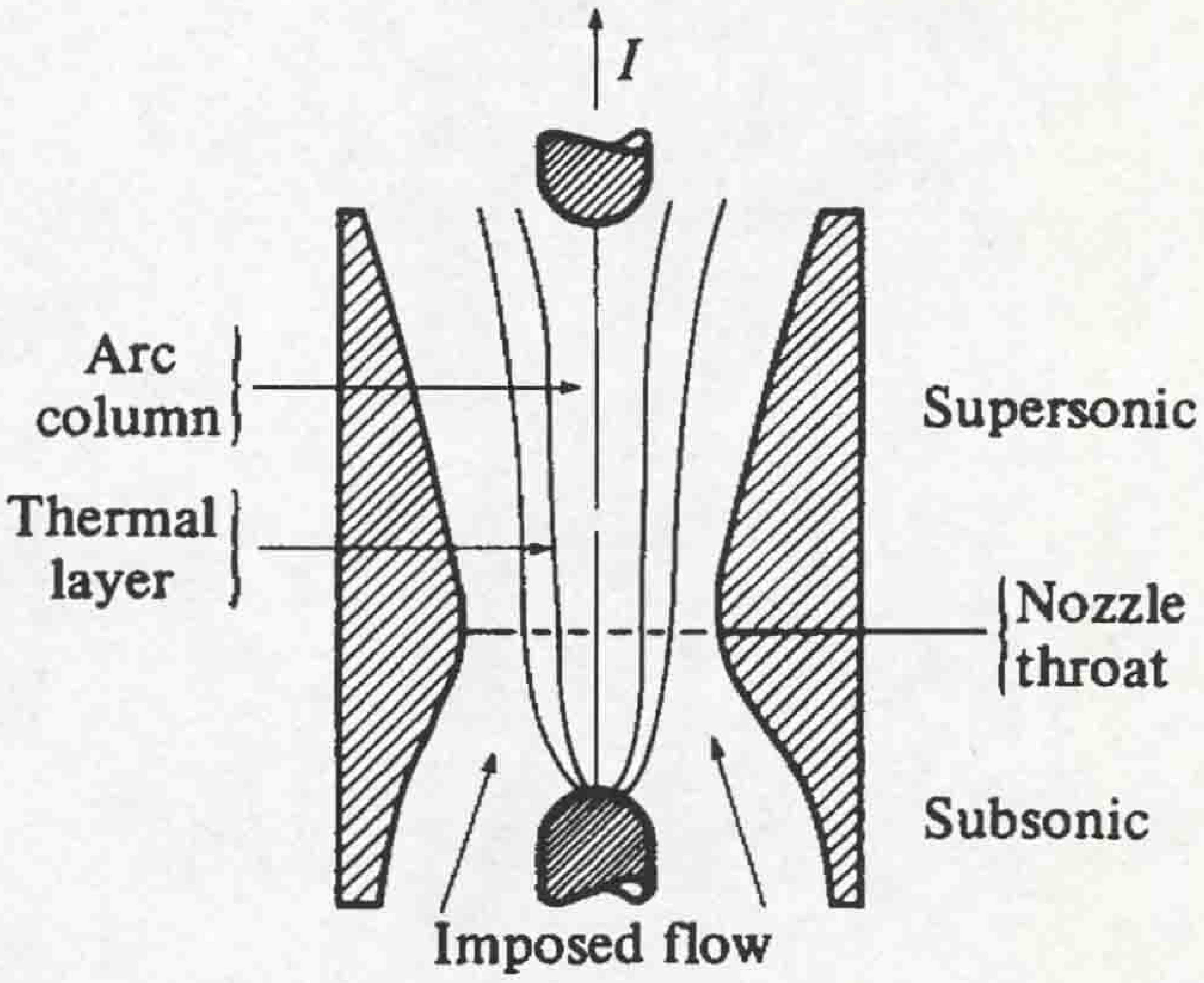

Figure 3.8 - Axial convection controlled axisymmetric arc (Jones, 1988)

Circuit breaker arcs, which are initiated by contact separation, generally have an initial phase where electrode vapour is the dominant source of charged particles (Slade and Hoyaux, 1972). However, after this initial transient phase, the plasma column increases in length well beyond the narrow regions directly affected by the electrodes (Heberlein *et al*, 1984). Thus, it is the physical properties of the plasma column which tend to dominate the overall behaviour of a circuit breaker arc. The plasma can be described by the equations of equilibrium thermodynamics and the conservation equations of a compressible, viscous fluid. However, the unique plasma properties necessitate the inclusion of the following effects (Heberlein *et al*, 1984):

1. The plasma column is composed of chemically reacting species, so that rate equations are required to take account of the different reactions and their effect upon the material properties of the plasma.
2. The conservation of momentum equation must account for the interaction of the arc with magnetic fields, which may be external or induced by the arc current itself.
3. Energy conservation considerations need to account for volumetric heat generation in the plasma, which may be incorporated via Ohm's law for resistive heat dissipation of electrical energy.

4. The plasma emits a significant amount of electromagnetic radiation, which constitutes a major energy dissipating mechanism under many operating conditions.
5. There is one thermodynamic equation of state for every component species - electrons, ions, atoms and molecules - present in the plasma.

The incorporation of all of these effects without any simplification results in a comprehensive set of equations, with a large number of often unknown parameters. Consequently, measurements are required of suitable parameters (eg. arc current, pressure or electric field) to assist in simplifying and solving the equations. Even so, the solution of each equation simultaneously in three dimensions (axial, radial, time) is computationally difficult and prohibitive in effort and cost. Simplifications are, therefore, sought, which, for a high-pressure arc, take the following form (Jones and Fang, 1980):

Conservation of mass
$$\frac{\partial \rho}{\partial t} + \nabla.(\rho \mathbf{v}) = 0 \qquad (3.2)$$

Conservation of momentum
$$\rho \frac{d\mathbf{v}}{dt} = -\nabla p + \mathbf{j}x\mathbf{B} + \rho F g + F(\eta) \qquad (3.3)$$

Conservation of energy
$$\frac{\partial}{\partial t}\left[\rho\left(\frac{1}{2}v^2 + e'\right)\right] + \nabla.\left[\rho\mathbf{v}\left(\frac{1}{2}v^2 + e'\right)\right]$$
$$= \nabla.(K\nabla T) - \nabla.(p\mathbf{v}) - \nabla.(\mathbf{F}) + \phi + \mathbf{j}.\mathbf{E} \qquad (3.4)$$

Maxwell's equations
$$\nabla x\mathbf{E} = -\frac{\partial \mathbf{B}}{\partial t} \qquad (3.5)$$
$$\nabla x\mathbf{B} = \mu_0 \mathbf{j} \qquad (3.6)$$

Simplified Ohm's law
$$\mathbf{j} = \sigma \mathbf{E} \qquad (3.7)$$

Equation of state
$$p = f(\rho, T) \qquad (3.8)$$

Radiation $$\nabla.(\mathbf{F}) = 4\pi \int_0^\infty \kappa'_\nu (B_\nu - J_\nu) d\nu \qquad (3.9)$$

where t is time, σ,ρ,η and K are the electrical conductivity, mass density, viscosity and thermal conductivity of the gas. T, **v** and p are the temperature, velocity and pressure of the gas. e′ is the internal energy per unit mass, ϕ is the viscous friction heat dissipation function, **j** the current density, **E** the electric field strength, $F(\eta)$ the viscous stress and Fg the sum of all other volume forces per unit mass. **F** is the radiation flux vector, defined by eqn.3.9, where κ_ν' is the effective spectral absorption coefficient, B_ν the black-body spectral intensity, J_ν the average spectral intensity and ν the radiation frequency.

Again, the solution of this set of equations in three dimensions is difficult and further simplifications are needed, based on the type of arc and operating conditions involved.

3.2.2.1 Axial convection-controlled arc

The axial convection-controlled arc burns in a coaxial imposed flow. At high powers its overall behaviour is governed by a combination of the convective effects of the flow field and self-magnetically-induced convection (Jones and Fang, 1980). The behaviour of the arc is also strongly influenced by the type of flow, which can range from uniform flow, with negligible spatial gradients of pressure and flow velocity, to an accelerating flow with substantial pressure and velocity gradients.

In gas blast circuit breakers the imposed flow is accelerated through a nozzle and the flow characteristics are influenced by the nozzle geometry. The nozzle usually operates above the critical pressure ratio for supersonic flow to be supported, so that the arc column section upstream of the throat burns in a high pressure, convergent subsonic flow, whereas the downstream section of the column burns in a lower pressure diverging supersonic flow.

The cross-section of an arc column in an axial flow field is more constricted than for the free-burning arc due to increased entrainment of cool gas from the surrounding flow field into the arc plasma column. The degree of arc constriction increases with flow acceleration, as does the electric field strength driving the current through the arc (Barrault and Jones, 1974). Also, the electrical conductivity is axially fairly constant.

For an arc in an axial accelerating flow field, the axial gradient of a physical quantity is usually much less than its radial gradient (Jones and Fang, 1980) so that boundary layer approximations (Schlichting, 1968) may be used to simplify the general equations (3.2-3.9). The following simplifications can be incorporated:

1. Momentum diffusion and thermal conduction in the axial direction are negligible compared with the radial components.
2. The radial flow kinetic energy is negligible compared with the axial flow component.
3. The radial components of current density and electric field strength are negligible compared with their axial components.
4. The axial electric field strength is radially constant.

Further simplifications were achieved (Cowley, 1974) through the formulation of radially integrated conservation equations, known as the boundary layer integral method. This method describes arc behaviour on the assumption of similarities between the radially integrated properties of various arc types. Thus a detailed knowledge of the radial arc structure becomes redundant, if the scaling laws relating the various radial integrals can be established (Ryan and Jones, 1989). The advantage of the integral method is its ability to incorporate empirical data, so that discharge conditions which are difficult to define mathematically, such as radiation, may be accommodated quantitatively. Each radial integral is known as a "characteristic area", examples of which are defined as follows:

Thermal $$\theta_\delta = \int_0^\infty (1 - \rho/\rho_\infty) 2\pi r dr \tag{3.10}$$

Displacement $\theta_d = \int_0^\infty (1 - \rho v/\rho_\infty v_\infty) 2\pi r dr$ (3.11)

Momentum $\theta_m = \int_0^\infty (1 - \rho v^2/\rho * v *^2)(1 - v_\infty/v) 2\pi r dr$ (3.12)

Magnetic $\theta_B = \pi r_1^2 \exp\left[-2 \int_0^1 (B/B_1)^2 (r/r_1) d(r/r_1) \right]$ (3.13)

Enthalpy $\theta_\Delta = \int_0^\infty (\rho h/\rho * h *)(1 - h_\infty/h) 2\pi r dr$ (3.14)

Enthalpy flux $\theta_h = \int_0^\infty (\rho v h/\rho * v * h *)(1 - h_\infty/h) 2\pi r dr$ (3.15)

Kinetic energy $\theta_{ke} = \int_0^\infty (\rho v^3/\rho * v^3)(1 - v_\infty^2/v^2) 2\pi r dr$ (3.16)

Radiation $\theta_Q = \int_0^\infty (Q/Q *) 2\pi r dr$ (3.17)

Conductance $\theta_Q = \int_0^\infty (\sigma/\sigma *) 2\pi r dr$ (3.18)

The conducting arc core is discretised from the external flow in the analysis so that the generalised arc equations now evolve into the following:

$$\frac{\partial}{\partial t}\left[\rho_\infty (A - \theta_\delta)\right] + \frac{\partial}{\partial z}\left[\rho_\infty v_\infty (A - \theta_d)\right] = 0 \qquad (3.19)$$

$$\frac{\partial}{\partial t}\left[\rho_\infty v_\infty (\theta_\delta - \theta_d)\right] - \rho_\infty \theta_\delta \frac{\partial v_\infty}{dt} + \frac{\partial}{\partial z}\left(\rho * v *^2 \theta_m\right) - \rho_\infty v_\infty \theta_d \frac{\partial v_\infty}{dt}$$

$$= \frac{\mu I^2}{8\pi}\frac{\partial}{\partial z}\left(\ln\theta_B\right) \qquad (3.20)$$

$$\frac{\partial}{\partial t}\left[\rho^* h^* \theta_\Delta + \frac{1}{2}\rho^* v^{*2}\theta_m + \frac{1}{2}\rho_\infty v_\infty^{\;2}\left(\theta_\delta - \theta_d\right)\right] - \rho_\infty\theta_\delta\frac{\partial}{\partial t}\left(h_\infty + \frac{1}{2}v_\infty^{\;2}\right) +$$
$$\frac{\partial}{\partial z}\left(\rho^* v^* h^* \theta_h + \frac{1}{2}\rho^* v^{*3}\theta_{ke}\right) - \rho_\infty v_\infty \theta_d \frac{\partial}{\partial z}\left(h_\infty + \frac{1}{2}v_\infty^{\;2}\right) = EI - Q^*\theta_Q \qquad (3.21)$$

$$I = \sigma^* E\theta_c \qquad (3.22)$$

$$\rho_\infty \frac{\partial}{\partial t}\left(\frac{1}{2}v_\infty^{\;2}\right) + \rho_\infty v_\infty \frac{\partial}{\partial z}\left(h_\infty + \frac{1}{2}v_\infty^{\;2}\right) = 0 \qquad (3.23)$$

This new set of equations is closed by using shape factors, which relate the various arc characteristic areas to the thermal area θ_δ. The relationship between the shape factors is dependent upon the flow characteristics involved.

3.3 CIRCUIT BREAKER MODELLING

3.3.1 Introduction to circuit breaker modelling

The aims of circuit breaker modelling are:

- To improve the understanding of the physical processes occurring within an interrupter, in order to identify the significance of test data, and improve the strategy of circuit breaker testing.
- To produce an analytical or semi-empirical tool for the design of improved performance circuit breakers and to provide a means for predicting the behaviour of the circuit breaker in a power system.

In order to produce an effective circuit breaker model, account needs to be taken of (Shimmin, 1986):

1. The interrupter geometry and contact movement.
2. The interrupting gas (SF_6) properties.
3. The gas flow during operation.
4. Variations in the gas thermodynamic state.
5. The effect of the arc on 2 to 4.

Coldflow modelling (in the absence of an arc) may be comfortably achieved. For most purposes the SF_6 gas can be regarded as an ideal gas, without any significant loss of accuracy. However, incorporation of the arc into the model is difficult, since complex processes, such as nozzle ablation and electrode melting may need to be incorporated.

Part of the work described in this thesis has involved the development of an optical fibre linear travel recorder (**chapter 5**), to monitor the contact and piston motion, and prototype testing of a recently developed optical fibre pressure sensor (**chapter 8**), to measure the piston chamber pressure of the test circuit breaker during operation. Therefore, the predictions of piston pressure rise, produced by a theoretical model for the test circuit breaker (Christodoulou, 1995), based upon the above equations, and using the measured interrupter stroke as input, may be compared (**chapter 11**) with the pressure rises recorded by the optical fibre pressure sensor in the piston chamber (**chapter 10**).

Christodoulou's model for the test breaker also incorporates the arc in pressure rise calculations within the piston chamber. Therefore, the pressure rises predicted by this model may be compared with the measured values from the optical fibre transducer, for different arc currents (**chapter 11**).

3.3.2 Coldflow modelling

For coldflow circuit breaker modelling, it is often convenient and sufficiently accurate to treat the SF_6 gas as ideal (Shimmin, 1986) and, therefore, it can be described by the ideal gas equation of state

$$P = \rho RT \tag{3.24}$$

where P, ρ and T are the gas pressure, mass density and temperature respectively. In order to calculate the piston chamber pressure, during operation, the circuit breaker can be treated as a system, where conservation of energy will apply

$$dE = dQ - dW \tag{3.25}$$

where E is the total energy of the system, Q is the heat added to the system and W is the work done on the system. In the absence of an arc, there will be no heat added. Eqn.3.25 then evolves to, in time differential terms (Shimmin, 1986)

$$\frac{d}{dt}(M.u) = \left[P\frac{dV}{dt} + \frac{dm}{dt}\left(h + \frac{1}{2}v^2\right)\right] \tag{3.26}$$

where M is the mass of gas remaining in the piston chamber, u is the specific internal energy, $P(dV / dt)$ is the work done by the piston and dm/dt(h + 1/2v^2) is the heat associated with gas escaping from the piston chamber. Further manipulation of eqn.3.26 gives

$$MC_v \frac{dT}{dt} = PA_p s - \frac{dm}{dt}\frac{P}{\rho} \tag{3.27}$$

where C_v is the specific heat capacity of SF_6 (constant volume), P is the piston chamber pressure, A_p is the area of the piston, s is the speed of the interrupter (provided by measured travel records) and dm/dt the mass flow rate of gas out of the piston chamber. The mass density of gas in the piston chamber is calculated by using the conservation of mass

$$M = M_0 - \int_0^t m\,dt \tag{3.28}$$

and the relationship $\rho = M/V$, where M is the instantaneous mass of gas in the piston chamber, M_0 the initial mass of gas, m the net outflow of mass from the chamber and V the instantaneous volume of the piston chamber. The temperature can then be calculated using eqn.3.27 and the pressure from the equation of state (eqn.3.24).

This shows, in principle, how the piston chamber pressure rise may be calculated during coldflow operation. For real situations different equations are needed to calculate the mass flow rate dm/dt out of the piston chamber, depending upon whether the flow is choked by sonic conditions at the nozzle throat. Therefore, a theoretical model, which computes the piston chamber pressure at discrete time intervals, will check for choked flow at each time step in order to identify the appropriate mass flow equation to apply.

3.3.3 Arc-incorporated circuit breaker modelling

Circuit breaker modelling, including the effects of arcing, have been the subject of significant widespread research (eg. Shimmin, 1986, Ueda *et al*, 1982 and Yanabu *et al*, 1982). Central to all the models is the prediction of piston pressures at various arc current levels to identify the required mechanical input power from the interrupter drive mechanism. To progress from the coldflow prediction of pressure rise nozzle blocking, arc heating, cool gas entrainment into the arc and nozzle and electrode ablation may need to be considered. Furthermore, the following problems exist to hinder the advancement of circuit breaker models (Fang, 1993):

1. A scarcity of reproducible and generally accepted test results for arcs in SF_6.
2. Arc instability under realistic circuit breaker conditions is not well understood.
3. There is uncertainty about the transport properties of SF_6 (thermal and electrical conductivity) below 10000K.
4. There is uncertainty regarding the upstream boundary conditions.

In order to minimise the uncertainties associated with these complexities, recent research conducted collaboratively between Reyrolle Switchgear, Rolls Royce Advanced Research Laboratories and the University of Liverpool has led to the incorporation of a sophisticated arc model, based upon eqns.3.2 to 3.23, into a commercial computational fluid dynamics package (Phoenics), produced by Cham. This modelling is based upon finite element computation and the results obtained by Christodoulou (1996), for the test circuit breaker, are used in **chapter 11** for comparison with the experimentally measured pressure rises for different arc currents.

3.4 RADIATION EMISSION FROM CIRCUIT BREAKER ARCS

3.4.1 The need to quantify radiation loss

A knowledge of the amount of power, which is dissipated by various processes from the arc, is important for understanding the mechanism of arc control and quenching. One of such processes is radiation energy transport from the arc. It is important to be able to quantify the total radiation which escapes from the arcing environment to solve the conservation of energy equation (eqn.3.4), since this energy is not absorbed by the plasma nor heats the surrounding gas (i.e. it is effectively lost).

Radiation effects also play a role in dielectric breakdown in circuit breakers (Lowke, 1978). Assuming thermal reignition of an arc does not occur (for which turbulence rather than radiation is significant) then, for dielectric reignition to occur (typically ≥100μs after current zero), a new conducting channel has to be formed by electron ionisation processes. A thermal mantle of hot gas forms around the arc plasma before current zero. Ragaller and Reichert (1977) have shown that the diameter of this mantle can be ~5mm even 100μs after current zero. The mantle thickness which would correspond to thermal conduction processes alone is shown by Lowke to be <0.1mm. Thus, the much larger measured diameter of 5mm is attributed to radiation processes. (Turbulence and flow instabilities can increase the diameter of the thermal mantle but radiation determines the lower limit).

The photoabsorption threshold for cool SF_6 (300K) is 130nm (Aubrecht and Gross, 1994). Wavelengths below this value are absorbed within much less than 1mm, while wavelengths above this value generally escape from the circuit breaker.

This far UV radiation (<130nm) contributes to the thermal mantle diameter and, consequently, the probability of dielectric breakdown.

Radiation losses can be calculated or measured. Neither is an easy task on account of the wide range of continuum radiation (from ~10nm to ~10μm), on which nearly 2000 spectral lines are superimposed. Furthermore, the radiation-producing species may have a complex time and spatial concentration and temperature variation. In calculating the radiation losses from circuit breaker arcs the most severe assumption is that the plasma is isothermal. This causes significant errors in determining the radiation loss beyond the relatively flat temperature profile of the plasma core. This problem does not exist, of course, in experimental measurements of radiation loss. However, detection systems all possess finite response times and spectral responsivity ranges (eg. thermopiles may operate typically between 180nm to 4000nm). Hence, some of the emitted radiation (eg. between the 130nm photoabsorption threshold for SF_6 and lower limit of the detector) will not be captured, causing errors in total radiation measurements. Both methods of radiation emission determination, therefore, possess advantages and disadvantages and comparison of results from both is often necessary.

3.4.2 Calculations of radiation loss

3.4.2.1 The radiation transfer equation

Theoretical calculations of the radiation emitted by gas blast circuit breaker arcs have been the subject of research by several workers (eg. Lowke, 1974; Liebermann and Lowke, 1976; Gleizes *et al*, 1991 and Aubrecht and Gross, 1993). Calculation of the net emission of radiation from an SF_6 arc plasma is difficult since both continuum and line spectra need to be considered over the spectral range of far UV to far IR (from ~10nm to ~10μm - Lowke, 1978). There are nearly 2000 spectral lines in this range, the strongest of which (~400) are used in theoretical calculations (Aubrecht and Gross, 1994). Line radiation dominates over continuum at 1bar, by an order of magnitude, but at higher pressure the extent of this domination reduces.

The radiative transfer equation, which determines the radiation emitted from an SF_6 arc plasma, is given by (Heberlein *et al*, 1984)

$$\frac{dI_\nu}{ds} = \varepsilon_\nu - I_\nu \kappa'_\nu \tag{3.29}$$

where I_ν is the intensity of radiation emitted at a frequency ν, ds an arbitrary path length, ε_ν the emission coefficient and κ_ν' the spectral absorptivity at the frequency ν. dI_ν/ds is known as the net emission coefficient, $\varepsilon_{N\nu}$, taking absorption effects into account. It can be shown (Aubrecht and Gross, 1994) that the total net emission coefficient for an isothermal, homogeneous, cylindrical SF_6 plasma in local thermal equilibrium, and of radius R, is given by

$$\varepsilon_N = \int_0^\infty B_\nu \kappa'_\nu e^{(-\kappa'_\nu R)} d\nu \tag{3.30}$$

where B_ν is the Planck function. ε_N is the fraction of power radiated per unit volume and solid angle, on the axis of a cylindrical column, that escapes from the plasma of radius R. Several steps are performed in order to calculate the total net emission coefficient, which is a function of temperature, plasma radius and pressure:

1. The equilibrium composition of the plasma is calculated. This is necessary, since the spectral absorptivity of each species is proportional to the concentration of that species.
2. The continuum absorption coefficient, which is determined by electron transitions within the plasma, is calculated as a function of frequency, ν (or wavelength, λ), including the effects of photo-recombination radiation, "bremstrahlung" radiation and radiative attachment (Gleizes *et al*, 1992).
3. The spectral line profiles are used to determine the line absorption coefficients. Line broadening due to, for example, resonance, Stark and Doppler effects and line overlapping are taken into account in determining the absorption coefficients.

4. The absorption effects of the continuum and line spectra are combined to give a spectral absorptivity, κ_v'.
5. Using eqn.3.30 the total net emission coefficient of radiation can be calculated.

3.4.2.2 The spectral absorptivity function κ_v'

Aubrecht and Gross (1994) calculated the spectral absorptivity, κ_v', of an SF_6 plasma, using the assumptions described above, as a function of wavelength and temperature at a pressure of 1bar (fig.3.9). In order to reduce computation time only the major equilibrium constituents of SF_6 were used in the calculations i.e. S, F, S+, S2+, F+, F2+ and electrons. Shown on the results is the spectral absorptivity at 300K. The form of the 300K spectral absorptivity is interesting, since it shows the threshold wavelength (130nm) for photoabsorption in cool SF_6. Radiation at wavelengths below this value acts to sustain the plasma rather than being "lost" to the surroundings.

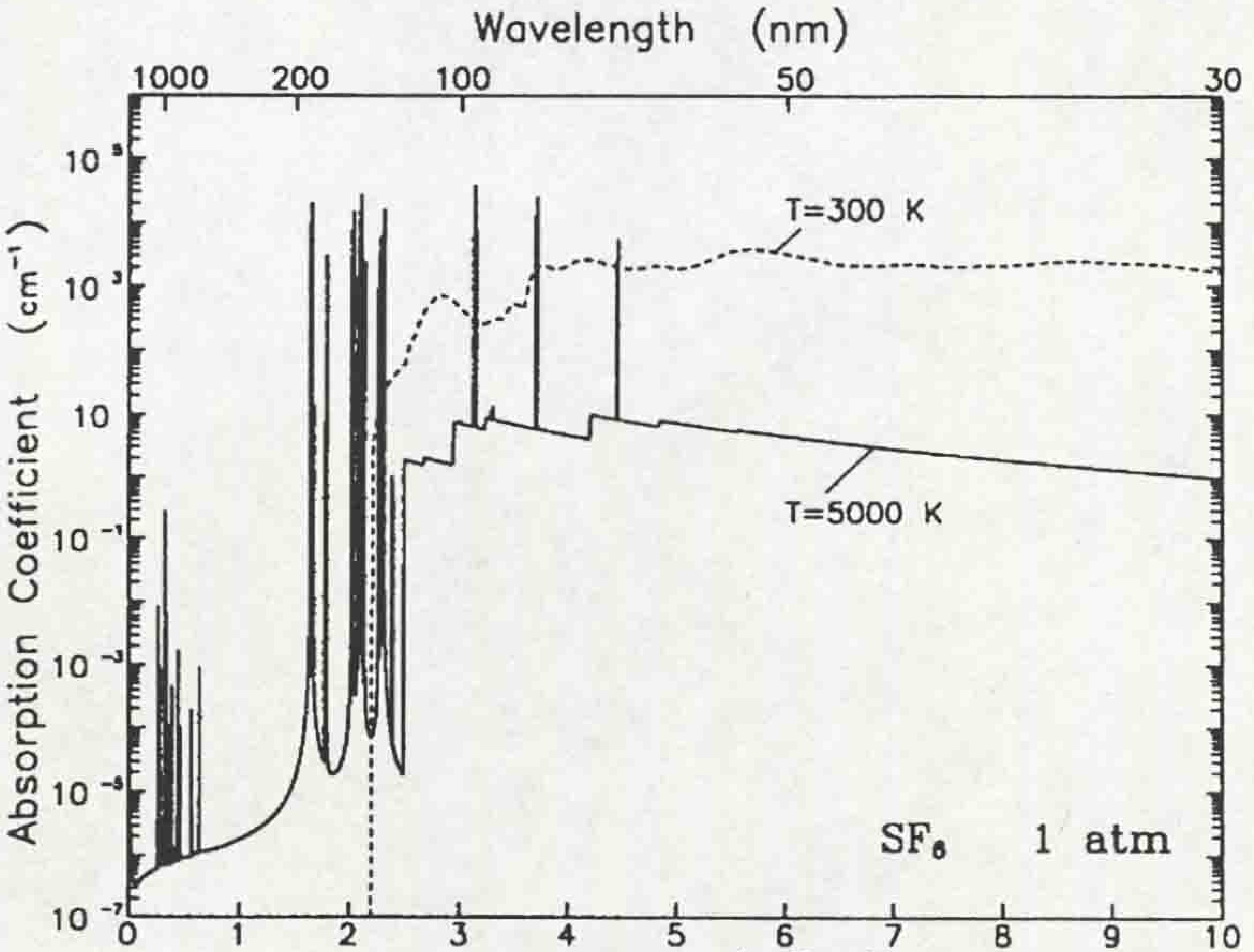

Figure 3.9a - κ_v' as a function of wavelength at 300K and 5000K (Aubrecht and Gross, 1994)

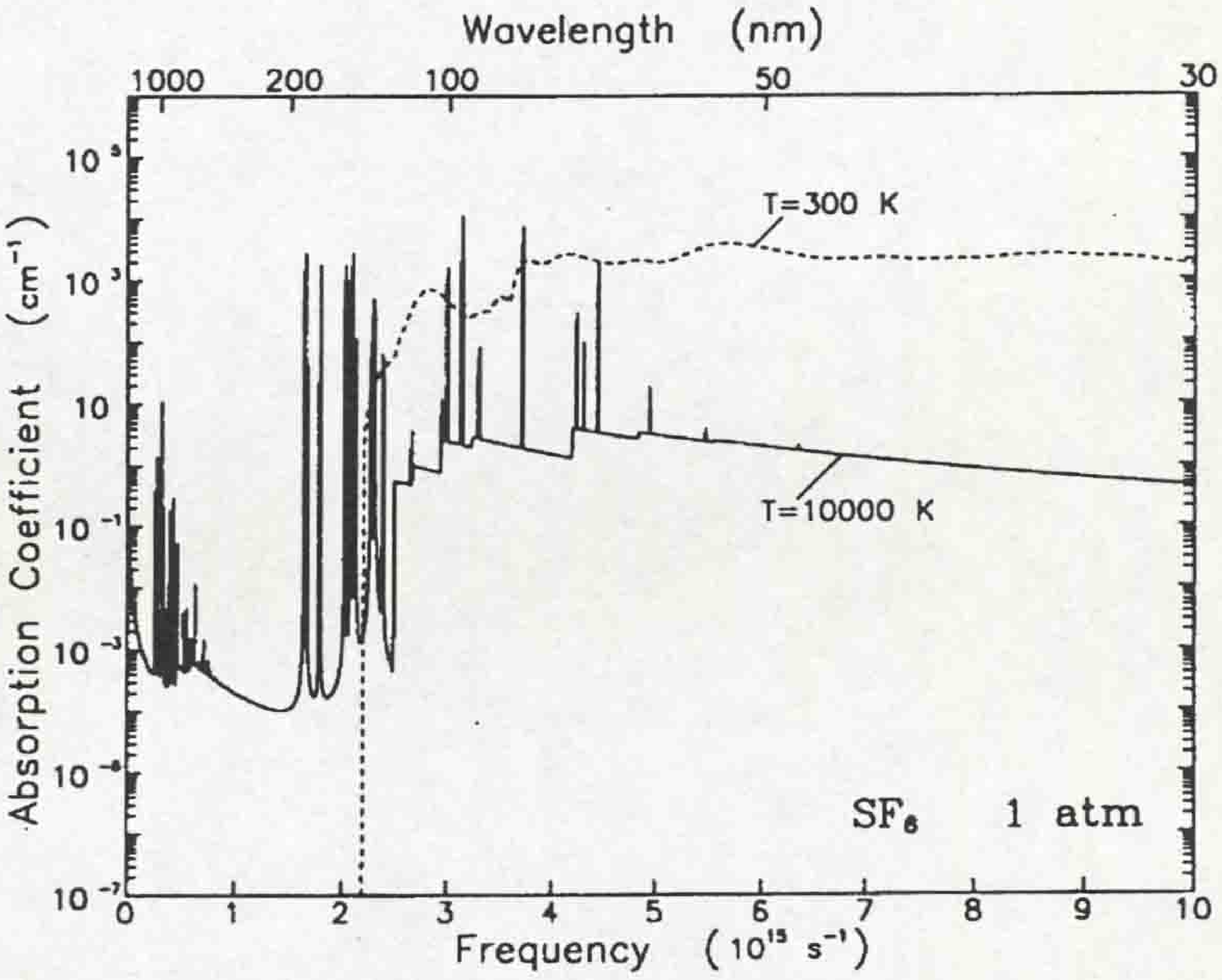

Figure 3.9b - κ_ν' as a function of wavelength at 300K and 10000K (Aubrecht and Gross, 1994)

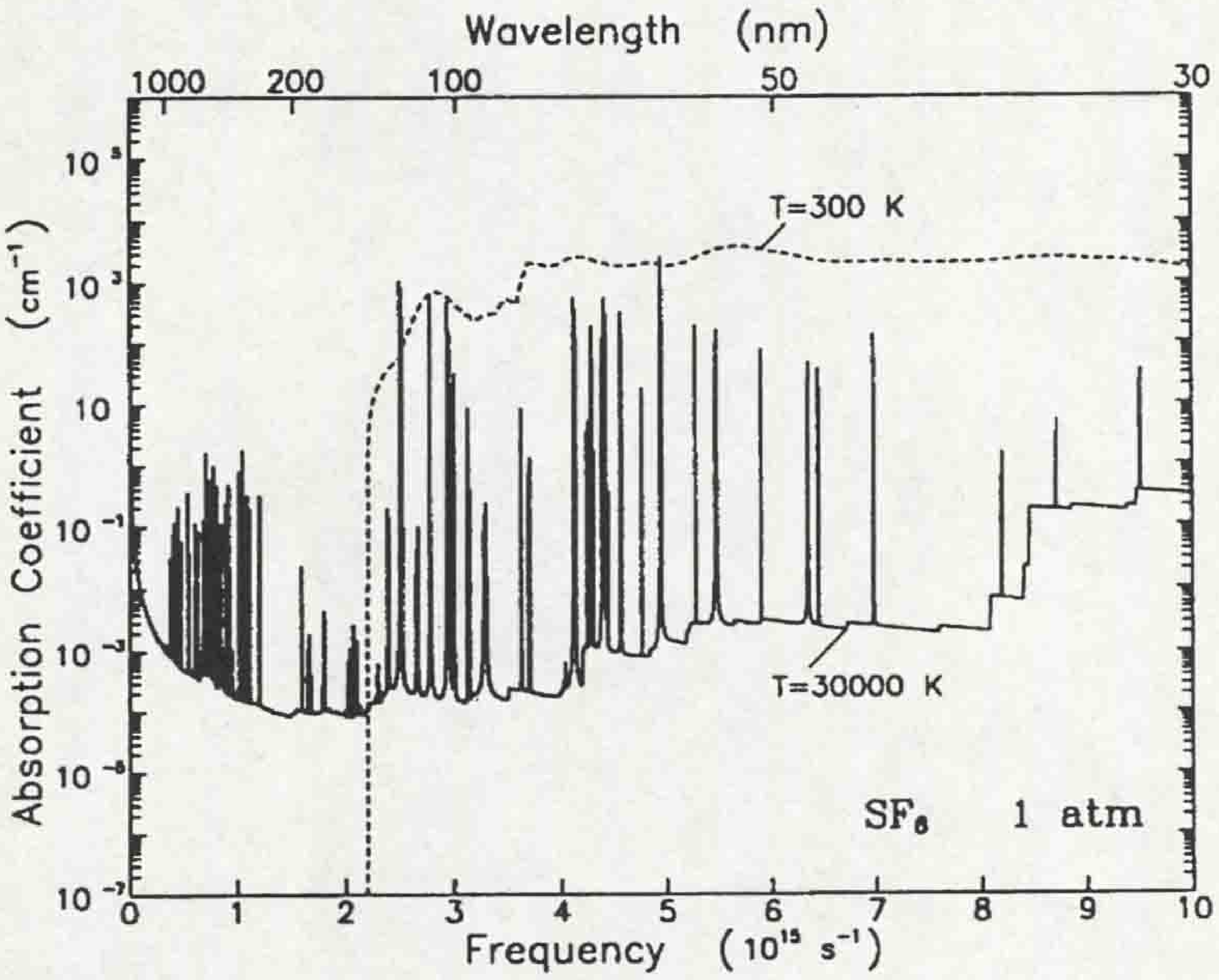

Figure 3.9c - κ_ν' as a function of wavelength at 300K and 30000K (Aubrecht and Gross, 1994)

It is apparent from fig.3.9 that at lower temperatures (eg. 5000K - fig.3.9a) the spectral absorptivity is reasonably similar in form to the spectral absorptivity at 300K, while at higher plasma temperatures (30000K - fig.3.9c) the spectral absorptivity tends to equalise across the spectrum.

3.4.2.3 The total net emission coefficient ε_N

Using eqn.3.30 and the results of fig.3.9, Aubrecht and Gross calculated the total net emission coefficient as a function of temperature, plasma radius and pressure. The results (fig.3.10) show that a steep gradient exists in the ε_N/T relationship up to 10000-15000K, at each pressure, which then tends to level off after this temperature. Also, the total net emission coefficient reduces as the plasma radius increases, due to self-absorption within the plasma; R=0 corresponds to a neglect of self-absorption effects. Finally, it is noted that a change in pressure of an order of magnitude results in a corresponding approximate order of magnitude change in ε_N. The results of Aubrecht and Gross compare well with the calculated results of Liebermann and Lowke (1976) and Gleizes *et al* (1991) and the experimental results of Mottschmann (1968) for wavelengths greater than 200nm (it is difficult to measure emissions in the far UV range of the spectrum).

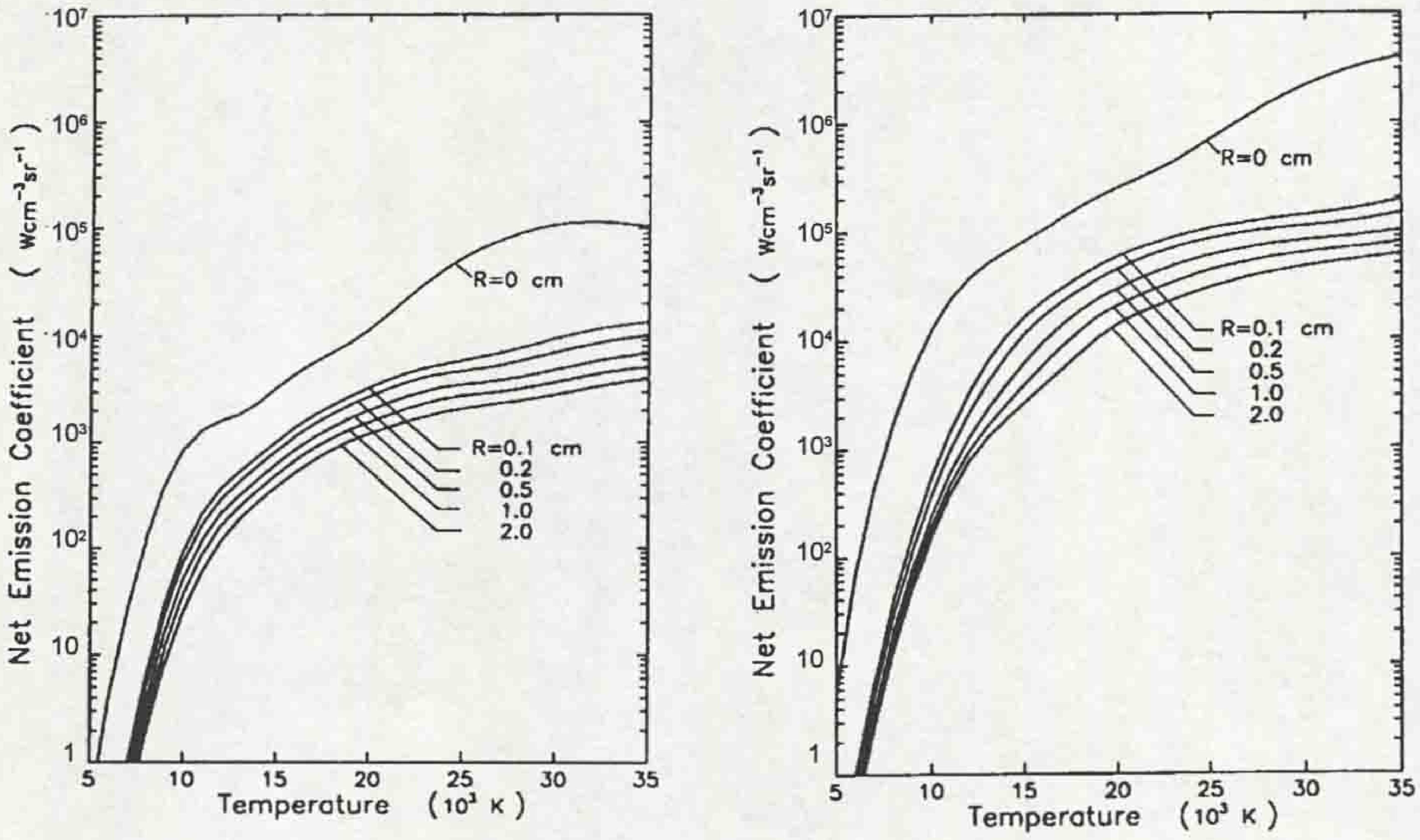

(a) P = 1bar

(b) P = 10bar

Figure 3.10 - ε_N for SF_6 as a function of temperature, radius and pressure

3.4.2.4 The effect of metal vapour on ε_N

The analysis described above, for evaluating ε_N, applies to pure SF_6 plasmas only. However, in high power gas blast circuit breakers, as used in this project, the plasma is composed of a mixture of SF_6 decomposition species and metal vapour, produced by electrode melting. The effect of metal vapour in the plasma, on the total net emission coefficient, was investigated theoretically by Gleizes *et al* (1992). Fig.3.11 shows the ε_N/T relationship at 1bar, for a mixture of SF_6 and 1% copper by volume. This result can be compared directly with the result of Aubrecht and Gross (fig.3.10a) at the same pressure for pure SF_6 (taking into account the different units). It is apparent that at lower plasma temperatures (~5000K) the mixture has a value for ε_N of an order of magnitude higher than the pure SF_6 plasma. At higher temperatures the difference is reduced.

The practical consequence of a higher radiation loss for an SF_6-Cu mixture, combined with the increased electrical conductivity, is a temperature reduction of the plasma (Gleizes *et al*, 1992).

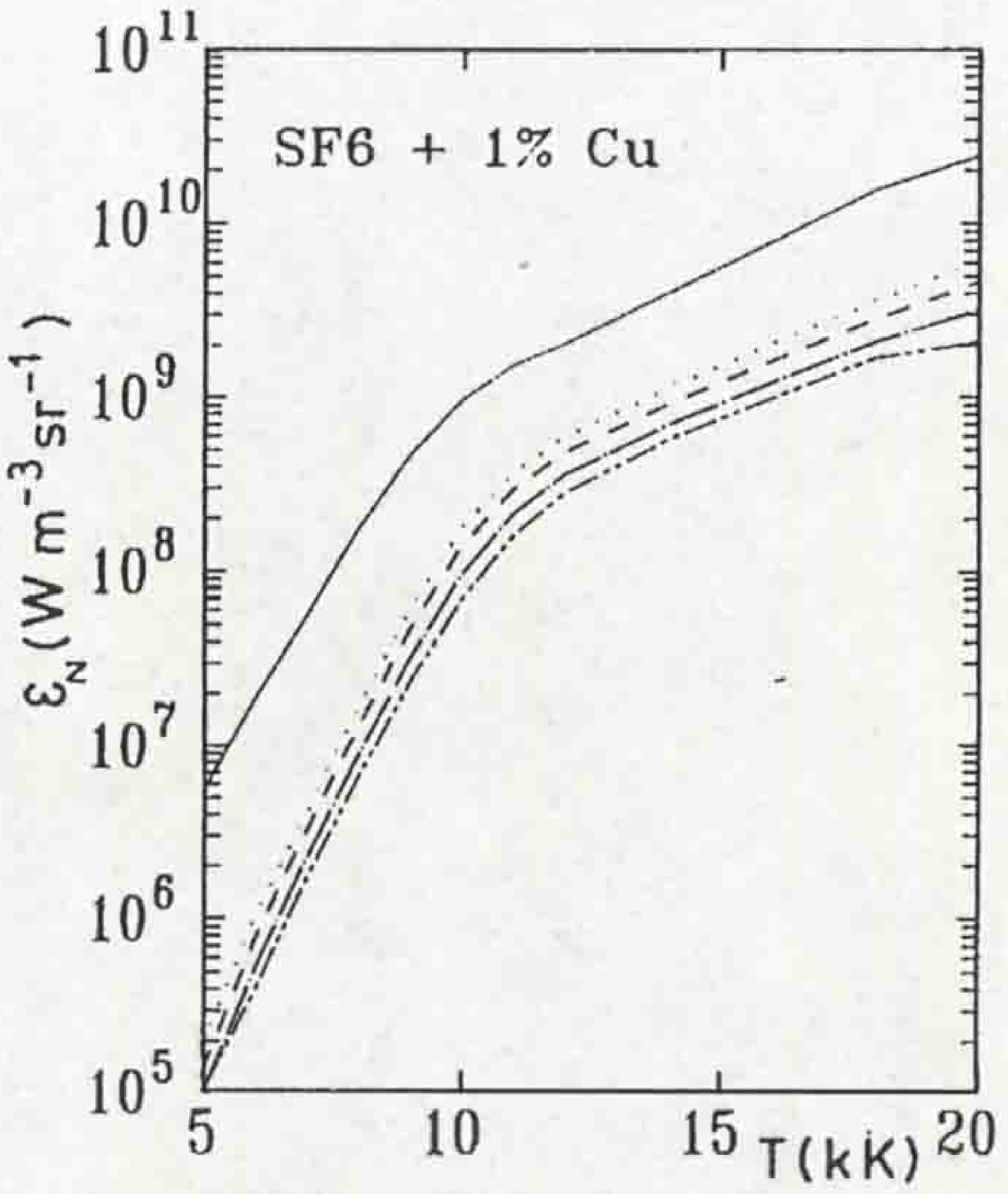

Figure 3.11 - The effect of metal vapour on ε_N

3.4.3 Measurements of radiation loss

3.4.3.1 Total radiation loss

The total radiation loss is the only energy dissipation process that can be measured directly (Leclerc and Jones, 1982). Its measurement requires a flat detector response over a wide spectral range. Ideally this range should be from 130nm (the photoabsorption threshold for cool SF_6) to ~10μm. Thermopiles have a good spectral detection range (typically 180nm to 4μm) and are useful for high current measurements, because they offer good protection against spurious signals from vibration or shock waves. However, their limited transient response restricts their use to observing phenomena on a time scale of 10ms or longer (Jones, 1988). For more rapid and sensitive radiation measurements, photomultipliers may be used. Their general disadvantage is a narrower detection range than thermopiles (eg. the RCA type 60 ER (4832) has a flat detection response between 250 to 900nm). In measuring the total radiation loss from a circuit breaker arc a collimating slit is usually employed (~1mm) so that, in positioning the detector a suitably large distance away (~1m), the inverse square law can be applied to the radiation measured.

Strachan *et al* (1977) investigated the total radiation loss, with respect to the upstream pressure P_0 and instantaneous arc current, measured at the downstream edge of the orifice, for an orifice flow arc in air. The results (fig.3.12) show that there is a unique correlation with arc current and that there is a dependency on the upstream electrode material (copper, copper-tungsten and carbon electrodes were investigated). Strachan derived an empirical relationship for the radiation loss, Q_R

$$Q_R = \alpha I E \sqrt{P} \tag{3.31}$$

where I is the instantaneous current, E the local electric field strength, P the local gas pressure and α a constant whose value is determined by the upstream electrode material.

Leclerc and Jones (1982) determined the total radiation for a 50mm orifice flow arc at higher currents, both in air and SF_6. Fig.3.13 shows the radiation loss upstream of the orifice and arc current as a function of arc duration, in SF_6, from this study. It can be seen that at around 2ms, after which time a well defined core of electrode vapour is formed, the radiation loss increases quite rapidly. The decreasing portion of the half-cycle provides a much higher radiation loss than the increasing portion, due to this metal vapour entrainment.

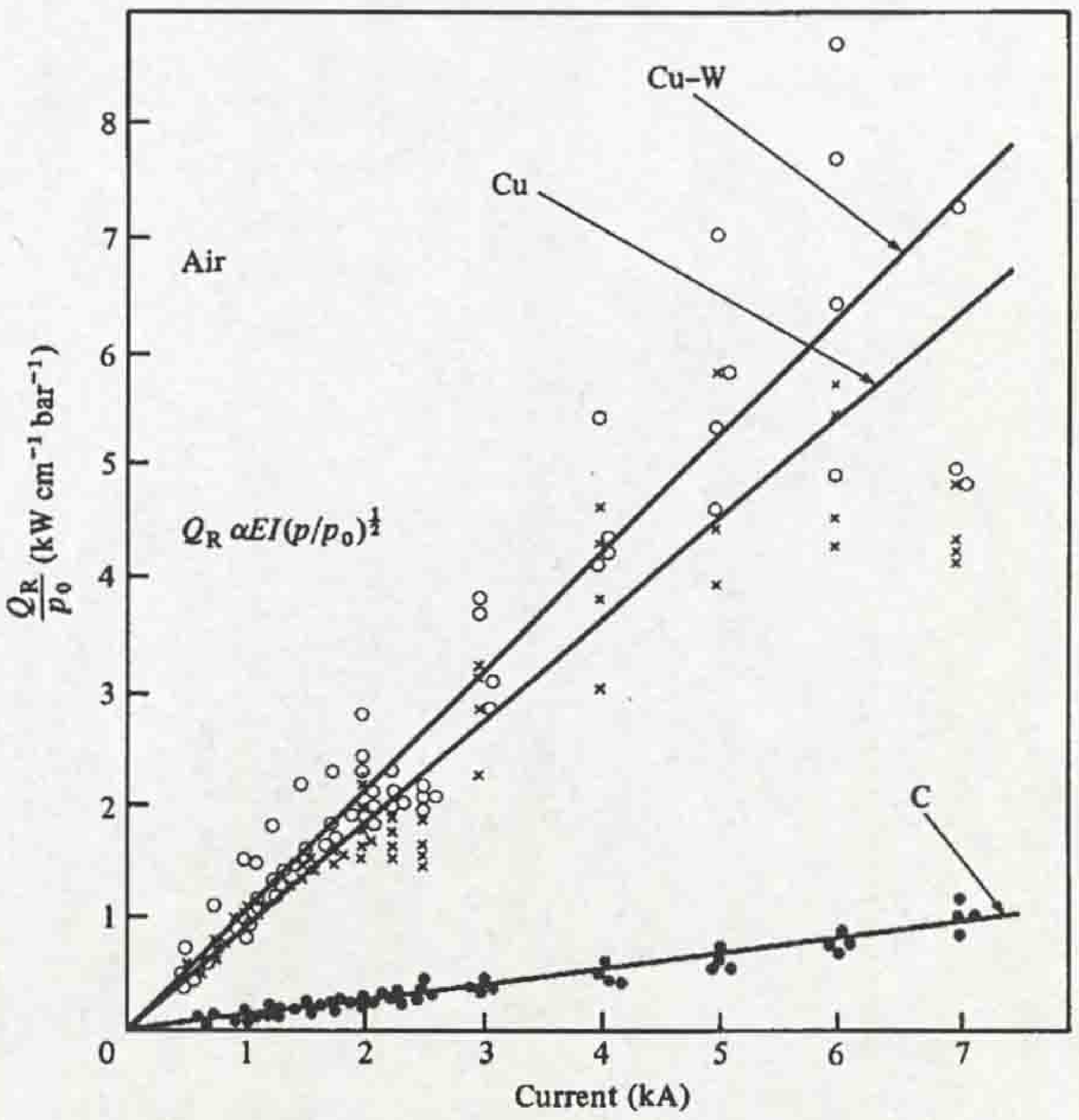

Figure 3.12 - Radiation loss with respect to upstream pressure and current for an orifice flow arc (Strachan *et al*, 1977)

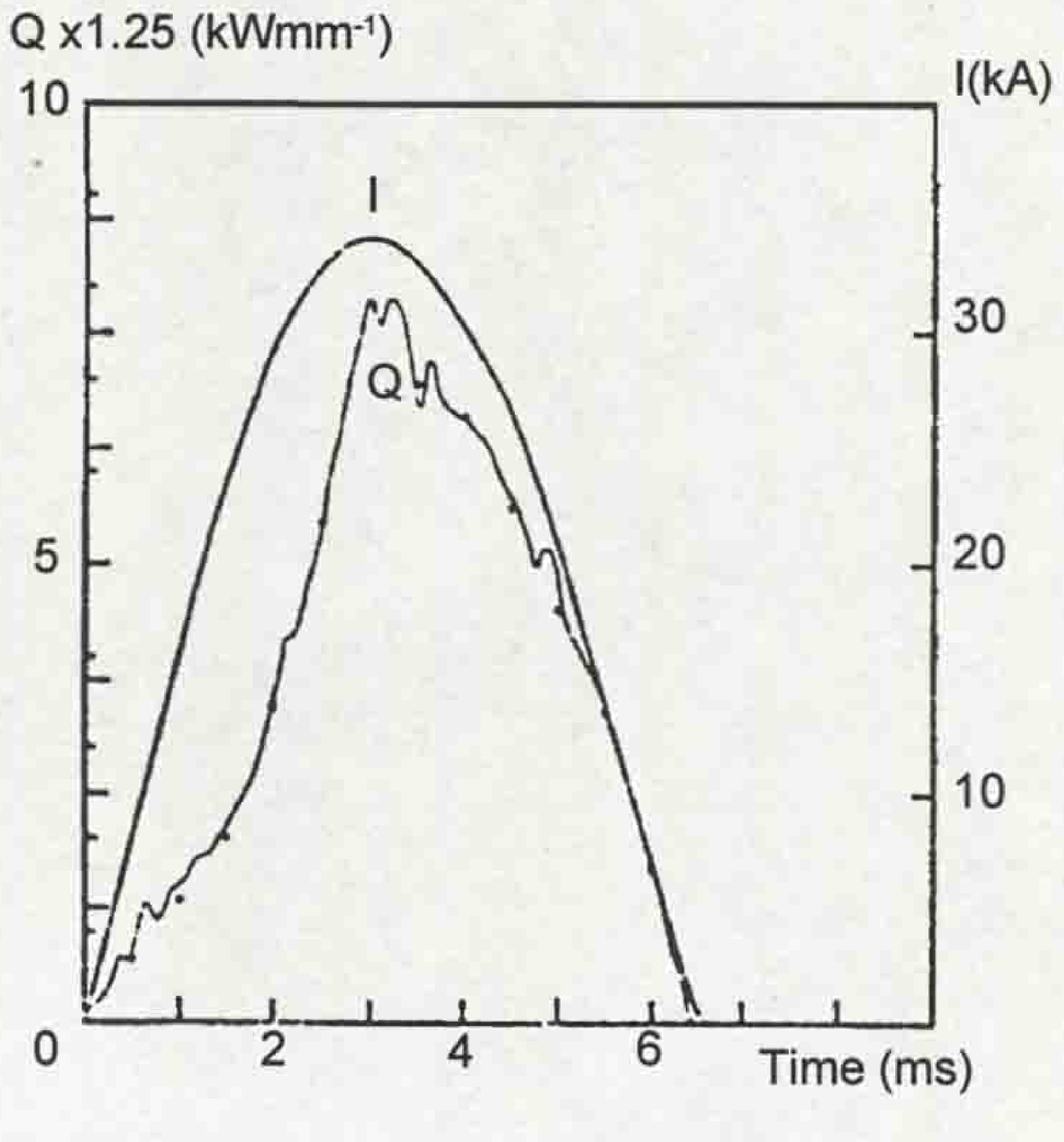

Figure 3.13 - Radiation loss measured upstream for a 50mm orifice flow arc in SF_6 (Leclerc and Jones, 1982)

Fig.3.14 shows the variation of radiation loss, as a function of instantaneous current, with peak current as parameter, in air, from the same study. The results show an appreciable difference in radiation loss recorded upstream and downstream of the orifice. Upstream (fig3.14a) the radiation loss is approximately proportional to the instantaneous current and independent of peak current. However, downstream (fig.3.14b) there is a sharp increase in the radiation loss for peak currents greater than ~20kA, corresponding to electrode vapour (Cu-W) entrainment. Following the peak current, the radiation loss during the decreasing portion of the half-cycle is much lower than during the increasing portion. This phenomenon was attributed to ablation of the wall of the flow confining nozzle and subsequent absorption of much of the radiation by the ablation products.

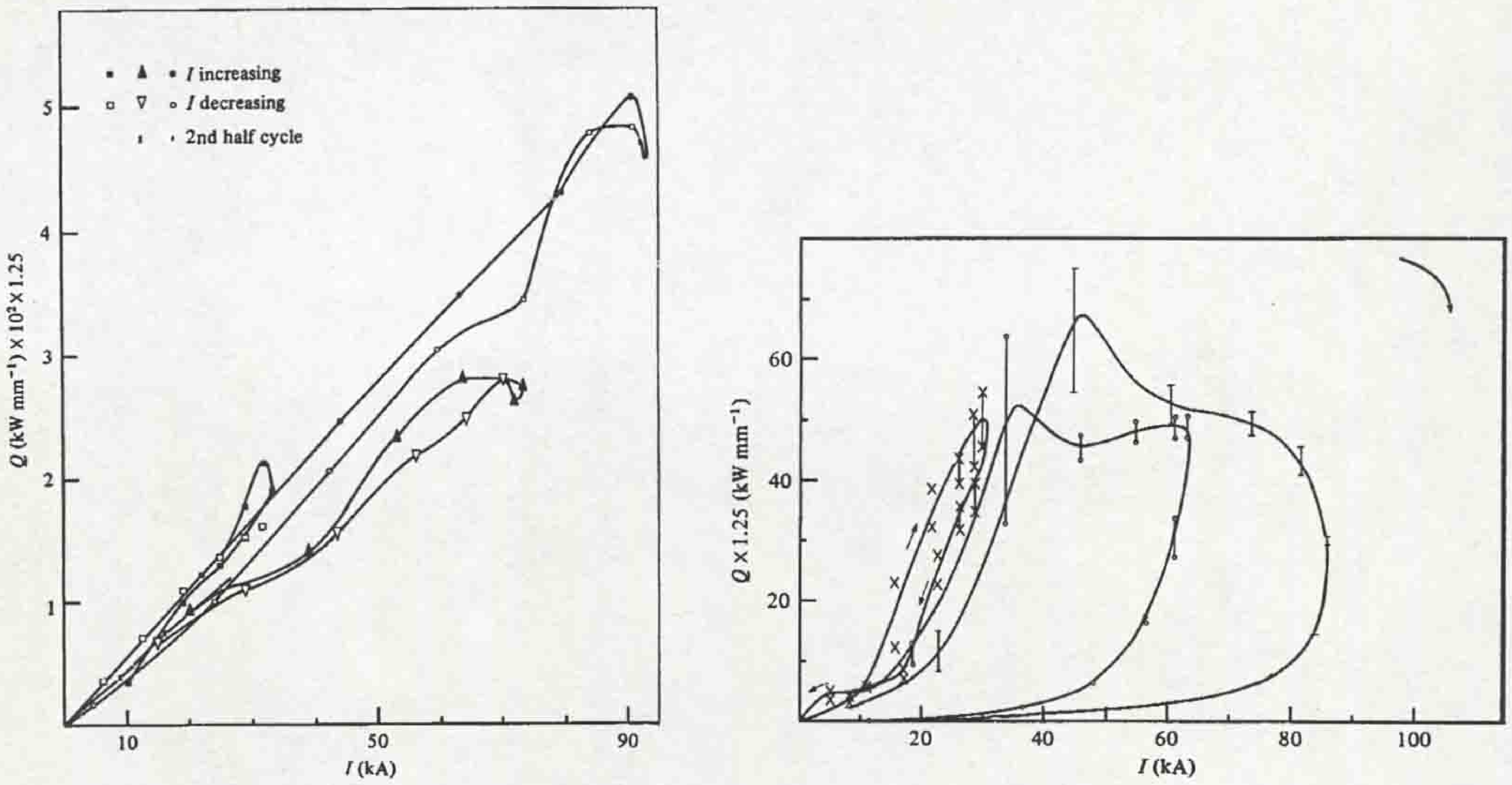

(a) Upstream

(b) Downstream

Figure 3.14 - Radiation loss as a function of instantaneous current with peak current as parameter (Leclerc and Jones, 1982)

Total radiation loss measurements were taken on a commercial 420kV 63kA SF_6 puffer circuit breaker (Shimmin, 1986). Although repeatability of the radiation loss amplitudes was not observed between shots at the same current, Shimmin found similar effects to Leclerc and Jones; in particular the relatively small hysteresis effects upstream of the nozzle throat (as on fig.3.14a), compared with much larger hysteresis (probably due to nozzle ablation) at the nozzle throat (as on fig.3.14b).

3.4.3.2 Spectroscopic radiation investigations

Spectroscopic measurements of arc plasma columns have been performed by many researchers (eg. Mottschmann, 1968; Airey, 1977; Housby-Smith and Jenkins, 1978 and Ikeda *et al*, 1982). Jones (1988) has described the methods by which plasma temperature, electron density and species concentrations can be derived from spectroscopic measurements.

Spectrometers, which may be prism or grating based, have a sensitivity which varies with the wavelength of the incident light (eg. fig.3.15, Ibuki, 1979) and their calibration using standard source (eg. tungsten lamp) is necessary. The intensity of a spectral line is given by (Sanjani, 1973)

$$I_L(\lambda)=\alpha(\lambda)I(\lambda,T_L)\frac{d\lambda}{dx}(\lambda)\frac{t_2}{t_1}W(\lambda,T_L) \tag{3.32}$$

where $\alpha(\lambda)$ is the ratio of the width of the image at the film plane of the spectrometer entrance slit to the true slit width, $I(\lambda,T_L)$ is the continuum radiation intensity from a standard tungsten lamp used for calibration, at a wavelength λ and temperature T_L, $d\lambda/dx(\lambda)$ is the slope of the dispersion curve at the wavelength λ, dx being the lateral displacement along the recording film, t_1 and t_2 are the exposure times for the observed spectral line and the tungsten calibration respectively and $W(\lambda,T_L)$ is the equivalent width of the calibration source.

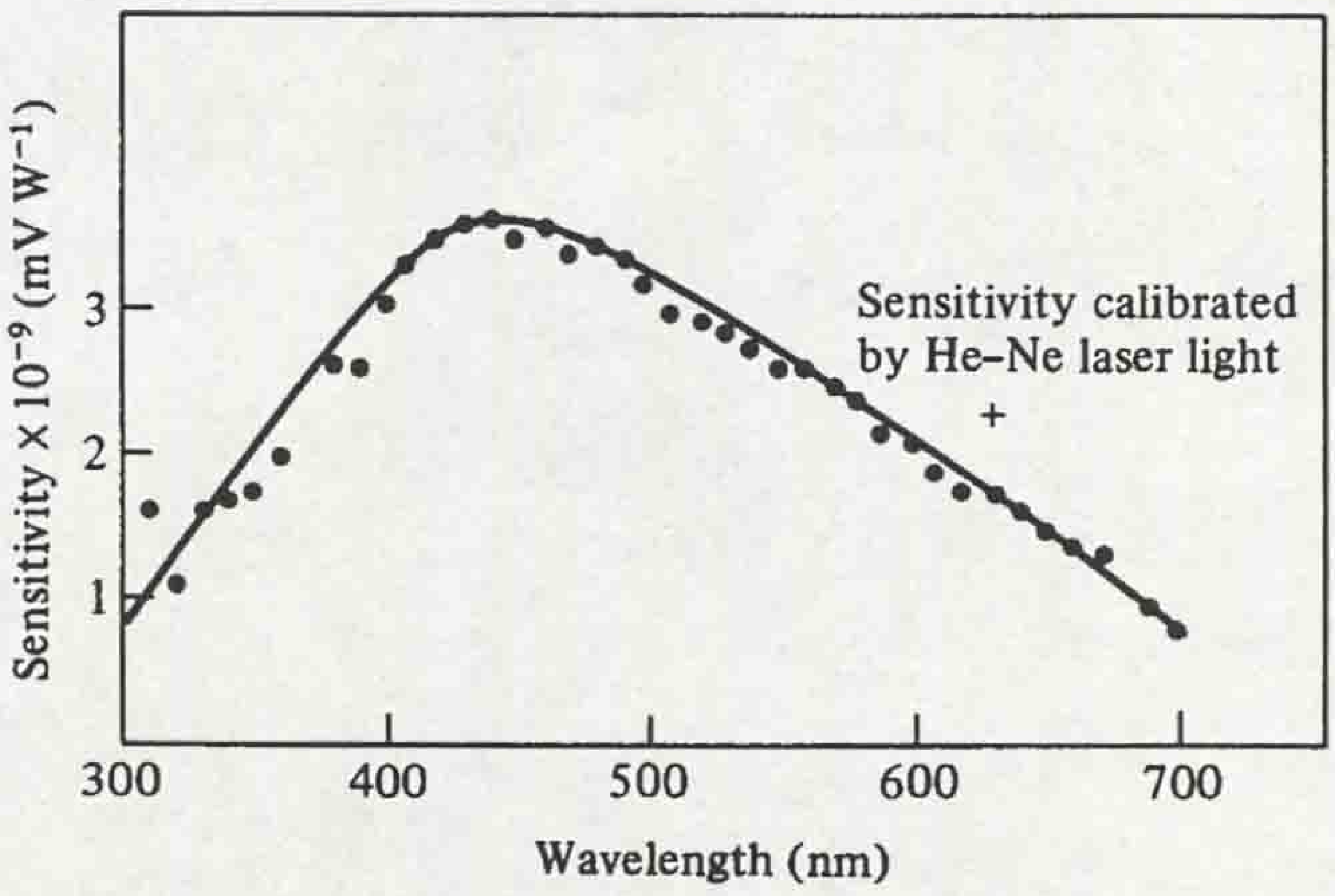

Figure 3.15 - Spectrometer sensitivity as a function of wavelength (Ibuki, 1979)

Typical emission spectra from an SF_6 circuit breaker arc (Airey, 1977) are shown in fig.3.16. The effect of electrode material in the form of copper lines is shown superimposed on the sulphur lines of the host plasma. Housby-Smith and Jenkins (1978) showed that the number of contact vapour lines in the spectrum changes according to the upstream electrode material. More lines are produced in the order carbon, copper, mild steel and copper-tungsten. The consequence of more lines in the emission spectrum is a higher radiation loss as discussed above. The disadvantage of this is the significant increase in electrical conductivity during the current zero period, causing a greater likelihood of reignition. To overcome this problem, the partial duo-flow device was produced and is shown in the lower spectrum of fig.3.16 to significantly reduce the level of contact vapour in the arcing region.

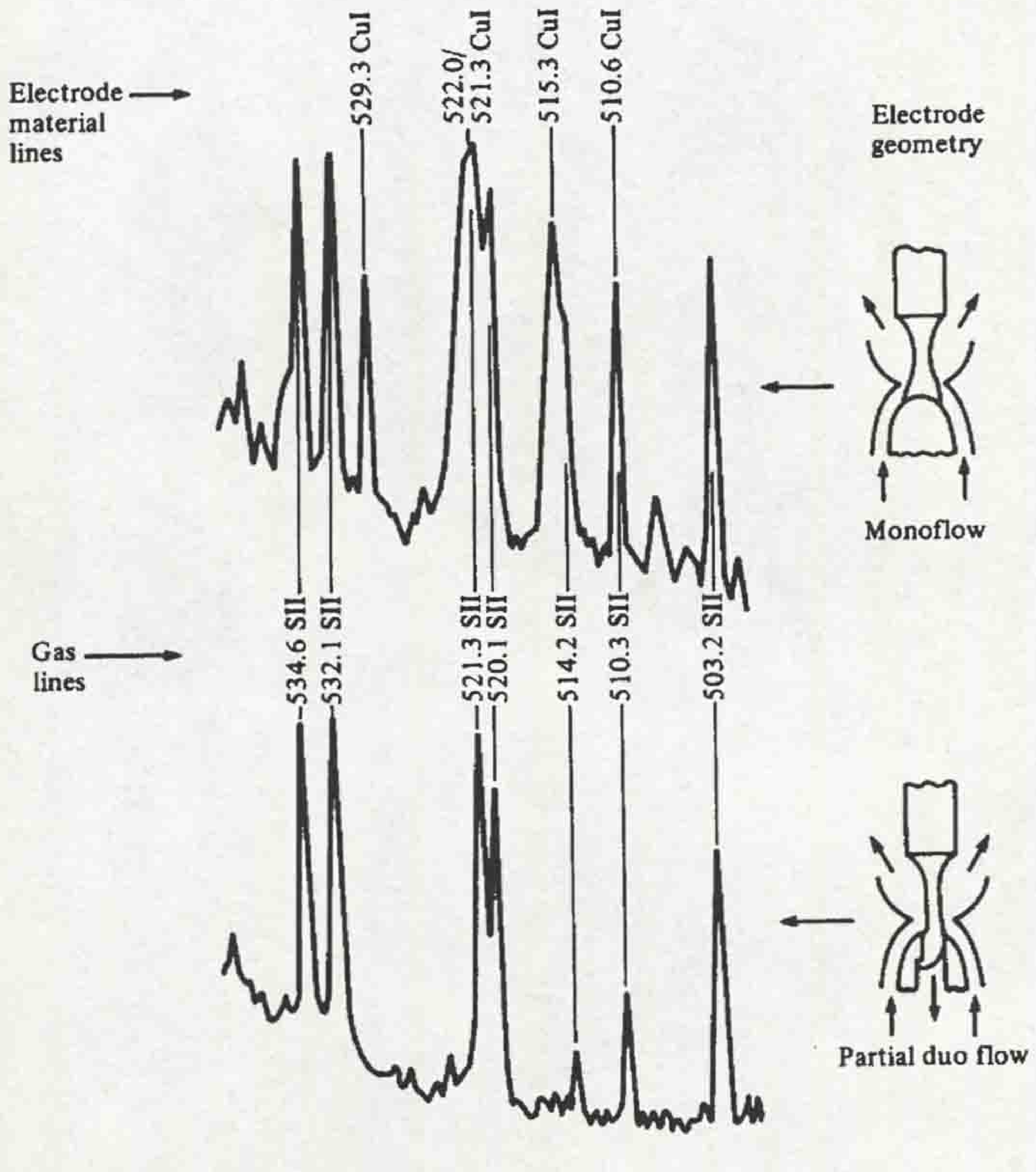

Figure 3.16 - Typical emission spectra from an SF_6 circuit breaker arc (Airey, 1977)

Ikeda *et al* (1982) measured the downstream radial distribution of various spectral line intensities for an orifice flow 30kA arc in SF_6 with Cu-W electrodes. The result (fig.3.17a) showed that the copper line distribution had a smaller diameter than the host plasma. Subsequent calculation of the radial intensity variation of the plasma and copper lines (fig.3.17b) showed that a copper concentration of 70% in the copper vapour core, which exists for arc currents ≥20kA (Jones, 1988 - fig.3.18), would correspond to the spectral line intensities measured.

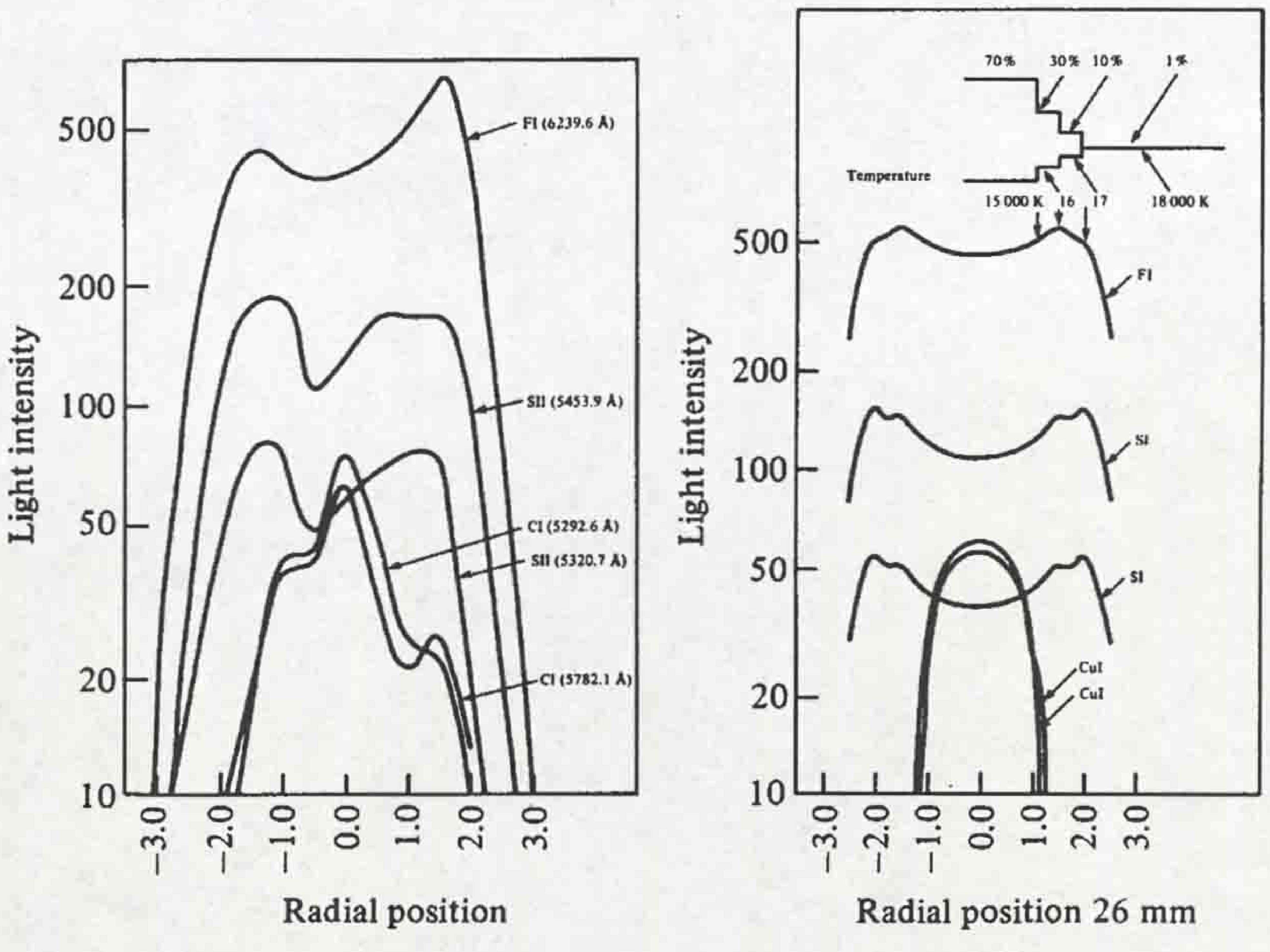

(a) (b)

Figure 3.17 - Radial distribution of various spectral line intensities for an orifice flow 30kA arc (a) Downstream experimental results (b) Calculated profiles (Ikeda, 1982)

Inspection of the spectra from very high current arcs confined by flows in copper nozzles shows that many copper lines are strongly absorbed (Jones, 1988). This is evidence of strong ablation of the nozzle wall producing relatively cool copper vapour around the arc periphery, which absorbs the copper lines from the arc plasma. This ablation layer is shown on fig.3.18.

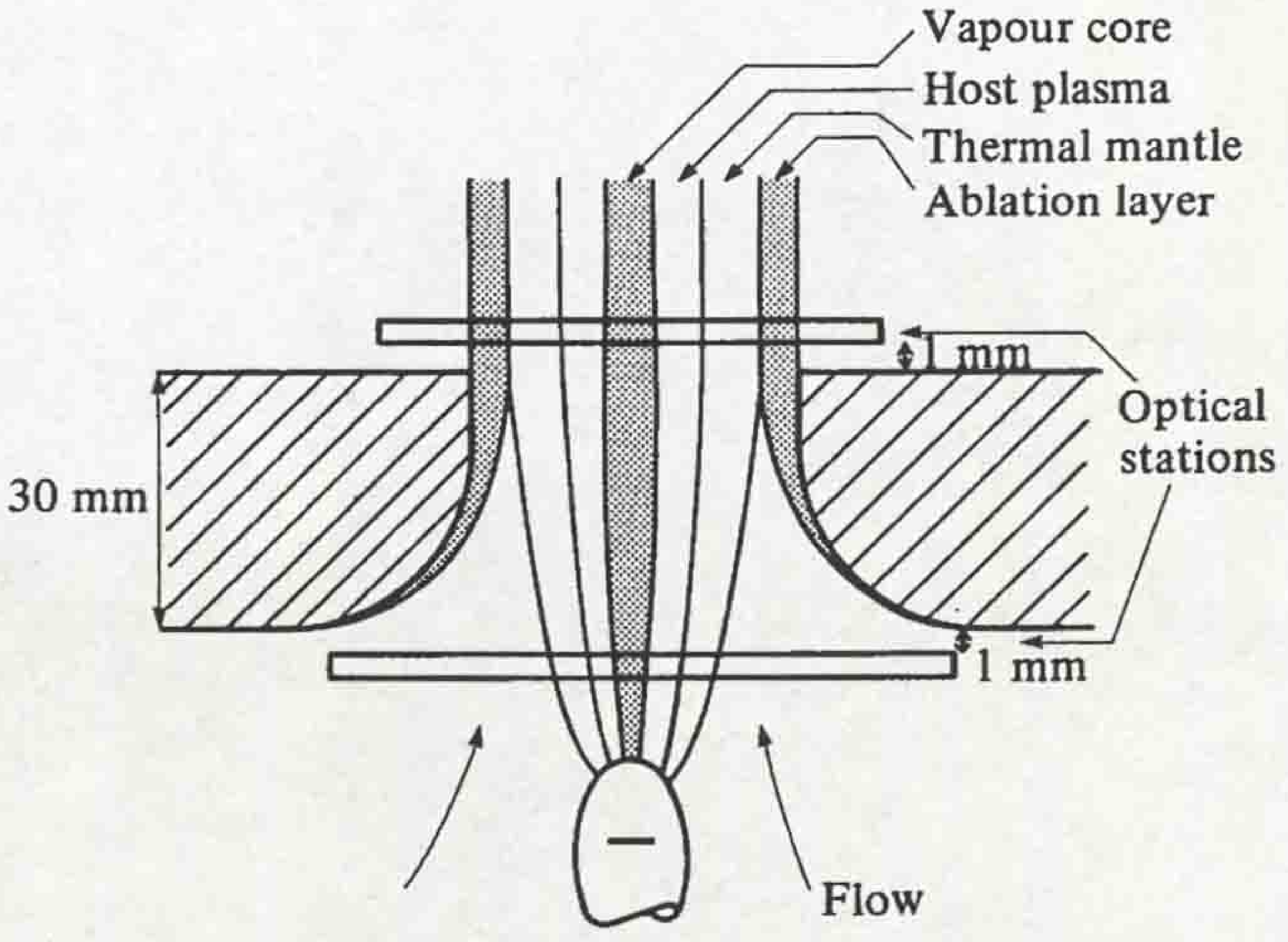

Figure 3.18 - Structure of nozzle flow arc at very high currents showing electrode vapour core and nozzle wall ablation layer (Jones, 1988)

3.4.4 The chromatic approach to radiation measurement

In this project a different approach to the total loss or spectroscopic investigations, described above, was used. The system (**9.4.1.2**) captured the radiation emitted from the circuit breaker with an optical fibre in the spectral range of 500-1000nm. This radiation spectrum was interrogated by a PD150 type double photodiode, having two overlapping spectral responsivities with a crossover point at ~750nm. The PD150 photodiode, together with its processing circuitry (LIBIDO system - **4.3.3.2**) gave a “dominant wavelength” value (**4.3.2**) to the arc radiation spectrum, which is the weighted mean wavelength, with respect to the PD150 detector.

Thus, the system was able to monitor changes in the ratio of the intensity of the lower wavelength range of the spectrum (500-750nm) to the intensity of the higher wavelength range (750-1000nm). This system, with a detector of two overlapping spectral responses, is characteristic of a distimulus monitoring system, the simplest form of chromatic measurement. Greater discrimination of spectral changes can be obtained using detection systems with a greater number of overlapping spectral responses. Tristimulus chromatic monitoring (3 overlapping detectors - Messent, 1995) of SF_6 puffer circuit breaker arcs is currently being investigated at Liverpool University as a successor to the distimulus approach described in this thesis.

3.5 CONCLUSIONS

Observation of voltage and current waveforms, during interruption of a fault, can indicate the instant of arc initiation and extinction and the effect of the arc on the external circuit (**3.1**). However, they do not provide an understanding of the physical processes occurring within a circuit breaker arc and its interaction with the surrounding medium (usually SF_6 gas).

In order to understand the physical processes occurring within an axial convection-controlled arc (which prevails in the test circuit breaker in this project), significant theoretical research has been undertaken. However, due to the complex processes occurring, simplifications are necessary to describe the problem mathematically. Furthermore, it is often necessary to produce semi-empirical arc models, since processes, such as radiation and nozzle ablation are difficult to define mathematically (Fang, 1993). The extent of the problem is evident in the complexity of eqns.3.2 to 3.23.

Circuit breaker modelling aims to produce an analytical tool for the design of circuit breakers with improved interrupting performance. Coldflow modelling is relatively straightforward and a common approach is shown (**3.3.2**). However, incorporation of the arc into a circuit breaker model is difficult, on account of the mathematical complexities discussed above. Nevertheless, a model for the test circuit breaker, used in this project, has been produced (Christodoulou, 1995), which uses the travel records for the interrupter, produced by the optical fibre linear travel recorder, OFLTR (**chapter 5**), to predict the piston chamber gas pressure rises during operation of the circuit breaker. These predictions are compared, in **chapter 11**, with the experimentally measured pressure rises from the optical fibre pressure sensor (**chapter 8**).

Determination of radiation loss from circuit breaker arcs provides an important contribution to the understanding of arc control and quenching and, in particular for circuit breaker modelling. The radiation loss from circuit breakers can be calculated or measured, both methods having advantages and disadvantages (**3.4.1**). Theoretical and experimental evaluation of radiation emission from circuit breaker arcs has been discussed, including the significance of metal vapour entrainment into the arc and nozzle wall ablation. A novel method of radiation emission measurement was introduced, namely chromatic processing of the radiated spectra (**3.4.4**). A distimulus chromatic system was used to monitor radiation emissions from the test circuit breaker in this project, for a range of interrupted fault currents. The results are presented in **chapter 10** and further analysed in **chapter 11**.

Part II - Development of optical fibre sensors

CHAPTER 4 - PRINCIPLES OF OPTICAL FIBRE SENSING

4.1 ELEMENTS OF AN OPTICAL FIBRE SENSING SYSTEM

An optical fibre sensing system consists of four fundamental components (fig.4.1); a source, optical fibre links, a modulator and a detector. The source light is characterised by its inherent properties, including its intensity, phase, polarisation, wavelength (for narrowband sources) or spectral distribution (for broadband sources). The light from the source is transmitted to the modulator through an optical fibre. The reaction of the modulator to the measurand (eg. displacement, pressure or temperature) causes a change in at least one of the source light properties. The modulated light is then fed to a detector, where it is converted into a convenient parameter for recording, such as an electrical voltage. Calibration of the sensor allows the relationship between the measurand and the final output to be determined.

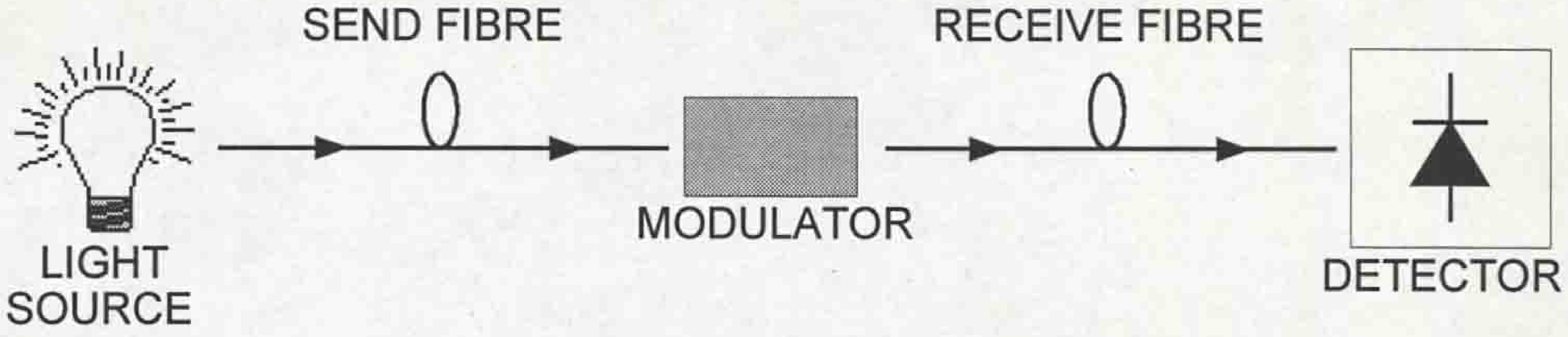

Figure 4.1 - Basic optical fibre sensing system

Optical fibre sensors can be classified as intrinsic, extrinsic or hybrid (Moghisi, 1989). In an intrinsic sensor the source and detector are connected by a continuous optical fibre. Modulation of the light is achieved within the fibre itself. In an extrinsic sensor the source light actually leaves the transmitting fibre before it is modulated. The same fibre, or a separate one, is used to return the modulated light to a detector. Extrinsic sensors, therefore, generally suffer from greater attenuation than intrinsic sensors, although there is a much greater variety of modulation schemes possible. Hybrid sensors use a conventional electrical transducer combined with optical fibre transmission by incorporating appropriate electro-optic and opto-electronic conversion (eg. Pilling, 1992). Such systems are often useful in electric power environments where the fibres provide isolation between live high voltage elements and control room instrumentation. Other advantages of optical fibre sensors were discussed earlier (**2.2.3**).

4.1.1 Sources

Optical light sources can be categorised as (Senior, 1992):

- Narrowband incoherent sources (light emitting diodes - LEDs).
- Monochromatic coherent sources (lasers, laser diodes).
- Wideband continuous sources (quartz tungsten halogen lamps).

Semiconductor sources, i.e. laser diodes and LEDs, are used extensively for optical fibre sensing applications. They are small, reliable and consume relatively little power. The main disadvantage with semiconductor sources is that they are affected by ambient temperature variations (Culshaw, 1984). Thus, systems using these sources often need to incorporate a temperature compensation facility. Lasers can provide a coherent high power output with a very high bandwidth (GHz). However, their use in optical fibre sensing is limited due to their cost and large size. For sensing applications which involve modulation of the source light spectrum, wideband sources, such as quartz tungsten halogen lamps, offer good stability and relatively high optical power over a broad spectral range.

Table 4.1 (Moghisi, 1989) summarises the performance characteristics of the sources described above.

Table 4.1

Parameter	LED	LD	Other lasers	Filament lamp
Phase shift	N/A	10^{-6} to 10^{-7} Hz	N/A	N/A
Line width	20 to 100nm	0.01nm typ.	<0.001nm	(see fig.4.16)
Lifetime	Years	Years	Years	10,000hrs
Wavelength	550 to 1500nm	680 to 1550nm	632 (He-Ne)	400-10000nm
Max. power	10s mW	100s mW	mW to 10W	~1kW
Temp range	-55 to 125°C	various	N/A	N/A
Efficiency	60 to 80%	40 to 60%	few %	~50%
Power i/p	2V, 10mA	12V, 0.5A	240V, mW	150W, 20V

4.1.2 Optical fibres

There are essentially three types of optical fibre; multimode step index, multimode graded index and single mode step index fibre. The structure and transmission characteristics of each type is shown on fig.4.2 (Senior, 1992).

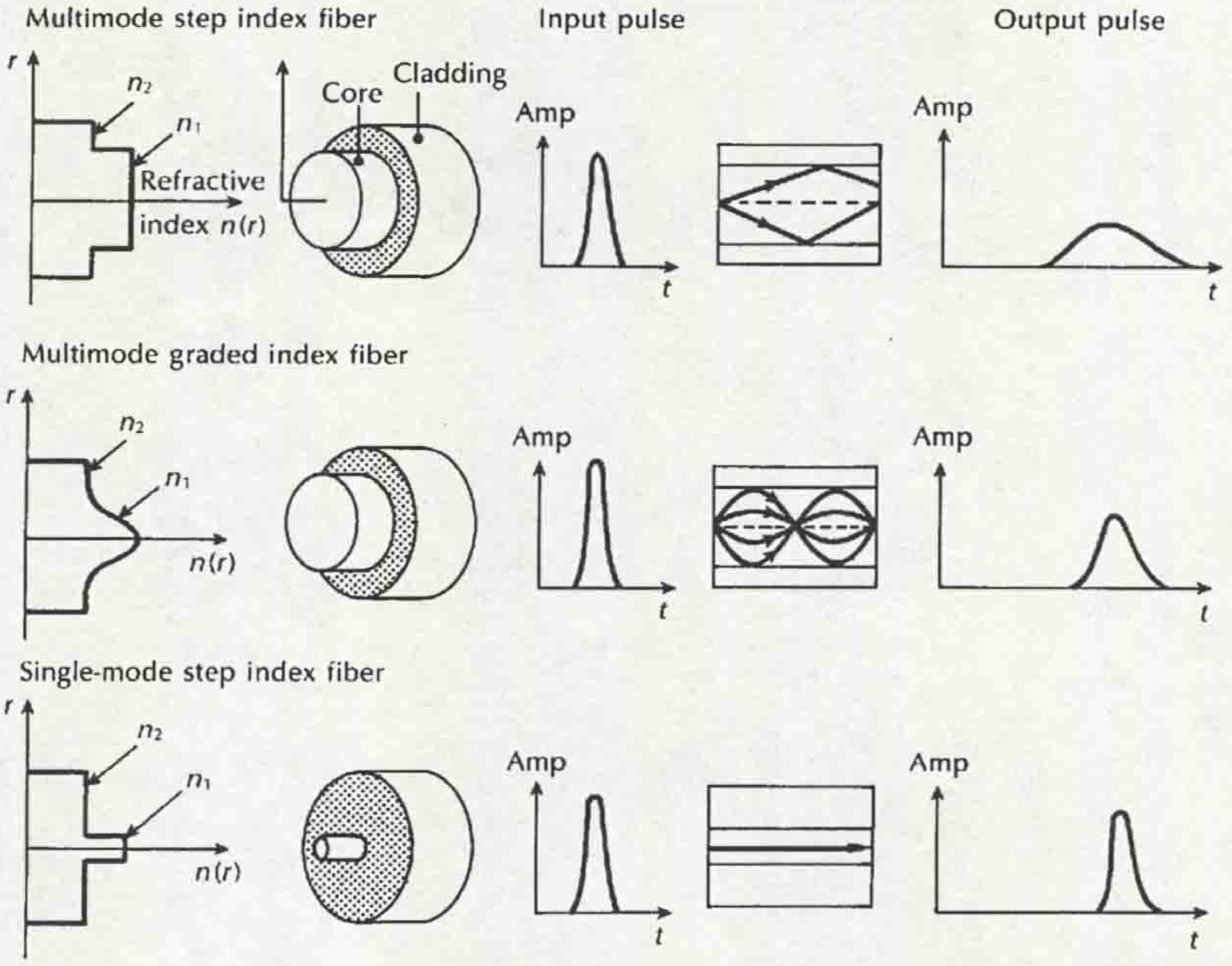

Figure 4.2 - Transmission characteristics of the three fibre types (Senior, 1992)

Multimode step index fibres consist of a core of constant refractive index n_1 and a cladding of slightly lower refractive index n_2. Made from glass or doped silica, they have relatively large core diameters (50-400μm, typically) and large numerical apertures (0.16-0.5) to facilitate coupling to incoherent light sources such as LEDs and filament lamps. Multimode step index glass fibre are best suited to short haul, limited bandwidth and relatively low-cost applications. Their use is widespread in optical fibre sensing systems.

Multimode graded index fibres have a radial refractive index variation, as shown on fig.4.2. The gradual decrease in refractive index from the centre of the core means that, although rays travelling close to the fibre axis have shorter paths than those in the outer regions, the higher refractive index on the axis causes these rays to travel at a lower velocity than the more extreme rays, thus reducing signal dispersion and increasing the bandwidth capability. Core diameters are typically 30-

100μm, with numerical apertures from 0.2-0.3. They are commonly used in medium haul, medium to high bandwidth applications, using incoherent and coherent multimode sources (LEDs and lasers).

Single-mode step index fibres have a very small cored diameter (typically 5-10μm), with a correspondingly low numerical aperture of 0.08-0.15. They are used to preserve the coherence of laser sources and possess high bandwidth capability, since ray transmission occurs along the axis of the fibre only and signal dispersion is, therefore, very low. Their use in optical sensing is limited to phase-modulated sensors, where preservation of source coherence is necessary. In communications, they are used for high bandwidth, very long haul applications, using laser sources.

Typical performance characteristics of the fibres discussed above (glass/silica core) are shown in table 4.2.

Table 4.2

Fibre type	Core diameter	N.A.	Attenuation	Bandwidth
Multimode step index	50-400μm	0.16-0.5	2.6-50dB/km	6-50MHz km
Multimode graded index	30-100μm	0.2-0.3	2-10dB/km	0.3-3GHz km
Single-mode step index	5-10μm	0.08-0.15	2-5dB/km	0.5-40Ghz km

Optical sensing applications, which require a large diameter output beam and/or greater optical power transmission, often employ glass fibre bundles. A fibre bundle consists of a large number of small diameter fibres (typically 100μm core, multimode step index) packed together to provide an overall diameter of, typically, 2mm. A bifurcated fibre bundle is split into two tails (often one for source, the other for detector), usually containing a random distribution of fibres in each tail, with respect to the common end.

4.1.3 Detectors

Photodetectors convert the received optical signal into an electrical signal, which can then be amplified and further processed using suitable circuitry. The choice of photodetector for a particular application depends on the available optical signal power, the optical background level and the required signal-to-noise ratio (SNR) (Culshaw, 1984). Semiconductor detectors include the PIN photodiode, avalanche photodiode (APD) and the photoconductor. Other detectors include the photomultiplier tube (PMT).

The silicon PIN diode (fig.4.3) is the most commonly used photodetector, with a useful wavelength detection range of, typically, 400 to 1600nm. It has a high bandwidth (≥1GHz) and a small temperature coefficient. Further, it possesses good linearity and is simple to use. The absence of internal gain means that PIN diodes require an incident radiation of, typically, ≥100nW.

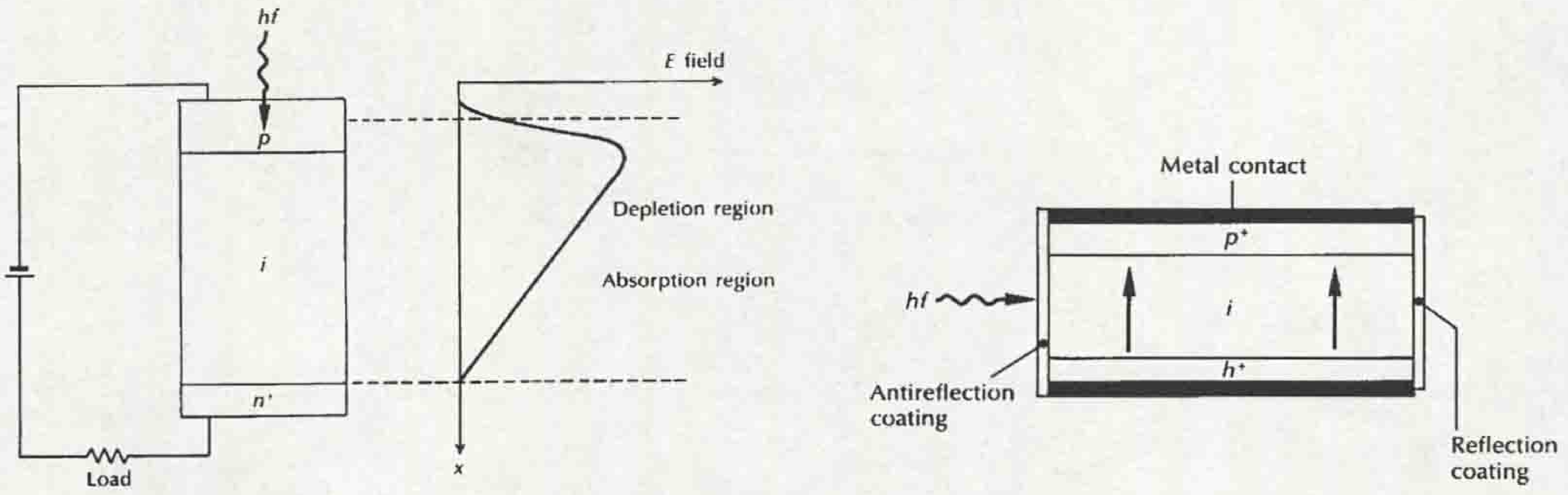

Figure 4.3 - Structure and characteristics of a silicon PIN photodiode

APDs can detect lower incident powers than PIN diodes due to an internal gain mechanism, caused by an extremely high electric field region (~3×10^5Vcm^{-1} - Senior, 1992) created by the more sophisticated structure on fig.4.4. They can operate over a similar wavelength range and bandwidth. However, they require temperature compensation and a relatively high operating voltage (~200V). APDs are principally used in long-haul communications systems; they are generally only used for sensing purposes when the received SNR is inadequate for a PIN diode.

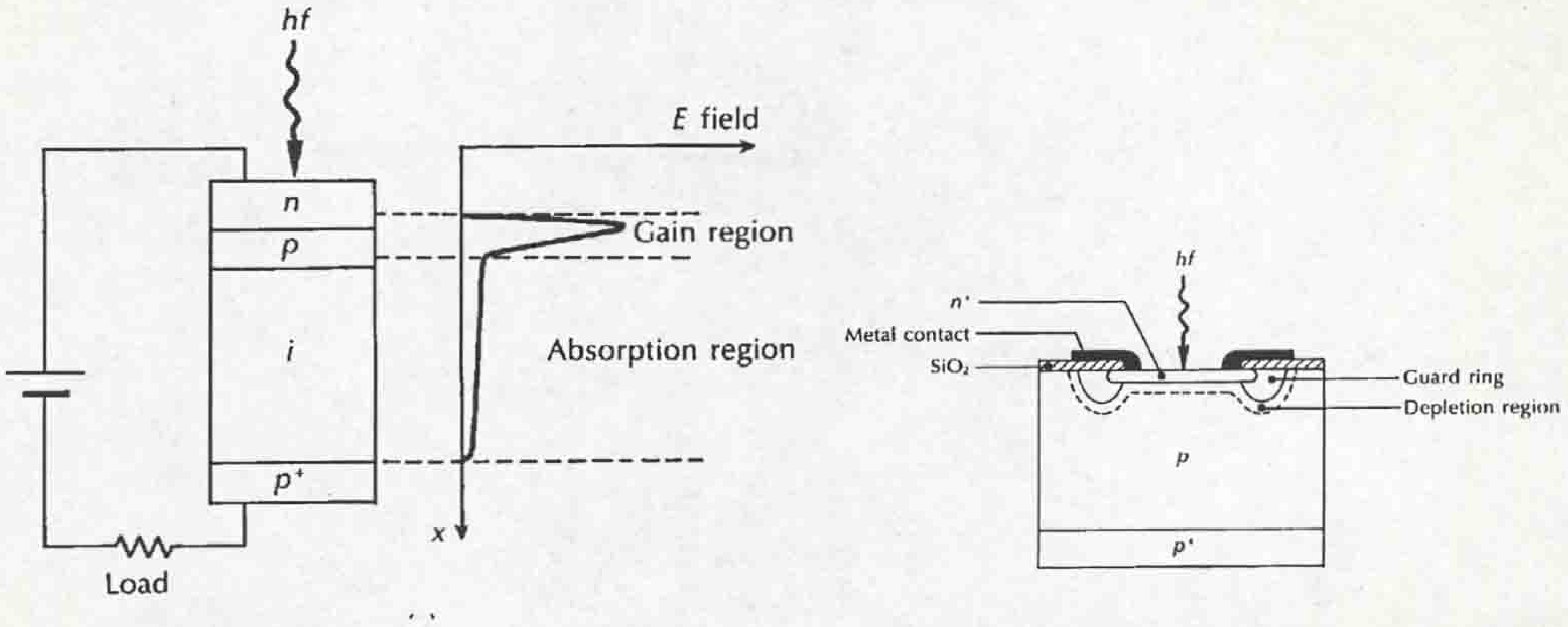

Figure 4.4 - Structure and characteristics of a silicon avalanche photodiode

A typical photoconductor structure is shown on fig.4.5. In operation the incident light upon the channel region is absorbed, thereby generating additional electron-hole pairs. These photogenerated carriers increase the channel conductivity, which results in an increased current in the external circuit. Photoconductors can detect a wider range of wavelengths than PIN diodes and APDs (up to tens of microns). They are usually only used for mid to far infra-red applications where diode detectors are not available. Therefore, they require cooling to reduce noise and improve the detector resolution.

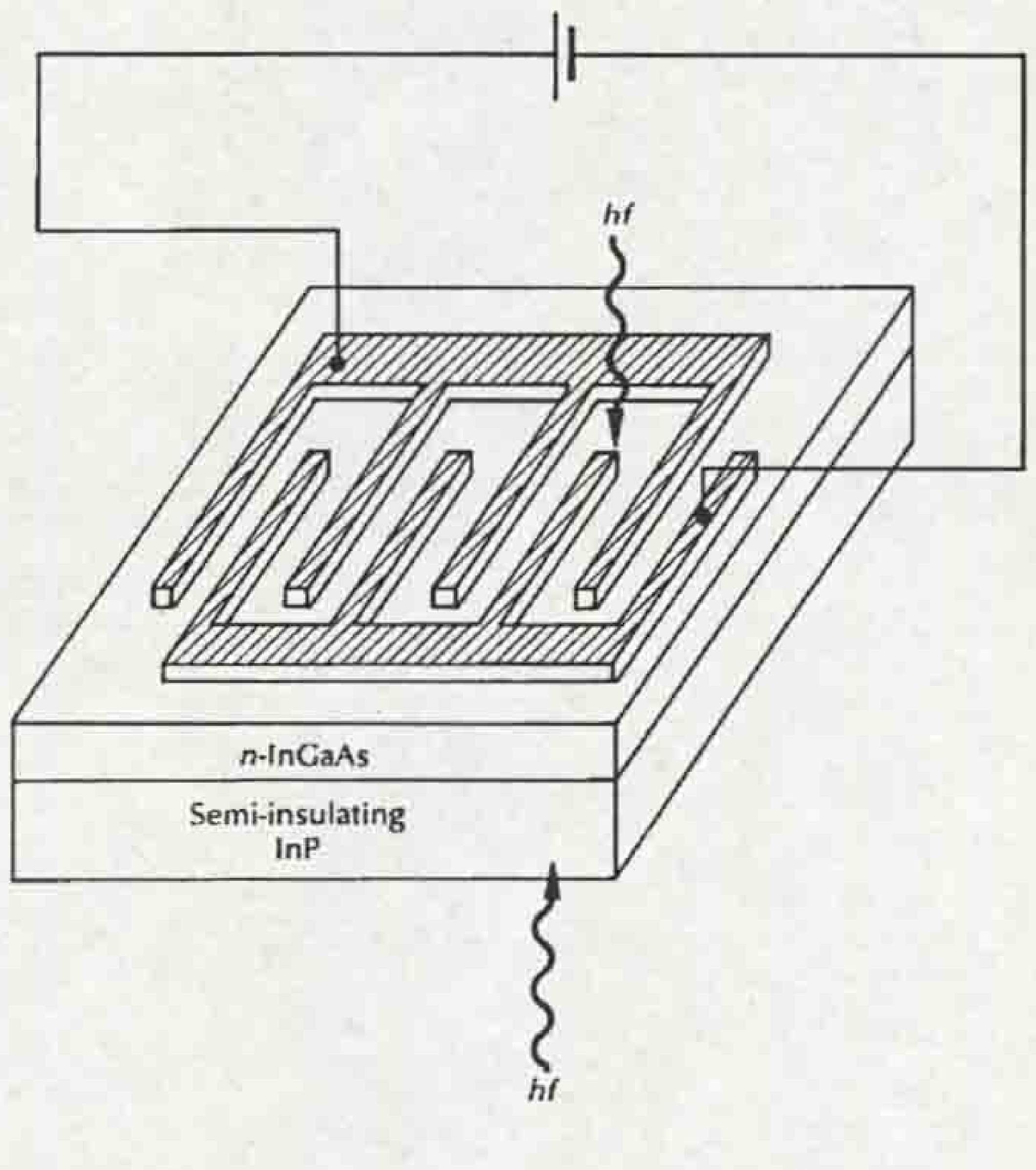

Figure 4.5 - Typical photoconductive device structure

Photomultiplier tubes are extremely sensitive, low noise devices, which can detect incident radiation as low as 1 photon/sec. They consist of a vacuum photodiode and an electron multiplier in the same envelope (fig.4.6). The electron multiplier amplifies the photocurrent by secondary emission. PMTs are generally only used for incident radiation ≤1nW over a wavelength range of, typically, 300 to 1000nm. The disadvantages of the PMT are the high operating voltage requirement (kilovolts), relatively large size, fragile nature and cost.

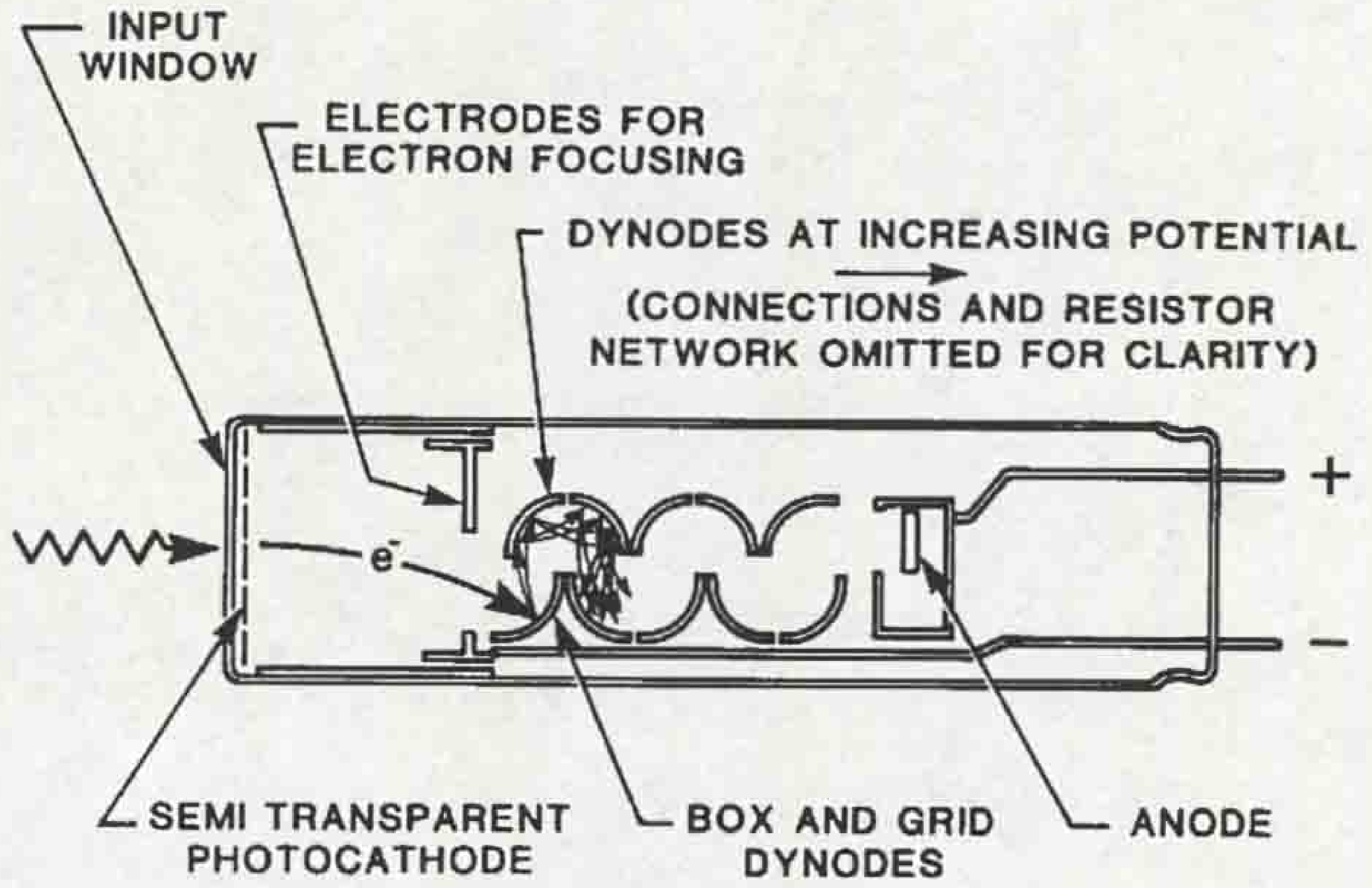

Figure 4.6 - Structure of a photomultiplier tube

Table 4.3 (Culshaw, 1984) summarises the performance characteristics of the detector types described above.

Table 4.3

Device	Power Detection	Wavelength range (μm)	Quantum Efficiencies	Frequency Response
PIN	P>100nW	0.4-1.6	Over 50%	Up to 1GHz
APD	P<100nW	0.8-0.9 1.3-1.5	Over 50%	Up to 1GHz
Photoconductor	P~10^{-18}W	To tens	Can be >50% Usually less	100MHz available
PMT	P~10^{-19}W	0.3-1.0	Low, typically below 10%	100MHz possible

4.1.4 Modulation schemes

Rather than discuss individual examples of modulators, of which there are a large number of possibilities, it is convenient to discuss the methods of modulation available. Sections **4.1.4.1** to **4.1.4.4** review conventional modulation methods. Later, section **4.3** introduces a more recent modulation concept, chromatic modulation (Jones *et al*, 1987), which was used in this project.

4.1.4.1 Intensity modulation

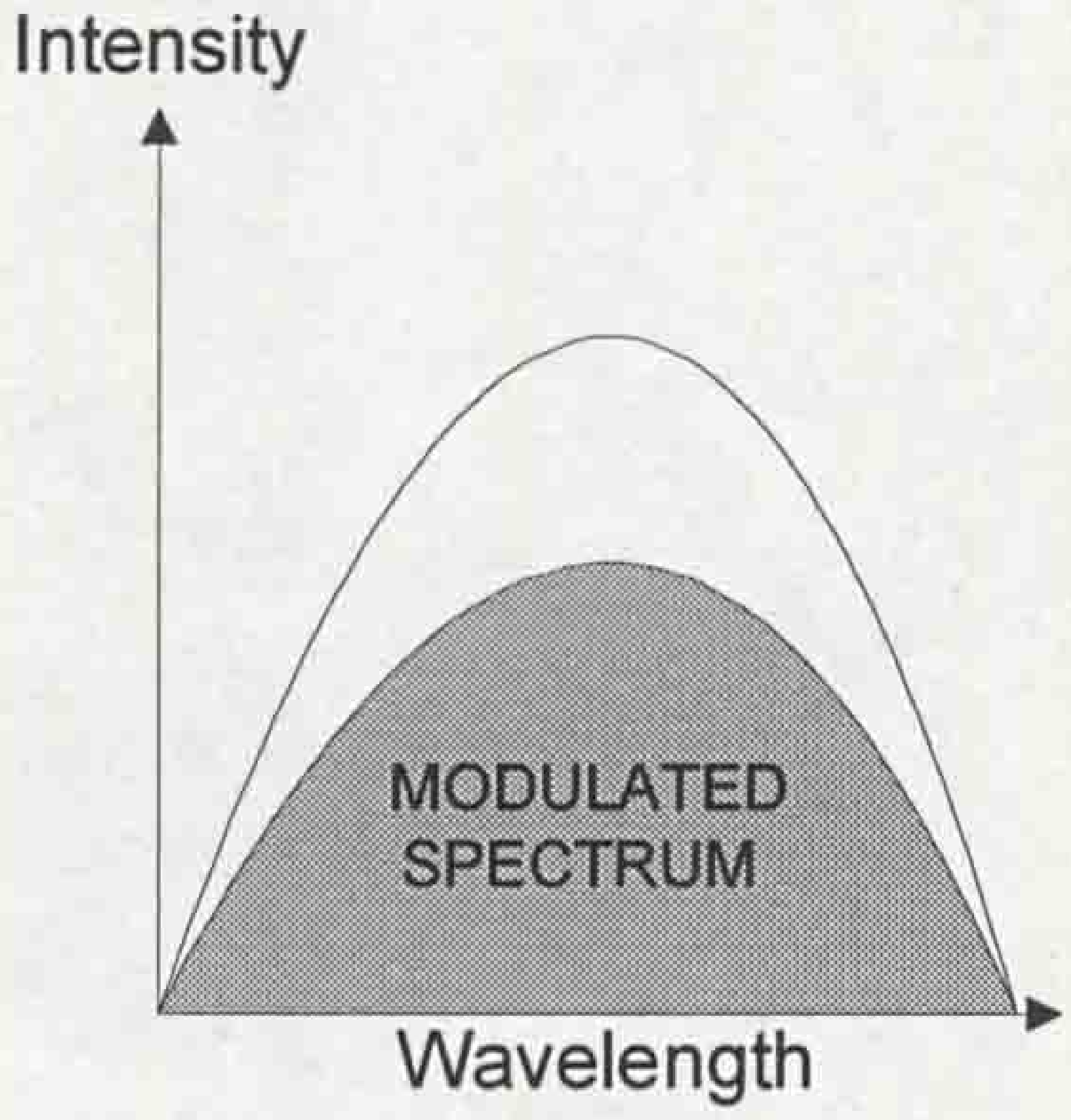

Figure 4.7 - Effect of intensity modulation

Referring to fig.4.7, intensity modulation involves the attenuation of an optical signal between the source and detector, the extent of modulation being related in some way to the external measurand. Intensity modulated sensors may be intrinsic or extrinsic.

Extrinsic modulation occurs when the signal is attenuated outside the optical fibres. The simplest arrangement to achieve this involves the lateral or longitudinal displacement of a source fibre relative to a receive fibre, as in fig.4.8 (Krohn, 1992).

The use of modulating masks between fixed fibres has proved a popular method of extrinsic intensity modulation. Simple shutters (eg. Roos *et al*, 1985) and focusing/defocusing spheres (Dotsch *et al*, 1983) are examples of intensity modulating masks. A further method is using reflective techniques (Bejczy *et al*, 1980 and Krohn, 1984). Here, the signal is modulated by rotation or retraction of a mirror, the source and receive fibres located on the same side of the reflector.

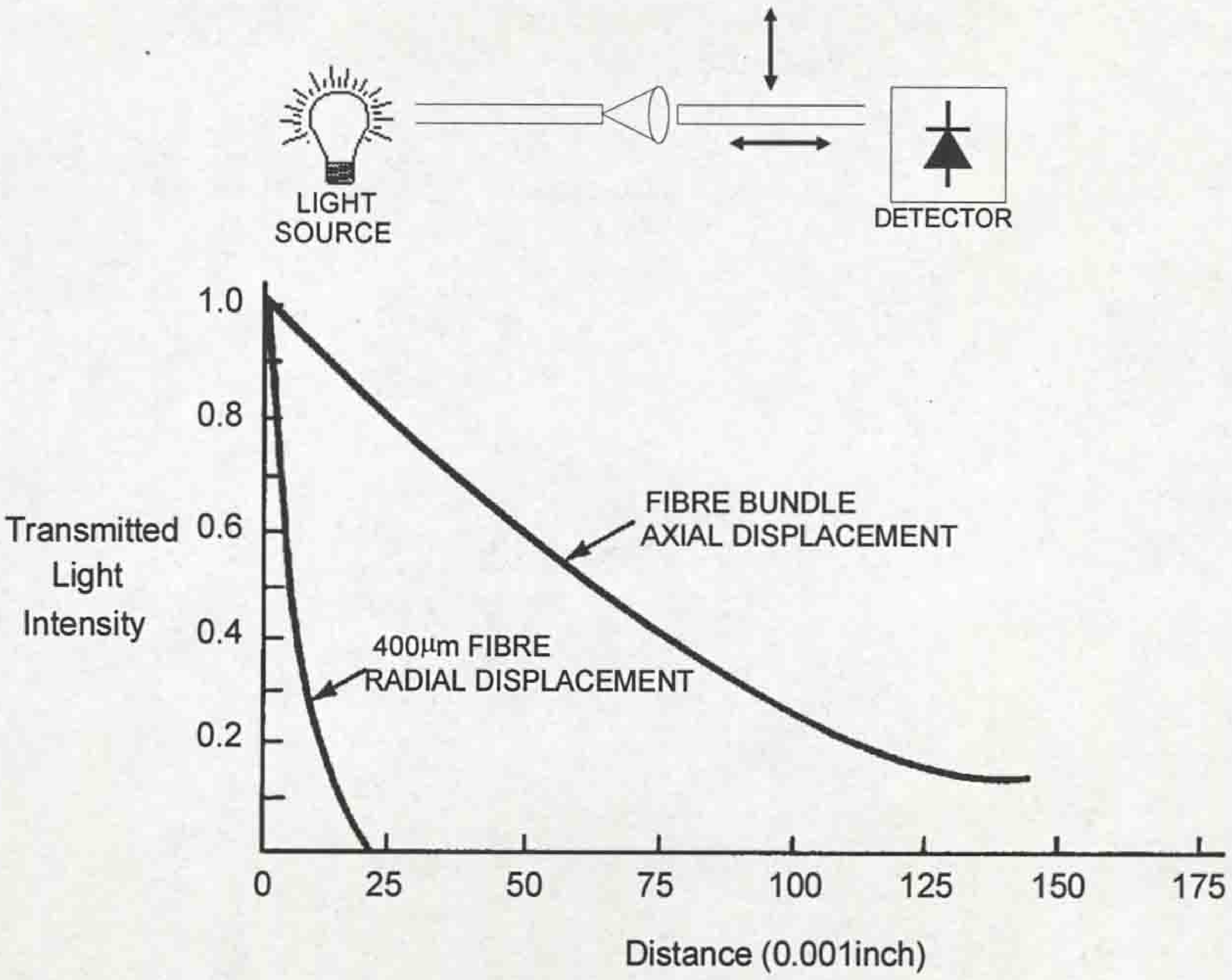

Figure 4.8 - Intensity effect of displacing two fibres with respect to each other (Krohn, 1992)

Intrinsic intensity modulation, where the light is modulated within the fibre, has been achieved using fibre microbending to measure strain (Asawa *et al*, 1982). Also, temperature measurements have been made intrinsically (Gottleieb and Brandt, 1983), using temperature induced changes to the refractive index of a fibre cladding.

Intensity modulation is the simplest method to use for sensing and has been employed in a wide range of optical fibre sensing applications. However, it is difficult to discriminate between intensity changes caused by the external measurand (eg. displacement, temperature, pressure) and spurious intensity changes caused by, for example, source drift and mechanical fibre disturbance (Dakin, 1984). For circuit breaker diagnostics, in particular, there are additional, undesirable, intensity changes caused by contamination of sensor surfaces with particles produced from arcing and direct arc radiation infiltrating exposed optical elements. Compensation schemes have been devised (eg. Jones, 1983 and Ostrowsky *et al*, 1990) to reduce errors caused by spurious intensity changes.

4.1.4.2 Phase modulation

The phase angle ϕ, for a light wave travelling in a fibre, is defined in fig.4.9. The phase angle for a lightwave with a given wavelength, λ, having propagated a distance L, is given by

$$\phi = \frac{2\pi L}{\lambda} = \frac{2\pi n_1 L}{\lambda_0} \tag{4.1}$$

where n_1 is the refractive index of the fibre core and λ_0 is the wavelength of light in vacuum. A change in path length and/or refractive index will cause a phase change as defined by the following equation

$$\phi + \Delta\phi = \frac{2\pi}{\lambda_0}\left(n_1 L + n_1 \Delta L + L \Delta n_1\right) \tag{4.2}$$

Assuming that the refractive index does not change, then eqn.4.2 will simplify to

$$\phi + \Delta\phi = \frac{2\pi}{\lambda_0}\left(n_1 L + n_1 \Delta L\right) \tag{4.3}$$

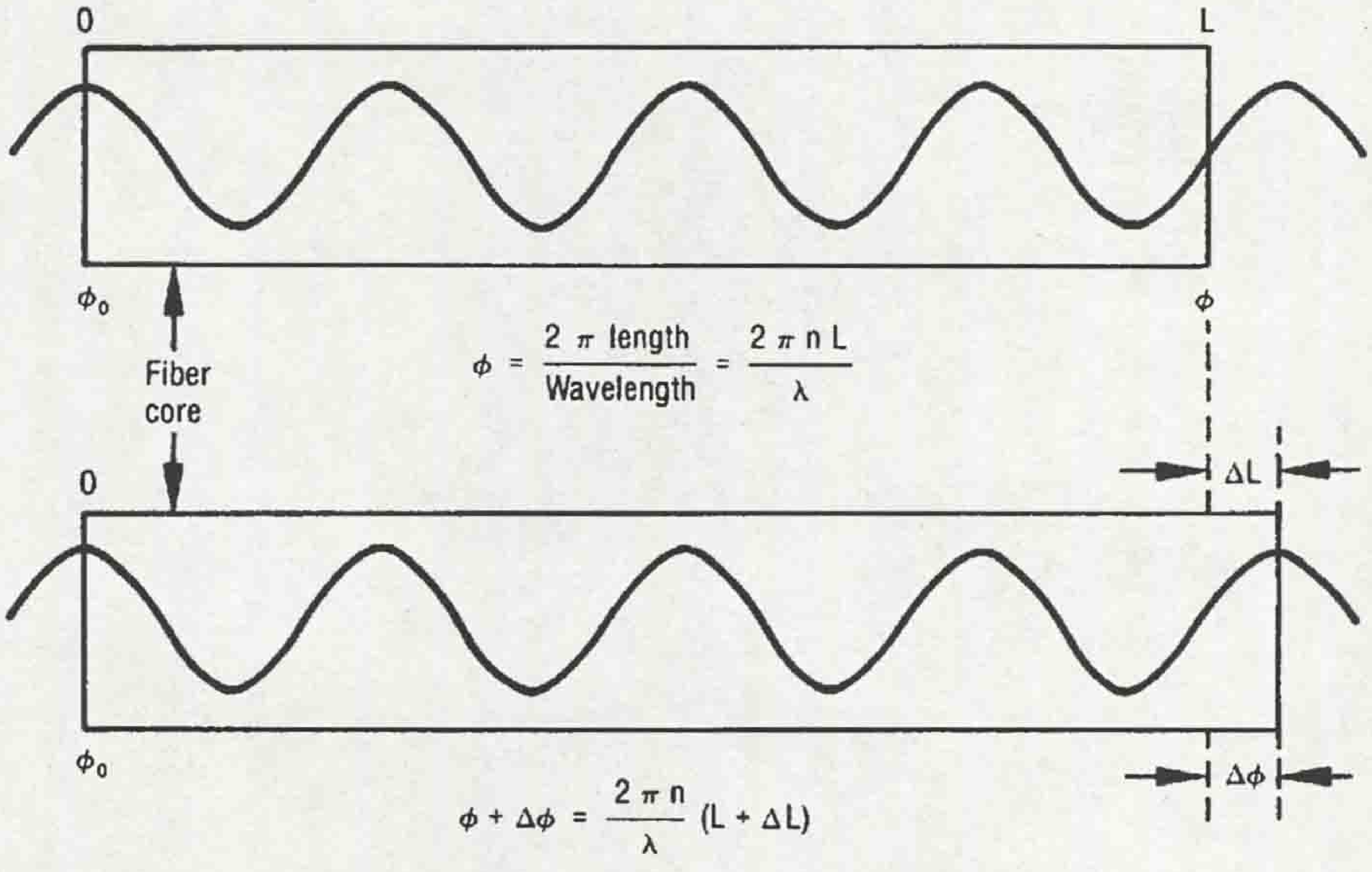

Figure 4.9 - Phase change of a light wave through an optical fibre of original length L that has been stretched by a length ΔL (Krohn, 1992)

An example of how this effect is utilised in optical sensing is the Mach-Zehnder interferometer (fig.4.10). It consists of two fibres, a reference fibre and a sensing fibre. If the sensing fibre is unperturbed, then the optical path lengths in both fibres have the same value L. In this case the outputs of the two fibres interfere constructively and give the maximum intensity output. If the sensing fibre experiences a mechanically or thermally applied strain, the sensing fibre increases in length by ΔL. Under such circumstances the intensity output decreases due to destructive interference. A modulation of 100% occurs over 1/2 wavelength of light change in fibre length. This sensitivity allows movements as low as 10^{-13} metres to be detected. Other interferometric configurations include the Michelson, the Fabry Perot and the Sagnac (Krohn, 1992 and Culshaw, 1984).

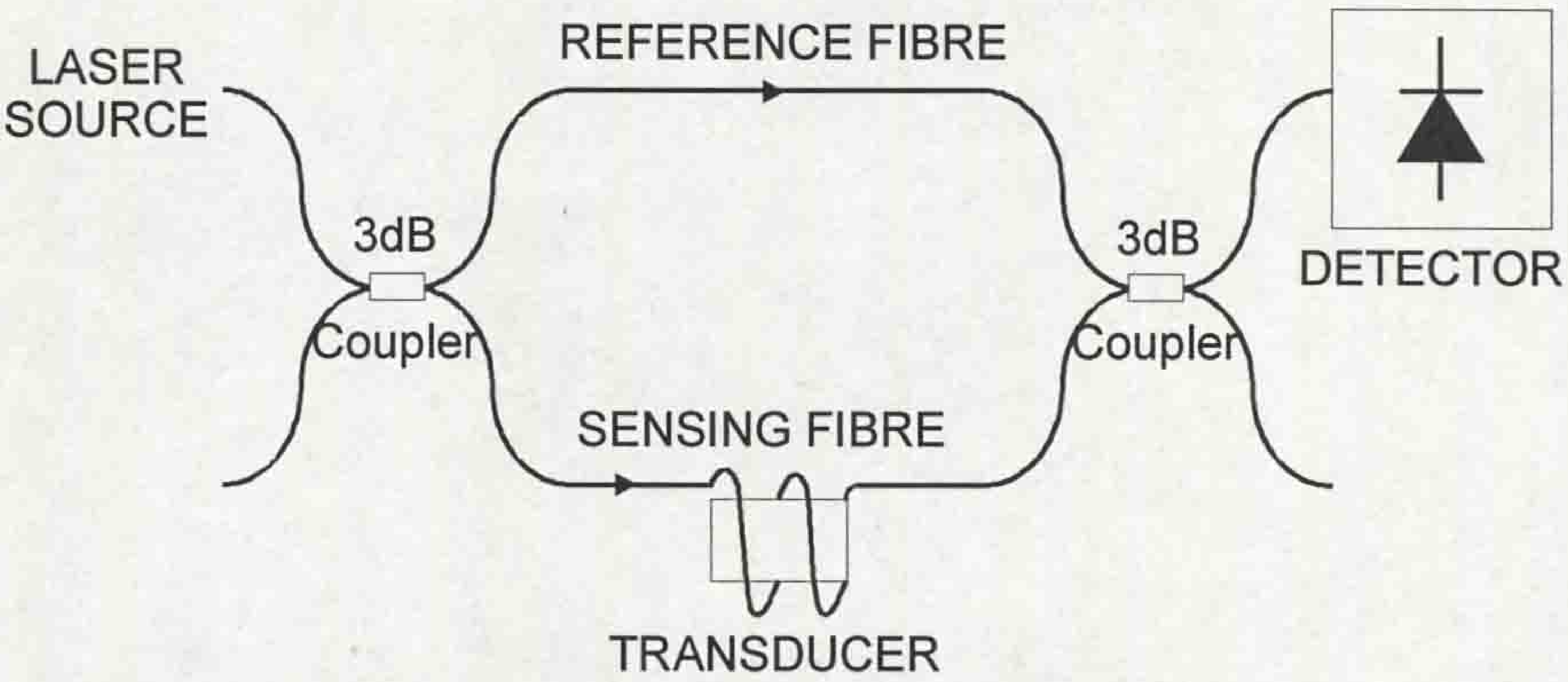

Figure 4.10 - Mach-Zehnder interferometer configuration

Phase modulated sensors have been used for temperature, pressure and strain measurements, and also electric and magnetic fields (Moghisi, 1989). Sagnac interferometers, in particular, have found an application in optical fibre gyroscopes (Bergh, 1984). However, the complexity of phase modulated sensors and their susceptibility to temperature and vibration effects reduce their suitability for circuit breaker research.

4.1.4.3 Wavelength modulation

If a broadband light source (eg. quartz tungsten halogen lamp) is passed through a narrowband optical filter, such that a particular wavelength is transmitted (in practice a narrow band of wavelengths), and this wavelength varies due to the effect of the external measurand on the optical filter, then wavelength modulation is said to occur. The effect is shown on fig.4.11.

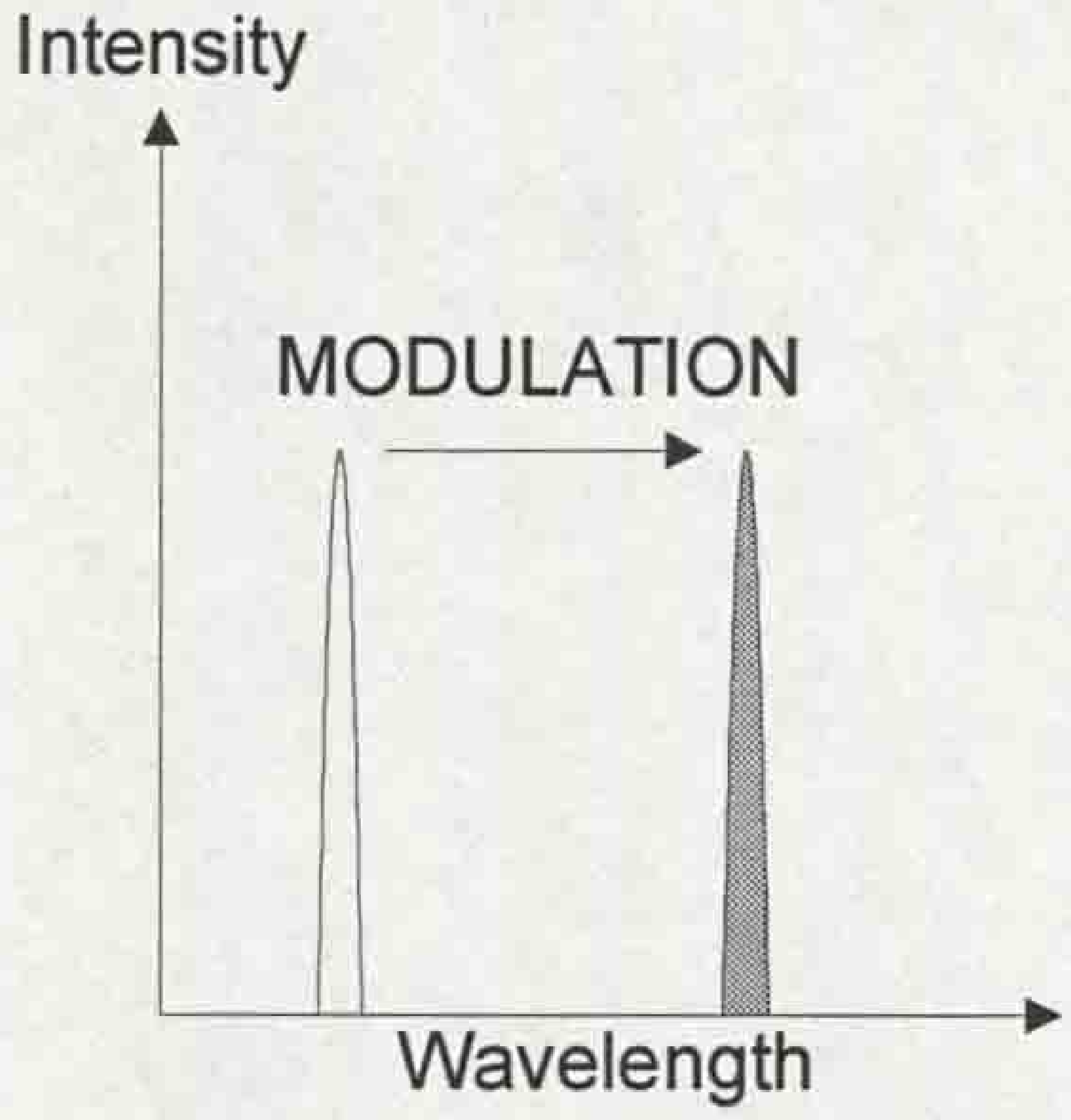

Figure 4.11 - Effect of wavelength modulation

Wavelength modulation has been used for temperature measurement (McNutt *et al*, 1984), where modulation is achieved by a temperature induced fluorescent wavelength shift.

The advantage of wavelength modulation is the insensitivity to the effects of spurious intensity variations, since it is the wavelength, not the quantity of radiation being measured. However, it is an inefficient use of the available optical power as only a narrow band of wavelengths are utilised for any particular condition of the external measurand. Further, the expense associated with the wavelength detector, a spectrometer, means that this type of modulation can only be used for highly specialised applications, where cost is a minor design criterion.

4.1.4.4 Polarisation modulation

Natural light is unpolarised; it is a mixture of light polarised in different ways and to different degrees (Meyer-Arendt, 1984). These differences result because such light is emitted by atoms, or groups of atoms, most of them oscillating independently. If the electric field oscillates in a certain, constant orientation, the light is said to be linearly polarised (fig.4.12). In circular polarisation, the electric field vector no longer oscillates in a plane, as in linear polarisation. Instead, the vector is constant in magnitude and proceeds in the form of a helix around, rather than through, the axis of propagation. Elliptical polarisation is the most general type of polarisation, where circular and linear are the two extremes.

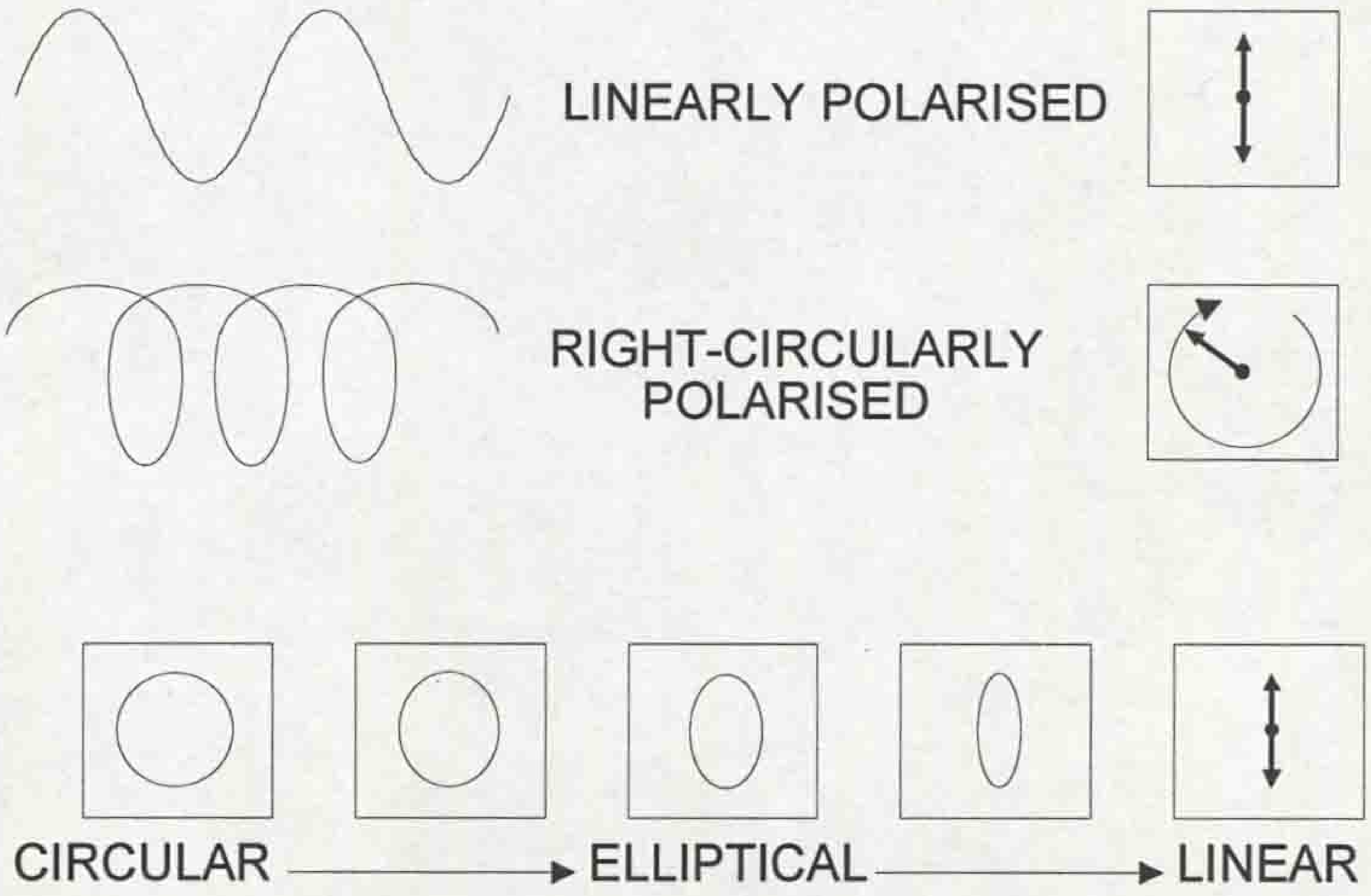

Figure 4.12 - States of polarised light

Polarised light may be modulated by using birefringence or rotation effects (Murphy, 1992). Electrically induced birefringence phenomena, such as the Pockel effect and Kerr Effect (Smith, 1988) are used in optical electric field sensors (Moghisi, 1989). The photoelastic effect is a mechanical stress-induced birefringence, which has been used for a variety of optical fibre strain sensors (eg Murphy, 1992 and Tranter, 1995). The Faraday magneto-optic effect is an example of light polarisation rotation, which has been used for optical fibre current sensors (Lewis *et al*, 1995). Polarisation modulation is often used as an intermediate step in an intensity modulated system by employing pre and post modulator polarisers at different angles, and, in such circumstances, the drawbacks of intensity modulation may apply.

4.2 SYSTEM DESIGN CONSIDERATIONS

When designing an optical system, whether for sensing or communication purposes, there are several important fibre transmission characteristics to be taken into account, but bandwidth and attenuation are the most significant.

4.2.1 Bandwidth

The system bandwidth is effectively determined by the lowest of each individual bandwidth of the source, detector and optical fibres. Sources and detectors can readily achieve bandwidths approaching 1GHz. The bandwidth of optical fibres can vary from (typical values) 10MHz.km for multimode step-index, to 1GHz.km for graded index, to 10GHz.km for single mode (Senior, 1992). Thus, in a communication system of appreciable length it is the optical fibres which determine the system bandwidth.

The bandwidth of the fibres is determined by optical dispersion effects, of which there are two types, intermodal and intramodal (or chromatic) (Senior, 1992). In a step index fibre low order propagation modes are excited by light rays entering at small angles to the fibre axis, while high order modes are excited by rays entering at large angles. Therefore, the higher the mode, the longer is the distance travelled by the ray inside the fibre and, consequently, the longer is the transit time. The difference in transit times between low and high order modes produces intermodal dispersion. Intermodal dispersion is high for step index fibre, but can be reduced by the use of graded index fibre, because the radially dependent refractive index reduces the difference in transit times between the high and low order modes (Jones, 1995). The use of single-mode fibre virtually eliminates intermodal dispersion, since their structure only allows the transmission of a single mode (excited by the ray propagating parallel to the fibre axis).

Intramodal, or chromatic, dispersion may occur in all types of optical fibre and results from the finite spectral linewidth of the optical source (Senior, 1992). Since all optical sources emit a band of frequencies then there may be propagation delays between the different spectral components of the transmitted signal. This causes broadening of each transmitted mode, known as intramodal dispersion. This effect is greatest for broad spectral sources and least for lasers.

Bandwidth is a factor which is usually more critical for communications, rather than optical sensing systems. Optical sensing often considers the effect of a modulator on a stabilised D.C. source with sampling frequencies which rarely extend to MHz. Thus, for optical fibre sensing, bandwidth is not usually a design problem.

4.2.2 Attenuation

In 1970 the emergence of an optical fibre with a total attenuation of below 20dB/km (Kapron *et al*, 1970) represented a major breakthrough in optical fibre development. Since then further improvements in optical fibres have produced better attenuation characteristics than the competing metallic conductors (~5dB/km) to the point that recent silica based glass fibres have achieved an attenuation of <0.2dB/km (Nagel, 1987). For this discussion it is convenient to class the type of attenuation as intrinsic i.e. caused by the fibre itself, or extrinsic i.e. occurring external to the fibre at, for instance, a coupling.

4.2.2.1 Intrinsic attenuation

Fig.4.13 shows an attenuation spectrum for a typical low loss fibre. Absorption and scattering effects are responsible for the attenuation spectra produced by fibre manufacturers (Senior, 1992).

Ultraviolet absorption is caused in pure glass by electron transitions to higher energy levels within the glass, while infra-red absorption occurs due to longer wavelength radiation being absorbed by molecules to excite them to higher energy levels. The UV and IR absorption effects are increased by transition metal impurities in the glass. Their boundaries can be seen in fig.4.13. Another significant impurity is the OH ion produced by water absorbed in the glass. This has a vibration corresponding to wavelengths between 2.7 and 4.2μm with overtones that extend to the usual working wavelength range, one of which can be seen in fig.4.13.

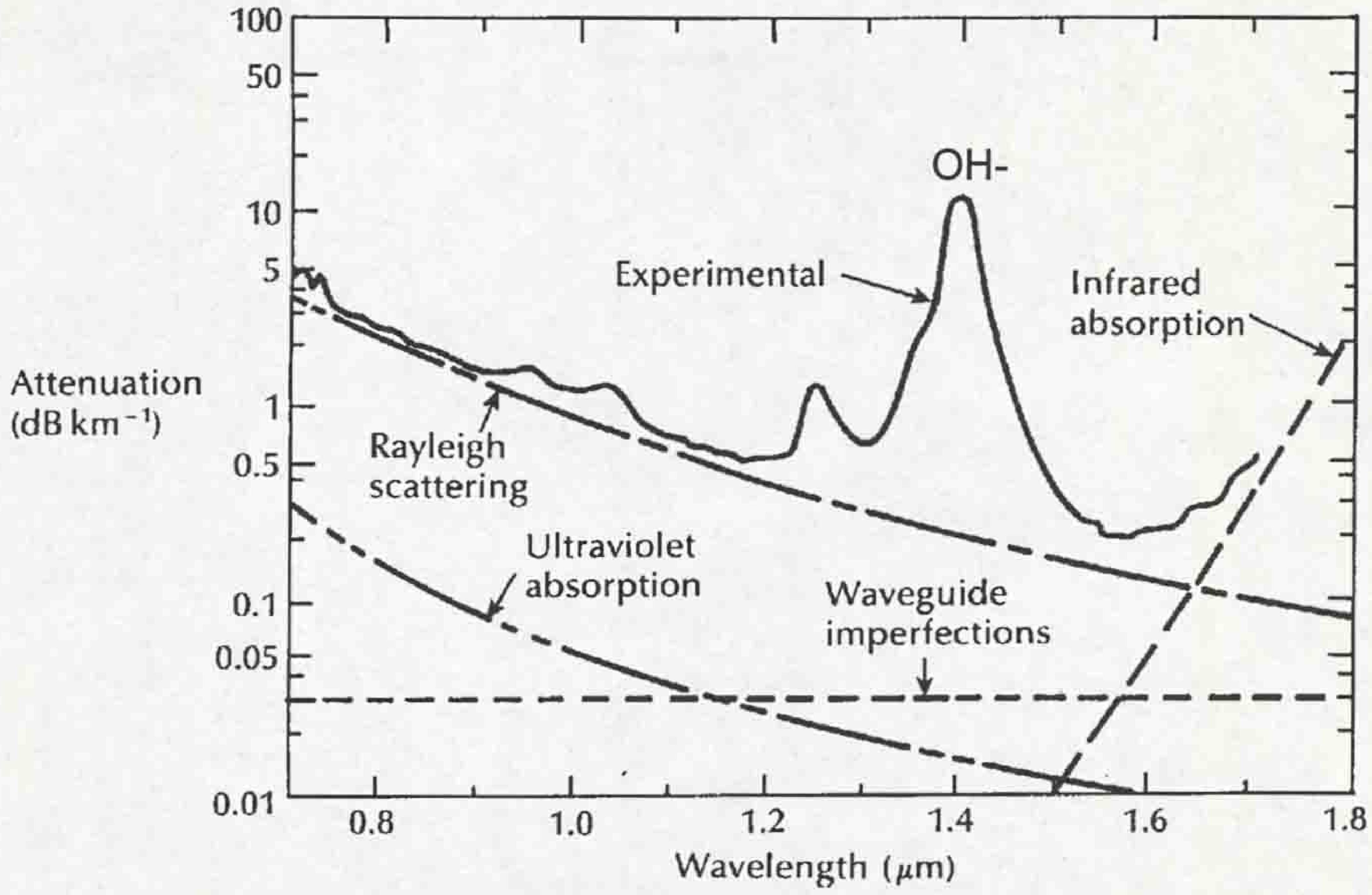

Figure 4.13 - Typical attenuation spectrum for a low loss fibre (Senior, 1992)

Material scattering entails linear and non-linear scattering. Linear scattering causes some or all of the optical power contained within one propagating mode to be transferred, proportional to the mode power, into a different mode. The attenuation occurs due to the transfer being made to a mode which is subsequently lost from the fibre. Linear scattering occurs due to imperfections within manufactured fibres. In Rayleigh scattering the imperfections are small compared to the light wavelength and the attenuation is proportional to $1/\lambda^4$ (Olshansky, 1979). For imperfections which are comparable to the wavelength Mie scattering occurs. Non-linear scattering, such as stimulated Brillouin and stimulated Raman scattering, causes the transfer of power from one mode to either the same mode or another, but at a different frequency (Senior, 1992).

Optical fibres can also suffer intrinsic attenuation due to bending losses, which may be macrobending or microbending losses (Jones, 1994). In macrobending, the attenuation occurs as a result of the transition of high order modes in the core to the cladding as the corresponding rays exceed the critical angle for total internal reflection (Murphy, 1992). Microbending loss occurs at very small periodic bends, typically with separations of ~mm. Such bends can be introduced during the fibre production process or during handling. Losses arising from microbending can be appreciable; for example, tightly winding a drum of 3dB/km fibre may increase its losses to over 20dB/km (Culshaw, 1984).

4.2.2.2 Extrinsic attenuation

Extrinsic attenuation is caused by fibre connection losses. These occur at source-fibre, fibre-modulator, fibre-detector and fibre-fibre connections. Losses at the first three types of connection are generally system specific. Losses due to fibre-fibre connections can occur due to the use of different fibre types, with incompatible core diameters or numerical apertures, or mechanical misalignment of the fibres. The misalignment losses may be longitudinal (~0.01dB/μm), lateral (~0.1dB/μm) or angular (~0.2dB/°) (Murphy, 1992).

Even assuming a perfectly symmetrical joint between the two fibres there will still be attenuation caused by Fresnel reflection (Senior, 1992), where some of the light is reflected back into the transmitting fibre at the glass-air interface. Fresnel losses can be reduced by using index matching compound in the coupling.

4.3 CHROMATIC MODULATION

Chromatic modulation is a relatively recent optical modulation concept (Jones *et al*, 1987). It is described as "the utilisation of polychromatic light for sensing changes in a physical system". The mechanism of chromatic modulation can be explained by extending the theories of colorimetry using the human eye as a detector.

4.3.1 Traditional colorimetry

One of the most fascinating aspects of colorimetry is the fact that totally different spectra can give exactly the same appearance in terms of brightness and colour to the human eye. In fact this phenomenon of "metamerism" can yield an infinite number of different spectra which can appear to have the same colour (Stiles and Wysecki, 1962). The human eye simplifies the situation by interpreting any colour as the algebraic sum of three primaries, the choice of which is arbitrary. This is known as the "trivariance of vision" (Le Grande, 1968).

In 1931, the CIE (Commission Internationale de l'Eclairage), the body responsible for international recommendations for photometry and colorimetry, adopted the average results of different experiments performed by Wright (1929) and Guild (1931) on a total of seventeen humans to standardise colorimetry. For convenience, the three primaries chosen were red (700nm), green (546.1nm) and blue (435.8nm). It was found that the photometric amounts of each primary to exactly match the appearance of an equi-energy white light, S_E, which has an equal radiant energy across the visible spectrum, was as follows:

$$5.6508cd/m^2 WHITE \equiv 1.0000cd/m^2 RED + 4.5907cd/m^2 GREEN + 0.0601cd/m^2 BLUE \tag{4.4}$$

The extremely small amount of blue luminance in eqn.4.4 shows how intensely colourful blue appears to the eye. In order to standardise the equation so that the bias of any colour towards any of the primaries could readily be seen, new luminous units were chosen for each of the stimuli:

1 luminous unit of RED	$R = 1.0000cd/m^2$.
1 luminous unit of GREEN	$G = 4.5907cd/m^2$.
1 luminous unit of BLUE	$B = 0.0601cd/m^2$.
$\therefore$ 1 luminous unit of WHITE	$W = 5.6508cd/m^2$.

Now eqn.4.4 can be expressed more simply in terms of the tristimulus values, R,G and B:

$$W \equiv R + G + B \tag{4.5}$$

The experiments performed by Wright and Guild evaluated how much of each tristimulus value was required to produce a match to each monochromatic colour of the visible spectrum. These values, known as the spectral tristimulus values / colour matching functions / distribution coefficients, are shown in fig.4.14 (LeGrande, 1968 and Hunt, 1987).

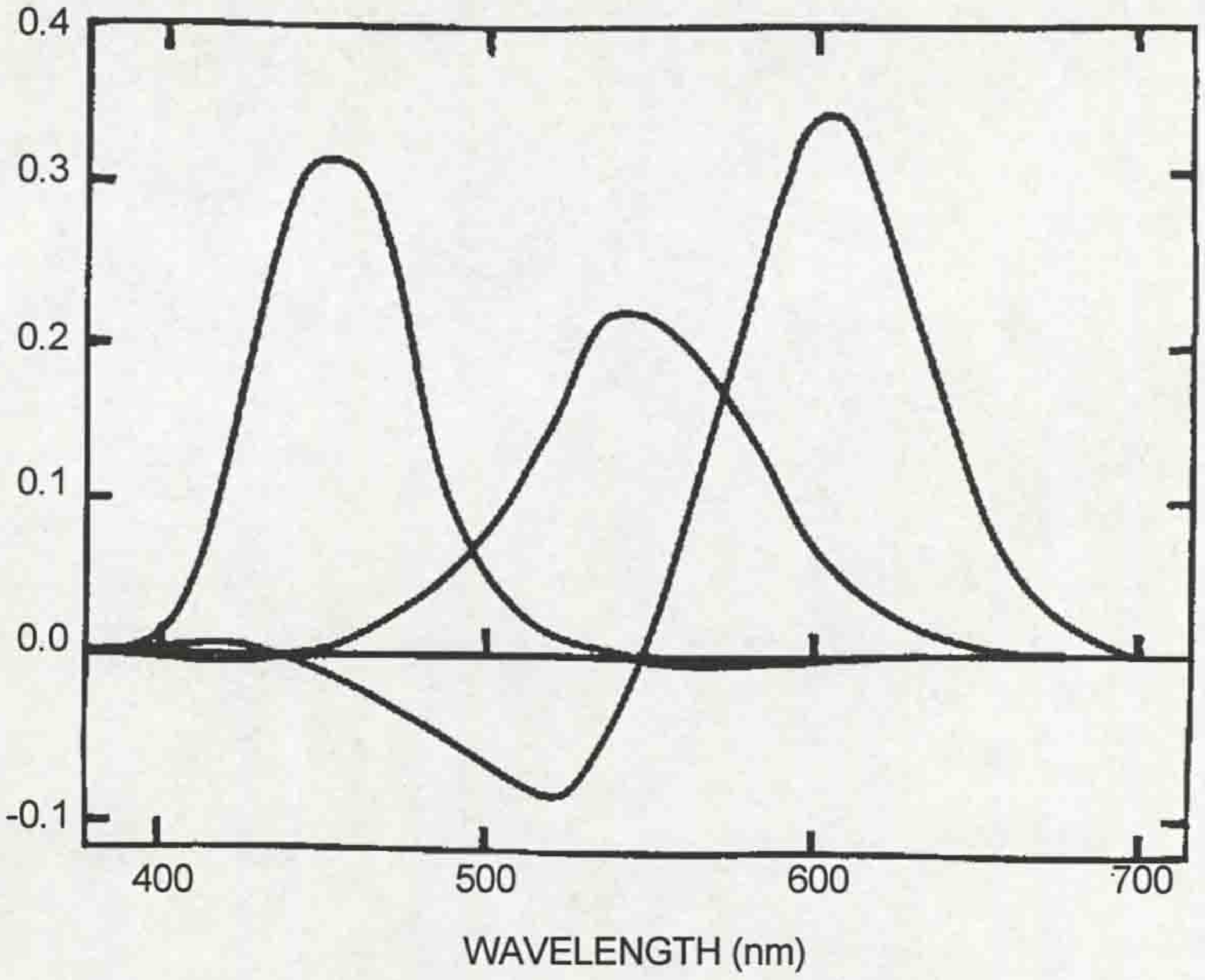

Figure 4.14 - Spectral tristimulus values for the RGB primary stimuli system (Hunt, 1987)

It can be seen that to obtain a tristimulus value of 1 (1 trichromatic unit, 1TU) of monochromatic 500nm, the tristimulus values are:

$$1(500nm) \equiv -1.1685R + 1.3905G + 0.7780B \tag{4.6}$$

The actual luminances of each primary are obtained by multiplying the tristimulus value by its corresponding luminous unit. Also, the luminance of the monochromatic 500nm must equal the sum of the three primary luminances. This yields:

$$5.2616cd/m^2(500) \equiv -1.1685cd/m^2 RED + 6.3834cd/m^2 GREEN + 0.0467cd/m^2 BLUE \tag{4.7}$$

The negative sign in these equations indicates that it is not physically possible to add red, green and blue light to get a match with 500nm. Rather, it is necessary to mix 1TU of monochromatic 500nm with 1.1685TU of red to get a match to the mixture of 1.3905TU of green and 0.7780TU of blue. Unfortunately, eqn.4.7 will always have a negative sign on the right hand side, according to fig.4.14. To avoid this, and consequent confusion, the CIE defined three imaginary primaries X,Y and Z, such that their tristimulus values are always positive, as in fig.4.15 (Padgham and Saunders, 1975).

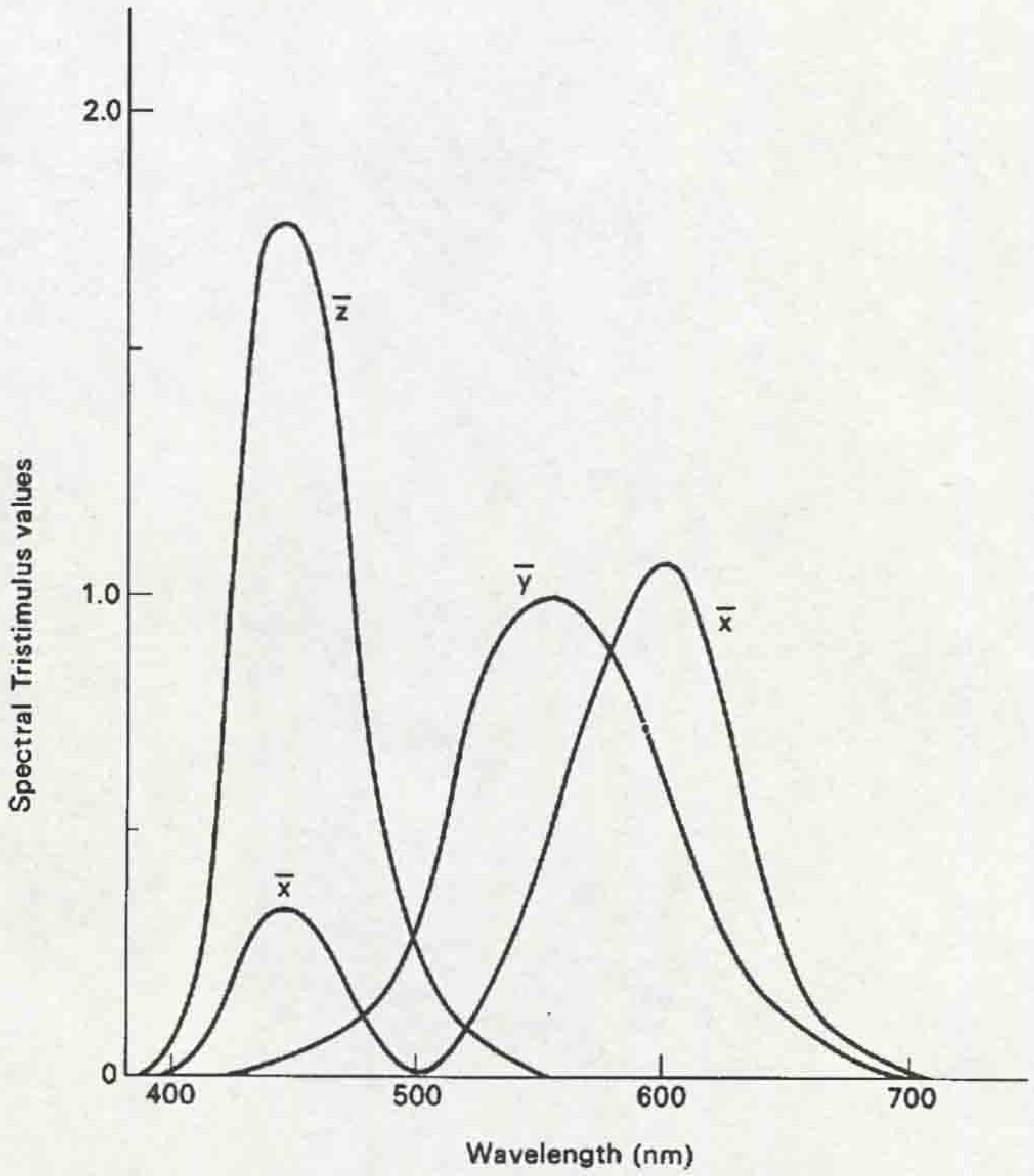

Figure 4.15 - Spectral tristimulus values for the XYZ primary stimuli system (Padgham and Saunders, 1975)

Generally, it is necessary to calculate the tristimulus values X,Y and Z to define the colour of a spectrum rather than a monochromatic light. This can be done simply with the following equation (Le Grande, 1968):

$$X = a \int \bar{x}(\lambda) E(\lambda) d\lambda \tag{4.8}$$

where $E(\lambda)$ is the spectral energy distribution of the light, a is a constant depending on the units chosen for $E(\lambda)$ and $\bar{x}(\lambda)$ are the spectral tristimulus values corresponding to primary stimulus X. Similar equations apply to the Y and Z tristimulus values.

4.3.2 Chromaticity

In general, the appearance of any light whatsoever can be exactly reproduced by the addition of a white light luminance and a monochromatic light luminance. This is an extension to the trivariance of vision. The wavelength of this monochromatic luminance is known as the dominant wavelength and the ratio of the monochromatic luminance to the total luminance defines the colorimetric purity (Hunt, 1987). Thus:

$$L_S(S) \equiv L_W(W) + L_\lambda(\lambda) \qquad (4.9)$$

where L_S is the luminous variable, λ the dominant wavelength and $p_c = L_\lambda / L_S$ the colorimetric purity. λ and p_c are known as the chromatic variables. In order to deduce the chromaticity of a light, in other words the objective colour content, the total luminance does not need to be known; it is the relative magnitudes of the tristimulus values that are important. The chromaticity co-ordinates are defined as:

$$x = \frac{X}{X+Y+Z} \qquad y = \frac{Y}{X+Y+Z} \qquad z = \frac{Z}{X+Y+Z} \qquad (4.10)$$

Since $x + y + z = 1$, it is only necessary to specify two chromaticity co-ordinates, x and y; z will automatically follow.

The CIE x,y chromaticity diagram (fig.4.16) is a colour map on which the chromaticities of all colours can be plotted. The equi-energy white light point S_E is marked (1/3,1/3). The point N is the position on the diagram of the achromatic point i.e. where white and shades of grey are located, with respect to the eye (equi-energy white light will actually appear pale blue to the eye). The curved boundary in the diagram is the line on which all the monochromatic colours lie, known as the spectral locus. The straight line connecting red and blue is the line containing pure purples.

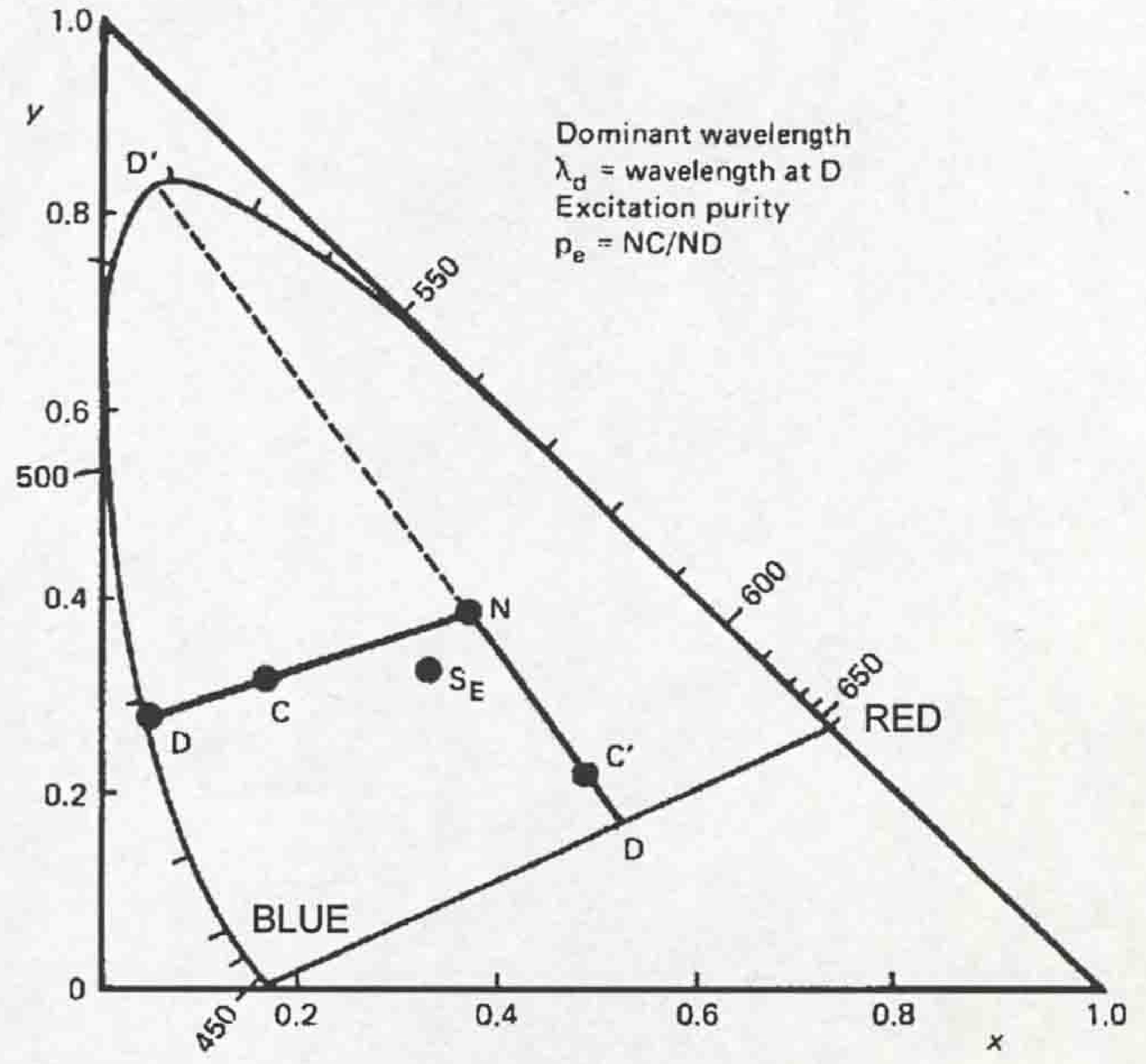

Figure 4.16 - The CIE x,y chromaticity diagram (Hunt, 1987)

Any colour on the diagram can be described chromatically by its dominant wavelength and its excitation purity (which is directly related to colorimetric purity). Consider the colour C on the diagram. The dominant wavelength can be found by drawing a straight line from the achromatic point through C, extended to the spectral locus, where the dominant wavelength will be at D. This dominant wavelength is defined relative to the white point N; the dominant wavelength could also be given relative to S_E if desired. The excitation purity is defined by the ratio of lengths NC/ND. It is a useful indication of how "saturated" a colour is i.e. how close it is to being monochromatic.

The essence of chromatic modulation is to modulate a broadband white light source such that a colour change (dominant wavelength and/or purity) occurs upon the action of the external measurand. The use of spectrally overlapping tristimulus photodiodes, which mimic the spectral tristimulus values of the eye, allows a relationship between colour - more strictly chromaticity, since colour is a subjective interpretation, whereas chromaticity is an objective quantification of colour - and the external measurand to be obtained.

4.3.3 Distimulus colorimetry

For the purposes of optical fibre sensing it is often not necessary to calibrate an external measurand, such as displacement, pressure or temperature, against two variables. The system can be simplified so that only one chromatic variable is produced (the dominant wavelength), which can then be related to the external measurand. If a distimulus arrangement is used i.e. only two overlapping detectors instead of three, then one of the previous tristimulus values, say Z, becomes redundant and can be made equal to zero. Eqns.4.10 now become:

$$x = \frac{X}{X+Y} \qquad y = \frac{Y}{X+Y} \tag{4.11}$$

Since x + y = 1, only one variable, x or y, is sufficient to define the distimulus chromaticity of a colour. The CIE x-y chromaticity diagram now reduces to a one dimensional straight line as in fig.4.17 (Jones *et al*, 1987).

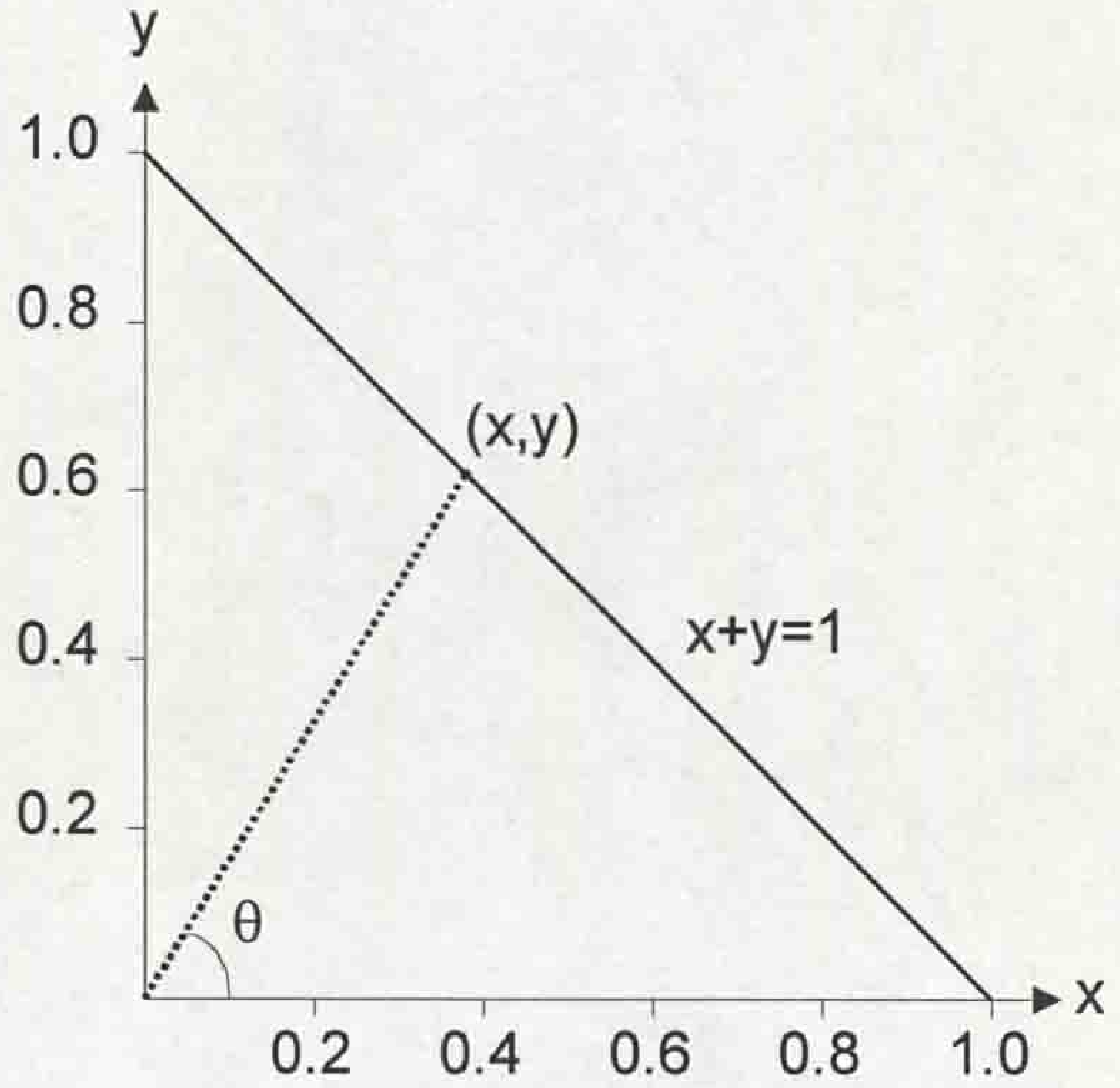

Figure 4.17 - Collapse of x-y chromaticity diagram to a straight line for a distimulus system (Jones *et al*, 1987)

This line is a spectral locus containing monochromatic wavelengths only. The distimulus chromaticity can be conveniently expressed as a polar co-ordinate ($\tan\theta = y/x$), whose relationship to dominant wavelength depends on the chosen detector characteristics. Thus, the distimulus system can only measure one of the chromatic variables, the dominant wavelength. It cannot indicate the purity of a colour. However, this one variable is sufficient for many optical sensing and colorimetry purposes.

Further, there is no reason why the colorimetry arguments, which apply to the visible range of the electromagnetic radiation spectrum, cannot also apply to other wavelengths, such as infra-red, provided that suitable practical photodetectors are available. This is discussed in the next section.

4.3.3.1 A practical distimulus detector

An example of a suitable practical distimulus detector is the Sharp PD150 double layer sequential photodiode (Beavan, 1989 and Henderson, 1989). This consists of two photodiodes PD1 and PD2 in a single semiconductor substrate (fig.4.18).

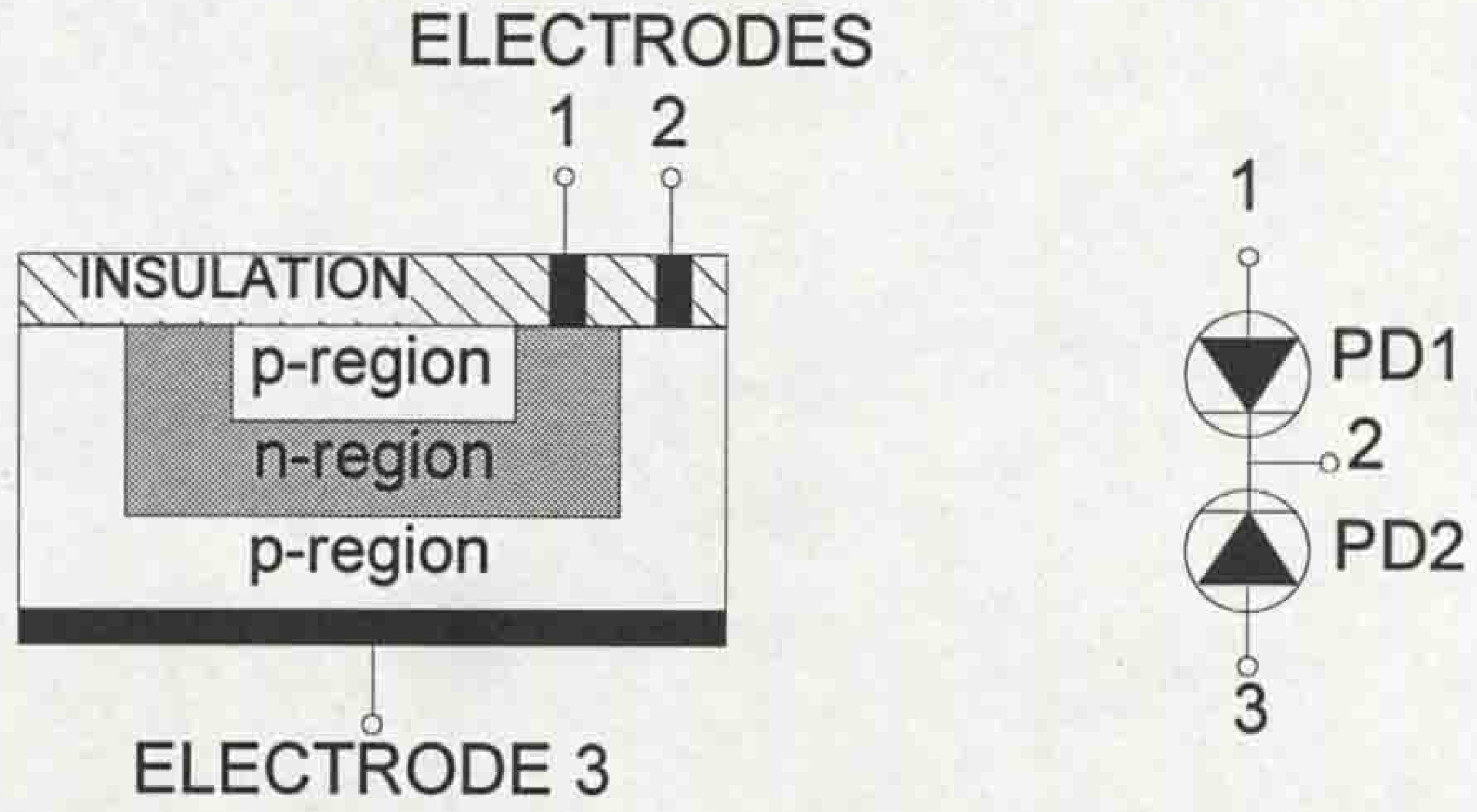

Figure 4.18 - Cross-section of the PD150 double photodiode (Sharp, 1982)

The detector has a response range of ~450-1100nm, PD1 having maximum short wavelength sensitivity and the converse for PD2 (fig.4.19). Hence, this photodiode is a distimulus detector, which can detect dominant wavelengths outside the range of the human eye (380-780nm).

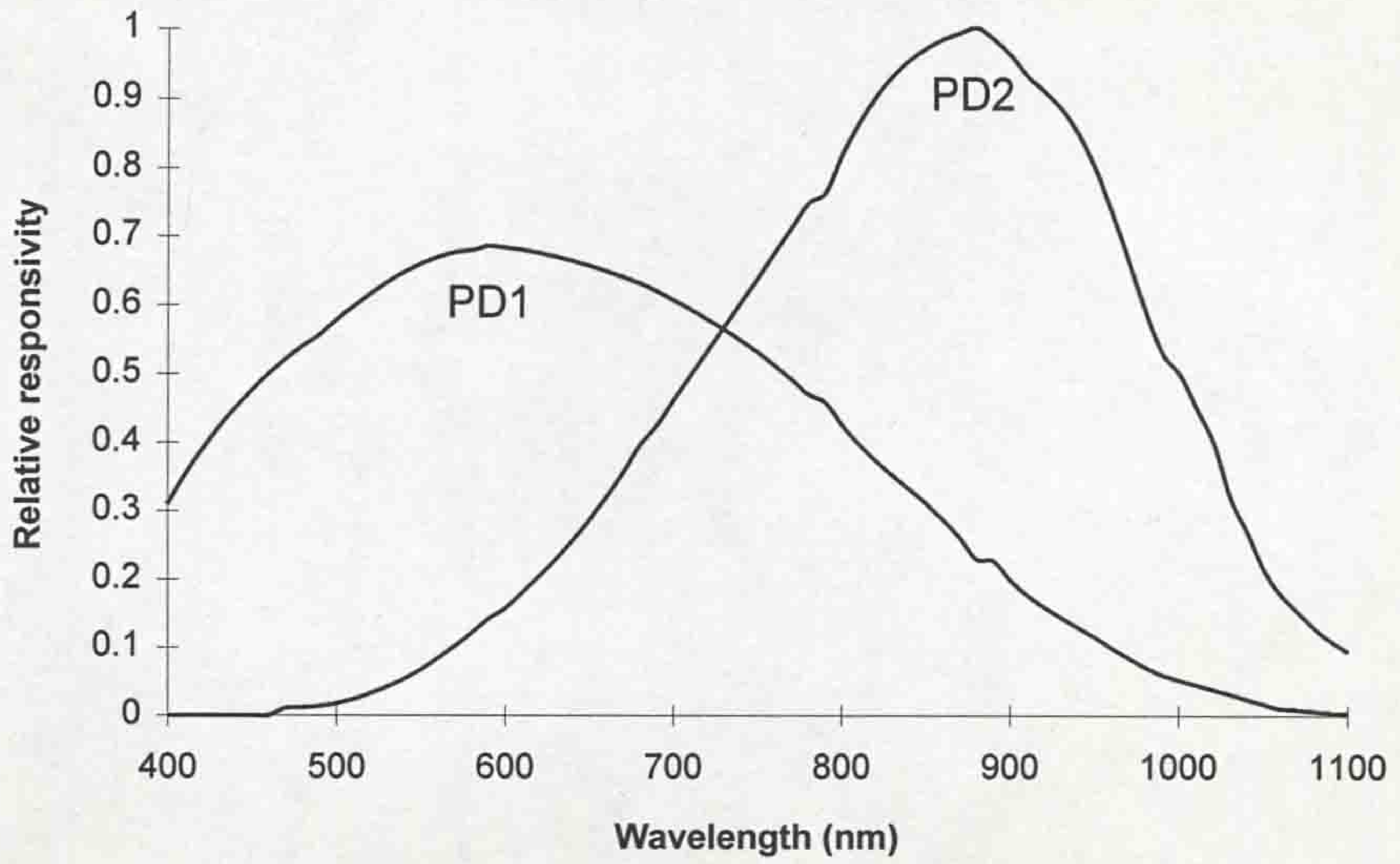

Figure 4.19 - Spectral responsivities for the PD150 double photodiode (Sharp, 1982)

The outputs from PD1 and PD2 are two short circuit currents I_1 and I_2, where

$$I_1 = a_1 \int R_1(\lambda) E(\lambda) d\lambda \tag{4.12}$$

which can be directly compared with eqn.4.8, $R_1(\lambda)$ being the spectral responsivity of PD1, which is analogous to the spectral tristimulus values $\bar{x}(\lambda)$ of the human eye. A similar equation applies to I_2. The chromaticity is the ratio of the two short circuit currents I_1/I_2. This is related to the dominant wavelength as in fig.4.20.

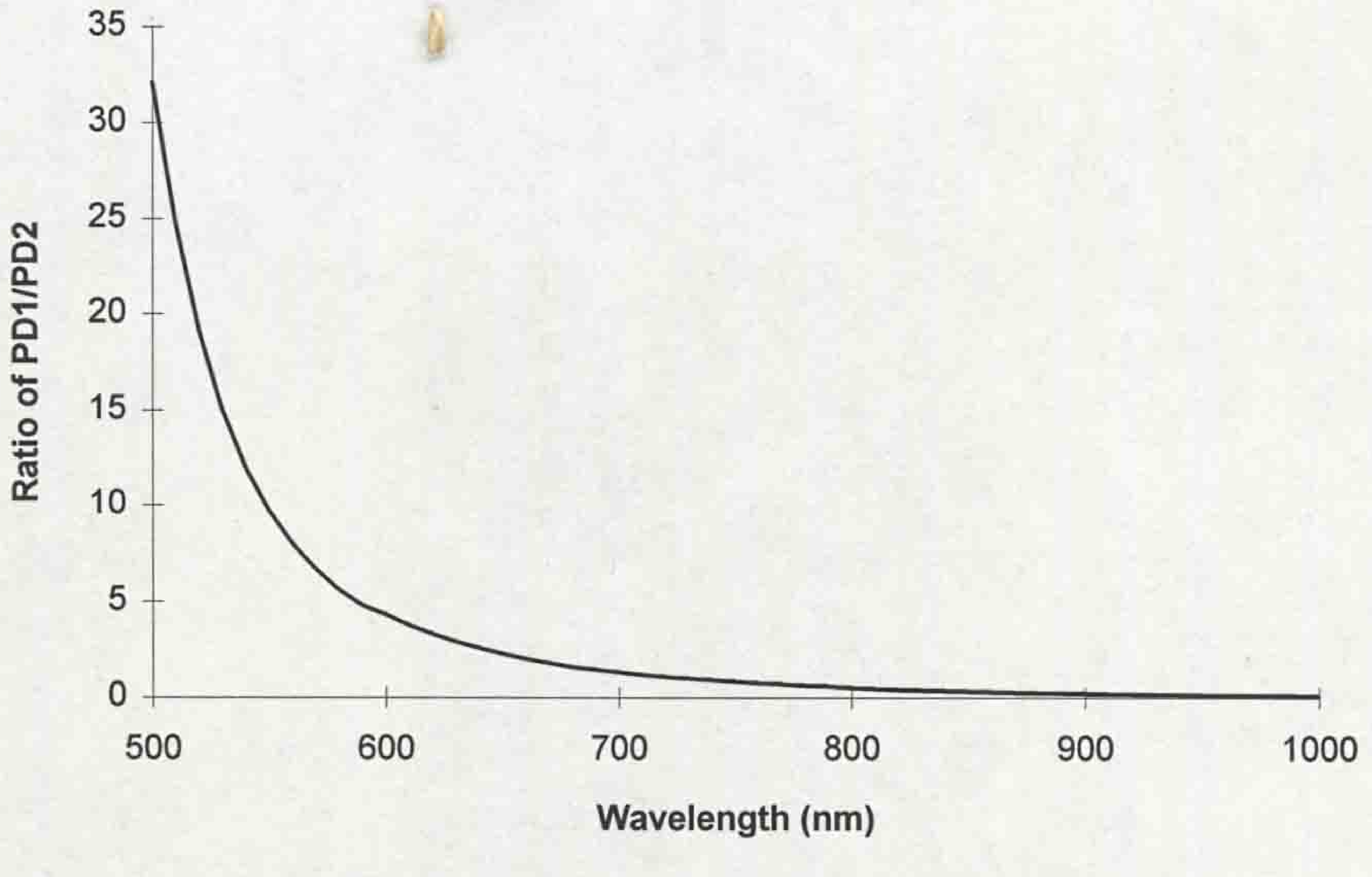

Figure 4.20 - Relationship between s/c current ratio and dominant wavelength

4.3.3.2 A commercial distimulus chromatic detection system

The project described in this thesis used a commercial distimulus chromaticity monitor, built around the PD150 device. This system was a complete source/detection unit, manufactured by Lucas Control Systems Products, known as LIBIDO - "**LI**ght **BI**stimulus **DO**minant wavelength detection". This acronym is used frequently in the thesis to indicate the detection system. The system can be seen in fig.4.21. It incorporates a broadband white light source, a quartz tungsten halogen lamp, with a spectral energy distribution as in fig.4.22.

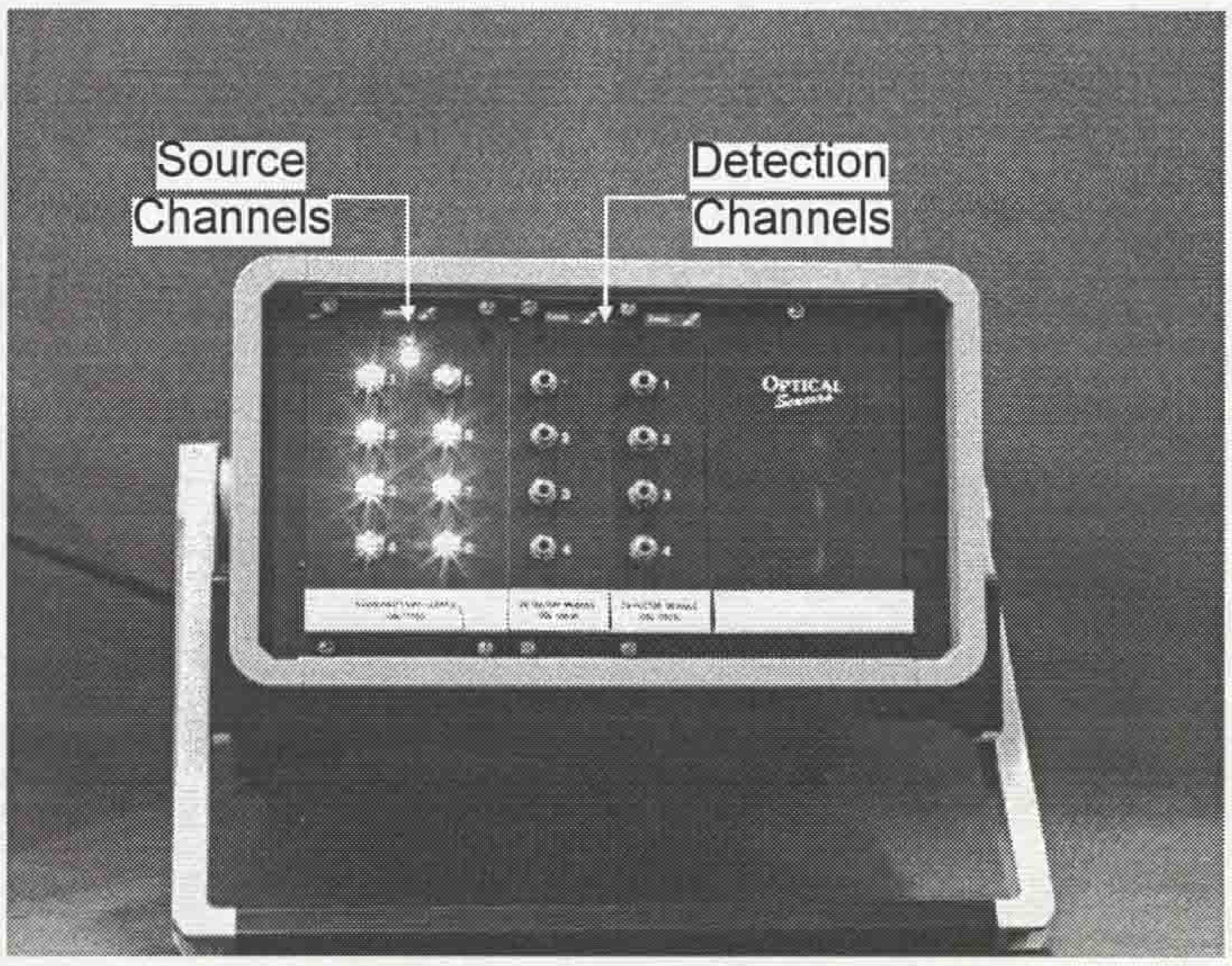

Figure 4.21 - LIBIDO distimulus chromaticity monitor

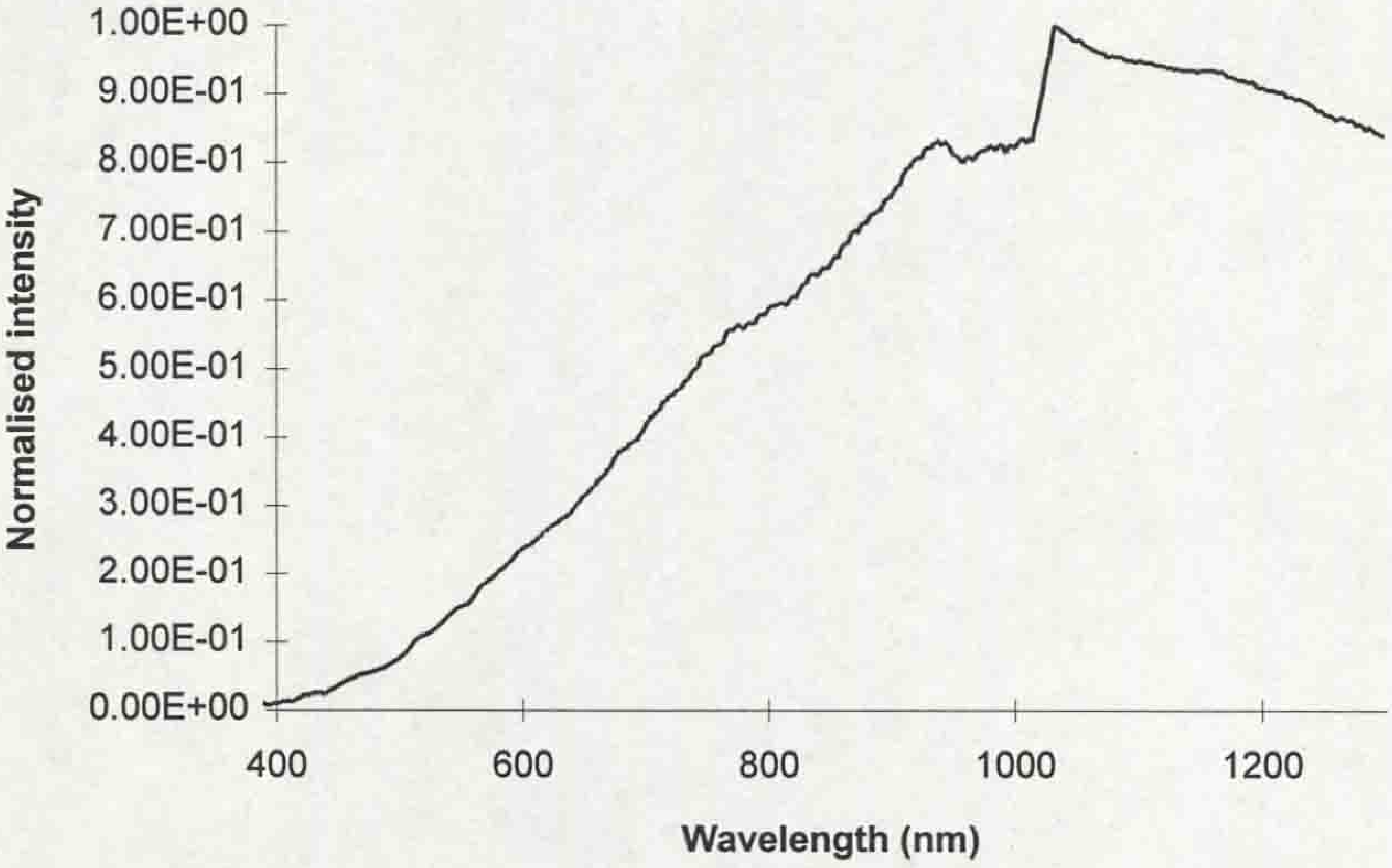

Figure 4.22 - Spectral energy distribution of light transmitted by LIBIDO source

There are eight source channels fed by the lamp, each of which can be connected to SMA-terminated optical fibres. At the other end of the transmission fibres the source light is modulated by a suitable optical sensor, which reacts to the external measurand. The modulated light is then returned to the LIBIDO detection unit, again via SMA-terminated fibres. There are up to eight detector channels available, each having its own PD150; hence, up to eight separate sensors can be operated simultaneously from one LIBIDO module. The outputs of each detector are converted by software into the corresponding dominant wavelength of the modulated light spectrum.

The system uses the high sensitivity range of the PD150, from 500-1000nm. The detector channels can be sampled at up to 4kHz, with dominant wavelength data stored on an IBM compatible personal computer interfaced to the unit. The LIBIDO system has an overall resolution of 0.01nm and is accurate to 0.1nm.

4.3.4 Advantages of chromatic modulation

Chromatic modulation offers significant advantages over traditional modulation techniques (Jones *et al*, 1987).

Intensity modulation makes effective use of source optical power but is susceptible to errors arising from spurious intensity variations due to, for example, source instability (Dakin, 1984). In distimulus chromatic modulation the chromaticity is obtained by taking the ratio of PD150 short circuit currents. Thus,

$$Chromaticity = C = \frac{I_1}{I_2} = \frac{a_1 \int R_1(\lambda) E(\lambda) d\lambda}{a_2 \int R_2(\lambda) E(\lambda) d\lambda} \qquad (4.13)$$

Assuming that an intensity fluctuation occurs consistently over the working range (500-1000nm), then the chromaticity will not change. In practice, intensity variations will be non-linear to some extent, with respect to wavelength, but chromatic modulation will minimise their significance.

Wavelength modulation is insensitive to spurious intensity variations, but utilises only a narrow band of the source light spectrum and is, therefore, an inefficient use of the system optical power. Chromatic modulation, on the other hand, uses a broad spectral range of the source. This improves the signal-to-noise ratio and allows much smaller signal powers to be transmitted without the need for regeneration. Hence, chromatic modulation combines the advantages offered by intensity and wavelength modulation.

The sensitivity offered by chromatic modulation has been shown to exceed other popular methods, such as intensity modulation and wavelength referencing (Jones *et al*, 1987). Furthermore, the sensitivity of the method is not strongly dependent upon optical wavelength, so that the most appropriate part of the optical spectrum, compatible with the transmission characteristics of the optical fibre, may be chosen.

Finally, the great many possibilities for modulating the chromaticity of a white light spectrum makes chromatic modulation the most versatile of the optical modulation methods. Indeed, practical chromatic modulators used previously represent a small fraction of those yet to be discovered. These include ruby spheres (Henderson, 1989, and Kwan, 1987), various non-linear spectral filters (eg. Henderson *et al*, 1993), photoelastic elements (Murphy, 1992), intrinsic fibre bending (Beavan,1989) and, more recently, micromachined silicon interference cavities (Dancaster, 1993).

A potential drawback of chromatic modulation is the phenomenon of metamerism (see **4.1.3**), that different spectra can give the same chromaticity (Culshaw, 1984). However, careful design of the modulator, with reference to the source spectrum and x,y chromaticity diagram, can avoid this. Further, it is essential for chromatic sensing systems to ensure that each fundamental component (i.e. source, fibres, modulator and detector) all operate over the desired working wavelength range i.e they are spectrally matched.

4.4 CONCLUSIONS

Optical fibre sensing requires a suitable choice of source, fibres, detector and modulation method. Careful consideration of the cost of each component, its attenuation and other factors is necessary to arrive at a combination of these four basic elements, which will most suitably meet the design requirement.

Taking these factors into account, it was decided for this work that a suitable source providing relatively high power and good stability at low cost would be a quartz tungsten halogen lamp. The fibres chosen were generally multimode doped silica fibres (core diameter 400μm, numerical aperture 0.4) to provide high power launching capability at a relatively low cost. The optical fibre linear travel recorder, described later (**chapter 5**), used fibre bundles, rather than single fibres, to provide a large output beam diameter (2mm), to minimise optical noise on the system (**5.3.1.2**).

For the reasons discussed earlier (**4.3.4**), chromatic modulation was chosen to be the most suitable modulation method. The versatility of the method is verified later in this thesis, which describes several optical sensors, all employing chromatic modulation to measure different parameters (displacement, pressure and particle concentration). The readily available commercial LIBIDO system was chosen as a convenient chromatic source/detection unit, which could be easily interfaced to a personal computer. The cost of an eight source, eight detector unit of ~£3000 compares favourably with many other systems, the cost per source/detector channel pair being under £400.

CHAPTER 5 - OPTICAL FIBRE LINEAR TRAVEL RECORDER (OFLTR)

5.1 INTRODUCTION

5.1.1 Review

Early fibre optic displacement sensors were predominantly based on intensity-modulated reflective techniques. The simplest form involved the use of two adjacent fibres, which emitted and received a cone of light reflected by a perpendicular mirrored surface, which was displaced longitudinally with respect to the fibres (Kissinger, 1967). Many other variations have evolved from this basic principle (eg. Sridharan, 1984, and Murphy and Coursolle, 1990), some of which incorporated loss compensation schemes to overcome the disadvantages of intensity modulation (eg. Beheim, 1987). However, the emphasis with these types of displacement sensors is on short range (≤1mm) and high resolution (~nm).

Such types of displacement sensors were not feasible in this project. The specification (**5.1.2**) demanded a long range device (200mm), with a resolution of 1%, but, importantly, simple and robust enough to withstand the extremely harsh circuit breaker environment. Therefore, the review concentrated on devices with a long dynamic range.

A zone plate was used (Liu *et al*, 1991) with a two-wavelength referencing method to produce a sensor which was monotonic up to 50mm, still far short of the required range. Earlier, Ura *et al* (1989) had reported a position sensitive, integrated interferometric sensor with a 150mm range. However, the sophisticated nature of the device, and the requirement for on-board electronics, made this unsuitable for use on a circuit breaker. A position sensor utilising photoluminescent material was reported (Lang and Ryan, 1992), with a range of 35 inches. This system had a relatively high standard deviation error of 1cm; furthermore, there would be problems in installing such a device in the very limited space within the interrupter.

Direct monitoring of the displacement of the moving contact stalk of a puffer circuit breaker, with an optical fibre displacement sensor, has been achieved (Shimmin, 1986 - fig.2.11). This device consisted of a rotating wheel which pressed against the interrupter contact shaft, the displacement being measured by counting successive, equi-distant reflecting bands on the wheel by optical fibre interrogation. However, due to the high velocity of a puffer interrupter moving contact during operation, the possibility of slippage between the wheel and contact stalk could not be totally ruled out. This factor prohibited the use of this technique in this project.

It became evident that the most convenient approach was to design and develop a custom device for the circuit breaker. Ideally, this could be based on a chromatic modulation method (**4.3**), as with several other sensors used on the project, to provide a generic monitoring approach, involving the commercially available distimulus chromatic detection system LIBIDO (**4.3.3.2**).

5.1.2 Specification

The project required an optical fibre displacement sensor (referred to here as "optical fibre linear travel recorder" - OFLTR) to be designed in order to monitor the contact separation of the puffer circuit breaker electrodes during fault current interruption (up to 56kA peak). A review of optical fibre displacement sensors (**5.1.1**) did not reveal any methods suited to the extremely harsh environment and limited space within the circuit breaker. Therefore, a novel transducer was required. A stringent specification needed to be satisfied:

- The device must be optical fibre based to provide freedom from electromagnetic interference produced by the arc.
- The device must monitor the contact movement in a linear, non-contact manner.
- The device must be analogue i.e. able to provide an absolute position for the contact stalk in case of a malfunction of the circuit breaker. A digital, fringe counting method (eg. interferometry) was, therefore, not permitted.
- The device and its associated data acquisition system must be able to record dynamically, at velocities up to 4m/s.

- The device must monitor the full displacement of the interrupter stroke i.e. 190mm.
- The resolution of the complete system must be within 2mm.
- The device must be located on the contact stalk itself, within the interrupter unit. Firstly, this is to provide an accurate record of the interrupter motion. Secondly, this would reveal any faults in the linkages which connect the interrupter contact and piston to the driving mechanism.
- The device must tolerate potential rotation of the contact shaft of up to 3°.

5.2 DESIGN CRITERIA

5.2.1 Proposed arrangement of OFLTR within the puffer circuit breaker

In view of the extreme mechanical forces imposed on the interrupter during operation and the severe space limitations within the interrupter unit, it was decided that the most effective arrangement for the OFLTR would be a reflection based system. It was proposed that the transducer be attached to the moving contact stalk, as in fig.5.1, with the optical fibres housed in the stationary interrupter casing, perpendicular to the transducer.

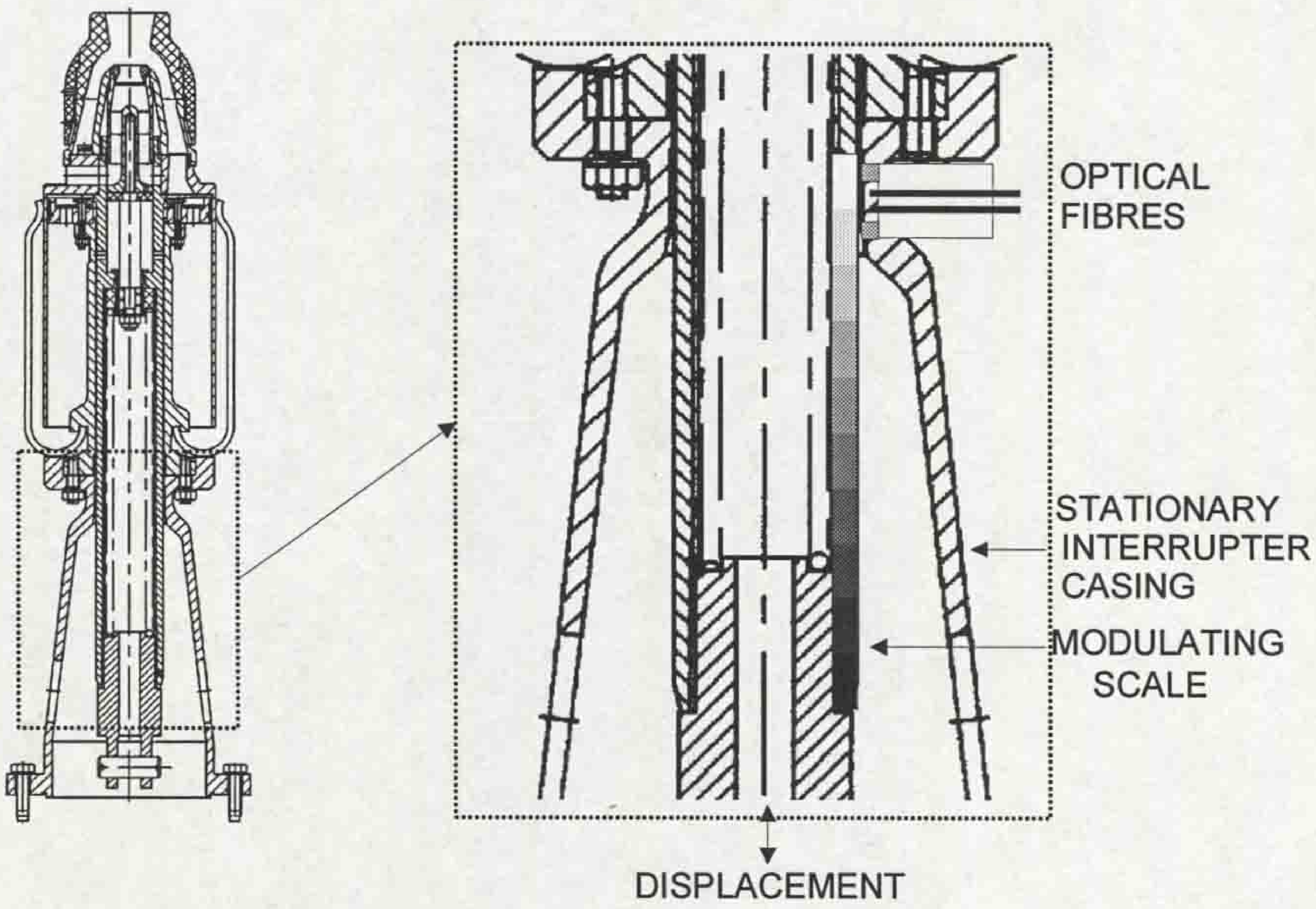

Figure 5.1 - Chosen position for OFLTR within interrupter unit

The sensor-addressing light is delivered by optical fibres and reflected by the transducer scale into the receiving fibres, for transmission to the detection system. The transducer was required to produce a linear change in the modulation parameter, which could be calibrated against its length. The transducer was also required to have an overall length of 200mm, to account for the 190mm stroke of the interrupter. Thus, as the moving contact of the interrupter was operated, the transducer would move past the fibres, causing a corresponding change in the modulation parameter, which could then be converted into displacement.

Since the moving stalk of the interrupter was subjected to extreme acceleration forces and vibration during operation, it was decided not to use a conventional glass mirror as the reflecting part of the transducer. Polished steel has been shown to provide a high level of reflectance (Bois *et al*, 1989). Combined with the ease of machining, low cost and robustness, it was, therefore, decided to use polished steel as the reflecting element of the transducer.

5.2.2 Choice of modulation method

Having decided the basic form for the sensor, the next requirement was to choose the most appropriate method of optical modulation. The two methods that could be most conveniently employed in a reflective system are intensity modulation (**4.1.4.1**) and chromatic modulation (**4.3**). The corresponding modulation parameters from each of these methods are intensity and dominant wavelength (**4.3.2**). To assess the suitability of each of these methods for use with a steel reflector, two tests were performed.

Test 1 *- To investigate errors caused by reflectance variations of the steel on the intensity and chromaticity of a broadband optical source.*

The set up simply consisted of a bifurcated glass fibre bundle and a polished piece of steel, as shown on fig.5.2. One of the tails of the fibre bundle was used as the signal input, while the other tail was used to measure the intensity and dominant wavelength of the signal (using a power meter and the LIBIDO detection system - **4.3.3.2**). The intention was to investigate the extent to which the intensity of the signal was affected by imperfections in the polished steel surface compared with the chromaticity signal. Twenty random positions on the steel reflector were addressed by the fibre and for each position the intensity and dominant wavelength were measured. It was found that the intensity varied by 15%, while the dominant wavelength varied by only 0.5% of the potential modulation depth (a difference of x30). This verifies the high degree of independence of chromatic modulation to intensity fluctuations (**4.3.4**) and indicates a major advantage offered by the chromatic approach.

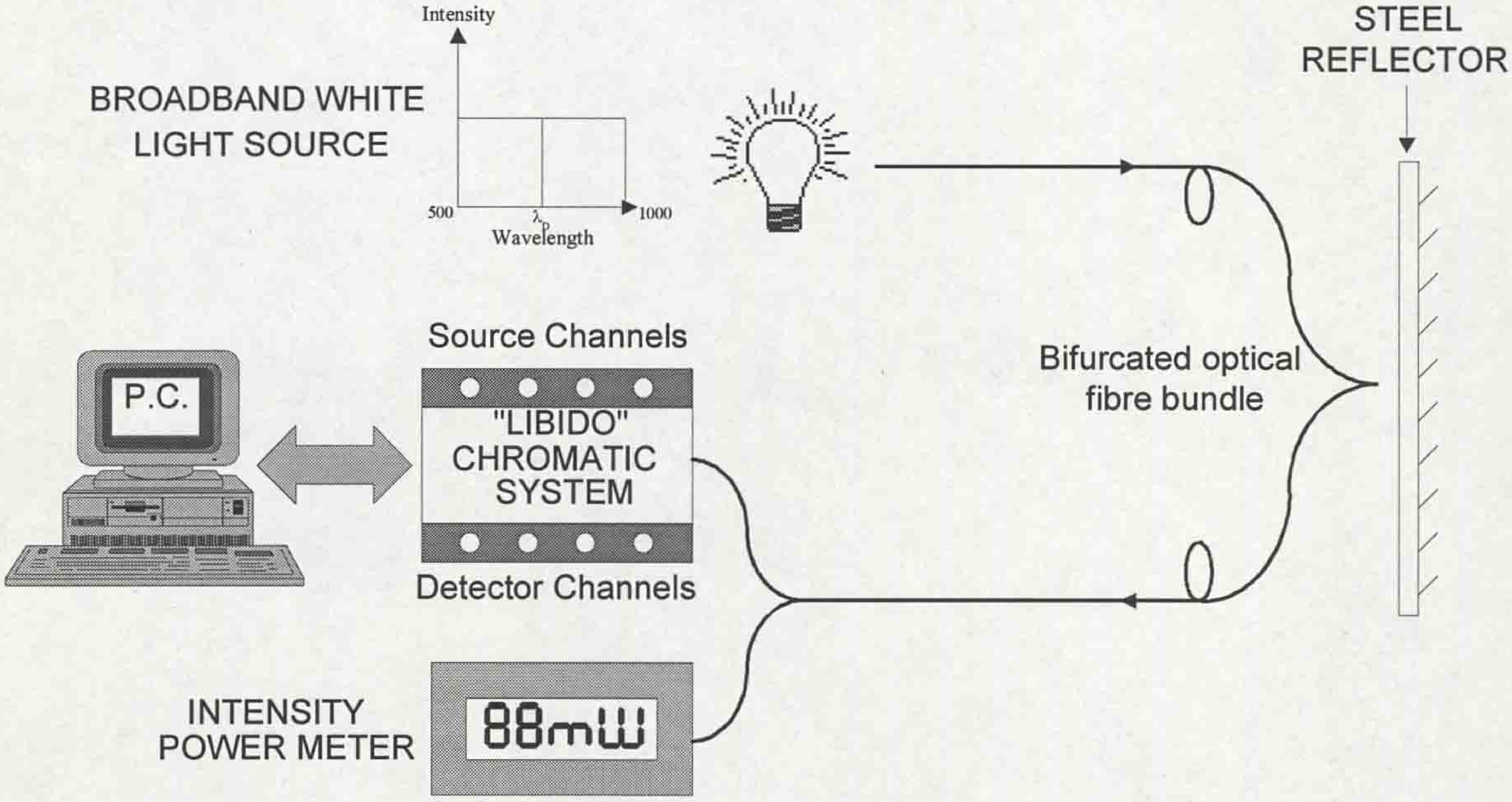

Figure 5.2 - Set-up to compare chromatic and intensity performance

Test 2 - *To predict errors caused by rotation of the interrupter shaft on the intensity and chromaticity of the signal.*

It was indicated above (**5.1.2**) that the OFLTR needed to tolerate shaft rotation of up to ±3°. Therefore, in this test (using the same set up as test 1 above) the steel reflector was rotated by ±3°. It was found that the intensity varied by 16%, while the dominant wavelength varied by only 0.8%. Again the chromatic approach was found to be far less susceptible to errors than the intensity method (an improvement of x20).

Compounding the errors from the two tests, the total potential error on the signal intensity was 22%, while the chromaticity error was less than 1%, a x22 improvement from the chromatic approach for this application. From these results it was decided that chromatic modulation would be the most suitable method to employ. Although the intensity errors could have been reduced by using a referencing system, chromatic modulation does this implicitly, in addition to having other advantages (**4.3.4**).

5.2.3 Proposed calibration characteristic

Although the chromatic modulation method kept errors to under 1% (**5.2.2**), additional errors could arise from, for example, detector noise and mechanical vibration of the interrupter shaft. This meant that if a modulating scale, consisting of a single track was used, then the resolution might not achieve the 2mm specified limit. It was, therefore, proposed that a dual track modulating scale be used. The coarse track of the scale was to provide ten levels of modulation, each step being of 20mm length, to ideally give the characteristic **(a)** of fig.5.3. The fine track of the scale, which determined the resolution of the sensor, was to ideally provide the periodic modulation characteristic **(b)** in fig.5.3.

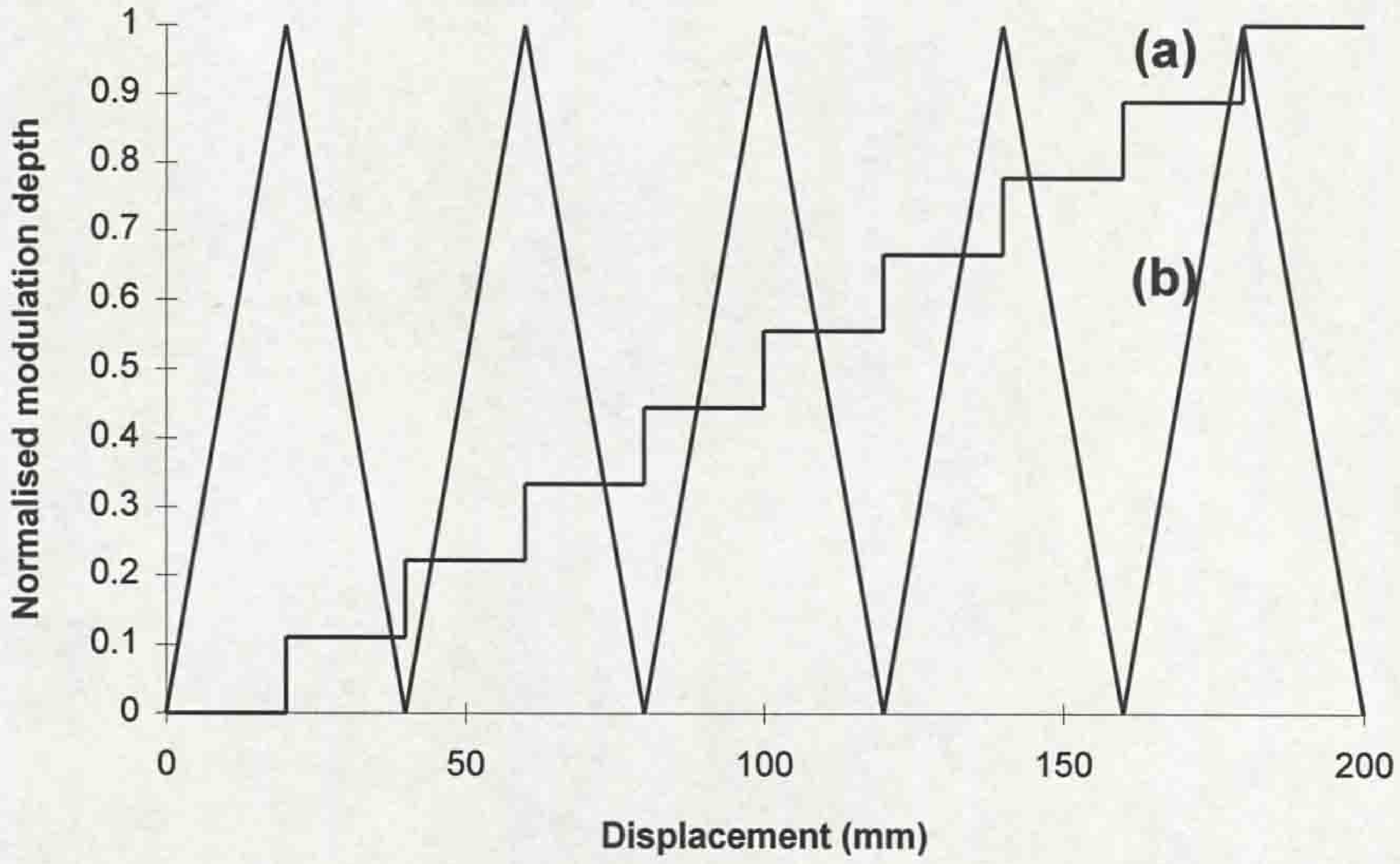

Figure 5.3 - Ideal modulation characteristics for (a) coarse track and (b) fine track of OFLTR modulating scale

For each coarse step there is a full linear sweep of the modulation depth on the fine scale. Each track of the scale would be interrogated by its own fibre. The outputs from the two fibres, after chromatic detection, would provide an unambiguous position for the transducer and, hence, the interrupter contact.

5.3 LABORATORY DEVELOPMENT

Laboratory development of the OFLTR involved identifying a suitable method for chromatically modulating the source light spectrum, and then honing the principle to provide control over the linearity of modulation.

5.3.1 The practical chromatic modulator

A convenient method for controlling the modulation of a broadband white light source, to provide a dominant wavelength variation in the range of 500 - 1000nm - the working range of the LIBIDO distimulus chromatic detection system (**4.3.3.2**) - was to use a variable density deposition of organic type ink, as found in conventional inkjet printers. In such printers the specified printing resolution determines the density of ink dots that can be deposited on a given area. This dot density matrix can be controlled with software (**5.3.1.1**). To illustrate the method an acetate slide was half covered with black ink from an inkjet printer (model HP Paintjet XL300, 300dpi resolution). The slide was then attached to a polished steel reflector with optically transparent adhesive. Using a bifurcated fibre bundle (fig.5.4), the signal from a white light source was reflected after passing through the clear portion of the modulator and the "opaque" portion.

In each case the reflected signal was processed with, firstly, a spectrum analyser and, secondly, the LIBIDO detection system, to provide a signal dominant wavelength. The two spectra obtained from the spectrum analyser, corresponding to the clear **(a)** and black **(b)** portions of the scale, are shown on fig.5.5.

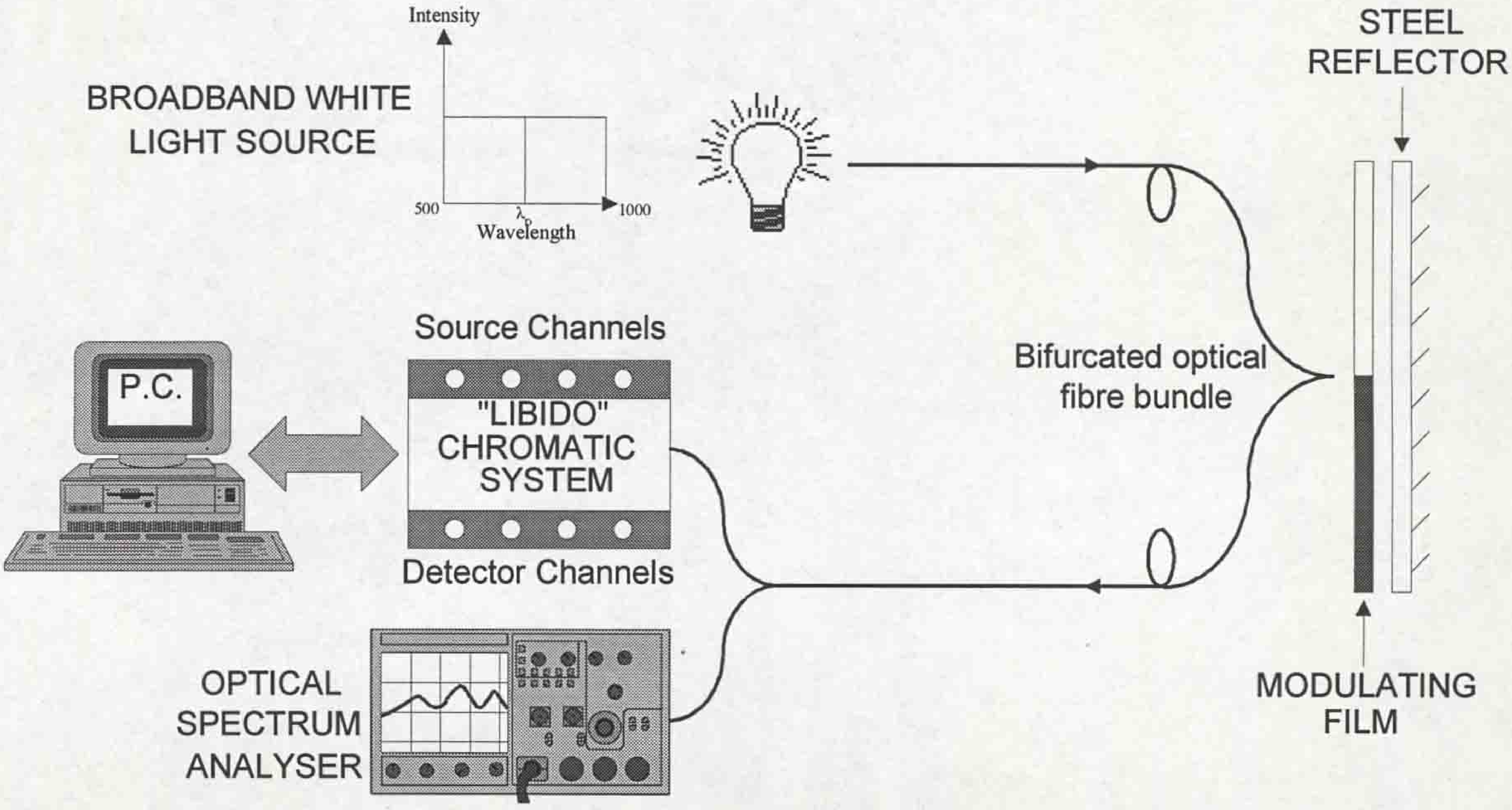

Figure 5.4 - Set-up to investigate chromatic effect of ink deposition

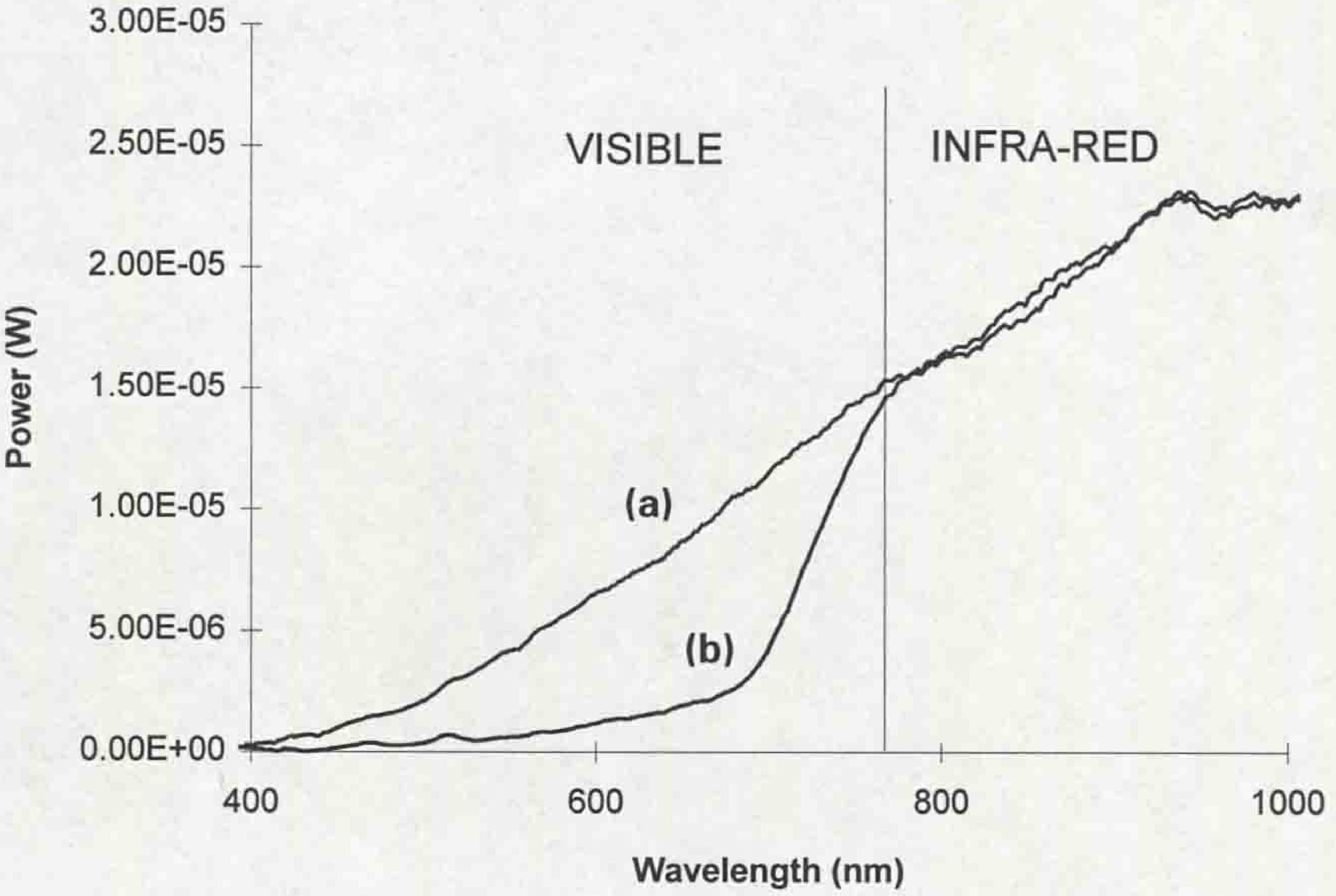

Figure 5.5 - Spectra obtained from (a) clear and (b) black portions of scale

The ink absorbs much of the visible part of the spectrum but transmits the infra-red part. Therefore, although appearing to the human eye to be a total colour absorber, the ink causes an effective colour change in the working wavelength range of the monitoring system (500-1000nm). The two spectra on fig.5.5 yield corresponding dominant wavelengths which differ by approximately 30nm, when analysed by the LIBIDO distimulus chromatic detection system (**4.3.3.2**). This defines the potential chromatic modulation depth of the OFLTR, which, when taken with the dominant wavelength resolution capability of the LIBIDO system of 0.01nm, yields a potential resolution of 1:3000.

5.3.1.1 Controlling the extent of modulation

The next step was to grade the density of ink dots deposited so that the extent of modulation could be controlled from zero (no ink) to full (black). To achieve this a software package was used (Micrografx Designer v4), which allows the deposition of varying levels of "greyness", from 0% (clear) to 100% (black), in steps of 1%. The greyness is actually determined by the density of black dots per unit area deposited by the printer on the slide. By taking dominant wavelength readings for different percentage greyness levels a relationship between the two parameters was obtained. This is shown on fig.5.6.

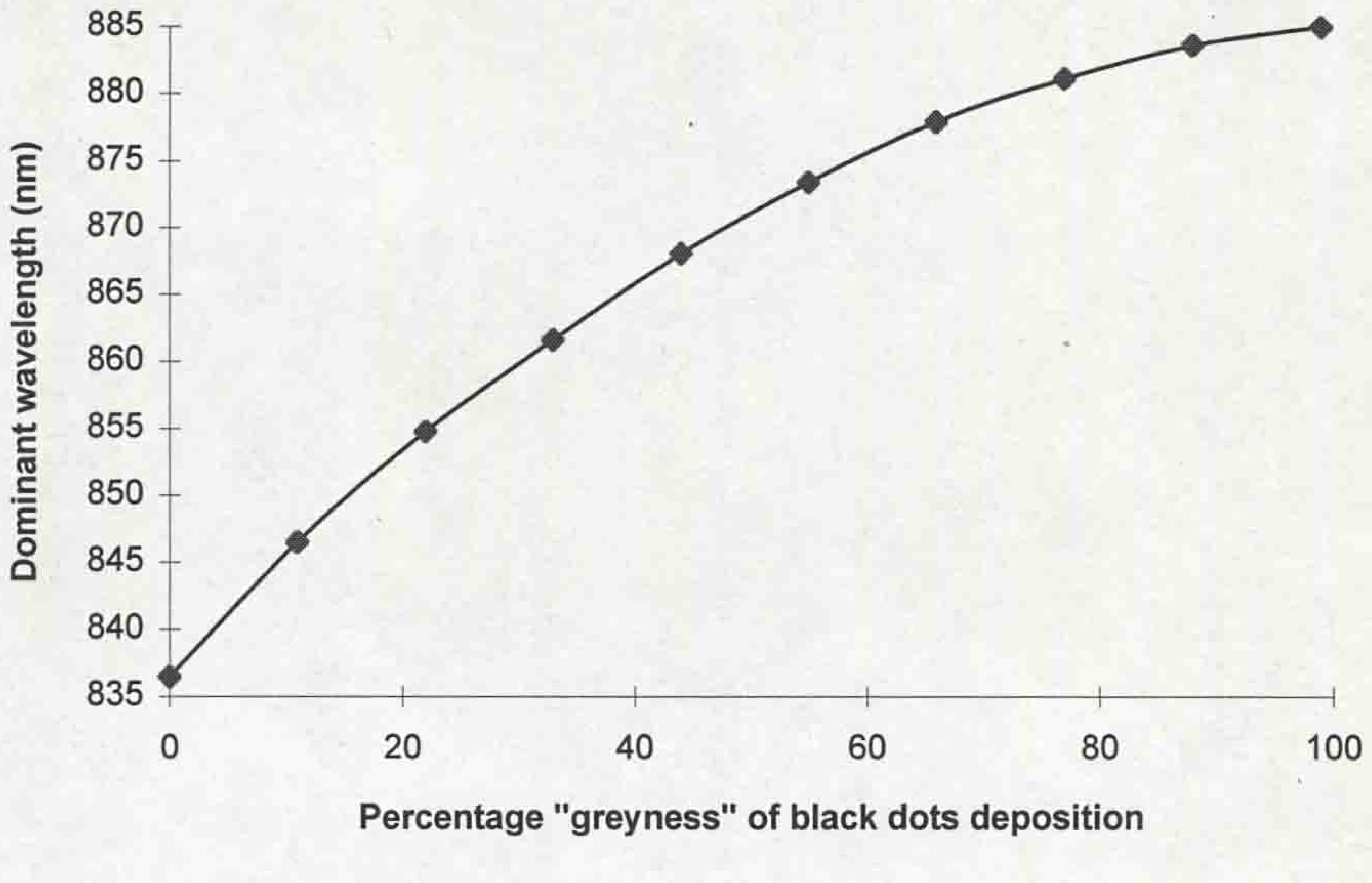

Figure 5.6 - Relationship between ink dot density and dominant wavelength

5.3.1.2 Producing a dual track linear modulating scale

It was mentioned above (**5.2.3**) that the modulating scale should consist of two tracks, coarse and fine. The coarse track required ten modulation levels which were equally spaced with respect to dominant wavelength. By using the characteristic in fig.5.6 ten different percentage levels of "greyness" were selected, in order to provide a linear step change in dominant wavelength. The fine track of the scale was a condensed version of the coarse track, each modulation step reduced in width to 2mm. To address each track of the scale a bifurcated glass fibre bundle, 2mm diameter at the common end, was chosen. One reason for this was to smooth the steps on the fine track and thus produce a linear correlation between dominant wavelength and displacement, with only a small amount of ripple. Additionally, the relatively large interrogation area, provided by the 2mm bundles, ensured that individual dots entering or leaving the beam did not cause significant noise on the signal, in the form of random quantised steps. An example of the dual track linearised scale, designed in this manner, is shown on fig.5.7 (actual width, half the length used), along with the greyness levels selected to provide a chromatically linear output.

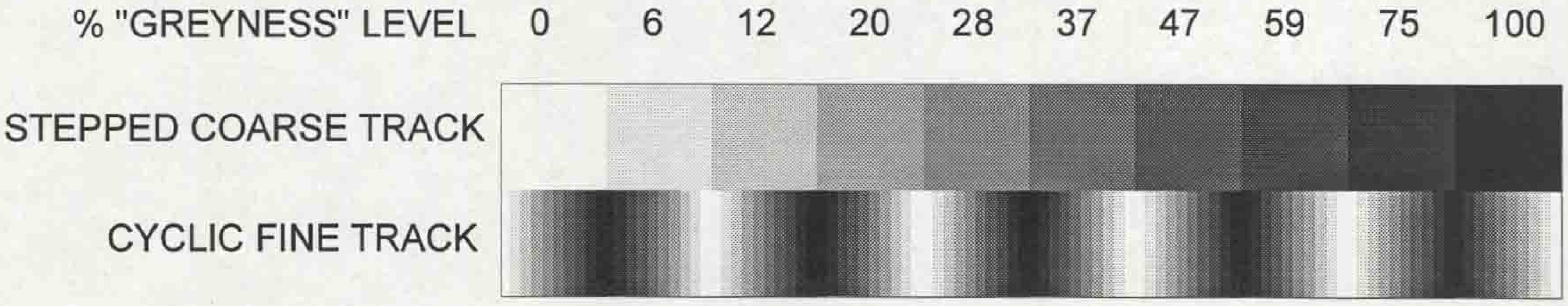

Figure 5.7 - Dual track scale with linearised dot density deposition

5.3.2 Prototype design

The prototype OFLTR consisted of three basic components (fig.5.8):

- Modulating transducer.
- Addressing fibre bundles.
- Distimulus chromatic source/detection unit (LIBIDO).

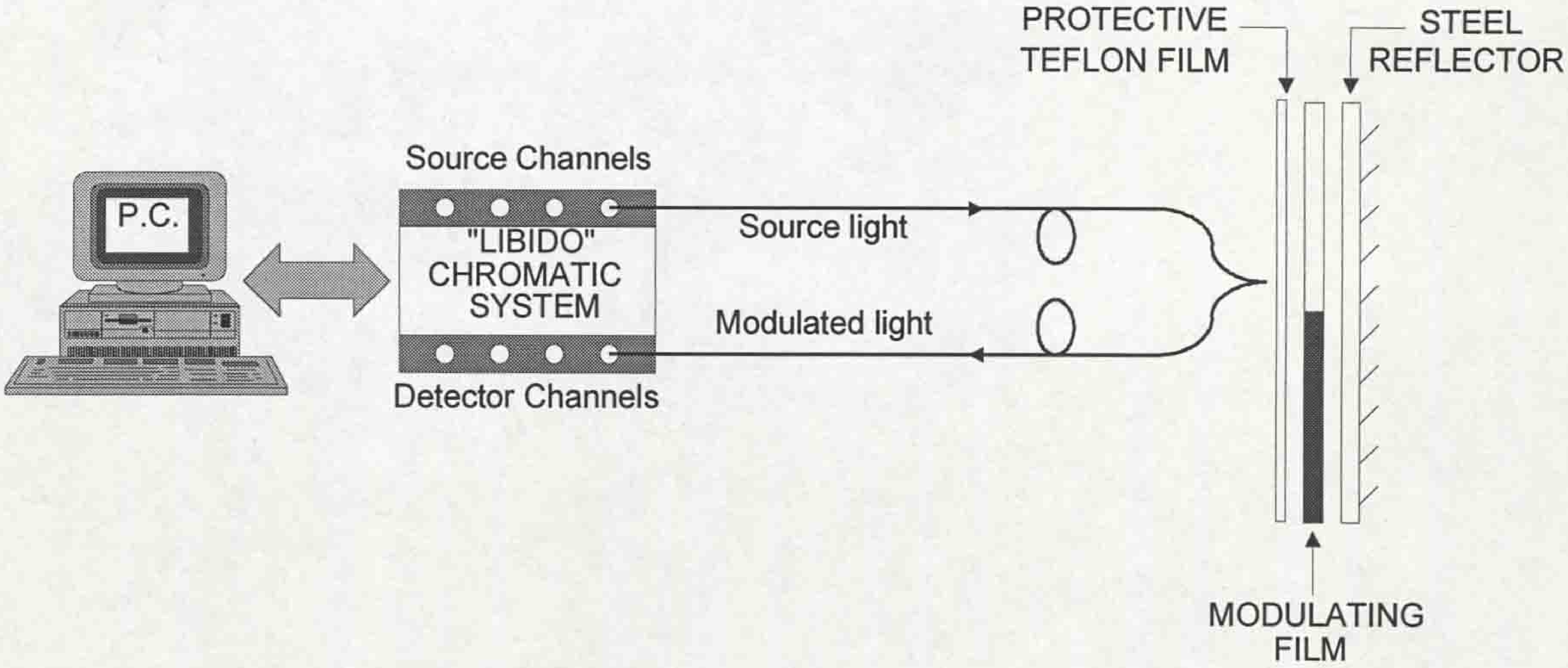

Figure 5.8 - Elements of the prototype OFLTR system

The modulating transducer was attached directly to the moving shaft of the interrupter (fig.5.1), so that upon operation of the circuit breaker the graded scale moved across the open ends of the addressing fibre bundles, which were housed in the stationary puffer case. The transducer itself consisted of three elements:

- Polished steel reflector.
- Modulating dual track scale.
- Protective Teflon film cover.

The polished steel reflector, of dimensions 220x25x2mm, had four countersunk screw holes (size 6BA) at each corner for attachment to the interrupter shaft. The modulating scale (fig.5.7), printed on an acetate slide, with dimensions 200x20mm (negligible thickness), was attached to the steel using optical grade adhesive. The scale and steel reflector were covered by a protective layer of clear Teflon™ fluorocarbon resin film, 100μm thick. This film was cemented to the scale and steel, again using optical grade adhesive. The film was used to provide temperature protection from the arc and also resistance to volatile, arc-induced degradation products, such as hydrogen fluoride, to which the film is inert. The sandwich arrangement was attached to the moving shaft of the interrupter, following successful laboratory tests.

A special jig was manufactured to allow simple installation of the fibre bundles in the interrupter casing. Two bifurcated fibre bundles were used, one for each track of the scale. These were connected at the split ends to source and detector channels of the LIBIDO system. The complete sensor arrangement can be seen schematically on fig.5.9 and on the photograph of fig.5.10.

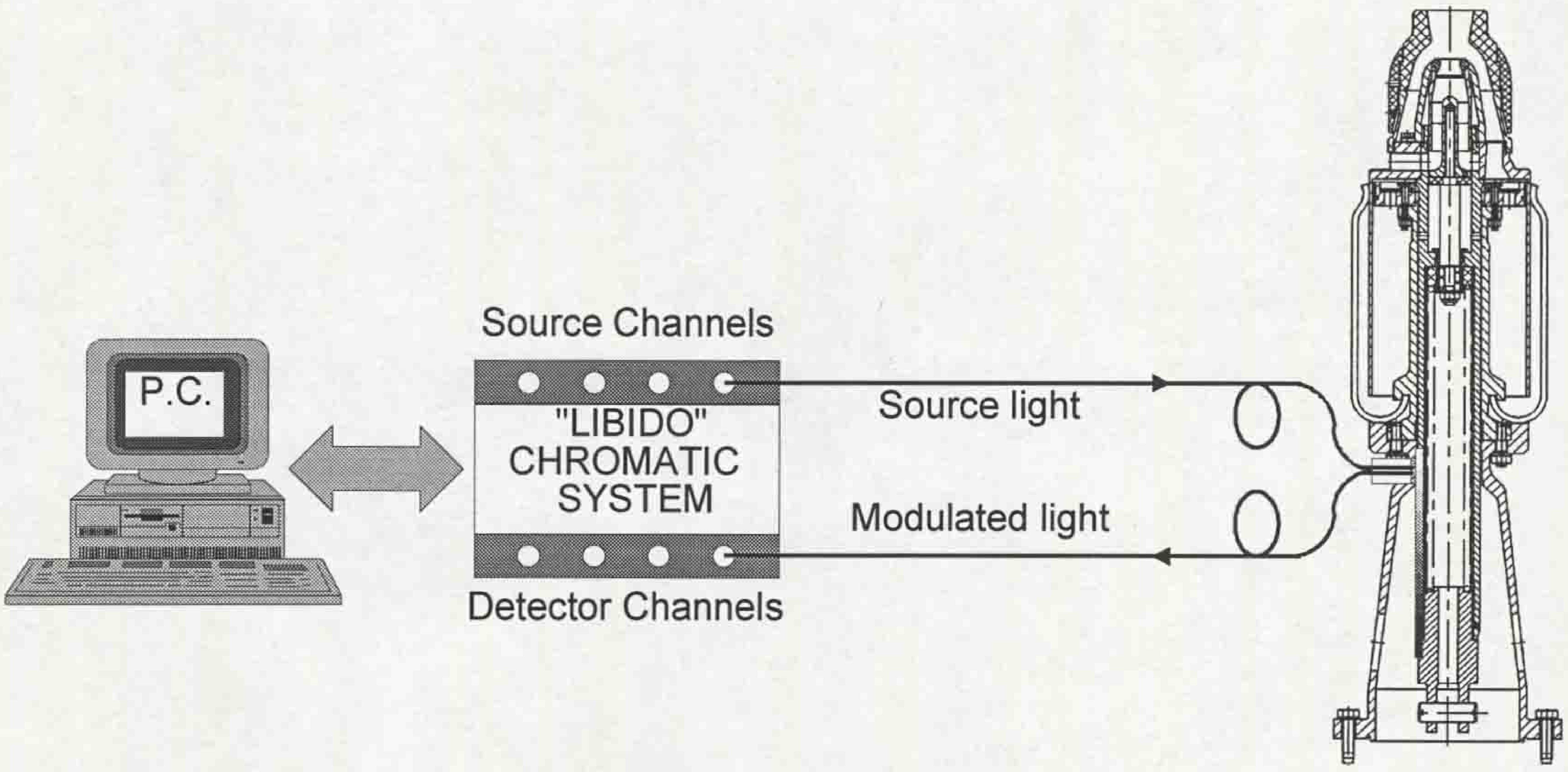

Figure 5.9 - Complete OFLTR sensing arrangement

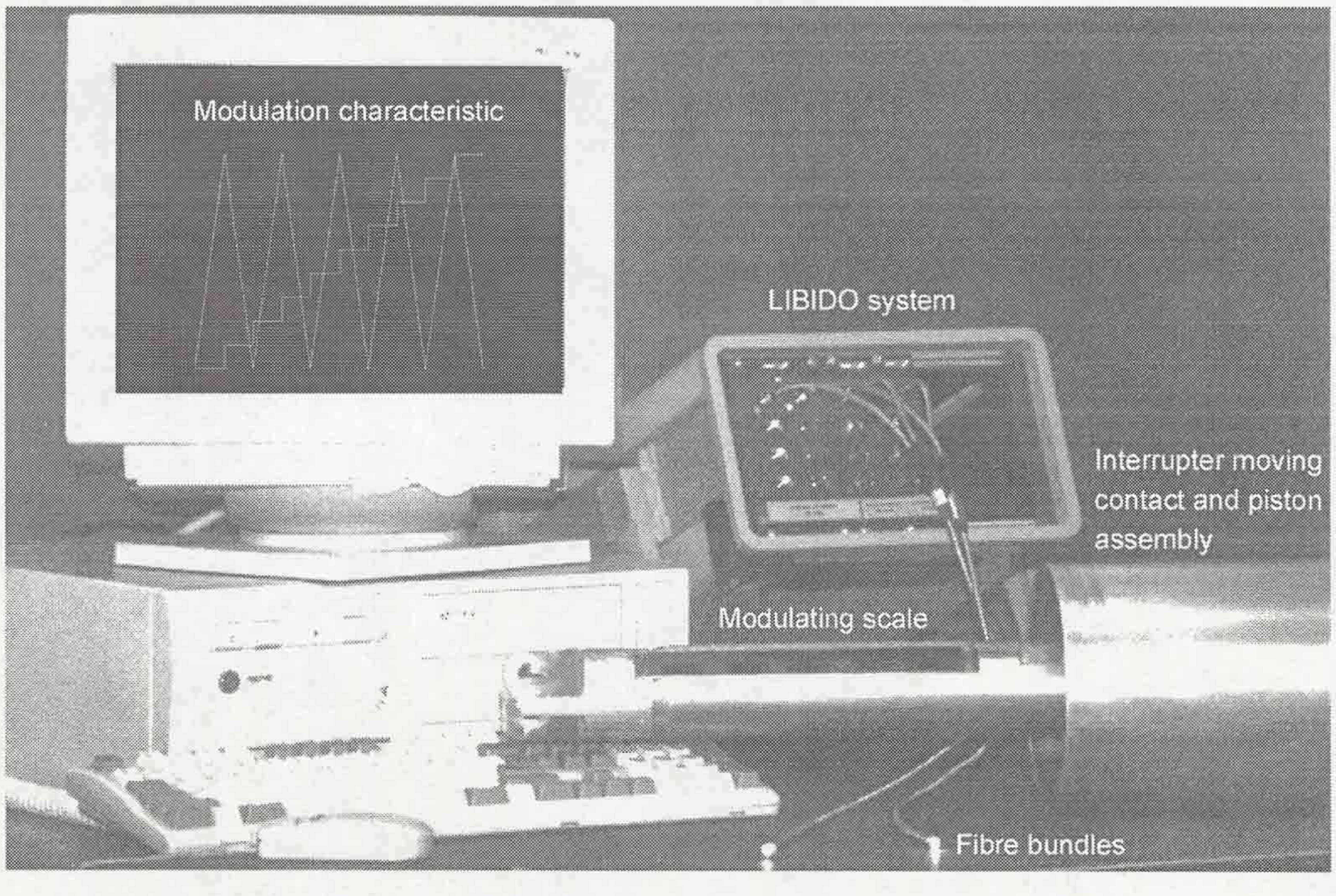

Figure 5.10 - Photograph of OFLTR system

5.3.2.1 Laboratory test on prototype

Before installation in the puffer interrupter, the prototype OFLTR was tested for linearity between scale displacement and dominant wavelength. The fibre bundles were held perpendicular to the scale with an intervening gap corresponding to that which would exist in the interrupter. The results of the test showed a behaviour in good agreement with the ideal characteristics of fig.5.3. (This is evident in the dynamic circuit breaker test on fig.5.11). Further, the results showed that the noise levels on the coarse scale step characteristic are within a tolerable level for step identification. The noise ripple on the fine scale defines a resolution of <1mm, well within the specified limit of 2mm.

5.4 CIRCUIT BREAKER TESTS

Following a successful bench-top calibration (**5.3.2.1**), the prototype OFLTR was installed in the puffer circuit breaker interrupter under test to commence dynamic testing. For the dynamic tests, software was written (Taylor, 1994) to interface the distimulus chromatic detection system (LIBIDO) to an IBM compatible PC, so that the chromatic outputs from the LIBIDO (dominant wavelength values) could be acquired at a rate of 4kHz. This enabled a time discrimination for the movement of the scale to be achieved of the order of 250μs.

5.4.1 Coldflow results

The initial tests performed were coldflow tests, where the circuit breaker was operated in the absence of fault current. Fig.5.11 shows the variation in dominant wavelength with time, for each track of the sensor, during an opening operation of the circuit breaker.

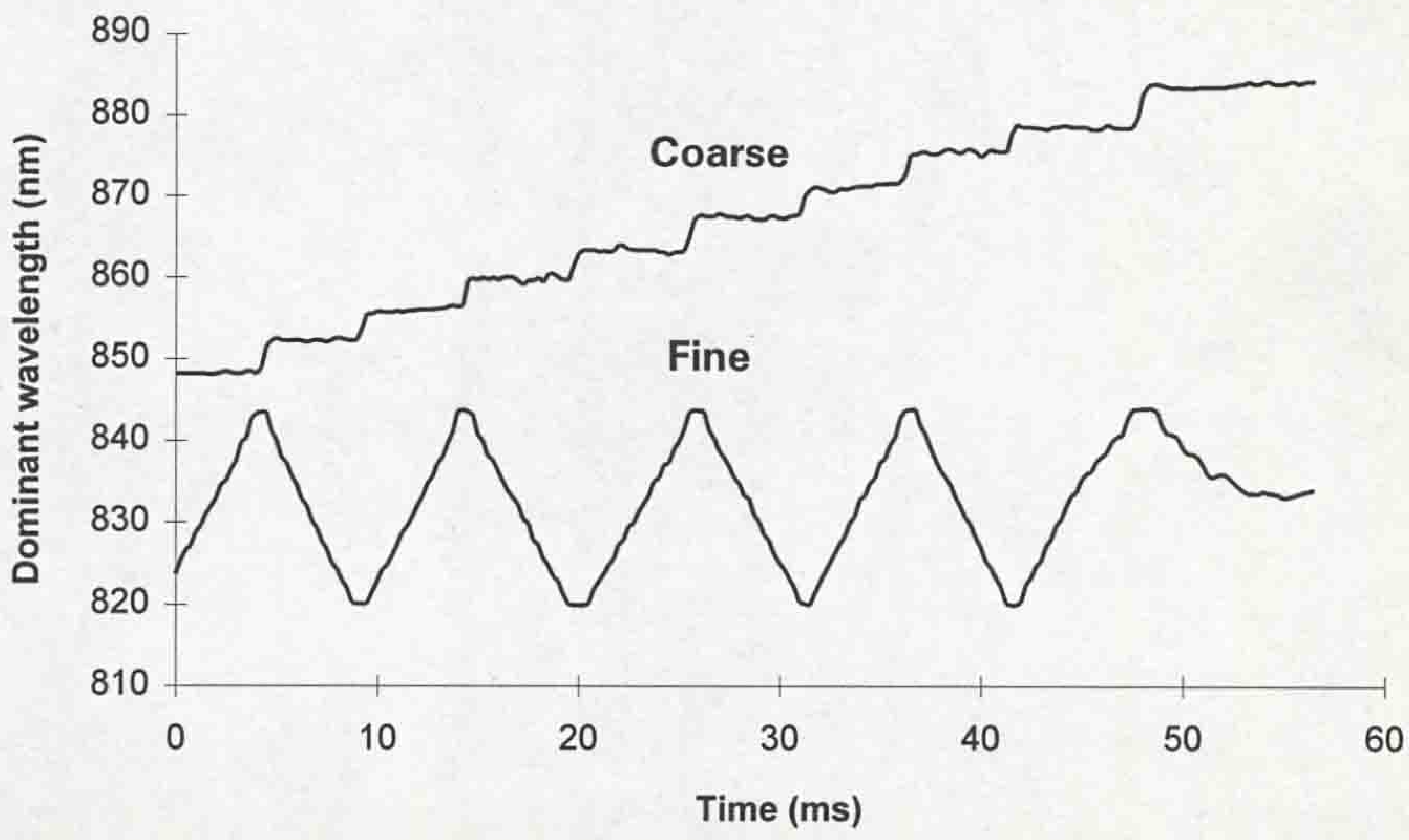

Figure 5.11 - Variation in dominant wavelength for dual track scale during opening

The dominant wavelength data was converted into spreadsheet format (Microsoft Excel), and a spreadsheet "macro" program written (**Appendix II**) to convert the dominant wavelength data into the corresponding displacement values. This allowed a travel record for the interrupter opening stroke to be produced (fig.5.12).

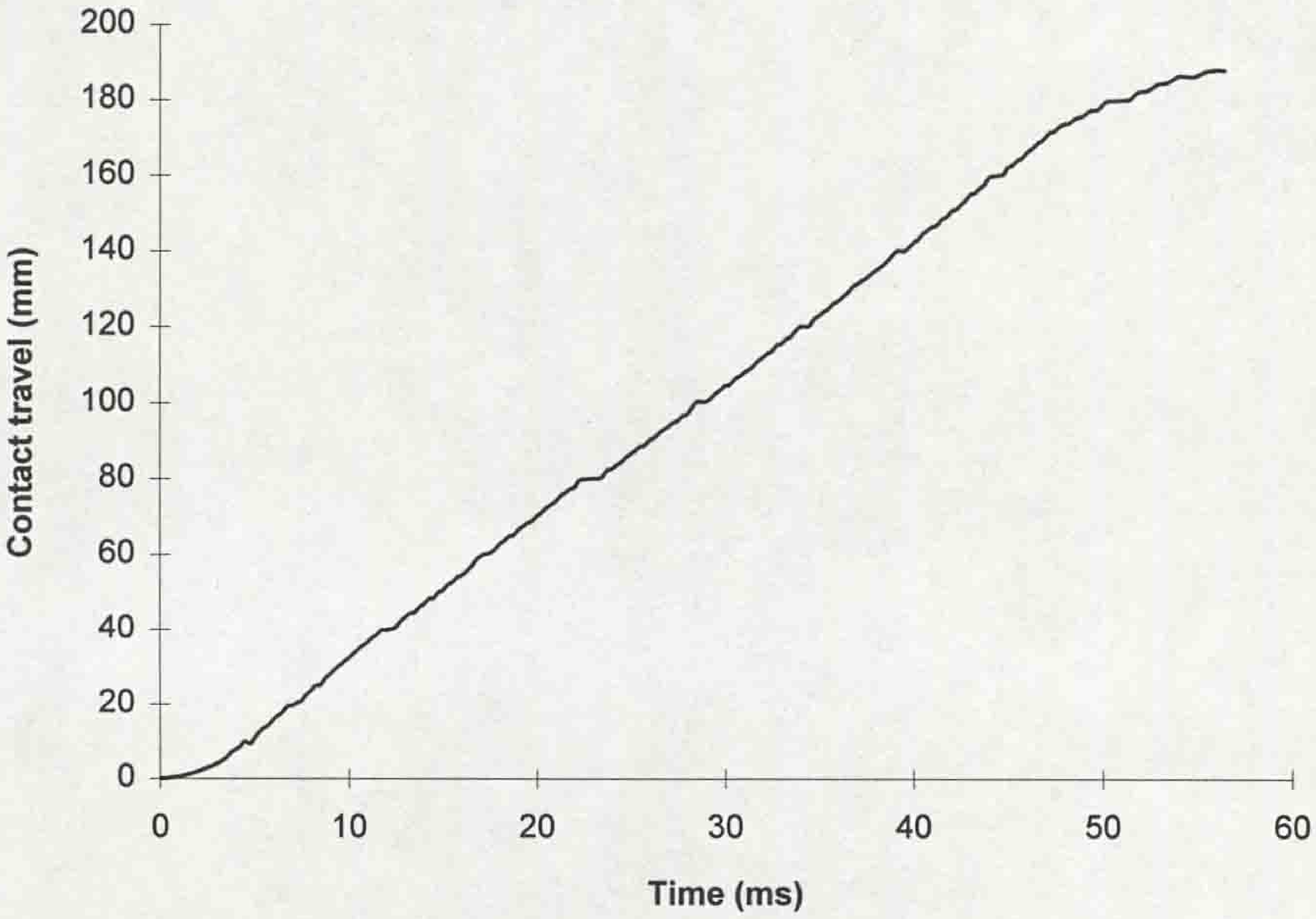

Figure 5.12 - Travel record for opening stroke of test circuit breaker

The differentiation, with respect to time, of a suitable travel curve-fit equation, corresponding to the travel record above, yielded a velocity profile for the interrupter (Fig.5.13).

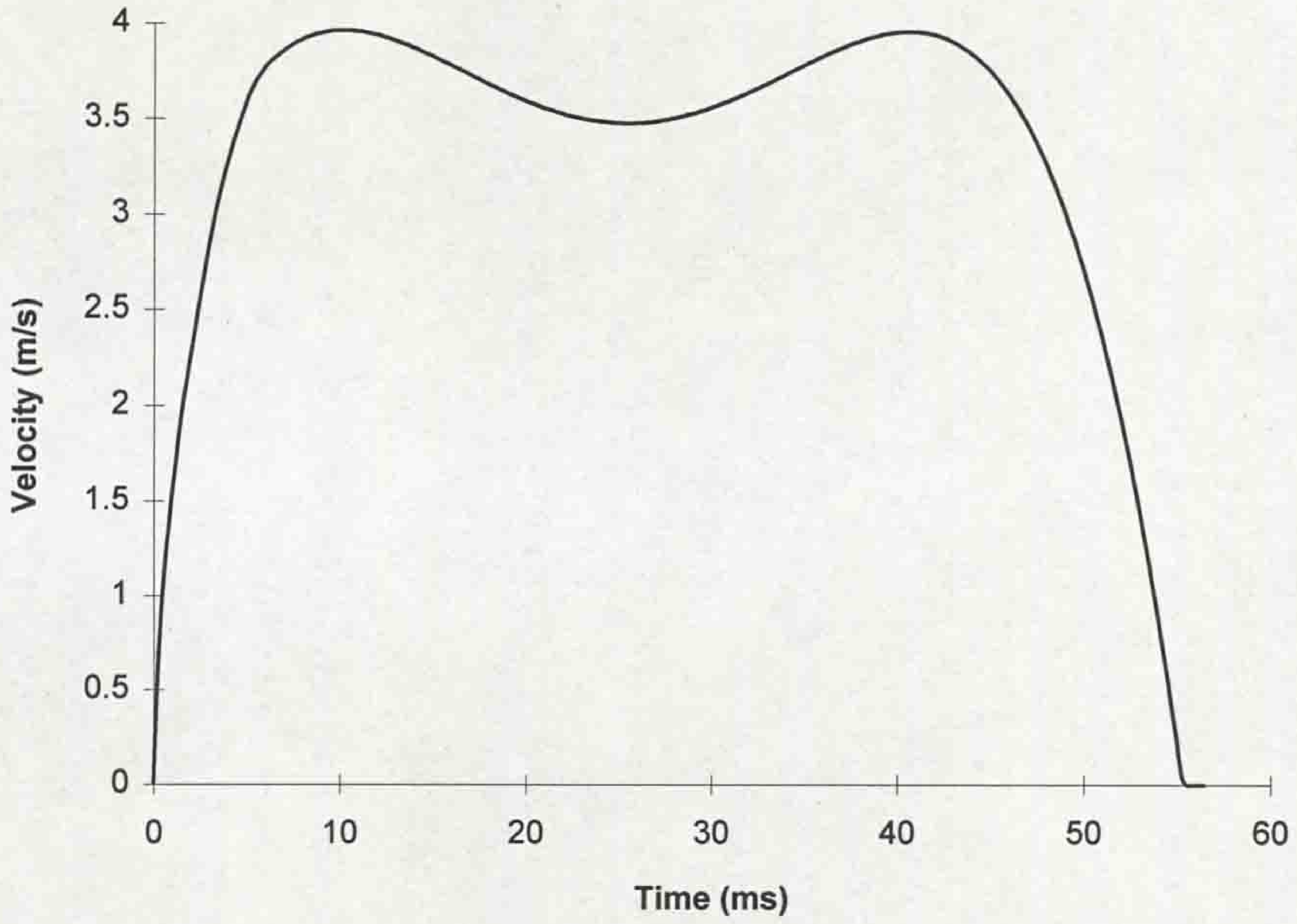

Figure 5.13 - Velocity profile for opening stroke of test circuit breaker

Several coldflow operations were performed to test the repeatability of the OFLTR. Within the resolution of the measurement system, all of the tests were reproducible, so confirming the ability of the system to accurately monitor the displacement of the moving contact within the mechanically demanding circuit breaker environment.

5.4.2 Arcing tests

Although the OFLTR had performed well for coldflow operation, the main test of the device would be during the interruption of high fault currents (up to 56kA peak). Several potential problems existed:

- Radiation from the arc could cause excessive optical noise on the transducer signal.
- High post-arc temperatures may cause damage to the transducer components.
- A continual build up of SF_6 degradation particles with operation of the circuit breaker could coat the transducer and affect the optical output signal.

Subsequent tests of the OFLTR at high fault currents showed that the first two potential problems did not arise, due to the secluded position of the transducer in the circuit breaker and its relatively remote location from the arc. However, the third problem did materialise. Fig.5.14 shows the first result obtained from a series of tests at a 15kA peak fault current. It can be seen that the OFLTR provided a clean dominant wavelength characteristic for each track of the sensor, since there were initially no degradation particles within the breaker. However, after twenty shots at the same arc current, the sensor output deteriorated optically (fig.5.15). It became clear upon stripdown of the breaker that this noise was caused by a build up of particles on the transducer surface.

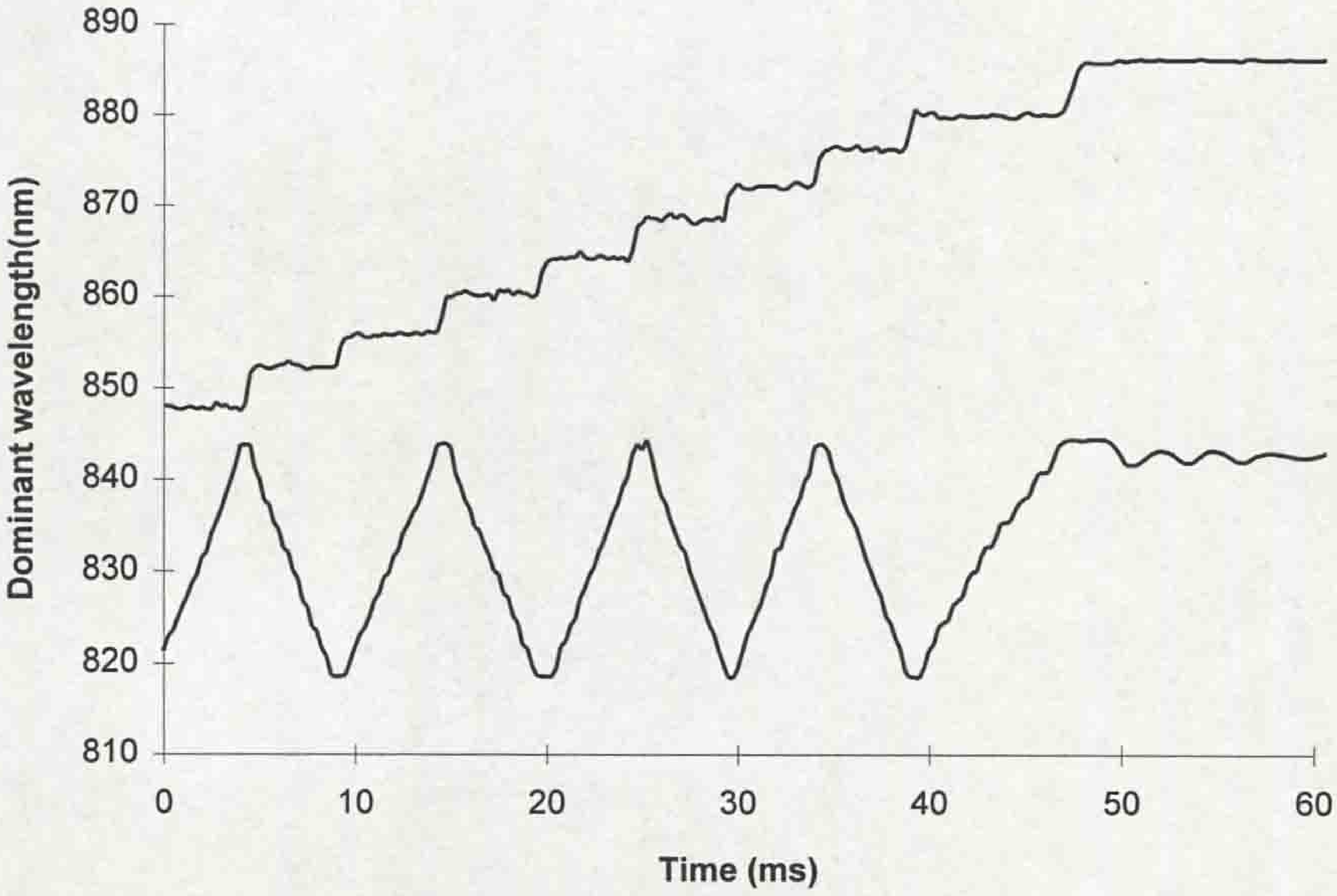

Figure 5.14 - OFLTR response during 1st operation at 15kA

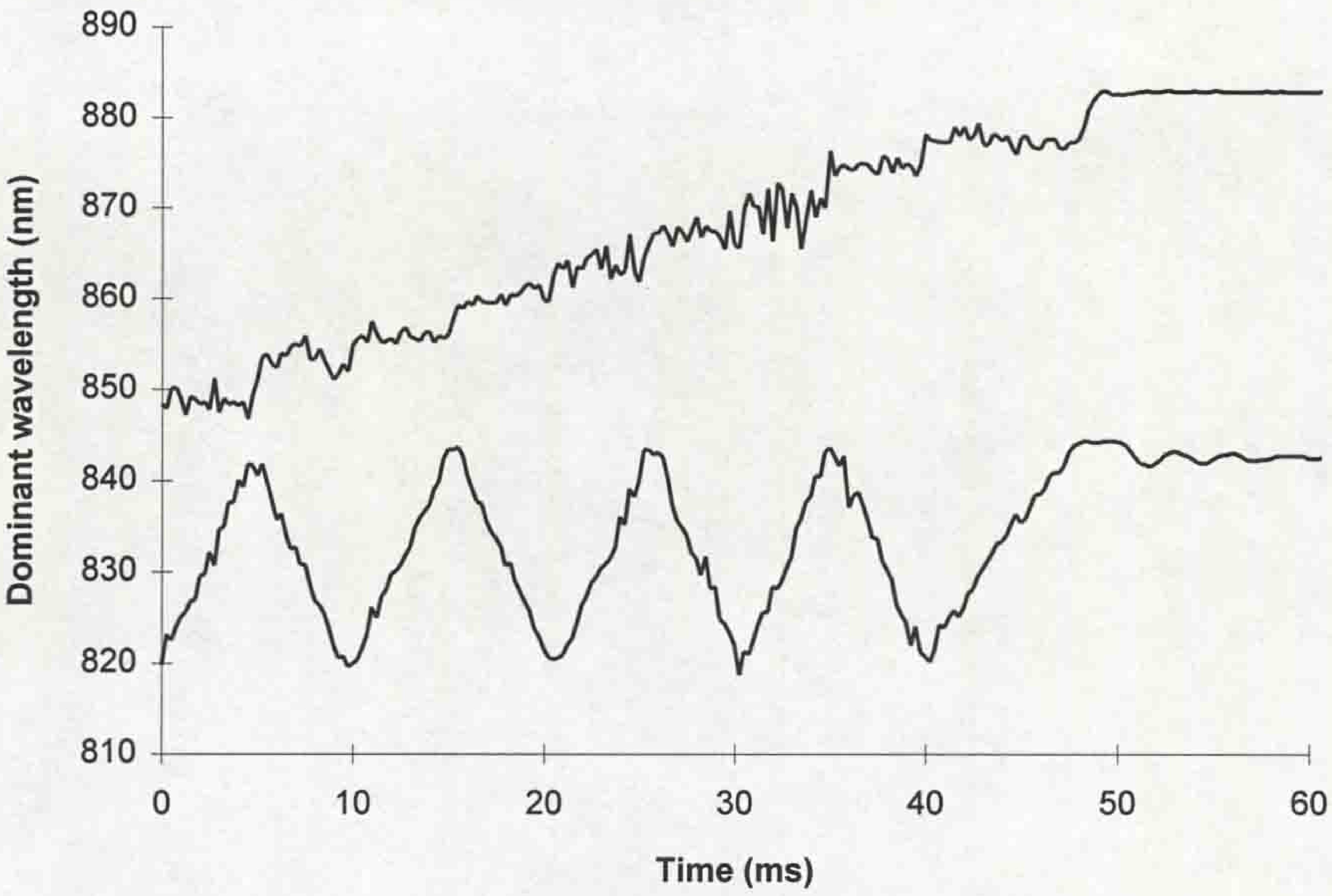

Figure 5.15 - OFLTR response during 20th operation at 15kA

5.4.2.1 Contaminant elimination

In order to overcome the build up of contamination particles on the scale and fibres, an annular cork seal was incorporated (fig.5.16).

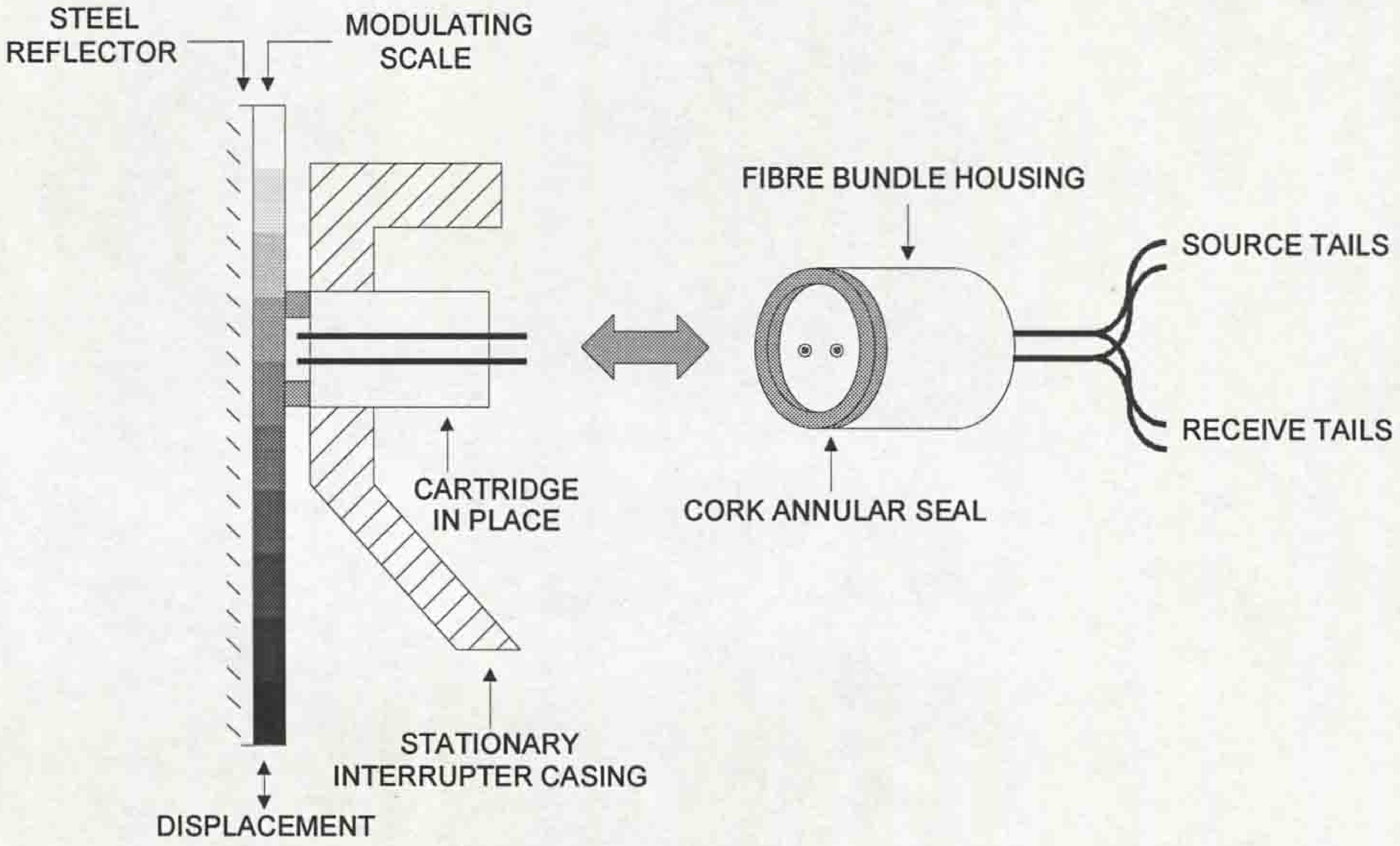

Figure 5.16 - Seal/wiper arrangement for OFLTR

This performed two functions: firstly, in pressing against the scale, the seal prohibited any particles from reaching the fibre tips; secondly, during operation of the interrupter, the seal wiped away any particles which had settled on the transducer from the previous test. This ensured a clear optical path for each operation of the breaker, giving highly repeatable performance of the OFLTR. This was verified by repeatability tests consisting of 30 operations at 15kA peak current. Figs.5.17 to 5.19 show the repeatability of the transducer signals throughout the test.

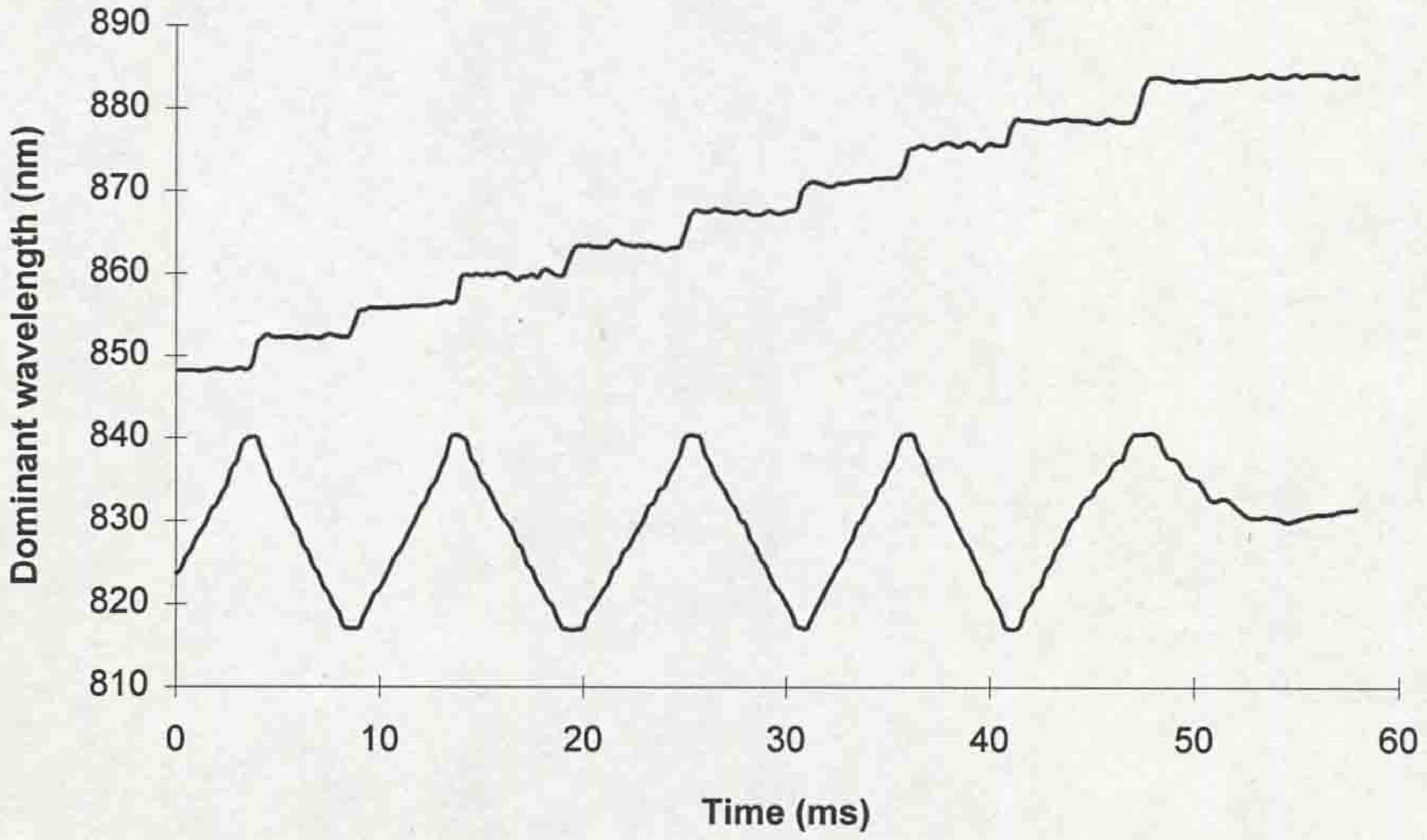

Figure 5.17 - 1st operation at 15kA with seal

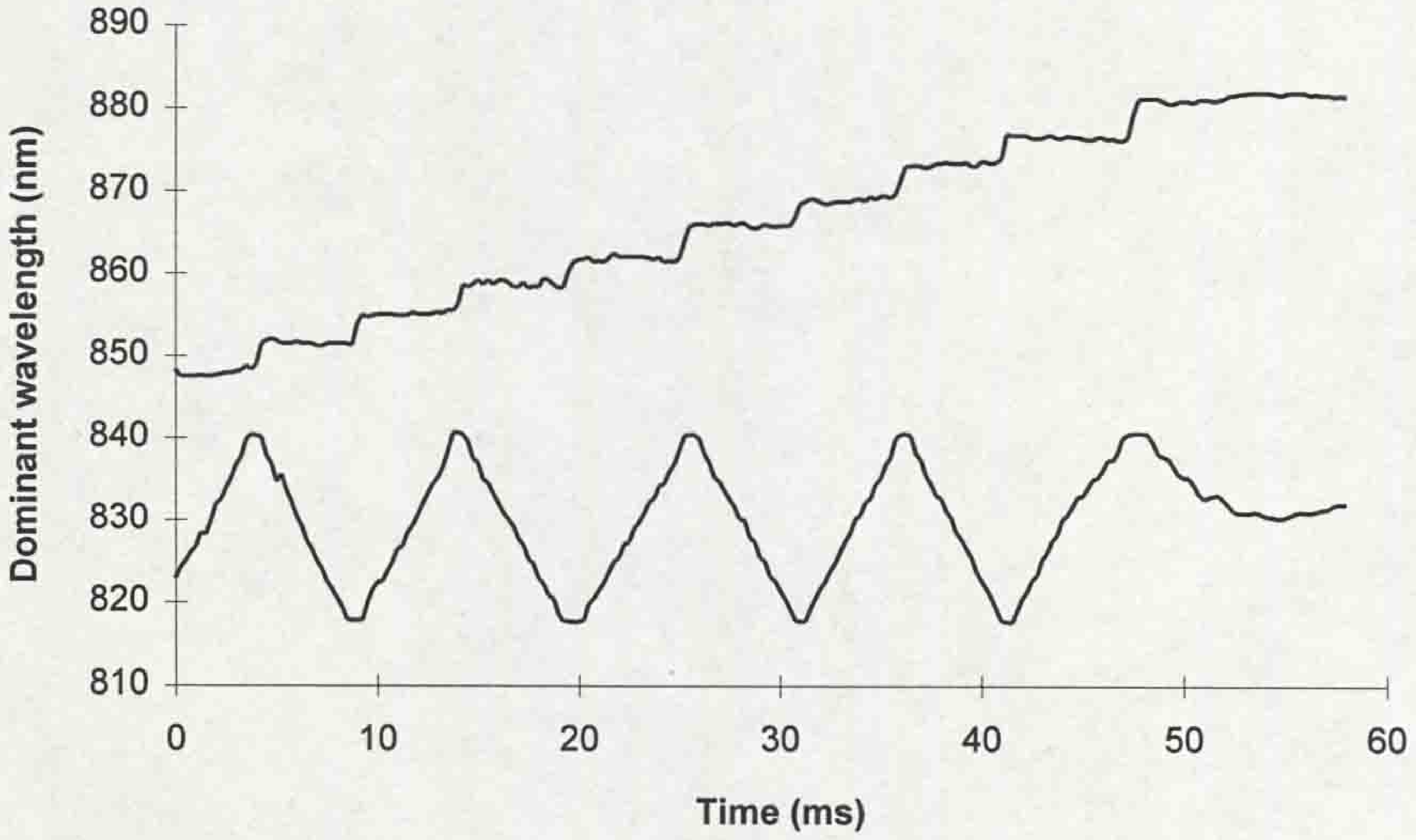

Figure 5.18 - 15th operation at 15kA with seal

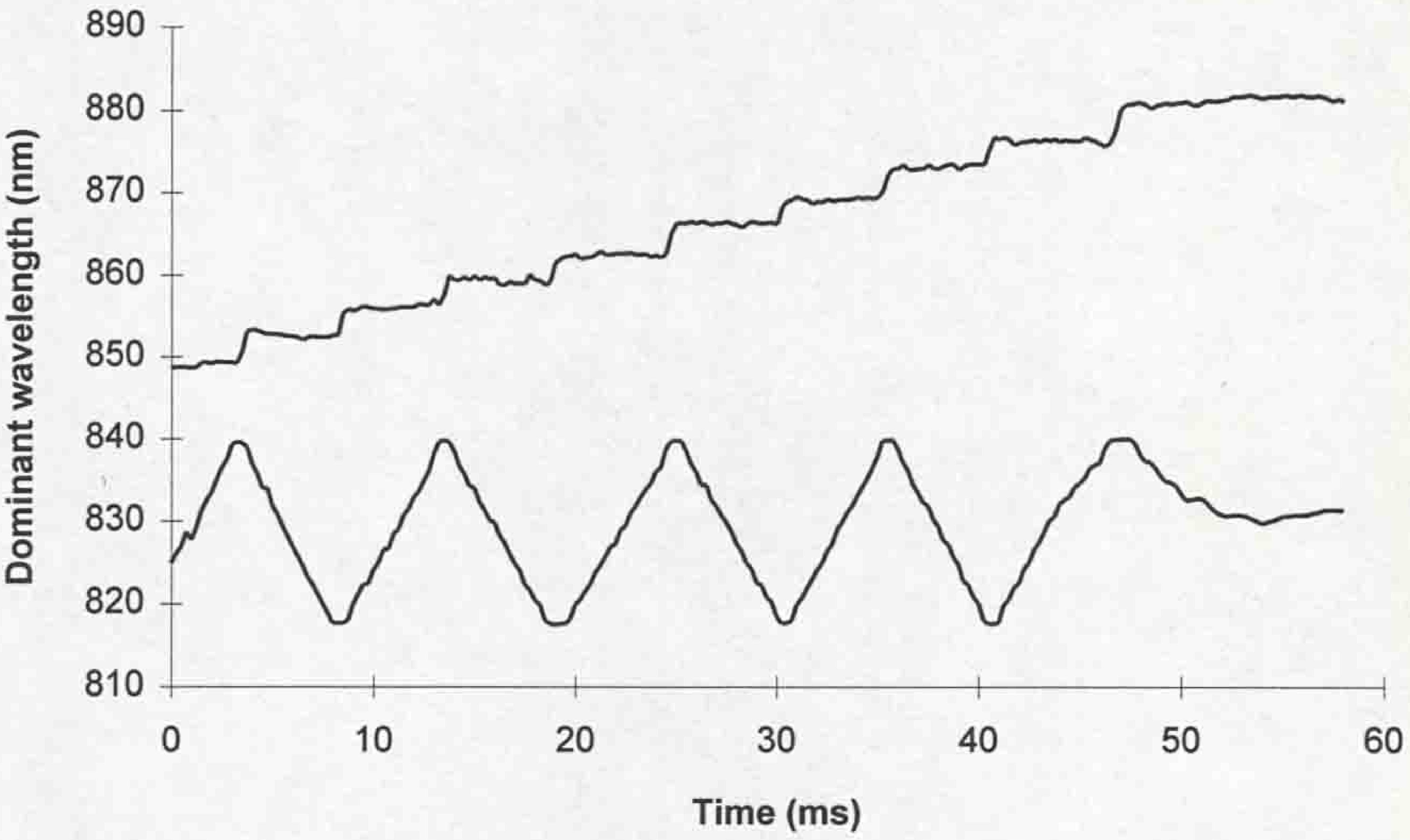

Figure 5.19 - 30th operation at 15kA with seal

The OFLTR was subsequently tested successfully at short circuit current levels up to 56kA peak, the rating of the breaker. The travel records obtained for all arcing situations were the same as the coldflow case (fig.5.12). Shimmin (1986) noted a similar result with his device on a commercial puffer circuit breaker and attributed the negligible effect of arc current on the records to the stiffness of the hydraulic driving mechanism.

5.4.2.2 Prototype lifetime

The prototype system was able to record over 100 operations of the circuit breaker, at various short circuit current levels and over a twelve month testing period, before overhaul was necessary. The lifetime was curtailed by etching of the glass fibre tips by hydrogen fluoride gas, another SF_6 degradation product, which permeated the porous cork seal. Therefore, the lifetime of the OFLTR could be extended, ideally to be maintenance free, by suitable choice of non-porous seal material. This would be the next appropriate development step towards realising a commercially viable OFLTR based upon this system.

5.5 CONCLUSIONS

As part of the project reported in this thesis it was necessary to monitor the electrode separation of the puffer circuit breaker during interruption of short circuit fault currents. Such travel records are essential for circuit breaker users to indicate the mechanical condition of the operating mechanism. They also contribute to circuit breaker research, since they provide a vital parameter for puffer circuit breaker modelling, by indicating accurate electrode position, arc length and piston volume as a function of time. An OFLTR would also be a primary sensing component of a circuit breaker condition monitoring system (**2.4.2**), which is being developed at the University of Liverpool and including sensors developed in this work.

A review of currently available optical fibre displacement sensors did not reveal any methods, which were suitable for use in the extremely harsh circuit breaker environment and also able to meet the design specification. Therefore, a novel device, based on chromatic modulation, was designed and developed.

The prototype OFLTR successfully monitored the interrupter stroke up to its full short circuit current rating. The only problem of significance to arise during initial tests was the build up of SF_6 degradation particles on the transducer, causing excessive noise on the optical signal. The introduction of a cork seal, which also acted as a wiper for the transducer, ensured a clear optical path and repeatable performance from the OFLTR.

The lifetime of the prototype OFLTR was governed by hydrogen fluoride etching of the glass fibre tips. The hydrogen fluoride gas, produced by SF_6 dissociation, was able to permeate the porous cork seal. Future development of the OFLTR should include an evaluation of seal materials to extend the lifetime to that of the circuit breaker and the use of the protective Teflon film, used to coat the scale itself, to also cover and protect the exposed optical fibre tips.

CHAPTER 6 - OPTICAL FIBRE PARTICLE CONCENTRATION MONITOR (OFPCM)

6.1 OBJECTIVES

When subjected to high power circuit breaker arcs, sulphur hexafluoride (SF_6) produces a wide range of decomposition products (Belmadini *et al*, 1991, Chu, 1986 and Ruegsegger *et al*, 1985). The decomposition products include small particles which form a mist-like suspension after arcing and take time to settle out of the gas. Since these particles contain metallic elements, their existence in the electrode region could compromise the dielectric strength of the gas (eg. Beavan, 1989). Therefore, an optical fibre particle concentration monitor (OFPCM), which could indicate the time taken for the particles to settle out of the gas, would be a useful tool in determining the extent of post-arc dielectric vulnerability.

The concentration of particles, produced during fault current interruption in a circuit breaker, is anticipated to be dependent upon the arc energy input, which also determines the wear of crucial circuit breaker components such as the electrodes and nozzle (Belmadini *et al*, 1991). When the wear of the components reaches a critical level, the circuit breaker is prone to failure. Therefore, an indication of such wear would be advantageous to circuit breaker users, in order to prevent one of the causes of future failure (Messent, 1995). An OFPCM may be useful as an element of a system capable of providing an indication of component wear caused in any given circuit breaker operation.

The objective of this part of the work was, therefore, to design, develop and test an OFPCM to indicate post-arc particle concentrations within the circuit breaker tank. As part of a unified optical sensing approach, it was decided that the system should be based, if possible, on a particle concentration - light chromaticity interaction, so that the generic LIBIDO distimulus chromatic monitoring system (**4.3.3.2**) could be used to interrogate the sensor simultaneously with other chromatic sensors developed in this work.

6.2 THEORY

6.2.1 Fundamentals of light scattering

Light scattering is a process whereby light energy is absorbed by particles and re-emitted without appreciable change in wavelength (Meyer-Arendt, 1984). Under the influence of electric fields molecules form an electric dipole, where positive and negative charges within the molecule are displaced in opposite directions. The dipole moment, **p**, of a molecule in such circumstances is given by

$$\mathbf{p} = \alpha \mathbf{E} \tag{6.1}$$

where α is the polarisability and **E** the local electric field strength. For a sinusoidal imposed electric field, such as electromagnetic radiation, the dipole moment will oscillate according to

$$\mathbf{p} = \alpha \mathbf{E} \sin \omega t \tag{6.2}$$

where ω is the frequency of oscillation and t the time. The oscillating dipole acts as an antenna causing re-radiation of the incident electromagnetic radiation. This is the fundamental process of light scattering. A dipole oscillating in the z axis of fig.6.1 will scatter light with an intensity which varies as $\cos^2\theta$ (fig.6.2):

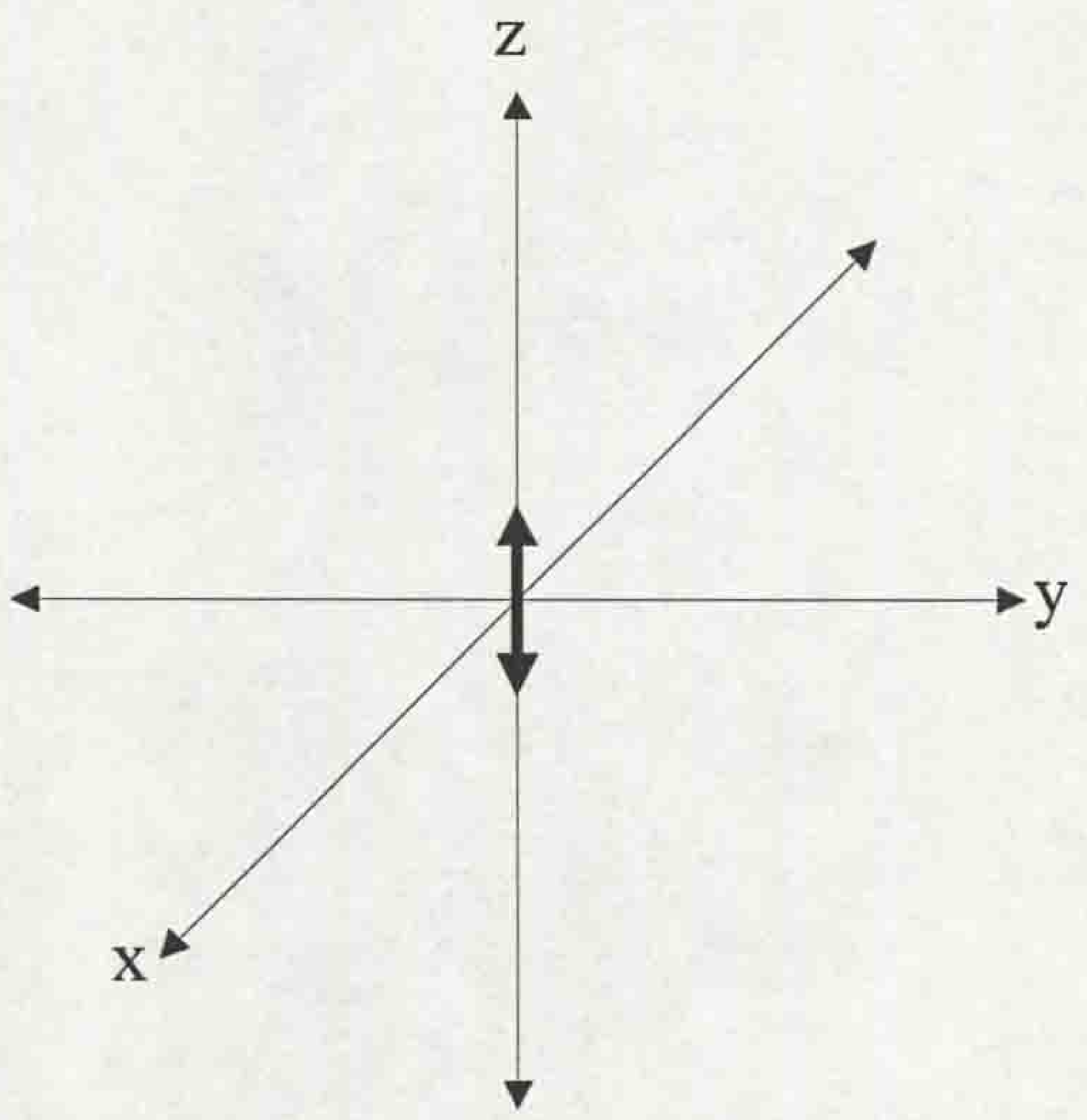

Figure 6.1 - Dipole oscillating in z-axis

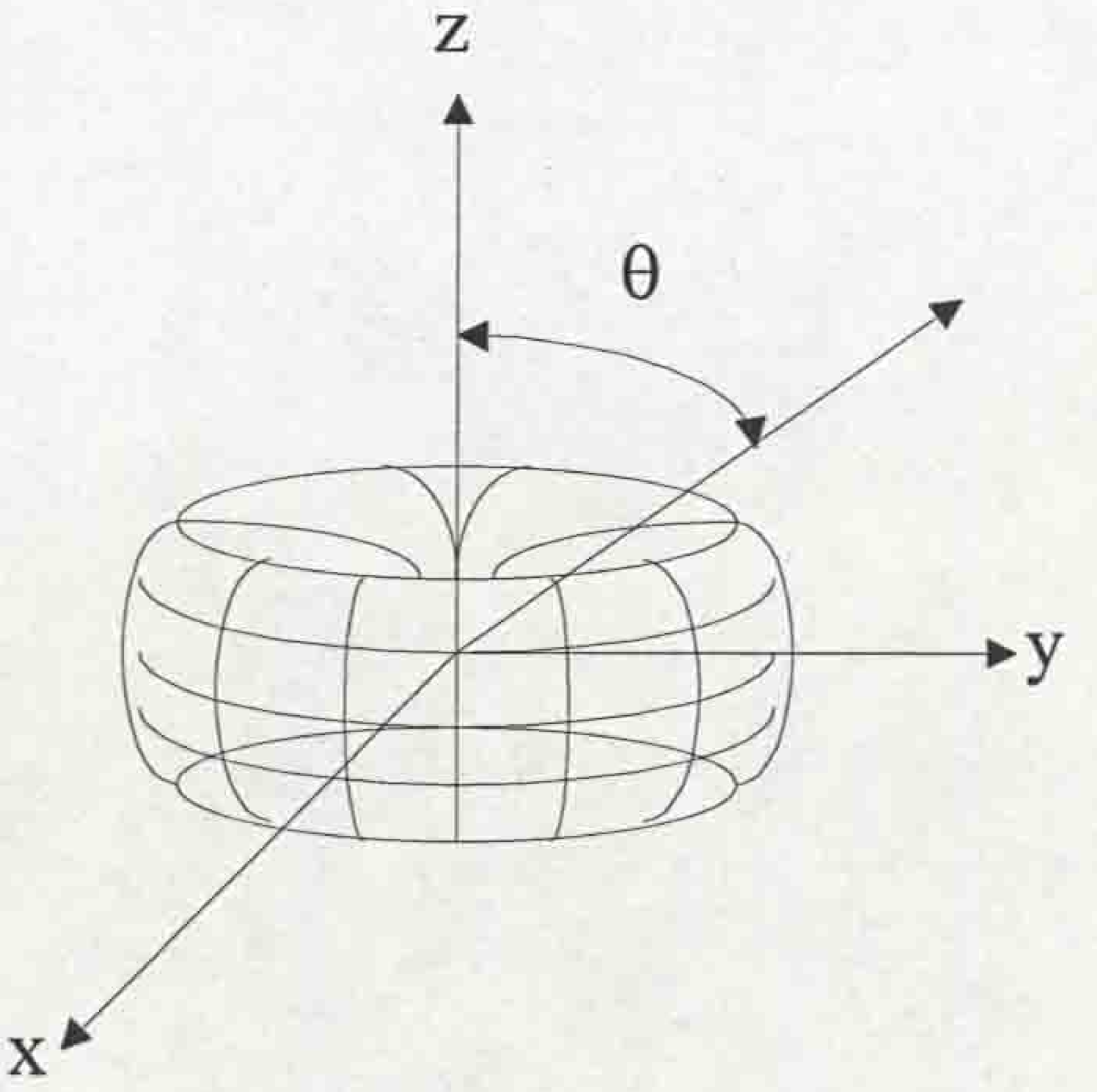

Figure 6.2 - $\cos^2\theta$ dependence of scattered intensity

6.2.1.1 Rayleigh scattering

Rayleigh scattering occurs for particles up to one tenth the wavelength of light (van de Hulst, 1957). If unpolarised light passes through a medium containing N scatterers per unit volume, then the intensity of the scattered light is (Meyer-Arendt)

$$i = \frac{I_0 8\pi^4 N\alpha^2}{\lambda^4 L^2}(1+\cos^2\theta) \tag{6.3}$$

where I_0 is the incident light intensity, N the number of particles per unit volume, α the polarisability of the particles and L the distance from the scatterers to the point of observation.

The total intensity of the scattered light will be given by

$$i_T = \frac{I_0 8\pi^4 N\alpha^2}{\lambda^4 L^2}\int_0^{2\pi}(1+\cos^2\theta)d\theta \tag{6.4}$$

It can be shown that $1+\cos^2\theta = \frac{1}{2}(3+\cos 2\theta)$. Thus, equation 6.4 becomes

$$i_T = \frac{I_0 8\pi^4 N\alpha^2}{\lambda^4 L^2} \int_0^{2\pi} \frac{1}{2}(3 + \cos 2\theta)\, d\theta \qquad (6.5)$$

which can be solved to provide an expression for the total scattered light intensity of

$$i_T = \frac{I_0 24\pi^5 N\alpha^2}{\lambda^4 L^2} \qquad (6.6)$$

The important implication of eqn.6.6 is that the intensity of scattered light is inversely proportional to the fourth power of the wavelength (fig.6.3):

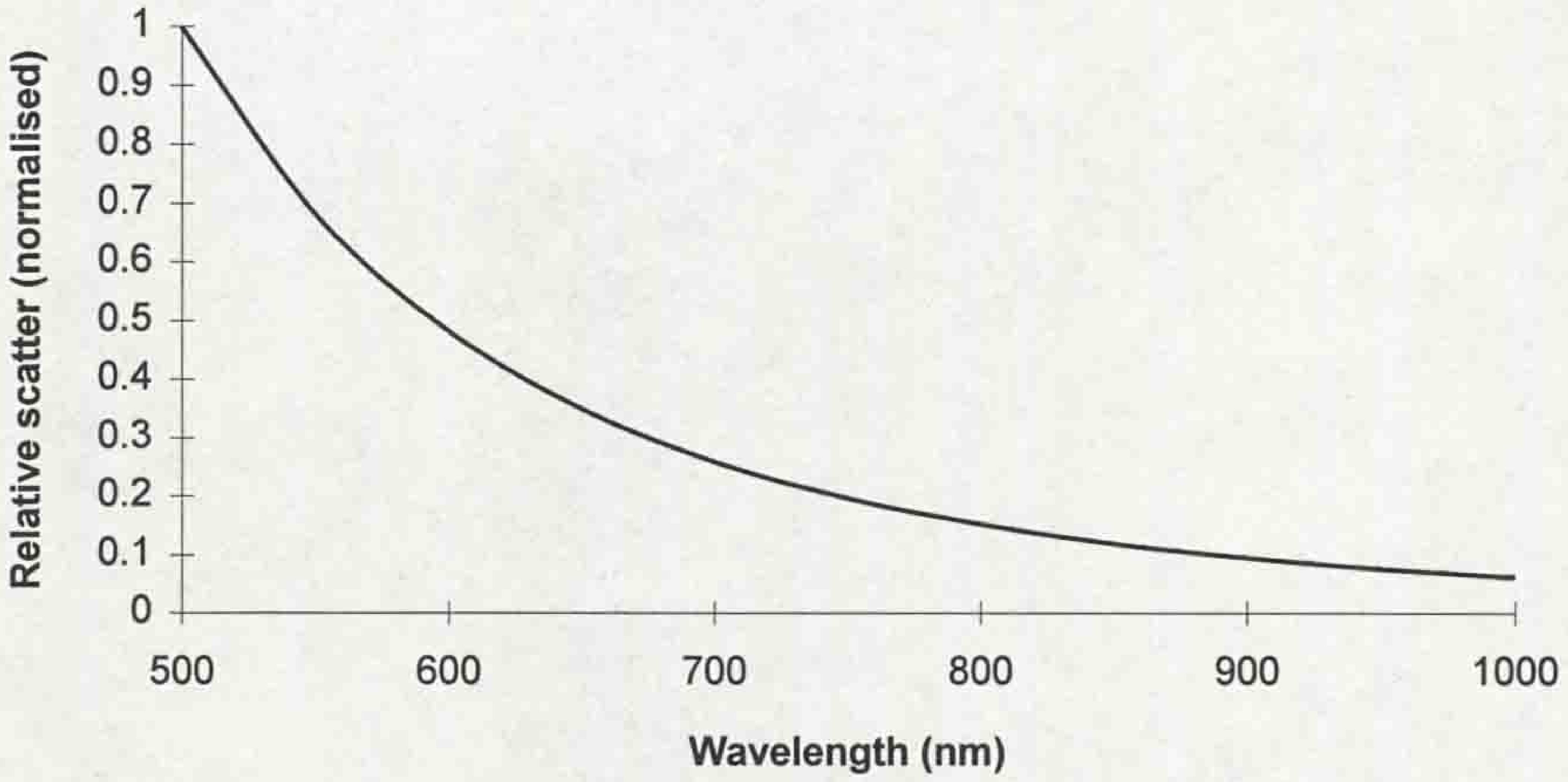

Figure 6.3 - Rayleigh scattered intensity as a function of wavelength

It follows that the unscattered light intensity will be given by

$$i_{UNSCATTERED} = I_0 \left[1 - \frac{24\pi^5 N\alpha^2}{\lambda^4 L^2} \right] \qquad (6.7)$$

6.2.1.2 Mie scattering

When the scattering particles are larger than one tenth of the wavelength of light, the light scattered from one point on the particle may be out of phase with light scattered from another point. The two contributions interfere and the scattered light is not symmetrically distributed as in the Rayleigh case. As the particle size increases the scattered light becomes more concentrated in the forward direction. Mie's theory (1908) is a generalised theory, encompassing all sizes of scattering particles, of which Rayleigh scattering is a special case.

If light of cross-section A is incident on a volume V of thickness Δx, containing N particles per unit volume and if r is the radius of a particle, such that each particle has a cross-section πr^2, then together they have a cross-section (Meyer-Arendt, 1984)

$$\sum = NA\Delta x\pi r^2 \tag{6.8}$$

However, since the particles will have a different refractive index to the surrounding medium, the "scattering cross-section" will not be the same as the particle cross-section. The ratio of the two cross-sections, known as the extinction factor K, is usually greater than one, indicating that the light scattering effect of a particle is greater than what would be expected from its physical size. The value $K\pi r^2$ is called the extinction cross section and the Mie extinction coefficient is given by

$$\mu = NK\pi r^2 \tag{6.9}$$

If the particles are of a size distribution, with radii ranging from r_1 to r_2 then

$$\mu = \pi \int_{r_1}^{r_2} NKr^2 dr \tag{6.10}$$

The ratio of the intensity of the scattered light, i, to the intensity of the incident light I_0 is given by

$$\frac{i}{I_0} = \mu\Delta x \tag{6.11}$$

Fig.6.4 shows how the extinction factor K varies with particle radius and wavelength (Meyer-Arendt, 1984).

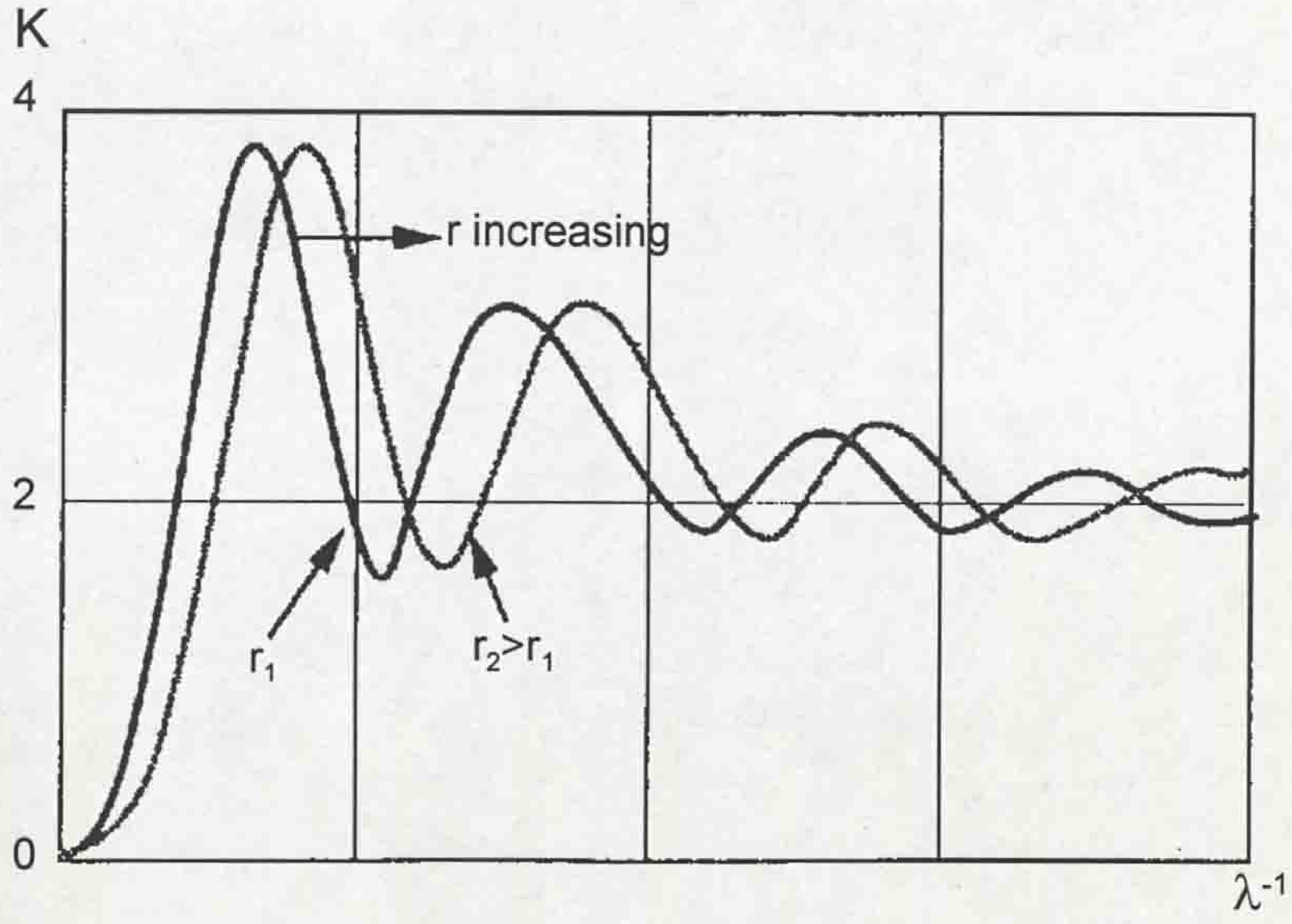

Figure 6.4 - Variation of extinction factor with wavelength and particle radius (Meyer-Arendt, 1984)

Jones and Russell (1993) indicated that the wavelength dependence of the extinction factor K could yield a chromaticity dependence on the particle radius, r, and concentration, N, of a polychromatic light, when transmitted through a particle conglomerate. This is discussed further below.

6.3 APPLICATION TO POST-ARC PARTICLE MONITORING IN A CIRCUIT BREAKER

6.3.1 The decomposition products of arced SF_6

The decomposition products of arced SF_6 have been listed in several studies (Belmadini *et al*, 1991, Chu, 1986, Sauers *et al*, 1986 and Ruegsegger *et al*, 1985). The principle reaction scheme (Sauers *et al*, 1986), which occurs when SF_6 is subjected to an arc in a circuit breaker is given in fig.6.5:

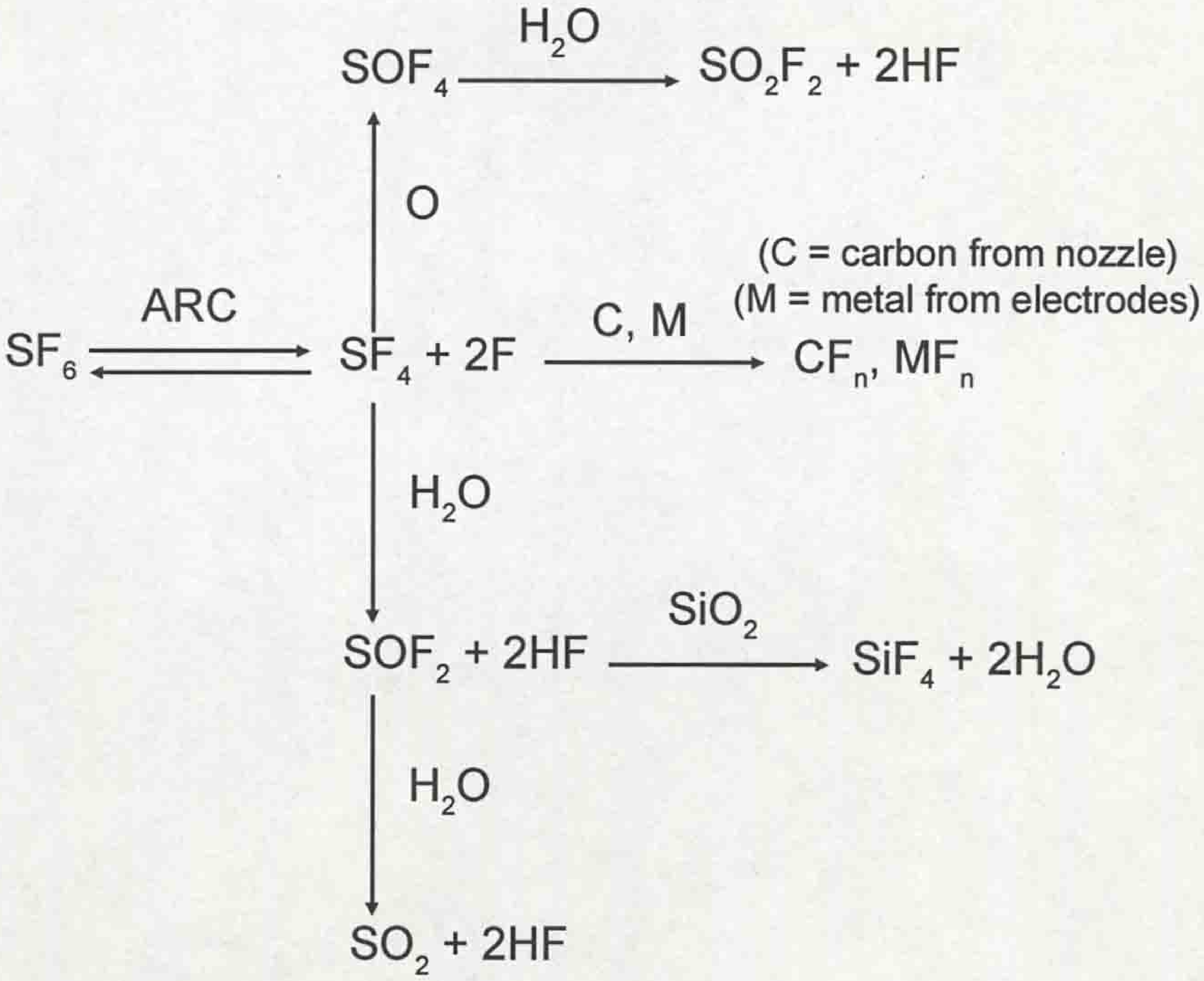

Figure 6.5 - Reaction scheme for arced SF_6

- The principal dissociation reaction of SF_6 gives SF_4 and F.
- The SF_4 combines with the unavoidable contaminants H_2O and O_2 to provide SOF_2 and SOF_4.
- SOF_2 is further hydrolysed to produce SO_2 and SOF_4 is hydrolysed to produce SO_2F_2.
- Carbon, which is present in the PTFE polymer nozzle reacts with dissociated fluorine to produce CF_4.
- Metals are also attacked by the fluorine to produce metal fluorides. The principal fluorides are WF_6 and CuF_2, since the circuit breaker electrodes are usually composed from copper tungsten alloy.

The decomposition of SF_6 in a circuit breaker is clearly complex. The major stable gaseous decay products are SOF_2, SO_2F_2, SO_2 and CF_4 (Belmadini *et al*, 1991). In addition to this solid particles are formed consisting of, in order of abundance, tungsten, copper, metal fluorides, iron, carbon and other minor constituents. These particles form a mist-like suspension, which takes time to settle following a short-circuit interruption.

6.3.2 The chromatic effect of light scattering

It was shown above that the decomposition products of SF_6 are considerably varied. In order to demonstrate the chromatic effect of light scattering, the generalised principles of Mie scattering are used, since the scattering particle sizes will generally exceed the λ/10 Rayleigh limit.

For a given broadband polychromatic light source E(λ), which is interrogated by a photodiode with response R(λ), having been modulated by the function M(λ), the short circuit current produced by the photodiode is given by:

$$I = \int_{\lambda_1}^{\lambda_2} E(\lambda)R(\lambda)M(\lambda)d\lambda \qquad (6.12)$$

The integrating range, λ1 to λ2, depends upon the working range of the detection system used (for this work the range was 500 to 1000nm). For light scattering by particles, the modulation function is itself a function of the Mie extinction coefficient, μ i.e. M=f(μ). Furthermore, according to eqn.6.9, μ=f(N,K,r) and fig.6.4 shows that K=f(r,λ). Hence, it follows that

$$M = f(N, r, \lambda) \qquad (6.13)$$

The significance of eqn.6.13 is that the modulation of a light source, when passed through a region of scattering particles, is a function of the concentration of particles, their size and the wavelength of the incident light.

The chromaticity of a light signal has been defined (**4.3.3**) in distimulus terms, with respect to the PD150 photodiode, as the ratio of the two photodiode short circuit currents I_1/I_2. Hence, for the PD150 based LIBIDO detection system, used in this work, the chromaticity of a broadband polychromatic source E(λ), after passing through a region of scattering particles, will be given by

$$C = \frac{I_1}{I_2} = \frac{\int_{\lambda_1}^{\lambda_2} E(\lambda)R_1(\lambda)M(N,r,\lambda)d\lambda}{\int_{\lambda_1}^{\lambda_2} E(\lambda)R_2(\lambda)M(N,r,\lambda)d\lambda} \tag{6.14}$$

The relationship between the value C and dominant wavelength, λ_D, for the modulated light spectrum, is given on fig.4.20. Therefore, solution of eqn.6.14 will yield a relationship between λ_D and particle size and radius i.e. λ_D=f(N,r). Hence, for a distimulus system, such as the PD150 based LIBIDO used for this project, the combined effect of particle size and concentration can be measured by the dominant wavelength change of a broadband signal, when passed through the particle conglomerate.

It is interesting to note that, if a tristimulus system were used (three overlapping detectors - **4.3.1**), then the modulated light signal would be described in terms of two chromatic variables i.e. dominant wavelength and colorimetric purity. These two output variables, to describe the effect of particle concentration, N, and radius, r, might provide discrimination between the two. This approach is recommended as an extension to this work in **chapter 12**.

6.3.3 Previous particle concentration monitoring in a circuit breaker

Beavan (1989) investigated the effect of changing the particle concentration, N, for a fixed particle radius, r, on the intensity of a broadband polychromatic light signal, when passed through a particle suspension. This result (fig.6.6) shows that as the particle concentration increases, the transmitted intensity of the shorter wavelengths is reduced by a larger amount than the longer wavelengths. Hence, as N increases, the ratio of infra-red / visible light also increases and the dominant wavelength of the modulated signal shifts to a higher value.

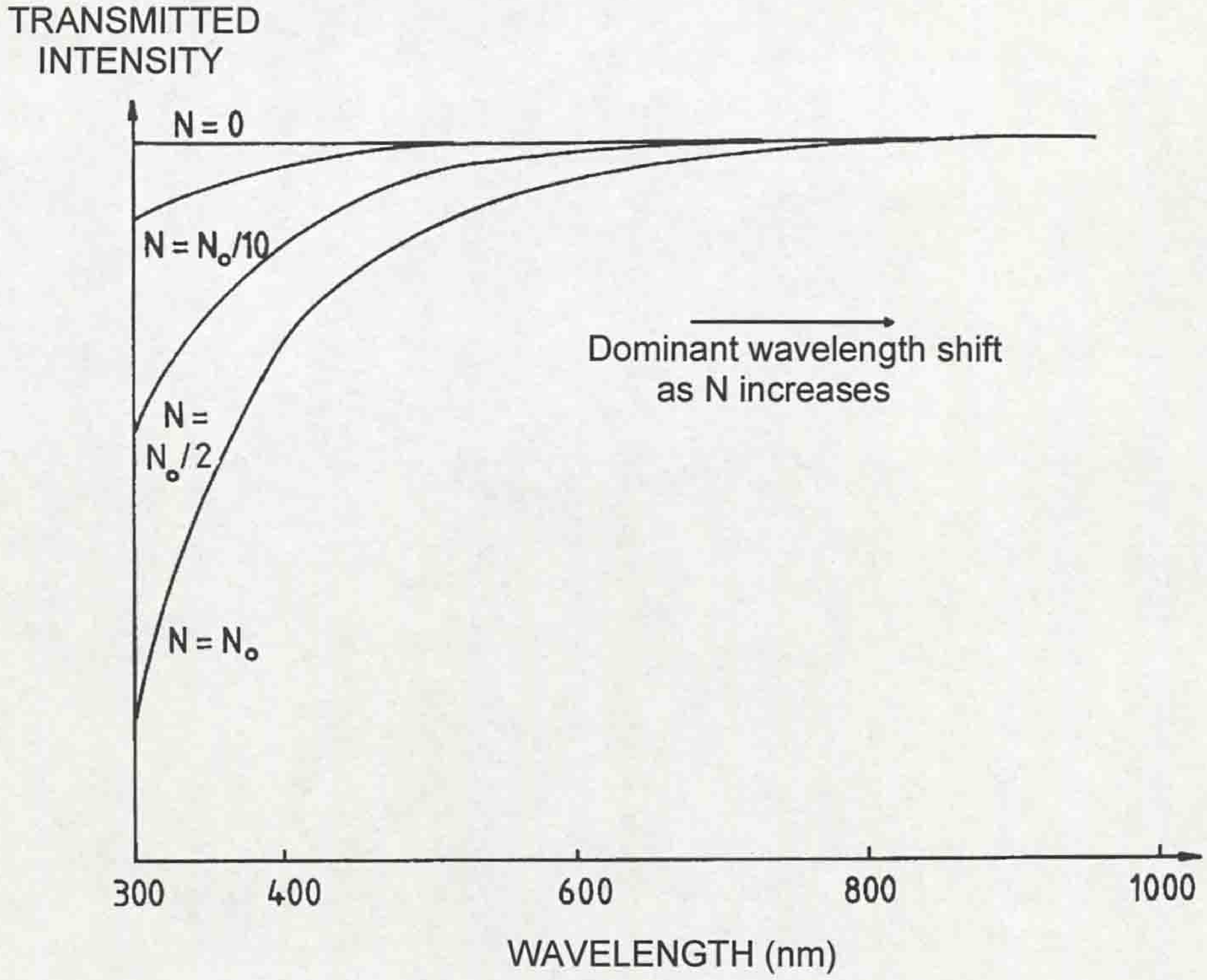

Figure 6.6 - Effect of particle concentration on transmitted intensity (Beavan, 1989)

Beavan verified the effect experimentally by monitoring the post-arc particle concentrations following a free burning arc in SF_6. A broadband "white light" source was transmitted through a region of the circuit breaker and a tristimulus detector received the modulated light spectrum. The result is shown on fig.6.7.

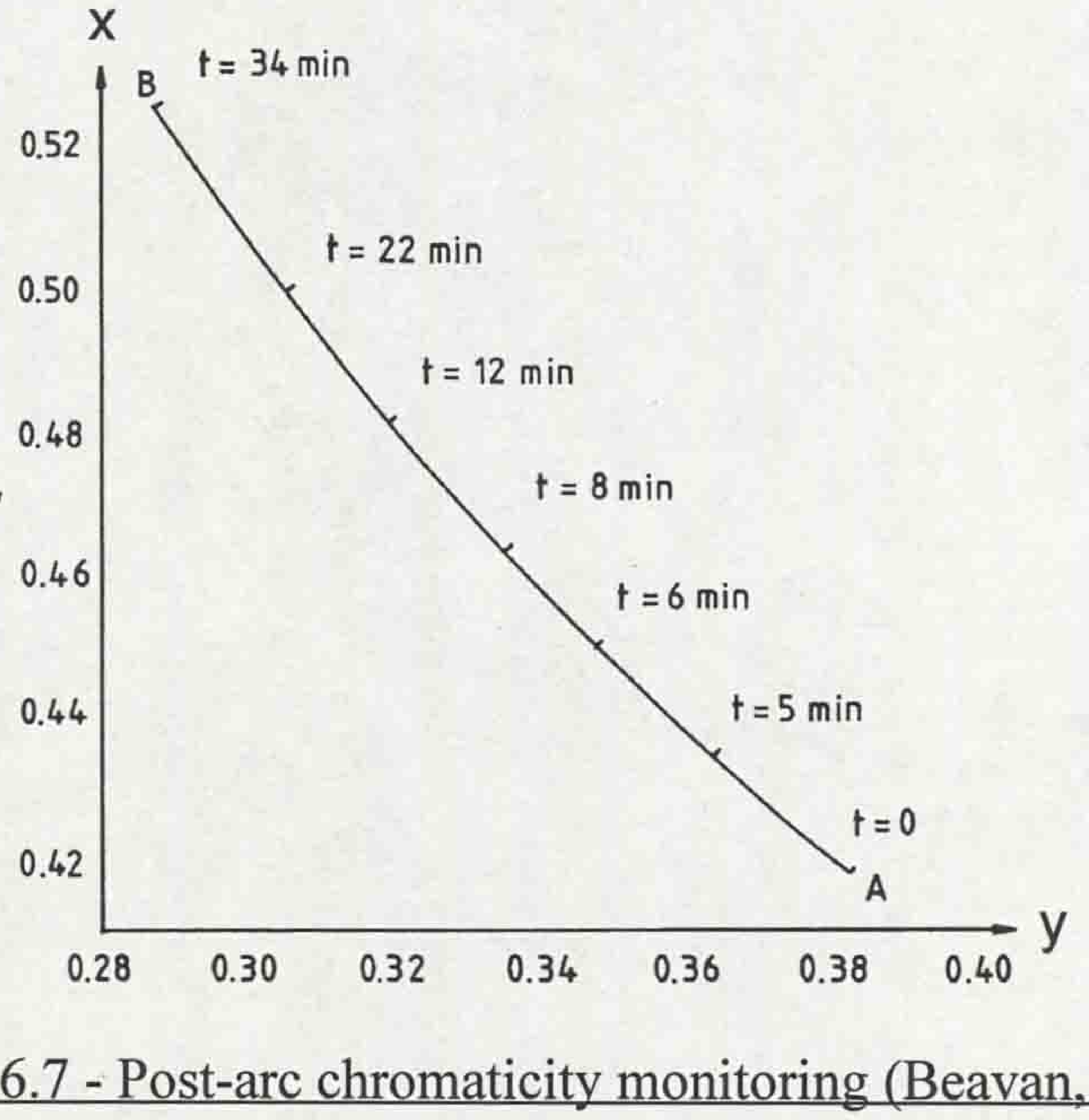

Figure 6.7 - Post-arc chromaticity monitoring (Beavan, 1989)

Point B is the chromaticity of the light transmitted through the test head before the interruption of the arc current. Point A is the chromaticity of the modulated light after arc current interruption, caused by scattering from the arc-induced SF_6 decomposition particles in suspension. The time-dependent chromaticity was monitored as the particle suspension settled out of the gas and is indicated by the locus AB. The chromaticity of the transmitted light moved towards the pre-arc chromaticity with time and gradually returned to that value.

In this way, the time taken for the particles to fully settle out of the gas was measured to be 34 minutes for this test. The direction of the locus from A to B on fig.6.7 corresponds to a reduction in dominant wavelength of the modulated light as the particles settle i.e. as N falls. This experiment proved that the light scattering caused by particles following heavy current arcing had a chromatic dependence on the particle concentration; however, the system was not calibrated to yield values of particle concentration from the modulated light chromaticity. The intention of this work, therefore, was to produce a particle concentration monitor, which could be calibrated so that actual levels of particle concentration within the test circuit breaker could be estimated. A distimulus system was used (the PD150 based LIBIDO) to determine a relationship between modulated light dominant wavelength, λ_D, and particle concentration, N. The practical system is described below (**6.3.4**).

6.3.4 Prototype optical fibre particle concentration monitor

The optical fibre particle concentration monitor (OFPCM), designed for the circuit breaker tests is shown schematically in fig.6.8. Broadband white light from the LIBIDO chromatic source/detection system (**4.3.3.2**) is collimated by a ball lens 10mm diameter. The light is passed through a gap of 10mm length before being refocused into a receiving fibre and transmitted to the LIBIDO detector. The modulation of the light beam is determined by the concentration of particles in the gap.

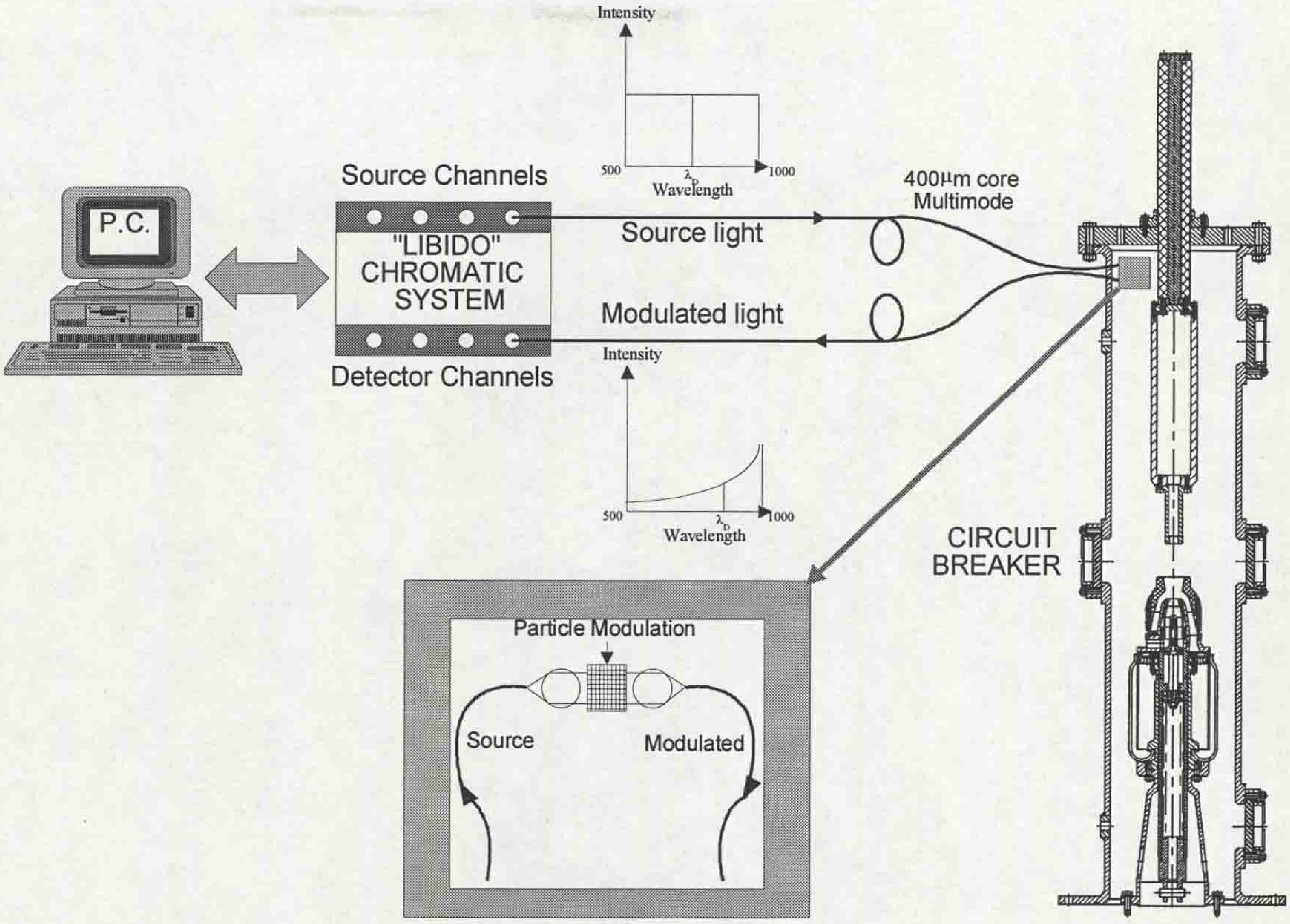

Figure 6.8 - Schematic of optical fibre particle concentration monitor

For calibration, the sensor was housed in an SF_6 filled chamber. Particles obtained from previous circuit breaker tests were added in a controlled manner so that the concentration in the chamber was known. A fan in the chamber was used to circulate the particles, producing the characteristic circuit breaker suspension. Each time particles were added to the test chamber the dominant wavelength of the modulated signal was measured by the LIBIDO system. The experimental set-up was as shown on fig.6.8, with the test chamber replacing the circuit breaker. Four tests were performed, to give the calibration characteristic shown on fig.6.9. A simple curve-fit to the results gives

$$\lambda_D = 820 + 0.167c \tag{6.15}$$

where λ_D is the recorded dominant wavelength and c the concentration. This result shows an apparent accuracy, with respect to the values on fig.6.9, of 10mg/l. Chapter 10 presents the results obtained from the prototype OFPCM, on the test circuit breaker, during interruption of fault currents up to 56kA peak.

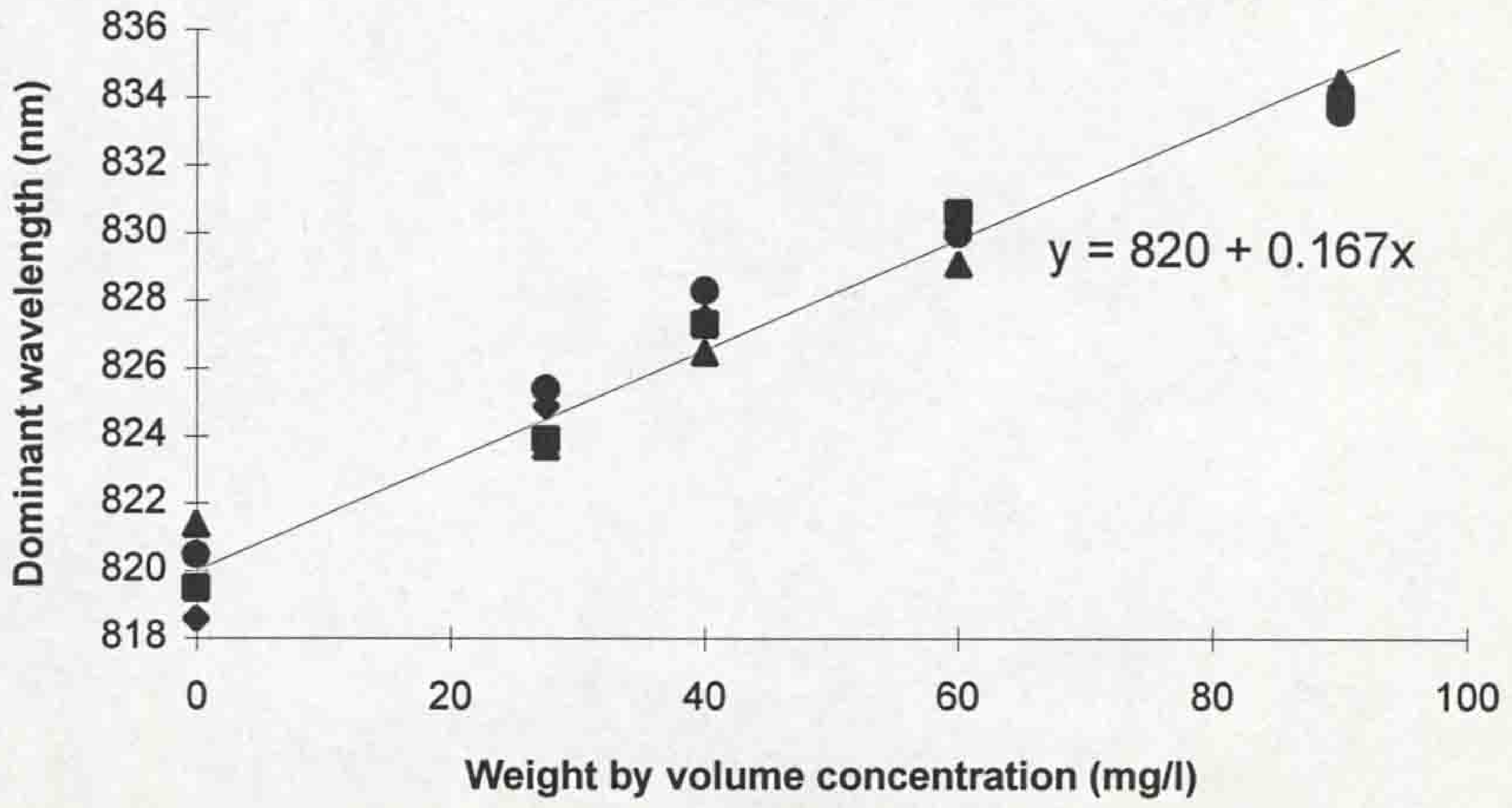

Figure 6.9 - Calibration curve for optical fibre particle concentration monitor

6.4 CONCLUSIONS

It has been shown that light scattering is wavelength dependent. For Rayleigh scattering (**6.2.1.1**), the scattered intensity is inversely proportional to the fourth power of the wavelength (eqn.6.6 and fig.6.3). As the particle size increases, then, according to Mie's generalised theory (**6.2.1.2**), the wavelength dependence is a complex relationship, as shown on fig.6.4.

The effect of light scattering on a polychromatic broadband light source is that the ratio of infra-red to visible light which emerges, after passing through a particle conglomerate, increases as the concentration of the particles increases (Beavan, 1989). Thus, the light undergoes a chromatic shift, with a corresponding shift in dominant wavelength, which is concentration dependent.

It was shown that, for the purpose of monitoring the post-arc particle concentrations in a circuit breaker, the decomposition products of SF_6 are many and varied (**6.3.1**) and the principles of Mie scattering may be applied to show in general how the dominant wavelength of a polychromatic light may be affected by the particle concentration and size within the circuit breaker. It was possible to reproduce the characteristic circuit breaker particle suspensions experimentally, using measured particle concentrations (weight by volume). Consequently, an approximate experimentally derived dependence of chromaticity on particle concentration was obtained (fig.6.9). This correlation can be used to convert the dominant wavelength values, obtained from the particle concentration monitor during the main circuit breaker tests (**chapter 10**), into their corresponding particle concentrations.

The OFPCM system developed was based on a distimulus detector. A distimulus system provides one chromatic variable output i.e. dominant wavelength, λ_D. Therefore, the values of λ_D obtained represent the combined effect of particle concentration, N, and radius, r, without any discrimination between the two. However, this was a convenient first development step, since it allowed the use of the PD150 based LIBIDO distimulus detection system, which was also used for other sensors in this project. Further development of the system could extend to tristimulus monitoring, which, by providing two chromatic output variables (dominant wavelength and colorimetric purity), may allow some discrimination between the individual contributions from N and r. This development step is recommended in **chapter 12**.

CHAPTER 7 - GAS DIELECTRIC STRENGTH PROBE

7.1 INTRODUCTION

7.1.1 Objective

Hot gas, generated by arcing in a gas blast circuit breaker, has a reduced mass density, causing its dielectric strength to decrease (Okamoto *et al*, 1991). Therefore, it is important to be able to characterise the behaviour of hot gas in a circuit breaker, in order to ensure that the post-arc dielectric strength is sufficient for the current interruption process to be completed. This chapter describes the design, assembly and testing of a dielectric probe for monitoring a particular region of the circuit breaker tank for hot SF_6 gas (i.e. reduced dielectric strength), where conventional thermal mapping, such as Schlieren, would be impractical (Yoshizumi *et al*, 1989).

It may be possible to estimate the temperature of the gas from the dielectric strength, using the results of Chervy *et al* (1994), provided that it is simply the reduction of mass density alone, which causes the dielectric strength change. In practice, other effects, such as the lack of thermodynamic equilibrium and the production of particulate material (**chapter 6**), may also influence the dielectric strength (Jones, 1996). Thus, as a first step in the process of estimating arc-induced after-effects in reducing the gas dielectric strength, regardless of the precise reason, the dielectric probe offers considerable advantages.

7.1.2 Principle of operation

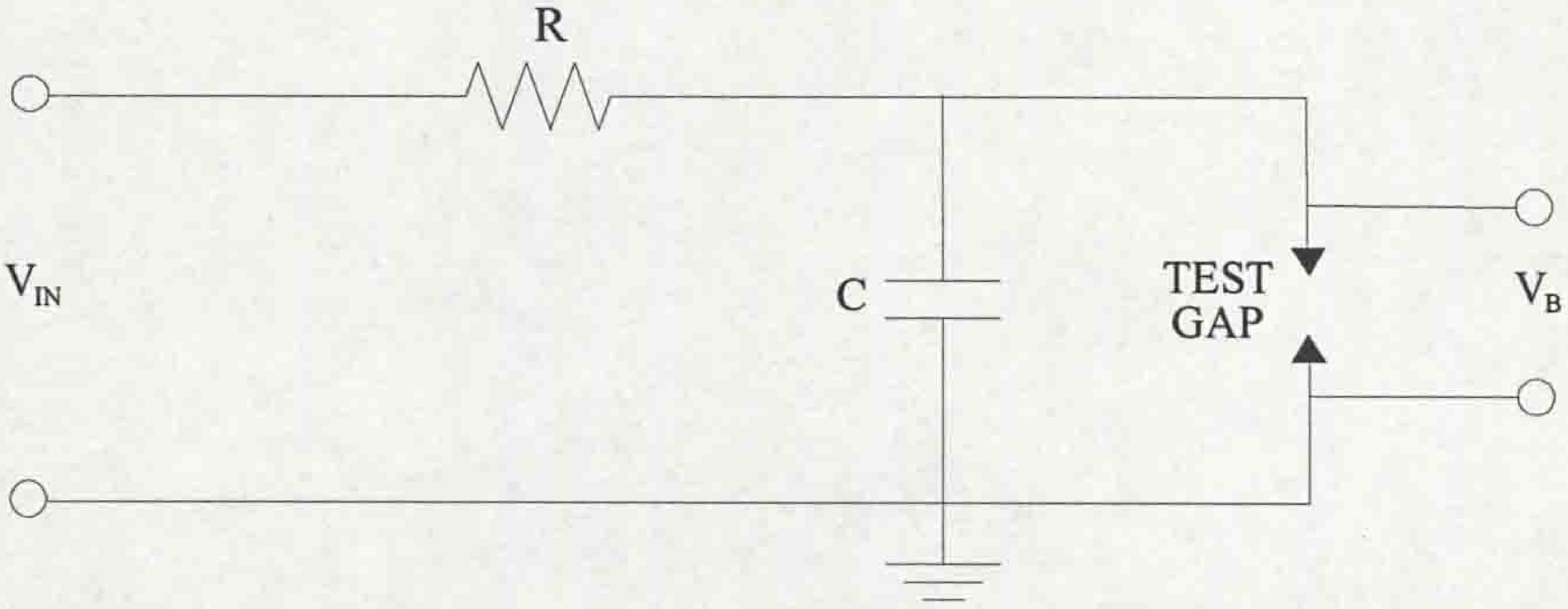

Figure 7.1 - Dielectric probe charging circuit

The operation of the dielectric probe is fundamentally based upon the circuit shown on fig.7.1. A high source voltage, V_{IN} (30kV), charges up a small capacitor C (20pF) through a large resistance R (100MΩ). When the voltage across C reaches the breakdown voltage of the gas, for a particular electrode test gap, the gap breaks down and the capacitor is discharged. After breakdown of the gap the voltage across the capacitor begins to rise as it is charged again. The gap breaks down once more when its voltage reaches the breakdown value and the process is repeated to set up a repetitive discharge waveform (shown from t_0 to t_1 on fig.7.2).

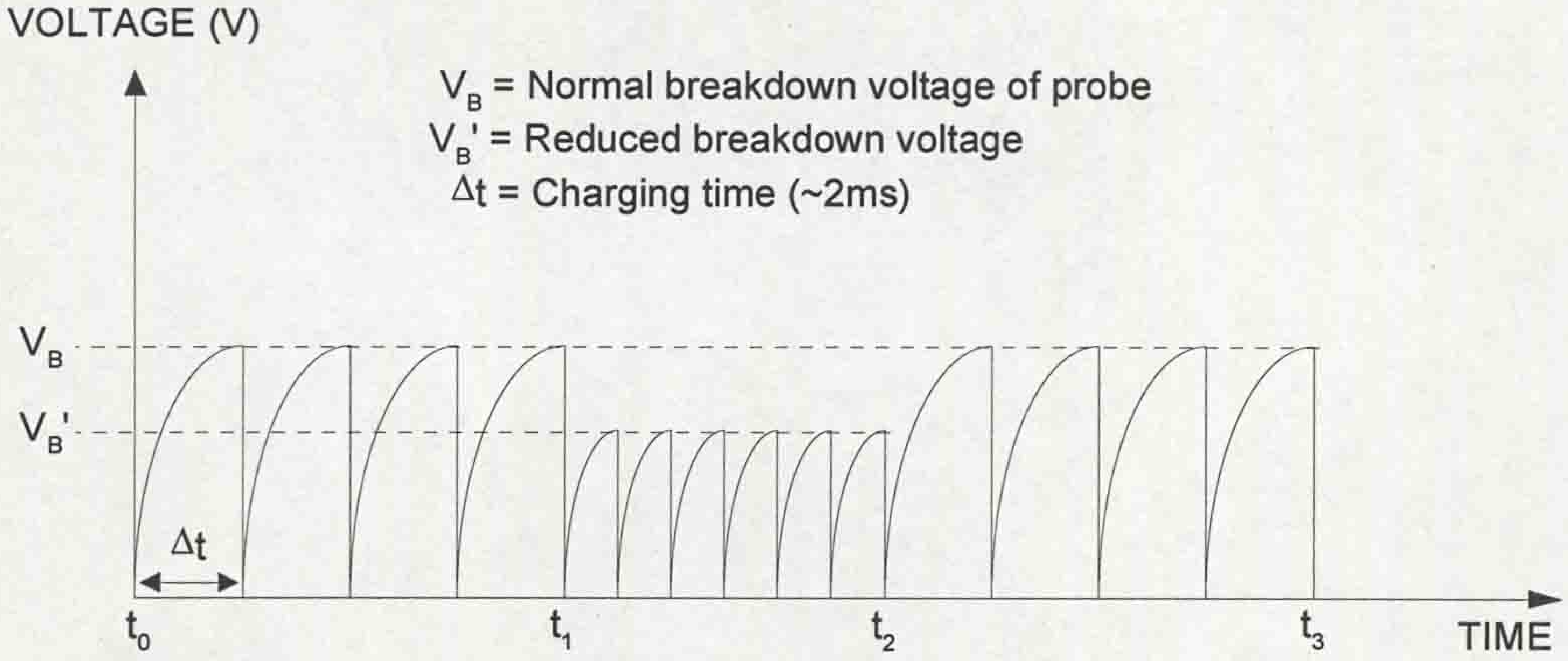

Figure 7.2 - Repetitive discharge waveform

The value of C is small so that the discharge energy is low and, consequently, erosion of the electrodes is minimal. (In practice C is the capacitance of the probe itself plus stray capacitance to ground). The value of R is chosen so that the charging time constant is 2ms. This provides a repetitive discharge of around 500Hz frequency in cool SF_6 (300K), which was chosen to be a suitable sampling rate.

If hot gas enters the test gap then its reduced mass density would decrease the breakdown voltage of the gas and the amplitude of the discharge waveform would be lowered. (This is shown between t_1 and t_2 in fig.7.2). From t_2 to t_3 the waveform has re-established itself to the previous level indicating full dielectric recovery. The waveform in fig.7.2 provides two important pieces of information; firstly, the extent of the dielectric loss and, secondly, the duration of reduced dielectric strength. It is also possible to estimate the temperature of the hot gas, by the reduction in breakdown voltage, assuming that this is the only factor causing the reduction. This is discussed in **7.2** below.

7.2 RELATIONSHIP BETWEEN BREAKDOWN VOLTAGE AND GAS TEMPERATURE

To arrive at a correlation between breakdown voltage and the temperature of the SF_6 requires two steps. Firstly, the test gap is calibrated to identify the relationship between the breakdown voltage of SF_6 and mass density (converted from pressure measurements), for the particular electrode configuration chosen. The second step is to use results of previous studies to convert the mass density into the corresponding SF_6 temperature.

7.2.1 Relationship between breakdown voltage and mass density

The electrode test gap, with the configuration shown in fig.7.3, was calibrated in cool SF_6 (300K), to produce a relationship between breakdown voltage and mass density (fig.7.4).

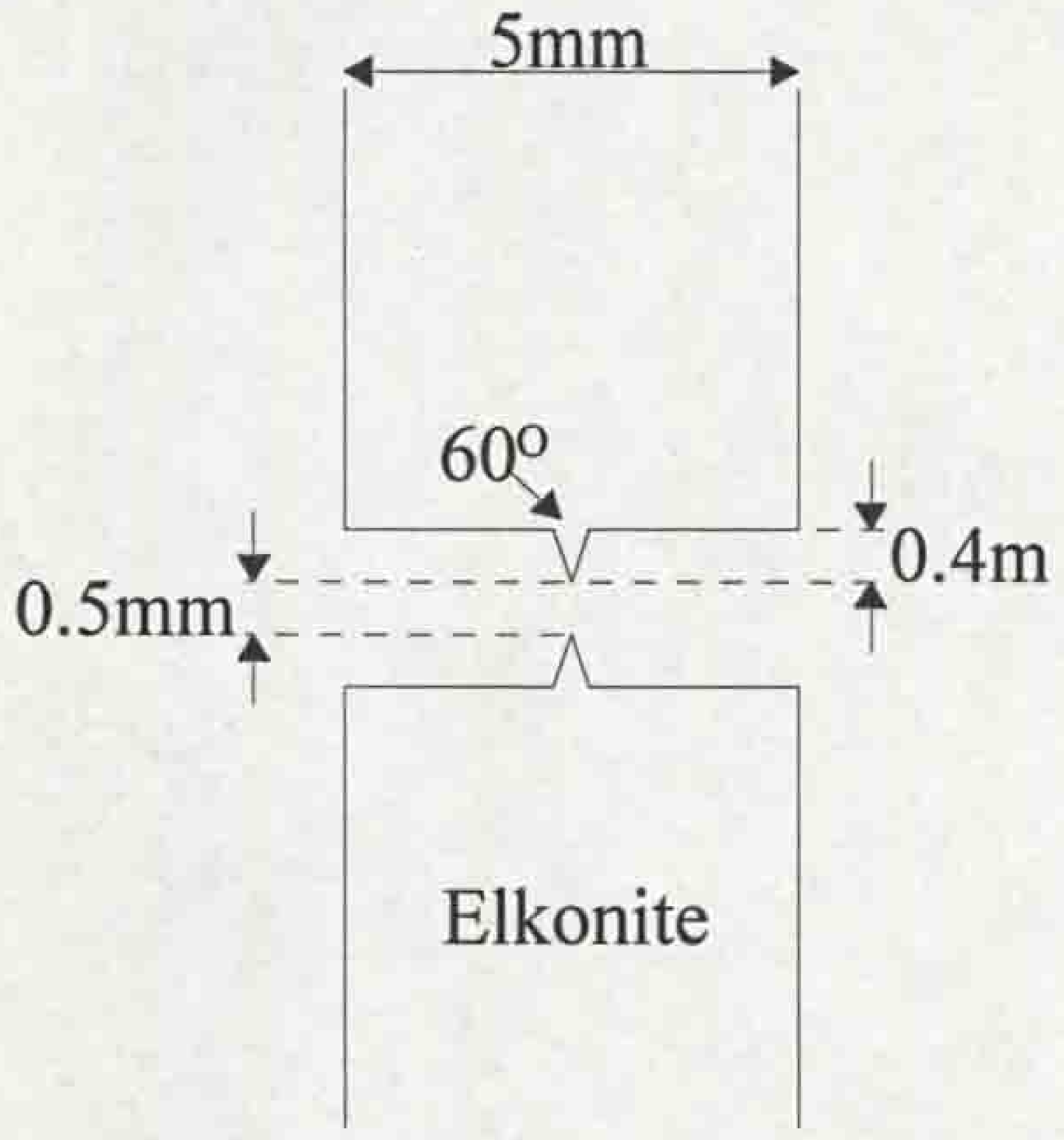

Figure 7.3 - Electrode configuration used in dielectric probe test gap

The calibration was achieved by altering the pressure of the SF_6 at 300K and subsequently converting these pressures into mass density values, using results of previous researchers (eg. Frost and Liebermann, 1971 and Chervy *et al*, 1994).

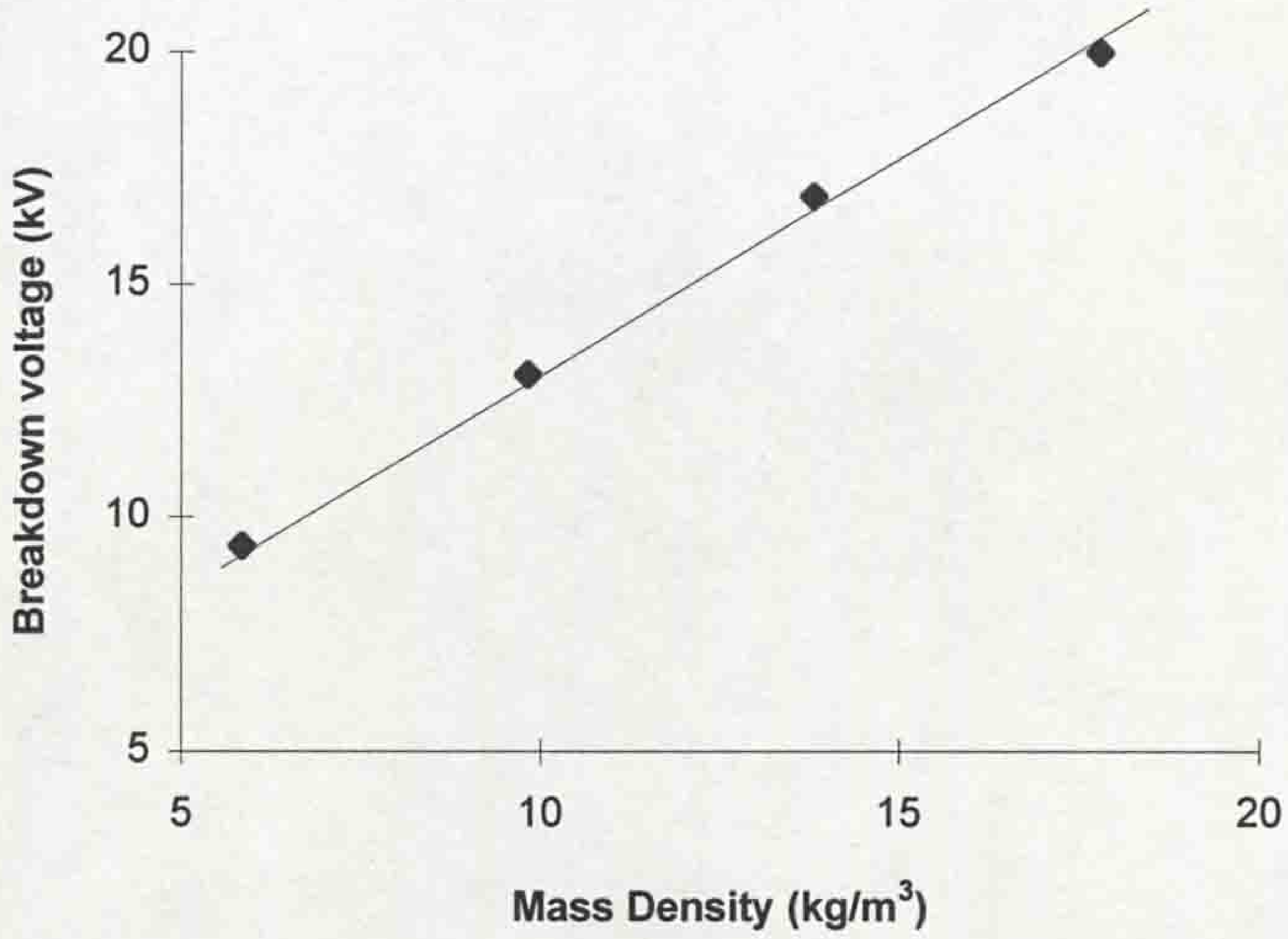

Figure 7.4 - Calibration of dielectric probe test gap

7.2.2 Relationship between mass density and temperature

Frost and Liebermann (1971) calculated the equilibrium composition of SF_6 for temperatures from 1000 to 45000K and pressures from 1 to 16bar. Mass density was computed for these temperatures and pressures. Similar studies have followed (Dienemann, 1983 and Chervy *et al*, 1994). The mass density results of Chervy agree closely with Frost and Liebermann and, since they extend down to 300K, they are used in this work.

The equilibrium composition of an SF_6 plasma at 1bar, as computed by Chervy, is shown in fig.7.5. Dissociation of SF_6, initially into F and SF_4, first occurs at around 1600K. This means that the calibration curve of fig.7.4 should be valid up to 1600K, thus defining the limit of temperature measurement with this approach. The onset of dissociation occurs at a higher temperature as the SF_6 pressure is increased (Dienemann, 1983). Therefore, since the SF_6 pressures used in this work were always above 1bar, the temperature measurement limit of 1600K is a conservative one.

The density - temperature relationship for SF_6 for pressures of 1 to 10bar, up to 2000K, is shown in fig7.6 (Chervy *et al*, 1994).

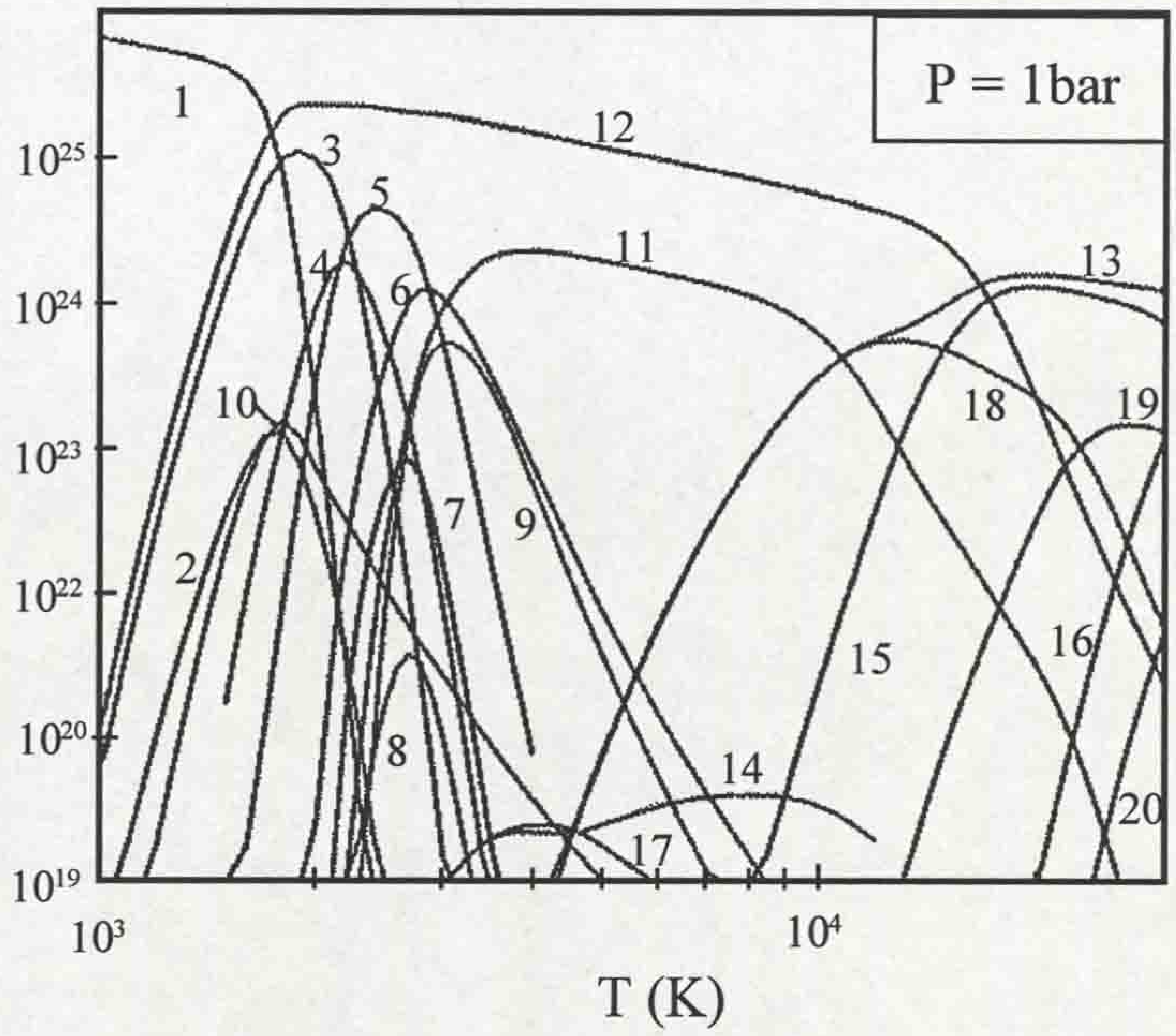

1. SF_6 2. SF_5 3. SF_4 4. SF_3 5. SF_2 6. SF
7. SSF_2 8. FSSF 9. S_2 10. F_2 11. S 12. F
13. e^- 14. F^- 15. F^+ 16. F^{2+} 17. S_2^+ 18. S^+
19. S^{2+} 20. S^{3+}

Figure 7.5 - Equilibrium composition of pure SF_6 between 1000 and 30000K

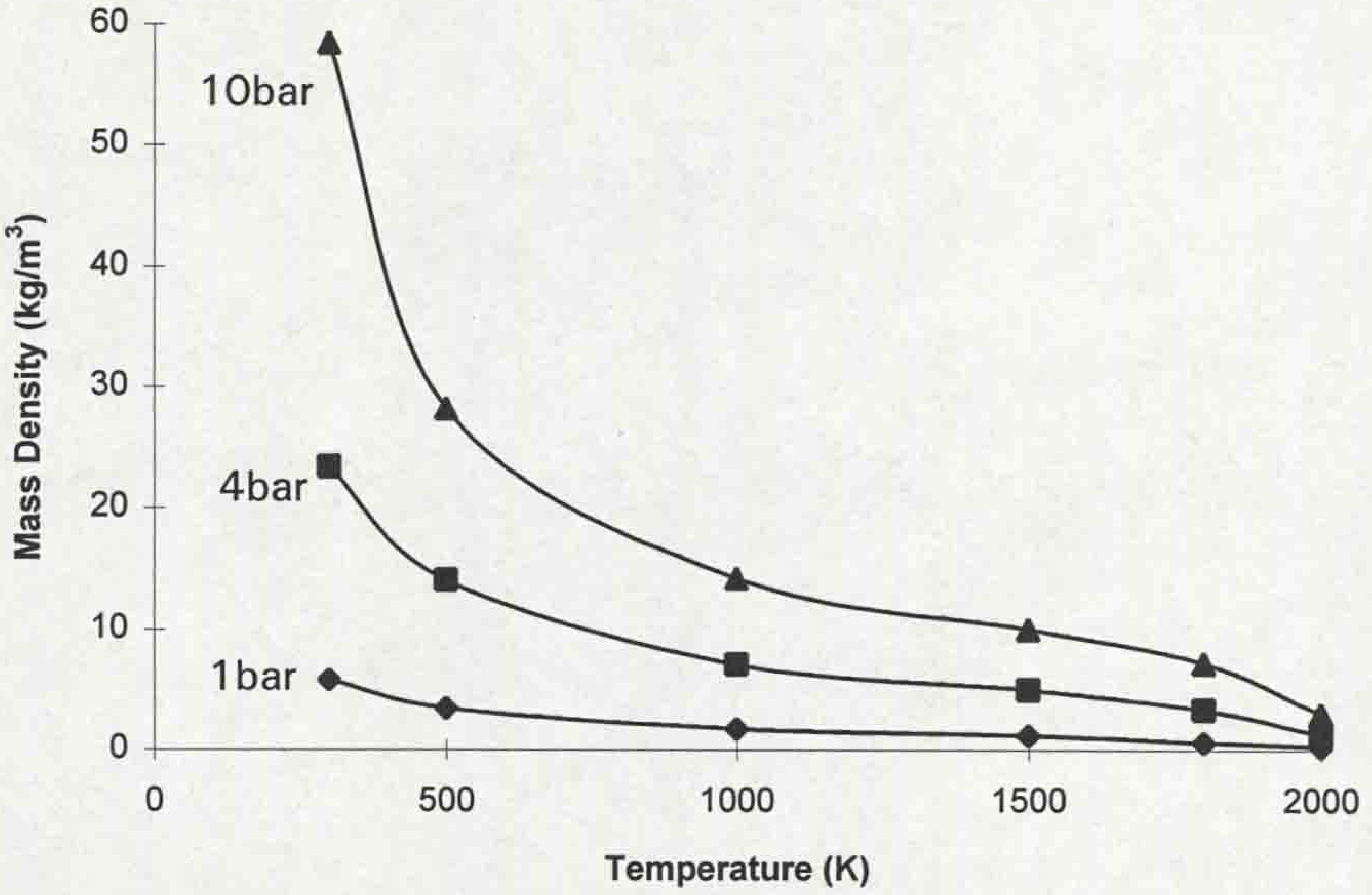

Figure 7.6 - Density / Temperature relationship for SF_6 (Chervy *et al*, 1994)

Up to the dissociation temperature (1600K) the characteristic ideal gas behaviour applies (ρ is inversely proportional to T), while above 1600K the dissociation of SF_6 reduces the mass density even further. By combining the calibration curve of fig.7.4 with the results in fig.7.6, it is possible to arrive at a relationship between breakdown voltage and temperature (for the electrode configuration in fig.7.3). This relationship will be valid for estimating SF_6 gas temperatures up to 1600K. The following assumptions are implicit in this reasoning:

1. The pressure of the hot gas flow after interruption is equal to the ambient pressure. For a puffer circuit breaker this has been verified to within several percent (Yoshizumi *et al*, 1989). Alternatively, if it is suspected that the pressure of the gas close to the dielectric probe test gap differs significantly from ambient, then it can be measured to permit a more accurate temperature estimation.
2. The nature of the discharge waveform and its frequency should be such that the breakdown voltage levels in the waveform are equivalent to the D.C. breakdown level (i.e. not reduced by the repetitive discharging process), so that the calibration characteristic of fig7.4, formed using D.C. voltages, also applies to the transient waveform breakdown voltages. This was verified experimentally for this dielectric probe system.
3. Thermodynamic equilibrium exists, so that the composition calculations of fig.7.5 are valid. In practice, recombination effects may lead to departures from such equilibrium (Jones, 1996).
4. The particles formed following arcing do not have an influence themselves on the dielectric strength or on the thermodynamic equilibrium. (The presence of the particles may be an indication that thermal recombination does not proceed as per fig.7.5, since there are no particle components shown on this result).

Section 7.4 uses the approach discussed above to monitor the dielectric strength, after arc interruption in a rotary arc distribution circuit breaker, and subsequently estimates the gas temperature based on the above assumptions.

7.3 ELEMENTS OF THE DIELECTRIC PROBE SYSTEM

7.3.1 Probe design

The dielectric probe was designed to be similar to a conventional spark plug. Fig.7.7 shows a cross-section of the design:

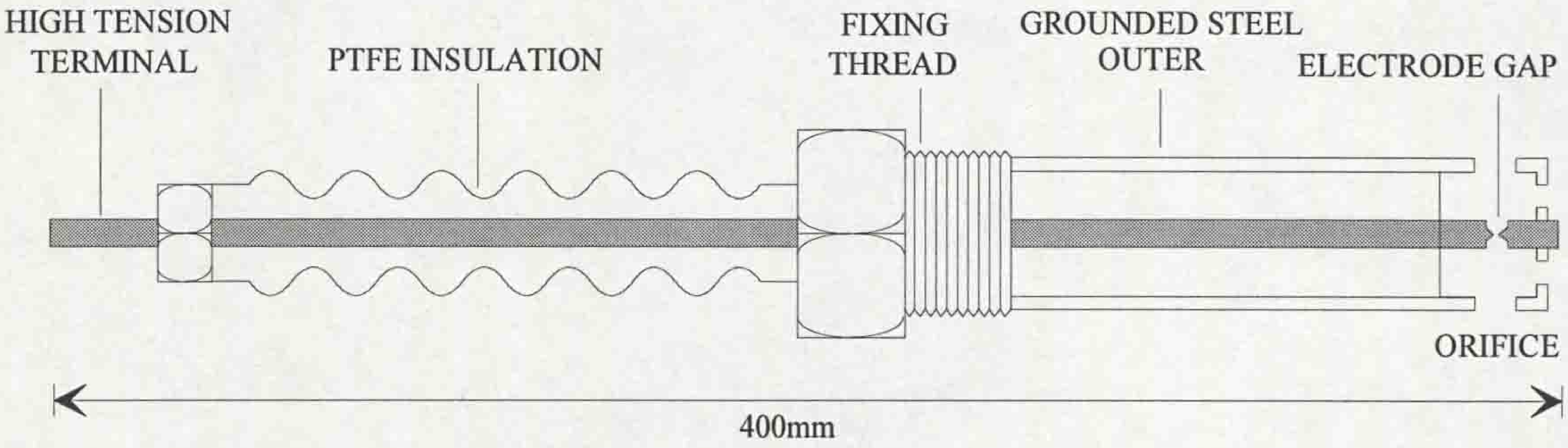

Figure 7.7 - Cross section of dielectric probe

The outer steel tube is locally grounded. The high tension electrode is connected to a copper rod which runs through the centre of the probe along its whole length and is insulated from the outer body by a PTFE sleeve. The high voltage connection is made where the copper emerges from the left hand end of the probe. It is insulated from the main body by a length of PTFE to prevent flashover in atmospheric air, since this part of the probe would lie outside the circuit breaker. The thread in the centre of the probe screws into the circuit breaker (usually the endplate) and the test gap is at the right hand end of the probe. Fig.7.8 shows a photograph of a completed probe.

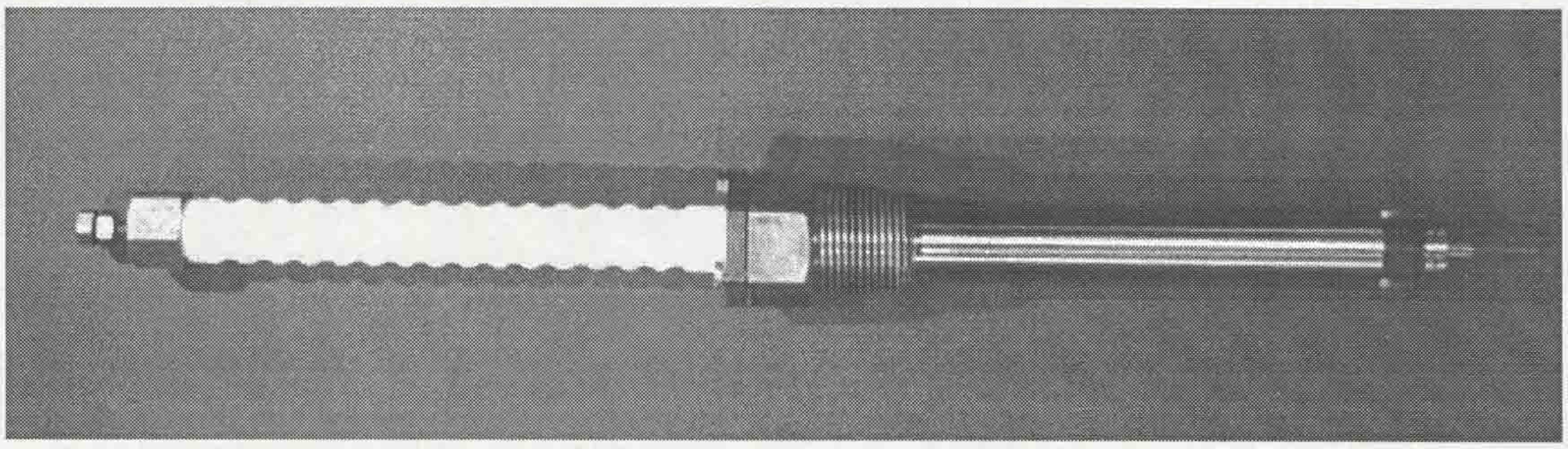

Figure 7.8 - Photograph of completed probe

7.3.2 Electro-optic measurement of breakdown voltage

In order to derive an approximate temperature for the gas, the breakdown voltages on the discharge waveform must be measured. It is often convenient to use a high voltage oscilloscope probe (eg. Tektronix P6015 1000:1). However, this creates an electrical link between the control room instrumentation and the circuit breaker, which is undesirable. A more satisfactory method to use is some form of electro-optic voltage measurement. This allows the measured signal to be returned to the control room via optical fibres, thus providing electrical isolation between the control room and circuit breaker.

Electro-optic materials are generally classified as exhibiting the Pockels effect or the Kerr effect (Krohn, 1992). Both phenomena affect the linear birefringence in electro-optic materials. Linear birefringence is that phenomenon whereby light polarised in two orthogonal linear directions propagates in the medium at different velocities, due to differences in refractive index of the medium in the two directions. The electro-optic effect is the name given to the dependence of the linear birefringence on the external field. For the Kerr effect this dependence is proportional to the square of the field, while the Pockels effect shows a direct proportionality to the field (Krohn, 1992). A Pockels cell was used to measure the breakdown voltage in this work.

Fig.7.9 shows the Pockels cell arrangement used to measure the breakdown voltage:

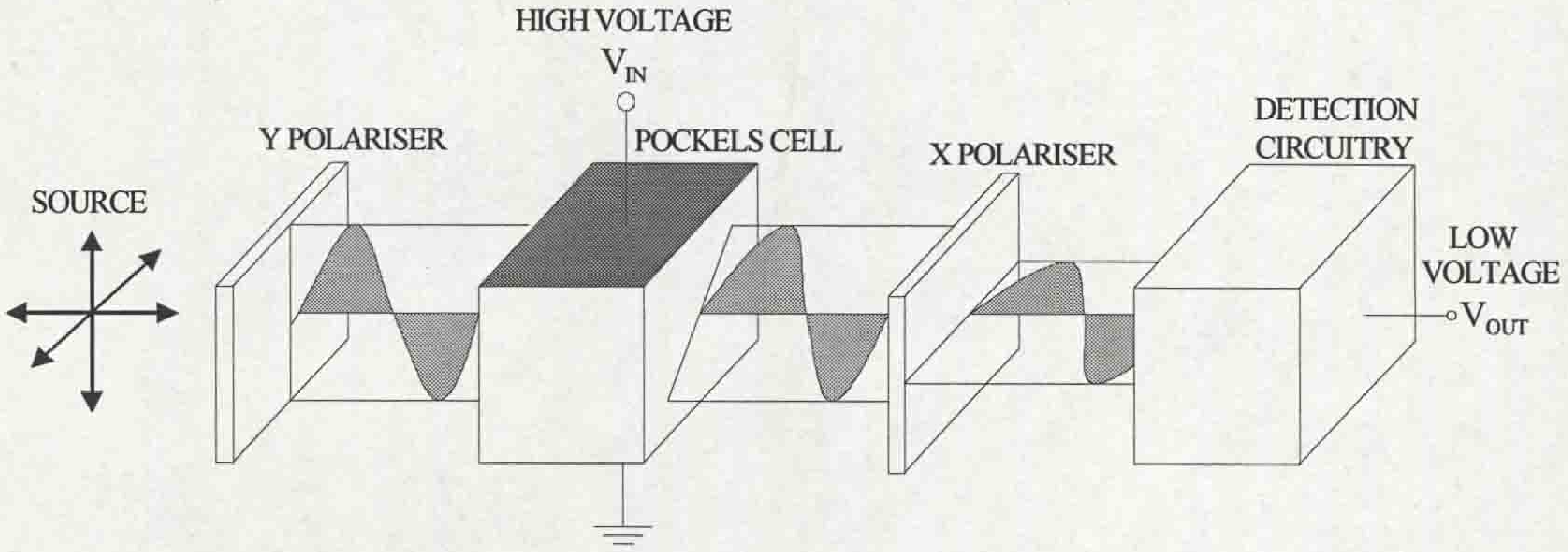

Figure 7.9 - Use of a Pockels cell to measure high voltage

The light emitted from an unpolarised source close to the Pockels cell is linearly polarised before it passes through the cell. In the presence of an electric field (in this case the voltage across the dielectric probe test gap) the Pockels effect essentially rotates the plane of polarisation as a function of applied voltage. Therefore, a linear polariser at the output of the cell, orthogonal to the input polariser, will transmit a light intensity into the detector fibre which depends upon the applied voltage amplitude according to (Krohn, 1992)

$$I = \frac{1}{2} I_0 \left(1 + \sin V / V_0\right) \tag{7.1}$$

where I is the transmitted intensity, I_0 the input intensity, V_0 the half wave voltage of the Pockels cell (a property of the material) and V the applied voltage. This light intensity can also be experimentally calibrated against the applied voltage.

7.3.3 High voltage power supply

The ultimate aim with the dielectric probe system would be to have no electrical connections between the control room and circuit breaker. Therefore, it was necessary to develop a high voltage D.C. supply, which could be powered from a 12V battery source (Wood, 1993). Whilst this supply was being developed, it was convenient to use a mains-fed high voltage D.C. supply in conjunction with an isolation transformer. A Brandenburg type supply, rated at 30kV 1mA, was used for this purpose.

7.3.4 Control system

A control circuit was incorporated into the system, such that during a circuit breaker test the high voltage supply would only be turned on for a short time (100ms). This time was long enough to record the post-arc dielectric strength of the gas in the circuit breaker, but sufficiently short, such that electrode wear on the test gap would be minimised. The complete system is shown on fig.7.10.

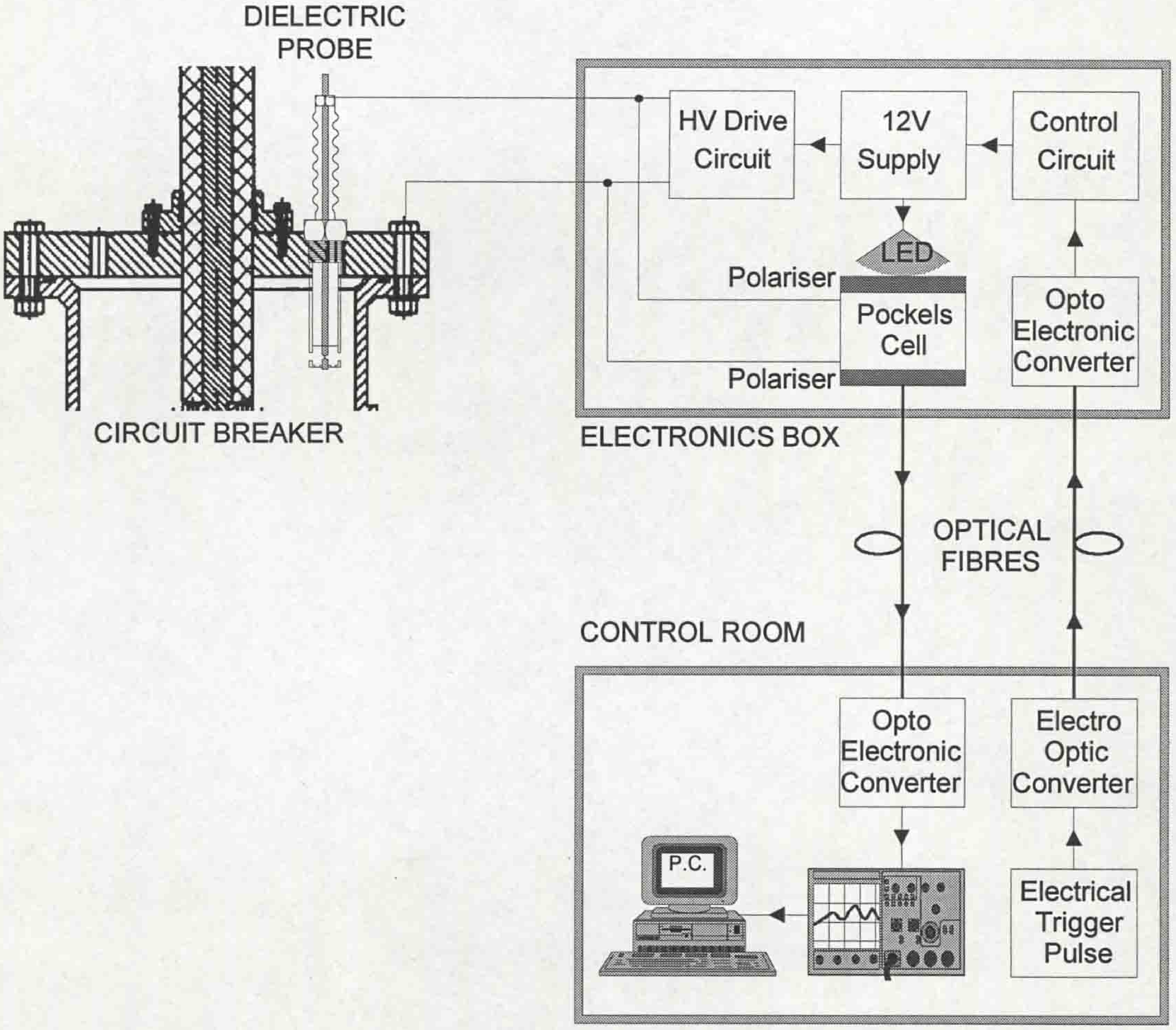

Figure 7.10 - Complete dielectric probe control system

The sequence for testing was as follows:

1. At the start of the test an electrical pulse is received at the control room to indicate that separation of the circuit breaker contacts has been initiated.
2. This signal is electro-optically converted (using a simple LED circuit) into a light pulse, which is transmitted via an optical fibre to the electronics box, mounted close to the circuit breaker.
3. The light pulse activates the control circuit, which turns on the high voltage for 100ms.
4. The high voltage supply charges up the capacitance of the probe (20pF) through a 100MΩ resistor. The process of repetitive discharge begins.

5. The breakdown voltage of each discharge is converted into a light intensity by the Pockels cell, the light being transmitted back to the control room via an optical fibre. The light source for the Pockels cell was an infra-red LED.
6. At the control room the light pulses corresponding to the breakdown voltage waveform are opto-electronically converted into an electrical signal and fed to a storage oscilloscope.

The overall system can be calibrated (Henderson, 1993) to obtain the relationship between the high voltages applied to the Pockels cell (the breakdown voltages) and the small voltage signals recorded on the oscilloscope.

7.4 DIELECTRIC STRENGTH TESTS ON A ROTARY ARC DISTRIBUTION CIRCUIT BREAKER

To demonstrate the potential of the dielectric probe system, it was used to monitor the dielectric strength of SF_6 gas after D.C. arc interruption in a rotary arc distribution circuit breaker (Ennis, 1994), the operation of which is described in **Appendix III**. The probe was situated 100mm downstream of the point of arc initiation, as shown on fig.7.11. Two results from these tests are analysed here, as an illustration of the method, using the principles described above (**7.2**). The first test monitored the breakdown voltage following an arc of 550A D.C., while the second test was performed with an arc current of 890A.

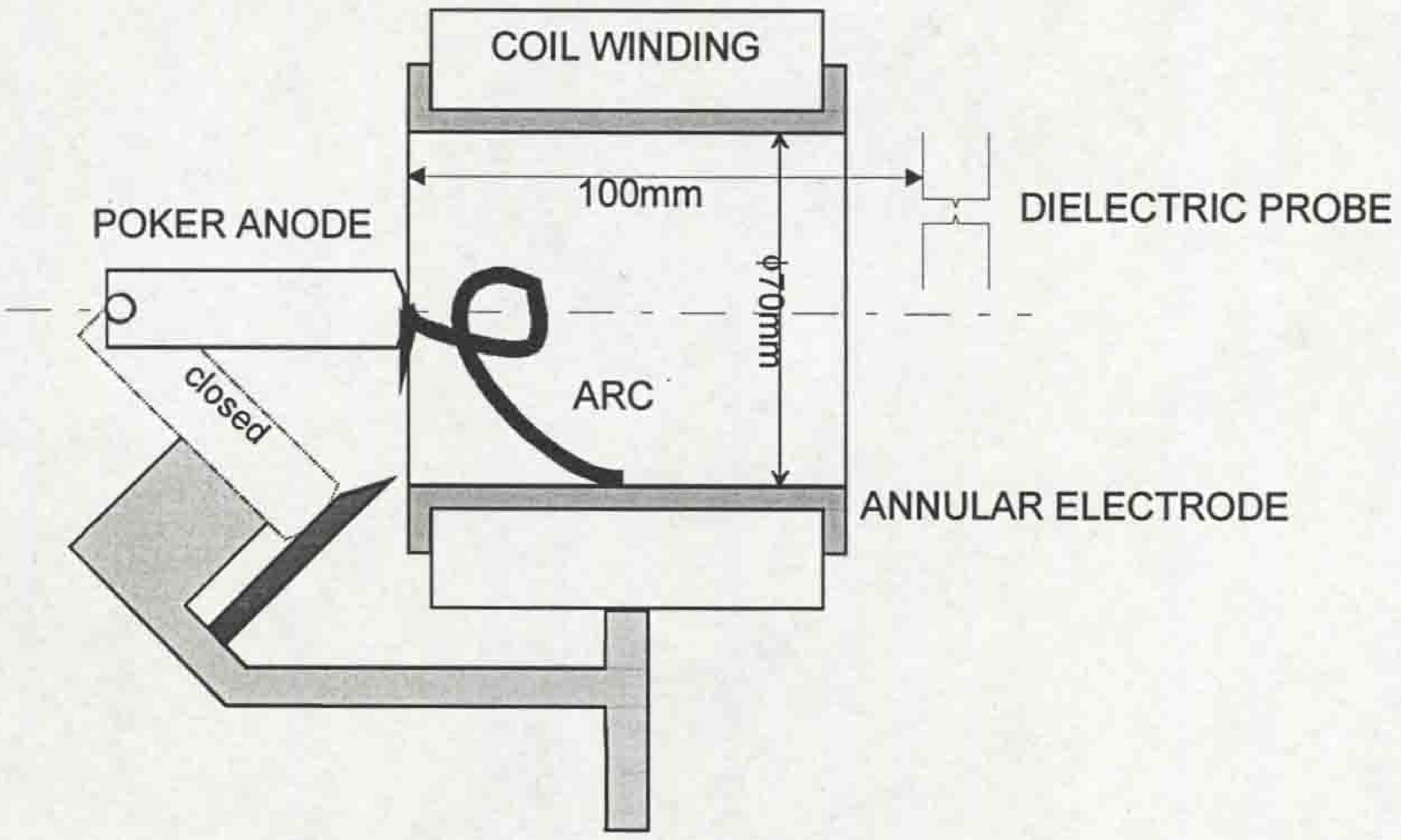

Figure 7.11 - Position of dielectric probe with respect to rotary arc circuit breaker

The breakdown voltages from the two tests have been plotted against time on figs.7.12.a and 7.12b respectively. On these traces 0ms represents circuit breaker tripping and arc initiation is at 4-5ms. The dielectric strength reduction is more pronounced following the 890A arc. Furthermore, the onset of dielectric strength reduction occurs more quickly, following extinction of the 890A arc (~5ms sooner) and the recovery of gas dielectric strength also takes longer (~45ms for the 890A arc compared with ~35ms for the 550A arc).

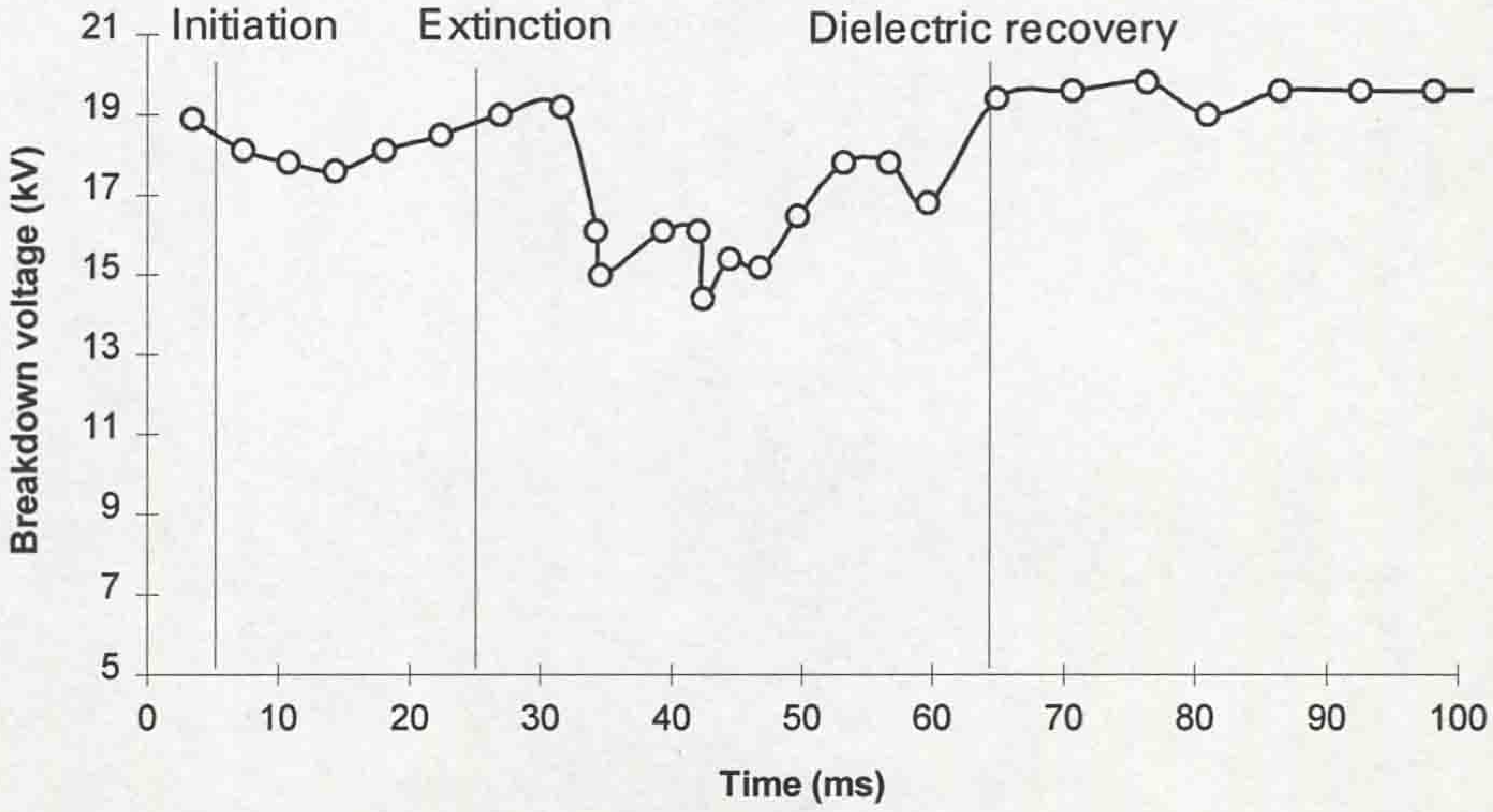

Figure 7.12a - Breakdown voltages recorded for 550A D.C. arc

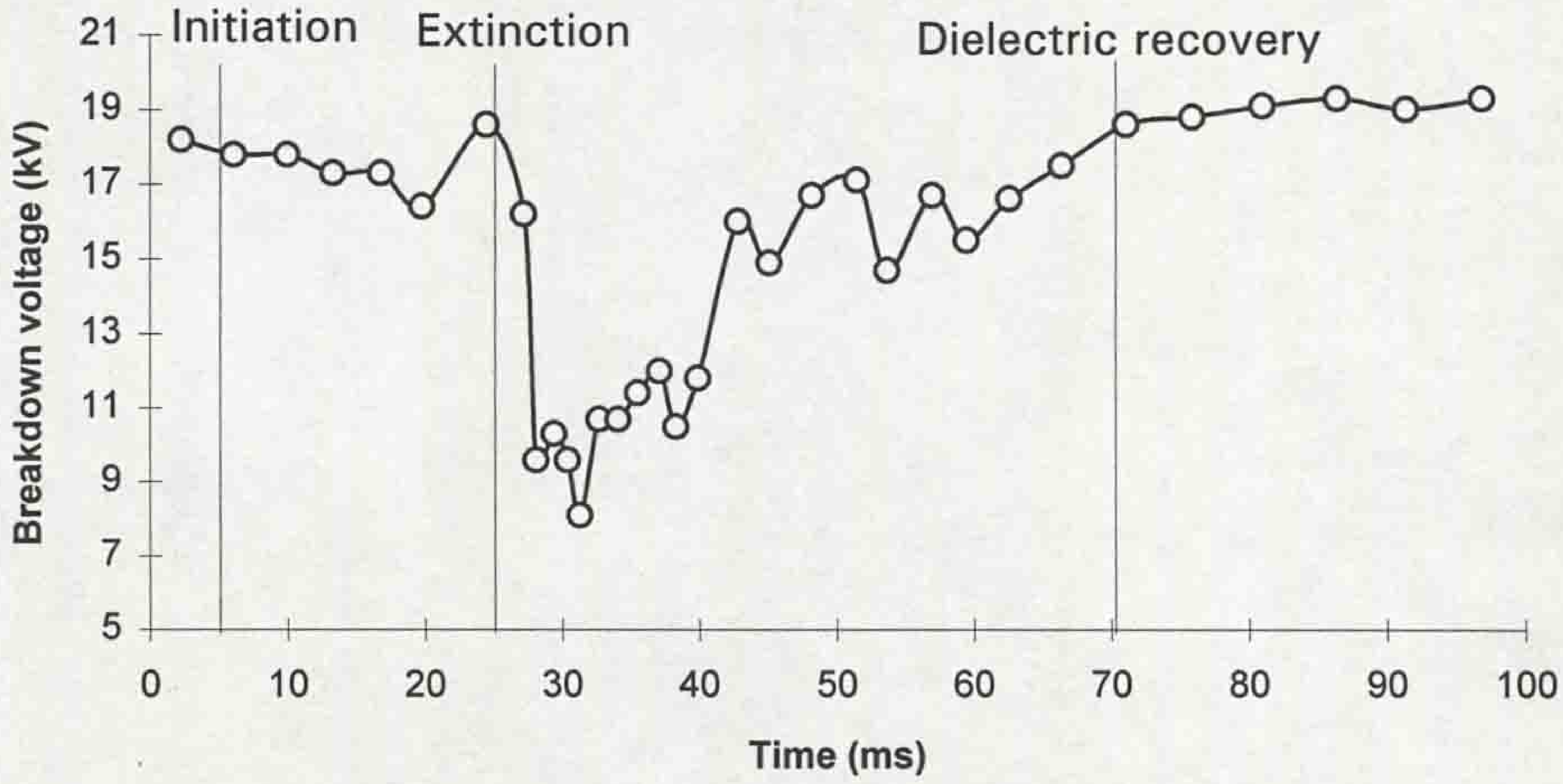

Figure 7.12b - Breakdown voltages recorded for 890A D.C. arc

7.4.1 Estimation of gas temperature

Using the procedure outlined in **7.2.1** the breakdown voltage variations in figs.7.12a and 7.12b can be converted to gas temperature variations, based on the assumptions made in **7.2.2**. Firstly, the calibration curve for the probe gap in these tests is shown in fig.7.13. Fig.7.13 allows the breakdown voltages in figs.7.12a and 7.12b to be assigned their corresponding mass densities. Next, interpolation of the results of Chervy *et al*, 1994) in fig.7.6 allows a density - temperature relationship for SF_6 at 3bar to be produced (fig.7.14).

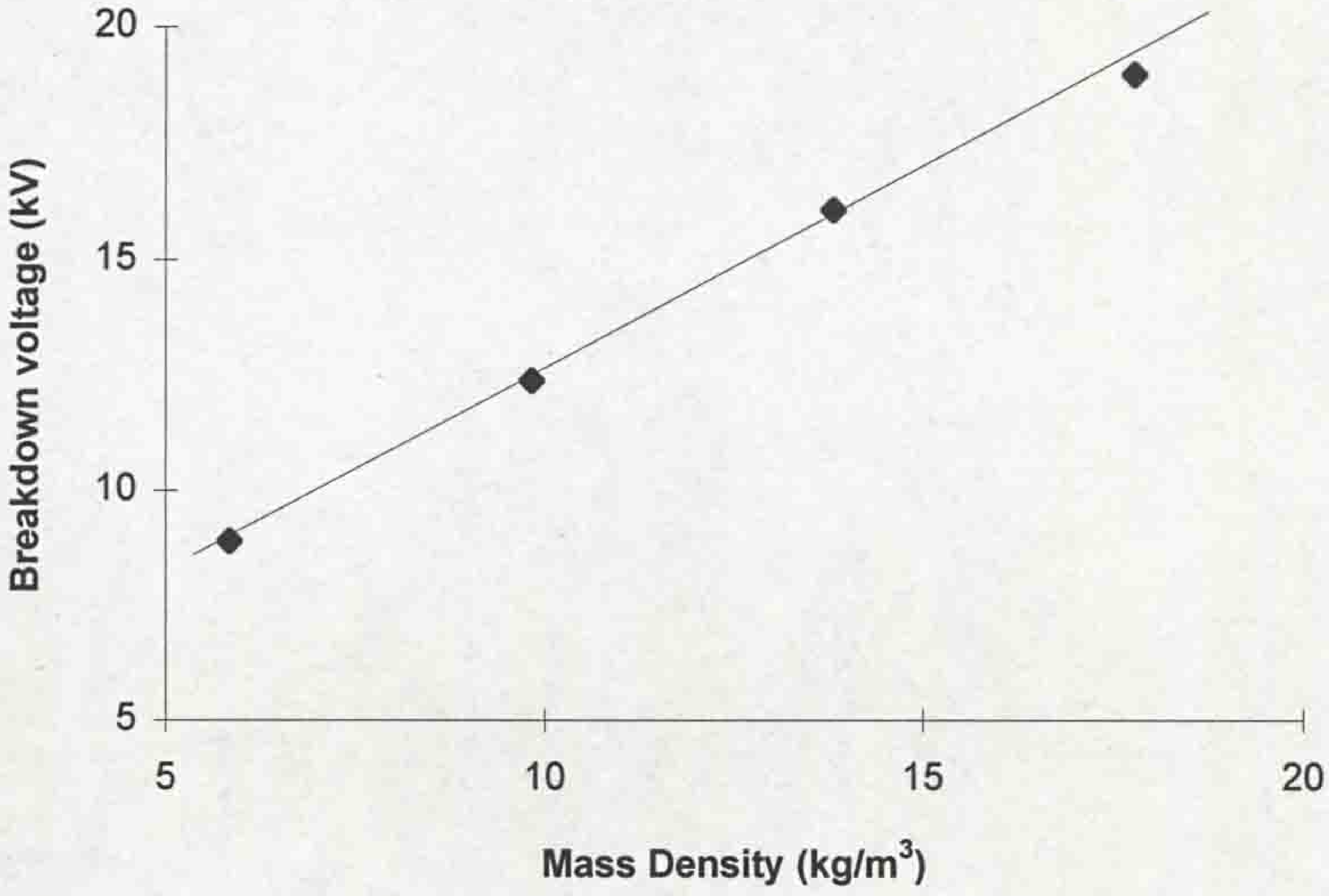

Figure 7.13 - Calibration of test gap for rotary arc results

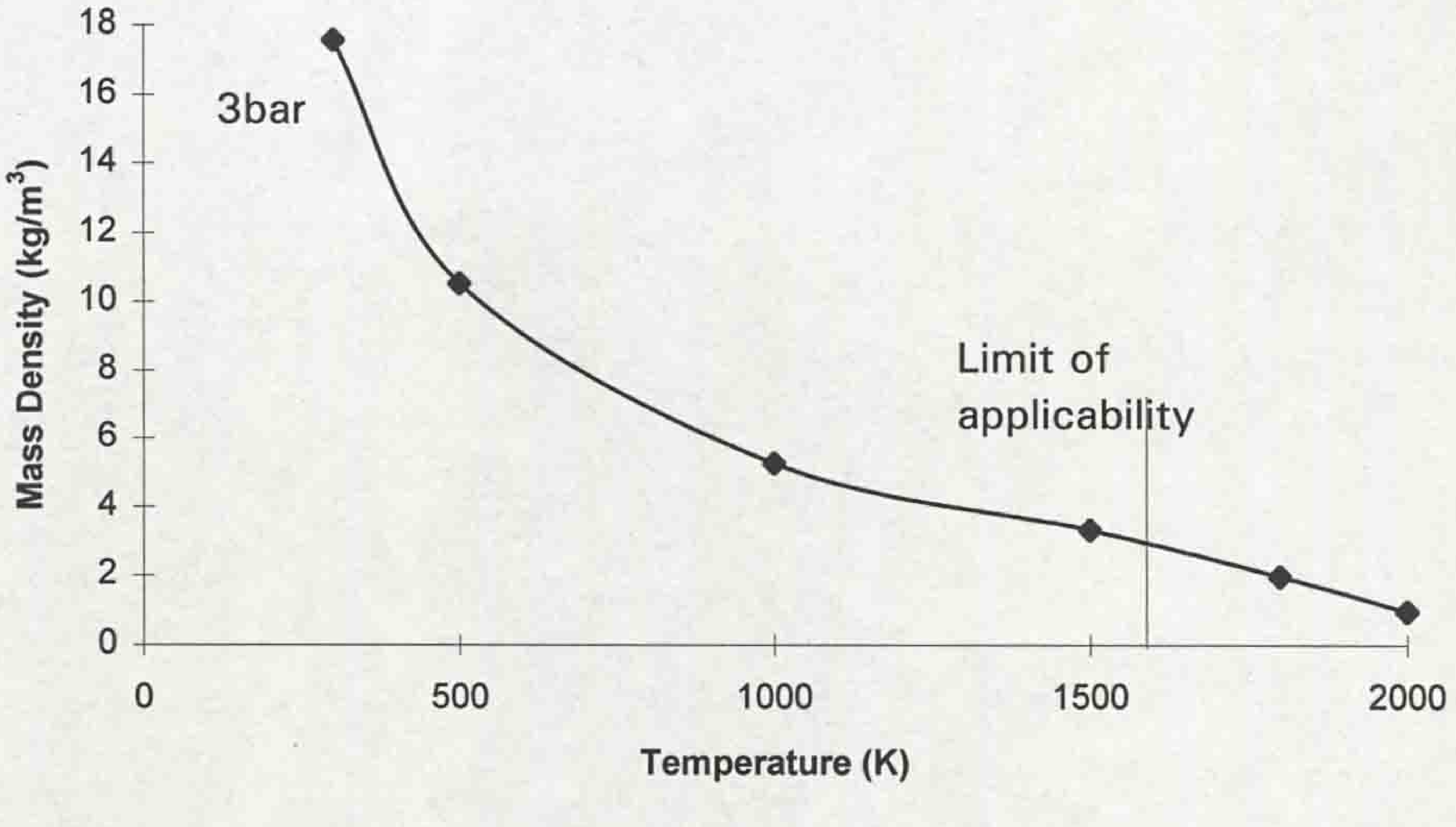

Figure 7.14 - Density / Temperature relationship for SF_6 at 3bar

The two results can then be combined to provide a direct correlation between temperature and breakdown voltage (fig.7.15):

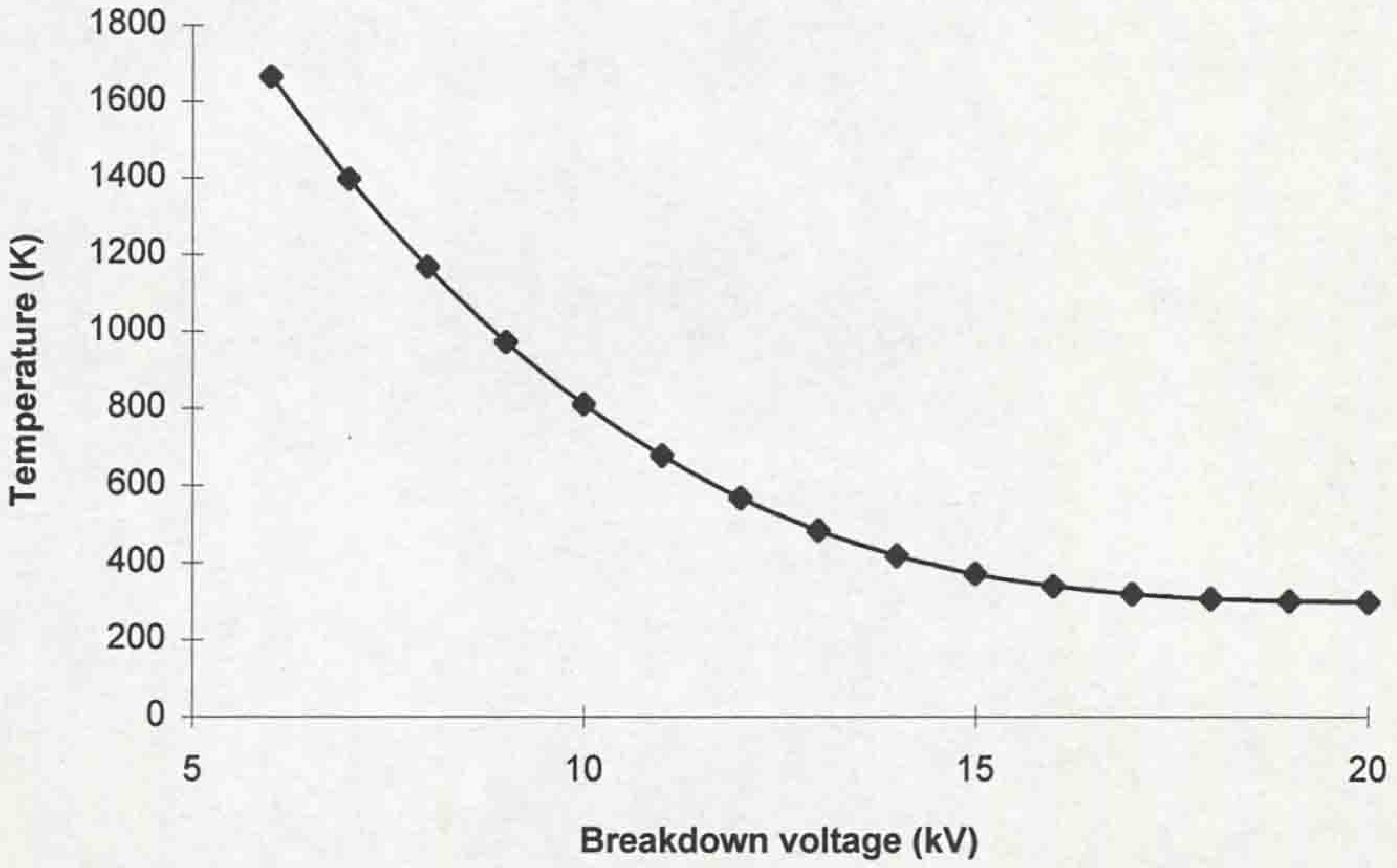

Figure 7.15 - Correlation between temperature and breakdown voltage

Fig.7.15 can now be used to convert figs.7.12a and 7.12b into temperature - time curves (figs.7.16a and 7.16b).

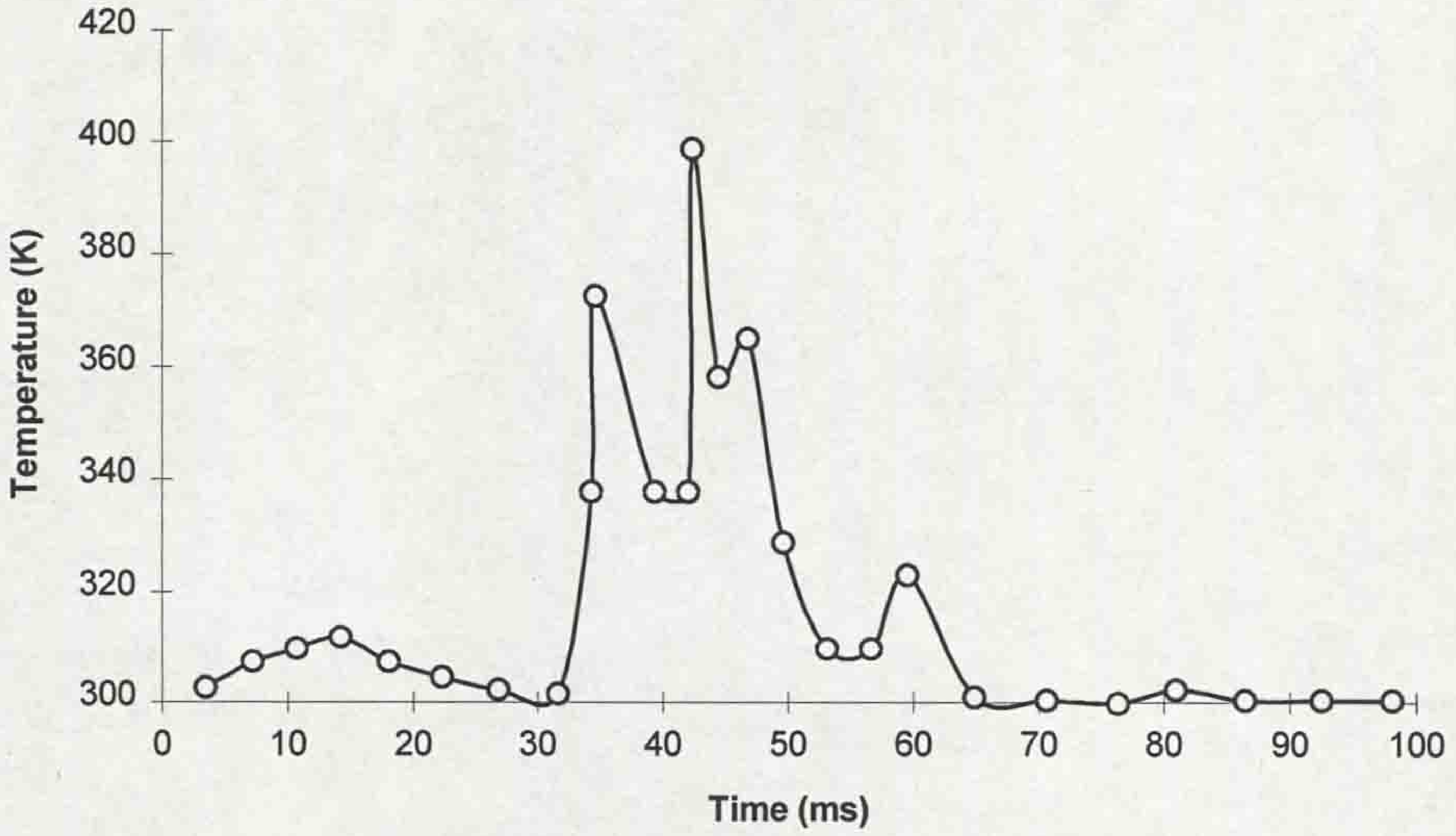

Figure 7.16a - Temperature / time profile for 550A test

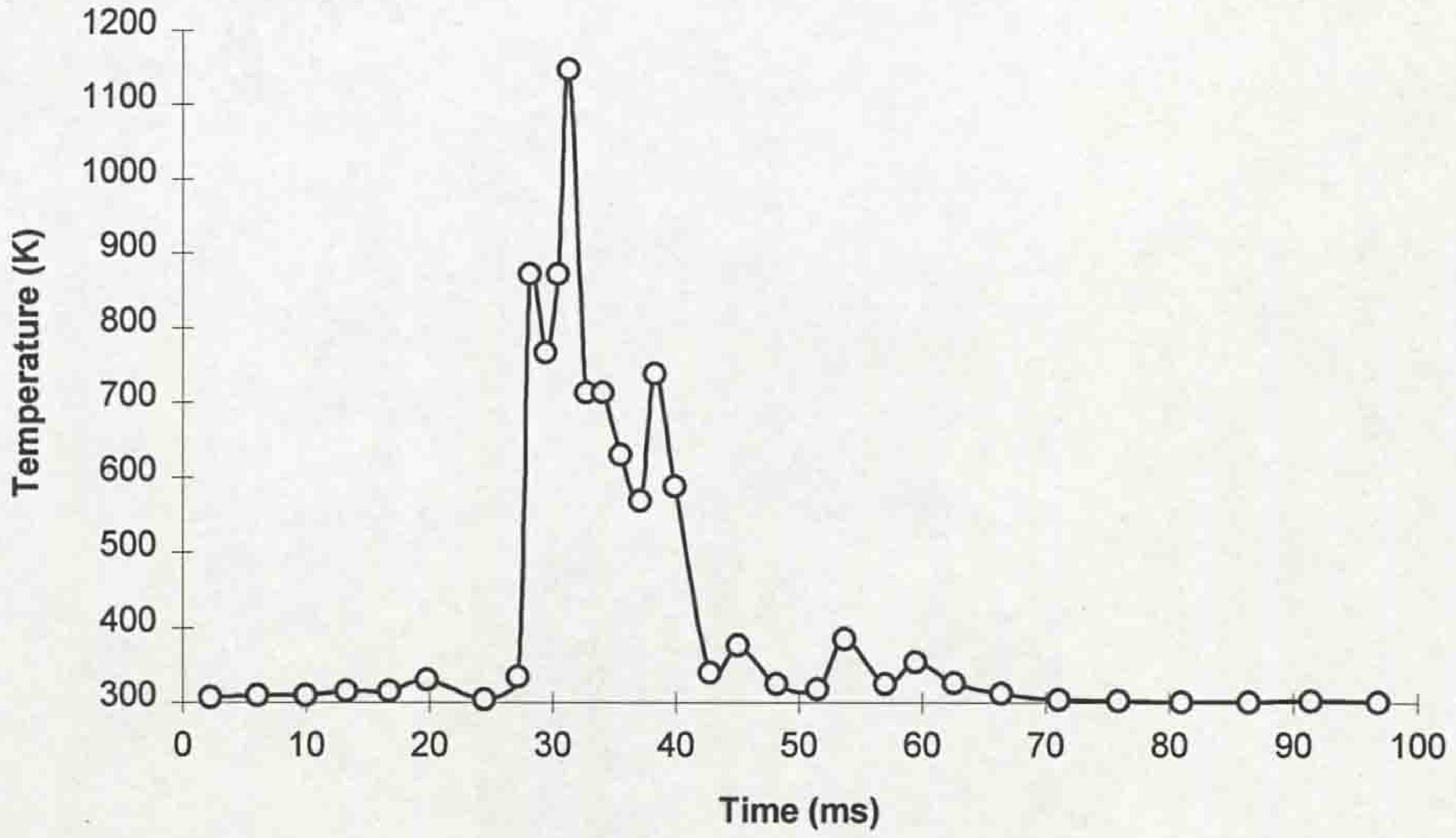

Figure 7.16b - Temperature / time profile for 890A test

From the results on fig.7.16 it appears that a higher gas temperature was recorded following interruption of the 890A arc (note the difference in temperature scales). However, the assumptions in **7.2.2** must be valid for these temperature estimations to be accurate. Also, fig.7.15 shows that, at lower values of breakdown voltage, the sensitivity of the system reduces. Thus, the higher estimates of temperature will be less precise than those close to ambient temperature (300K). Nevertheless, the system has, firstly, successfully monitored the gas dielectric strength following arc interruption and, secondly, provided at least a good qualitative indication of the temperature variation with time.

7.5 CONCLUSIONS

A dielectric probe system was designed, assembled and successfully tested, to monitor the dielectric strength of SF_6 gas, within a gas blast circuit breaker, following arc interruption. Such information is important to circuit breaker manufacturers to identify regions of dielectric weakness, which may subsequently lead to arc reignition and, hence, circuit breaker failure.

Using results from previous studies (eg. Chervy *et al*, 1994 and Frost and Liebermann, 1971) it is possible to relate the breakdown voltages recorded by the system to gas temperature (**7.2**), up to the onset of dissociation (~1600K). However, this process requires several assumptions (**7.2.2**), which may degrade the accuracy of temperature estimations with this method.

By measuring the breakdown voltages electro-optically (**7.3.2**), the system can be arranged such that the links between the circuit breaker and control room can be made entirely with optical fibres. This provides electrical isolation between the circuit breaker and control room and improves the independence of the signals to electromagnetic interference, thus resulting in a system suitable for on-site as well as laboratory research use.

Successful operation of the system was proved with tests on a rotary arc distribution circuit breaker (**7.4**). Changes in dielectric strength of the gas were recorded, following arc interruption at different current levels. These dielectric strength changes were converted into gas temperature variations, acknowledging the necessary assumptions (**7.2.2**).

The system was also used on the main test circuit breaker for this project (**9.2**). These results are presented in **chapter 10** of this thesis.

CHAPTER 8 - OPTICAL FIBRE PRESSURE SENSORS

8.1 INTRODUCTION

Gas pressure measurements, within gas blast circuit breakers, are important for circuit breaker modelling, both for the verification of theoretical models and incorporation into semi-empirical models. Furthermore, measurement of gas pressure is considered to be one of the primary parameters for inclusion in a circuit breaker condition monitoring system. Therefore, substantial research has been undertaken to attempt to monitor gas pressure within circuit breakers.

Shimmin (1986) and Tominaga *et al* (1980) measured piston pressures and axial pressure distributions within SF_6 puffer circuit breakers. However, these measurements were made using piezo-type devices, which can be susceptible to errors caused by electromagnetic interference from the arc. Moreover, care has to be taken to avoid compromising the electrical isolation from ground, of the circuit breaker, by transmitting signals along metal wires. With the rapid developments in optical fibre sensing over the past two decades and the advantages they possess, such as inherent insulation and freedom from electromagnetic interference, it was appropriate to direct research towards optical fibre pressure transducers, for application to circuit breakers.

Noeske *et al* (1983) monitored pressure in the nozzle of a gas blast circuit breaker using intensity modulation (**4.1.4.1**). However, an intensity modulated system is susceptible to spurious intensity changes in the monitoring region, which, in circuit breakers, can be produced by mechanical vibration of the optical fibres and optical radiation from the arc. These problems have been minimised by utilising the chromatic modulation technique applied to pressure sensing (Henderson *et al*, 1993).

A recent collaborative project between the University of Liverpool and Lucas Control Systems Products (Humphries *et al*, 1996) has resulted in the production of small, micromachined silicon, optical fibre pressure sensors, based on Fabry-Perot interferometry. These devices employ the chromatic modulation technique; hence, the LIBIDO distimulus chromatic source/detection system (**4.3.3.2**), which was also used with the optical fibre linear travel recorder (OFLTR - **chapter 5**) and optical fibre particle concentration monitor (OFPCM - **chapter 6**), can be used to interrogate the micromachined silicon pressure sensors.

As part of this project, two prototype pressure sensors were designed around the silicon devices, one for measuring the gas pressure near the top-plate of the test circuit breaker tank and the other to monitor pressure rises in the interrupter piston chamber, during fault current interruption. The prototype sensors were installed in the circuit breaker and their suitability for the task assessed; in particular, their performance with respect to vibration and arc radiation during operation of the circuit breaker was investigated.

8.2 FABRY-PEROT INTERFEROMETRY

The operation of a Fabry-Perot interferometer may be explained with the arrangement shown on fig.8.1.

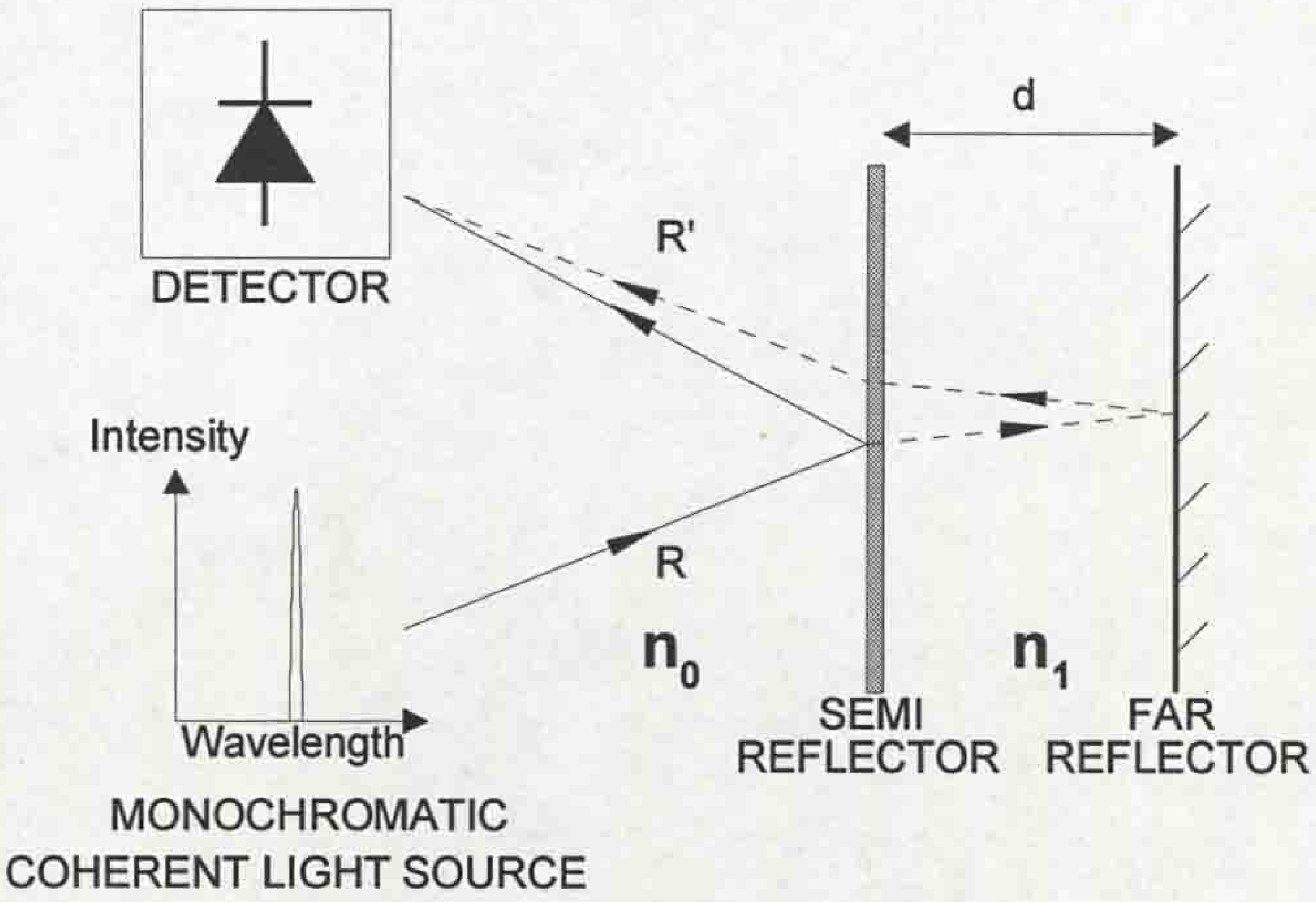

Figure 8.1 - Fabry-Perot interferometer

Light from a monochromatic, coherent source is directed towards a Fabry-Perot cavity, which consists of a semi-reflecting front surface and a totally reflecting back surface, separated by a distance d, such that d is within the coherence length of the light source. The ray shown, R, is partially reflected and partially transmitted at the semi-reflector. The portion of R, which is transmitted (R′), is reflected at the back of the cavity, returning through the semi-reflector and onwards to the detector. At the detector both rays, R and R′, interfere, since they have travelled different optical path lengths. Constructive interference will occur if

$$n_0 L - n_1 L' = m\lambda \tag{8.1}$$

where L is the path length of the ray R, L′ is the path length of the ray R′, m is an integer and n_0 and n_1 are the refractive indices of the media external to and within the cavity. This outcome results in an enhanced intensity, I_T, at the detector (fig.8.2), where I_R and I_R' are the intensities of each individual ray.

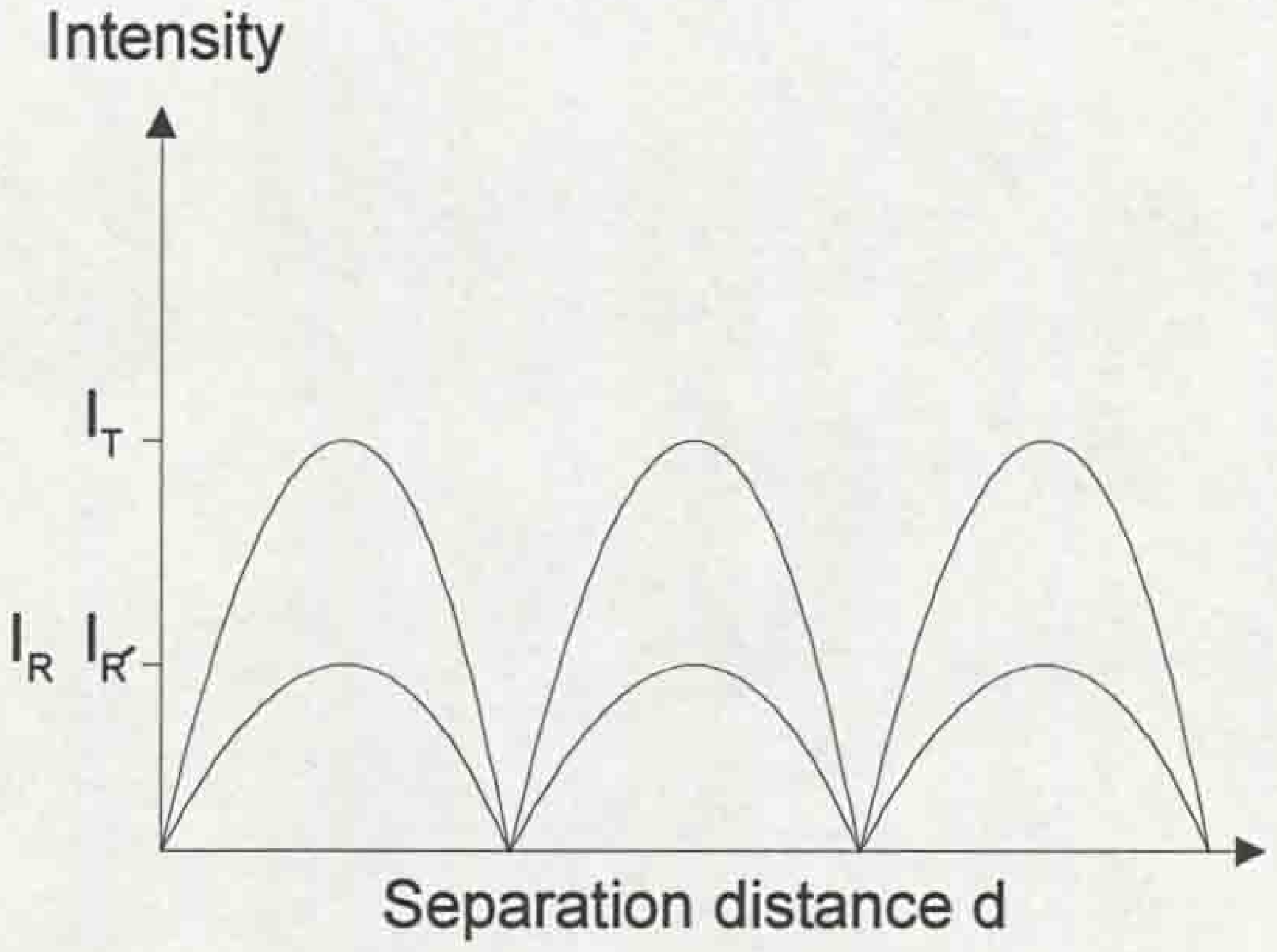

Figure 8.2 - Enhanced intensity at the detector caused by constructive interference

Conversely, destructive interference will occur if

$$n_0 L - n_1 L' = \frac{m\lambda}{2} \tag{8.2}$$

In this situation, the two waves will be in anti-phase and zero resultant intensity will be seen at the detector. Therefore, a displacement of $d = \lambda/2$, of the far-reflector with respect to the semi-reflector, will result in a change of light intensity at the detector from a maximum to zero. The general formula for the total intensity at the detector is (Jones, 1996)

$$I_T = I_R + I_R' + 2\sqrt{I_R I_R'}\cos^2 \delta \tag{8.3}$$

where $\delta = n_0 L - n_1 L'$.

8.2.1 White light interferometry

If a broadband source, rather than a monochromatic one, is used in the Fabry-Perot interferometer, the monochromatic fringe pattern of fig.8.2 is replaced by a polychromatic one. Each wavelength in the polychromatic light, on interfering with the reference beam R (fig.8.3), will have a different phase difference with respect to its reference partner. Thus, if for a wavelength λ_B (short wavelength - blue light), the situation is such that $n_0 L - n_1 L' = m\lambda_B$, leading to constructive interference, then for a different wavelength λ_R (eg. long wavelength - red light), the same difference in path length may yield $n_0 L - n_1 L' = m\lambda_R / 2$, which would result in destructive interference. Intermediate wavelengths would show intermediate phase differences and, consequently intermediate states of interference.

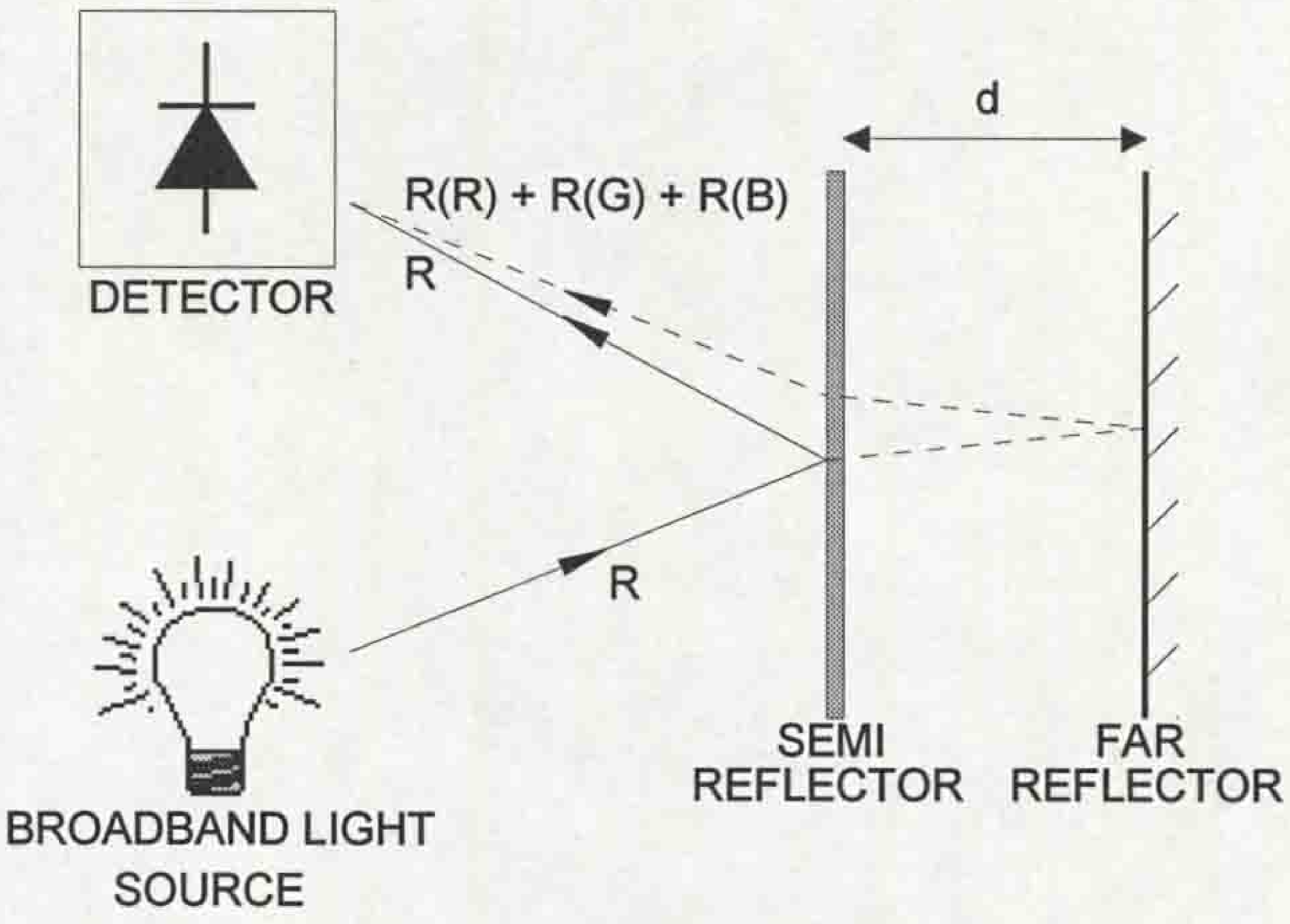

Figure 8.3 - White light interferometry

Therefore, at the detector, the rays R(B), R(G) and R(R) will be out of phase with each other. Depending upon the separation distance, d, some wavelengths will be more in phase with their corresponding partners in the reference beam R than others. Thus, the situation shown in fig.8.4, results.

In fig.8.4 the resultant light spectrum, at the detector, will have an intensity variation, where blue wavelengths have a higher intensity than the green, which, in turn, will have a higher intensity than the red. Therefore, the dominant wavelength of the source spectrum will be shifted towards the blue end of the visible spectrum. As the separation d varies, the phase relationships shown on fig.8.4 will change.

There will exist particular separation distances, which will cause resultant dominant wavelengths, of the modulated light, in the red range of the visible spectrum and others that will cause resultant dominant wavelengths in the green range of wavelengths. Therefore, rather than an intensity/separation relationship, as for the monochromatic source case, for the broadband source there is a resultant relationship between dominant wavelength and separation, d (fig8.5).

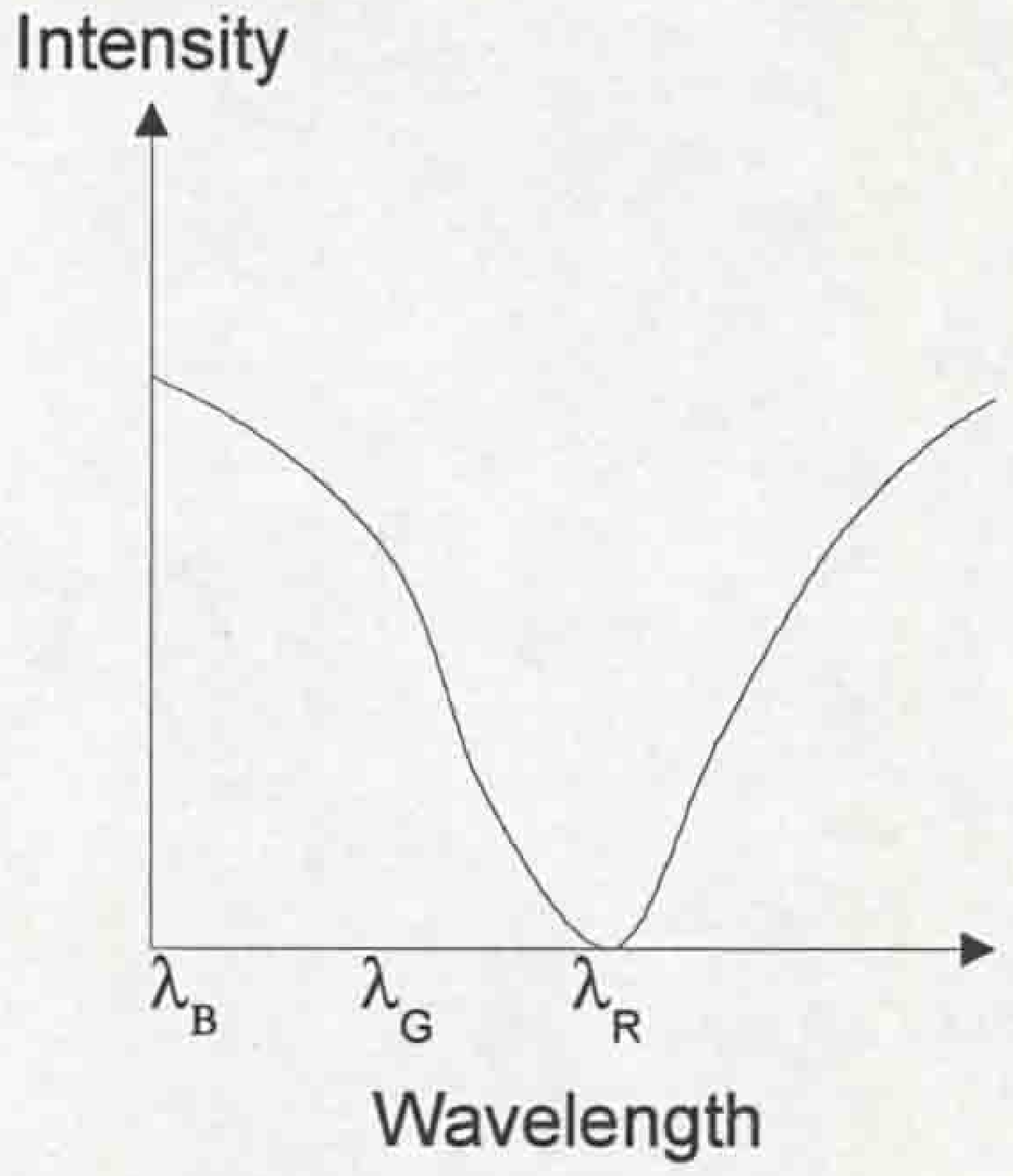

Figure 8.4 - Intensity variation with wavelength due to chromatic interference

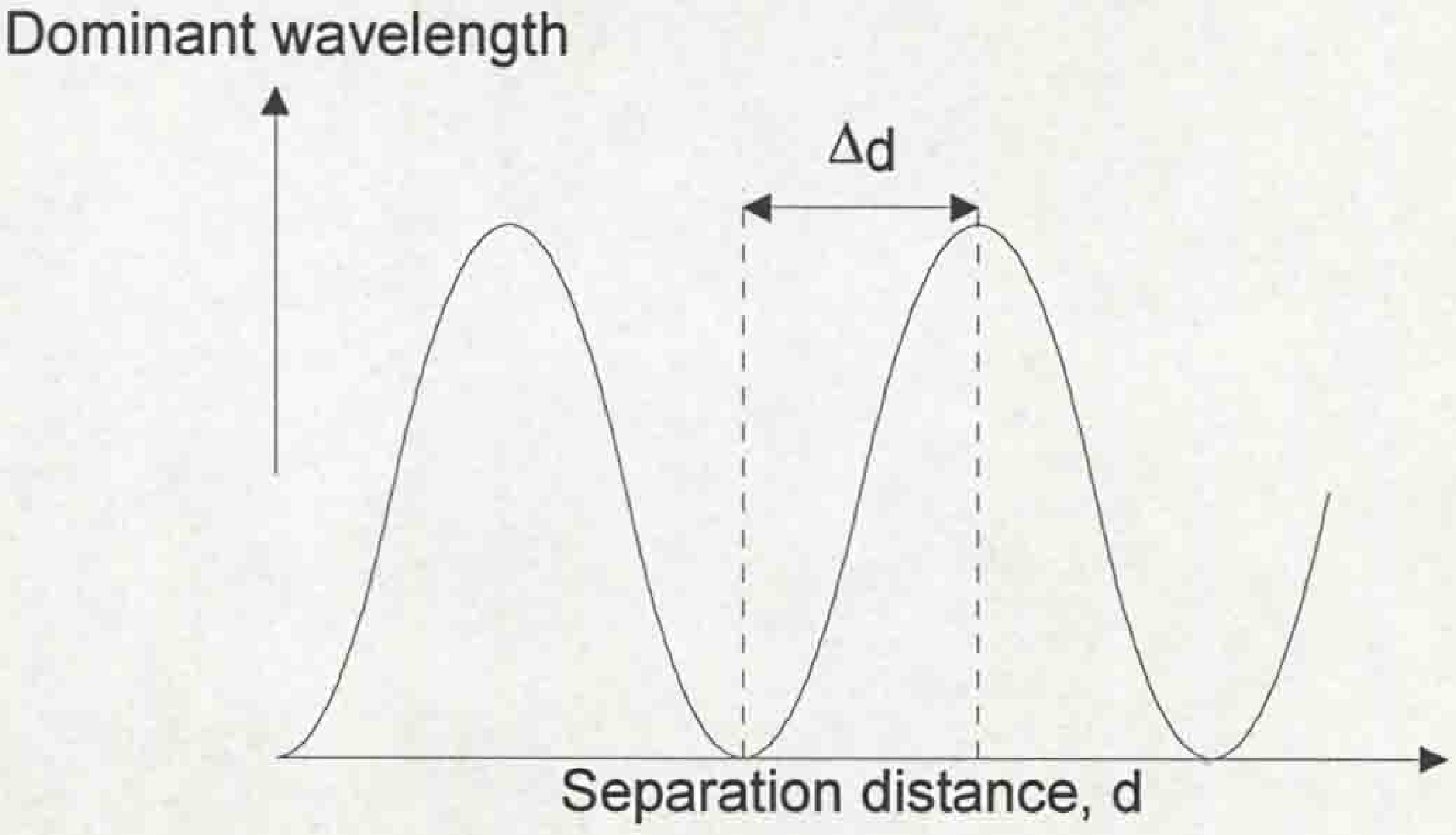

Figure 8.5 - Relationship between dominant wavelength and separation distance, d

If the far reflector of a Fabry-Perot cavity is made to be the diaphragm of a pressure sensor, then flexing of the diaphragm, caused by pressure changes, will result in a change in d and a consequent shift in the dominant wavelength of the light spectrum received at the detector. In such circumstances it is possible to relate pressure directly to dominant wavelength. This argument is valid provided that the coherence length of the polychromatic light is greater than the cavity depth, d. Hence, d in practice needs to be of the order of the wavelength of light (~μm).

8.3 OPTICAL FIBRE PRESSURE SENSOR

8.3.1 Structure of micromachined silicon Fabry-Perot cavity

The structure of the silicon Fabry-Perot cavities, which were incorporated into the prototype optical pressure sensors, is shown on fig.8.6 (Humphries *et al*, 1996).

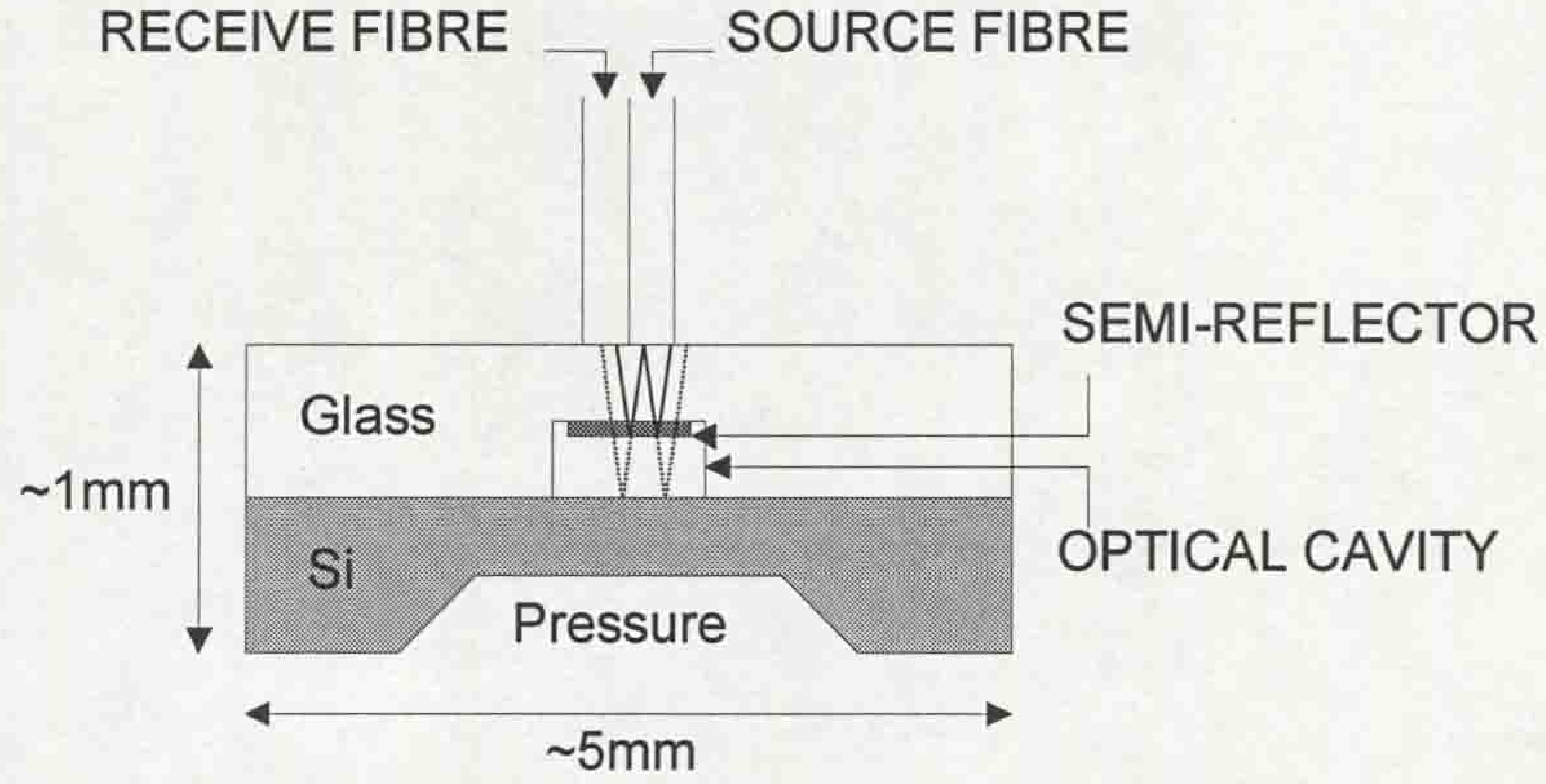

Figure 8.6 - Micromachined silicon Fabry-Perot cavity (Humphries *et al*, 1996)

A silicon diaphragm is formed by etching a cavity into the surface of a silicon wafer. This is electrostatically bonded to a 0.5mm thick glass plate, which has a semi-reflective metallised coating, to form the optical cavity. The temperature coefficients of the silicon wafer and glass plate are closely matched to minimise the temperature dependence of the sensor.

Two 400μm multimode step-index fibres, one source and one receiver, are butted up to the glass plate to address the sensor. Broadband "white" light, from the LIBIDO system light source is launched through the source fibre. Some of the light is reflected by the semi-reflective coating, while the rest of the light is reflected at the silicon wafer. The two rays interfere, resulting in a white light interference function (**8.2.1**). The light transmitted by the receiving fibre will have a corresponding dominant wavelength, which can be evaluated by the LIBIDO system.

When the pressure changes in the vicinity of the silicon diaphragm, the diaphragm flexes and the depth of the optical cavity will change. There will be a shift in the interference pattern (i.e. wavelengths which previously interfered constructively may now interfere destructively and vice versa). A corresponding dominant wavelength shift will occur. Using the LIBIDO distimulus chromatic detection system, the pressure at the transducer can be calibrated against the dominant wavelength of the modulated light.

As shown on fig.8.5, the variation of dominant wavelength with pressure will be periodic. The frequency of this characteristic, with respect to pressure, is determined by the dimensions of the optical cavity and diaphragm thickness in the structure on fig.8.6. Therefore, for the required operating pressure range, the device can be structured so that the dominant wavelength/pressure relationship is monotonic (range Δd on fig.8.5). For the circuit breaker application, the devices were designed to operate monotonically in a pressure range of 6-12barg.

8.3.2 Design of prototype transducers for application to the test circuit breaker

Two prototype optical fibre pressure sensors were designed around the silicon Fabry-Perot cavities for use on the test circuit breaker. The general form of the transducers is shown on fig.8.7. The sensors were housed in modified bolts (M16 thread) to provide a rugged sensor body and so that they could be conveniently screwed into the appropriate measuring regions of the circuit breaker. One sensor was used to monitor the SF_6 gas pressure near the top-plate of the main circuit breaker tank, during fault current interruption, while the other sensor simultaneously monitored the pressure rise in the piston chamber.

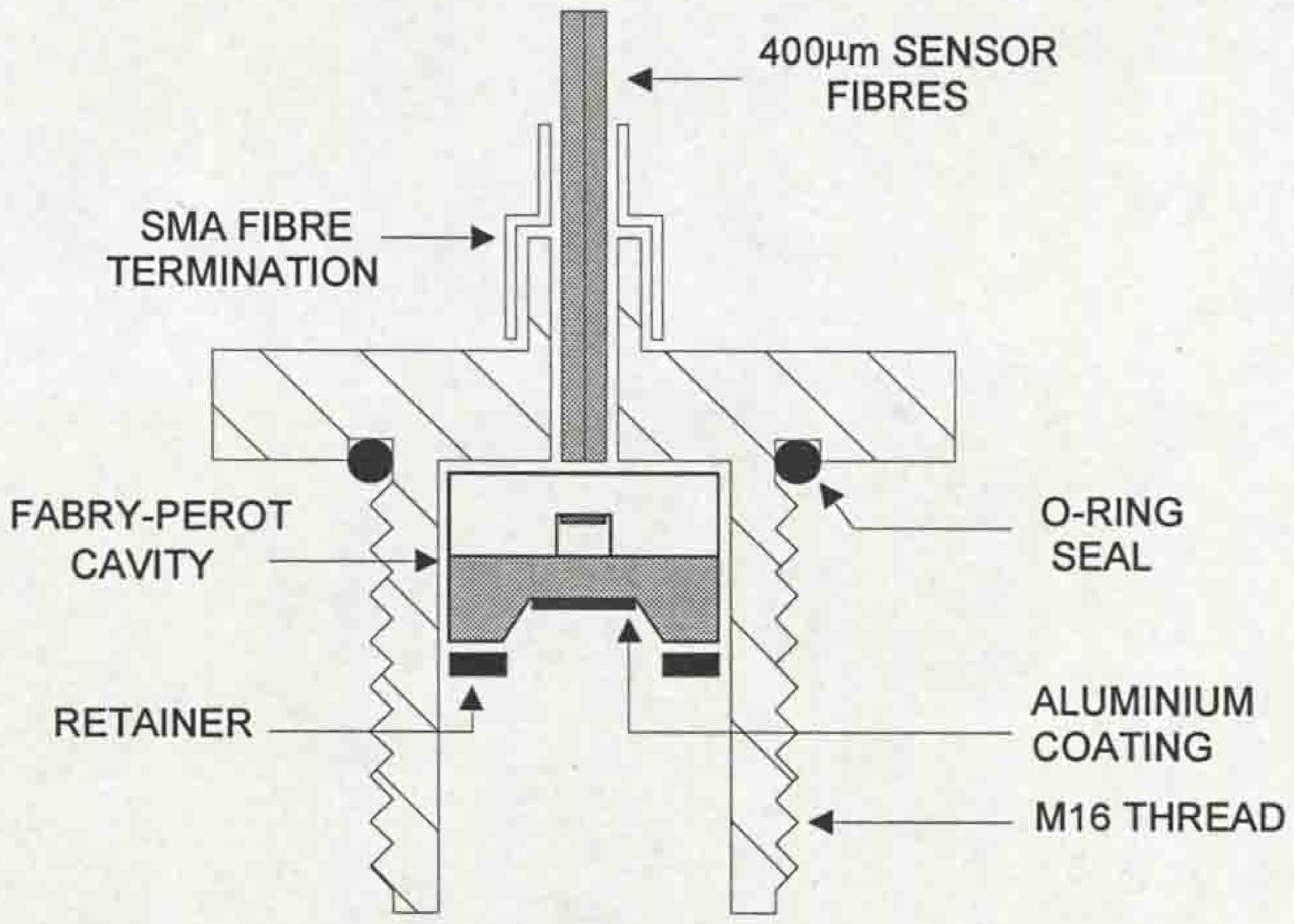

Figure 8.7 - Cross-section of optical fibre pressure sensor

The operating wavelength range for the sensors was 500-1000nm i.e. the detection range of the LIBIDO distimulus chromatic detection system. However, it was found that the silicon wafer of the sensor could transmit wavelengths above 950nm. Therefore, there was concern that stray optical radiation from the arc, between 950nm and 1000nm, during operation of the circuit breaker, might be transmitted through the silicon wafer to the sensor fibres, thus causing optical noise errors on the recorded pressure transients. To prevent this problem, the outer surface of the silicon diaphragm, which was exposed to the circuit breaker interior, was coated with a 5μm thick deposit of aluminium. This was sufficiently thin to avoid "loading" of the diaphragm, but also sufficiently thick optically to reduce transmission through the sensor, from external sources, by -50dB (to 0.001%). It transpired that, as a result of this preventative measure, no arc-induced optical noise was observed on the pressure records obtained from the sensors.

8.3.3 Complete optical fibre sensing system

The complete optical fibre pressure sensing system is shown on fig.8.8. The top-plate pressure sensor is shown only on this figure for convenience. A similar sensor was housed on the piston crown of the test circuit breaker interrupter, to monitor the piston chamber pressure.

A broadband "white" light source (the source unit of the LIBIDO source/detection system) was used. This meant that white light interference occurred in the Fabry-Perot cavity (**8.2.1**), so the gas pressure could be related to the dominant wavelength of the modulated spectrum. The LIBIDO distimulus chromatic detection system was used to convert the modulated light spectra into their corresponding dominant wavelengths. Therefore, it was possible to produce a dominant wavelength/pressure calibration curve for each of the two sensors.

The sensors were calibrated using a digital pressure controller (Druck model DPI500, 0.04% accuracy) to provide accurate measurements of gas pressure exposed to the sensors during calibration. The LIBIDO detection system was used to provide a measure of the dominant wavelength of the modulated light spectra (to 0.1nm accuracy). The calibration curve for the piston chamber pressure sensor is shown on fig.8.9 and for the top-plate pressure sensor on fig.8.10. The top-plate pressure sensor was calibrated over a smaller pressure range than the piston chamber sensor, since the pressure fluctuations near the top-plate, during operation of the circuit breaker, were expected to be much lower than those occurring in the piston chamber (a consequence of the design of puffer circuit breakers). The calibration ranges were chosen after consultation with industrial collaborators.

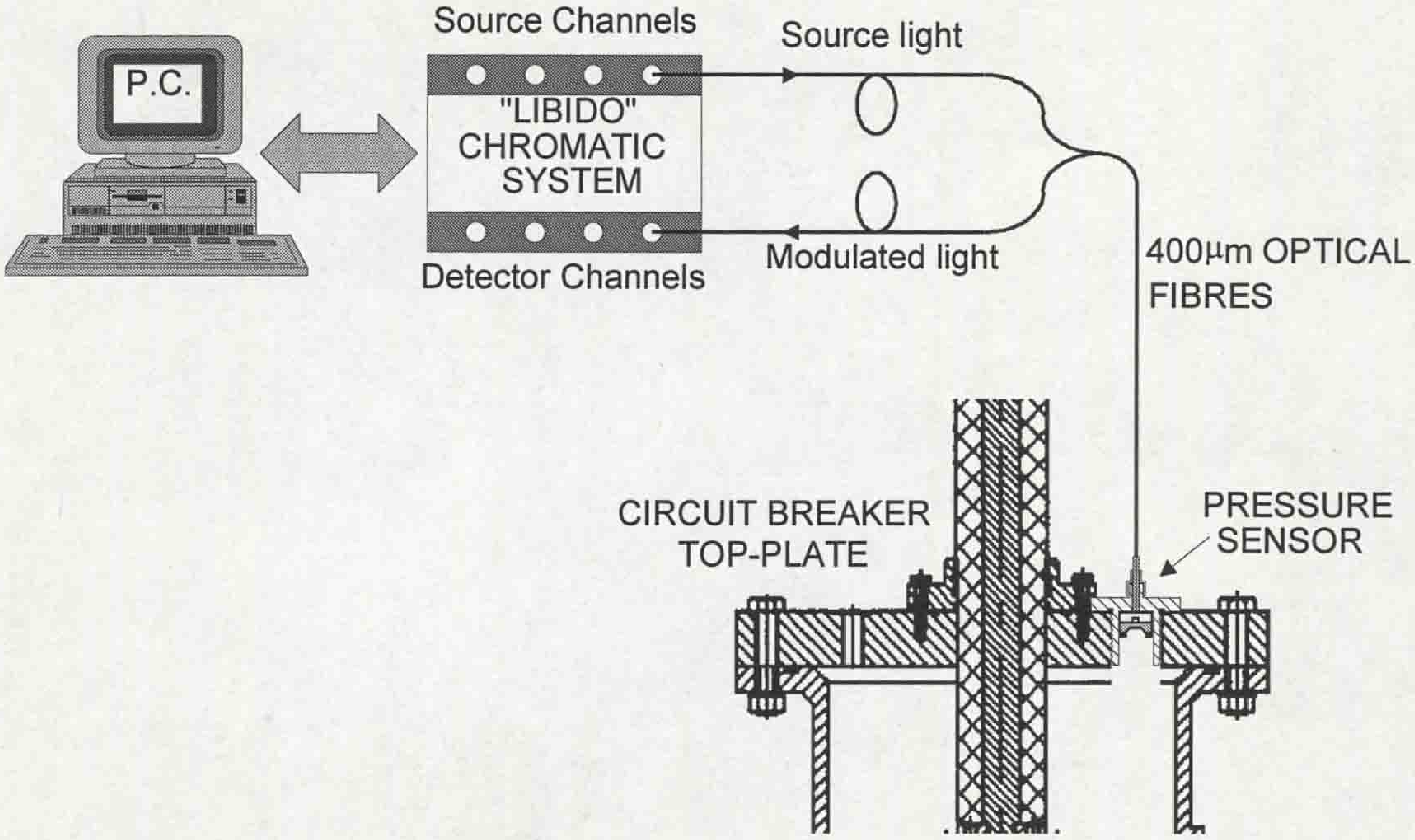

Figure 8.8 - Complete optical fibre pressure sensing system

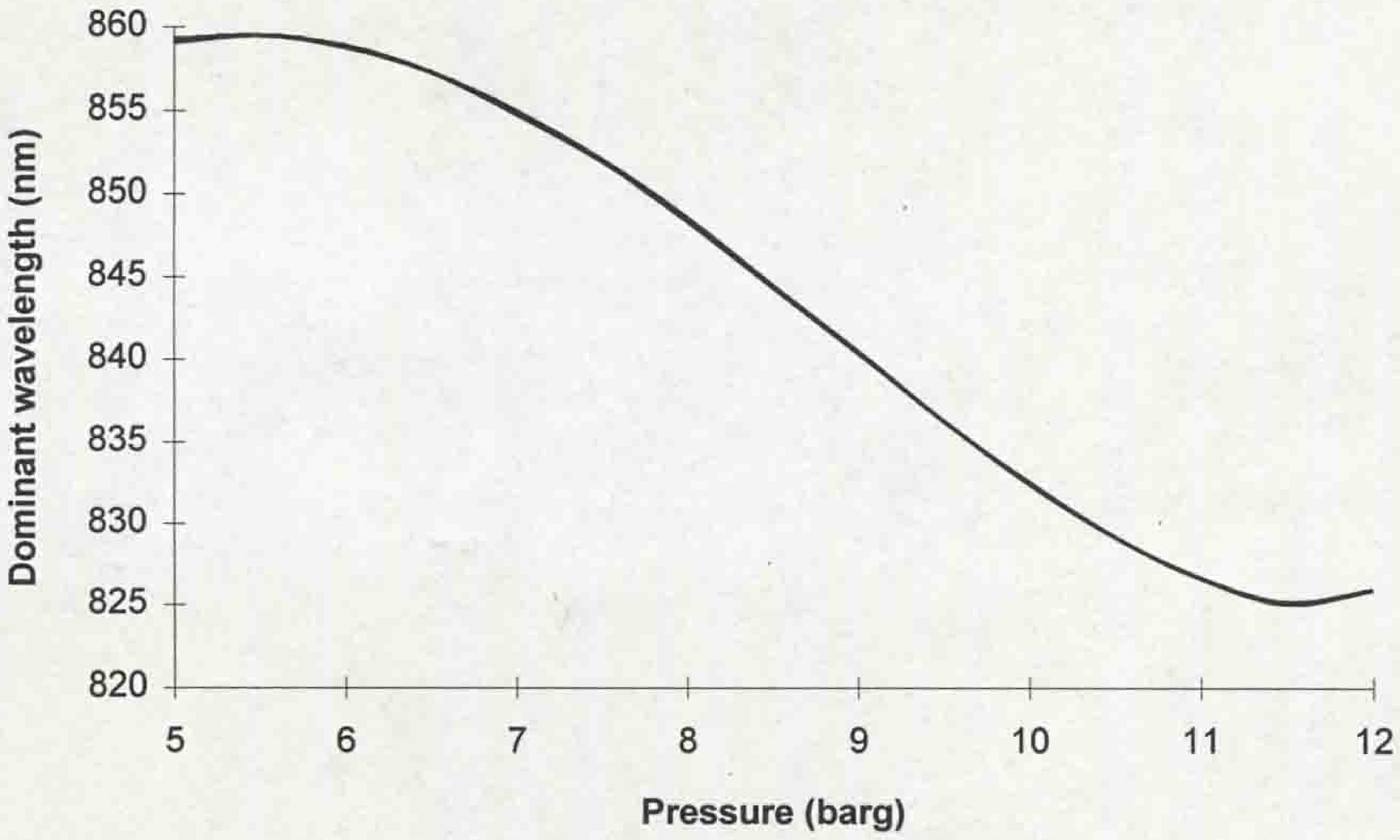

Figure 8.9 - Calibration curve for piston chamber pressure sensor

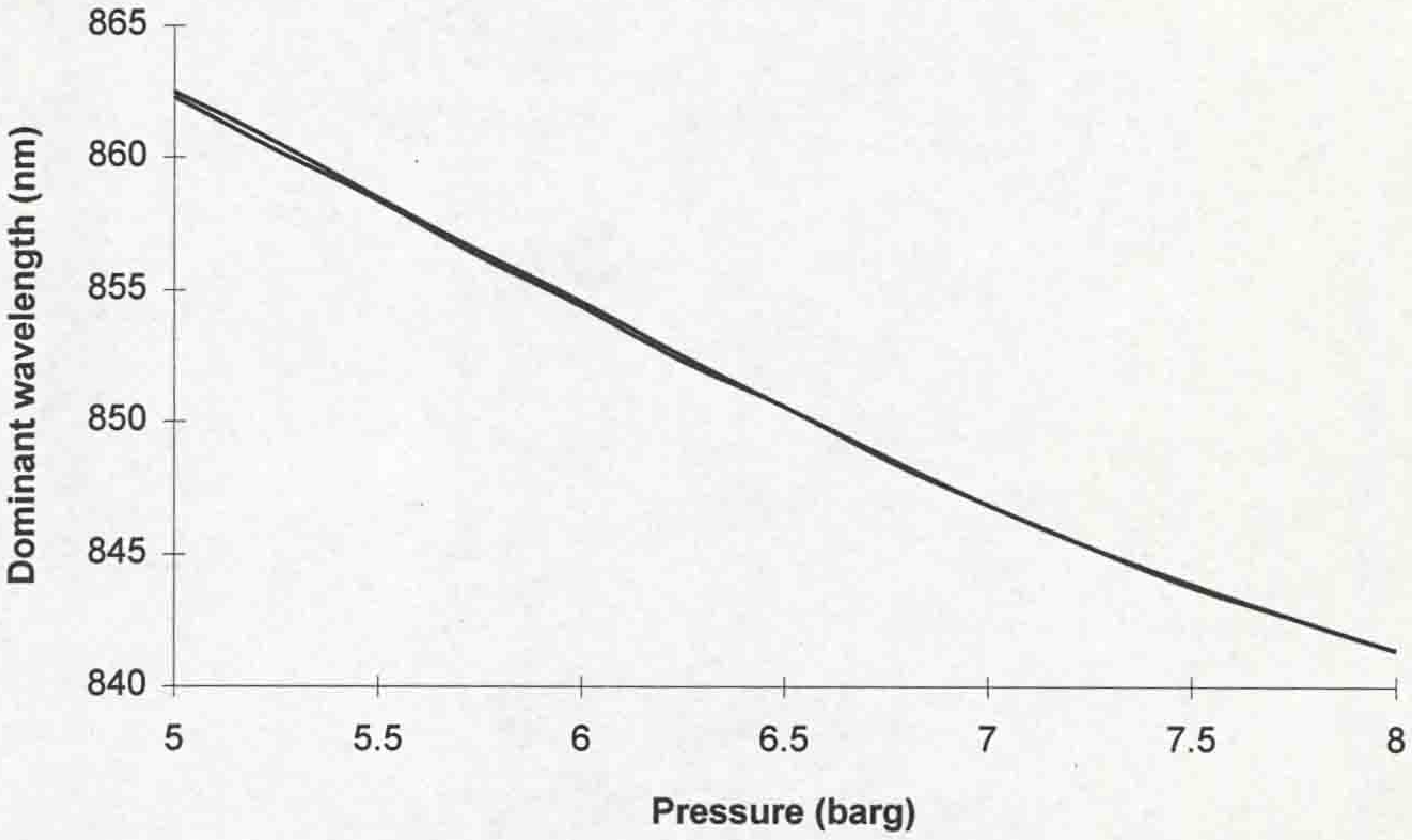

Figure 8.10 - Calibration curve for top-plate pressure sensor

On both figs.8.9 and 8.10 the sensors were calibrated against increasing and decreasing pressure. It can be seen that the hysteresis effects of the sensing system are slight. This hysteresis is due to the elastic deformation of the silicon diaphragm.

8.4 PRESSURE MEASUREMENTS ON THE TEST CIRCUIT BREAKER

The optical fibre pressure sensors were used on the test circuit breaker (**9.2**) to monitor the gas pressure near the top-plate of the main tank and in the piston chamber, during interruption of a wide range of fault currents. Pressure records for the two extremes of operation i.e. coldflow (no arc) and 56kA peak arc (the maximum short-circuit rating of the test circuit breaker) are presented in this chapter. The complete set of pressure records is presented (**chapter 10**) and analysed (**chapter 11**), later in this thesis.

8.4.1 Coldflow results

The time variation of the gas pressure in the piston chamber of the interrupter, in the absence of arcing, is shown on fig.8.11. Contact separation occurs at 0ms and interrupter movement begins at -18ms on the time scale used.

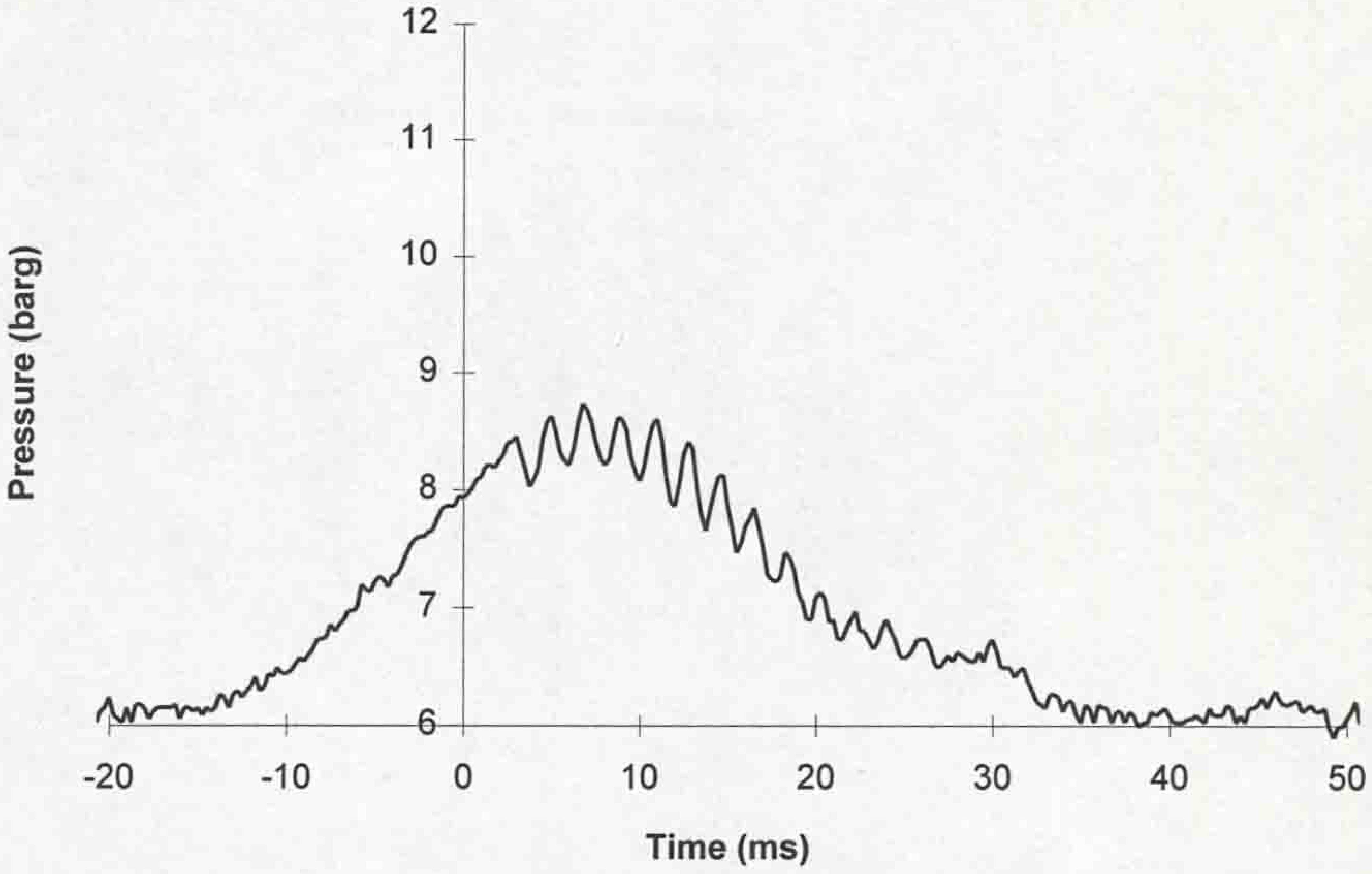

Figure 8.11 - Time variation of piston chamber pressure in absence of an arc

There are a number of features apparent in the transient. Firstly, the total pressure rise in the piston chamber is approximately 2.5bar above ambient. Further, distinct oscillations are apparent a few milliseconds after the instant of contact separation. The frequency of the oscillations is approximately 500-600Hz and their amplitude is, typically, 0.5bar (i.e. 20% of the maximum pressure rise).

The time variation of the gas pressure near the top-plate of the main circuit breaker tank, in the absence of arcing, is shown on fig.8.12. The result shows that the pressure fluctuations in this region are of a relatively low amplitude (typically 0.25bar pk-pk), against the background electrical noise of the detector, which corresponds to approximately 0.05bar. There appears to be a small pressure decrease immediately prior to contact separation (0ms), followed by a pressure transient consisting of frequencies, which are not immediately obvious. A full analysis of the frequency spectrum of fig.8.12 is given later in the thesis (**chapter 11**).

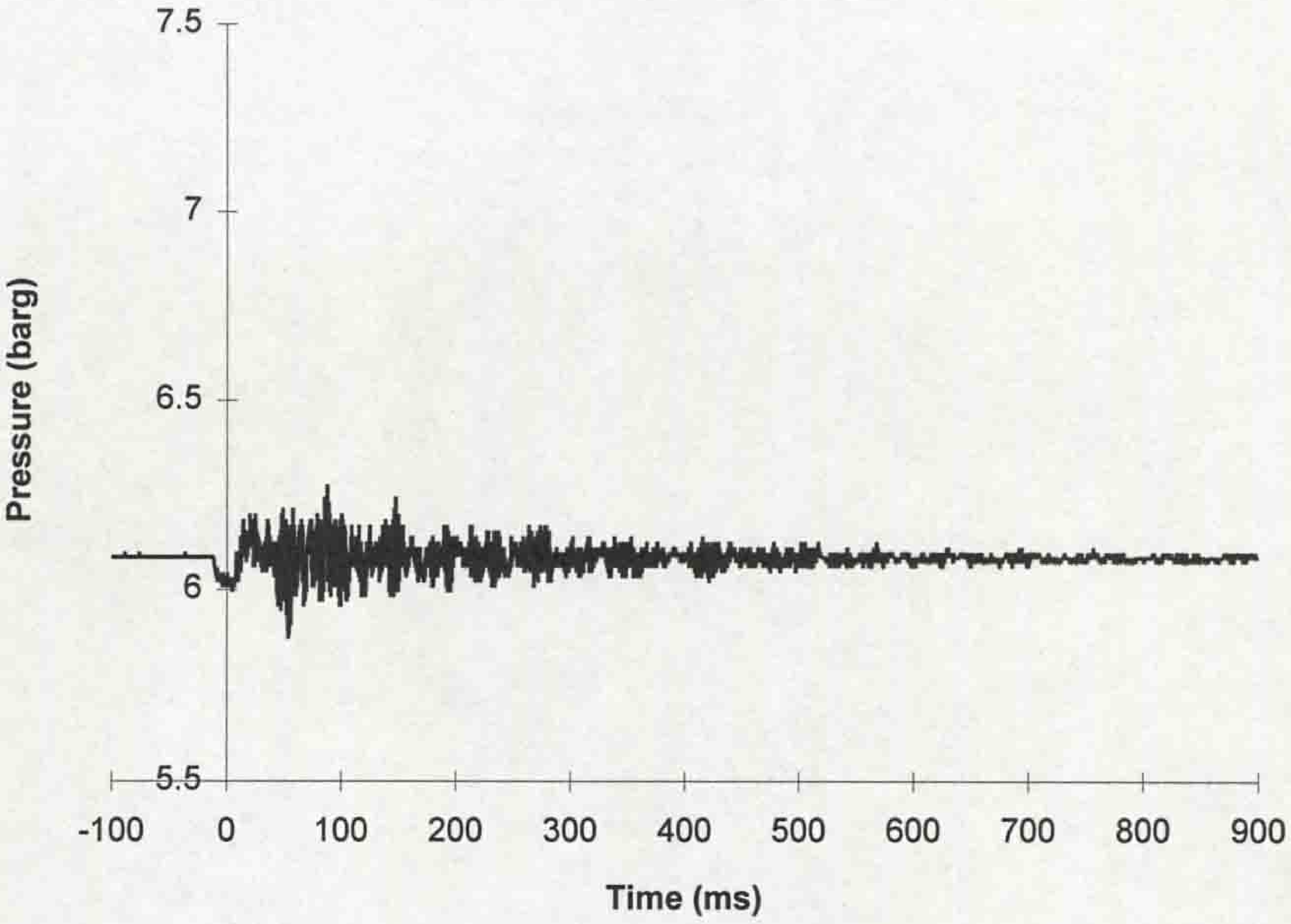

Figure 8.12 - Time variation of pressure near top-plate in absence of an arc

8.4.2 Results with an arc present

As for the coldflow case, pressure measurements were taken both in the piston chamber and near the top-plate of the main circuit breaker tank, under arcing conditions. The pressure results obtained, during interruption of a 56kA peak arc, the maximum current used in the tests, are presented below. Pressure results for the remaining range of arc currents are presented later (**chapter 10**).

The time variation of the gas pressure in the piston chamber is shown on fig.8.13, for a fault current of 56kA peak. The result shows that excess pressures are generated above the coldflow case. Further, the amplitude of the oscillations, which commence shortly after contact separation (0ms), have increased also. This result is discussed in more detail in **chapters 10** and **11**.

The time variation of the gas pressure near the top-plate of the main tank is shown on fig.8.14, for a fault current of 56kA peak. Again, the pressure fluctuations in this region are greatly increased with respect to the coldflow case. The peak-to-peak pressure fluctuation is greater than 1.5bar at some instances. It is interesting to note that, when the pressure transient decays, the post-arc tank pressure is higher than the pre-arc value by ΔP = 0.2bar. This is believed to be due to arc heating of the bulk gas volume within the circuit breaker and is discussed further in **chapter 11**.

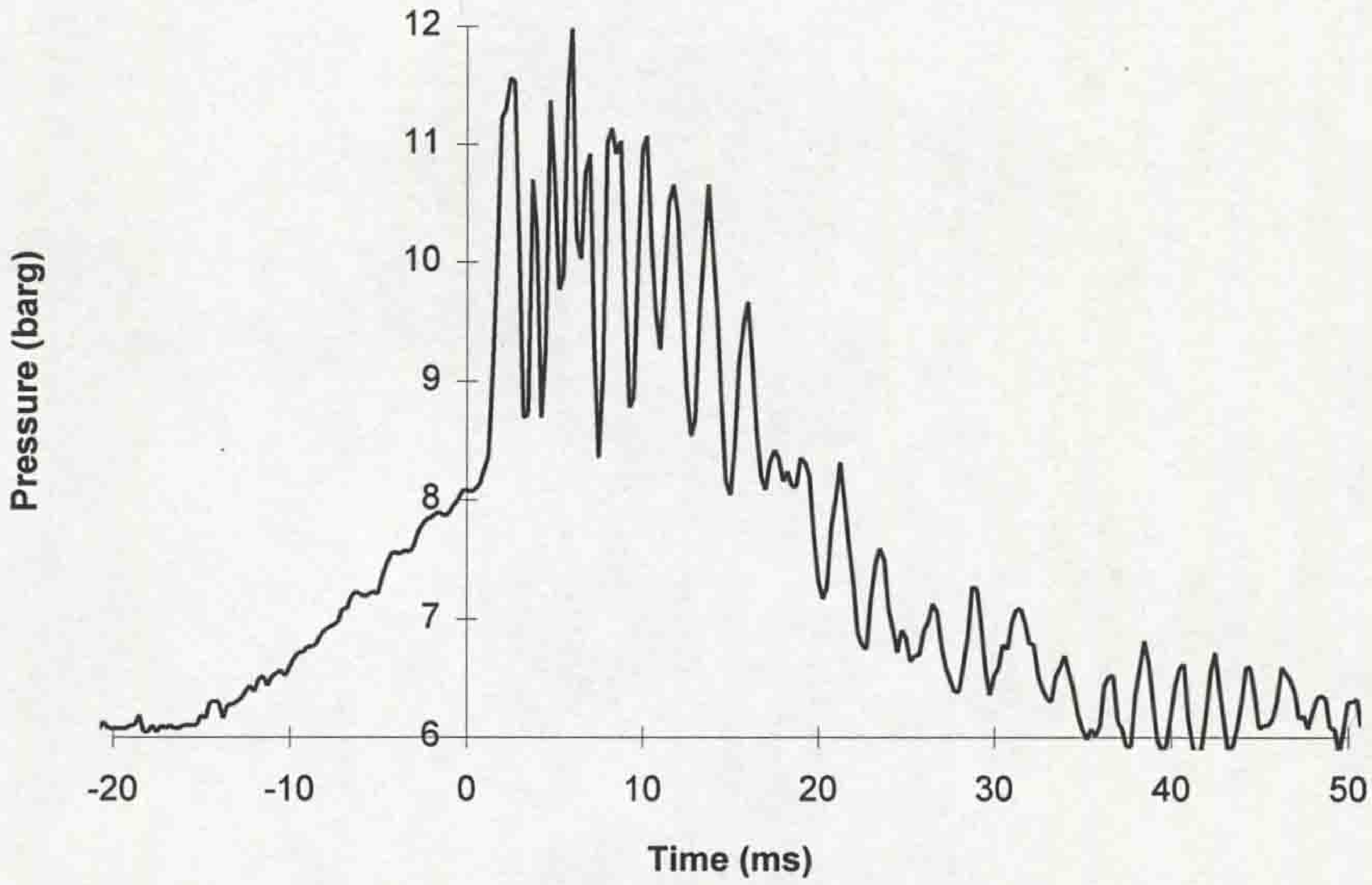

Figure 8.13 - Time variation of piston chamber pressure during interruption of 56kA peak fault current

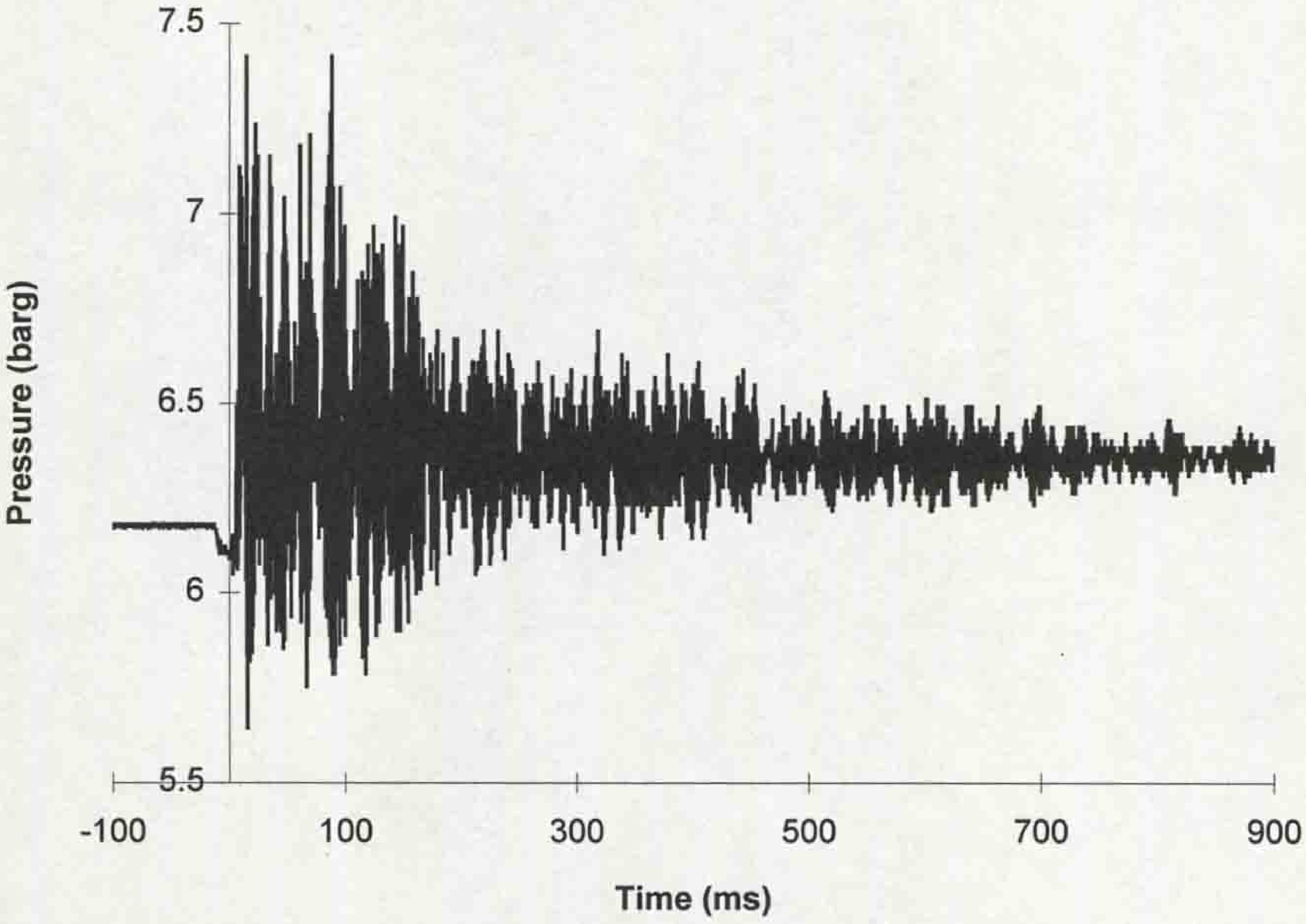

Figure 8.14 - Time variation of pressure near top-plate during interruption of 56kA peak fault current

8.4.3 Error analysis of results obtained from pressure transducers

In view of the large amplitude oscillations, which were evident on the pressure results recorded by the optical fibre pressure sensors (figs.8.11 to 8.14), it was important to check the effect of mechanical vibration, of the circuit breaker structure, on the sensor outputs. This was achieved by repeating the experiments, with the sensors blocked, so that they were only exposed to mechanical vibrations of the circuit breaker structure, not the pressure fluctuations.

The output from each sensor was processed to obtain an error value, expressed as a percentage of the full modulation depth of each sensor. Fig.8.15 shows the total percentage error from the top-plate pressure sensor, for an arc current of 56kA peak. This total error encompasses not only vibration, but also electrical noise of the LIBIDO detection system. The results show that, for the top-plate pressure sensor, the total error is 1%. Since this error is apparent before contact separation (0ms), the conclusion is that the error is solely due to detector noise and that the mechanical vibration-induced noise is negligible.

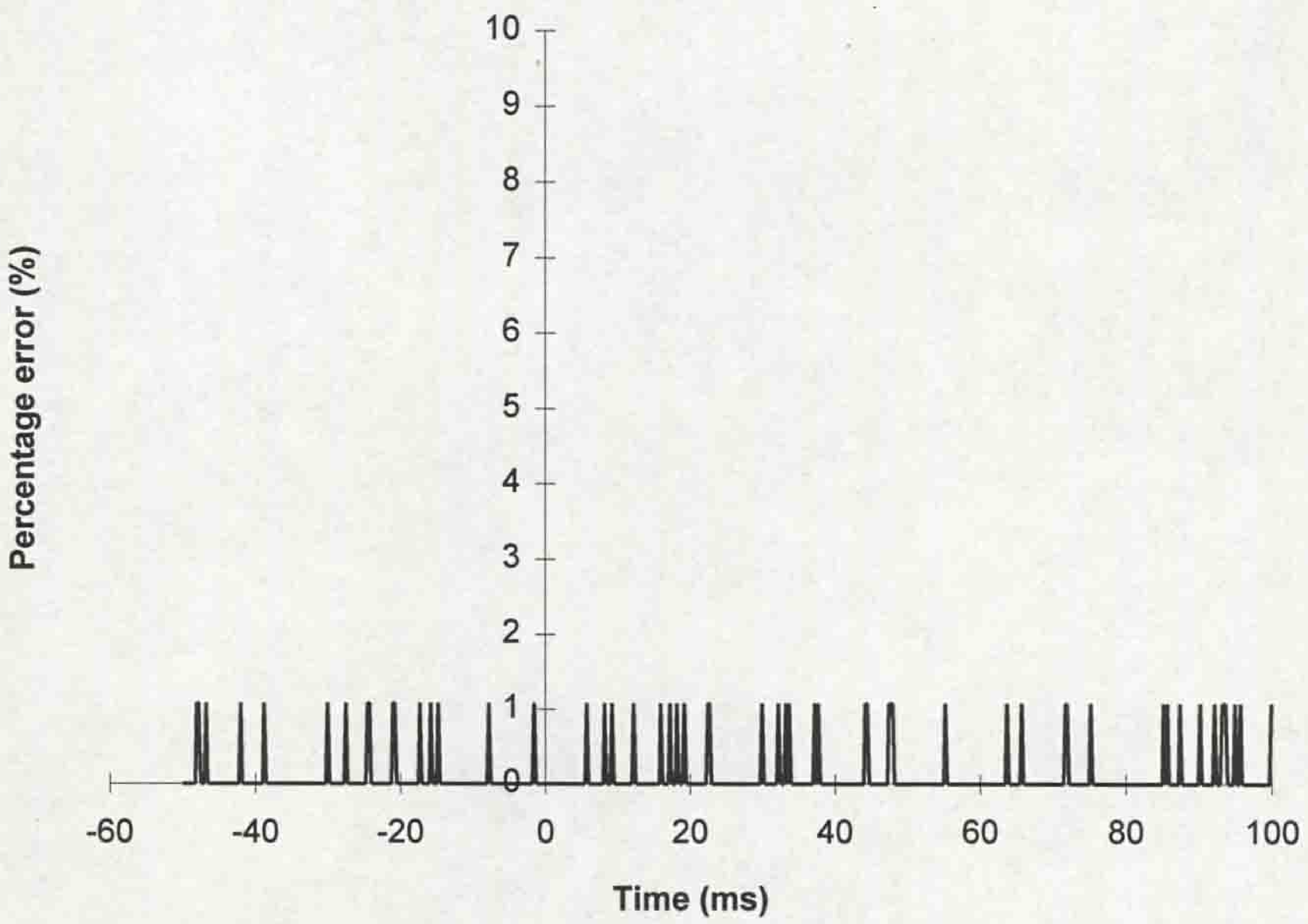

Figure 8.15 - Total error on top-plate pressure sensor during interruption of 56kA peak

Fig.8.16 shows the total error on the piston chamber pressure sensor, for the same arc current of 56kA peak. The detector noise is evident before contact separation (0ms) at 0.3%. Shortly after contact separation the error rises to a peak of 7%. This is likely to be due to mechanical vibration and is not unexpected, since the sensor is mounted on the piston crown of the interrupter, close to the arcing region. It was found, as anticipated, that this error increased with arc current. Thus, 7% is the worst possible error for all the piston pressure results obtained.

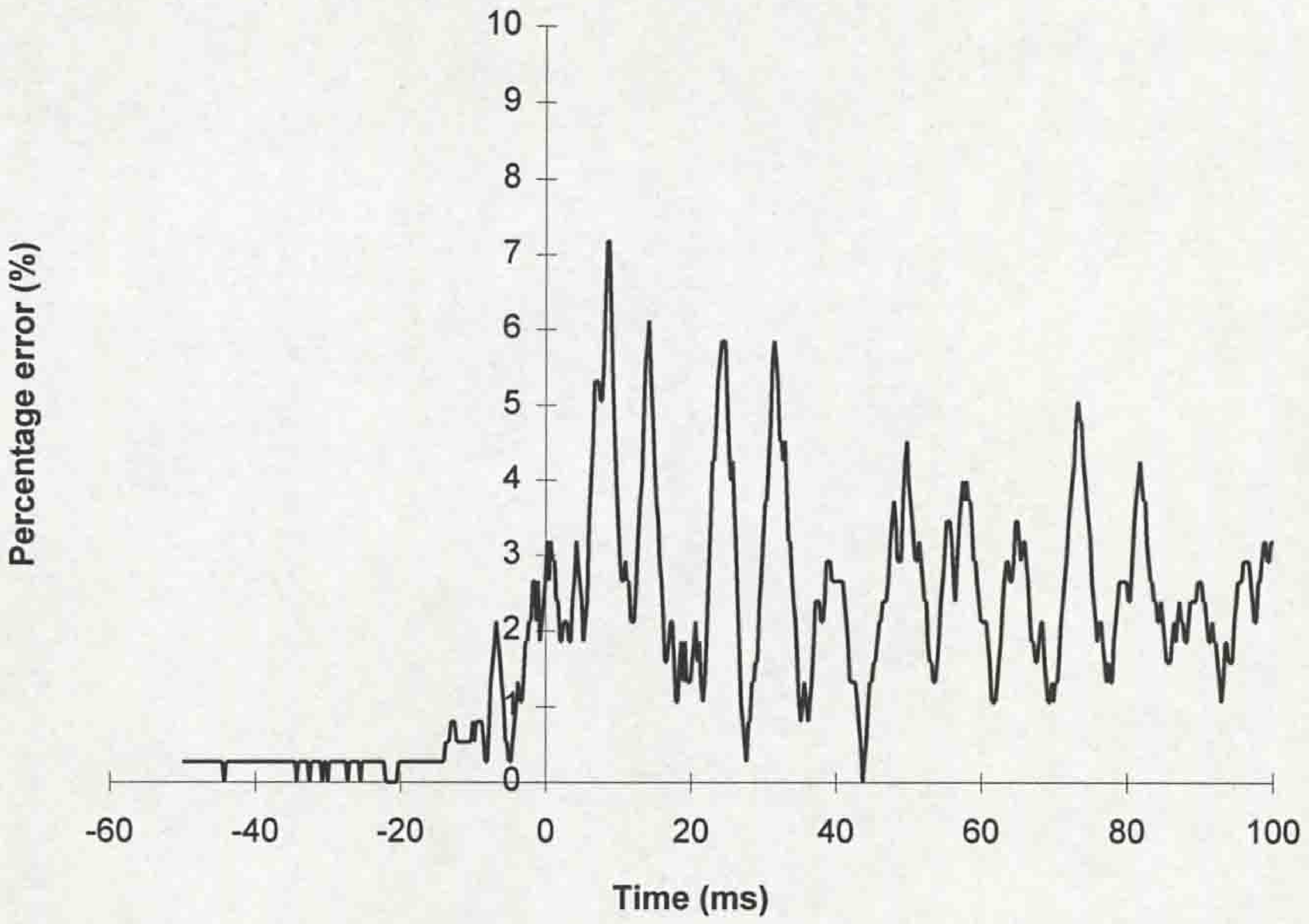

Figure 8.16 - Total error on piston pressure sensor during interruption of 56kA peak

Interestingly, there appears to be a post-arc D.C. error of 2.5% on fig.8.16. This change was probably due to arc heating of the gas pocket within the blocked sensor, causing the pressure change. Therefore, it is expected that this error would not exist during normal operation of the sensor, when there is no sealed gas pocket.

8.5 CONCLUSIONS

Pressure measurements are important in two areas of circuit breaker research, circuit breaker modelling and circuit breaker condition monitoring (**8.1**). Conventional pressure sensors are being superseded by optical fibre pressure sensors, since they have inherent freedom from electromagnetic interference and provide isolation between the circuit breaker and processing instrumentation, in the form of optical fibres.

Recently developed, micromachined silicon, Fabry-Perot pressure transducers (Humphries *et al*, 1996) were tested, as part of this project, to assess their suitability for circuit breaker application. Two prototype sensors were designed, built and tested. One sensor was used to monitor pressure near the top-plate of the main circuit breaker tank and the other was used to monitor pressure rises in the piston chamber.

Both of the sensors appeared to function successfully over the full range of arc currents interrupted. The results were found to be highly dependent upon arc current and are discussed in more detail in **chapters 10** and **11**. The total errors on each sensor, due to non-pressure effects, were experimentally derived. The top-plate pressure sensor had a maximum error of 1% for all tests. The piston chamber sensor had a total maximum error of 7%, which was found to occur during interruption of the highest fault current (56kA). It is possible that engineering refinements to the sensor housing could reduce this error, which is largely attributed to mechanical vibration of the circuit breaker structure. Nevertheless, the potential of this pressure sensing technique, for circuit breaker applications, was successfully proved.

Part III - Main circuit breaker experiments

CHAPTER 9 - CIRCUIT BREAKER EXPERIMENTS

9.1 INTRODUCTION

The initial period of research in this project involved the development of optical sensors to be used on the circuit breaker (**Part II**). The experimentation required for this was of a laboratory bench top nature. The experimental development and the theory pertaining to each individual sensor is discussed in the relevant chapters (**5-8**). Once a sensor was sufficiently advanced, a prototype was manufactured for testing on the circuit breaker. A proportionate amount of time was devoted to the development of each sensor, with the aim that they underwent prototype manufacture at roughly the same time. This allowed the use of several sensors on the circuit breaker during a single test phase, so that a large database of results could be obtained. This section describes the equipment used for this main series of circuit breaker experiments including the electrical circuit and instrumentation.

9.2 THE TEST CIRCUIT BREAKER

The circuit breaker, which was used to test sensors developed in this project, is shown on fig.9.1. It was a type SPLA, 145kV / 40kA (rms), livetank SF_6 partial duo-flow puffer circuit breaker, manufactured by NEI Reyrolle Switchgear. The operation of the interrupter is similar to that shown on fig.2.7 (**2.1.6.3.1**). The circuit breaker was modified specifically for research work. Instead of a conventional porcelain insulator to separate the top-plate (usually at line potential) from the earthed base-plate, a windowed steel tube was used. The purpose of the windows was to provide direct optical access to the circuit breaker interior, so that flow visualisation using laser-based techniques could be performed. This work (Heyes *et al*, 1995) was undertaken in parallel to the work reported in this thesis, as part of a global investigation into the circuit breaker behaviour. The top plate was electrically tied to ground for the circuit breaker tests and an insulating bushing installed to isolate the high voltage top electrode from the top plate.

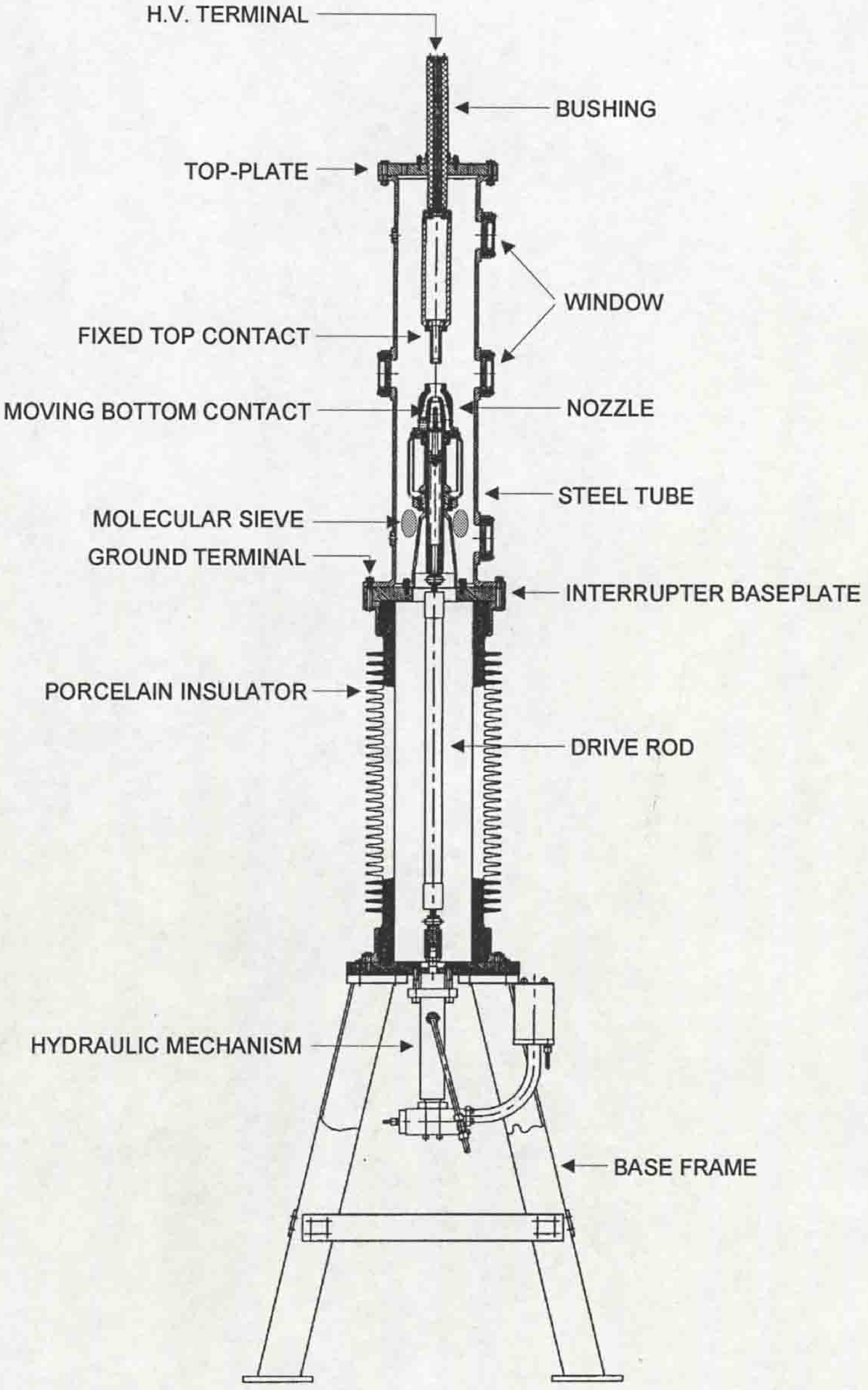

Figure 9.1 - Modified Reyrolle Switchgear SPLA 145kV - 40kA(rms) livetank puffer circuit breaker

9.3 ELECTRICAL TEST CIRCUIT

There were two main objectives to the experiments. Primarily they were undertaken to test the performance of the sensors in the presence of high-current circuit breaker arcs. Pending successful operation of the sensors, the secondary objective was to analyse the results and their applicability to circuit breaker modelling and circuit breaker condition monitoring. To achieve these aims a series resonant circuit was used (fig. 9.2) to pass high currents (up to 56kA peak) through the test breaker. A synthetic circuit, for producing extra high voltage restrike transients during the current zero period, was not used because the objectives were primarily concerned with the high current phase of interruption.

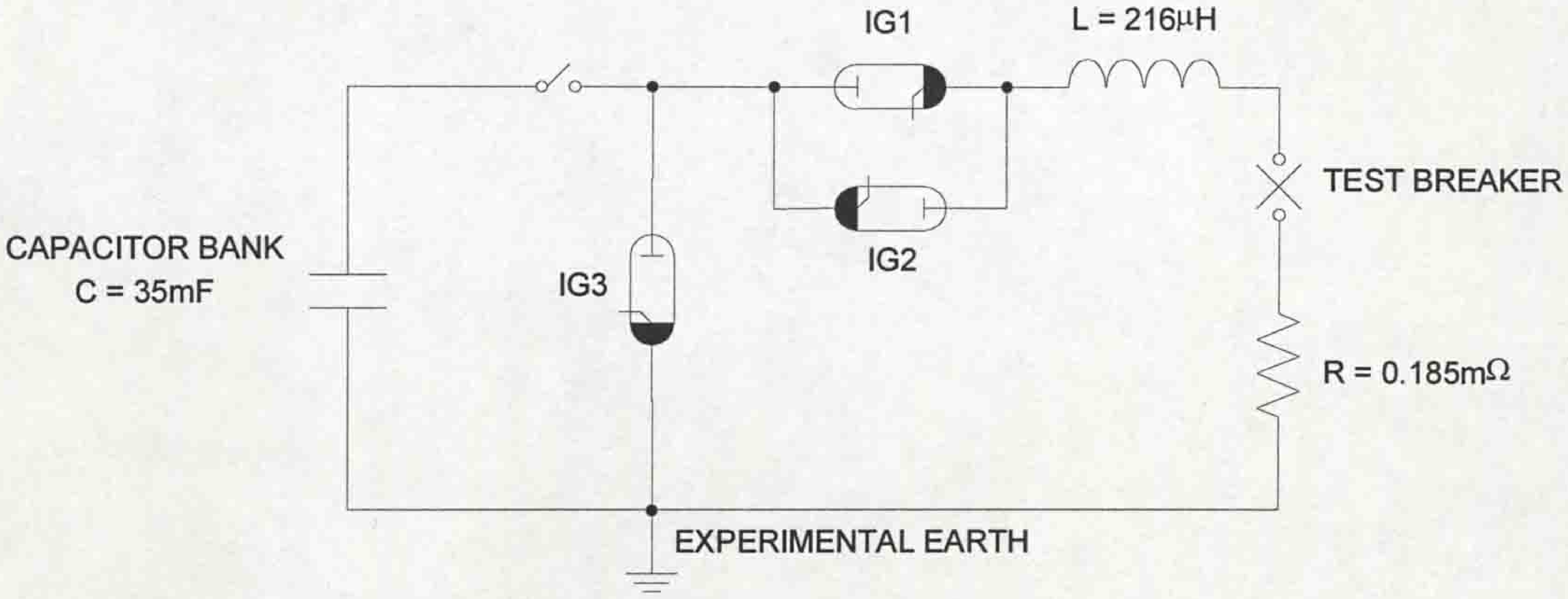

Figure 9.2 - Experimental test circuit

The capacitor bank, used for the circuit power source, had a capacitance of 35mF and was rated up to 6.3kV. A 216μH inductor was used to resonate the circuit at 58Hz (assuming a comparatively low circuit resistance). This was close enough to power frequency to emulate power system conditions. The circuit resistance, due to cables and connections, imposed a practical limit on the circuit discharge current, but the achievable current waveform peak was still sufficient to allow the breaker to be used up to its short circuit current rating (56kA peak).

Discharge of the capacitor bank was controlled by a number of ignitrons. One set of ignitrons were triggered by a central control unit (CCU) to discharge the capacitor bank into the circuit, such that two half-cycles of current were allowed to flow. A second set of ignitrons were triggered immediately after this operation to dump the residual energy, stored on the capacitors, to experimental earth. Only two half-cycles of current were necessary for the tests, since the breaker had a specified arc interruption time lying within this interval. However, for these tests the circuit breaker cleared all fault currents at the current zero following the first half-cycle, since the rate of rise of recovery voltage (RRRV) was much lower than that to which the circuit breaker would have been subjected in service.

9.3.1 Control unit and timing sequence

Operation of the experimental test facility was controlled by the central control unit (CCU). The CCU provided trigger pulses to various components of the high current circuit, with preset delays between pulses to achieve the correct timing sequence. The sequence of events for each test was as follows:

1. The capacitor bank was charged to the desired voltage, up to 6.3kV, depending on the short-circuit current amplitude required.
2. The CCU was activated to begin the test. The CCU provided its first trigger pulse to the hydraulic mechanism of the breaker to commence the opening stroke of the interrupter.
3. After 18ms the breaker contacts were just at the point of separating. The second trigger pulse from the CCU was delayed with respect to the first by a period of this duration. This second pulse was transmitted to the recording instrumentation to indicate the imminence of arc initiation, and to the ignitron IG1 (fig. 9.2) to discharge the positive first half-cycle of arc current through the circuit breaker.
4. After 8.5ms the first current zero on the high current waveform was reached and the CCU then triggered IG2 to discharge the negative second half-cycle of arc current. (As mentioned above this second half-cycle was not obtained during the tests, since the circuit breaker invariably extinguished the arc at the first current zero).
5) A further 8.5ms later, after the second half-cycle, the CCU triggered a second set of ignitrons (IG3), used to discharge any residual energy, stored on the capacitor bank, to the experimental earth.

This represents the standard test sequence which was followed for a range of arc currents to enable the prototype sensors to be tested. The experimental results obtained in this manner are presented later (**chapter 10**).

9.3.2 Practical considerations

It was essential to have a single earth point in the high current circuit of fig.9.1. This was provided by an experimental earth, which consisted of a copper rod rooted in the foundations of the building, close to the experiment. The use of low impedance interconnecting cables, with a high current rating, allowed the experimental circuit to discharge up to 56kA peak fault current for short periods (one cycle of power frequency). The mains earth, on the other hand, was only rated to carry a fault current of up to ≈30kA. Furthermore, discharging high fault currents into the mains earth could have caused dangerous voltage surges throughout the remainder of the building. Thus, it was vital to use the experimental earth as the only earth point for the experiment.

Any mains-fed equipment, e.g. oscilloscopes, which needed to be electrically connected to the experiment were powered through 1:1 isolating transformers, which isolated the mains earth from the instruments. The equipment was then connected at a suitable point to the experimental earth (in the case of oscilloscopes, for example, this was achieved via the outer sheath of a coaxial signal cable).

The other main consideration during the tests was to avoid any electromagnetic interference from the power circuit, which could cause errors in the signals transmitted from any electrical transducers (the optical transducers should have inherent immunity). Although the power circuit was operating at effectively power frequency (58Hz), higher frequency transients could, nevertheless, be produced during current interruption. Thus, it was necessary to ensure that there were no effects from earth loops. To ensure this, the main circuit cables were electromagnetically screened and the recording instruments were shielded in an experimentally earthed copper enclosure.

9.4 INSTRUMENTATION

This section briefly describes the range of transducers employed during the circuit breaker tests, together with the instrumentation for processing the signals. The transducers can be broadly classified as either being electrical, optical or hybrid.

The electrical transducers were used to monitor electrical parameters, i.e. current through and voltage across the circuit breaker terminals and required a direct electrical link between the circuit breaker and the recording instrumentation. Careful attention was, therefore, required to avoid earth loops and electromagnetic interference problems.

The optical transducers (**chapters 5-8**) were used to monitor several parameters, and involved transmitting signals which were optically encoded along optical fibres to the processing instrumentation. The optical fibres provided inherent insulation and freedom from electromagnetic interference.

A special case of transducer used was the dielectric probe (**chapter 7**). This actually measured an electrical parameter, the dielectric breakdown strength of the SF_6 gas within the circuit breaker. The measurement was performed electro-optically using a Pockels cell (**7.3.2**). The dielectric probe utilised battery-powered on-board electronics at the circuit breaker, which were optically triggered from the control room via optical fibres. Thus, the only link between the control room and dielectric probe was by optical fibres. This optical control of on-board electronics is characteristic of a "hybrid" optical sensor. At the control room the optical signals, representing breakdown voltage values for the SF_6 gas, were opto-electronically converted into electrical pulses and fed to a channel of a storage oscilloscope.

The signal processing instruments may also be classed as either electrical or optical. The electrical device was a four channel digital storage oscilloscope, while the optical device was the commercially available distimulus chromatic detection system, LIBIDO (**4.3.3.2**). Each of these instruments was interfaced to an IBM compatible PC so that the data could be downloaded into a spreadsheet.

9.4.1 Transducers

9.4.1.1 Electrical transducers

The two electrical transducers monitored the following parameters:

Current flowing through the circuit breaker

The current flowing through the circuit breaker was measured by recording the voltage drop across a 0.185mΩ coaxial current shunt positioned in the earth return cable of the power source circuit (fig.9.1). The output from the shunt was transmitted to one of the channels of the storage oscilloscope, via a coaxial signal cable.

Voltage across the circuit breaker

The circuit breaker voltage, during operation, was measured by using a Tektronix P6015 high voltage probe with a 1000:1 voltage division ratio. The output from the voltage probe was connected to another channel of the storage oscilloscope.

9.4.1.2 Optical transducers

The optical transducers were used to monitor several parameters during the tests:

- Travel of the interrupter moving contact.
- Pressure of the gas (in the interrupter piston chamber and main circuit breaker tank).
- Concentration variations of SF_6 degradation particles between tests.
- Chromaticity of the emitted arc radiation.

Travel of moving contact

The stroke of the interrupter was monitored during each test by the optical fibre linear travel recorder (OFLTR) developed as part of this project (**chapter 5**). The OFLTR provided a resolution of 1mm and accuracy of 1% over the 190mm displacement of the moving contact of the interrupter. The output from the OFLTR was a modulated polychromatic spectral signature, which, when interrogated by the LIBIDO chromatic detection system, provided a linear correlation of dominant wavelength (**4.3.2**) to displacement.

Pressure of SF_6 gas

Pressure sensors were designed around micro-machined silicon diaphragms (**chapter 8**). Two prototype sensors were constructed, one for monitoring pressure fluctuations near the top plate of the circuit breaker enclosure, and another for monitoring the pressure rise inside the piston chamber of the puffer interrupter. The LIBIDO distimulus chromatic detection system was used to process the signals, simultaneously with the OFLTR signals.

Particle concentrations within circuit breaker enclosure

The optical fibre particle concentration monitor (OFPCM), developed during the project (**chapter 6**), was used to monitor the post-arc levels of decomposition particles produced by arcing in the SF_6 gas. Again, the generic LIBIDO chromatic system was used to process the signals from this sensor.

Chromaticity of the optical radiation emitted by the circuit breaker

This sensor completed the range of optical sensors used during the circuit breaker tests. It was the least complex of all the sensors developed in the project, since it consisted of a single 400μm core multimode glass optical fibre mounted externally on the central viewing window of the circuit breaker. The fibre received optical radiation from the circuit breaker during arcing, and transmitted the light to the LIBIDO system, where it was converted into a dominant wavelength value. The dominant wavelength of the radiation emitted by the circuit breaker was monitored as a function of time with this method. This method of radiation measurement (introduced in **3.4.4**) can then be compared with more conventional radiation measurements (**3.4.3**).

9.4.1.3 Hybrid transducer

Gas dielectric strength

The dielectric strength of the SF_6 gas during fault current interruption was monitored by the dielectric probe, which was developed earlier in the project (**chapter 7**). The method of operation is detailed in chapter 7 and a cross-section of the probe is given (fig.7.7). The output from the dielectric probe system, following opto-electronic conversion of the optical signals, was a wavetrain of electrical voltage pulses (**7.1.2**), representing the breakdown strength variation of the SF_6 gas with time, which were fed into the third channel of the storage oscilloscope.

9.4.2 Signal processing equipment

9.4.2.1 Electrical signal processing instrument

A Tektronix digital storage oscilloscope (model 420) was used to receive and process electrical signals from the current shunt, high voltage probe and dielectric probe system. The oscilloscope was a four channel device, which was interfaced to an IBM compatible PC via a GPIB connection, to download the electrical signals into spreadsheet format. The channels were used as follows:

CH1- Current through circuit breaker.
CH2- Voltage across circuit breaker.
CH3- Dielectric probe waveforms.
CH4- External trigger from central control unit (CCU).

9.4.2.2 Optical signal processing instrument

The LIBIDO distimulus chromatic detection system (**4.3.3.2**), manufactured by Lucas Control Systems Products, was used to receive and process optical signals from the optical fibre linear travel recorder (OFLTR), optical fibre particle concentration monitor (OFPCM), optical fibre pressure sensors (in the piston chamber and near the top-plate of the circuit breaker) and the circuit breaker radiation monitoring fibre.

The output of this system was in the form of a chromatically processed dominant wavelength of the incoming light spectra. The LIBIDO provided the facility of having up to eight detector channels simultaneously processing and storing dominant wavelength values at up to 4kHz, for optical spectra in the wavelength range of 500-1000nm. This was also interfaced to an IBM compatible PC to download the dominant wavelength values into spreadsheet format.

9.5 TEST STRATEGY

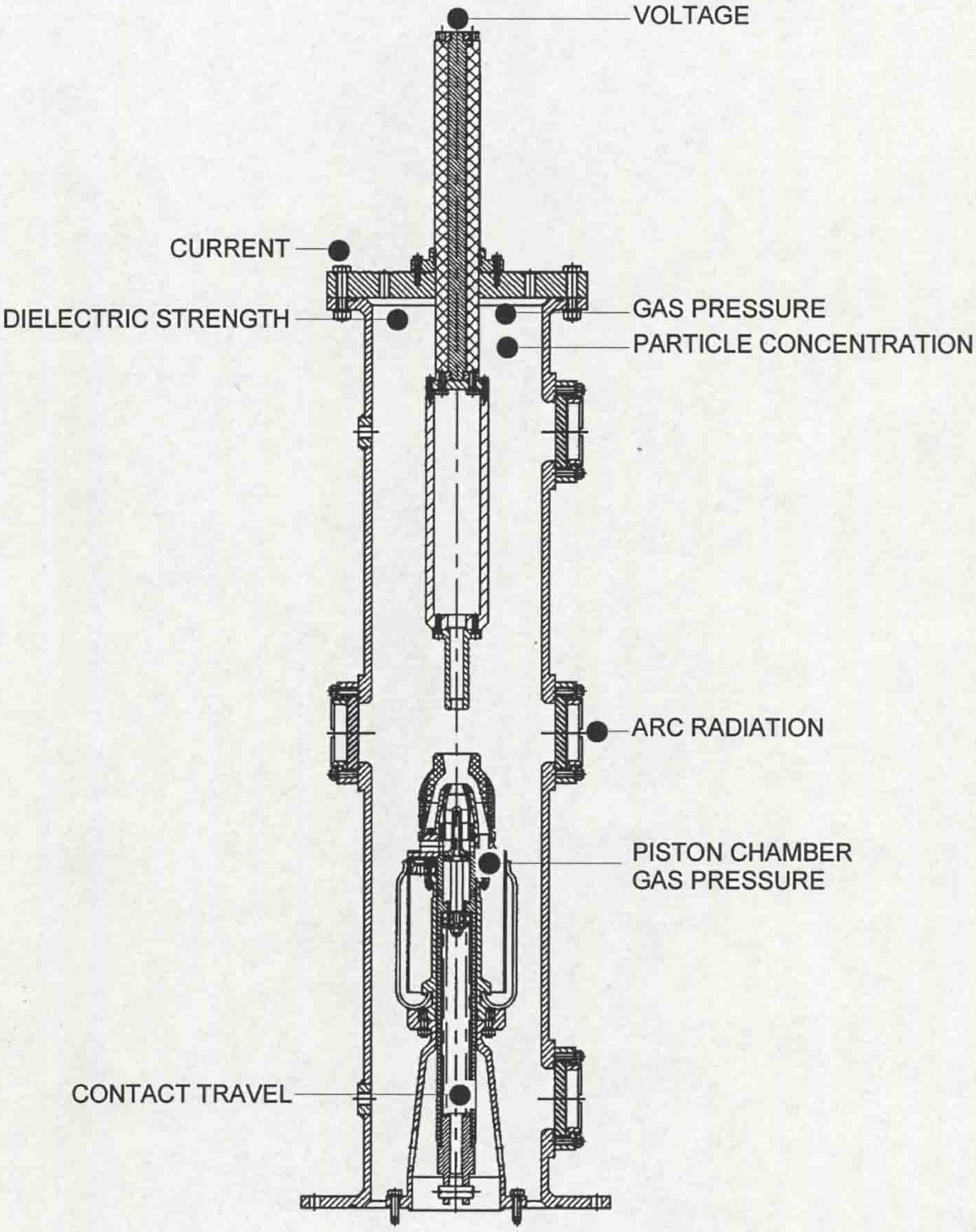

Figure 9.3 - Measurement points on test circuit breaker

Fig.9.3 shows the locations of transducers described above to monitor the appropriate electrical and optical parameters during the circuit breaker tests. The gas dielectric strength probe, gas tank pressure sensor and particle concentration monitor (OFPCM) were housed in the top-plate, since this is the easiest point of internal access on a circuit breaker in service. The travel recorder (OFLTR) and piston pressure sensor were housed within the actual interrupter unit. (Therefore, the use of these two sensors on a practical circuit breaker would require installation before the breaker was put into service, or a removal from service).

The full test and measurement system is shown on fig.9.4. The sequence of events for each test has been described above (**9.3.1**). The general strategy was to repeat the standard test on all of the sensors for a range of arc currents up to 56kA peak. The results obtained from these tests are presented, analysed and discussed later in this thesis (**chapters 10-11**).

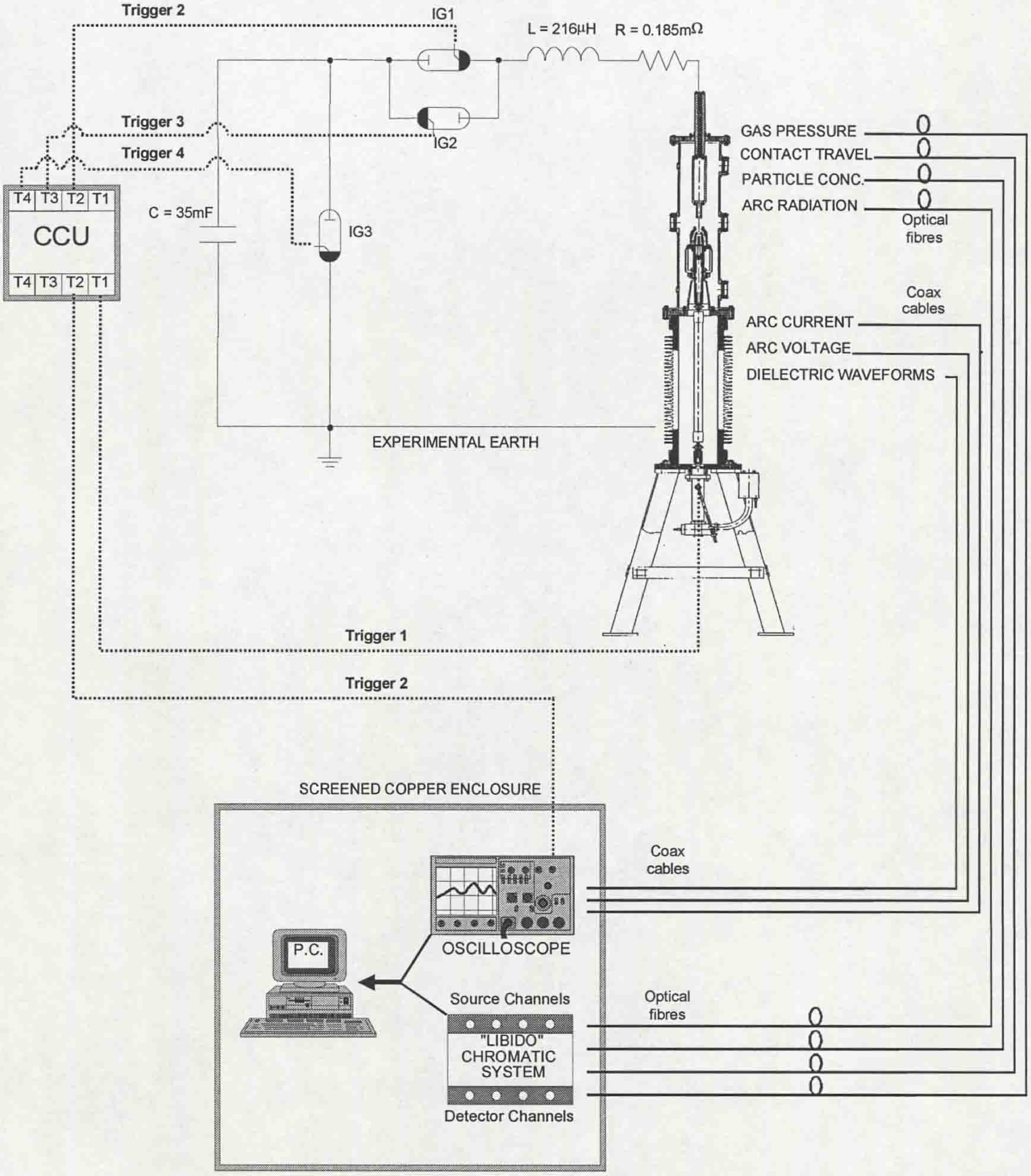

Figure 9.4 - Complete test and measurement system

9.5 CONCLUSIONS

This chapter has laid the foundation for **Part III** of this thesis, which describes and analyses the main circuit breaker test results. These results were gained from sensors, whose development was discussed in **Part II**. An LC series circuit (fig.9.2) was used to provide the high current waveforms, necessary to operate the test circuit breaker at its short-circuit fault current rating of 56kA peak (40kA rms). The capacitor bank used in fig.9.2 was rated to 6.3kV, much lower than the circuit breaker rating of 145kV. This did not matter, however, since it was the high-current phase of interruption (where the sustaining arc voltage is low with respect to the supply voltage) which was of interest.

The sensors, which were employed for this main set of tests, fall into three categories; electrical, optical and hybrid. The current passing through the circuit breaker and the voltage across the circuit breaker terminals were the two electrical parameters measured, using a conventional current shunt and high voltage oscilloscope probe. On the other hand, several parameters (contact travel, gas pressure, particle concentration and circuit breaker radiation chromaticity) were measured using optical sensors, which were developed earlier in the project (**Part II**). The gas dielectric strength probe (**chapter 7**) was classed as a hybrid sensor, since it incorporated on-board electronics, which were optically controlled from the control room.

Two data acquisition instruments were used to record the test results. The first, a Tektronix 420, 4 channel, digitising storage oscilloscope, was used to record the circuit breaker current and voltage and the gas breakdown voltage waveforms produced by the dielectric probe system. The second instrument, the generic LIBIDO distimulus chromatic source/detection system, was used to record data from the travel, pressure, particle concentration and arc radiation chromaticity optical sensors. This device had the facility for 8 detection channels datalogging simultaneously at up to 4kHz. Both of the data acquisition instruments were interfaced to an IBM compatible computer (486DX2 processor @ 66MHz) to convert the data into a spreadsheet format.

CHAPTER 10 - CIRCUIT BREAKER RESULTS

10.1 INTRODUCTION

This chapter presents the results obtained during the main set of circuit breaker tests. The results were obtained using the optical and hybrid sensors, described in **PART II** (**chapters 5-8**) of this thesis. The results are shown here to provide direct evidence of successful operation of the sensors developed during the project. The position of the sensors on the circuit breaker is shown on fig.9.3. Their performance was initially assessed in the absence of fault current arcing (coldflow), before being tested at various short-circuit current levels up to 56kA peak (the short-circuit current rating of the circuit breaker).

10.2 COLDFLOW RESULTS

10.2.1 Coldflow travel characteristics of the moving contact of the interrupter

Fig.10.1 shows the coldflow travel record (position / time) of the moving contact of the interrupter, obtained from the optical fibre linear travel recorder (OFLTR), described previously in **chapter 5**.

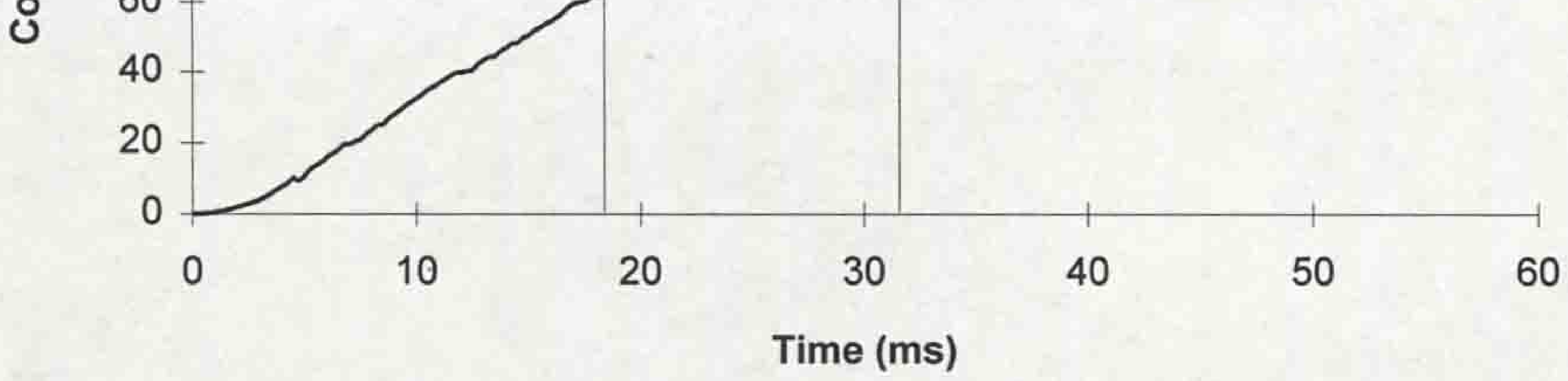

Figure 10.1 - Coldflow travel record of interrupter moving contact

The result on fig.10.1 was smoothed with a suitable curve-fit and differentiated, with respect to time, to obtain the corresponding velocity profile (fig.10.2). On each result the time taken for contact separation, and for the top fixed contact to emerge from the moving nozzle, are indicated.

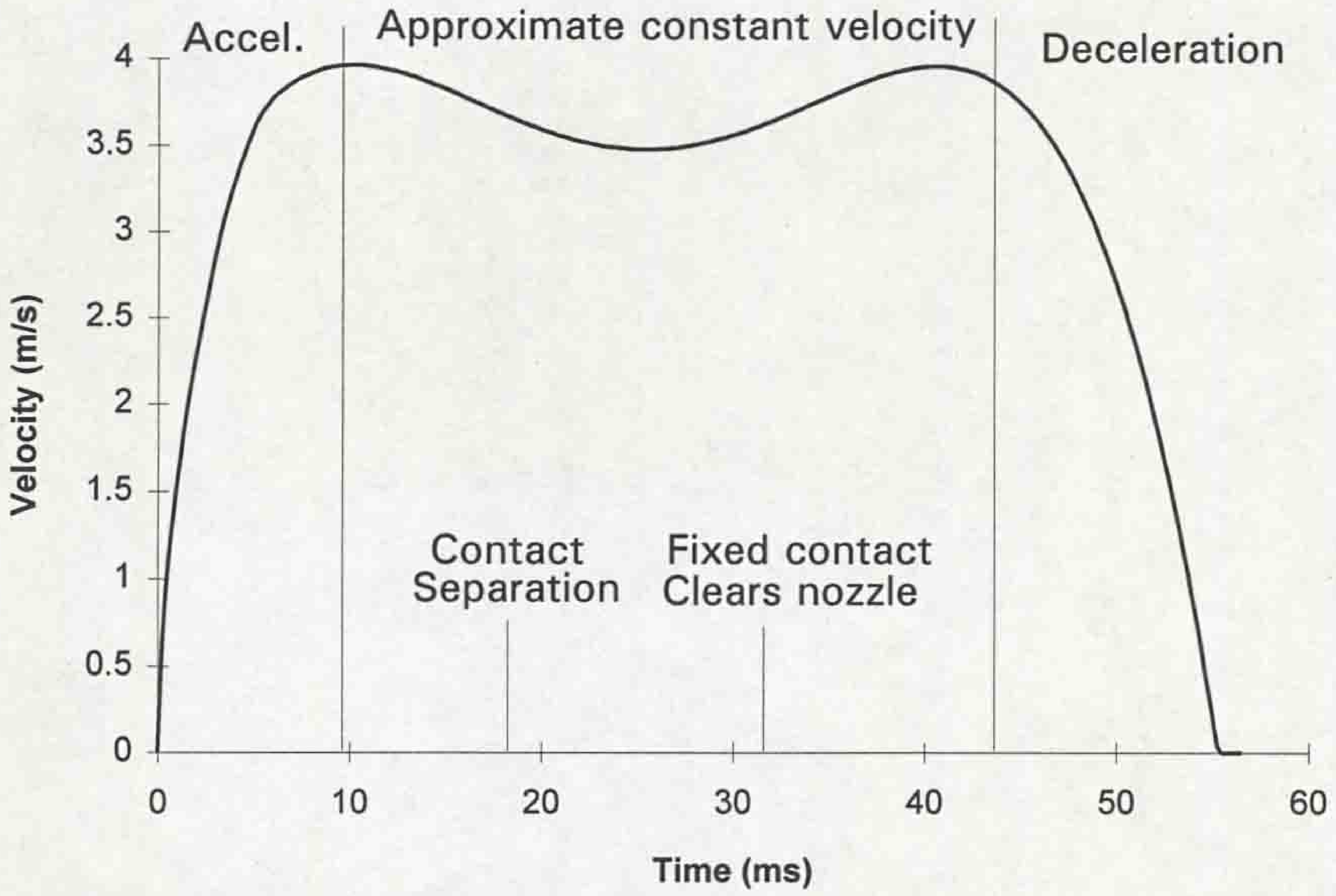

Figure 10.2 - Velocity profile of moving contact

These results show that, following an initial accelerating period, which lasts for ~9ms, the moving contact assembly moves at an approximate constant velocity of 3.5-4m/s for 35ms. At the end of the stroke there is a decelerating period of ~12ms, before the interrupter comes to rest. The displacements shown on fig.10.1 are accurate to within 2mm, which met the specified criterion for accuracy.

It was noticed that, during the arcing tests, the travel records obtained were similar to those in fig.10.1 and, therefore, independent of fault current, due to the stiffness of the hydraulic mechanism. (On figs.10.1 and 10.2, t = 26ms would represent arc extinction during the arcing tests).

(It should be noted that the modified rig was operated, for convenience, using an existing hydraulic mechanism at the University of Liverpool (ETNA type 5239). The SPLA 145kV / 40kA (rms) breaker in service employs a pneumatic mechanism, which may display different travel characteristics. It is intended that the OFLTR will be used on this and other puffer circuit breakers in service in the future).

10.2.2 Coldflow pressure variations within the test circuit breaker

The optical fibre pressure sensors (**chapter 8**) were used to monitor the gas pressure variations, both near to the top-plate of the main circuit breaker tank and also in the piston chamber, during operation of the circuit breaker without an arc present. These results have been presented in **chapter 8**, as figs.8.11 and 8.12 in **8.4.1**. The features of the coldflow pressure transients are discussed in **11.1**.

10.2.3 Relationship between interrupter velocity and peak piston pressure

Previous studies (eg. Shimmin, 1986) have shown that the piston chamber pressure rise is highly sensitive to the travel characteristic of the interrupter. This aspect of performance was investigated by monitoring the piston chamber pressure rise (with the optical fibre pressure sensor) and the interrupter velocity (with the OFLTR), for various levels of hydraulic pressure in the driving mechanism. The peak piston pressure, as a function of interrupter velocity, is shown on fig.10.3. The interrupter velocity quoted on fig.10.3 is the average value of the relative plateau region on fig.10.2.

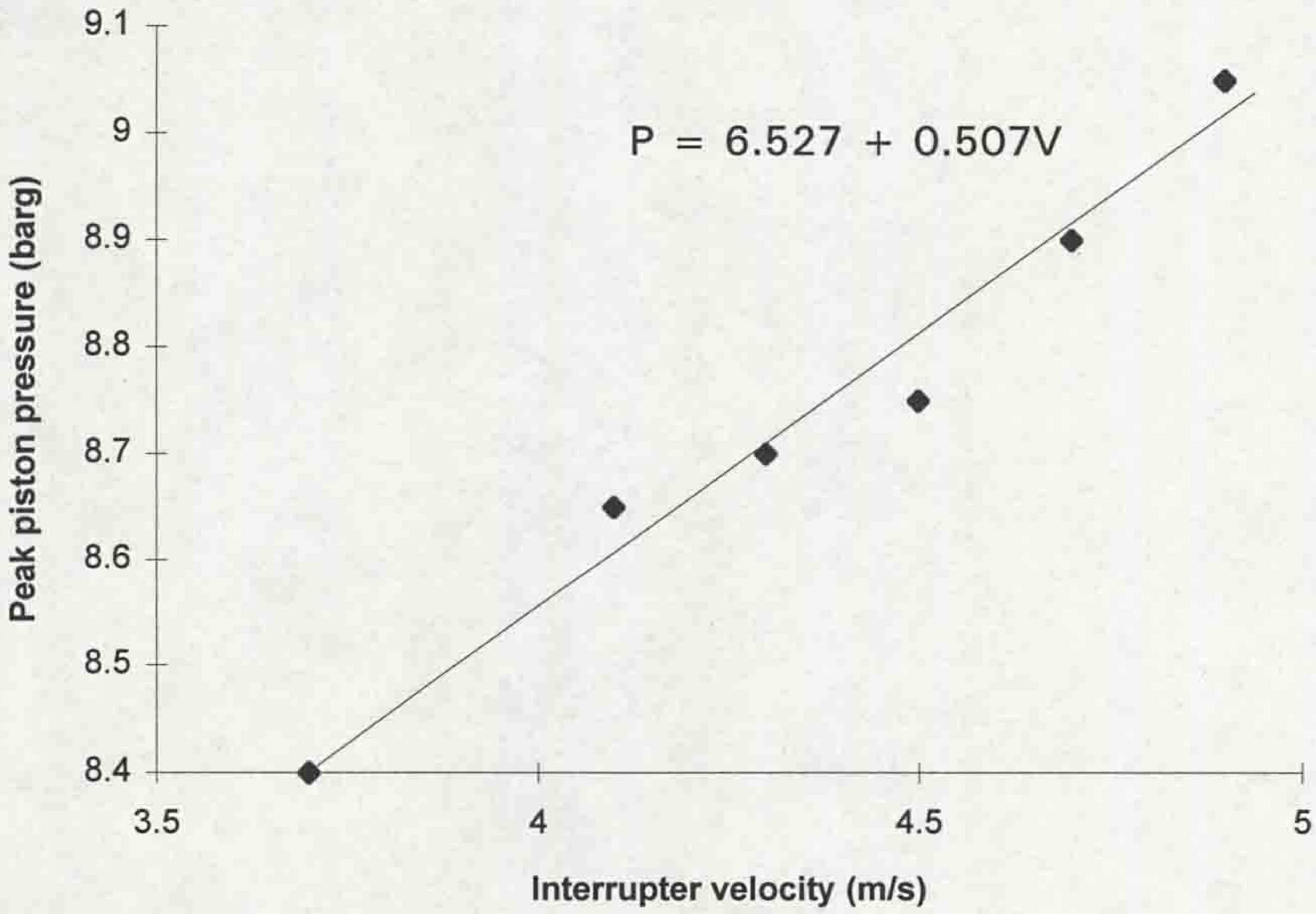

Figure 10.3 - Relationship between interrupter velocity and peak piston pressure

A linear curve-fit to fig.10.3 yields the simple relationship P = 6.527 + 0.507V, where P represents the peak piston pressure and V the interrupter velocity. This result is accurate to 0.05bar, for the pressure range on fig.10.3.

10.3 ARCING TESTS RESULTS

Live tests on the circuit breaker were performed for a range of arc currents up to 56kA peak and results obtained using the optical, hybrid and electrical transducers.

10.3.1 Typical current and voltage waveforms

Fig.10.4 displays the type of waveforms obtained for the current through and voltage across the circuit breaker terminals, during the arcing tests. These waveforms were obtained using a 0.185mΩ coaxial current shunt and a 1000:1 high voltage probe (**9.4.1.1**). The series resonant circuit of fig.9.2 was used to provide the high current discharge through the circuit breaker and the method of operation is described in **9.3.1**. The first ignitron IG1 discharged the positive half-cycle of current through the circuit breaker, at the instant of contact separation. At the first current zero the second ignitron IG2 (fig.9.2) automatically discharged the negative half-cycle of current. After this procedure any residual charge on the capacitor bank was dumped to the experimental earth. Thus, the circuit was capable of discharging one full cycle of power frequency high current through the circuit breaker.

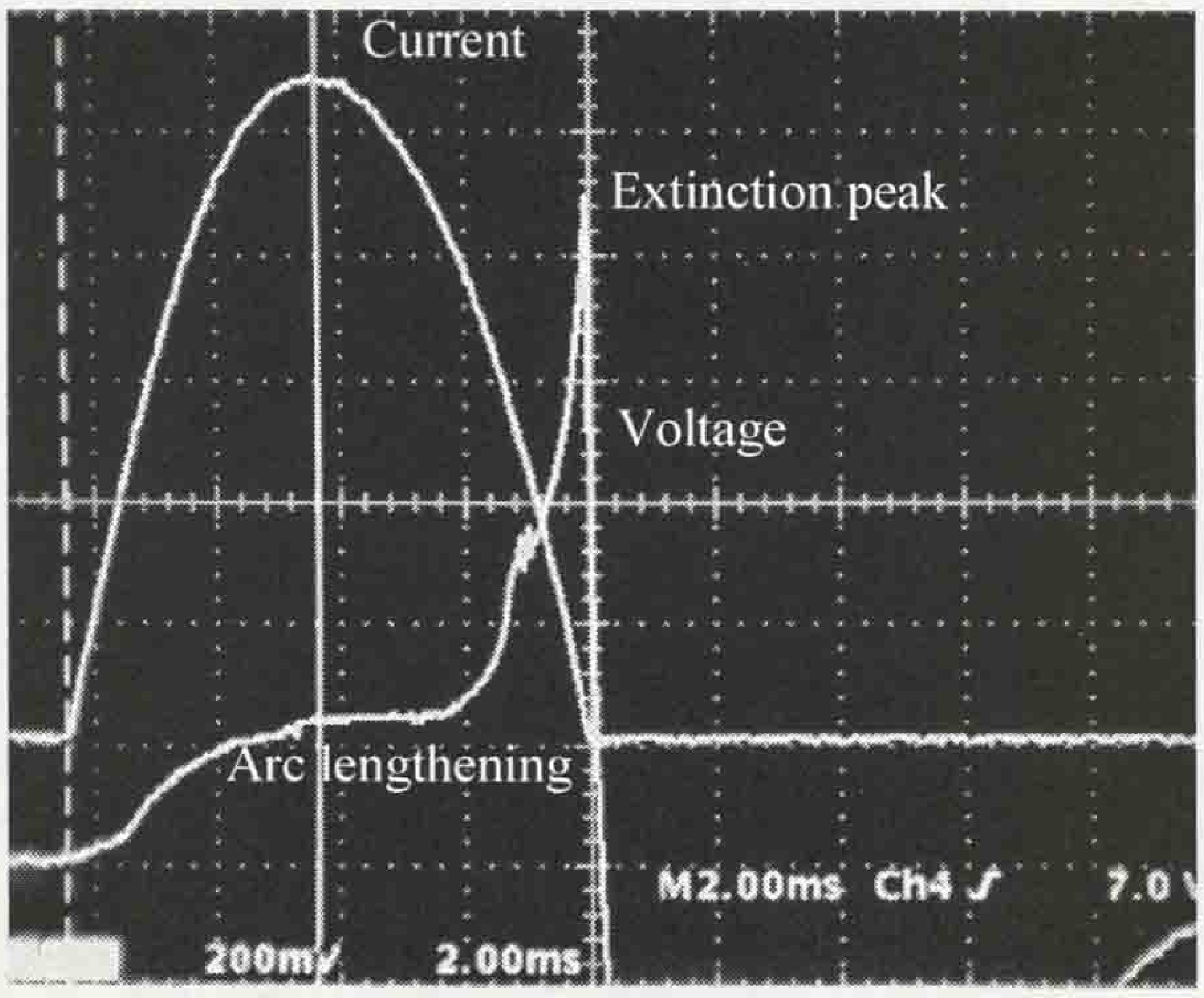

Figure 10.4 - Typical current and voltage waveforms

The current amplitude was controlled by the voltage to which the capacitor bank in fig.9.2 was charged (up to 6.3kV maximum). Since this voltage is low compared with transmission voltage levels, the inherent restrike voltage which could be provided by the circuit was limited. Consequently, for the conditions investigated here, the circuit breaker always interrupted the arc at the first current zero following contact separation. This is evident in fig.10.4, where only one half-cycle of current is apparent.

The voltage waveform, shown on fig.10.4, is typical of that for a puffer circuit breaker arc. The initial slow rise in voltage (t = 0-7ms) is mainly due to the arc increasing in length, as the contacts separate, and the flow being generated through the circuit breaker nozzle as the nozzle is unblocked by the moving contact. The final spike observed on the voltage trace, immediately prior to current zero, is the usual extinction voltage peak of the arc, which normally precedes a successful current interruption.

10.3.2 Pressure variations within circuit breaker during fault current interruption

As for the coldflow case (**10.2.2**), pressure measurements were taken near the top-plate of the circuit breaker tank and in the piston chamber, during interruption of short-circuit arcs.

10.3.2.1 Pressure variations near top-plate

The time variation of the SF_6 gas pressure, near the top-plate of the circuit breaker, is shown on figs.10.5a to 10.5d, for fault currents of 5, 15, 30 and 45kA peak respectively. The 56kA pressure waveform has been shown previously as fig.8.14 in **8.4.2**.

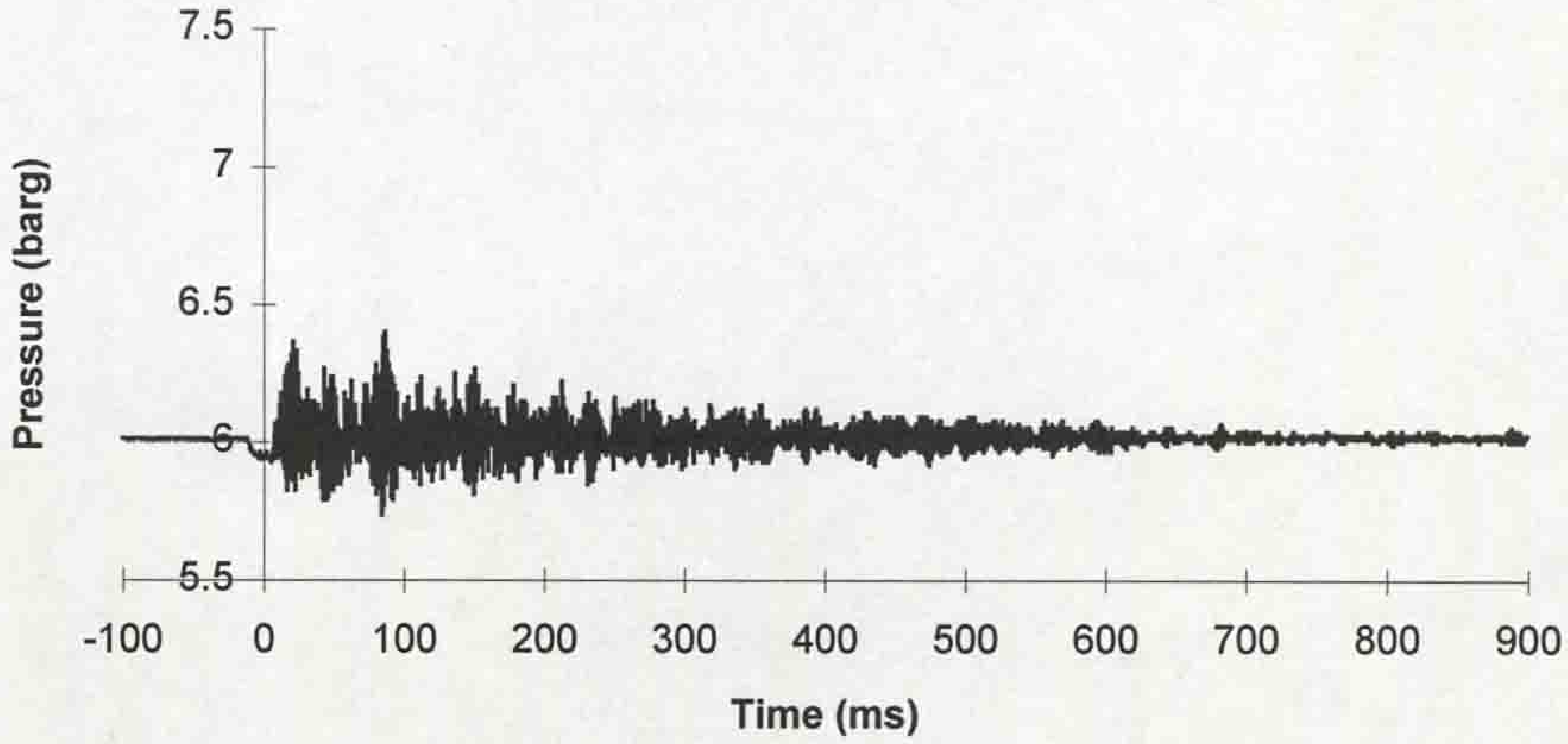

Figure 10.5a - Time variation of pressure near top-plate (5kA)

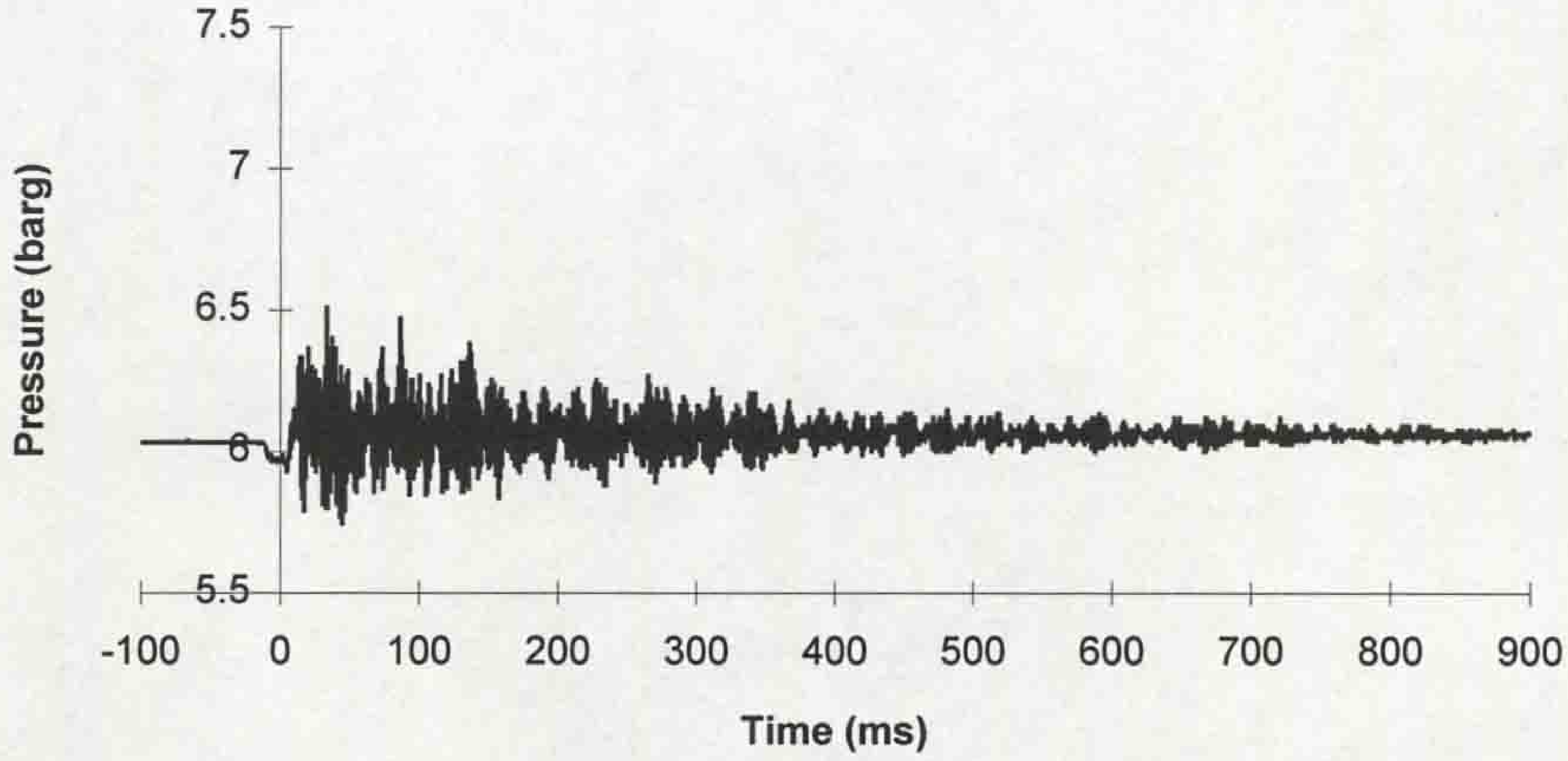

Figure 10.5b - Time variation of pressure near top-plate (15kA)

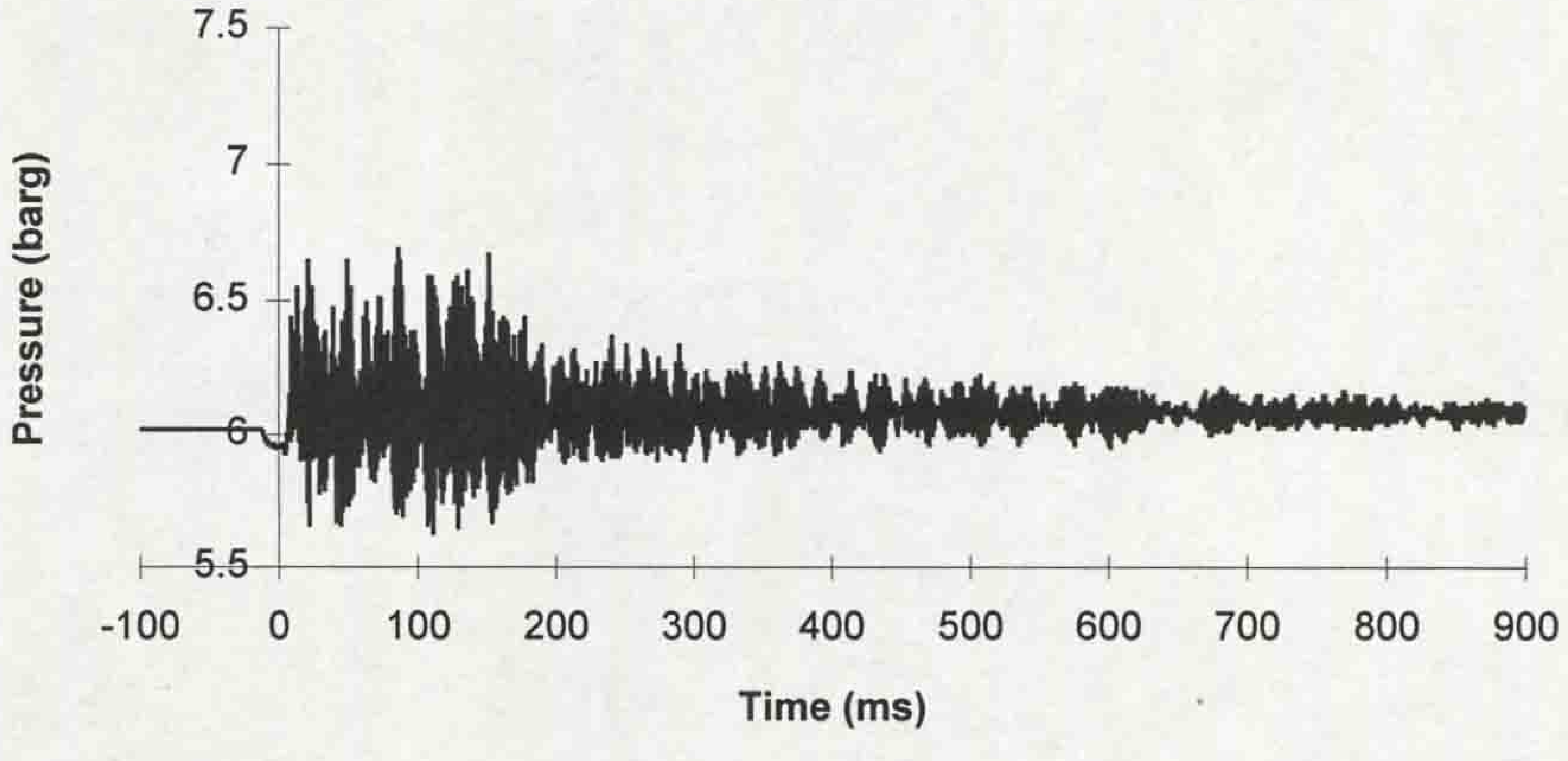

Figure 10.5c - Time variation of pressure near top-plate (30kA)

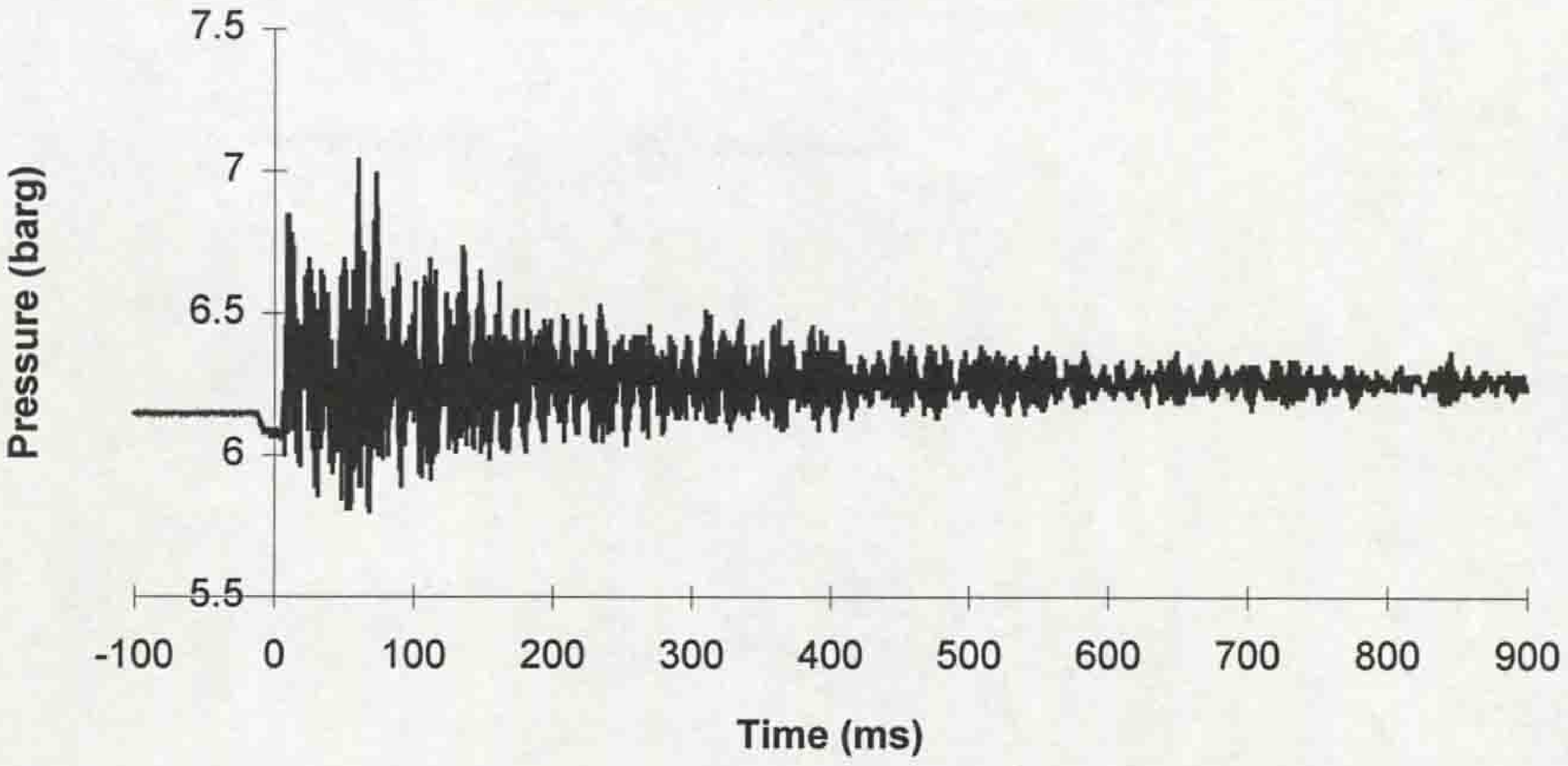

Figure 10.5d - Time variation of pressure near top-plate (45kA)

As with the coldflow case, the frequency spectra of the transients are analysed in **chapter 11**. The amplitudes of the oscillations increase with arc current, indicating a peak pressure over 7barg at the higher currents (45kA and 56kA), a rise of more than 1bar above ambient. Interestingly, when the pressure transient decays, the post-arc tank pressure is higher than the pre-arc value. The variation of this incremental increase in the tank pressure after arcing is shown as a function of fault current on fig.10.6. Since this pressure rise is small with respect to the ambient pressure (~2% at the highest current level), it would not be expected to affect the interruption capability of the circuit breaker while it lasted. For this reason it was not necessary to monitor the gradual decay in the tank pressure rise.

The features of the pressure transients are discussed further in **chapter 11**.

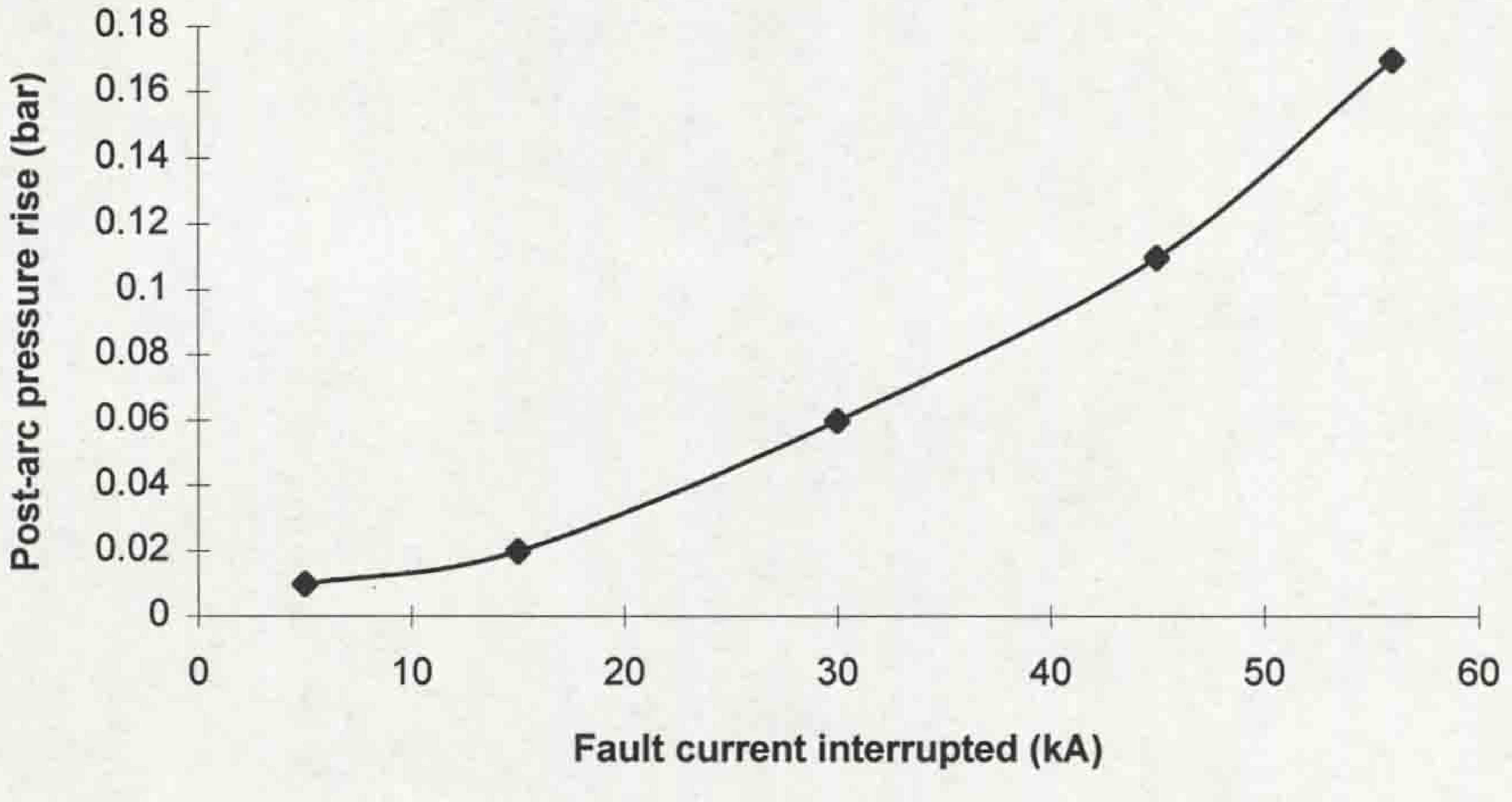

Figure 10.6 - Variation of post-arc pressure rise as a function of the fault current

10.3.2.2 Pressure rise in piston chamber

The time variation of the gas pressure in the piston chamber is shown on figs.10.7a to 10.7d for the same range of fault currents (5, 15, 30 and 45kA peak). The 56kA was shown previously as fig.8.13. The results show that excess pressures are generated above the coldflow case (fig.8.11) soon after contact separation (0ms). These excess pressures increase with fault current, apparently reaching a peak of approximately 12barg for a fault current of 56kA.

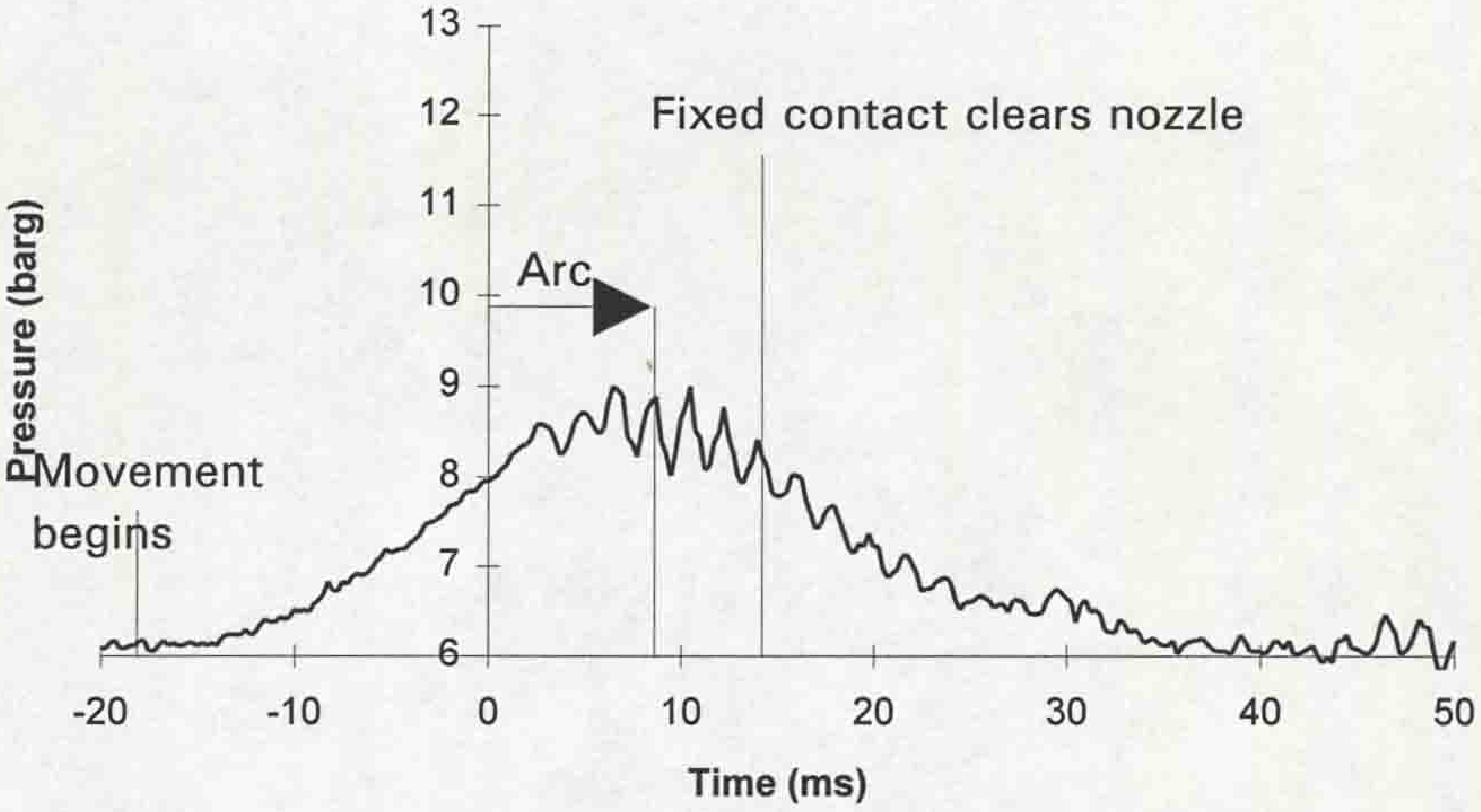

Figure 10.7a - Time variation of piston chamber pressure (5kA)

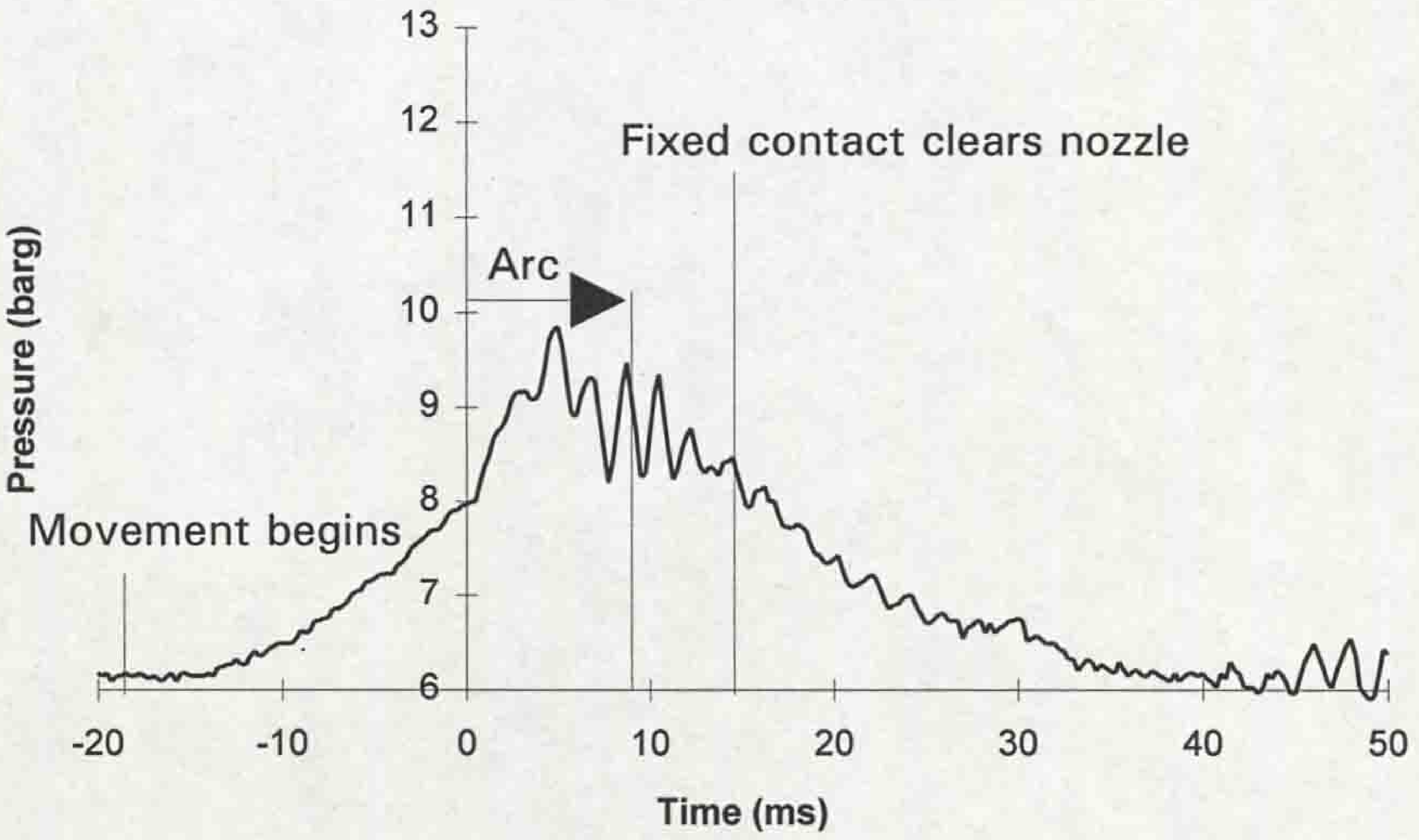

Figure 10.7b - Time variation of piston chamber pressure (15kA)

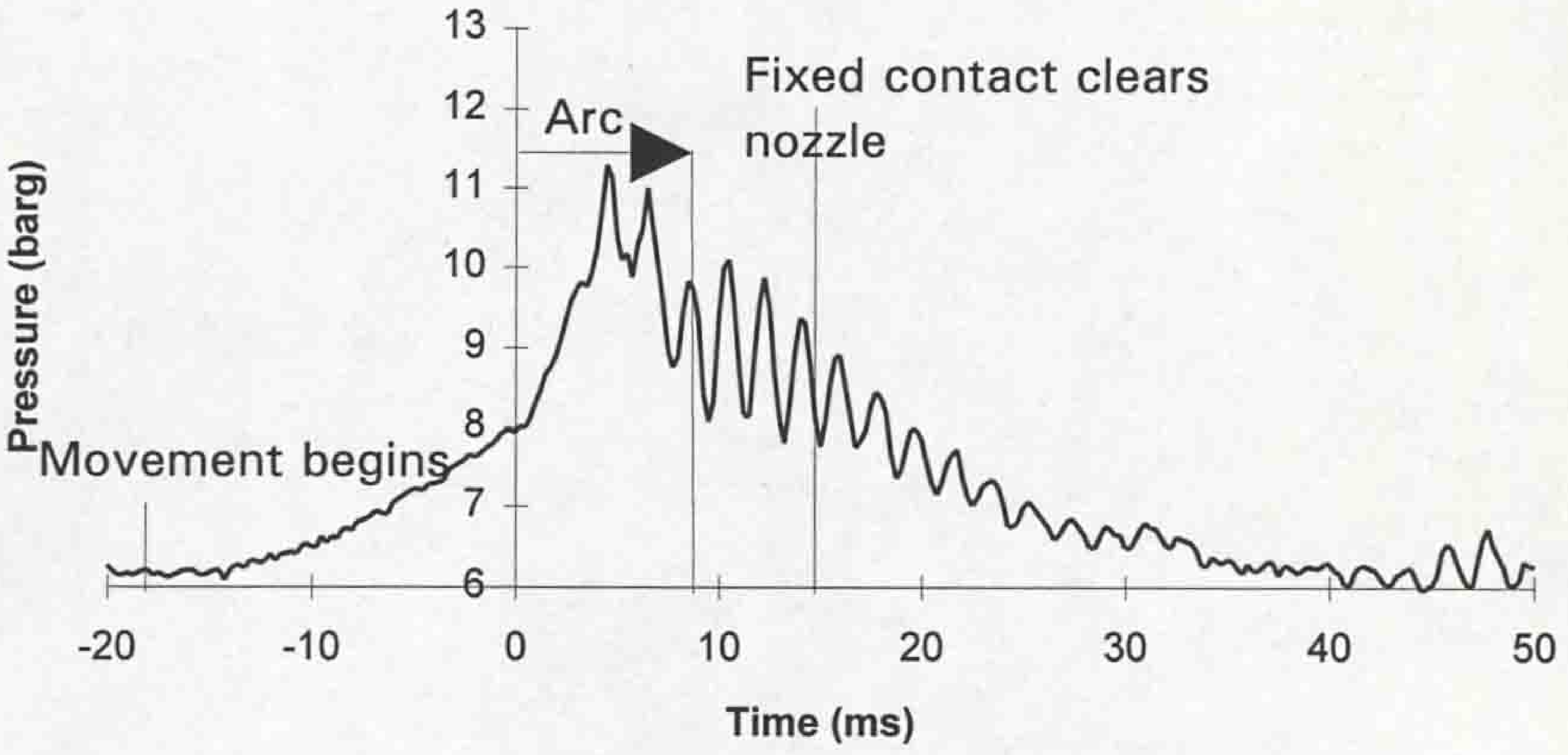

Figure 10.7c - Time variation of piston chamber pressure (30kA)

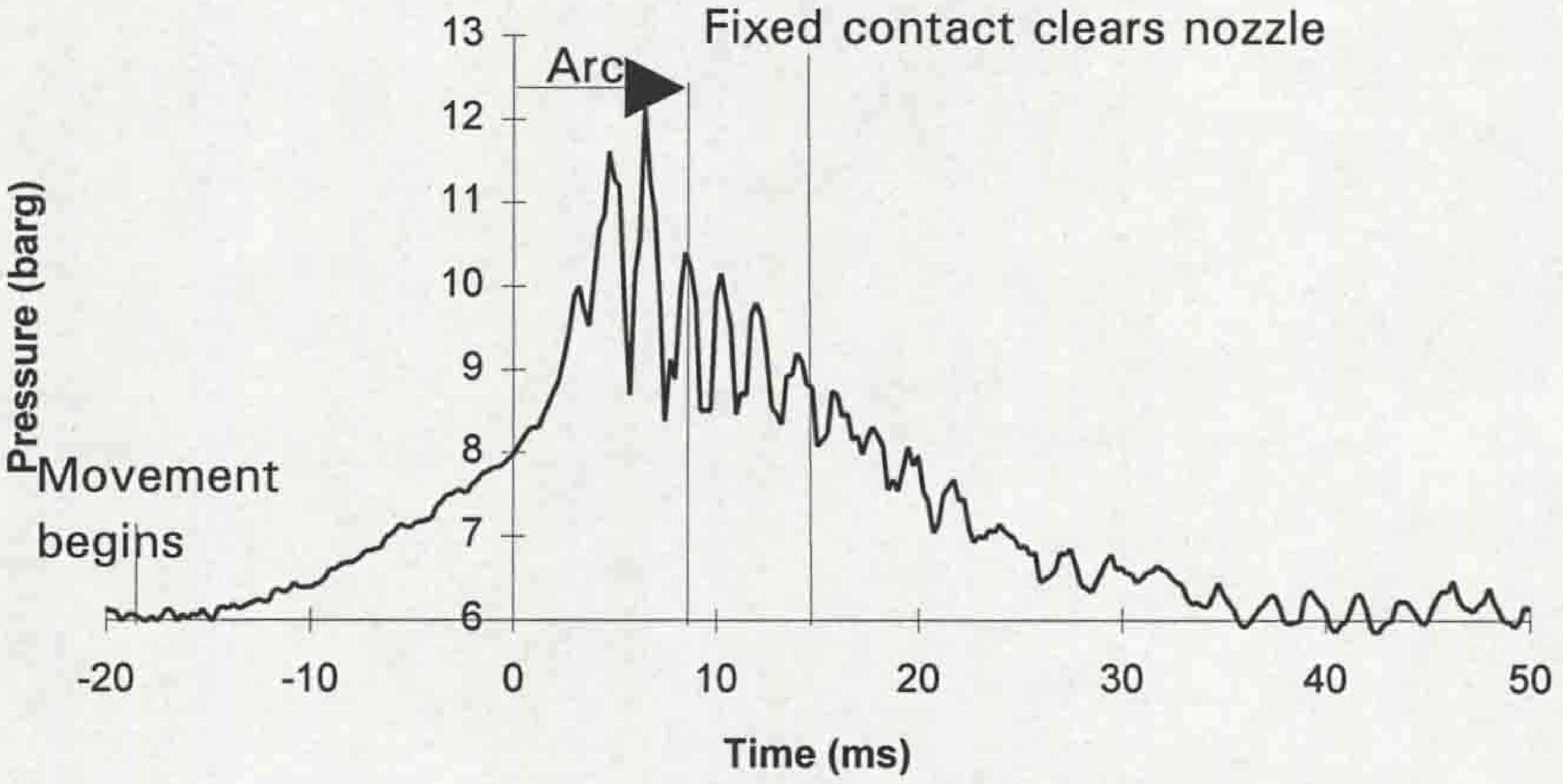

Figure 10.7d - Time variation of piston chamber pressure (45kA)

However, a note of caution is required concerning the 45kA and 56kA results (figs.10.7d and 8.13). It was shown on fig.8.9 that the calibration curve for the piston pressure sensor reached a trough in its characteristic cyclic function (fig.8.5) at 11.5barg. At higher pressures, the dominant wavelength begins to rise again. Hence, a pressure of 12barg would give a similar dominant wavelength output, by the sensor, as a pressure of 11barg.

Therefore, any piston pressure measurements which reach this 11.5barg possess a degree of ambiguity. This seems to apply to the 45kA and 56kA piston pressure results. On the other hand, at 30kA and below, the recorded pressures are below this 11.5barg limit and are, therefore, unambiguous.

This situation is highlighted by plotting the peak piston pressure rise, above ambient (6barg), as a function of the interrupted fault current peak. The result on fig.10.8 highlights the uncertainty in the 45kA and 56kA piston pressure results. It would be expected that the recorded pressures would continue the trend of the results up to 30kA. This is not apparent on fig.10.8. It is possible, therefore, that, at the highest currents (46kA and 56kA peak), the piston chamber pressures exceeded the monotonic dynamic range of the pressure sensor.

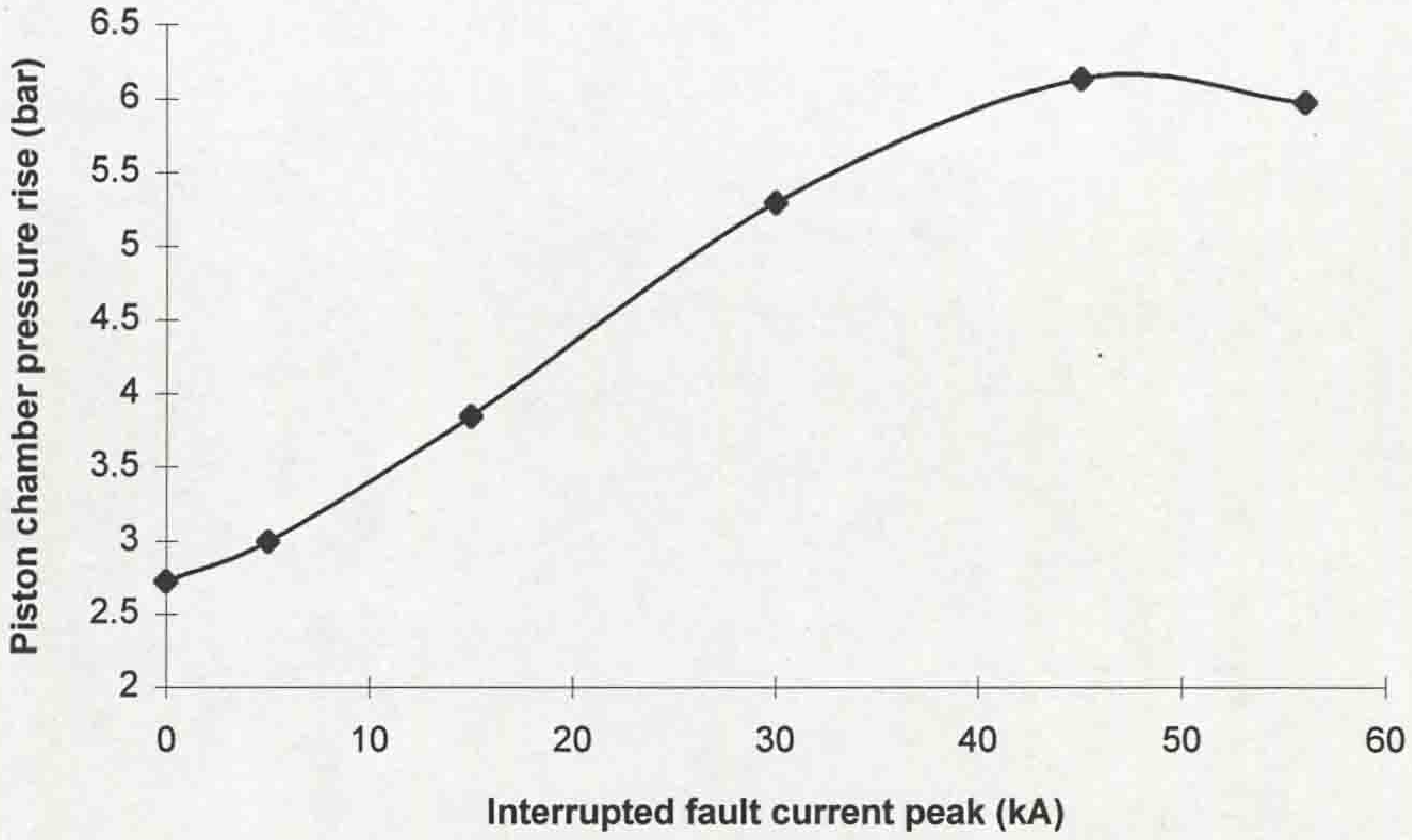

Figure 10.8 - Peak piston pressure rise as a function of peak fault current

In view of the result on fig.10.8, it is recommended (**chapter 12**) that the dynamic range of the micromachined silicon, Fabry-Perot cavities should be increased to more than the designed for 6-12barg current range, for pressure monitoring at high currents (≥30kA) in the piston chamber of a puffer circuit breaker. For pressure monitoring in the main tank, where recorded pressures were much lower (figs.10.5), the present cavities are suitable.

10.3.3 Circuit breaker radiation chromaticity results

The chromaticity of the optical emission from the fault current arcs at 15, 30, 45 and 56kA peak was monitored using a 400μm core, multimode glass fibre, situated at a central window of the experimental rig (fig.9.3). and interfaced to the LIBIDO distimulus chromatic detection system (**4.3.3.2**). Four sets of test results were recorded at each current level. Figs.10.9 display the dominant wavelength variation with time at each individual current level, showing the mean variation and the spread of values over the four tests. Fig.10.10 shows the mean variation in dominant wavelength for each current level tested. 0ms represents contact separation and the arc burns for 8.5ms at each current level.

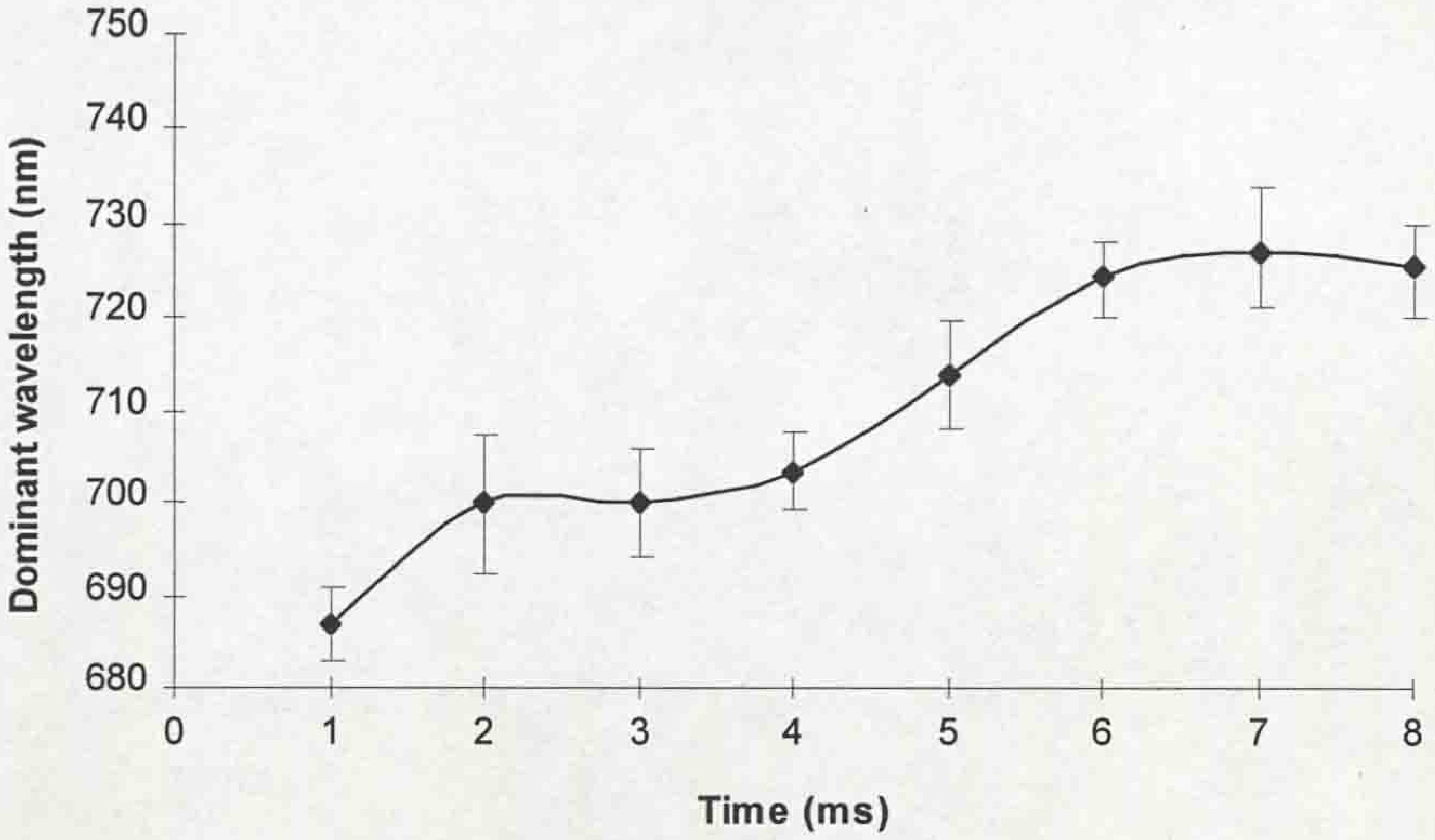

Figure 10.9a - Time variation of arc radiation chromaticity at 15kA

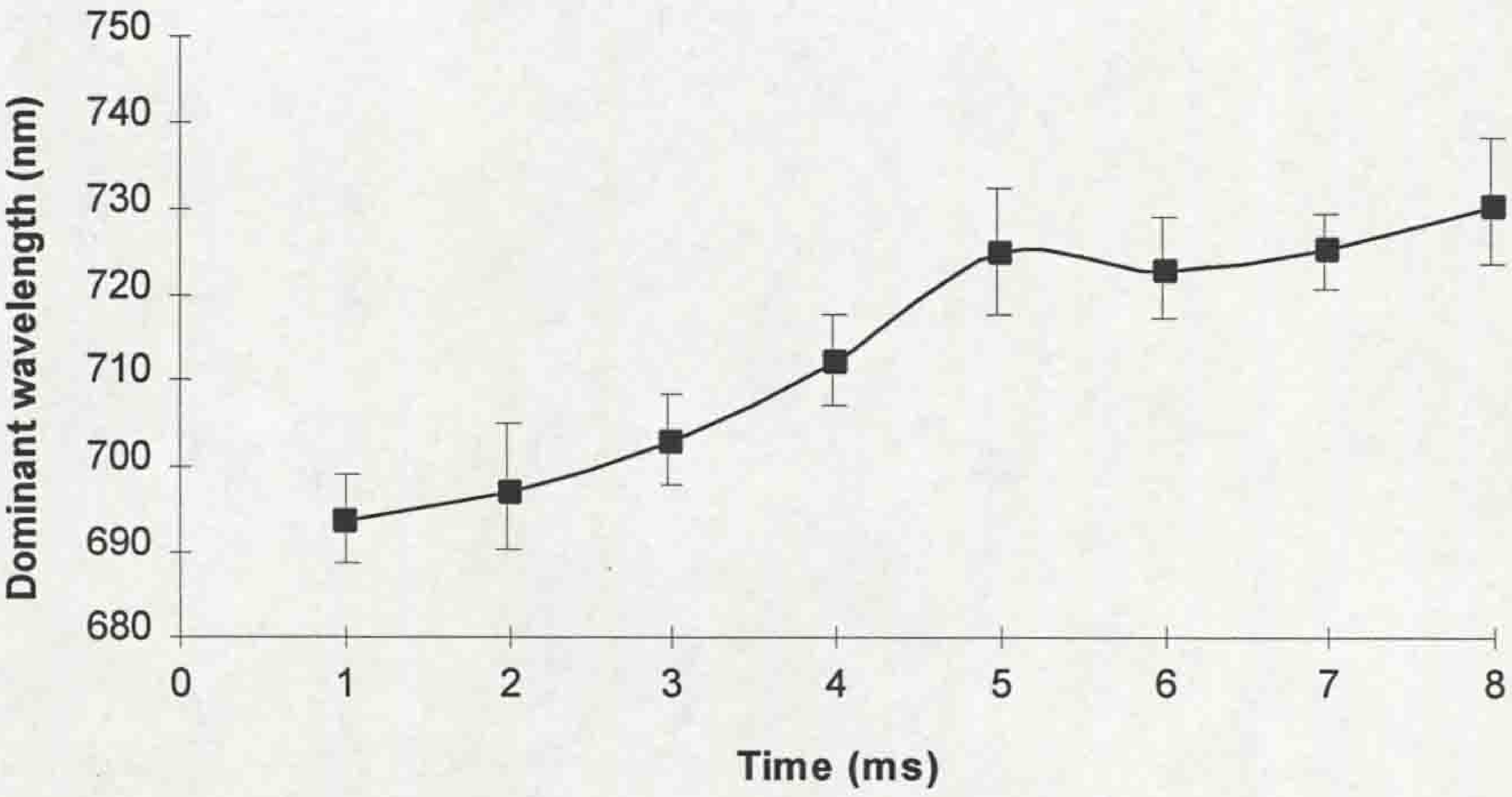

Figure 10.9b - Time variation of arc radiation chromaticity at 30kA

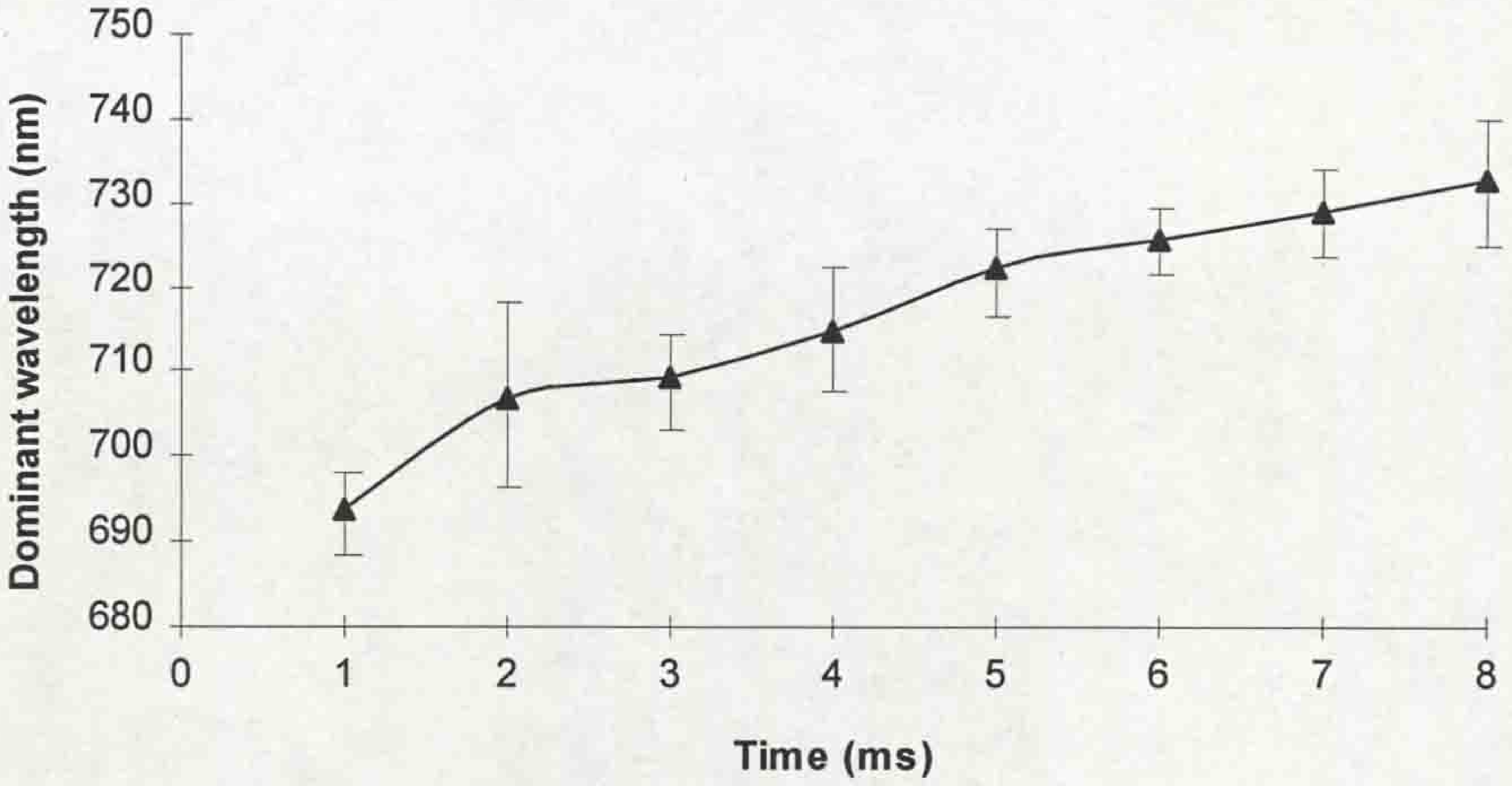

Figure 10.9c - Time variation of arc radiation chromaticity at 45kA

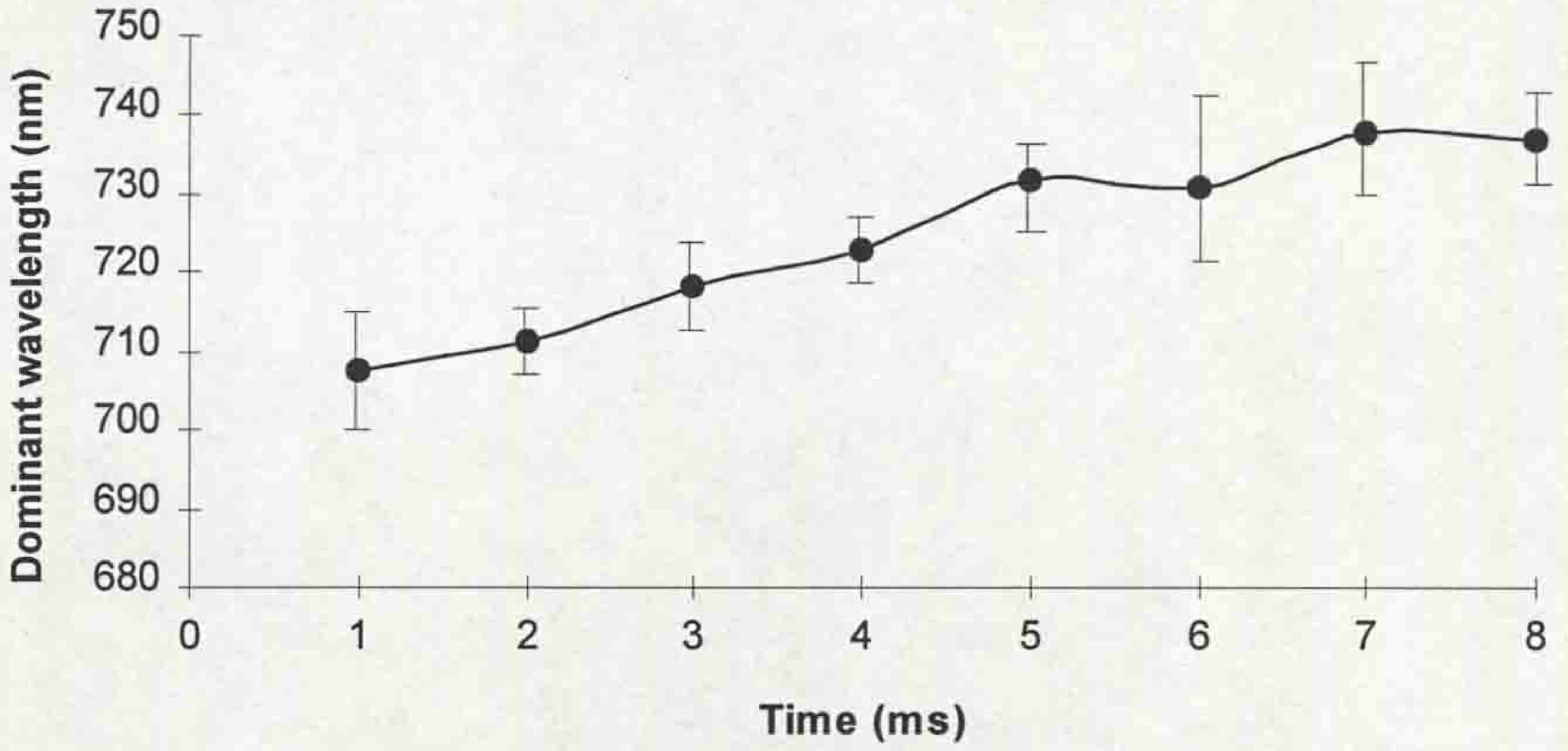

Figure 10.9d - Time variation of arc radiation chromaticity at 56kA

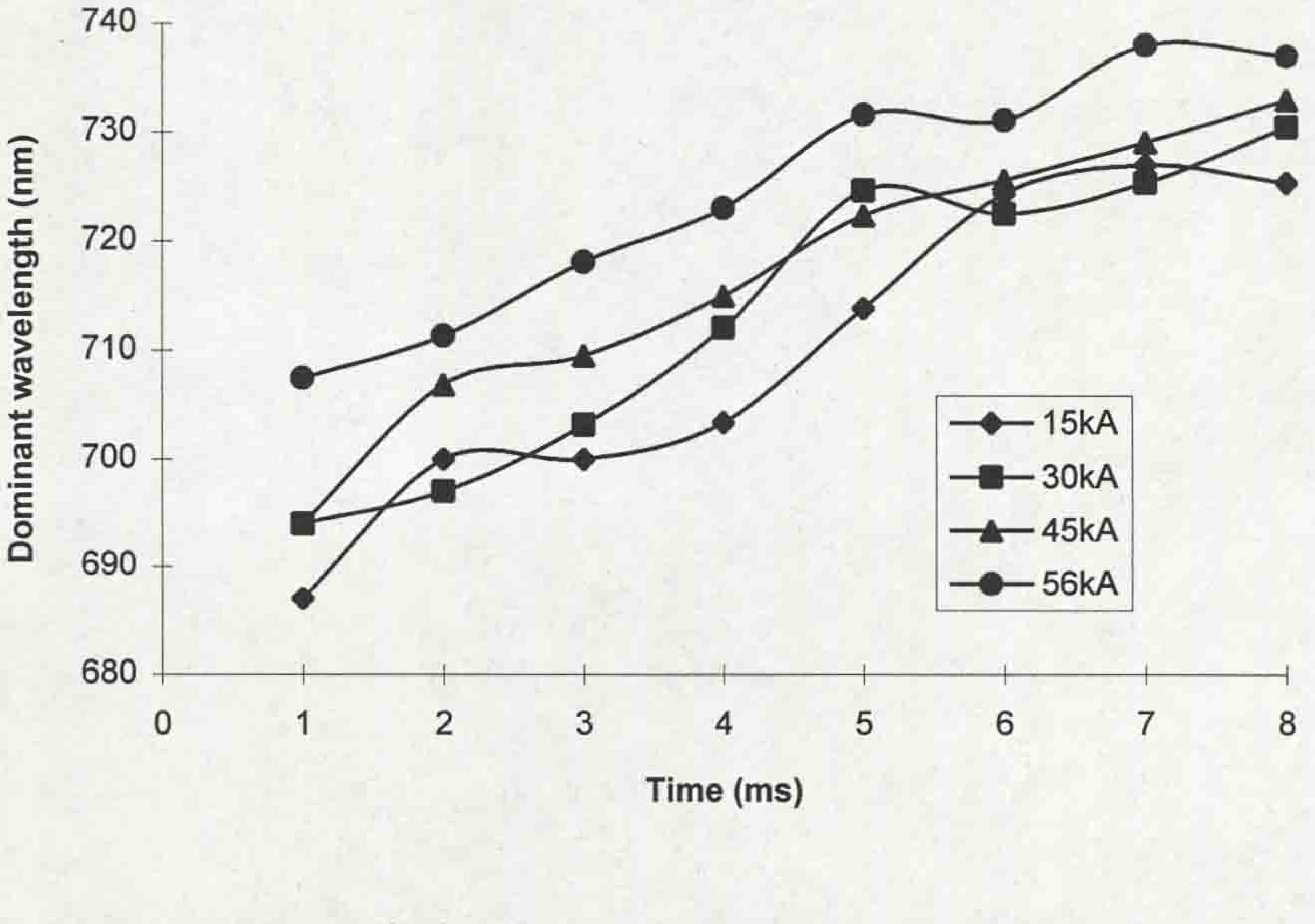

Figure 10.10 - Mean variation in dominant wavelength for each current level

Although the results on figs.10.9 exhibit a degree of scatter, some interesting trends may, nevertheless, be deduced from them. Fig.10.10 shows the mean dominant wavelength as a function of time for each peak current value. These results show that the dominant wavelength generally increases with time by ~30-40nm over the arcing period i.e. the emission tends towards the longer wavelengths of the near infra-red.. In addition, there is an apparent tendency for the dominant wavelength to also increase with the fault current being interrupted. This increase is typically 20nm between the 56kA and 15kA results, again the trend being for longer wavelengths to be more prevalent as the peak current increases. Despite the test to test variations and the relatively small dominant wavelength shift, the trend towards longer wavelengths seems to be genuine.

These results, taken together with the contact travel results, indicate that, for the whole duration of these measurements, the arc remained within the confines of the PTFE nozzle (as shown on fig.10.1 the top contact is not clear of the nozzle until 15ms after contact separation i.e. ~7ms after arc extinction). The radiation results, therefore, relate not to pure emission from the arc itself but rather to arc radiation, which is transmitted through the PTFE nozzle wall. Further consideration to the effect of radiation transmission through the nozzle wall is given in section **11.2**.

Several authors (eg. Leclerc and Jones, 1982, fig.3.14) have plotted total radiation loss measurements as a function of instantaneous current, with peak current as a parameter, in order to investigate the effects of nozzle ablation and electrode vapour entrainment into the arc plasma. Therefore, in **chapter 11**, as part of further analysis of the results on fig.10.10, the mean dominant wavelength is plotted against the same parameters, to investigate any similarities between radiation loss and dominant wavelength measurements.

10.3.4 Particle concentration results

The optical fibre particle concentration monitor, OFPCM (**chapter 6**), was used to investigate the concentrations of particles within the circuit breaker tank, produced by decomposition products of arced SF_6. This system utilised the effect of non-linear light scattering by the particles, when a broadband white light source is transmitted through a particle-containing region. This results in a quantifiable relationship between the dominant wavelength of the source and the concentration of particles (**6.3.4**).

The system was used to monitor particle concentrations within the circuit breaker tank, during a series of relatively low fault current tests (up to 15kA peak) and also during a series of high fault current tests (15kA to 56kA peak). A short time scale (~30ms recording time) was used for the low current tests to investigate the effect of the arc radiation on the signals from the OFPCM. For the high current tests, where relatively higher concentrations of particles were anticipated, a long time scale (tens of minutes) was used for the test results to investigate how the particles settled in the circuit breaker tank with time. The low current test results are described first.

The time variation of the dominant wavelength of the white light scattered by the particles and captured by the OFPCM is shown on fig.10.11, for fault currents ranging from 2kA to 15kA peak. These current levels were chosen for initial tests to provide a steady build up of particles in a controlled manner. The results show a D.C. shift in dominant wavelength, sequentially from test to test (current increasing), indicating a small increase in particle concentration, according to the calibration of fig.6.9.

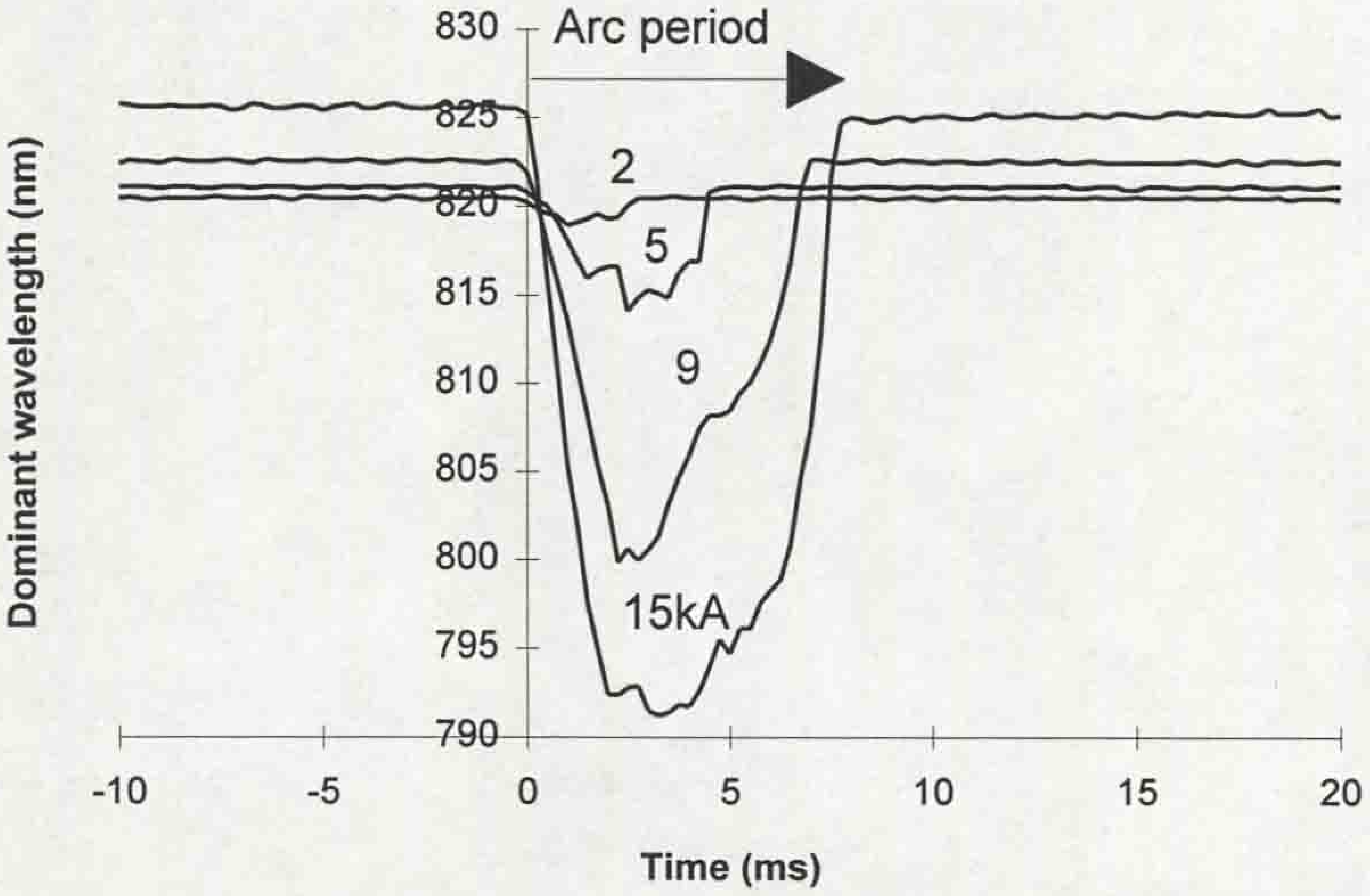

Figure 10.11 - Time variation of dominant wavelength from the OFPCM for a range of low arc currents (2kA to 15kA)

The results on fig.10.11 also show that during the arcing period the sensor picks up the optical radiation from the arc, which is initiated in each case at t = 0ms. The arc radiation, which was shown on fig.10.10 to have a dominant wavelength of ~690-730nm, is superimposed on the sensor's own source (the tungsten halogen lamp of the LIBIDO system), which has a dominant wavelength of ~820nm. Thus, the arc radiation reduces the dominant wavelength for the period that the arc burns.

It should be noted that the pre and post-arc white light dominant wavelengths are similar for individual currents, indicating that no particles are detected at the probe location, at the top of the tank, on these time scales. However, the dominant wavelength for each current is different, indicating that the particles are indeed formed, as described above, but only reach the measurement location on longer time scales. Thus, for the high current arc tests, the particle monitoring was extended over far longer time scales in order to attempt to observe the nature of the particle diffusion and settling.

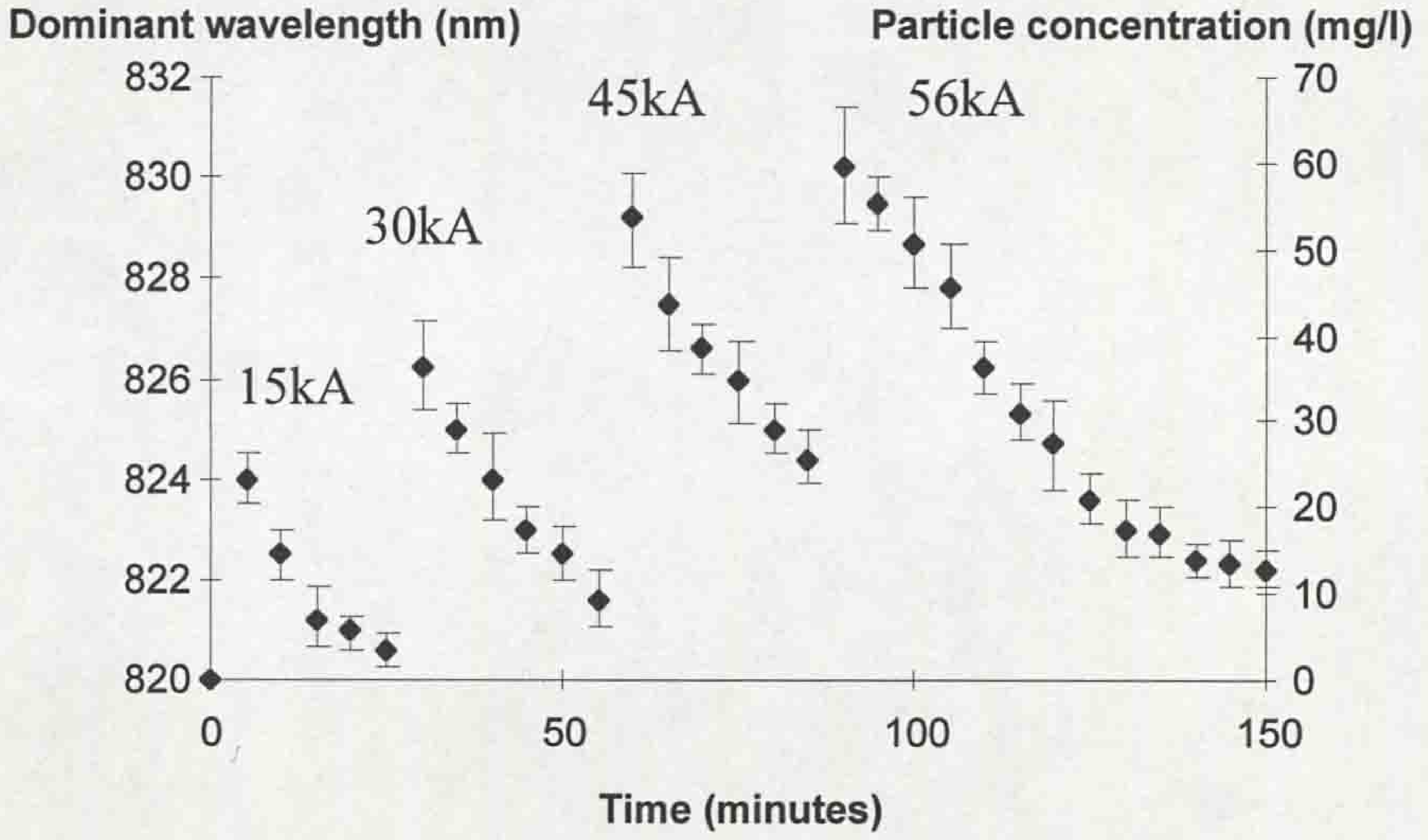

Figure 10.12 - Time variation of dominant wavelength from the OFPCM for a range of high fault currents (time measured from initiation of the first arc at 15kA)

For the high current tests four consecutive circuit breaker operations were performed, at 15kA, 30kA, 45kA and 56kA peak, with a 30 minute gap between each operation, during which the particles were continuously monitored. Dominant wavelength readings were taken every 5 minutes between each test. After the final test (56kA) the particle concentration was monitored until it appeared to settle at a steady value. Fig.10.12 shows the dominant wavelength variation with time, from the OFPCM, during these tests.

This series of four tests was repeated a further three times, with the OFPCM cleaned between each test series. Fig.10.12 represents the average variation in dominant wavelength for all of the tests performed, with error bars showing the deviation from this mean.

It is apparent that, after the 15kA test, the mean dominant wavelength rose to ~824nm from the zero concentration level of 820nm, and then gradually started to fall as the particles settled out of suspension. When the 30kA arc is interrupted, at t = 30mins, the mean dominant wavelength increased again after arcing to ~826nm. The characteristic decay in dominant wavelength occurred again as the particles began to settle. A similar situation occurred for both the 45kA and 56kA tests. However, after the 56kA test the mean dominant wavelength values from the sensor did not return to 820nm, as expected; the final value remained just over 822nm. When the circuit breaker was dismantled, between each test series, it was found that the particles had coated the optical surfaces of the optical fibre particle concentration monitor (OFPCM). This is believed to be the reason why the dominant wavelength did not return to its value corresponding to zero concentration (820nm). This effect may provide a means for recording the history of conditions experienced by the circuit breaker, by using the particles, which have settled on the sensor, as a memory to the current levels interrupted. Upon removal and cleaning of the optical surfaces of the sensor the dominant wavelength did return to 820nm as expected.

The results on fig.10.12, for these tests, were converted into particle concentrations, using the calibration characteristic for the OFPCM (fig.6.9); they are shown by the secondary axis of fig.10.12.

10.3.5 Gas dielectric strength results

During the project the industrial collaborators indicated that it would be interesting to monitor the gas dielectric strength in the circuit breaker tank, during arc interruption. The reason for this was that during the research and development of puffer circuit breakers evidence of very hot gas pockets was recorded inside the main tank, following arc extinction. This evidence was in the form of burn holes in a molecular sieve, which is located beneath the arcing region (see fig.9.1). The molecular sieve is used to absorb SF_6 by-products, following arcing, to reduce chemical attack on the interrupter components. The burn holes can be seen on fig.10.13.

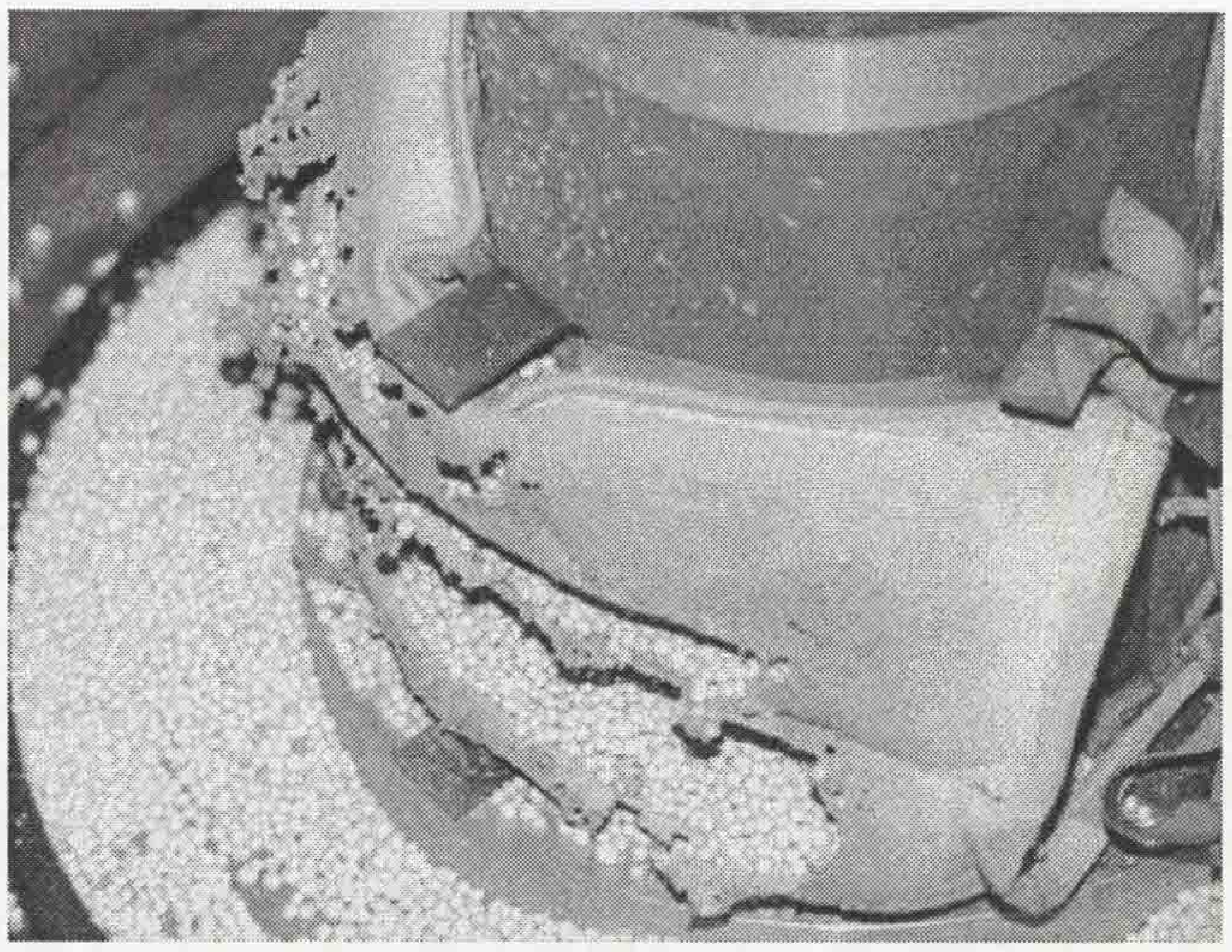

Figure 10.13 - Burning of molecular sieve following arc extinction

One suggested explanation for this was the reflection of hot gas at the top-plate, back towards the arcing region. It is important to identify the path of hot, dielectrically weak gas in order to assess the possibility of a “late breakdown” (reignition of the arc caused by hot gas re-entering the arcing zone). The most convenient place to monitor the gas dielectric strength was close to the top-plate of the circuit breaker, where hot gas reflections at the top-plate could be investigated.

The system for measuring the gas dielectric strength (**chapter 7**) was used to monitor the dielectric strength close to the top-plate during arcing (as in fig.9.3). The results are shown on figs.10.14a to 10.14d, which give the time variation of the probe output for peak currents of 15, 30, 45 and 56kA. It is apparent that there are no significant changes in post-arc dielectric strength at this position (0ms represents contact separation). These results were found to be repeatable and showed that it was improbable that hot gas was reaching the top-plate region on these time scales.

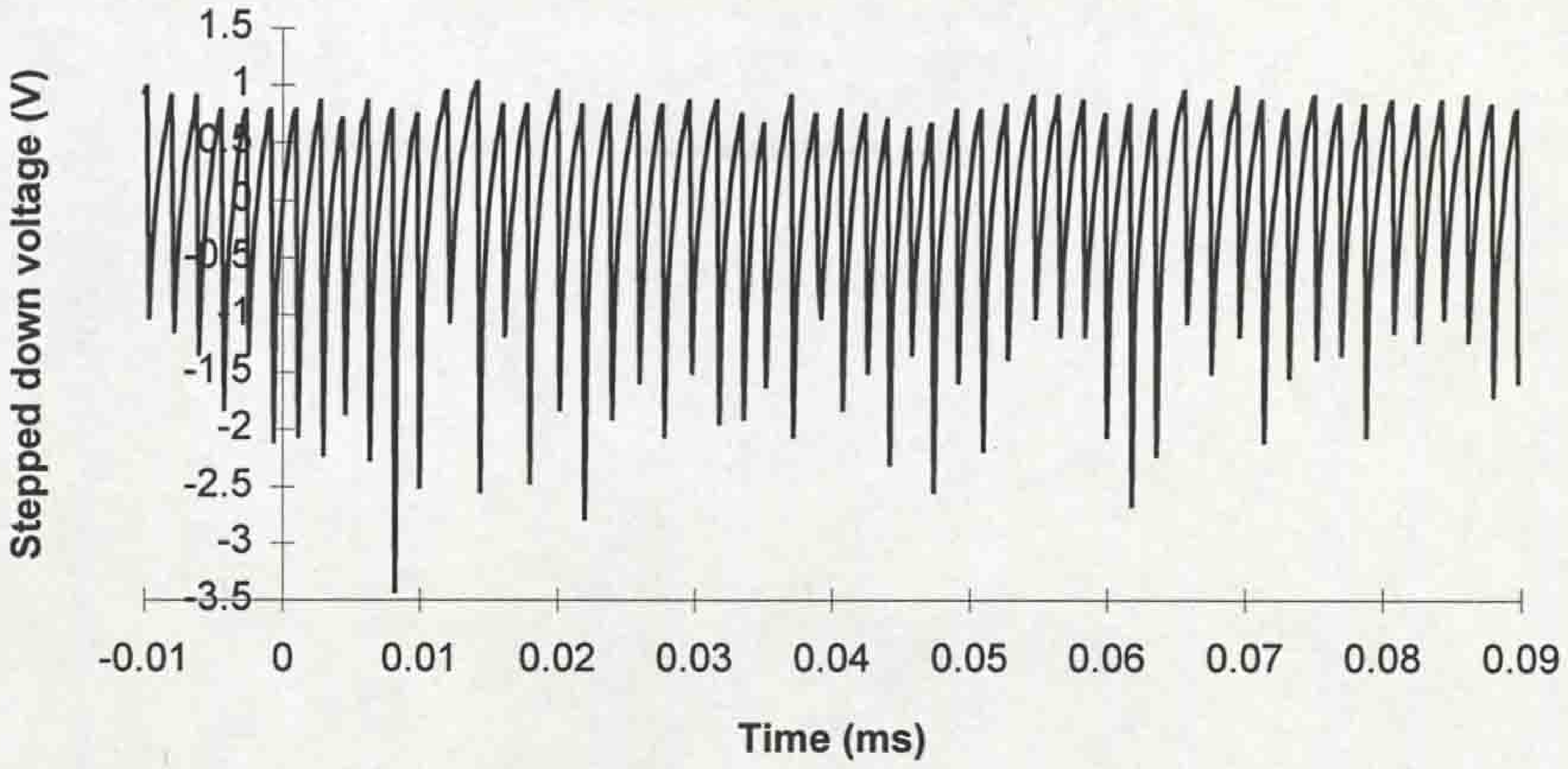

Figure 10.14a - Gas dielectric strength near top-plate after arcing (15kA)

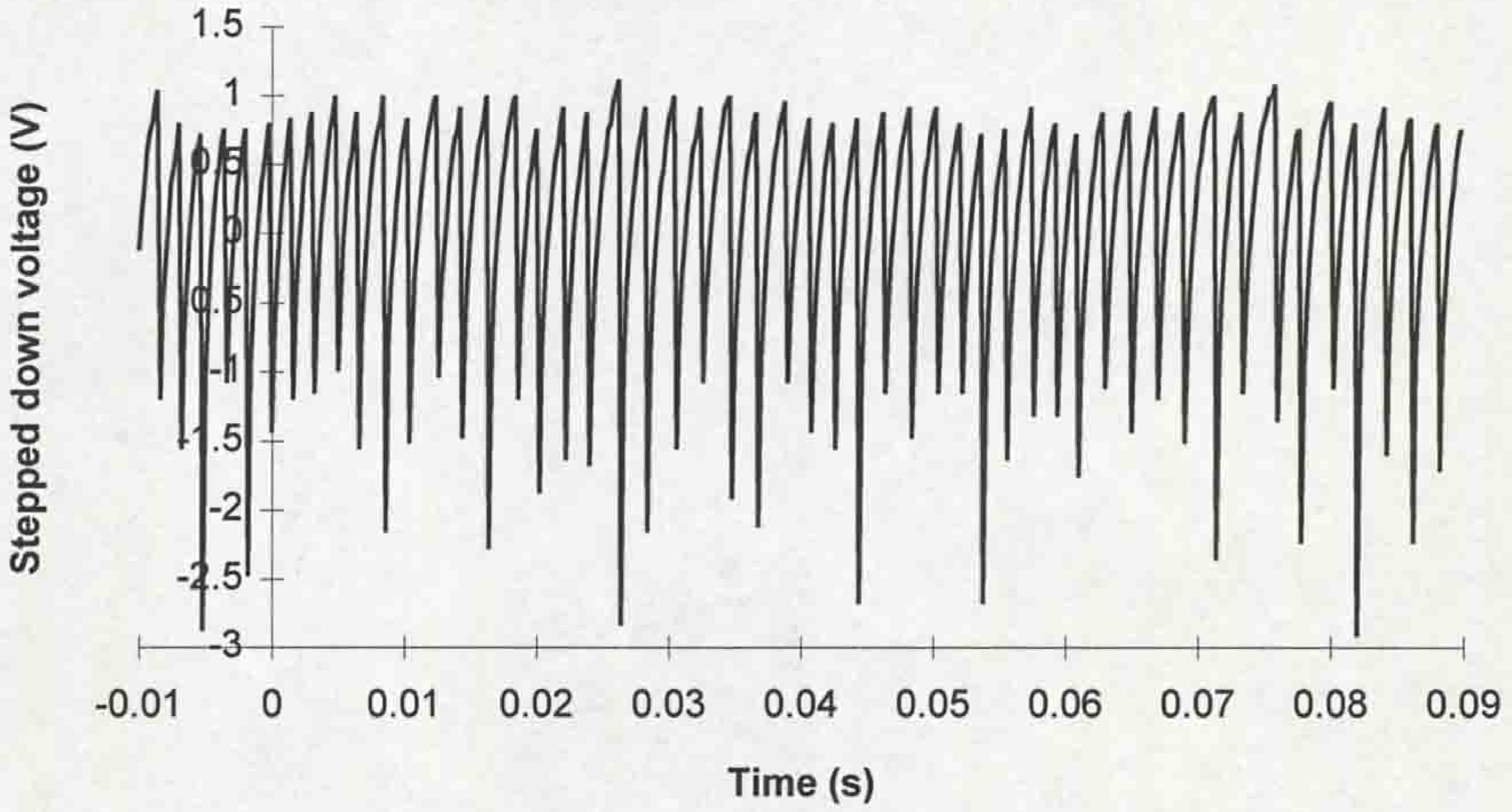

Figure 10.14b - Gas dielectric strength near top-plate after arcing (30kA)

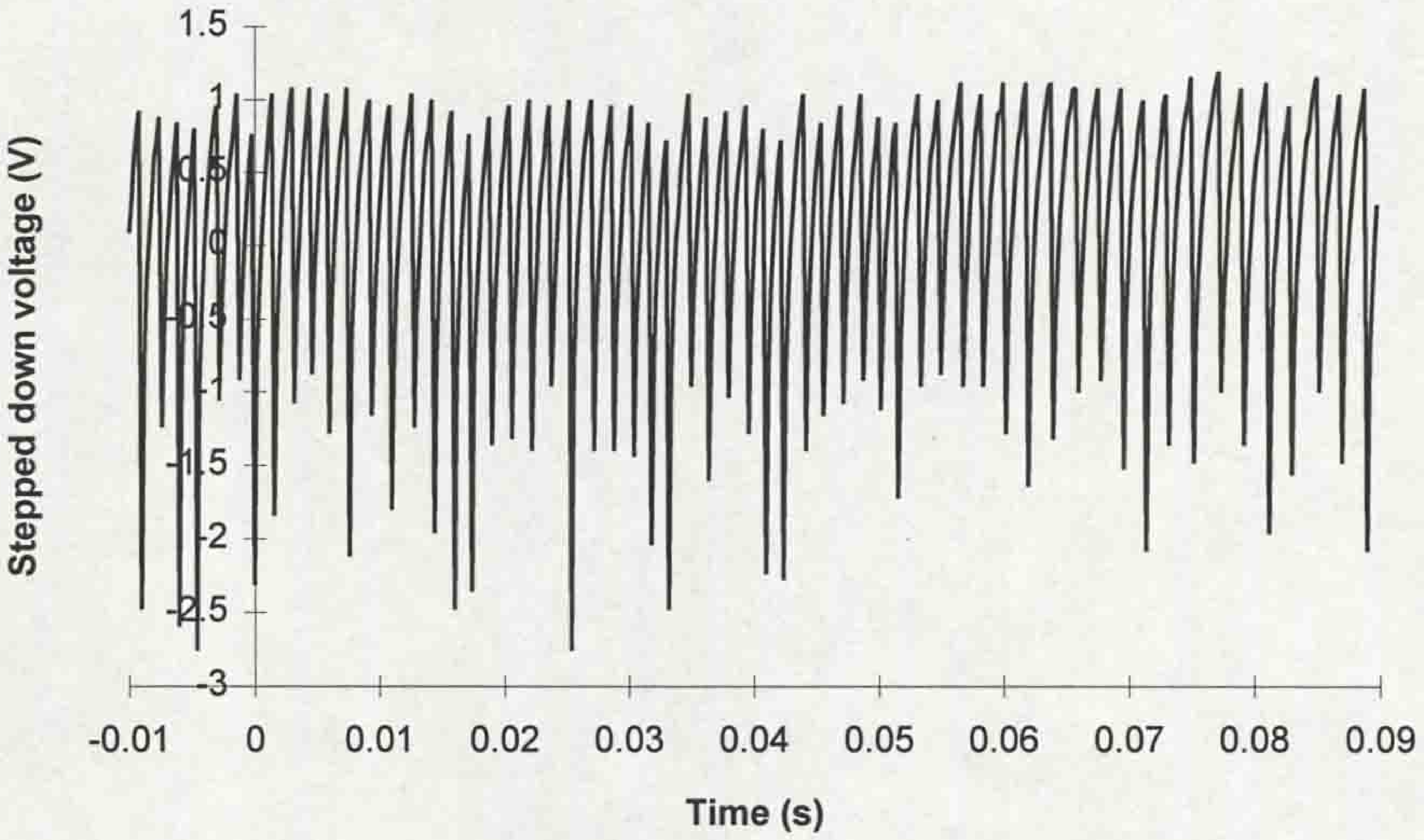

Figure 10.14c - Gas dielectric strength near top-plate after arcing (45kA)

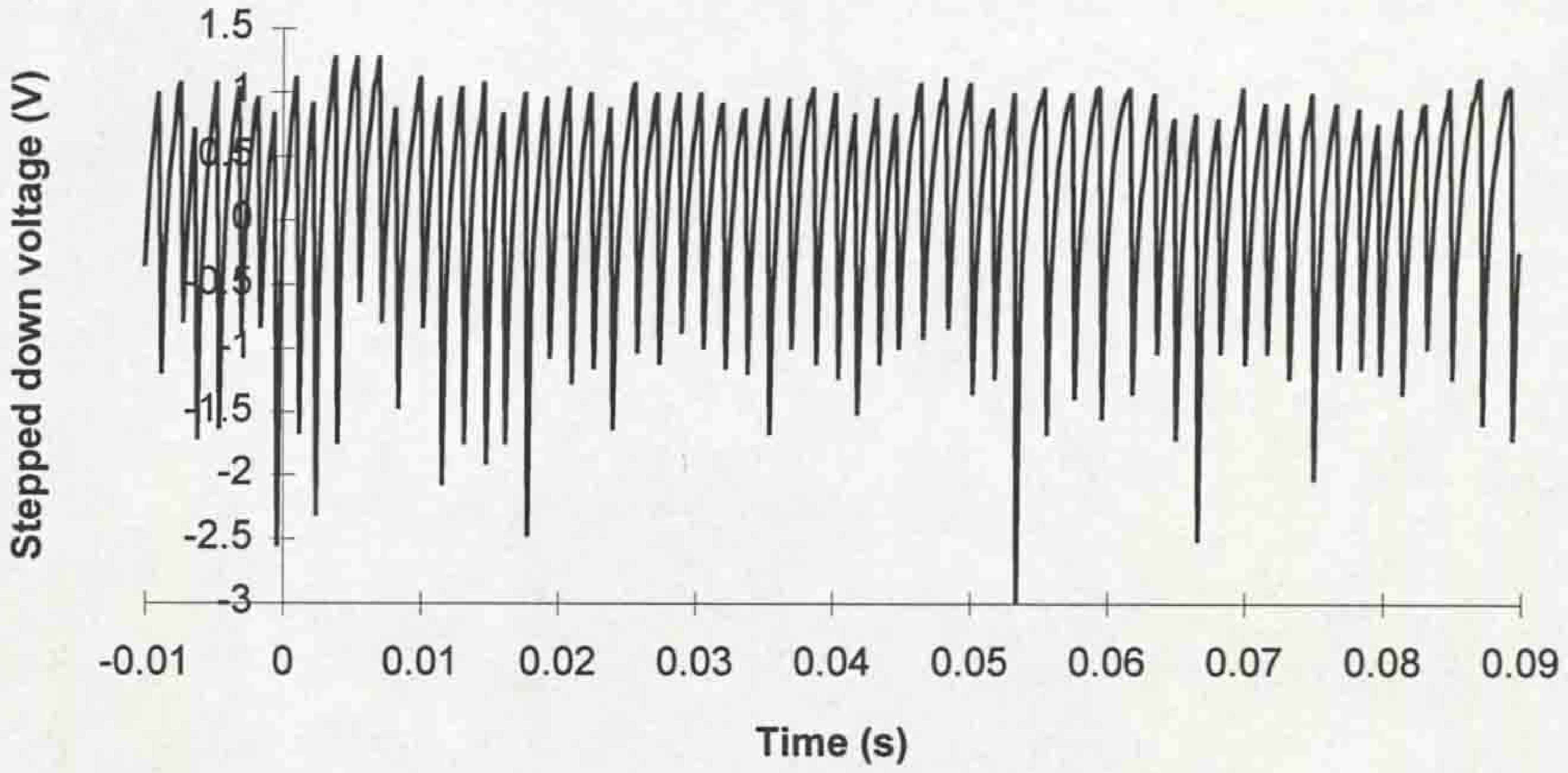

Figure 10.14d - Gas dielectric strength near top-plate after arcing (56kA)

As a result of these tests laser-based flow visualisation experiments (Heyes *et al*, 1995) were performed on the test circuit breaker, at the central viewing window, in order to further investigate the flow of hot gas during interruption. Results from these experiments (fig.10.15) showed major recirculation of gas at the shoulders of the fixed contact.

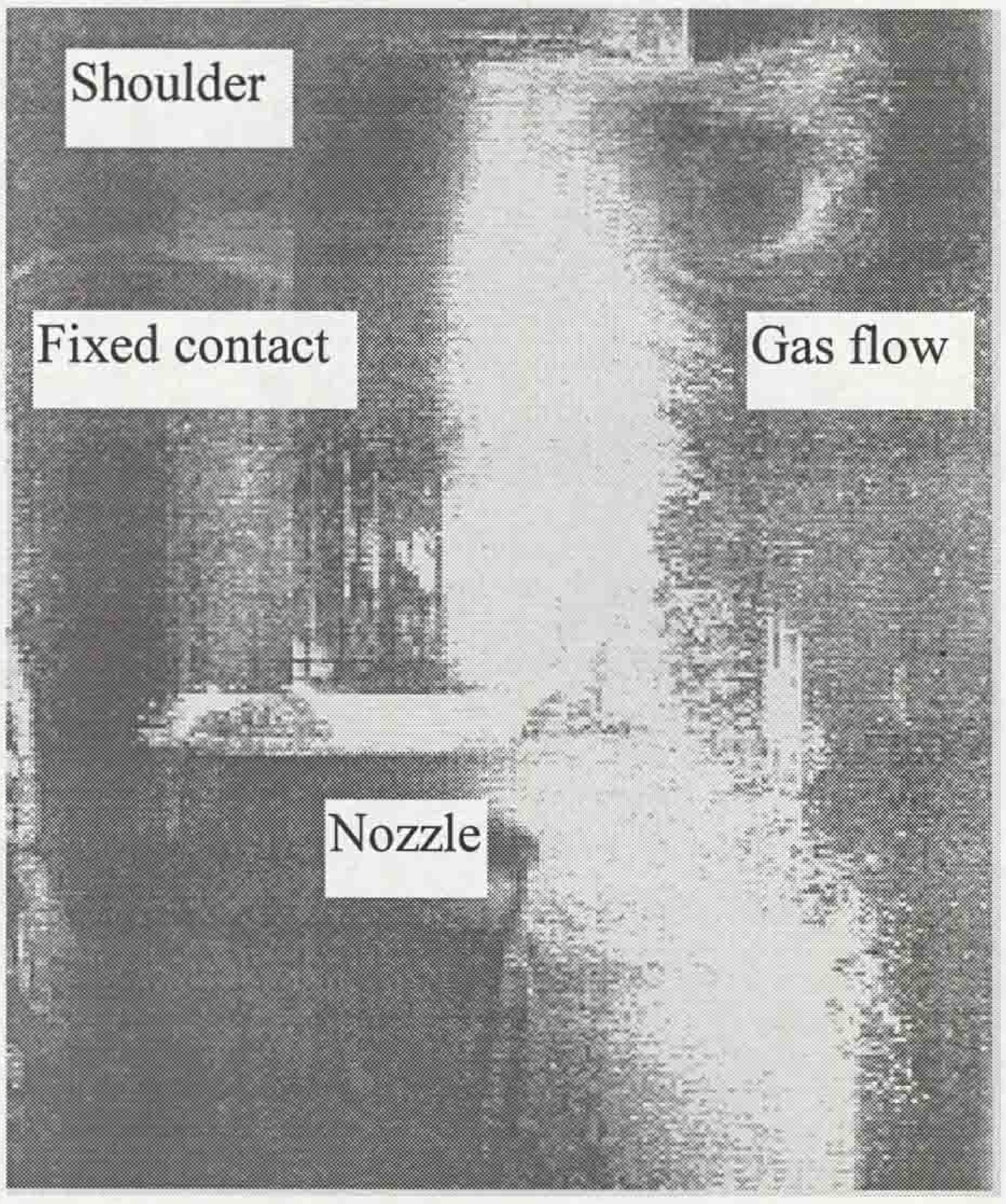

Figure 10.15 - Re-circulation of hot gas at shoulders of fixed contact during arcing

This circulating flow, when taken with the dielectric strength results, reinforce the unlikelihood of hot gas reaching the top-plate on the timescales considered. It is recommended, therefore, that further investigations with the dielectric probe system should concentrate on the region close to the electrodes. The central viewing window of the circuit breaker (shown on fig.9.3) would provide access for the probe. The extent of dielectric deterioration of the recirculating hot gas could then be ascertained to investigate the likelihood of arc reignition.

10.4 CONCLUSIONS

Detailed results, obtained with a range of optical fibre based transducers, have been presented in this chapter. These indicate measurements of pressure (piston chamber and circuit breaker tank), contact travel, optical emission from the arc through the PTFE nozzle, particle concentration and dielectric strength of the post-arc gas.

Some of the inter-relationships between these various measured parameters have already been indicated (eg. piston pressure rise and contact travel) and the time location of various events noted (eg. contact separation, arcing duration and fixed contact clearing the nozzle). The gas pressure, radiation and particle concentration results can be analysed further; this is described in **chapter 11**.

CHAPTER 11 - FURTHER ANALYSIS AND DISCUSSION OF RESULTS

In this chapter results presented in **chapter 10** are analysed in greater depth, in order to explore correlations between the various measurements and the effect of the arc on these inter-relationships.

11.1 FURTHER ANALYSIS OF PRESSURE RESULTS

11.1.1 Prediction of frequency of oscillations on pressure transients

Figs.10.5 and 10.7 showed that the results from both the top-plate pressure sensor and piston chamber pressure sensor exhibited significant superimposed oscillations. It is possible that these oscillations would be produced as a result of standing waves set up close to the sensors, caused by the circuit breaker operation. As shown on fig.8.7 the pressure sensors were housed in modified hollow bolts in order to provide a robust surrounding for the micromachined Fabry-Perot cavities. As a result the pressure cavities were effectively situated at the closed end of a pipe, as shown on fig.11.1. This pipe might be subjected to acoustic standing waves superimposed on the local gas pressure due to operation of the circuit breaker, whose amplitude may be dependent on arc current. The standing waves would be set up by the superposition of the incoming longitudinal pressure waves with reflections at the closed end of the pipe.

At the left hand end of the pipe the gas is stationary, thus forming a displacement node, with a corresponding pressure antinode (on fig.11.1 molecular displacement to the right is taken as positive and displacement to the left as negative). This is the simplest form of standing wave that can be set up in a closed pipe, known as the fundamental. The length of the pipe is one quarter of the wavelength of the fundamental and the fundamental frequency of the standing wave is then given by

$$\nu_0 = \frac{c}{\lambda_0} = \frac{c}{4l} \tag{11.1}$$

where c is the speed of sound in SF_6 (135m/s).

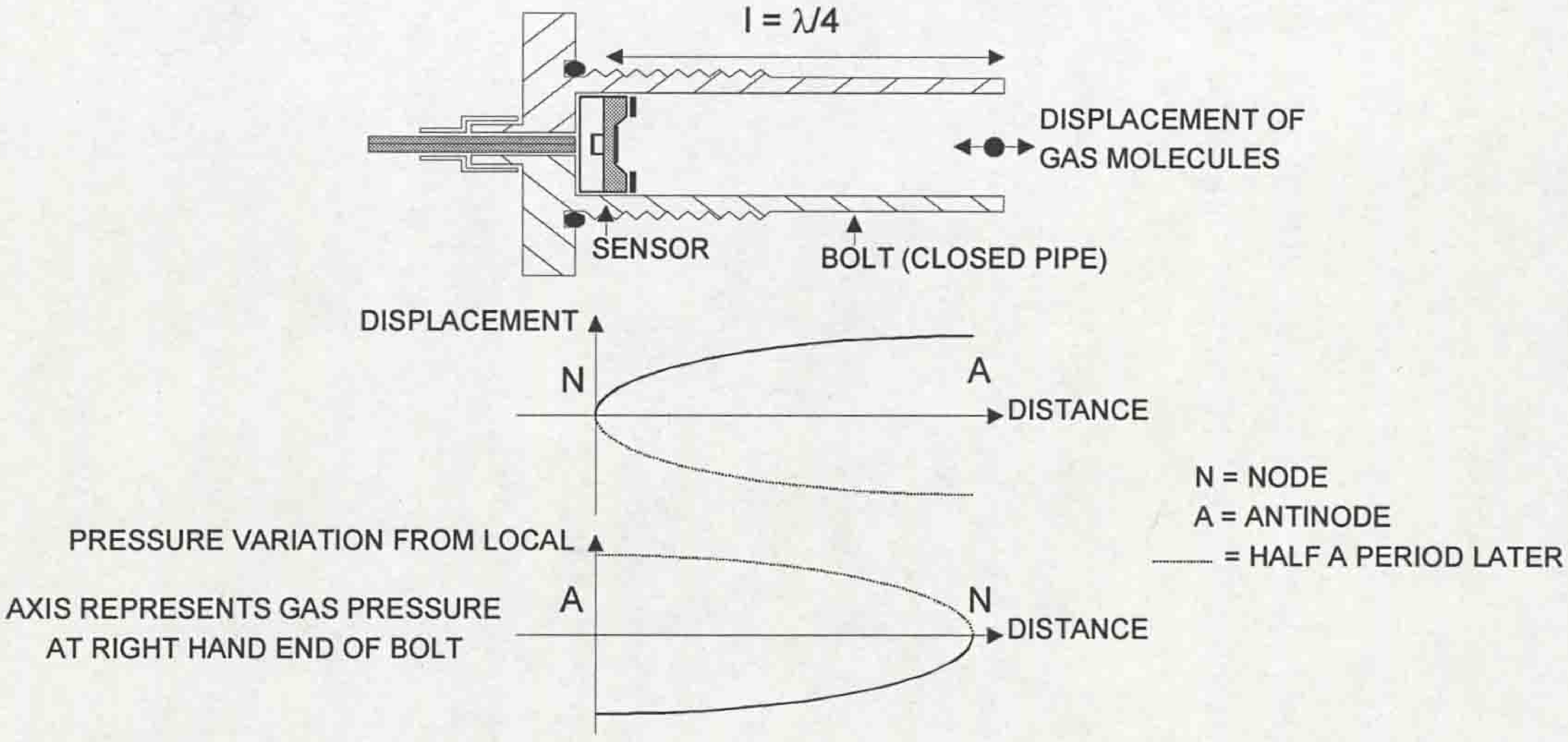

Figure 11.1 - Standing waves produced in a closed pipe

For the pressure sensor housed in the top-plate of the main circuit breaker tank the distance l was 40mm. From eqn.11.1, allowing for end correction (0.6 x pipe radius should be added to l) the fundamental frequency of the standing wave set up in the pipe housing of this sensor should be ~795Hz. For the piston chamber pressure sensor, with a slightly longer distance l of 60mm, the fundamental frequency of the standing wave should be ~560Hz. These predictions are compared in **11.1.3.1** and **11.1.4.1** with the frequencies obtained from a Fourier analysis of the experimental pressure transients on figs.10.5 and 10.7.

11.1.2 Frequency analysis technique for pressure waveforms

The frequency components of a time-dependent signal may be evaluated using the Fourier Transform, given by (Ramirez, 1985):

$$X(\nu) = \int_{-\infty}^{\infty} x(t) e^{-j2\pi\nu t} dt \tag{11.2}$$

where t is time, ν frequency and x(t) a non-periodic signal. To analyse a list of sampled digitised data, such as the pressure measurements made with the pressure sensors and LIBIDO system, the Discrete Fourier Transform is used

$$X_d(k\Delta\nu) = \Delta t \sum_{n=0}^{N-1} x(n\Delta t) e^{-j2\pi k\Delta\nu n\Delta t} \qquad (11.3)$$

where N is the number of samples, Δt the sampling interval, Δν the frequency domain resolution (=1/NΔt), n the time sample index, k the computed discrete frequency component index, x(nΔt) the set of time samples describing the signal to be analysed and $X_d(k\Delta\nu)$ the set of Fourier coefficients obtained from the DFT of x(nΔt).

In practice the DFT is computationally intensive. The computing time can be reduced by use of the Cooley-Tukey algorithm, or Fast Fourier Transform (Ramirez, 1985). The FFT allows individual frequency components present in a signal, and their relative amplitudes, to be visualised through a power spectral density function, in which the DFT of an individual frequency component is multiplied by its complex conjugate to eliminate the imaginary part. Thus

$$P(\nu) = (\alpha + j\phi)(\alpha - j\phi) \qquad (11.4)$$

where P(ν) is the power spectral density, α the amplitude component of the FFT and ϕ the phase component of the FFT.

The pressure waveforms obtained near the top-plate of the main circuit breaker tank and in the piston chamber were analysed using an FFT routine in the mathematics software package Matlab. A rectangular time-domain window was used in the frequency analysis. Under certain circumstances this can lead to a distortion of the results obtained. However, for this purpose of identifying the main frequency component in the signal, the use of a rectangular time-domain window was acceptable. The results of these analyses are presented in **11.1.3.1** and **11.1.4.1** for comparison with the predicted frequencies in **11.1.1**.

11.1.3 Pressure transients near the top-plate of circuit breaker tank

11.1.3.1 FFT analysis of pressure transients near the top-plate

Using the method of frequency analysis described in **11.1.2**, the pressure results obtained near the top-plate of the circuit breaker tank (figs.10.5) were processed to obtain their corresponding frequency spectra (figs.11.2). On each frequency spectrum the dominant frequency components are located around 800Hz, thus verifying the predicted standing wave frequency of 795Hz (**11.1.1**). The spread of frequencies present on figs.11.2 is a possible indication of second order effects within the main tank, such as radial resonance modes and gas turbulence.

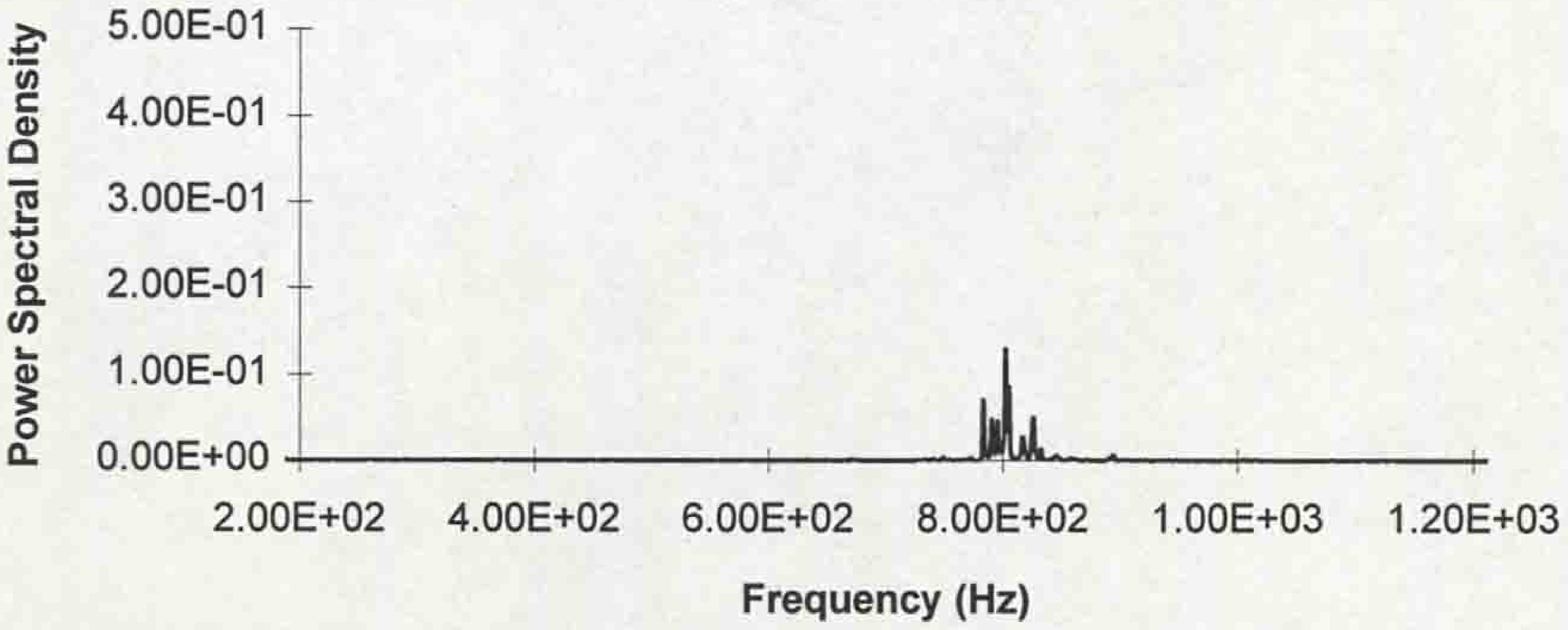

Figure 11.2a - Fourier analysis of top-plate pressure transient (coldflow)

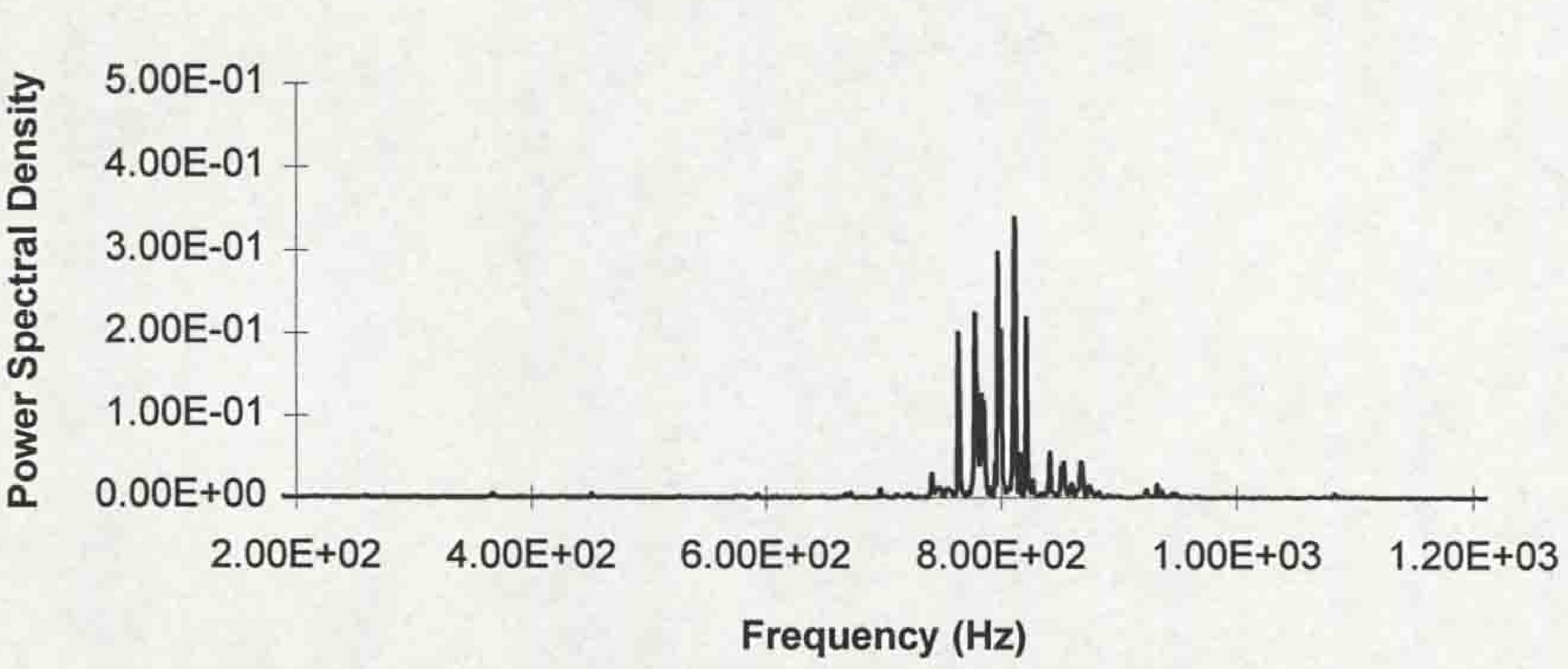

Figure 11.2b - Fourier analysis of top-plate pressure transient (5kA)

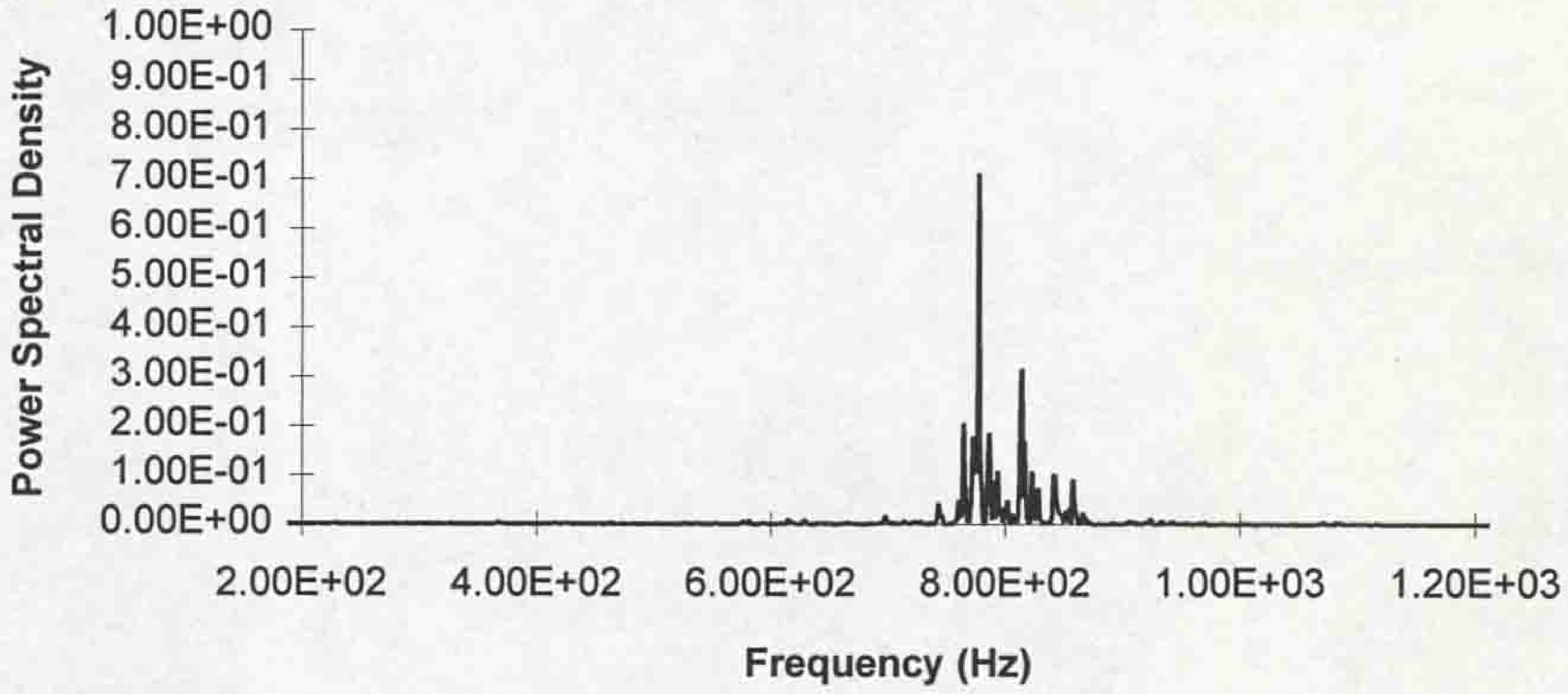

Figure 11.2c - Fourier analysis of top-plate pressure transient (15kA)

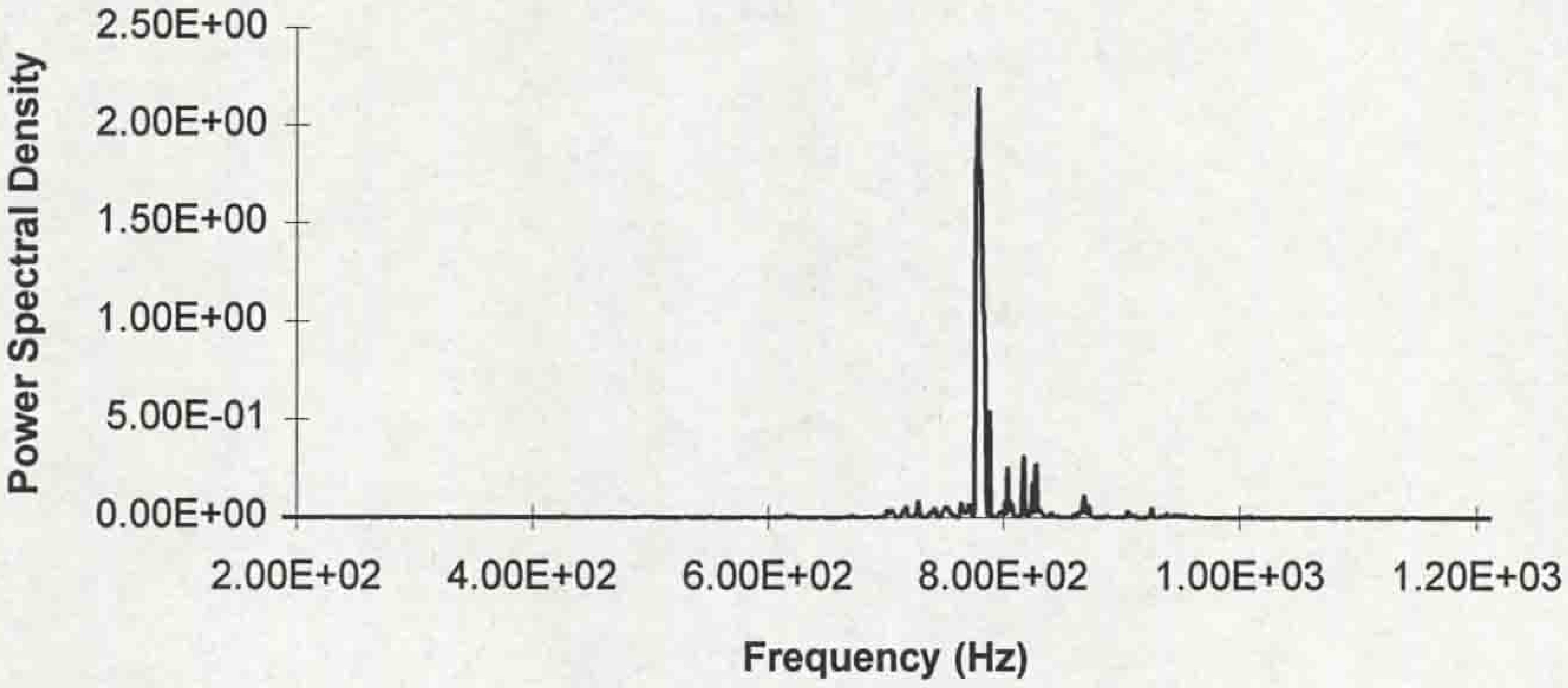

Figure 11.2d - Fourier analysis of top-plate pressure transient (30kA)

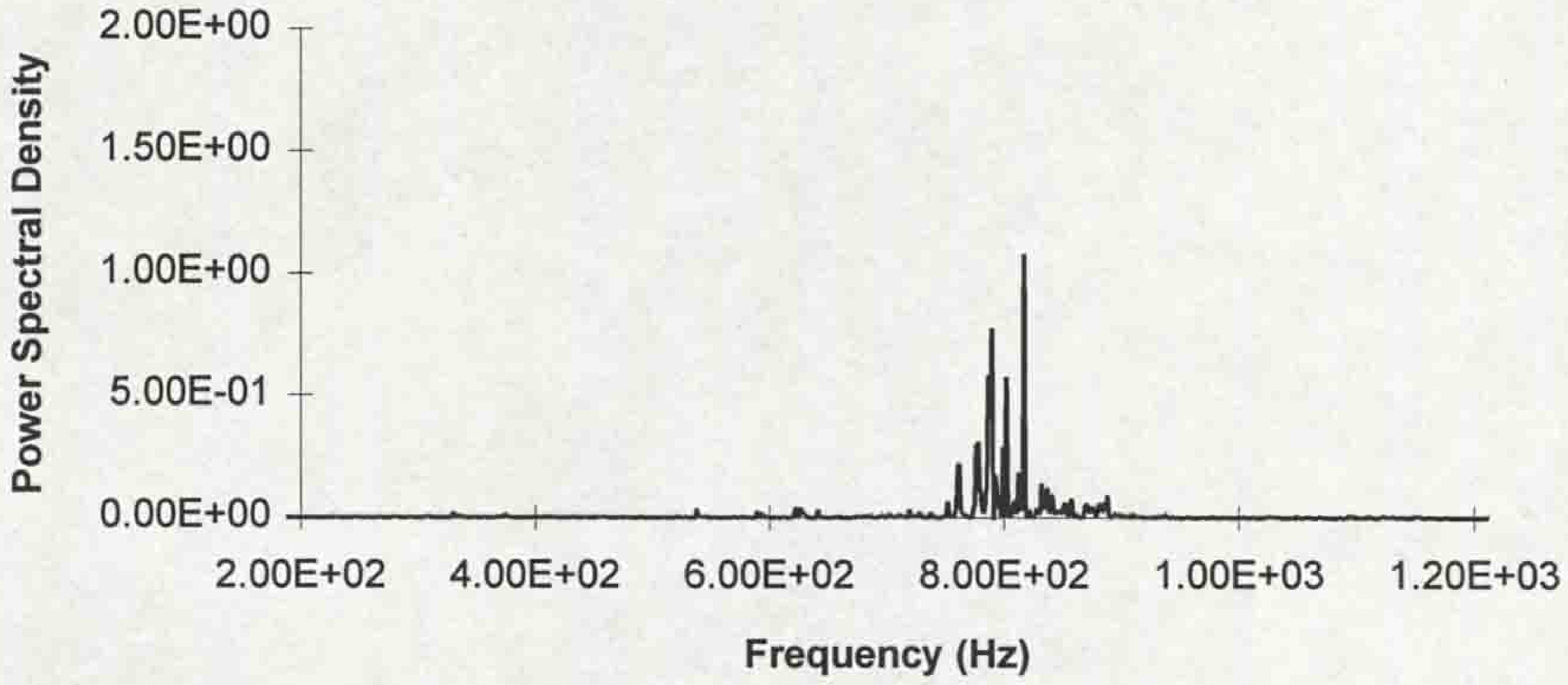

Figure 11.2e - Fourier analysis of top-plate pressure transient (45kA)

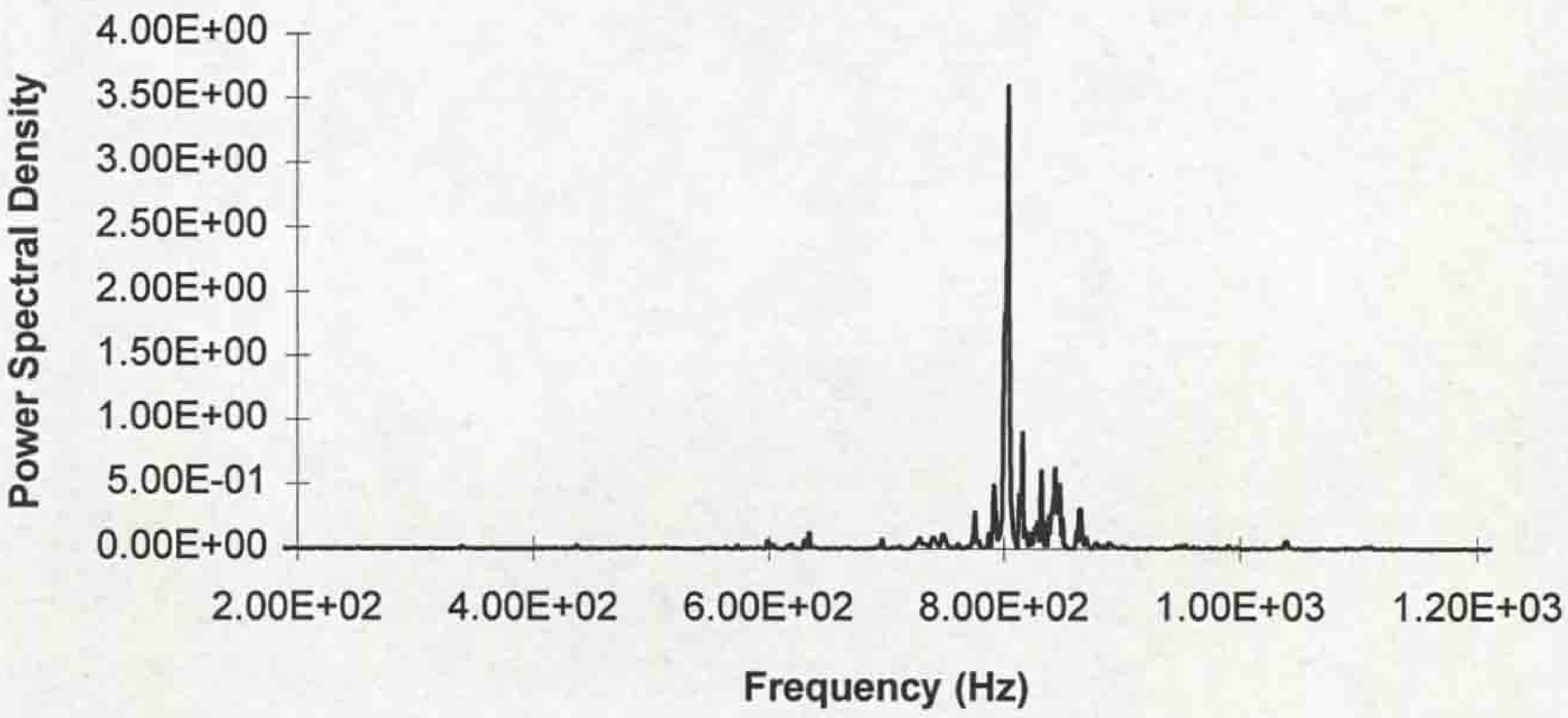

Figure 11.2f - Fourier analysis of top-plate pressure transient (56kA)

11.1.3.2 Analysis of post arc pressure rise in the circuit breaker tank

In **10.3.2.1** it was noted that, after arcing, the pressures recorded by the top-plate pressure sensor were higher than the pre-arc values when the transient oscillations had decayed (~1s after arcing). This incremental increase in tank pressure was shown as a function of arc current on fig.10.6. This pressure rise may also be plotted as a function of the electrical energy input into the gas, which is calculated using the formula

$$E = \int_{t_1}^{t_2} VI\,dt \qquad (11.5)\ .$$

where E is the total electrical energy input and V and I are the measured arc voltages and currents, examples of which are shown on fig.10.4. Fig.11.3 shows the experimentally measured pressure rise as a function of electrical input energy, which is termed $\Delta P_{TANK/POST\text{-}ARC/MEASURED}$ here and is referred to again in **11.3**.

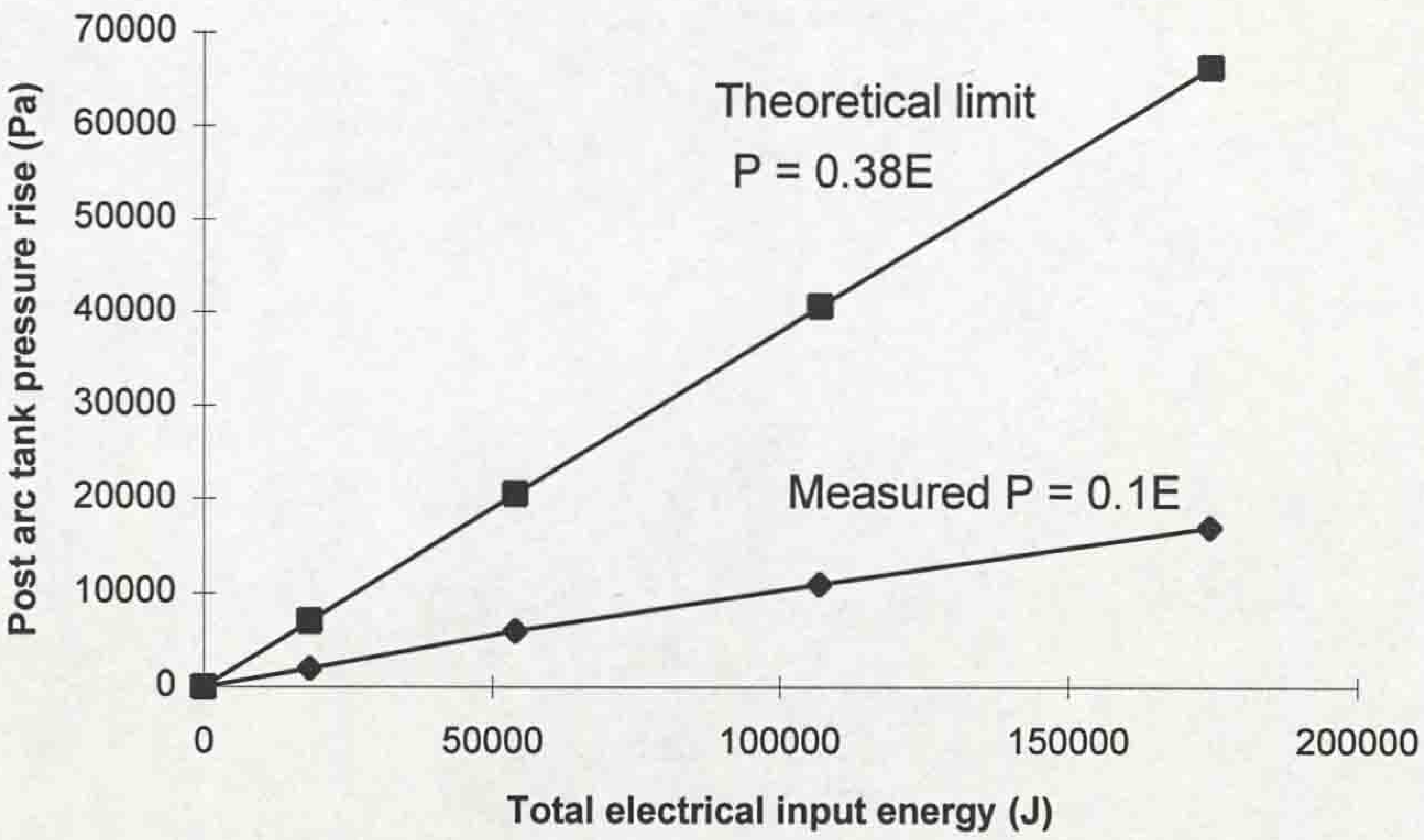

Figure 11.3 - Post-arc tank pressure rise as a function of electrical energy input

Fig.11.3 shows that the tank gas pressure rise, $\Delta P_{TANK/POST\text{-}ARC/MEASURED}$, is given by

$$\Delta P_{TANK/POST-ARC/MEASURED} = 0.1E \tag{11.6}$$

where ΔP is in Pa and E is the electrical input energy (J), defined by eqn.11.5. It is possible to calculate what percentage of the electrical input energy is retained by the bulk gas in the tank, 1 second after arc extinction. Firstly, if the gas were ideal then before arcing

$$M = \frac{PVM_r}{RT} \tag{11.7}$$

where M is the mass of SF_6 gas in the circuit breaker tank, P is the ambient pressure ($7\text{x}10^5$Pa), T is the ambient temperature (293K), M_r is the relative molecular mass of SF_6 (146), R is the universal gas constant ($8.314\text{x}10^3 JK^{-1}kmol^{-1}$) and V is the volume of the circuit breaker tank (estimated to be $0.25m^3$). This gives a value for the mass of gas before arcing of 10.5kg. If all of the energy dissipated by the arc were used to heat the gas uniformly, which is the simplest approximation (isothermal), then the increase in gas temperature would be given by

$$\Delta T = \frac{E}{MC_v} \tag{11.8}$$

where C_v is the specific heat of SF_6 at constant volume ($606Jkg^{-1}K^{-1}$). Also, for an ideal gas in a constant volume

$$\frac{P}{T} = \frac{P + \Delta P}{T + \Delta T} \tag{11.9}$$

Substituting values for P($7x10^5$Pa), T(293K), M and C_v in eqns.11.8 and 11.9 and rearranging gives the following theoretical limit between the tank gas pressure rise (Pa) and the electrical energy input from the arc (J)

$$\Delta P_{TANK/POST-ARC/LIMIT} = 0.38E \tag{11.10}$$

By rationalising equations 11.6 and 11.10 it is implied that the percentage of input energy, which is retained by the bulk gas in the circuit breaker chamber 1 second after arcing, is (0.1/0.38)x100 = 26%. The remainder of the input energy is dissipated via a number of energy loss mechanisms, which are discussed in detail in **11.3**.

11.1.4 Pressure transients in piston chamber

11.1.4.1 FFT analysis of pressure transients in piston chamber

The pressure waveforms recorded in the piston chamber (figs.10.7) may also be analysed using the Fast Fourier Transform method (**11.1.2**), as for the tank pressure analysis. The results are shown on figs.11.4.

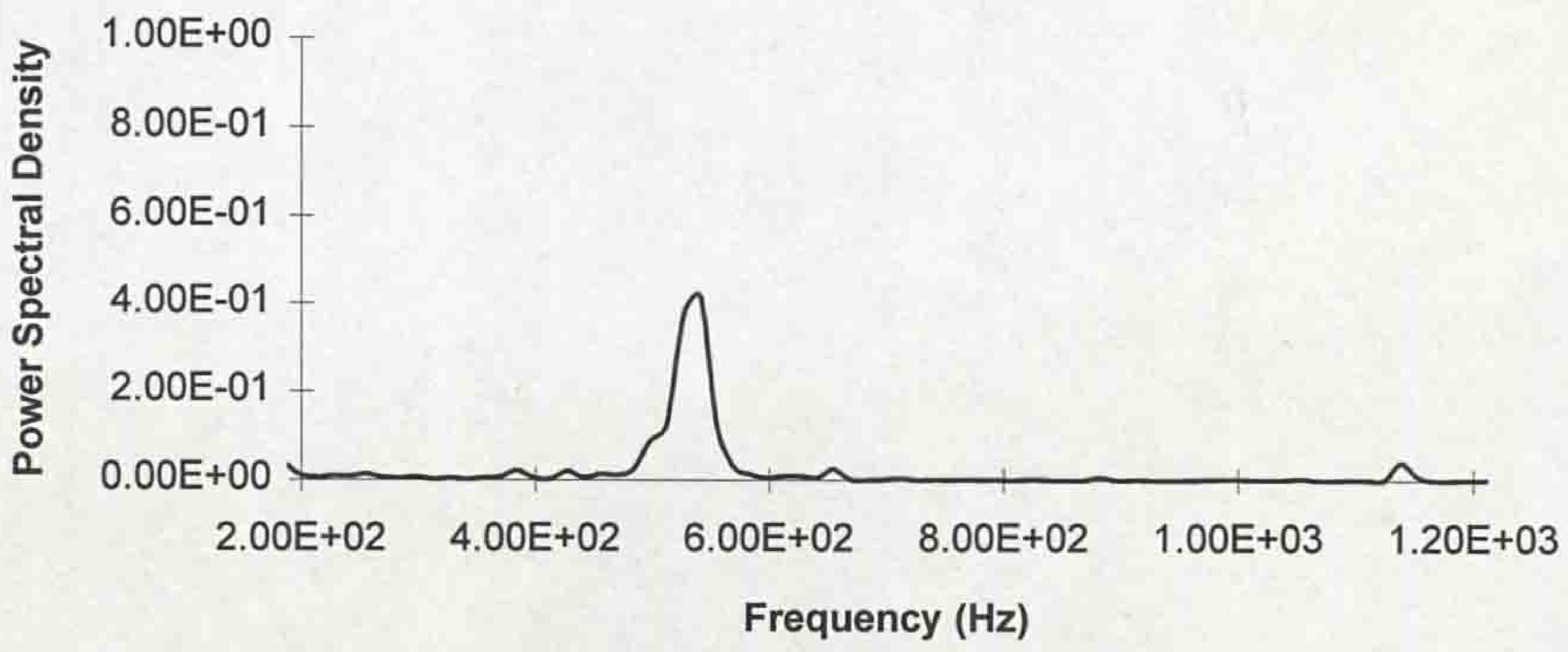

Figure 11.4a - Fourier analysis of piston chamber pressure transient (coldflow)

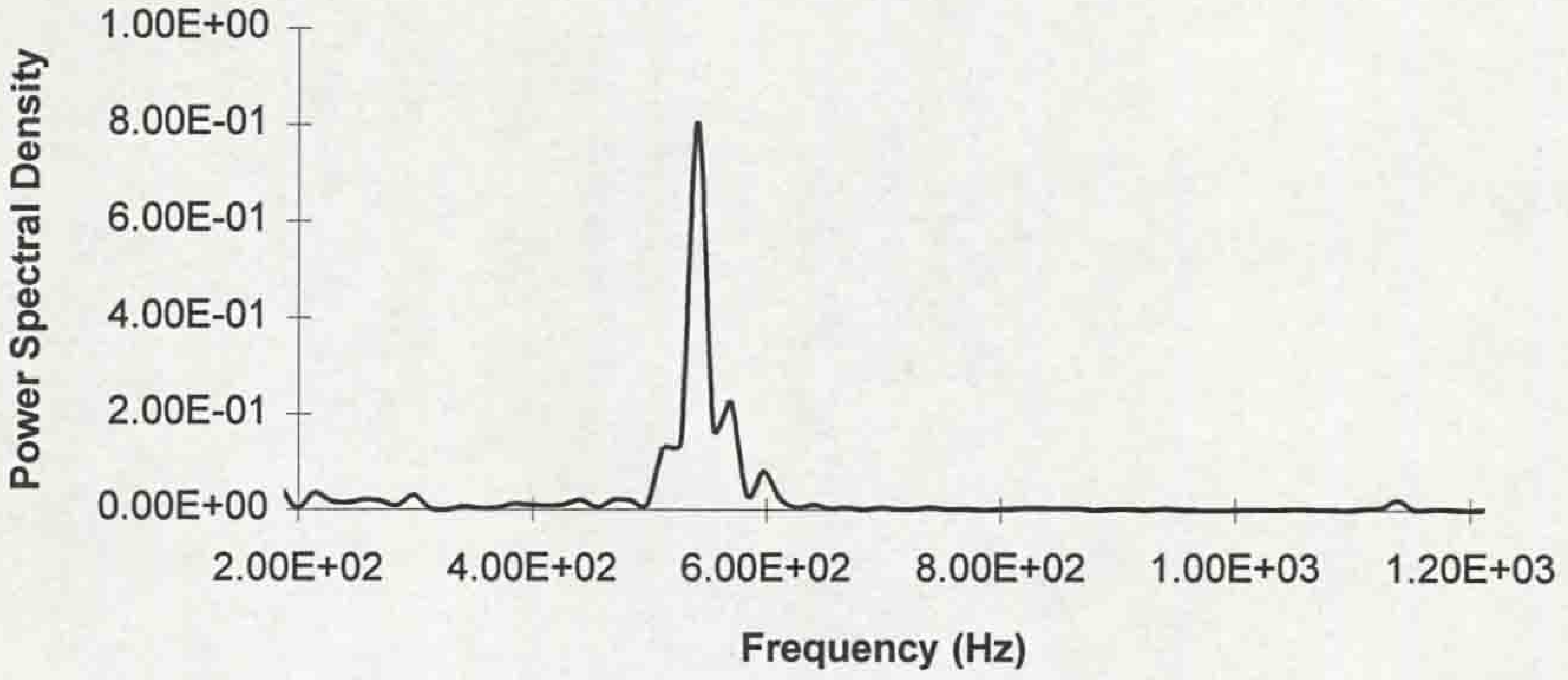

Figure 11.4b - Fourier analysis of piston chamber pressure transient (5kA)

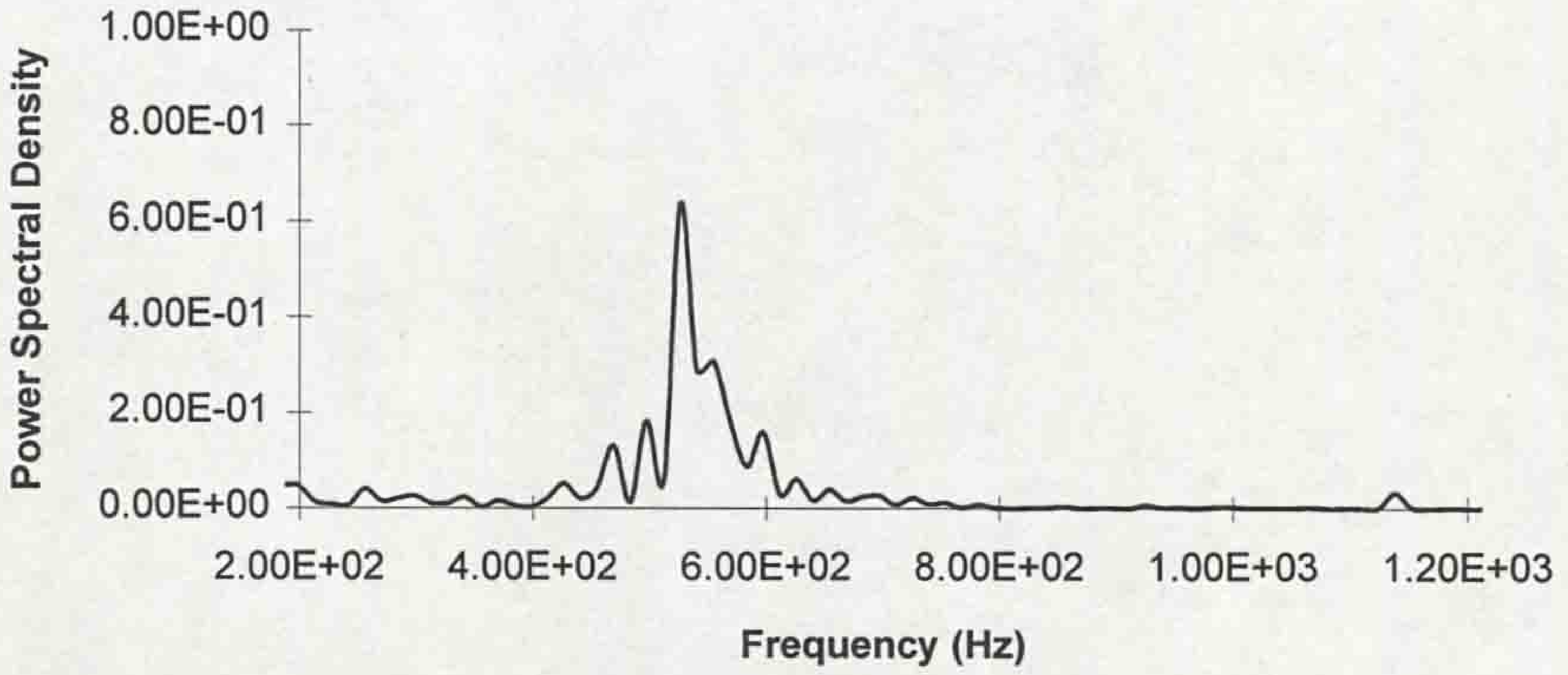

Figure 11.4c - Fourier analysis of piston chamber pressure transient (15kA)

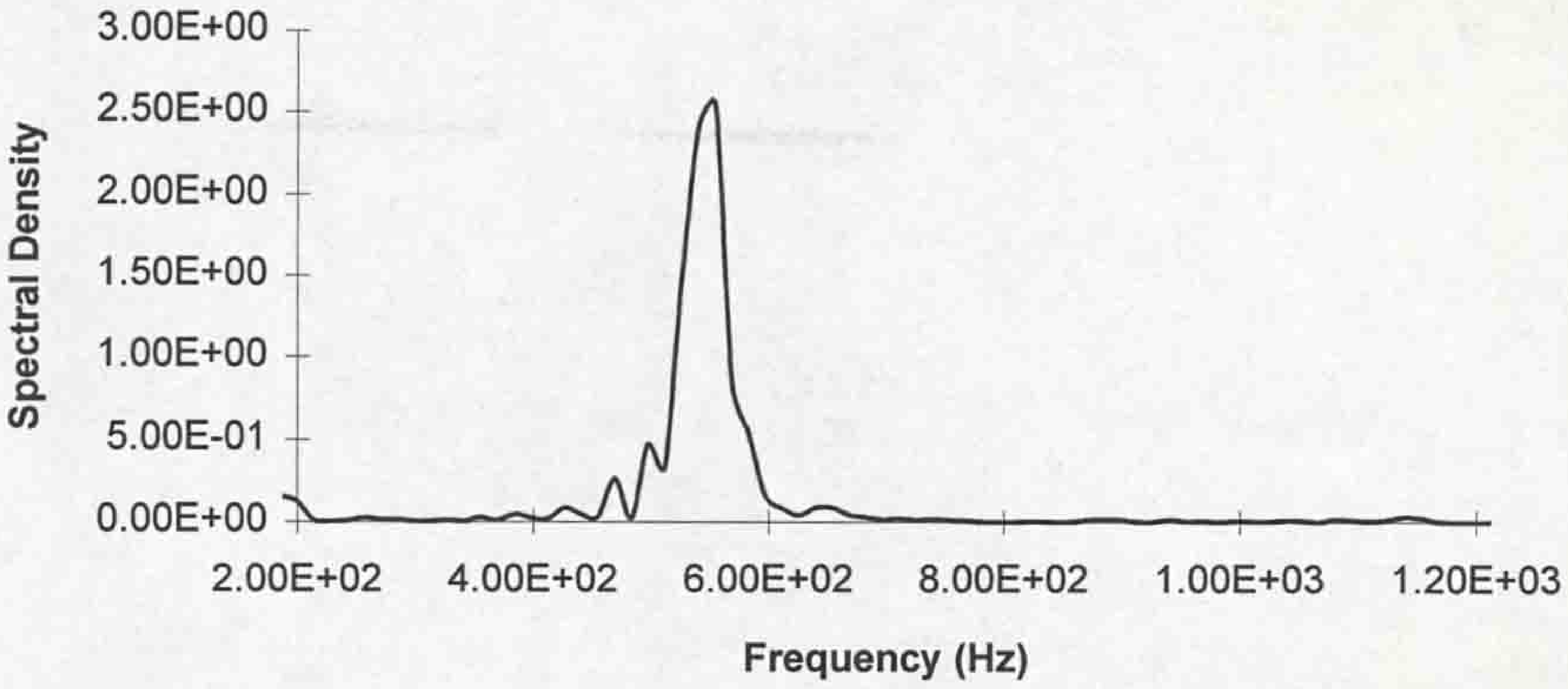

Figure 11.4d - Fourier analysis of piston chamber pressure transient (30kA)

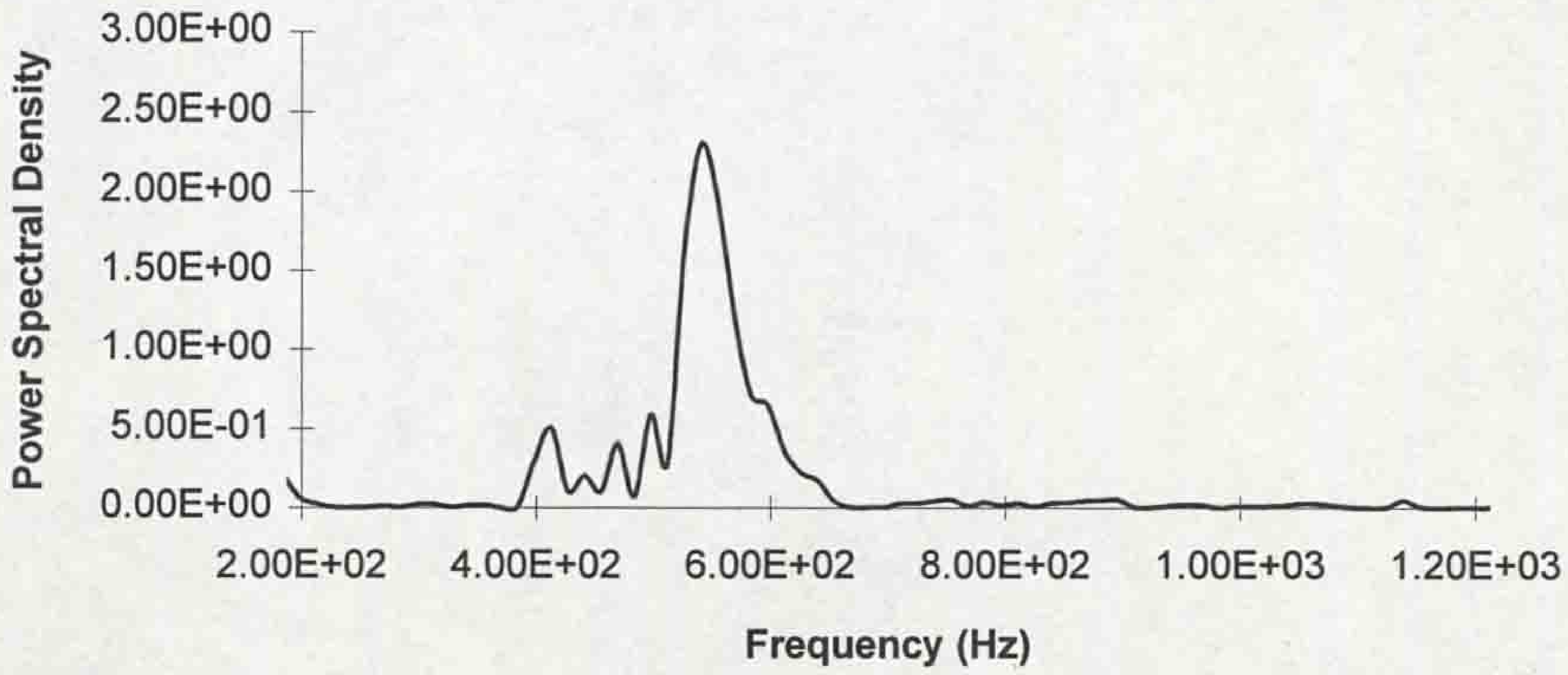

Figure 11.4e - Fourier analysis of piston chamber pressure transient (45kA)

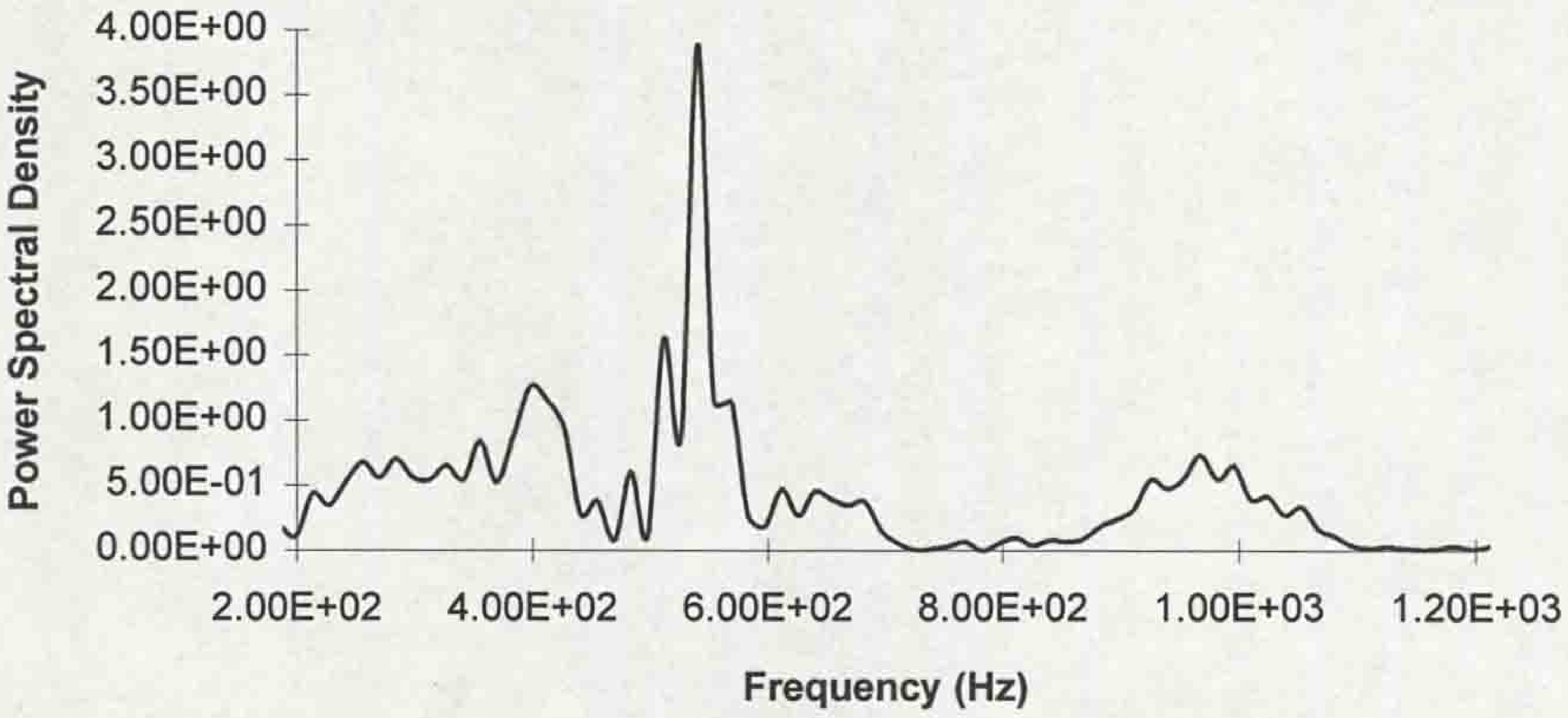

Figure 11.4f - Fourier analysis of piston chamber pressure transient (56kA)

Apart from fig.11.4f, the oscillation frequencies on the piston chamber pressure transients agree fairly well with the predicted standing wave frequency of ~560Hz (**11.1.1**). It was previously noted (**10.3.2.2**) that the piston chamber pressure results may become ambiguous, if pressure oscillations on these results exceeded the 11.5bar.g limit of the sensor. This may be the case in fig.11.4f, for the 56kA pressure transient, although the results up to 45kA appear to be unaffected, since their frequency spectra are similar.

11.1.4.2 Comparison of experimental and theoretical pressures in the piston chamber

Using the principles outlined in **chapter 3** for theoretically modelling the performance of a puffer circuit breaker (sections **3.2** and **3.3**), a model for the test circuit breaker has been developed (Christodoulou *et al*, 1996), in parallel to the experimental work reported in this thesis, using the CFD (computational flow dynamics) package Phoenics, produced by Cham. In the early stages of development some preliminary results of piston chamber pressure predictions by the model have been produced for comparison with experimentally measured pressures. For this, Christodoulou used the travel record, produced by the OFLTR, for the test circuit breaker, together with measured arc current and voltage waveforms (to deduce the energy dissipated by the arc) as the primary inputs. The experimental results provided in this section relate to a higher hydraulic mechanism pressure to that used for the piston pressure measurements described in **chapter 10**. Thus the measured pressure waveforms used in the comparison differ slightly to those in **chapter 10**. (Consequently, the repeatability of the measured pressure waveforms cannot yet be discussed, although this work is ongoing).

The piston chamber pressure is determined by the combined actions of piston compression, nozzle blocking and arc heating of the gas in the piston volume. Fig.11.5 summarises the major design parameters employed by the model in solving the complex set of conservation equations described in **3.2**.

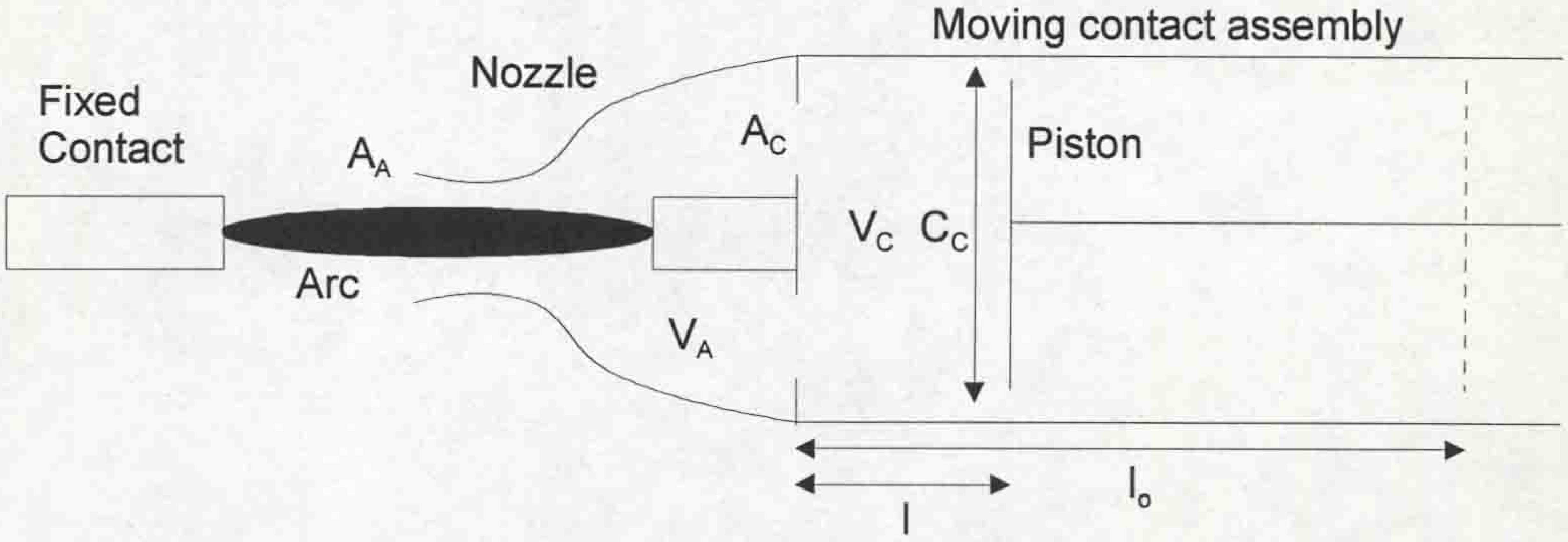

Figure 11.5 - Design parameters included in the puffer model

A_A = Effective area of nozzle throat, taking into account blocking of the nozzle, firstly by the fixed contact and then by the arc.

A_C = Area of nozzle / cylinder interface, where gas mixing takes place between the arc space and piston volume.

V_A = Volume of arc space.

V_C = Volume of piston chamber.

C_C = Cross section of piston cylinder.

l_0/l = Compression ratio.

The values of C_C, A_C, V_A and l_0 are fixed for a particular interrupter. V_C and l are provided by the optical fibre linear travel recorder (OFLTR), to which a polynomial curve-fit can be assigned (fig.11.6)

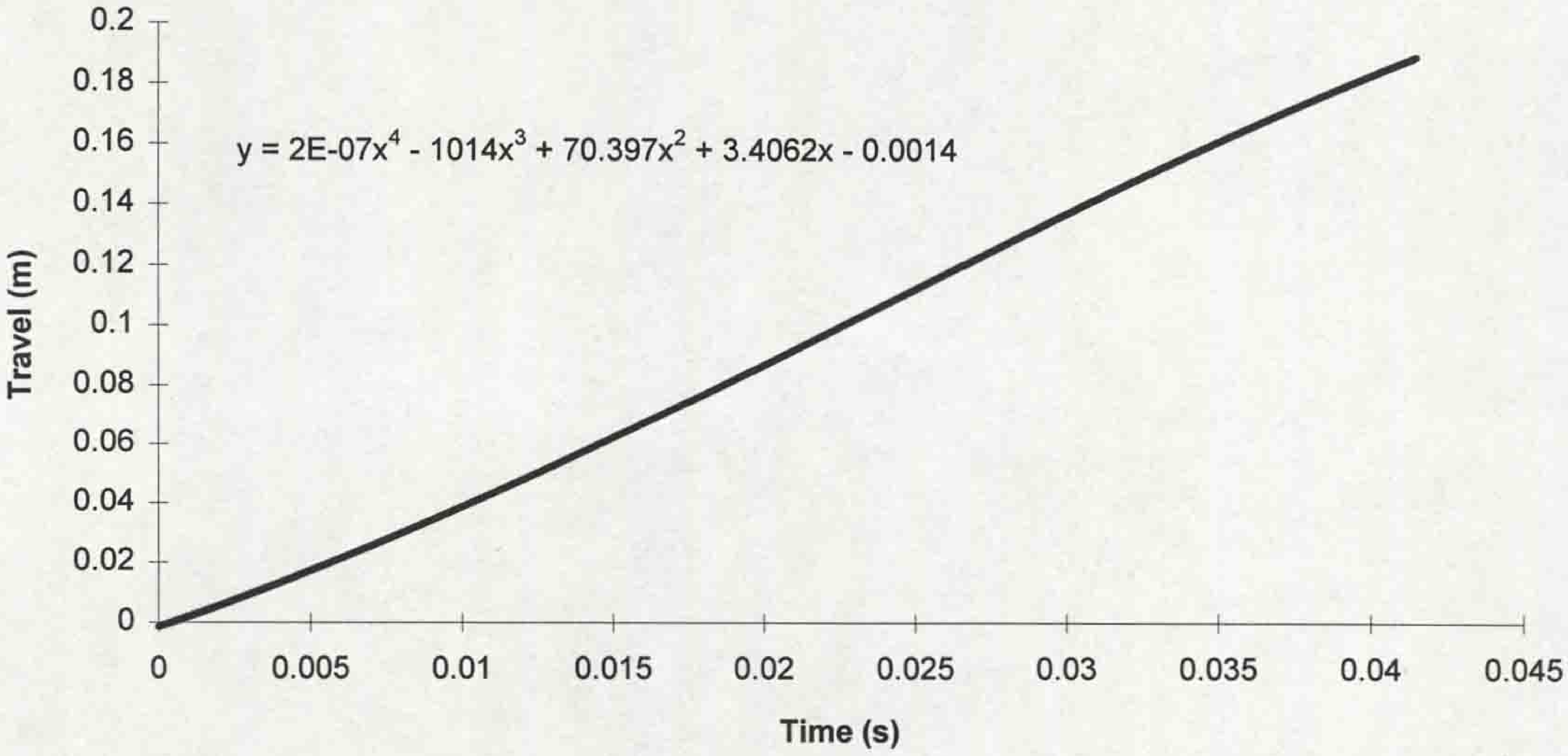

Figure 11.6 - Interrupter travel record with polynomial curve-fit

In the absence of arcing the pressure rise in the piston chamber is determined by the result of gas compression by the piston in the total volume ($V_A + V_C$) and mass transfer through the effective nozzle throat area A_A. This pressure rise, predicted by the model, is shown on fig.11.7, together with the result taken with the optical fibre pressure sensor.

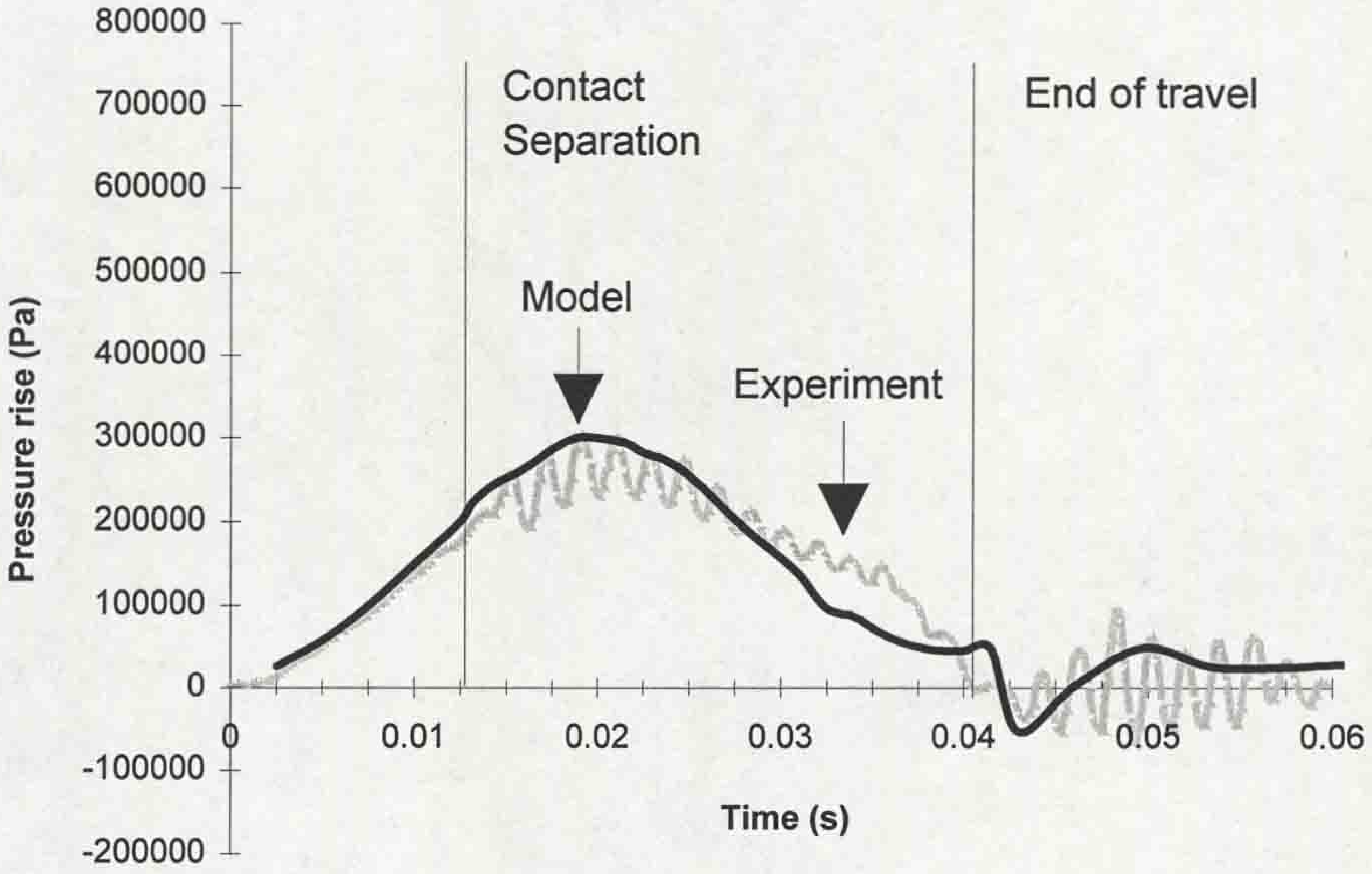

Figure 11.7 - Coldflow comparison of model and experimental piston pressures

The results show a close agreement, if account is taken of the oscillations on the measured waveforms (which are discussed in **11.1.1**). The dip in pressure below ambient, at the end of travel, which is more pronounced in the model result, has been observed by Shimmin (1986) on a different puffer circuit breaker. Ryan and Jones (1989) indicated that this decompression effect may be due to flow inertia, which will cause a continued mass flow out of the nozzle at the end of travel, with a consequent reduction of pressure in the piston chamber.

When an arc is interrupted in the circuit breaker, the gas pressure is raised by a combination of piston compression, nozzle blocking (firstly by the fixed contact and subsequently the arc) and arc heating of the gas in the piston chamber. These processes are summarised on fig.11.8 (Ueda *et al*, 1982).

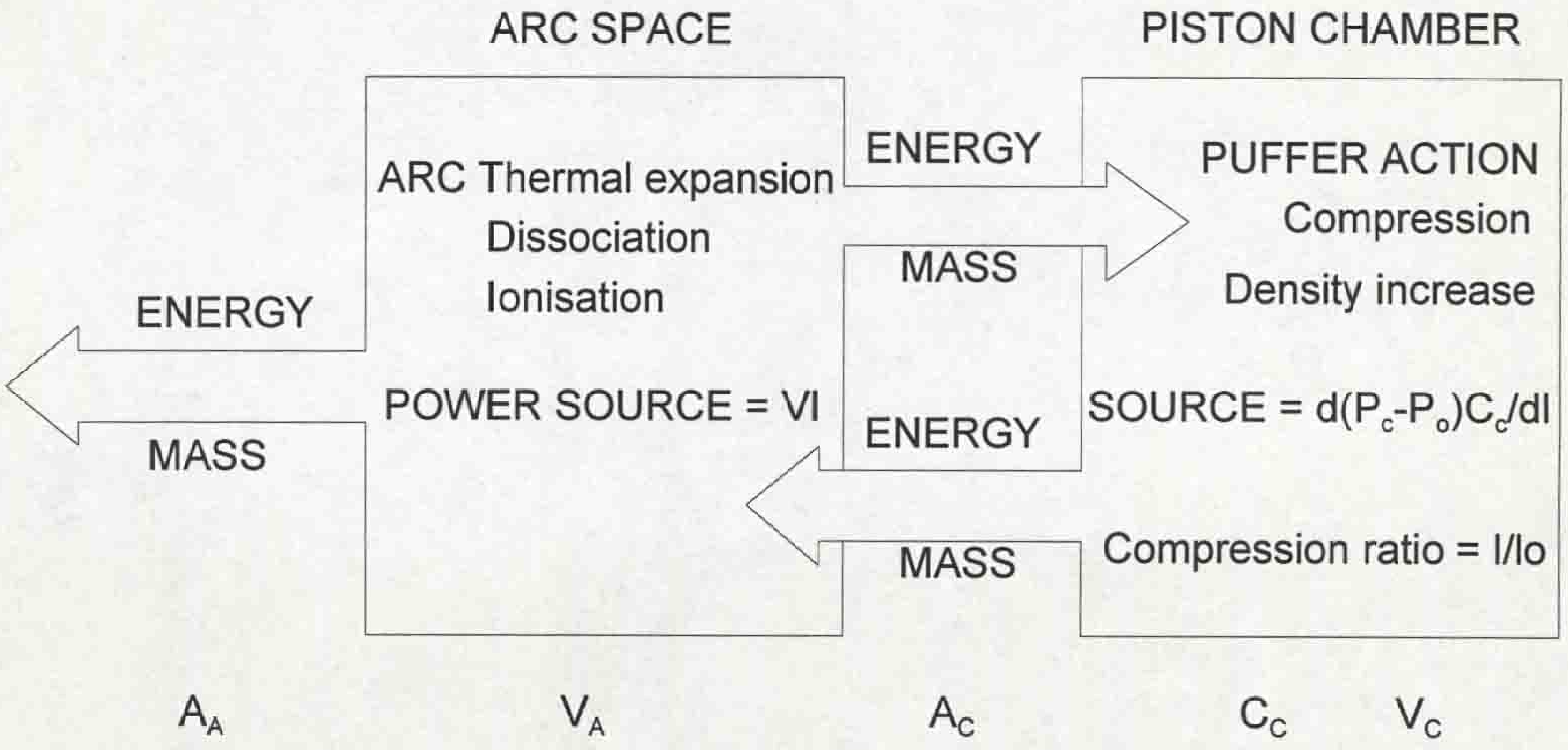

Figure 11.8 - Energy and mass exchange in the puffer circuit breaker

The electrical power input, which is the energy source for arc-induced gas heating, is calculated from the product of the arc voltage and current (fig.10.4), measured with the high voltage probe and current shunt respectively. This power input is shown, with respect to the interrupter travel, on fig.11.9, for arc currents of 15, 30 and 45kA.

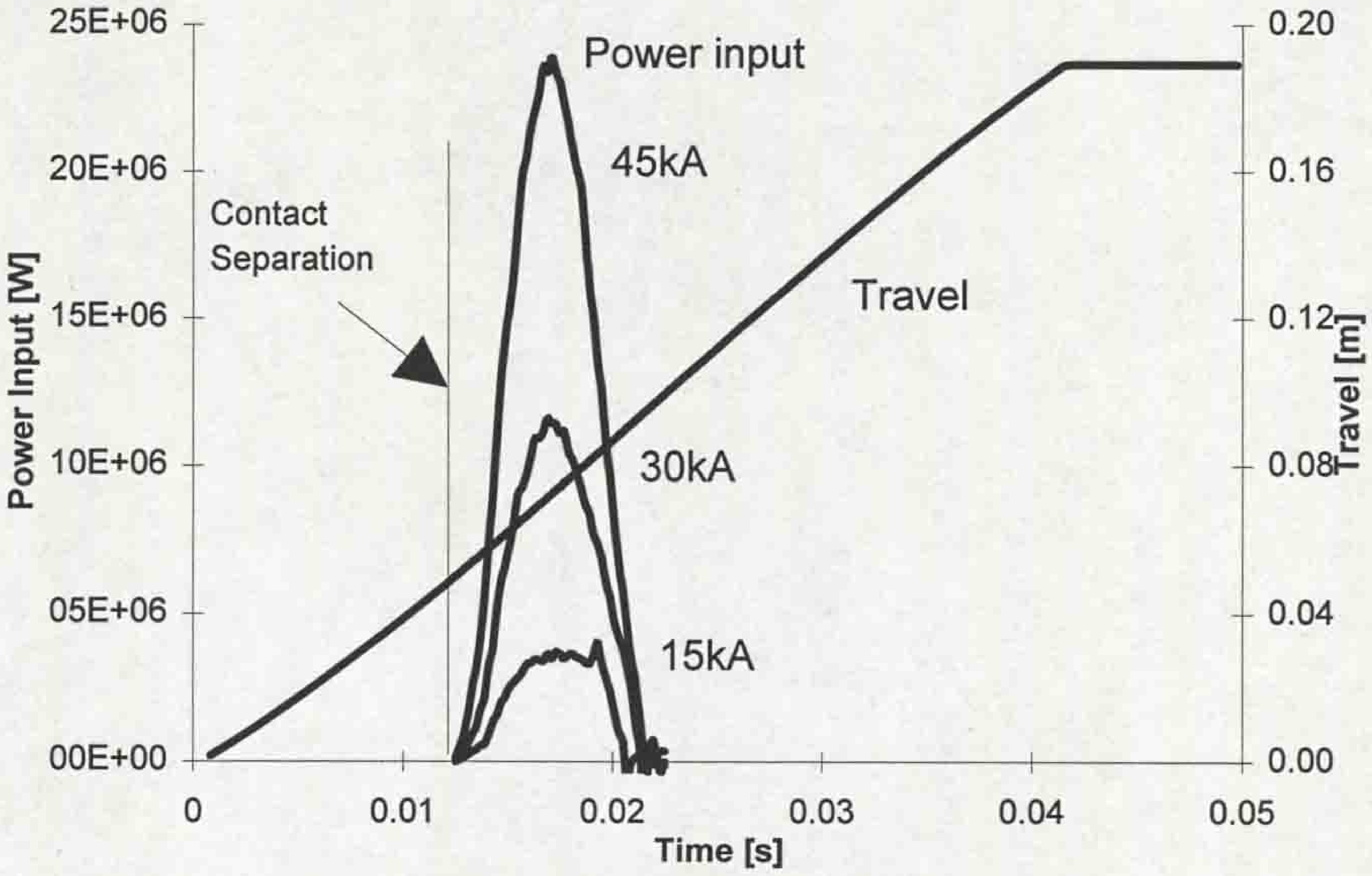

Figure 11.9 - Electrical power input at different current levels with respect to interrupter travel

The model incorporates terms to account for radiation loss of energy (which reduces the amount of energy available for gas heating) and nozzle ablation (which increases the mass flow into the piston chamber). Figs.11.10-12 show the comparisons between the model predictions of piston chamber pressure and the results taken with the optical fibre pressure sensor, for arc currents of 15, 30 and 45kA. There is a close agreement throughout the current range, which provides strong evidence of the validity of each method. Further refinements of the model are in progress to produce a design tool for commercial puffer circuit breaker development.

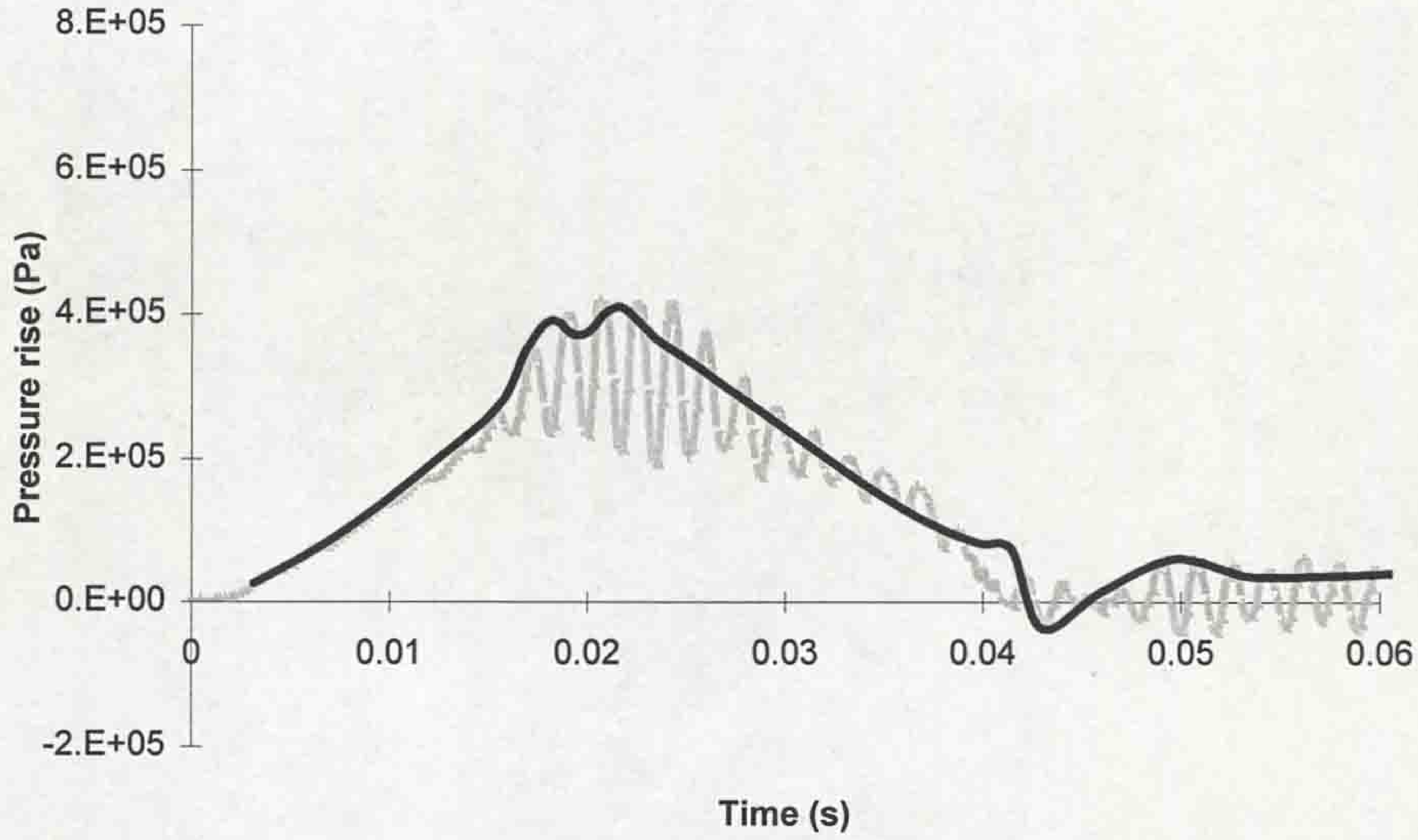

Figure 11.10 - Piston pressure comparison at 15kA

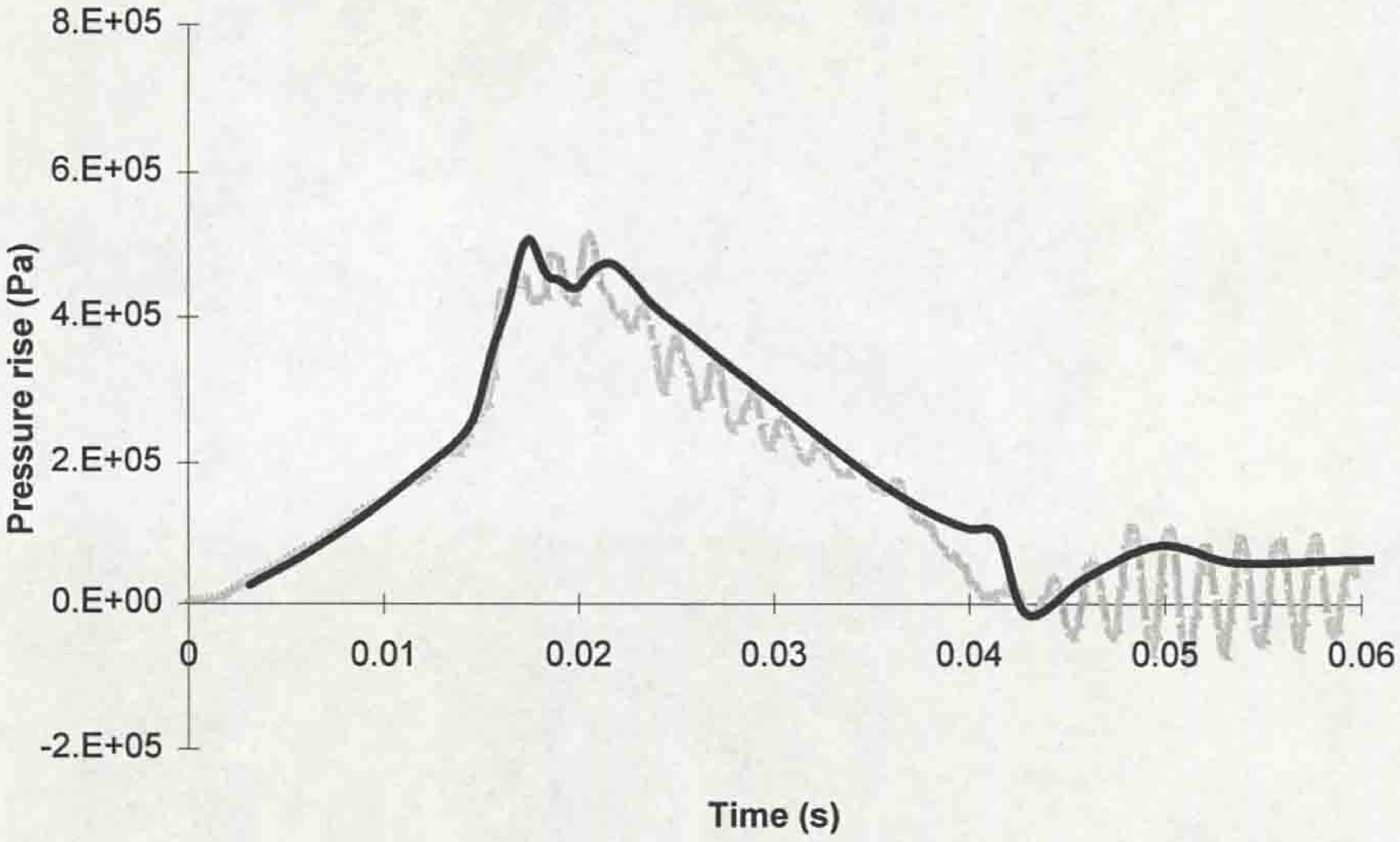

Figure 11.11 - Piston pressure comparison at 30kA

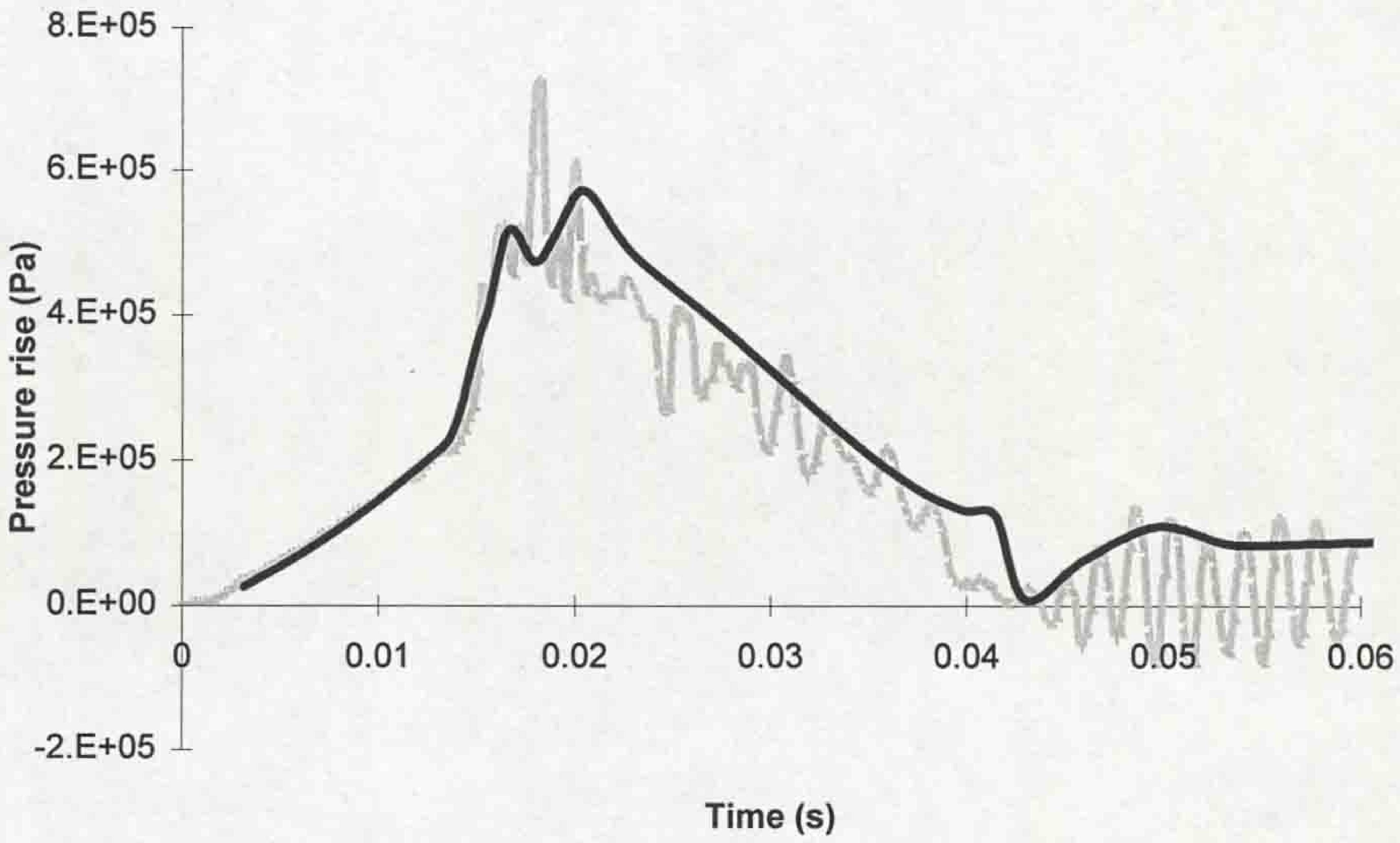

Figure 11.12 - Piston pressure comparisons at 45kA

11.2 FURTHER ANALYSIS OF THE OPTICAL RADIATION FROM THE CIRCUIT BREAKER ARCS

In **4.3** it was shown that for a chromatic distimulus detector, such as the PD150 used in this work, the detector responsivities of PD1 and PD2 (fig.4.19) will result in two short circuit currents, I_1 and I_2, when a spectrum of light is incident on the device. For a light spectrum E(λ), which has been modulated by the function M(λ), these short circuit currents will be given by

$$I_1 = \int_{\lambda_1}^{\lambda_2} E(\lambda)M(\lambda)R_1(\lambda)d\lambda \qquad (11.11a)$$

$$I_2 = \int_{\lambda_1}^{\lambda_2} E(\lambda)M(\lambda)R_2(\lambda)d\lambda \qquad (11.11b)$$

where R_1 and R_2 are the relative spectral responsivities of PD1 and PD2 and λ_1 and λ_2 are 500nm and 1000nm respectively (the working wavelength range of the PD150 based LIBIDO system). The ratio of the short circuit currents I_1/I_2 can then be used to identify the dominant wavelength of the incident light spectrum using the relationship on fig.4.20.

Figs.10.10 and 10.11 both showed the time variation of the dominant wavelength of the optical radiation received by the LIBIDO system, during interruption of varying levels of fault current. In fig.10.10 this radiation was that emitted directly from the arcing region. The results on fig.10.11, on the other hand, were obtained using the particle concentration monitor, which possessed its own tungsten halogen source. Therefore, the results on fig.10.11 correspond to the dominant wavelengths of the net spectrum of incident light, which is the combined effect of the sensor's source and the radiation emitted from the arcing region.

The potential sources of optical radiation which gave rise to the results on figs.10.10 and 10.11 can be identified as (fig.11.13):

- Radiation emission from the arc plasma column E_{col}. This may be expected to be influenced by the length of the column l (which is effectively the contact travel) and the power dissipated by the arc in the gas, vi where v is the arc voltage and i, the instantaneous arc current ($i = I_0 \sin\omega t$, where I_0 is the peak current and t the arc burning time). Hence $E_{col} = f(\lambda, vi, l)$.
- Radiation emission from the circuit breaker electrodes E_{elect}. It would be expected that $E_{elect} = f(\lambda, i)$.
- Radiation emission from the metal vapour core entrained into the arc plasma (see fig.3.18) E_{vap}. The radiative effect of the vapour core would be expected to depend on the contact travel l and the arc current. Thus, $E_{vap} = f(\lambda, i, l)$.
- Light from the tungsten halogen lamp source E_{lamp} (applies to fig.10.11 only). This is constant in time and independent of the arc current so $E_{lamp} = f(\lambda)$.

However, in addition to the sources of radiation described above, there are several modulating effects, which will affect the radiation from the arcing region. These effects are

- The modulating effect due to gas pressure M_{press}. Aubrecht and Gross (1994) and Strachan *et al* (1977) have identified the importance of gas pressure P on the total radiation loss (figs.3.10 and 3.12). Thus $M_{press} = f(P)$. (P itself depends upon the contact travel l, which determines the piston chamber volume, and electrical input energy vi from the arc).

- The modulating effect due to nozzle ablation M_{ablat}. This was considered to be an important effect on total radiation loss by Leclerc and Jones (1982) and Shimmin (1986), although it may also possess wavelength dependence. M_{ablat} is expected to be dependent upon the electrical power input by the arc, vi. Thus $M_{ablat} = f(\lambda, vi)$.
- The modulating effect of decomposition particles produced during arcing M_{part}. This has already been proved to possess a wavelength dependence in this thesis (**chapter 6**). This effect is dependent upon the concentration C of particles in the gas (which in turn will depend upon the power dissipated by the arc, vi). Thus $M_{part} = f(\lambda, C)$.

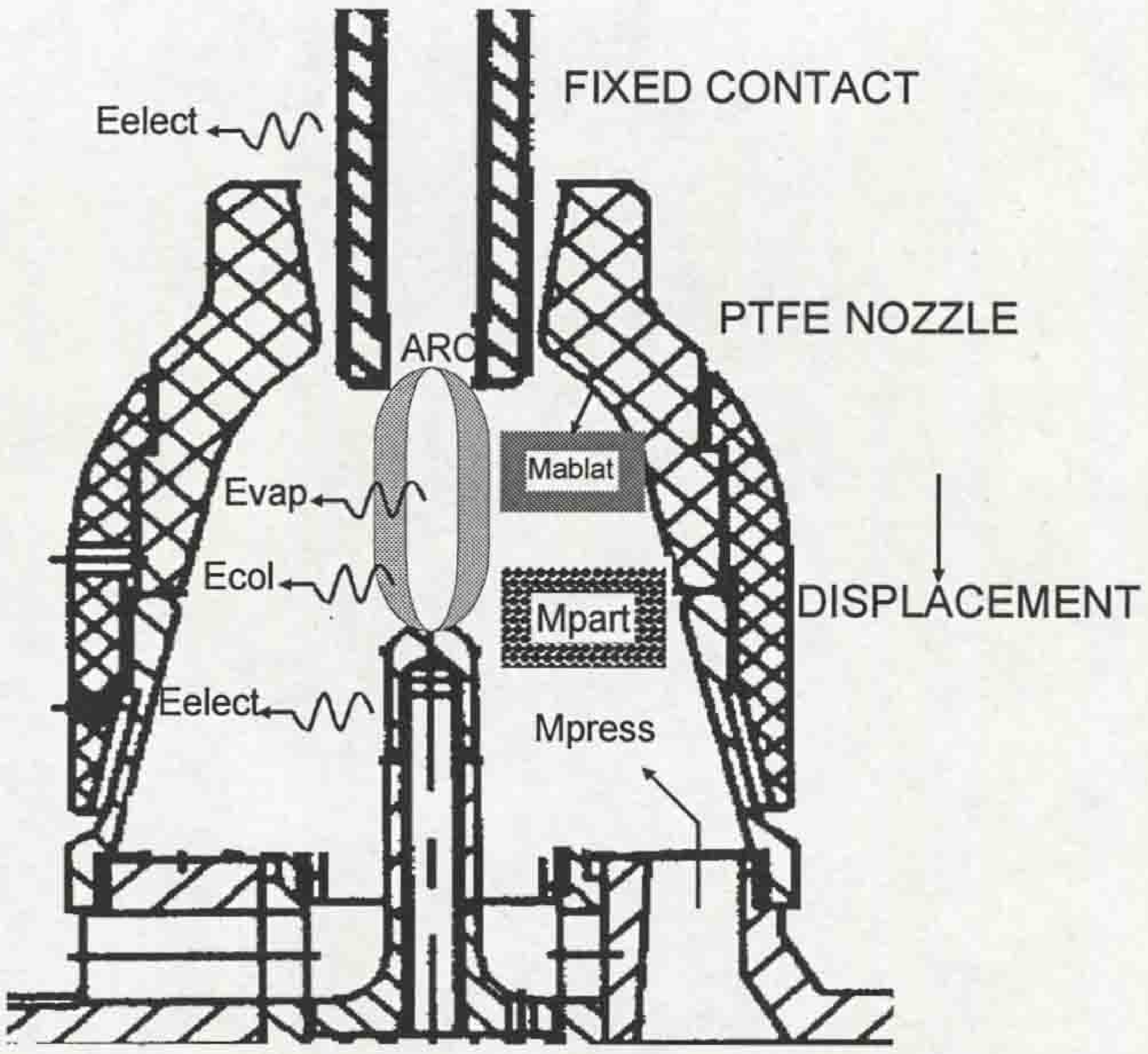

Figure 11.13 - Emissive and modulatory effects on radiation in the arcing region

The chromaticity of the net spectrum of light incident upon the detector may now be expressed by the following equation, which includes the tungsten halogen lamp source as well as the arcing region effects

$$C = \frac{I_1}{I_2} = \frac{\int_{\lambda_1}^{\lambda_2} \left(\left[E_{arcingregion}\right] * \left[M_{arcingregion}\right] + E_{lamp}(\lambda) * M_{part} \right) R_1(\lambda) d\lambda}{\int_{\lambda_1}^{\lambda_2} \left(\left[E_{arcingregion}\right] * \left[M_{arcingregion}\right] + E_{lamp}(\lambda) * M_{part} \right) R_2(\lambda) d\lambda} \qquad (11.12a)$$

where $E_{arcingregion} = E_{col}(\lambda, vi, l) + E_{elect}(\lambda, i) + E_{vap}(\lambda, i)$ (11.12b)

and $M_{arcingregion} = M_{press}(P) * M_{ablat}(\lambda, vi) * M_{part}(\lambda, C)$ (11.12c)

The results on fig.10.10 describe the chromaticity of the radiation from the arcing region alone i.e. no tungsten lamp source and, therefore, $E_{lamp} = 0$ in this situation. The chromaticity C would convert into the dominant wavelength λ_D for the resultant light spectrum at the detector with fig.4.20. It is evident that the dominant wavelength of this resultant spectrum is determined by a complex combination of radiative and modulatory effects. These effects themselves are functions of fundamental parameters, such as arc voltage, arc current, gas pressure, contact travel and particle concentration.

Figs.10.10 and 10.11 showed the time variation of dominant wavelength of the resultant optical radiation received at the detector. However, several authors (eg. Leclerc and Jones, 1982 - fig.3.14) have plotted total radiation loss measurements as a function of instantaneous current, with peak current as a parameter, in order to elucidate further information from the results. Fig.11.14 shows the dominant wavelength of the radiation emitted from the arcing region alone ($E_{lamp} = 0$), as a function of instantaneous current.

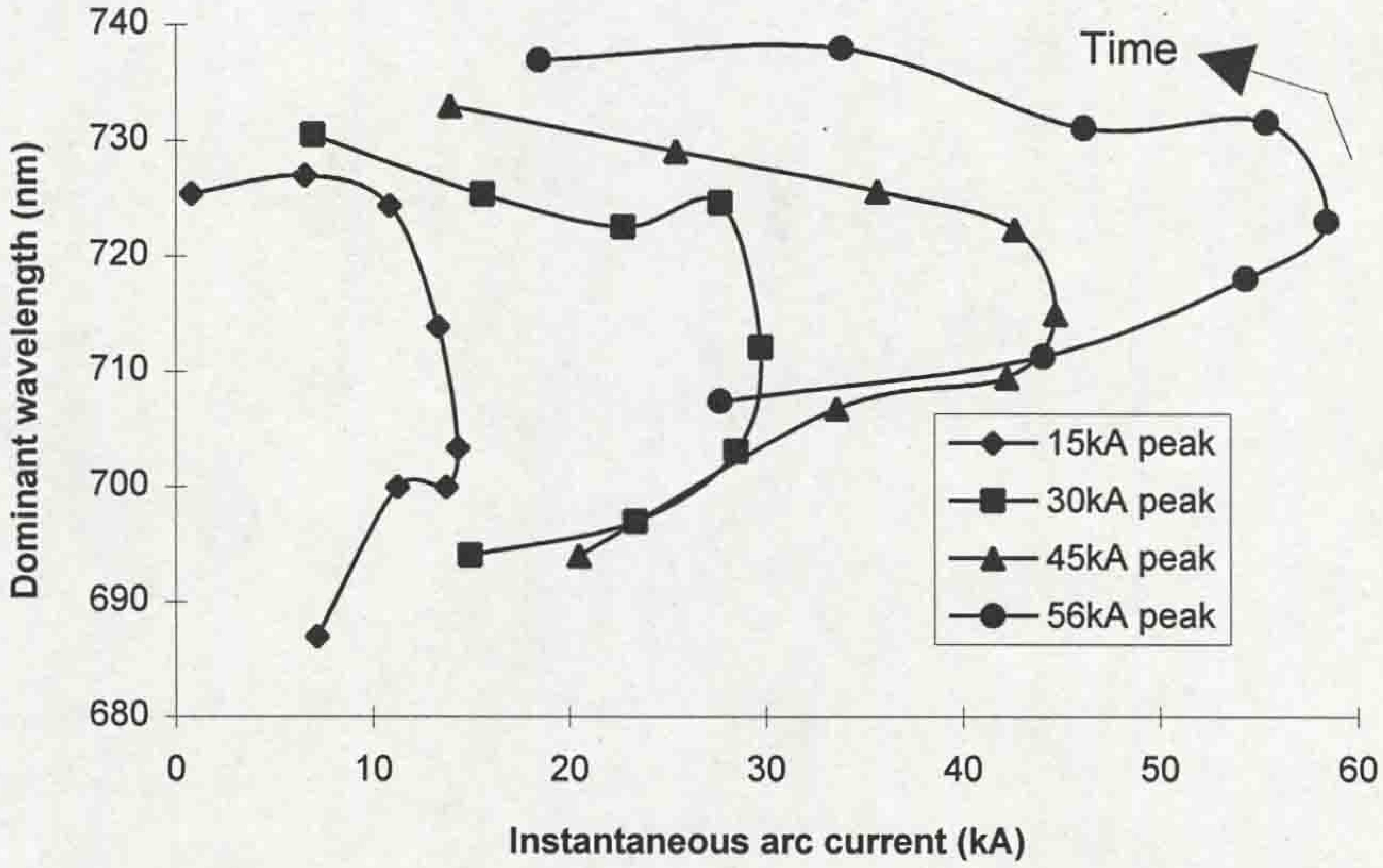

Figure 11.14 - Dominant wavelength of radiation emitted from arcing region as a function of instantaneous arc current for different peak currents (results from fig.10.10)

In the case of the results from the particle concentration monitor (fig.10.11) the dominant wavelength is that of the combined effect of the tungsten halogen source and the arc. Since the tungsten halogen source remains constant in amplitude, the dominant wavelength can be considered to be an indicator of the total radiation from the arcing region, since its variation reflects the relative intensity variation of the arc light. Fig.11.15 shows the dominant wavelength as a function of instantaneous current for the results of fig.10.11 (i.e. including the halogen source).

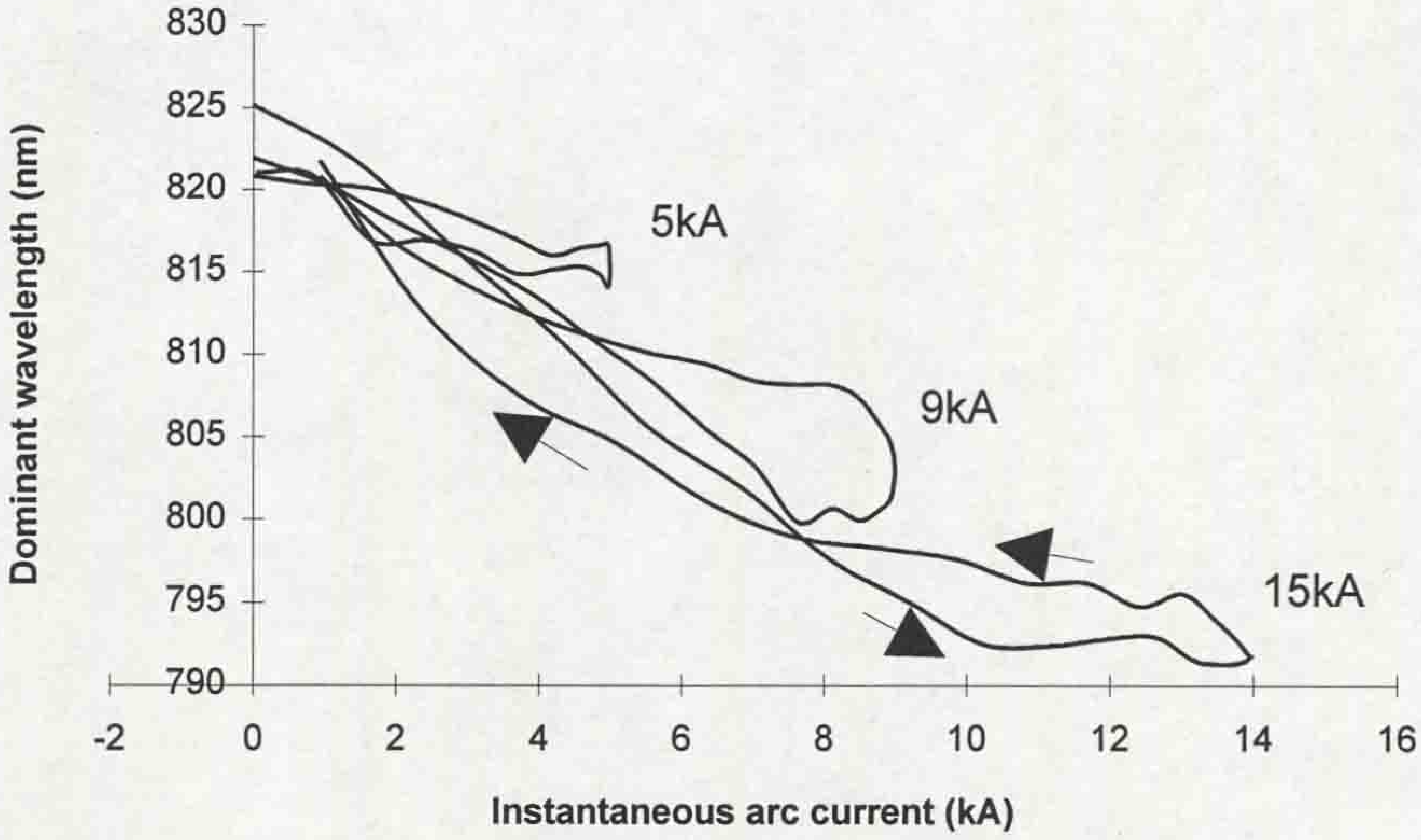

Figure 11.15 - Dominant wavelength of radiation emitted from arcing region combined with the tungsten lamp of the particle concentration monitor as a function of instantaneous arc current for different peak currents (results from fig.10.11)

Discussion of fig.11.14

The first observation from fig.11.14 is that during the increasing portion of the half-cycle of arc current, for peak currents of 30, 45 and 56kA, the dominant wavelength increases with instantaneous arc current, while peak current appears to have little effect. However, it is apparent that after the current peak is reached on the traces (~5ms, each point representing a 1ms time interval) the dominant wavelength shows some dependence on peak current.

The general increase of dominant wavelength with instantaneous current during the increasing portion of the half-cycle, irrespective of peak current, is similar to the trends reported by Leclerc and Jones (1982 - fig3.14b) for total radiation loss.

During this period the plasma radius increases with instantaneous current, suggesting that the emission term E_{col} in eqn.11.12 is influenced by instantaneous current.

Leclerc and Jones reported a radiation loss increase at 2ms following arc initiation, which was attributed to electrode vapour entrainment. Typical electrode line spectra are shown on fig.3.16 (Airey, 1977) to have wavelengths of ~510-530nm. Thus the effect of E_{vap} in eqn.11.13 would be to reduce the dominant wavelength of the resultant radiated spectrum. It is interesting, therefore, to note that from 2ms to 3ms on the 15kA and 45kA current traces on fig.11.14 there is a gradient reduction in the dominant wavelength, which may indicate electrode vapour entrainment consistent with the findings of Leclerc and Jones. However, the effect is not particularly pronounced and it is not seen on the 30kA and 56kA results, suggesting that the plasma column term E_{col} dominates.

If there is a chromatic modulation effect from gas pressure, M_{press}, it is difficult to identify at this stage. It has been shown (figs.10.7) that the pressure in the arcing region increases with peak current. The small increase of dominant wavelength with peak current may be due to a corresponding pressure increase, but the effect of instantaneous current on E_{col} is believed to dominate the resultant spectrum during the increasing portion of the half-cycle.

Leclerc and Jones concluded that the reduction in total radiation loss could be attributed to absorption by ablated products, which increase in concentration with current. Fig.11.16 shows the transmission characteristic of a 1mm thick slice of PTFE from the circuit breaker nozzle.

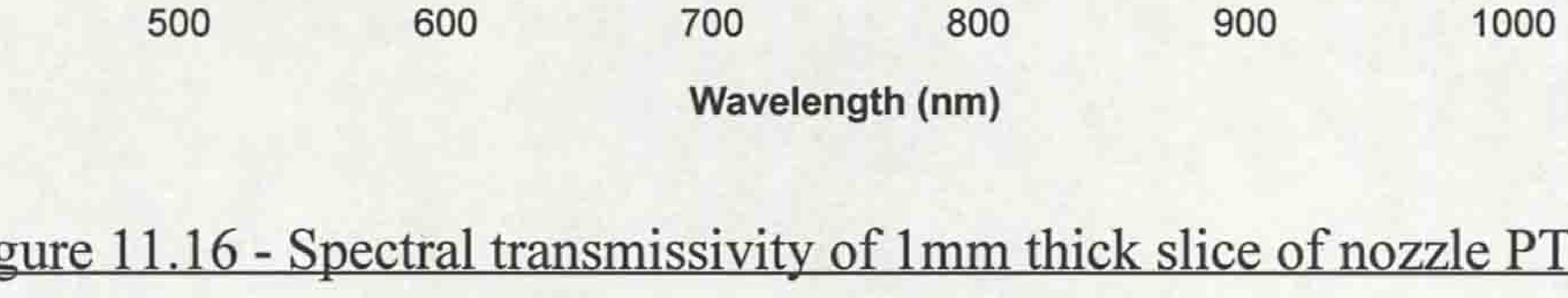

Figure 11.16 - Spectral transmissivity of 1mm thick slice of nozzle PTFE

It can be seen that the PTFE transmits more readily in the visible region of the spectrum. Therefore, in chromaticity terms, M_{ablat} in eqn.11.12 would tend to reduce the dominant wavelength of the resultant spectrum, as the concentration of ablated PTFE surrounding the arc increased. In opposition to this effect is the Mie scattering of radiation by arc-induced degradation particles, M_{part}, which was shown in **chapter 6** to shift the dominant wavelength upwards, due to increased scattering of the shorter wavelengths. Since both of these effects, M_{ablat} and M_{part}, are attempting to shift the dominant wavelength of the spectrum in opposite directions, they may tend to cancel each other's effect.

The remaining factor, which could then explain a higher level of dominant wavelength near arc extinction to that soon after arc initiation could be due to the electrode heating effect, E_{elect}. As the contacts get hotter with arcing they will emit a greater proportion of infra-red radiation. Since the contacts will dissipate heat more slowly than the plasma column collapses, during the decreasing portion of the half cycle, the term E_{elect} in eqn.11.12 will become more significant, while E_{col} will become less significant. The overall effect would then be an upward shift in dominant wavelength, as observed on fig.11.14.

Discussion of fig.11.15

It was noted above that in fig.11.14 the peak current had a relatively minor effect on the dominant wavelength of the resultant spectrum radiated from the arcing region. However, on fig.10.11, which showed the dominant wavelength variation observed at the detector with the tungsten lamp source (E_{lamp}) superimposed on the spectrum from the arcing region, the peak current showed a significant effect. The implication of this is that, since E_{lamp} is temporally constant, the dominant wavelength shifts on fig.10.11 are largely due to intensity changes of the arc. Therefore, by plotting dominant wavelength against instantaneous current, for different peak currents, as on fig.11.15, these results effectively represent total radiation loss trends, which may then be compared directly with the observations of Leclerc and Jones (fig.3.14).

There is good agreement between the two sets of results, since there is little hysteresis present on both sets for the current levels involved (up to 15kA peak). The looping effect on fig.11.15 for the higher current profiles (9kA and 15kA) indicates a reduction in radiation intensity from the arcing region, which may be indicative of the absorption effects reported by Leclerc and Jones and also Shimmin (1986).

The existence of several competing emissive and modulatory effects on the results obtained (figs.10.10, 10.11, 11.14 and 11.15) make it difficult to identify the precise role played by each effect, although the preceding discussion has highlighted the probabilities. Further investigations are, therefore, recommended (**12.5**), in which the overall problem may be simplified by performing a controlled set of experiments to eliminate some of the effects. This may result in an improvement in the understanding of the resultant radiated spectrum and also allow a quantitative assessment of the significance of the individual emissive and modulatory effects.

11.3 ANALYSIS AND DISCUSSION OF ENERGY TRANSFER MECHANISMS DURING FAULT CURRENT INTERRUPTION

In section **11.1.3.2** it was shown that the electrical energy input to the circuit breaker, during fault current interruption, is given by

$$E = \int_{t_1}^{t_2} VI\,dt \qquad (11.5)$$

The aim of this section is to investigate the transfer processes occurring for the redistribution of this energy during fault current interruption and, in doing so, to bring together collectively a number of the experimental and theoretical results reported previously in **chapter 10** and **chapter 11**.

11.3.1 Analysis and discussion of the energy transfer between the arc and the piston chamber based on estimates of gas temperature

It was calculated earlier (**11.1.3.2**) that the mass of gas within the circuit breaker was 10.5kg. The ratio of the piston volume to the main tank volume before arcing is calculated to be 1:40. From this ratio the mass of gas in the piston chamber can be estimated to be 0.263kg. The maximum possible temperature change in the piston volume during arcing, at the peak of the pressure waveform (here termed $\Delta T_{PISTON/ARCING/PEAK/LIMIT}$) can be calculated by assuming that all of the electrical input energy, E, is absorbed by the gas and equally distributed throughout the volume (isothermal). The temperature increase would then be calculated by eqn.11.8 (**11.1.3.2**) with M=0.263kg, which gives

$$\Delta T_{PISTON/ARCING/PEAK/LIMIT} = 0.0063E \qquad (11.13)$$

A graphical representation of this relationship is shown on fig11.17. This shows that the piston chamber gas temperature does not reach the dissociation temperature for SF_6 (1600K), for the operating current range of the circuit breaker, which means that the gas can be treated as ideal in this analysis.

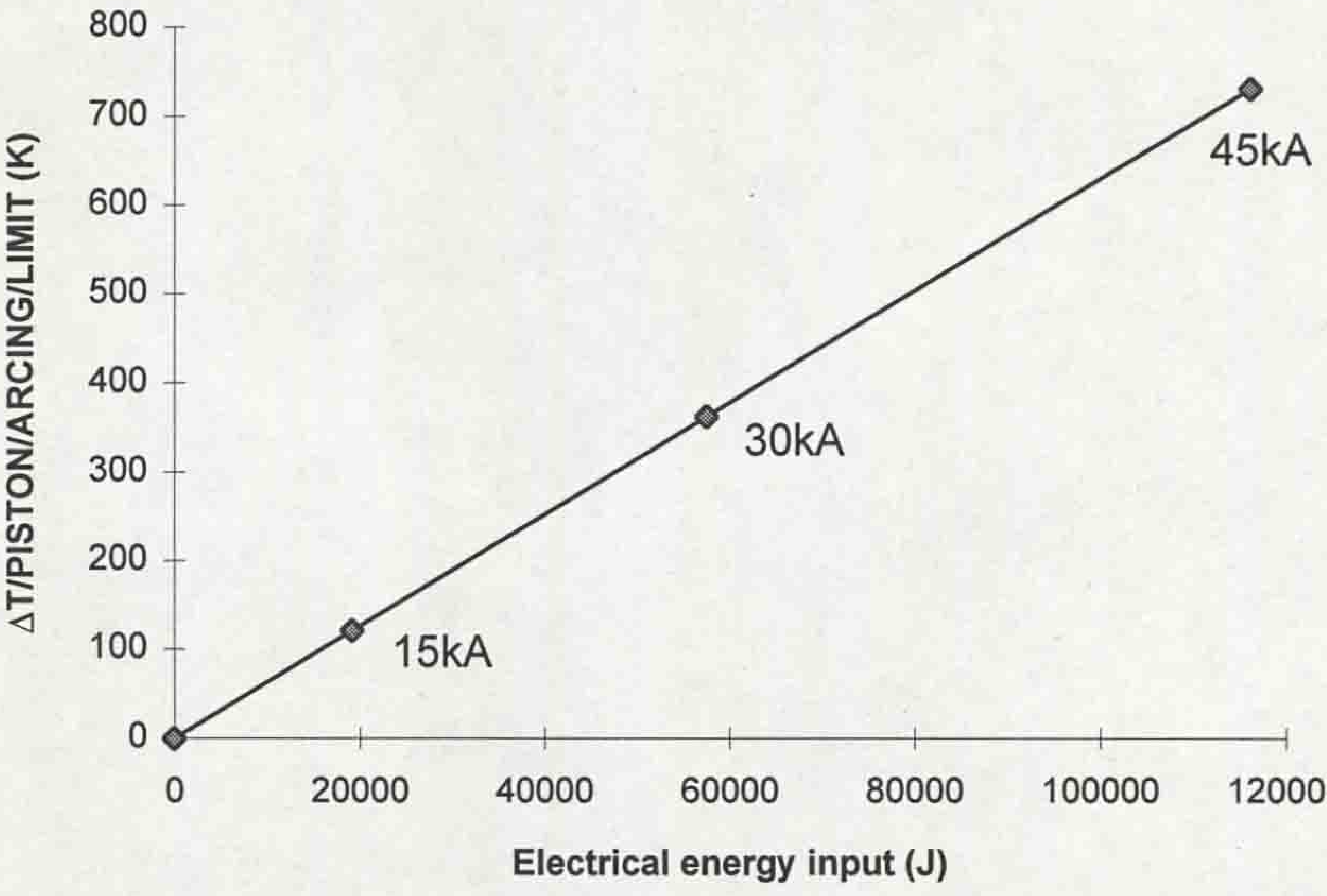

Figure 11.17 - Maximum possible temperature rise in piston chamber ($\Delta T_{PISTON/ARCING/PEAK/LIMIT}$) based on total isothermal absorption of input energy

The actual temperature change of the piston gas, during arcing, may be estimated by considering the piston pressure increases above the coldflow case for the range of currents in fig.11.17, again assuming isothermal conditions. Using the piston pressure results of **11.1.4.2** the parameter $\Delta P_{PISTON/ARCING/PEAK}$ may be plotted as a function of the electrical input energy, where $\Delta P_{PISTON/ARCING/PEAK}$ is defined as the increase in peak piston pressure caused by arc heating (i.e. the peak piston pressure at each current level minus the peak piston pressure during coldflow). $\Delta P_{PISTON/ARCING/PEAK}$ has been calculated using the CFD model results of figs.11.10, 11.11 and 11.12, subtracting the coldflow CFD results of fig.11.7. It was shown in **11.1.4.2** that these results agree well with the measured piston pressure waveforms at their peak, if account is taken of the oscillations in the measured values. Fig.11.18 shows the relationship between the CFD $\Delta P_{PISTON/ARCING/PEAK}$ and E.

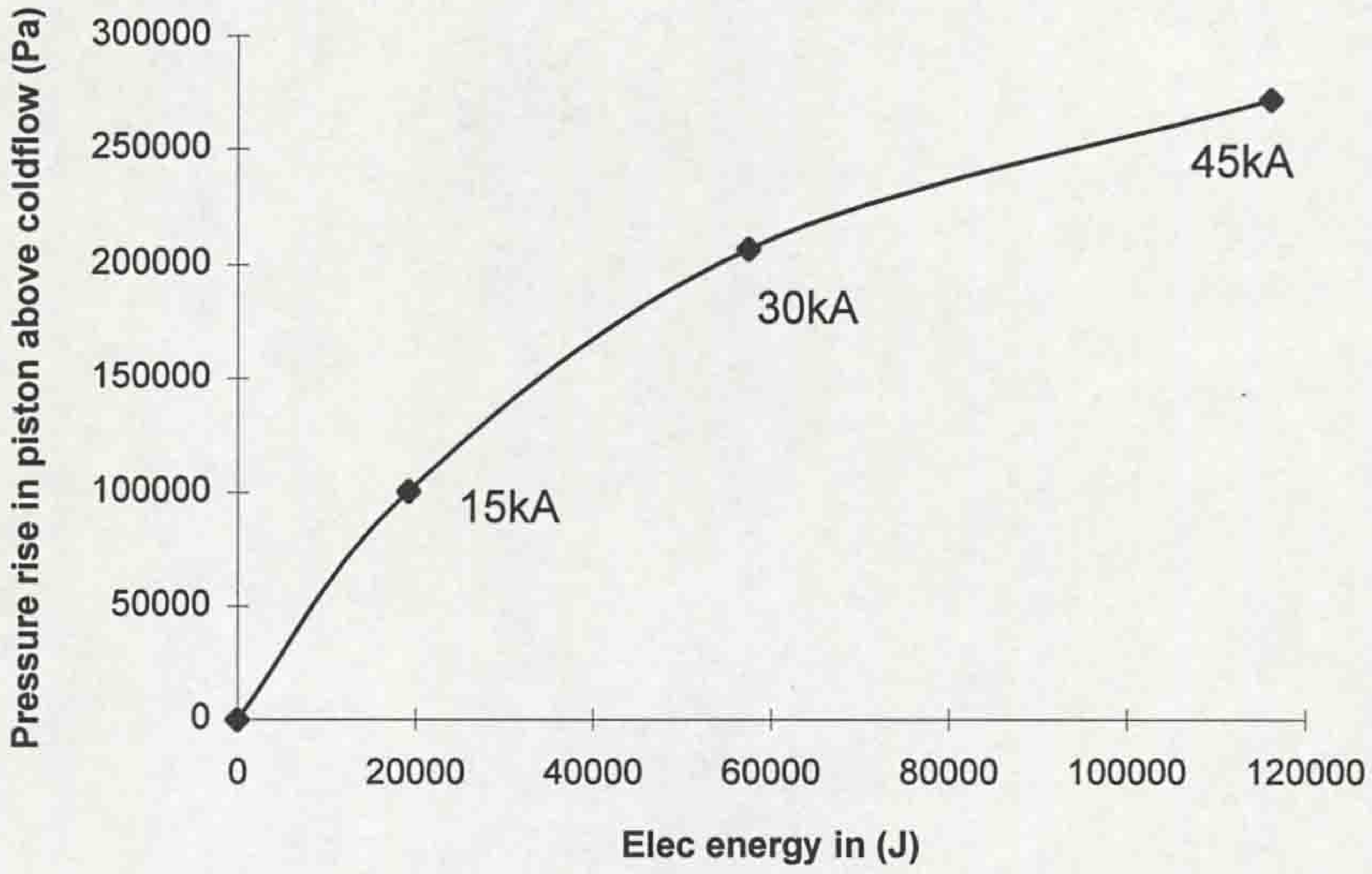

Figure 11.18 - Relationship between CFD $\Delta P_{PISTON/ARCING/PEAK}$ and electrical input energy

From the pressure results on fig.11.18 and using the ideal gas law it is possible to estimate the actual gas temperature increase in the piston chamber, $\Delta T_{PISTON/ARCING/PEAK}$. It can be assumed that the gas is ideal in the piston chamber, since fig.11.17 suggests that it does not dissociate. Thus

$$\frac{P}{T} = \frac{P + \Delta P_{PISTON/ARCING/PEAK}}{T + \Delta T_{PISTON/ARCING/PEAK}} \qquad (11.14)$$

where P and T are the peak pressure and temperature in the piston for coldflow ($10x10^5$Pa and 293K). This gives

$$\Delta T_{PISTON/ARCING/PEAK} = 2.93x10^{-4}\,\Delta P_{PISTON/ARCING/PEAK} \qquad (11.15)$$

By using the $\Delta P_{PISTON/ARCING/PEAK}$ values from fig.11.18 and eqn.11.15 above, the estimated values for $\Delta T_{PISTON/ARCING/PEAK}$ may be plotted against the arc energy input. The result is shown on fig.11.19, along with the maximum possible temperature, $\Delta T_{PISTON/ARCING/PEAK/LIMIT}$, from fig.11.17.

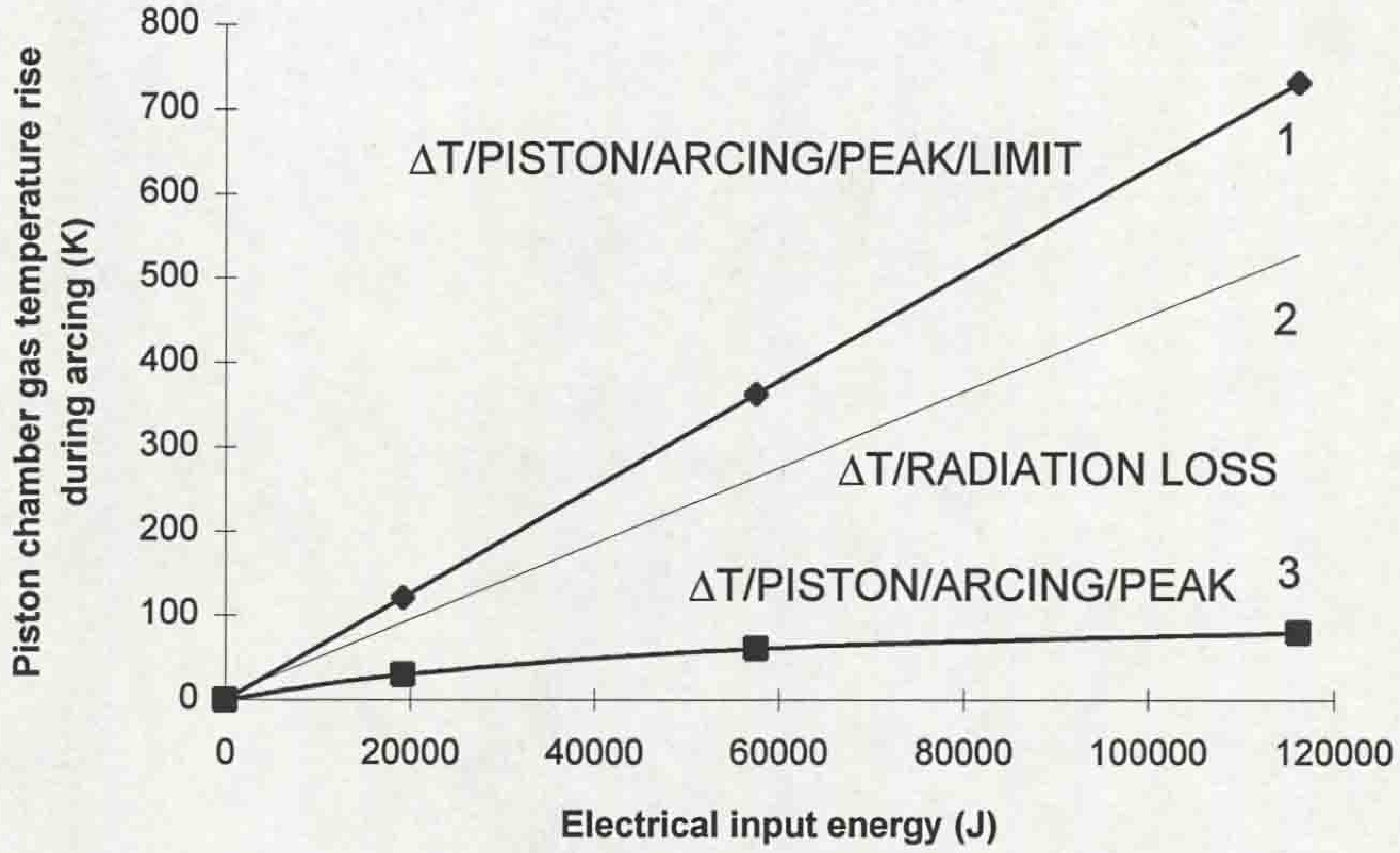

1. Estimated temperature rise from electrical input energy, E.
2. Radiation-corrected input energy.
3. Estimated temperature rise from measured piston gas pressure rise.

Figure 11.19 - Estimated increase in piston gas temperature based on pressure measurements in the piston chamber

According to fig.11.19, it is only a relatively small proportion of the arc energy which appears in heating the gas in the piston chamber. There are several reasons why this may be the case.

Firstly, there is energy lost due to optically thin radiation (i.e. radiation which is not re-absorbed by the SF_6 gas). This energy is difficult to define mathematically, since it is highly non-linear, but previous work by Shimmin (1986) has provided a reasonable yardstick, showing that around 25% energy loss under similar arcing conditions is by transparent transmission to the chamber walls. This radiated lost energy does not contribute to gas heating in the piston chamber and should, therefore, be subtracted from the total energy input used for these calculations (shown on fig.11.19).

Secondly, the partial duo-blast puffer interrupter (fig.2.8b) is designed with subsidiary flows to reduce contact vapour in the arcing zone, such that mass, and consequently energy, is directed through side vents in the interrupter rather than into the piston chamber. The energy lost in this process is difficult to quantify, but is accommodated within the CFD model, on which curve 3 is based.

A third energy loss mechanism relates to the ablation of the PTFE nozzle, due to its radiative loading from the arc. The effect is to inject the ablated mass into the piston chamber and, hence, to increase the pressure in the chamber (Ryan and Jones, 1989). This energy is also difficult to define mathematically, but again is accommodated in the CFD package.

The fourth energy loss process which may occur is due to absorption of heat by the particles produced during arcing. At present this is outside the scope of the CFD model. Fig.10.12 showed that particle concentrations of up to 60mg/litre might be produced at the higher currents. The circuit breaker volume of 250litres suggests that up to 15g may be produced during arcing, which represents only 0.1% of the mass of SF_6 gas in the whole circuit breaker, but 6% of the mass of gas in the piston chamber. **Appendix IV** includes calculations to investigate possible energy absorption by the particulate material, based on the specific heat capacities of its constituent elements. Such calculations show that the particle energy absorption is small with respect to the energy losses observed on fig.11.19, though the losses may become significant if the particles are assumed to be at elevated temperatures above the SF_6 gas.

To summarise, four energy loss mechanisms between the arc and piston chamber have been identified and discussed. They are the radiation loss during arcing, the lost energy caused by subsidiary flow from the arc to the main tank rather than the piston (via side vents), ablation of the PTFE nozzle and the retention of heat by the arc-induced particulates. The radiation loss and particle loss have been discussed quantitatively. The subsidiary flow and nozzle ablation losses are difficult to define mathematically; however, it is shown in **Appendix IV** that at a mid-range current of 30kA the combined losses from subsidiary flow, nozzle ablation and particle energy absorption (termed $\Delta E_{RESIDUAL\ LOSS}$) amount to 58% of the input electrical energy (E) from the arc.

11.3.2 Consideration of the energy exchange between the piston chamber and main tank

This section discusses further the energy transfer processes, based on comparisons of pressure measurements and theoretical predictions in the piston chamber and main tank. For such a consideration it is necessary to include a number of different transient pressure rises as indicated below.

The increase in peak piston pressure $\Delta P_{PISTON/ARCING/PEAK}$, caused by arc heating, is given by the peak piston pressure at each current level minus the peak piston pressure during coldflow (same definition as in **11.3.1**). $\Delta P_{PISTON/ARCING/PEAK}$ has been calculated using the CFD model results of figs.11.10, 11.11 and 11.12 and subtracting the coldflow results of fig.11.7 (it was shown in **11.1.4.2** that there is good agreement between these results and the measured transients).

The peak piston pressure rise, during arcing, $\Delta P_{PISTON/ARCING/PEAK}$ may be compared directly with the post-arc increase in tank gas pressure, $\Delta P_{TANK/POST-ARC/MEASURED}$, where , $\Delta P_{TANK/POST-ARC/MEASURED}$ is the increase in tank gas pressure caused by arcing and is calculated by subtracting the pre-arc ambient pressure from the tank pressure measured 1sec after arcing (as defined in **11.1.3.2**). The ratio of the piston volume (average) during arcing to the tank volume is 1:70. Therefore, the term $(\Delta P_{PISTON/ARCING/PEAK})/70$ is introduced to indicate 1/70th of the peak piston pressure rise, so that it may be plotted on fig.11.20 below with tank pressure rises.

The potential limit of the post-arc tank pressure rise, $\Delta P_{TANK/POST-ARC/LIMIT}$, is based on the assumption that all of the electrical input energy, E, is absorbed by the SF_6, which is isothermal and ideal (the same definition as in **11.1.3.2**).

The measured rise in piston chamber pressure above the coldflow case, after arcing has occurred and the interrupter has completed its travel, may be defined as $\Delta P_{PISTON/POST-ARC/MEASURED}$. On figs.11.10-11.12 it is the average of the oscillatory period between 0.05 and 0.06s.

The CFD model predicted rise in piston chamber pressure, above the coldflow case, after arcing has occurred and the interrupter has completed its travel is defined as $\Delta P_{PISTON/POST-ARC/CFD}$. On figs.11.10-11.12 it is the plateau region between 0.05 and 0.06s.

Fig.11.20 below shows each of the terms above plotted as a function of electrical input energy E.

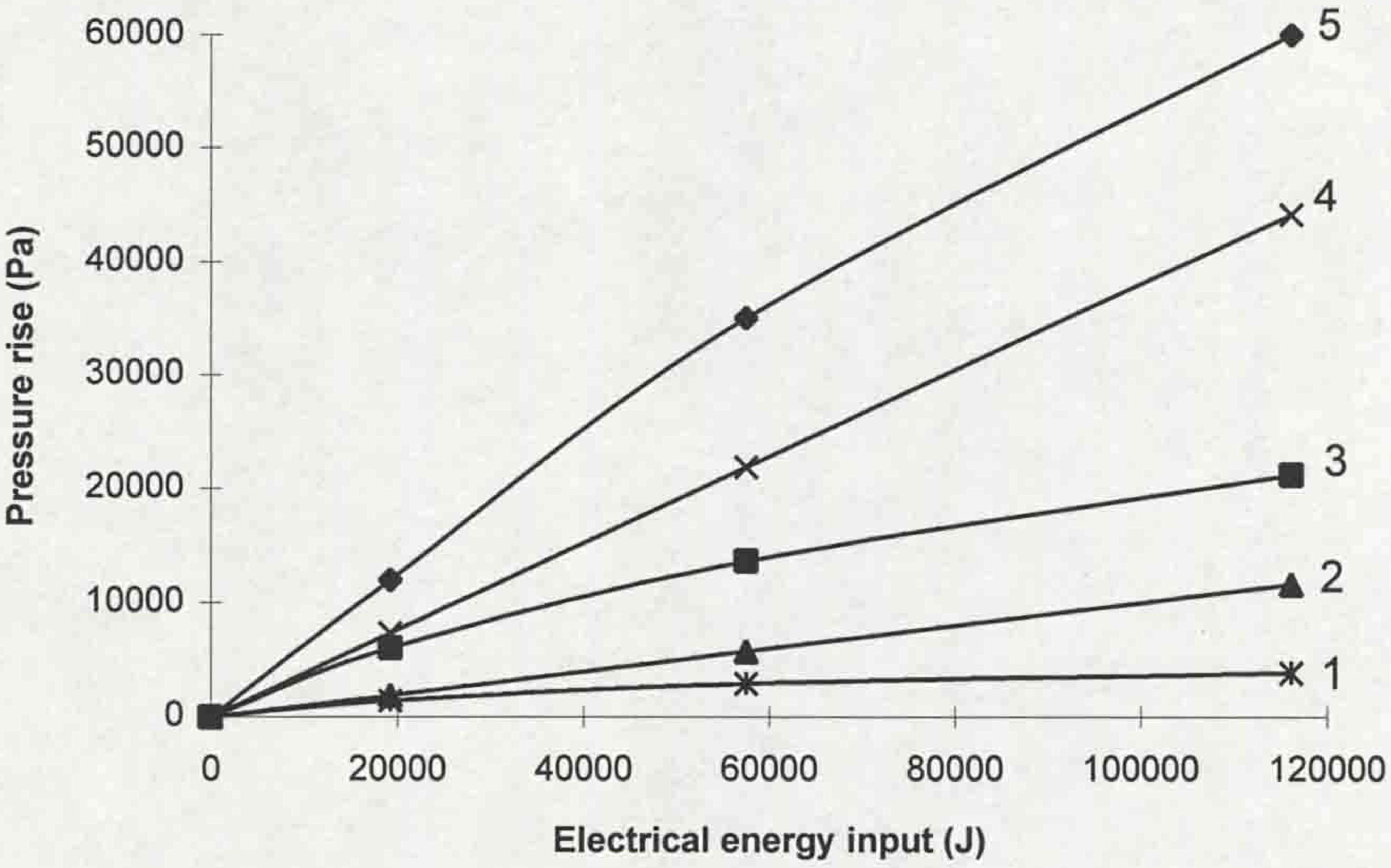

1. $(\Delta P_{PISTON/ARCING/PEAK})/70$.
2. $\Delta P_{TANK/POST-ARC/MEASURED}$.
3. $\Delta P_{PISTON/POST-ARC/MEASURED}$.
4. $\Delta P_{TANK/POST-ARC/LIMIT}$.
5. $\Delta P_{PISTON/POST-ARC/CFD}$.

Figure 11.20 - Comparison of the various measured and predicted pressure rises in the piston chamber and main tank.

The tank pressure (curve 2) is taken as the comparator curve. It is to be expected that this curve should be similar to the measured post-arc piston pressure (curve 3). Considering the need for sufficient time for gas mixing in the tank, the difference between curves 2 and 3 is not regarded as significant.

Superficially, the peak pressurisation in the piston chamber during arcing may also be compared with the post-arc tank pressure. Thus, converting the piston pressure rise for the greater volume (x70) of the tank, as described above, with the ideal gas law, produces curve 1. The pressures associated with curve 1 are lower than the measured tank pressures (curve 2). A possible explanation of this difference may be the leakage of gas from the piston chamber via the hollow contacts and side vents during arcing. The difference between curves 1 and 2 would therefore indicate the magnitude of this gas leakage.

Curve 5 on fig.11.20 corresponds to the CFD predicted post-arc piston pressure, which clearly exceeds both the measured piston and measured tank pressure. Indeed these CFD predicted values also exceed the values predicted from the electrical energy dissipated in the arc (represented by curve 4). These factors taken together suggest that the CFD results over-estimate the post-arc pressurisation.

11.3.3 Conclusions

The discussion concerned with integrating the results of the various measurements described in **chapter 11** show a general, although incomplete, coherence. There is a general correlation between the experimental pressure rises measured. The largest discrepancy appears to be associated with the CFD predicted post-arc pressure in the piston chamber, which may be due to the difficulty of theoretically modelling the auxiliary venting of the gas from the piston chamber, via a series of different orifices, during arc interruption.

Of particular significance from these analyses is that an approximate indication of the relevance of the particulate material formed by arcing in SF_6 has been gained. In general terms it is only about 0.1% of the mass of SF_6 in the circuit breaker, which appears as particulate material even after heavy duty arcing. Approximate calculations indicate that such a level of particulate material, after arcing, would not have a significant effect on the thermal storage of energy dissipated, if thermal equilibrium is assumed. However, if it is assumed that, during arcing, the particles are at an elevated temperature, with respect to the surrounding SF_6 gas, then 10-20% of the electrical input energy losses (radiation corrected) could be stored in the particles whose temperatures rise by 400-800K (**Appendix IV**).

This refers to longer term effects, which would be governed by diffusive and mixing effects. If this were indeed to be the case, the thermal absorption effects of the particles, close to their origin in the smaller volume piston chamber (~1/70th the volume of the main tank), could possibly become quite significant. Such aspects of the particle behaviour warrant further investigation.

CHAPTER 12 - CONCLUSIONS AND RECOMMENDATIONS

12.1 OPTICAL FIBRE LINEAR TRAVEL RECORDER

An optical fibre linear travel recorder (OFLTR) was developed to monitor the electrode separation of the puffer circuit breaker, during fault current interruption. The device provided a resolution of <1mm over the 200mm dynamic range, which was within the commercial specification (2mm). The prototype OFLTR showed that the opening stroke of the interrupter did not possess any significant dependence on the arc current, due to the stiffness of the driving mechanism.

The prototype travel recorder registered over 100 operations of the circuit breaker, at various levels of fault current, before overhaul was necessary. It was found that the tips of the optical fibres, which addressed the modulating transducer scale, had been attacked by hydrogen fluoride gas, which is produced within the circuit breaker during arcing. This caused a gradual weakening of the detected signal, which eventually fell below the detection threshold.

It is recommended that an investigation be conducted into suitable sealing materials, which are non-porous (the cork seal used was penetrated by the HF), to protect the fibre tips from HF attack. If this can be achieved then the OFLTR would be at a stage of commercial viability, with a lifetime extending beyond that of the circuit breaker electrodes and nozzle.

12.2 OPTICAL FIBRE PARTICLE CONCENTRATION MONITOR

Using the principles of non-linear Mie scattering, an optical fibre particle concentration monitor (OFPCM) was developed and used to indicate the levels of degradation particles within the circuit breaker, following short-circuit current interruption. It was found that these particle concentrations increased with fault current.

The present system uses distimulus chromatic detection (two spectrally overlapping detectors), providing one output parameter only i.e. dominant wavelength. Therefore, no discrimination between the particle numbers and radii, which both contribute to the Mie scattering effect, can be made. However, if the modulated light signals were processed using a tristimulus system (three overlapping detectors), then two chromatic outputs would be obtained i.e. dominant wavelength and colorimetric purity. It may then be possible to conduct a controlled series of experiments to evaluate the effects of separately altering particle numbers and radii on each of the two chromatic variables, to see if any discrimination can be made between the two. If possible then the circuit breaker particles may be described both in terms of their numbers and size. This would be a suitable next development step.

The OFPCM was successfully employed to determine particle concentration levels during fault current interruption. The results obtained, in conjunction with gas pressure and electrical measurements, were used to analyse the energy loss mechanisms during arc interruption.

12.3 GAS DIELECTRIC STRENGTH PROBE

A gas dielectric strength probe was developed to monitor the dielectric strength of SF_6 gas within circuit breakers, following interruption of short-circuit fault currents. The system is characteristic of a hybrid optical sensor i.e. it measures an electrical parameter (in this case the breakdown voltage of the gas) but uses electro-optic and opto-electronic conversion techniques to allow the sensor and control room instruments to be linked entirely by optical fibres, thus maintaining the isolation to ground of the live circuit breaker elements.

The system was used initially on a rotary arc distribution circuit breaker. Distinct changes in gas dielectric strength, following current interruption, were observed, which showed some dependence on the current amplitude. By acknowledging several assumptions, which are listed in **chapter 7**, the gas temperature was estimated from the breakdown voltage values.

The system was also used on the main test circuit breaker for this work, to investigate the possibility of late breakdown in the circuit breaker, caused by hot gas re-entering the arcing zone. It was shown that the gas dielectric strength near to the top-plate did not change significantly after arcing, for the timescales used. Flow visualisation techniques (Heyes *et al*, 1995) confirmed that this was due to major recirculation of hot gas at the shoulders of the fixed contact. It is proposed that further investigations with the dielectric probe system should concentrate close to the arcing region, with access provided by the central viewing ports on the experimental rig. The potential for arc reignition can then be assessed by the dielectric deterioration of the gas.

12.4 OPTICAL FIBRE GAS PRESSURE SENSORS

Two prototype optical fibre pressure sensors were designed around the recently developed micro-machined silicon Fabry-Perot cavities. The sensors were used to monitor gas pressure variations near the top-plate of the main circuit breaker tank and inside the piston chamber of the interrupter. Both sensors operated successfully, revealing pressure transients which varied with arc current. Oscillations were observed superimposed on the transients, which, on account of their oscillating frequency, might be due to standing waves set up in the housings.

It was shown that there is a direct relationship between the tank pressure rise after arcing (~1s) and the energy dissipated by the arc, which may be useful for condition monitoring purposes. It is suspected that the piston chamber pressures exceeded the upper limit of monotonicity of the silicon cavities at the highest currents. Therefore, it is recommended that commercial development of the sensors for circuit breaker application should include increasing their dynamic range. This is particularly important if the sensors are to be employed on other puffer circuit breakers, which may induce higher piston chamber pressures than the one tested in this project.

The gas pressure measurements proved to be of considerable relevance to the formulation of the energy transfer analysis section of the thesis (**11.3**).

12.5 CIRCUIT BREAKER RADIATION MONITORING

A novel technique for measuring the radiation emitted from the circuit breaker was employed. Rather than measuring the total radiation loss to investigate the effects of, for example, electrode vapour and nozzle ablation, as has traditionally been the case, the radiated spectra were processed chromatically to identify their dominant wavelength, with respect to the LIBIDO detection system used (500-1000nm range).

In principle it may be possible to identify the significance of each role played by the various radiative and modulatory effects during fault current interruption, which would yield an improved understanding of the physical processes occurring within the arcing region. This may require a further dismantling of the problem; for example, the nozzle of the interrupter may be removed to eliminate the modulation effect due to varying gas pressure (M_{press}) and nozzle ablation (M_{ablat}). Furthermore, by using a fuse-initiated arc between the fully open contacts, the variability of contact travel and arc voltage can be eliminated. Other possibilities include using a DC arc to eliminate the variation in instantaneous arc current. These are examples of how the problem of understanding the puffer circuit breaker radiative emissions can be dismantled into a manageable set of experiments. This approach is recommended as a continuation to the work in this project.

12.6 USE OF THE DIAGNOSTICS TO VERIFY THE MATHEMATICAL MODEL PRODUCED FOR THE TEST CIRCUIT BREAKER

A mathematical model for the test circuit breaker has been developed as the "sister project" to the experimental work described in this thesis. The model requires input from the travel recorder in order to calculate arc length, piston chamber volume and the position of the fixed contact in relation to the nozzle. Using the measured travel record, current through and voltage across the circuit breaker as primary inputs, the model predicted results which compared well with those measured by the piston chamber pressure sensor (figs.11.10-12). Since the piston chamber pressure sensor employs the recently developed micromachined silicon technique for optical fibre sensing, the agreement from the model reinforces the suitability of this technology for circuit breaker application.

12.7 APPLICABILITY OF THE DIAGNOSTICS TO CIRCUIT BREAKER CONDITION MONITORING

Fig.2.13 showed the potential circuit breaker interrupter failure mechanisms, which a condition monitoring system may aim to predict.

Gas pressures, both in the circuit breaker tank and piston chamber, would play an important role in such a system. The tank pressure sensor would fundamentally indicate gas leaks from the circuit breaker, but it has also been shown to be able to indicate the cumulative energy dissipated by the arc, which will, in turn, determine the amount of wear of the electrodes and nozzle. The nozzle wear can be more directly monitored by the piston chamber pressure sensor, since the piston chamber pressure will continue to reduce as the nozzle wears.

The travel recorder is regarded as an essential component of the future condition monitoring system. Since it has been shown that the opening stroke of the interrupter is largely independent of arc current, it can be assumed that any significant changes in the interrupter travel will most likely be caused by a mechanical malfunction, which may develop at the mechanism, at a defective link between the mechanism and interrupter unit, or at the interrupter unit itself. The location of the OFLTR in the interrupter unit could detect any of these problems, which is important if future mechanical failure is to be predicted.

Although the other sensors developed show promising initial results, further controlled experiments are recommended using, for example, electrodes and nozzles at various states of wear, to investigate whether patterns of behaviour can be observed on the sensors, which can be correlated against the internal conditions of the circuit breaker. If such patterns can be established then their role in the condition monitoring system could be identified. Overall, the development of the sensors has achieved the objectives described in **chapter 1**.

One of the major advantages of the optical fibre sensors developed in this work is that, apart from the gas dielectric strength probe, all of the sensors are operated by the commercially available LIBIDO distimulus chromatic source / detection system. This has the facility for eight source / detection channels sampling simultaneously at up to 4kHz. Therefore, a condition monitoring system based on this device may incorporate additional sensors (e.g. as shown on fig.2.13) to those developed in this work. Moreover, a condition monitoring system using a variety of sensors, which can all be operated by one piece of detection equipment (current cost ~£3000), has obvious cost advantages.

REFERENCES

AIREY, D.R. (1977)
Energy balance and transport properties of very high current SF_6 arcs.
PhD thesis, University of Bath.

ALI S.M.G., RYAN H.M., LIGHTLE D, SHIMMIN D.W., TAYLOR S and JONES G.R. (1985)
High power short circuit studies on a commercial 420kV 60kA puffer circuit breaker.
Trans. IEEE, PAS-104, No.2, February, pp459-467.

ALI S.M.G. and HEADLEY P. (1984)
Developments in modern EHV switchgear.
BEAMA - Tech. Seminar for PLN, Jakarta.

ASAWA C.K., YAO S.K., STEARNS R.C., MOTA N.L. and DOWNS J.W. (1982)
High sensitivity fibre-optic strain sensors for measuring structural distortion.
Electronics letters, Vol.18, No.9, 29 April, pp362-364.

AUBRECHT V. and GROSS B. (1994)
Net emission coefficient of radiation in SF_6 arc plasmas.
J. Phys. D: Appl. Phys., Vol.27, pp95-100.

BAKER B.P. and WILCOX H.W. (1930)
The use of oil in arc rupture.
Trans. Am. Inst. Elect. Eng. 49, pp431-446.

BARRAULT M.R. and JONES G.R. (1974)
Practical arcing environments - arc plasma diagnostics.
Proc. Invited Lectures 7th Yugoslav Symp. and Summer School on Physics of Ionized Gases (Rovinj, Yugoslavia) (Inst. of Physics, Zagreb Univ).

BEAVAN C. (1989)
Colour measurement in optical metrology.
PhD thesis, University of Liverpool.

BEHEIM G (1987)
Loss-compensation technique for fiber-optic sensors and its application to displacement measurements.
Appl. Opt. Vol.26, No.3, Feb, pp452-455.

BEJCZY A.K., PRIMUS H.C. and HERMAN W.A. (1980)
Fiber optic proximity sensor.
NASA Tech. Brief, Vol.4, No.3, item 63, JPL report NPO-14653/30-4279, March.

BELMADINI B., CASANOVAS J., CASANOVAS A.M., GROB R. and MATHIEU J. (1991)
SF_6 Decomposition under Power Arcs - Physical aspects.

IEEE Trans. on Elect. Insul., Vol.26, No.6, December, pp1163-1182.

BERGH R.A., LEFEVRE H.C. and SHAW H.J. (1984)
An overview of fibre optic gyroscopes.
J. Lightwave Technol., **2**, pp91-107.

BIERMANNS J. (1929)
Hochleistungschalter ohne OL.
Elektrotech. Z., 1929 - 2 pp1073-1079 and 1114-1119.

BIERMANNS J. (1938)
The AEG airblast breaker.
AEG Progress Report 1938-2.

BOIS E., HUARD S.J. and BOISDE G (1989)
Loss compensated fiber-optic displacement sensor including a lens.
Appl. Opt. Vol.28, No.3, Feb, pp419-420.

BROWNE (Jr.) T.E. (1948)
A study of arc behaviour near current zero by means of mathematical models.
Trans. Am. Inst. Electr. Eng., 67, Pt.I, pp141-153.

BROWNE (Jr.) T.E. (1984)
Circuit Interruption - Theory and Techniques.
Marcel Dekker, Inc.

CASSIE A.M. (1939)
Arc rupture and circuit severity.
CIGRE paper 102, pp1-14.

CHAARAOUI J.A. (1993)
Effects of high frequency arcing in SF_6 puffer interrupters from low inductive current switching.
PhD thesis, Univ. of Liverpool.

CHAPMAN A. (1977)
Electrical conductance of gas blast arcs.
PhD thesis, Univ. of Liverpool.

CHEN L. and VOUMARD P. (1992)
An intelligent condition monitoring, diagnosis and maintenance system for circuit breakers.
Proc. 1st Singapore Int. Conf. on Intelligent Systems, pp263-268.

CHERVY B., GLEIZES A. and RAZAFINIMANANA M. (1994)
Thermodynamic properties and transport coefficients in SF_6 - Cu mixtures at temperatures of 300-30000K and pressures of 0.1-1MPa.
J.Phys.D: Appl. Phys. 27, pp1193-1206.

CHRISTODOULOU M., DIXON C.M and HEYES A.L. (1996)
A moving boundary technique for modelling the operation of high voltage puffer type interrupters.
Rolls-Royce Applied Science Laboratory Internal Report.

CHU F.Y. (1986)
SF_6 decomposition in gas-insulated equipment.
IEEE Trans. Elect. Insul., Vol.EI-21, No.5, October, pp693-725.

COATES W.A. and PEARCE H. (1938)
Switchgear Handbook - Volume 1.
Pitman.

COOPER F.S. (1940)
Gas dielectric media, US Pat. 2221671.

COWLEY M.D. (1974)
Integral methods of analysing electric arcs.
J. Phys. D: Appl. Phys., Vol.7, pp2218-2245.

CROMER C.F. and FRIEDRICH R.E. (1956)
A new 115kV, 1000MVA gas filled circuit breaker.
AIEE Trans. 75 (ptIII), pp1352-1357.

CULSHAW B. (1984)
Optical fibre sensing and signal processing.
Peter Peregrinus Ltd., on behalf of the IEE.

DAKIN J.P. (1984)
Analogue and digital extrinsic optical fibre sensors based on spectral filtering techniques.
SPIE, Vol.468, Fibre optics 84 (SIRA), pp218-223.

DANCASTER J. (1993)
The development of a silicon optical Fabrey-Perot pressure sensor.
Report No. ADVE/S-E-0303, Lucas Advanced Engineering Centre.

DHAR P.K., BARRAULT M.R. and JONES G.R. (1979)
A multiring radio frequency technique for measuring arc boundary variations at high currents and close to current zero.
Univ. of Liverpool, Arc Research Report, ULAP-T64.

DIENEMANN H. (1983)
Material functions of sulphur hexafluoride.
J. Phys.D: Appl. Phys. 16, pp1651-1671.

DOTSCH H., MARTENS G. and MEYER, W. (1983)

Fibre optic components for industrial control.
1st Int. Conf. on Fibre Optic Sensors, London, April, pp67-71.

DUPLAY C. and HENNEBERT J. (1983)
The breaking process with Fluarc SF_6 *puffer and rotating arc circuit breakers and Rollarc contactors.*
Merlin-Gerin Service Information E/Ct 122.

EASLEY G.J. and TELFORD J.M. (1964)
New design 34.5-69kV intermediate capacity SF_6 *circuit breaker.*
IEEE Trans. Power Appar. Syst. 83 1172-1177.

EINSELE A. (1964)
The new Siemens F circuit breaker for 220kV, 15GVA.
Siemens Rev., 31, pp219-223.

ENNIS M.G., TURNER D.R., SPENCER J and JONES G.R. (1996)
Rotating arc interrupter with independent field excitation.
IEE Proc.-Sci. Meas. Technol. Vol.143, No.2 March, pp. 113-118.

ENNIS M.G.(1994)
Private communication.

FANG M.T.C. (1995)
Private communication.

FANG M.T.C. (1993)
Mathematical modelling of axially blown switching arcs.
Internal lectures, University of Liverpool.

FANG M.T.C. (1983)
A review of gas blast circuit breaker arc modelling.
Liverpool University, Arc Reasearch Report, ULAP-T69.

FLURSCHEIM C.H. (1965)
Development in power engineering.
Proc. IEE, 112, No.1, January, pp5-12.

FLURSCHEIM C.H. (Ed.) (1982)
Power circuit breaker theory and design.
IEE Power Engineering Series 1, Peter Peregrinus, 2nd Edition.

FRIEDRICH R.E. and YECKLEY R.N. (1959)
A new concept in power circuit breaker design utilizing SF_6.
AIEE Trans. PartIII, Vol.78, pp695-706.

FROST L.S. and LIEBERMANN R.W. (1971)

Composition and transport properties of SF_6 and their use in a simplified enthalpy flow arc model.
Proc. IEEE, Vol.59, No.4, April, pp474-485.

GLEIZES A., RAHMANI B., GONZALES J.J. and LIANI B. (1991)
Calculation of net emission coefficient in N_2, SF_6 and SF_6-N_2 arc plasmas.
J. Phys. D: Appl. Phys., Vol.24, pp1300.

GLEIZES A.,GONZALES J.J. and LIANI, B. (1992)
Net emission coefficient of mixtures of gas with metallic vapour and its influence on arc modelling.
Proc. 10th Int. Conf. Gas Discharges and their Appl., Swansea 1992, pp208-211.

HALL W.B. (1992)
Private communication.

HEBERLEIN J.V.R, KIMBLIN C.W. and LEE A. (1984)
Nature of the electric arc. (In Circuit interruption - Browne (Ed.)).
Marcel Dekker, Inc.

HENDERSON P. (1989)
Chromatic modulation systems for multiparameter measurement in physically demanding situations.
PhD thesis, University of Liverpool.

HENDERSON P.J., SPENCER J. and JONES G.R. (1993)
Pressure sensing using a chromatically addressed diaphragm.
Meas. Sci. Technol. 4, pp88-94.

HEYES A., CHRISTODOULOU M. and WISEALL S. (1995)
Arc Research Project Session, University of Liverpool, September 1995.

HOFF P., HOLM A., KARLEN O., LAGER U. and AKESSON U. (1992)
Condition monitoring of SF_6 circuit breakers.
CIGRE session 1992, paper 13-104.

HOLMES J.E. (1884)
UK Pat. 1256.

HOUSBY-SMITH C. and JENKINS J.E. (1978)
High current arcs in an orifice flow. Spectroscopic measurements under quasi steady state conditions.
University of Liverpool, Arc Research Report ULAP-T54.

HUMPHRIES J.E. *et al* (1996)
A chromatic interferometrically addressed micromachined silicon pressure sensor.
To be published, University of Liverpool.

HUNT R.W.G. (1987)
Measuring colour.
Ellis Horwood Ltd.

IBUKI K. (1979)
Spectroscopic study of the high current vacuum arc.
Ph.D thesis, University of Liverpool.

IKEDA H., JONES G.R., IRIE M. and PRASAD A.N. (1982)
Proc. 7th Int. Conf. Gas Discharges and their Appl., London, pp5-8.

JONES G.R. (1996)
Private communication.

JONES G.R. (1994)
Lectures on Optical Systems.
Internal lectures, University of Liverpool.

JONES G.R. and RUSSELL P.C. (1993)
Chromatic modulation based metrology.
Pure Appl. Opt. **2** pp87-110.

JONES G.R. and FANG M.T.C. (1980)
The physics of high power arcs.
Rep. Prog. Phys. 1980 **43**, pp1415-1465.

JONES G.R., LIDGATE D., COWLEY M.D. and EDELS H. (1973)
High current arcs in orifice air flow 1. Experiments during the high current phase.
Univ. of Liverpool, Arc Research Report ULAP-T12.

JONES G.R. (1984)
Predicting pressure transients due to arcing in two pressure, puffer, and rotary arc interrupters.
Proc. IEE Symp. on Trends in modern switchgear design 3.3-150kV, Newcastle, pp8.1-8.5.

JONES G.R., SHAMMAS N.Y. and PRASAD A.N. (1986)
Radiatively induced nozzle ablation in high-power circuit interrupters.
IEEE Trans. PS-14, pp413-422.

JONES G.R., KWAN S., BEAVAN C., HENDERSON P., and LEWIS E. (1987)
Optical fibre based sensing using chromatic modulation.
Opt. Laser Technol. 9 pp297-303.

JONES G.R. (1988)
High pressure arcs in industrial devices - Diagnostic and monitoring techniques.
Cambridge University Press.

KAPRON F.P., KECK D.B. and MAURER R.D. (1970)
Radiation losses in optical waveguides.
Appl. Phys. Lett., 10, pp423-425.

KISSINGER C.D. (1967)
Fiber optic proximity probe.
US. Pat. No. 327584.

KROHN D.A. (1992)
Fiber optic sensors - fumdamentals and applications.
2nd Ed., Instrument Society of America.

KROHN D.A. (1984)
Fiber optic displacement sensor.
Proc. of ISA Int. Conf., Houston, TX, Vol.39, part 1, pp331-340.

LANG S.R. and RYAN D.J. (1992)
Position sensing using an optical potentiometer.
IEEE Trans. Instrum. Meas., Vol.41, No.6, Dec, pp902-905.

LECLERC J.L. and JONES G.R. (1982)
The radiative characteristics of gas blast circuit breaker arcs at very high currents.
IEE Gas Discharge Conf, pp1-4.

LEE, GREENWOOD, CROUCH and TITUS (1962)
Development of power vacuum interrupters.
Trans. Am Inst. Electr. Eng. 81, Pt.III, pp629-639.

LEEDS W.M., BROWNE (Jr.) T.E. and STROM A.P. (1957)
The use of SF_6 *for high power arc quenching.*
AIEE Trans. 76(Pt. III), pp906-909.

LE GRANDE Y. (1968)
Light, colour and vision.
2nd Ed., Chapman and Hall Ltd.

LEWIS E., SHAMMAS N.Y. and JONES, G.R. (1985)
The current zero SF_6 *blast arc at high di/dt.*
Proc. Int. Conf. on Gas Discharges and their Applications, Oxford,pp35-38.

LEWIS K.G., JONES R.E. and JONES G.R. (1995)
A tap-changer monitoring system incorporating optical sensors.
2nd Int. Conf. on Reliability of transmission and distribution equipment, Warwick, March, pp97-102.

LIERBERMANN R.W. and LOWKE J.J. (1976)
Radiation emission coefficients for Sulphur Hexafluoride arc plasmas.
J. Quant. Spectrosc. Radiat. Transfer, Vol.16, pp253-264.

LINGAL H.J., STROM A.P. and BROWNE (Jr.) T.E. (1953)
An investigation of the arc quenching behaviour of sulfur hexafluoride.
AIEE Trans. 72 (Pt.III), pp242-246.

LIU X.P., SPOONCER R.C and JONES B.E. (1991)
An optical displacement sensor with extended range using two-wavelength referencing.
Sensors and Actuators A, 25-27, pp197-200.

LOWKE J.J. (1978)
Radiative energy transfer.
In "Current interruption in high voltage networks.", pp299-327.
Ed. Ragaller, Plenum Press.

LOWKE J.J. (1974)
J. Quant. Spectrosc. Radiat. Transfer, Vol.14, pp111-

LYTHALL R.T. (1972)
J & P Switchgear book.
Butterworth & Co. Ltd.

McNUTT W.J., McIVER J.C., LEIBINGER G.E., FALLON D.J., WICKERSHEIM K.A. (1984)
Direct measurement of transformar winding hot spot temperature.
Trans. IEEE, PAS-103, No.6, June, pp1155-1162.

MAYR O. (1943)
On the theory of the electric arc and its extinction.
ETZ, 64, pp645-652.

MESSENT D. (1995)
Private communication.

MEYER-ARENDT J.R. (1984)
Introduction to classical and modern optics.
2nd Ed., Prentice Hall Inc.

MOGHISI M. (1989)
Optical fibre current and voltage sensors.
PhD thesis, University of Liverpool.

MURPHY P.J and COURSOLLE T.P (1990)
Fiber optic displacement sensor employing a graded index lens.
Appl. Opt. Vol.29, No.4, Feb, pp544-547.

NAGEL S.R. (1987)
Optical fiber - the expanding medium.
IEEE Commun. Mag., 25(4), pp33-43.

NOESKE H.O, BENENSON D.M., FRIND G., HIRASAWA K., KINSINGER R.E., NAGAMATSU H.T., SHEER R.E. and YOSHIOKA Y. (1983)
Applications of arc-interruption fundamentals to nozzles for puffer interrupters.
EPRI Report EL-3293, Project 246-2.

NONKEN G.C. (1941)
High pressure gas as a dielectric.
IEEE Trans. 60, pp1017-1020.

OKAMOTO M., ISHIKAWA M., SUZUKI K. and IKEDA, H. (1991):
Computer simulation of phenomena associated with hot gas in puffer-type gas circuit breaker.
IEEE Trans. Power Deliv., Vol.6, No.2, April, pp833-839.

OLSHANSKY, R. (1979)
Propagation in glass optical waveguides.
Rev. Mod. Phys, 51(2), pp341-367.

OSTROWSKY D.B., SCHWIEZER P and NEVEUX L. (1990)
Instrically linear wavelength referenced fibre optic absolute angular displacement sensor.
Spectec., 15 Chemin de l'Archet, Nice, France.

PADGHAM C.A and SAUNDERS J.E (1975)
The perception of light and colour.
G. Bell and Sons Ltd.

PARK K.Y. (1993)
Mathematical modelling of SF_6 puffer circuit breakers.
PhD thesis, University of Liverpool.

PARRY J. (1984)
Further developments in SF_6 switchgear for distribution systems incorporating a rotating arc circuit breaking device.
Proc. IEE Symp. on Trends in modern switchgear design 3.3-150kV, Newcastle, pp2.1-2.6.

PILLING N. (1992)
Optical fibre measurement in power systems.
PhD thesis, University of Liverpool.

PILLING N. (1995)
Circuit breaker failure modes.
National Grid Research progress meeting, University of Liverpool, July 1995.

PRINCE D.C. and SKEATS W.F. (1931)
The oil blast circuit breaker.
Trans. AIEE, Vol.50, pp506-512.

PRINCE D.C. (1935)
Circuit breakers for the Boulder Dam line.
Trans. AIEE, Vol.54, pp366-372.

ROGERS A.J. (1976)
Method for simultaneous measurement of current and voltage on high-voltage lines using optical techniques.
Proc. IEE, Vol.123, No.10, Oct, pp957-960.

ROOS B.A. *et al* (1985)
Fibre optic transducer for use near MR magnetic fields.
Radiology, August, pp151-155.

RUEGSEGGER W., MEIER R. and KNEUBUHL F.K. (1985)
Mass spectrometry of arcs in SF_6 *circuit breakers.*
Appl. Phys. B 37, 115-135.

RYAN H.M., MILNE D. and POWELL C.W. (1985)
Site testing and the evaluation of a technique to differentiate between a gas or spacer flashover in SF_6 *GIS.*
Symp. on Gas insulated substations technology and practice, pp1-8.

RYAN H.M. and JONES G.R. (1989)
SF_6 *switchgear.*
IEE power Engineering Series 10, Peter Peregrinus Ltd.

SANJANI V. (1973)
Internal Report PL-73-10, University of Sydney.

SAUERS I., ELLIS H.W., CHRISTOPHOROU L.G., GRIFFIN G.D. and EASTERLY C.E. (1986);
Spark decomposition of SF_6*; toxicity of byproducts.*
Oak Ridge National Laboratory Report ORN/TM-9062.

SCHLICHTING H. (1968)
Boundary layer theory.
New York: McGraw-Hill.

SENIOR J.M. (1992)
Optical fiber communications - principles and practice.
2nd Ed. Prentice Hall International (UK) Ltd.

SHARP CORPORATION, ELECTRONIC COMPONENTS GROUP (1982)
Technical data for semiconductor color sensor, model PD150/151.
Sharp Corporation.

SHIMMIN D.W. (1986)
High power short circuit studies on an SF_6 puffer circuit breaker.
PhD thesis, Univ. of Liverpool.

SLADE P.G. and HOYAUX M.F. (1972)
The effect of electrode material on the initial expansion of an arc in vacuum.
IEEE Trans. Parts Hybrid Packag. PHP-8:35.

SLEPIAN J. (1929)
Theory of the de-ion circuit breaker.
Trans. AIEE , Vol.48, April, pp523-527.

SMITH F.G. and THOMSON J.H.(1988)
Optics.
Wiley and Sons Ltd.

SORENSON R.W. and MENDENHALL H.E. (1926)
Trans. Am. Inst. Electr. Eng., 45, pp1102-1107.

SPENCER J.W. (1985)
Some investigations of the behaviour of a rotating arc discharge.
PhD thesis, Univ. of Liverpool.

SRIDHARAN G. (1985)
Optical reflectance sensor measures displacement in magnetic suspension.
IEEE Trans. Instrum. Meas., Vol.IM-34, No.1, March, pp31-34.

STRACHAN D.C., LIDGATE D. and JONES G.R. (1977)
Radiative energy losses from a high current air blast arc.
J. Appl. Phys., 48, pp2324-2330.

STILES and WYSZECKI (1962)
J. Opt. Soc. Amer., 52, 313.

SUZUKI, K. TODA H., AOYAGI A., IKEDA H., KOBAYASHI A., OHSHIMA I. and YANABU S. (1993)
Development of 500kV 1-break GCB (PART I) - Investigation of interrupting chamber performance.
IEEE Trans. Power Delivery, Vol.8, No.3, July, pp1184-1191.

THOMEN H. (1941)
An a.c. high speed circuit breaker for very high service duty and breaking capacity.
BBC Eng., 28, pp292-294.

TODA H., KOBAYASHI A., TAKAGI H, SUZUKI K, IKEDA H and MURAYAMA Y (1993)
Develoment of 550kV 1-break GCB (PART II) - Development of prototype.
IEEE Trans. Power Delivery, Vol.8, No.3, July, pp1192-1198.

TOMINAGA S., KUWAHARA H., YOSHINAGA K. and SAKUMA, S. (1980)
Investigation on gas flow of puffer type gas circuit breaker based on observation of arc and pressure measurement.
Trans. IEEE, PAS-99, No.6, Nov/Dec, pp2040-2048.

TOMINAGA S., KUWAHARA H., YOSHINAGA K. and SAKUMA, S. (1981)
SF_6 gas analysis technique and its application for evaluation of internal conditions in SF_6 gas equipment.
IEEE Trans., PAS-100, pp4196-4206.

TUMA D.T. (!980)
A comparison of the behaviour of SF_6 and N_2 blast arcs around current zero.
IEEE Trans., PAS-99, pp2129-2137.

UEDA Y.; MURAI Y.; OHNO A. and TSUTSUMI T. (1982)
Development of 7.2kV - 63kA advanced puffer gas circuit breaker.
IEEE Trans. Power App. Syst., Vol. PAS-101, No.6, June 1982, pp143-149.

WALTY W. (1935)
The Brown Boveri airblast circuit breaker.
BBC Eng., 22, pp199-207.

WHITNEY W.B and WEDMORE E.B. (1930)
British Pat. 278764.

WOOD J.K. (1993)
Private communication.

YANABU S., MIZOGUCHI H., KOBAYASHI A., OZAKI Y. and MURAKAMI Y. (1982)
Factors influencing the interrupting capability of SF_6 puffer breaker and development of 300kV 50kA one-break circuit breaker.
IEEE Trans. Power Appar. Syst. PAS-101, No.6, June, pp1511-1517.

YANABU S., MIZOGUCHI H., IKEDA H., SUZUKI K. and TOYODA M. (1989)
Development of novel hybrid puffer interrupting chamber for SF_6 gas circuit breaker utilizing self-pressure-rise phenomena by arc.
IEEE Trans. Power Delivery, Vol.4, No.1, January, pp355-361.

YECKLEY R.N. and CROMER C.F. (1970)
New SF_6 EHV circuit breaker for 550kV and 765kV.
IEEE Trans. Power Appar. Syst. PAS-89, pp2019-2023.

YOSHIZUMI T., IKUBI K., HOSOMI M., YONEZAWAT. and KAWASAKI H (1989)
Hot gas flow analysis in SF_6 gas circuit breaker during the short circuit interruption.
IEEE Trans. Power Deliv., Vol.4, No.3, July, pp1757-1764.

APPENDIX I

The following pages show reprints of conference papers related to work reported in this thesis:

ISAAC L.T., SPENCER J.W., JONES G.R., JONES C., HALL W.B., TAYLOR B.
Live monitoring of contact travel on EHV circuit breakers using a novel optical fibre technique.
XIth Int. Conf. Gas Discharges and their Applications, Vol.2, pp.238-241, Tokyo, Japan, 1995.

ISAAC L.T., SPENCER J.W., HUMPHRIES J.E., JONES G.R., HALL, W.B.
Particle formation by SF6 circuit breaker arcs.
(To be presented at) XIIth Int. Conf. Gas Discharges and their Applications, Greifswald, September 1997.

LIVE MONITORING OF CONTACT TRAVEL ON EHV CIRCUIT BREAKERS USING A NOVEL OPTICAL FIBRE TECHNIQUE

L.T. Isaac, J.W. Spencer, G.R. Jones, C. Jones*, W.B. Hall* and B. Taylor**

Department of Electrical Engineering and Electronics
The University of Liverpool, P.O. Box 147, Liverpool L69 3BX, UK.
*Reyrolle Limited, Rolls Royce Industrial Power Group, Tyne and Wear, Newcastle NE31 1UP, UK.
**Lucas Control Systems Products, Shirley, Solihull, West Midlands, B90 4JJ, UK

ABSTRACT

A novel optical fibre based displacement sensor has been developed for use on a SF_6 puffer circuit breaker when interrupting fault currents of up to 50kA. The sensor can monitor dynamic displacements over 200mm with a resolution of 1.5mm at a velocity of 4m/s and with an accuracy of 1%. By mounting the sensor on to the moving contact shaft, with no mechanical linkages between the sensor and the arcing contact, the transducer monitors the contact movement directly. The sensor is based upon chromatic modulation [1], which overcomes many of the inherent problems of optical fibre sensing. Some sample test results are presented to indicate the important information which can emerge from the use of such a monitoring system.

INTRODUCTION

The environment inside a SF_6 puffer circuit breaker, when interrupting fault currents, is extremely hazardous for any type of transducer. There are a number of aspects of that environment which could interfere with the operation of the transducer. They can be broadly categorised as:

- mechanical shock and vibration arising from the mechanical operation of the interrupter.
- optical radiation emitted from the arc, which could decrease the signal-to-noise ratio of an optical based sensor.
- chemical reactivity arising from the dissociation of SF_6, which could produce species capable of degrading the transducer materials.
- electromagnetic interference produced by the current interruption process, which may degrade the output signal and its processing.

Account needs to be taken of these environmental factors when formulating the design philosophy of an optical electrode displacement monitor.

In addition, the manner in which the optical signal is modulated, and hence the type of system used to monitor the sensor, will also affect the design strategy. For example, simple optical intensity techniques are unacceptable on account of their vulnerability to optical noise caused by, for example, vibration. To overcome these difficulties a technique was chosen, with which experience already exists when used with other optical transducers in equally hazardous environments [1]. Tests with this type of system have shown it to be immune to many effects which cause serious problems for intensity based systems. For the present application, the chromatic approach is potentially more accurate than a simple intensity system, whilst simultaneously avoiding overcomplicated transducer design, and therefore reducing susceptibility to some of the environmental effects.

The chromatic system utilises a broadband light source rather than a laser, since the modulated signal returning from the transducer is in the form of a broadband spectrum, whose dominant wavelength is determined from the output of a pair of silicon diodes with overlapping wavelength responsivities. The displacement sensor is engineered such that the dominant wavelength of the detected optical signal is directly proportional to the measurand (i.e. electrode displacement).

This contribution describes the design and performance of the optical displacement transducer, based upon such a chromatic modulation system, which is used to monitor the travel of a contact shaft in a SF_6 puffer circuit breaker, during interruption of high fault currents.

THE COMPLETE OPTICAL SENSOR SYSTEM

The sensor system may be divided into three parts; the source/detection unit, the optical fibres and the optical displacement transducer (figure 1). The source/detection unit is a commercially available chromatic monitoring instrument, manufactured by Lucas Control Systems Products, which measures the dominant wavelength of a light signal. An optical displacement transducer for interfacing to this unit was designed to maximise the depth of modulation, resolution and accuracy and to minimise the effect of environmental factors. A further design consideration was the location of the transducer in order not to interfere with the design and operation of the circuit breaker. The number of practical locations, which would afford protection against interference from the arc light and arc induced contamination by-products, whilst permitting monitoring of the contact movement without intervening linkages, is limited. The shaft to which the contact is connected was chosen to be the most suitable position, requiring few changes to the interrupter structure. The location is shown in figure 1. The transducer was fitted to the shaft at this location and the addressing optical fibres contained within the surrounding housing. A further advantage of this location is that the optical path is well defined. The disadvantages are that the space is limited and rotation of the shaft could affect the optical signal.

THE OPTICAL DISPLACEMENT TRANSDUCER

The displacement transducer was based upon a computer designed scale along whose length the dominant wavelength is arranged to vary between prescribed limits [2]. This scale was mounted on a polished stainless steel reflective surface and covered with a chemically inert protective film. The stainless steel reflector was tested to ensure that imperfections on the surface did not cause changes in the optical signal. Such imperfections caused up to 0.5% errors on the chromaticity (dominant wavelength) of the optical signal but up to 15% errors on the intensity, confirming the superiority of the chromatic approach.

To monitor contact travel over 200mm with reasonable resolution requires two such scales operating in parallel, each having a different modulation function. The coarse scale produces a stepped change in the dominant wavelength (figure 2a) at regular intervals along the scale. These changes in modulation give well defined chromatic values over a relative large distance. The fine scale produces a periodic optical modulation (figure 2b). The combination of these two scales gives a unique pair of chromatic values which can be resolved to give the position unambiguously.

The purpose of the clear film, covering the transducer, is to provide protection against chemical attack from arc induced by-products of SF_6 dissociation on the ink deposited on the scale and to the stainless steel reflector itself.

MODULATION MECHANISM

The ink used to form the modulation pattern on each scale of the transducer modulates light non uniformly across the spectrum. The ink transmits the infrared portion of the light but not the visible. The density of ink dots on the film determines the proportion of visible and infrared light reaching the detectors. A change in this ratio represents a change in the weighted mean of the detected spectra and therefore a change in dominant wavelength. The detected spectra obtained using zero dot density (0% greyness) and full dot density (100% greyness), corresponding to the two extremes of the modulation range, can be seen in figure 3.

The design of the dot matrix pattern on the scale to produce a linear relationship between displacement and dominant wavelength λ_D requires the effect of the light beam divergence from the optical fibre to be taken into account. Simple analysis of the requirements indicates that the dominant wavelength is related to the percentage greyness of the dot pattern (X) according to

$$\lambda_D = \lambda_S + A.X - B.X^2 + C.X^3 \qquad ...(1)$$

where λ_S is the unmodulated dominant wavelength, and A, B, C are constants for a particular optical system.

OPTICAL FIBRES

The optical fibres for addressing the chromatic scale described above were chosen, using equation (1), to be 2mm diameter glass fibre bundles. Each scale (coarse figure 2a and fine figure 2b) was addressed by a separate fibre bundle, the light being delivered and the modulated light received by same bundle in each case. The fibres passed through a gas tight inlet and were then taken 20m to the detection unit. At this unit each fibre bundle was bifurcated, one tail being connected to the light source and the other to the detection system.

PERFORMANCE ASSESSMENT

The performance of the travel recorder has been assessed on a 145kV puffer interrupter being tested at the University laboratories. The following observations have been made:

The sensitivity of the optical transduction to the rotation of the contact shaft was assessed by marginally rotating the latter through +/- 3°. Whereas an intensity modulated signal varied by 16% for such a rotation, the chromatically modulated signal only changed by 0.8% again confirming the superior immunity of the chromatic approach. Tests with the circuit breaker operated a number of times indicated negligible rotation of the shaft.

The displacement transducer has a resolution of 0.5mm, and is accurate to 0.5%. When the system is used dynamically, as in this case, the main constraint upon the dynamic resolution is the sampling rate of the data capture software. Since the sampling rate is presently 4kHz, and the maximum speed of the interrupter 4m/s, the dynamic resolution of the recording system is 1mm (worst case). This gives an overall dynamic resolution of 1.5mm, and dynamic accuracy of 1%. Higher sampling rates are feasible so that these values can be improved if necessary.

The transducer was subjected to a controlled repeatability test by operating the circuit breaker 30 times to interrupt a 15kA arc. Each successive shot increased the amount of degradation powder within the breaker. Despite a considerable level of powder, the travel records produced by the sensor remained repeatable throughout. The typical result can be seen in figure 4, which corresponds to the raw chromatic values of figure 2. The sensor was also unaffected by the arc radiation throughout.

CONCLUSIONS

This contribution has described an optical fibre based displacement sensor, which is robust enough to survive the hostile environment within a SF_6 circuit breaker under fault current conditions. The transducer does not interfere with either the mechanical operation or electrical integrity of the interrupter. The use of chromatic rather than intensity modulation has been shown to provide greater immunity to imperfections in sensor components and contact shaft rotation. Furthermore, the transducer is not susceptible to undesirable mechanical, chemical, electromagnetic or optical effects.

Tests on prototype sensors of this type have indicated their capability to operate in a reproducible manner over a significant number of operations even with arcing sustained by fault currents of at least 15kA. More recent tests at 50kA indicate the transducer's immunity to heavy arcing conditions and probable extention to significantly higher fault current conditions without loss of performance.

The immunity of the system to the effect of arc interruption enables it to be applied with confidence to new interrution technologies where contact travel characteristics can be significantly influenced by the fault current being switched. For this purpose, the optical fibre displacement sensor is easily adaptable for measuring operating strokes of different magnitudes and speeds.

REFERENCES

(1) Jones, G.R. and Russell, P.C. (1993)
Chromatic modulation based metrology: Part I Basic Concepts p.87-99
Part II Illustrative Applications p.99-110 , Pure Applied Optics 2.

(2) Lewis, G., Jones, R.E. and Jones, G.R. (1995)
Tap changer monitoring system incorporating optical sensors , Proc. IEE 2nd Int. Conf. on Reliability of Transmission and Distribution Equipment (in the press).

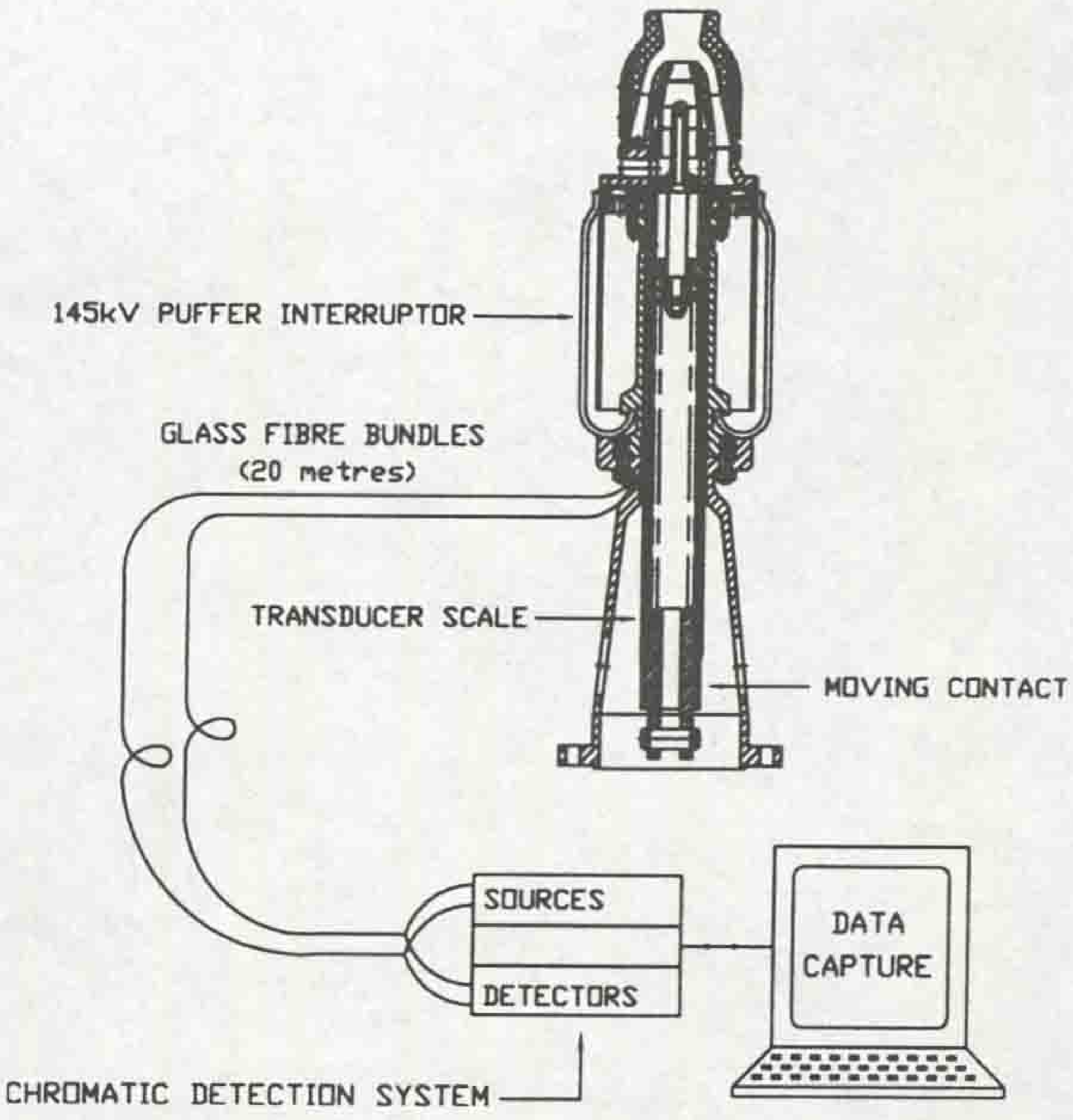

Figure 1 - Schematic of complete displacement sensor system

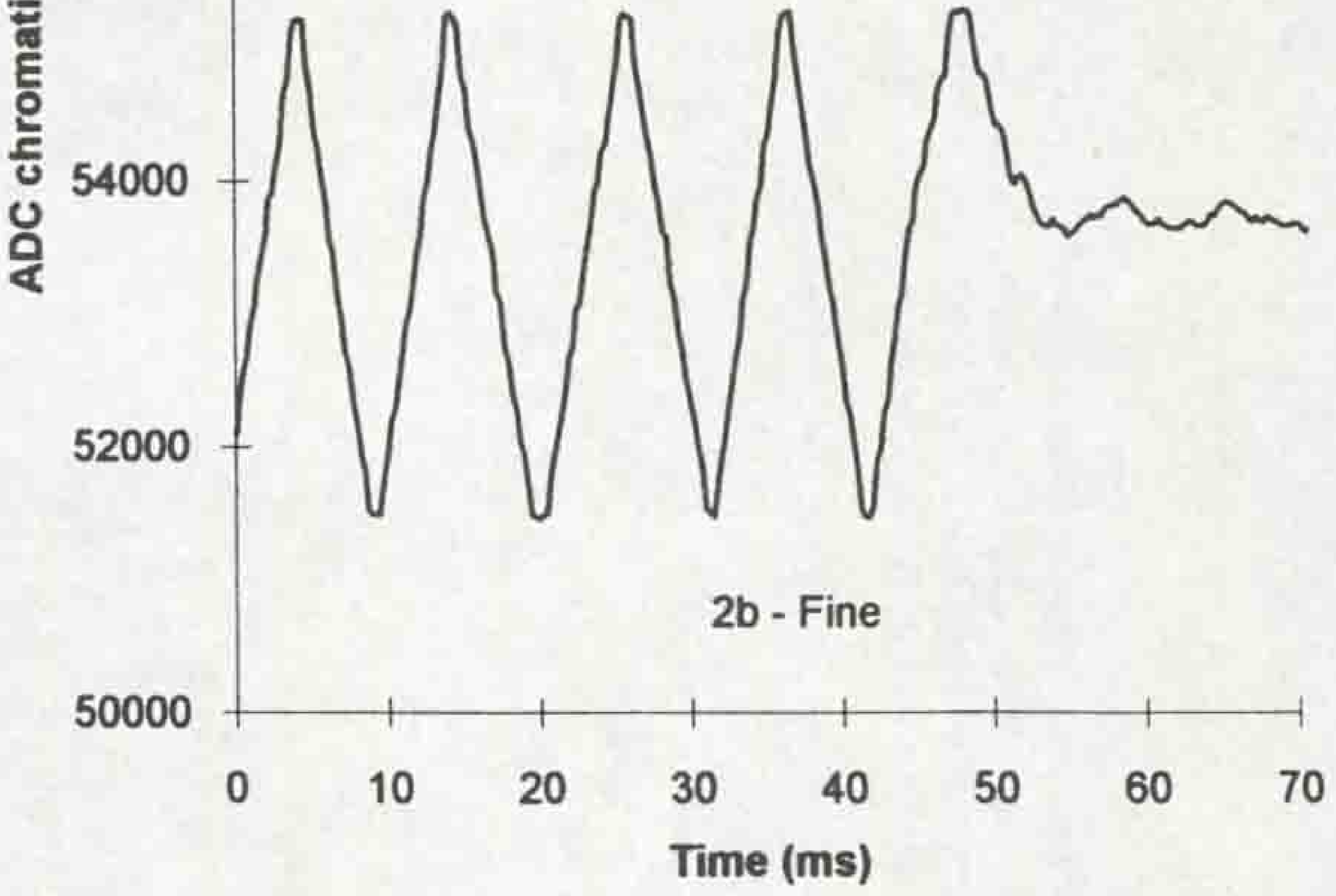

Figure 2 - Digital chromatic values of the modulation produced by the coarse and fine scales.

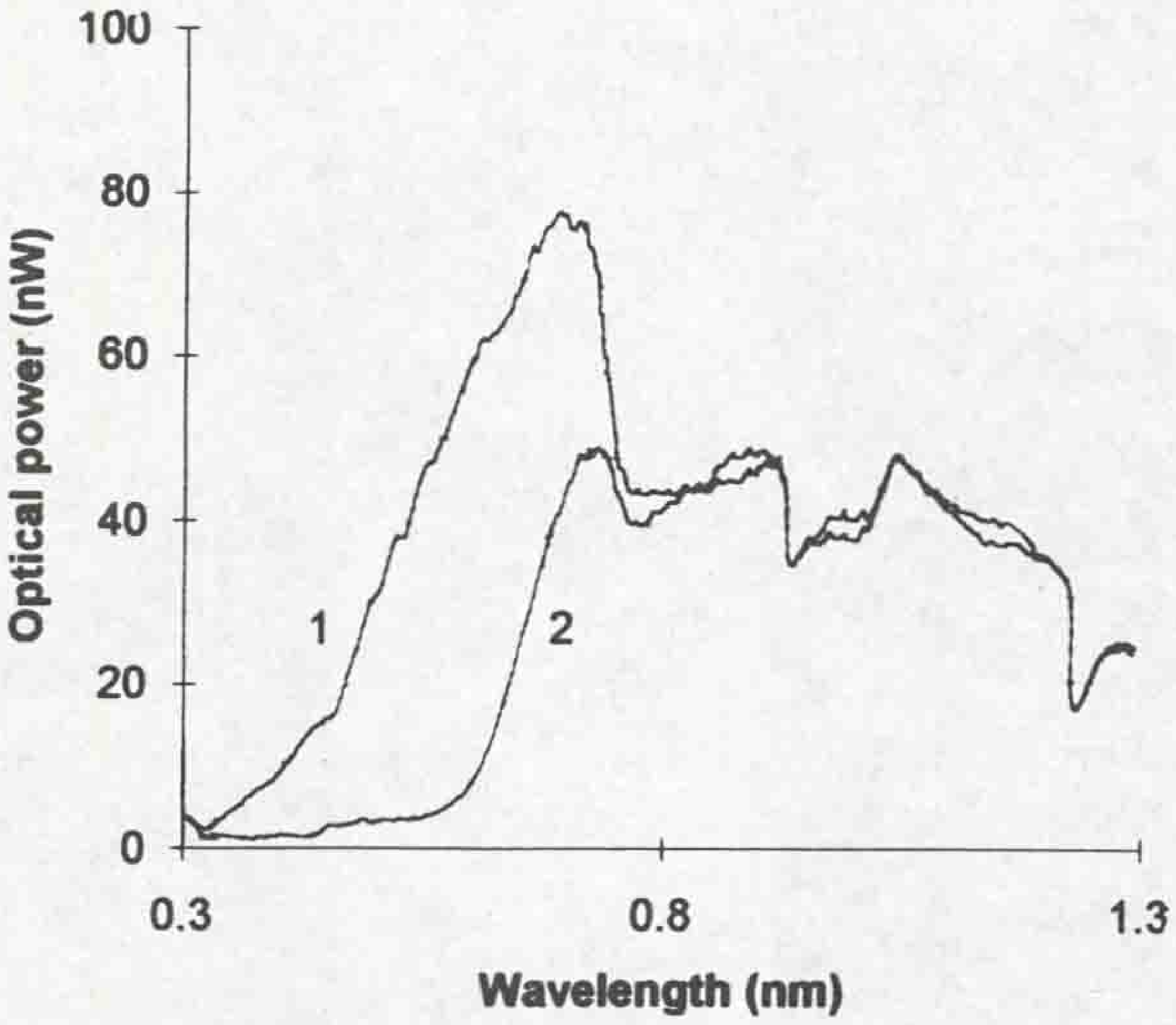

Figure 3 - Spectra for 0% greyness (1) and 100% greyness (2)

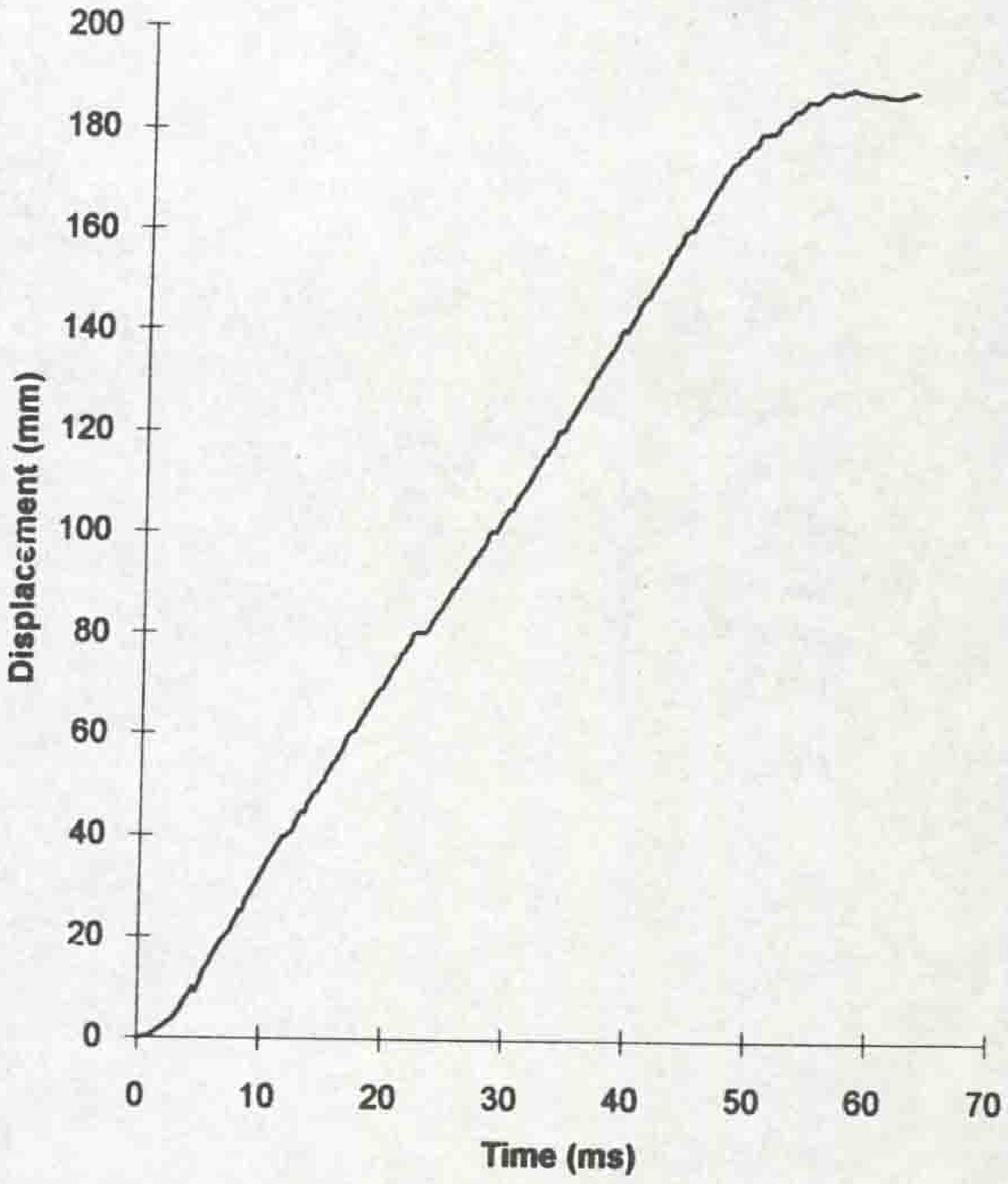

Figure 4 - Typical opening stroke travel record (15kA)

PARTICLE FORMATION BY SF_6 CIRCUIT BREAKER ARCS

L Isaac[1], J W Spencer[1], J Humphries[1], G R Jones[1], W Hall[2]

[1]CIMS, Dept of Electrical Engineering and Electronics, University of Liverpool,
Liverpool L69 3GJ, UK
[2]Reyrolle Switchgear, Rolls Royce Power, Hebburn, Tyne and Wear, UK

ABSTRACT

It is well established that SF_6 arcs produce copious amounts of particulate material much of which is believed to be metallic fluorides. Such particulate contamination may, under some circumstances, produce a weakening of the dielectric strength of the SF_6 environment. This contribution describes an optical fibre probe based upon chromatic modulation for monitoring the accumulation of such particulate material following arcing in an SF_6 puffer circuit breaker. The probe calibration characteristic is presented along with some test results showing how the particle formation varies with fault arc current.

INTRODUCTION

There is experimental evidence that particulate material produced during arcing to metallic electrodes in an SF_6 atmosphere can lead to a reduction in the breakdown strength of the SF_6 under some operating conditions (eg [1]). Because of the complicated structure and the severe operating conditions which exist within high voltage SF_6 puffer circuit breakers during fault current interruption and because of the difficulties in monitoring particle concentration in gaseous atmospheres there is little information in the literature regarding the rate at which particles are produced in such circuit breakers.

This contribution describes a small optical fibre probe for monitoring particle concentrations and which, because of its small size, can be inserted into a puffer circuit breaker housing for on line particle measurements. The probe detects the scattered light from the particles using chromatic signal processing to determine the dominant wavelength of the scattered light which is related to the particulate concentration per unit volume. Some test results obtained with such a probe inserted into a model 145kV SF_6 puffer circuit breaker are presented. These show how the particulate concentration varies with fault current arcs of different magnitudes and the manner in which the particulate material accumulates over prolonged periods.

PRINCIPLE OF OPERATION

The scattering of polychromatic light by micron sized particles is a complex function of optical wavelength (λ), particle radius $\left(R_p\right)$ and particle concentration (N) governed by [2], [3]:

$$I_F = I_o\left(1 - CN\alpha^2\left[\lambda^4 R_p^2\right]^{-1}\right)$$

where I_F is the intensity of the forward scattered light, I_o the incident intensity α the particle polarisability, C a constant.

The implication is that the wavelength of the forward scattered light is a function of the fractional volume of micron sized particles NR_p^2 / R_A^2 where R_A is the radius of the cylindrical volume being optically addressed. Thus the light detected in the forward direction will contain forward scattered light mixed with the range of wavelengths contained in the polychromatic addressing light beam and weighted towards a particular value governed by $\left(NR_p^2 / R_A^2\right)$.

In order to deduce the fractional particulate volume from the observation of such scattered light a monitoring technique is required which can identify changes in the weighted wavelength of the light and which can track such weighted wavelengths over substantial wavelength ranges. The chromatic modulation technique [2], [4] lends itself ideally for such an application. In its simplest form the chromatic approach involves detecting an optical signal with two photodetectors having different but overlapping wavelength responses. The dominant wavelength is given by the ratio of the outputs from these two detectors [2].

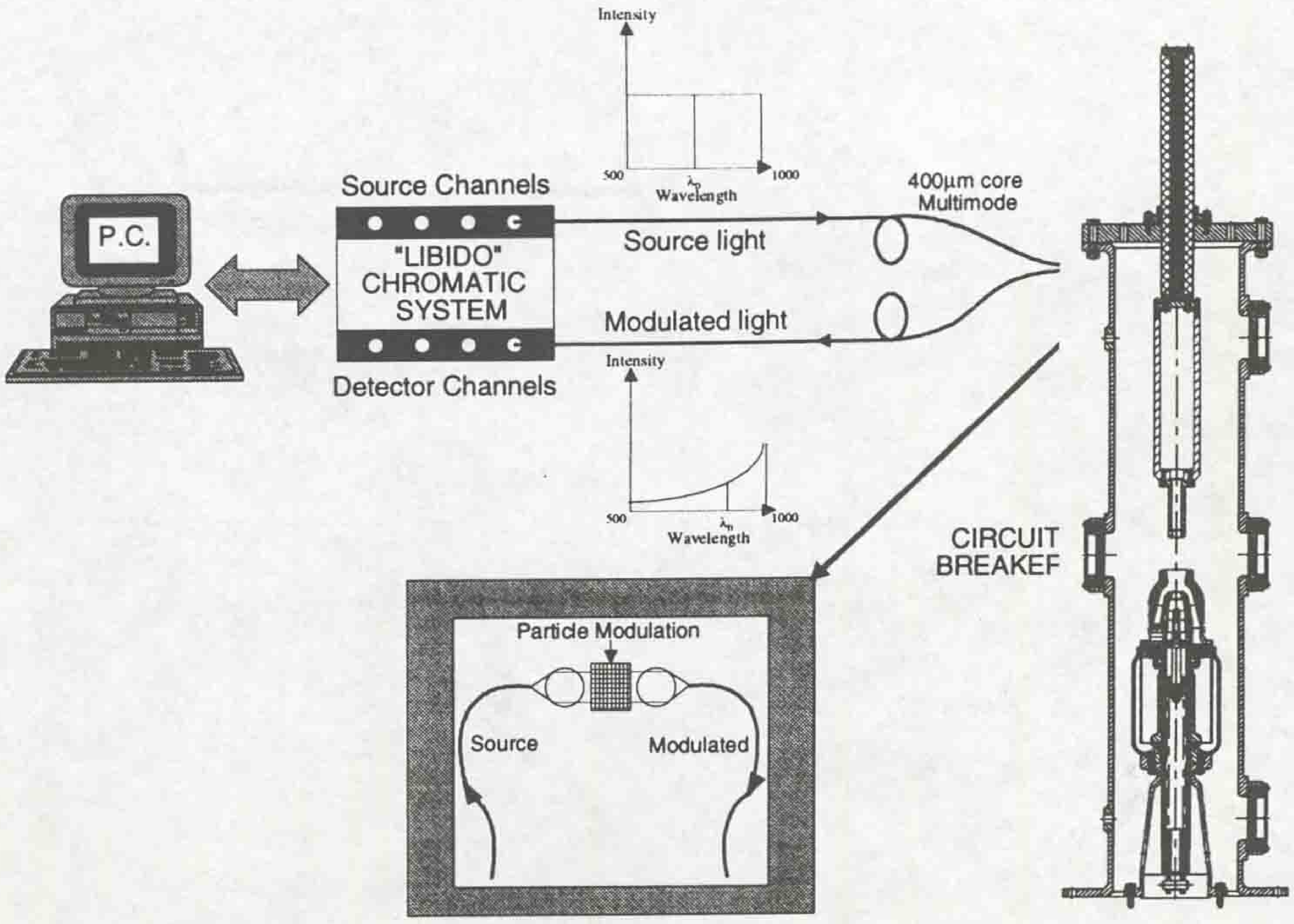

Figure 1 - Schematic of optical fibre particle concentration monitor

EXPERIMENTAL APPARATUS

The particle monitor consisted of a cell across which a beam of collimated white light propagated (figure 1). The light was provided by a high stability tungsten halogen source transmitted to and from the cell by 400µm multimode optical fibre. Collimation was provided by two spherical lenses (one for launching and the other for capturing the light across the cell). The light from the receiving fibre was monitored with a PD150 double layer photodiode which provided the two signals for determining the dominant wavelength of the captured light.

For the present investigations the particle monitoring cell was installed within a 145kV 63kA SF_6 puffer circuit breaker at the location shown on figure 1. Optical access was provided by the 400µm optical fibres passing through appropriate seals in the wall of the circuit breaker tank.

The output from the optoelectronic detectors was processed and displayed on an IBM personal computer.

EXPERIMENTAL RESULTS

The particle monitoring system was calibrated with a test chamber by using known concentrations of particles captured from prior arcing tests in SF_6. Known masses of particles were uniformly dispersed throughout the chamber by a fan and the scattered light monitored chromatically.

These experiments yielded calibration curves in the form of graphs of dominant wavelength versus the weight by volume concentration of particles as shown on figure 2. A particle concentration of 90mg/l produces a change in dominant wavelength of 14nm with a measurement uncertainty of ±1nm. the accuracy of the electronic monitoring instrumentation was ±0.1nm.

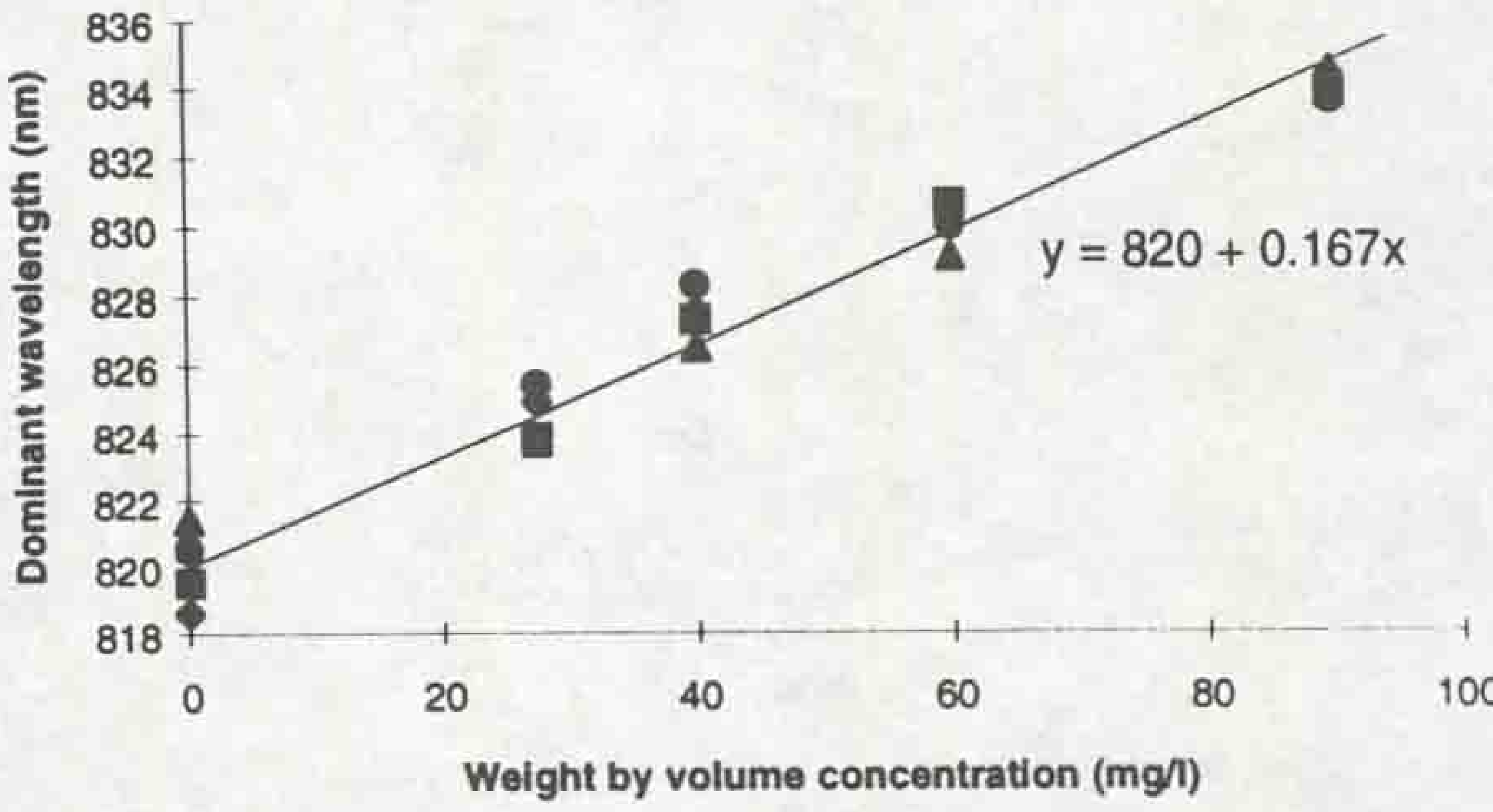

Figure 2 - Calibration curve for optical fibre particle concentration monitor

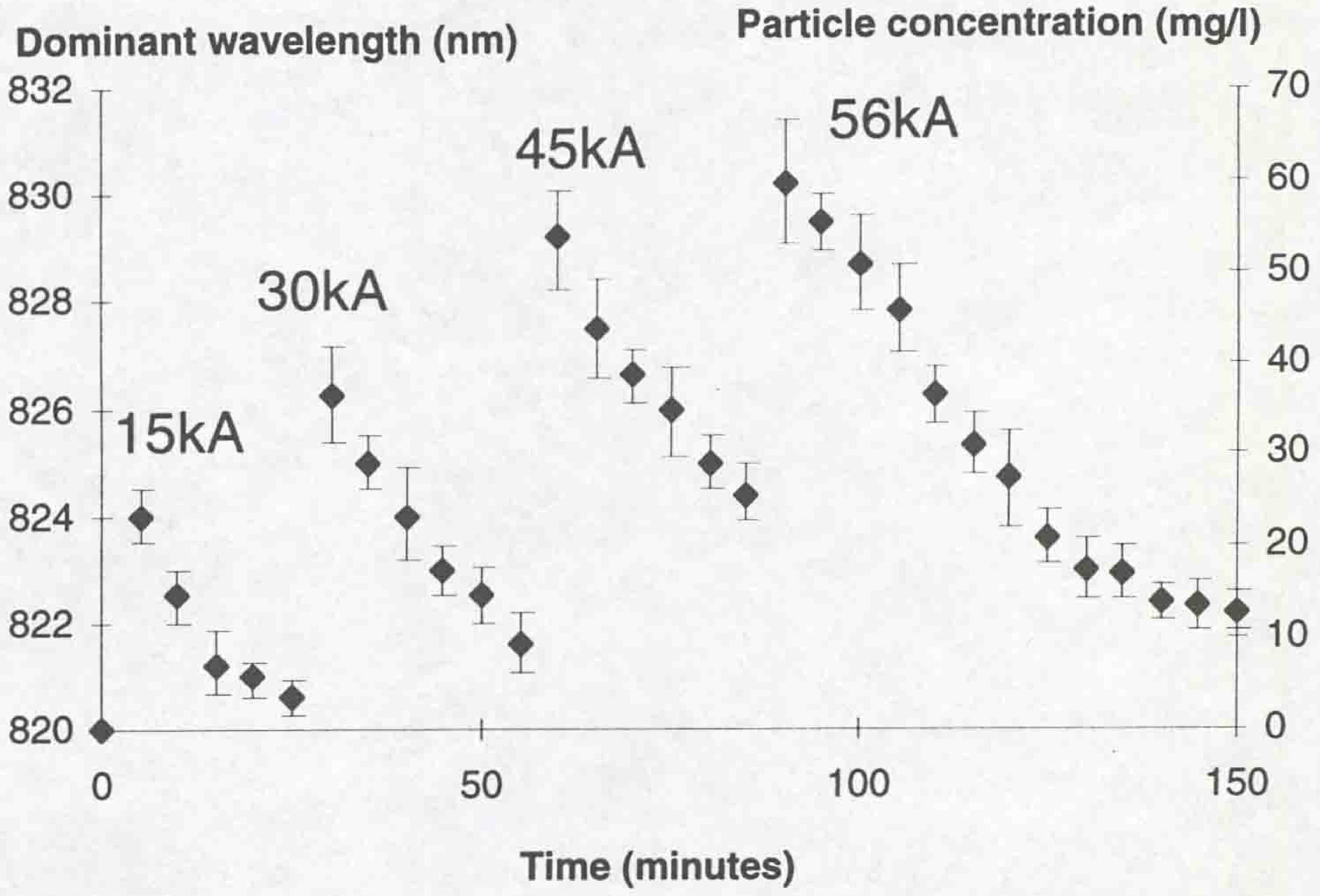

Figure 3 - Time variation of dominant wavelength from the OFPCM for a range of high fault currents

The results of a series of tests performed on the 145kV 63kA SF_6 puffer circuit breaker are given on figure 3. These show the variation of dominant wavelength with time after fault current arcing with peak arc current as parameter. The dominant wavelength scale is also shown transformed into particle concentration using the calibration curve from figure 2. Results for peak arc currents of 15, 30, 45 and 56kA are presented. Time is measured from the initiation of the first arc at 15kA so indicating the settling time for particles allowed between each sequential arcing test.

The results show that the amount of particulate material produced by arcing increases from about 23mg/l at 15kA to about 60mg/l at 56kA. (The results are for a full half cycle of arcing at 50Hz.) The results also show the rate at which the particulate material settles after arcing. The initial rate of decay of the particulate concentration following arcing appears to be similar for each peak fault current. These settling times are of the order of about 25 minutes at 15kA and 60 minutes at 56kA.

DISCUSSION OF RESULTS

The experimental investigation using the chromatic monitoring of the scattered light has shown that particle formation due to fault current arcing in SF_6 can be monitored on line with an optical fibre probe. The experimental results obtained at various peak currents and shown on figure 3 indicate that 0.8mg/l is produced per KA of fault current (50Hz half cycle duration). The mean settling rate is of the order of 1mg/l per minute. These approximate, empirically determined particle formation and settling rates form guidelines for any future particle related performance considerations relating to SF_6 circuit breakers.

There is evidence from the 56kA arc results of figure 3 in particular that the particle concentration level as seen by the probe at the end of the settling period (~12mg/l) does not return to the same level prearcing.

To investigate these effects more closely, the probe output was observed on shorter timescales (~30ms) around the arcing period itself. The results are shown on figure 4 in the form of dominant wavelength as a function of time for four arc currents observed in the direct sequence 2, 5, 9, 15kA peak respectively. These results confirm the longer timescale results of figure 3; the pre and immediately post arcing particle levels seen by the probe are identical for each current implying that the particles have not diffused to the probe location during at least 10ms after arc extinction. However the particle level preceding arcing at each current level is increased above the level observed for the previous arcing test confirming the results of

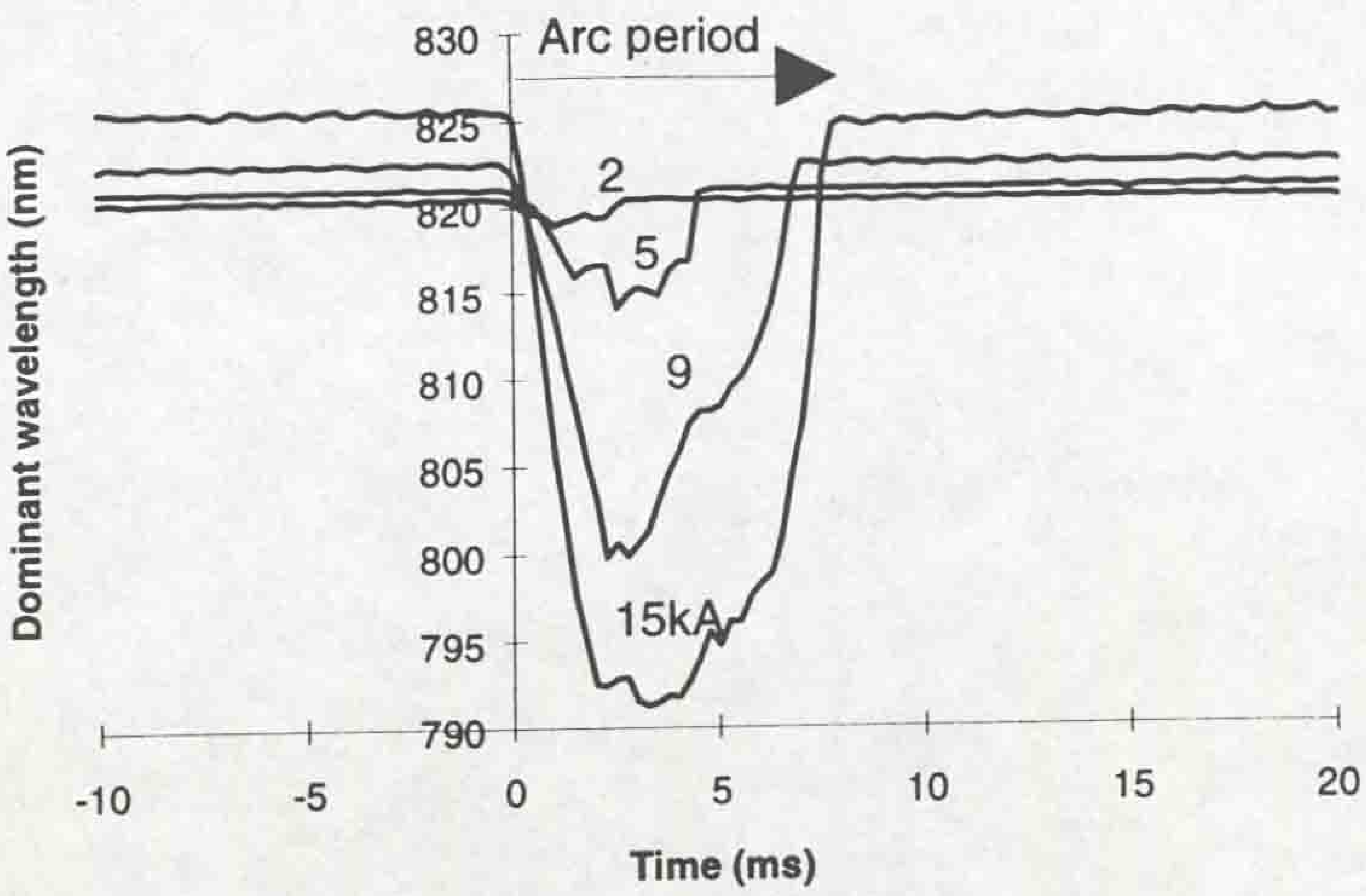

Figure 4 - Time variation of dominant wavelength for a range of low arc currents

figure 3 that the base level particle concentration at the probe increases after each test. This means that an intermittent, non continuous monitoring of the particle level with this kind of probe is capable of providing historical information about the arcing in the circuit breaker from the memory embedded in the particle film deposited on and directly observable from the probe.

The results of figure 4 also indicate that the particle probe detects the optical emission from the arcing event itself as a shift in dominant wavelength caused by the arc emission with respect to the dominant wavelength of the external polychromatic tungsten halogen source used for energising the probe. Consequently the probe output contains information about the severity of arcing (peak current level) as well as its duration so enabling the cause of the particle production and the consequence (particle concentration) to be derived from the intelligence provided by a single probe output.

CONCLUSIONS

An optical fibre probe based upon the Mie scattering of light has been shown to provide a range of empirical information concerning the formation and accumulation of particles in a 145kV 63kA SF_6 puffer circuit breaker. From the intelligence provided by the probe it has been shown that the following information is accessible

- time variation of particle distribution from continuous monitoring
- accumulated particle concentration from intermittent monitoring
- indication of severity of the arc producing particulate event

As such the approach provides a valuable tool for the research and development of high voltage SF_6 circuit breakers whilst also providing a possible building block for an intelligent circuit breaker condition monitoring system.

ACKNOWLEDGEMENTS

The authors appreciate the financial support provided by Rolls Royce Power which enabled this work to be undertaken.

REFERENCES

[1] G R Jones, *Proc. 2nd Electrical Workshop, Cocoyoc, Mexico,* 4.4, 1-30, (1993)

[2] G R Jones and P C Russell, *Pure and Applied Optics,* 2, 87-110, (1993)

[3] C Beavan, *PhD Thesis, University of Liverpool,* (1989)

[4] G R Jones, *Proc. XI Int. Conf. on Gas Discharges and their Applications,* Tokyo, p 11, 504-512, (1995)

APPENDIX II

Listing of Microsoft Excel (v4) Macro program to convert dominant wavelength data into the corresponding displacement values.

```
Record1 (a)
=SELECT("R2C5")
=FORMULA("=MAX(R[4]C[-3]:R[3998]C[-3])")
=SELECT("R3C5")
=FORMULA("=MIN(R[3]C[-3]:R[3997]C[-3])")
=SELECT("R2C6")
=FORMULA("=(RC[-1]-R[1]C[-1])/9")
=SELECT("R6C5")
=FORMULA("=ROUND(((RC[-3]-R3C5)/R2C6),0)")
=FILL.AUTO("RC:R[390]C",FALSE)
=VPAGE(-8)
=VSCROLL(1,TRUE)
=SELECT("R6C5")
=UNDO()
=COPY()
=SELECT("R7C5")
=VSCROLL(4003,TRUE)
=SELECT("R7C5:R4006C5")
=PASTE()
=SELECT("R2C7")
=CANCEL.COPY()
=FORMULA("=MAX(R[4]C[-4]:R[3998]C[-4])")
=SELECT("R3C7")
=FORMULA("=MIN(R[3]C[-4]:R[3997]C[-4])")
=SELECT("R2C8")
=FORMULA("=(RC[-1]-R[1]C[-1])/20")
=SELECT("R6C6")
```

```
=FORMULA("=ROUND(((RC[-3]-R3C7)/R2C8),1)")
=COPY()
=SELECT("R7C6")
=VSCROLL(4003,TRUE)
=SELECT("R7C6:R4006C6")
=PASTE()
=SELECT("R6C7")
=CANCEL.COPY()
=FORMULA("=IF(MOD(RC[-2],2)=1,20-RC[-1],RC[-1])")
=COPY()
=SELECT("R7C7")
=VSCROLL(4024,TRUE)
=VPAGE(-1)
=SELECT("R7C7:R4006C7")
=PASTE()
=SELECT("R6C8")
=CANCEL.COPY()
=FORMULA("=RC[-7]/4")
=COPY()
=SELECT("R7C8")
=VSCROLL(4003,TRUE)
=SELECT("R7C8:R4006C8")
=PASTE()
=SELECT("R6C9")
=CANCEL.COPY()
=FORMULA("=RC[-4]*20")
=SELECT("R6C9")
=FORMULA("=(RC[-4]*20)+RC[-2]")
=COPY()
=SELECT("R7C9")
=VSCROLL(4024,TRUE)
=VPAGE(-1)
```

```
=SELECT("R7C9:R4006C9")
=PASTE()
=SELECT("R6C10")
=RETURN()
```

APPENDIX III

Operation of rotary arc distribution circuit breaker (fig.7.11)

1. In the closed position the moving poker anode mates with the main stationary contact.
2. On opening an arc is drawn between them as the poker moves towards its fully open position on the axis of the coil.
3. The arc is “blown”, under its own magnetic force, towards the annular electrode.
4. Once the arc has transferred in this way, the magnetic field, produced by the coil, acts electromagnetically on the arc to both rotate it and drive it axially into the annular electrode, thus forming a helical arc.
5. The lengthening of the arc in this way and its rapid movement through cool gas are sufficient to extinguish the arc a current zero on the fault current waveform.

APPENDIX IV

Energy absorption by particulate material

To a first approximation it is assumed that the particulate material during arcing is composed of Tungsten, Copper (both from electrode erosion) and Sulphur (from gas decomposition) in equal quantities. The specific heat capacities of each of these substances are 134, 383 and 719Jkg^{-1}K^{-1} respectively. Therefore, the mean specific heat capacity of such a mixture, Cp_{PART}, is 412Jkg^{-1}K^{-1}.

It is possible that the particulates may possess a higher temperature than the SF_6 gas in the piston which might, in principle, explain the energy differences between the curves $\Delta T_{RADIATION\ LOSS}$ and $\Delta T_{PISTON/ARCING/PEAK}$ on fig.11.19. The relationship between the average particle temperature and corresponding energy loss can be predicted. The residual temperature loss in the gas, $\Delta T_{RESIDUAL\ LOSS}$, may be calculated from fig.11.19 according to

$$\Delta T_{RESIDUALLOSS} = \Delta T_{PISTON/ARCING/PEAK/LIMIT} - \Delta T_{RADIATIONLOSS} - \Delta T_{PISTON/ARCING/PEAK} \quad \text{(IV.1)}$$

Thus for an arc current of 30kA, this gives $\Delta T_{RESIDUAL\ LOSS}$ = 211K. The residual energy loss, $\Delta E_{RESIDUAL\ LOSS}$, corresponding to this "temperature loss", which is the energy loss after subtracting 25% radiation loss and the energy absorbed by the gas from the input energy E, is now calculated using eqn.11.8 (with M=0.263kg of SF_6) to be 33692J. Thus the percentage residual loss is $(\Delta E_{RESIDUAL\ LOSS})/E \times 100 = 58\%$ (since E = 57567J at 30kA). This residual energy loss accounts for the combined effect of the subsidiary flow loss, the nozzle ablation loss and the particle heat retention loss, each of which have been described in **11.3.1**. If it is assumed that $\Delta E_{RESIDUAL\ LOSS}$ is composed totally of particle heat retention then the maximum temperature rise of the particles can be calculated using

$$\Delta T_{PART} = \frac{\Delta E_{RESIDUALLOSS}}{M_{PART} Cp_{PART}} \quad \text{(IV.2)}$$

where M_{PART} is the mass of particles produced at 30kA (from fig.10.14) and Cp_{PART} is the mean specific heat of the particles (= 412$Jkg^{-1}K^{-1}$ from above). This gives ΔT_{PART} = 8177K. Curve 1 on fig.IV.1 shows the temperature rise of the particles (above ambient - 293K) during arcing at 30kA as a function of the percentage of $\Delta E_{RESIDUAL\ LOSS}$. For example, if the mean particle temperature rose by ~800K, then ~10% of $\Delta E_{RESIDUAL\ LOSS}$ could be attributed to energy absorbed by the particles.

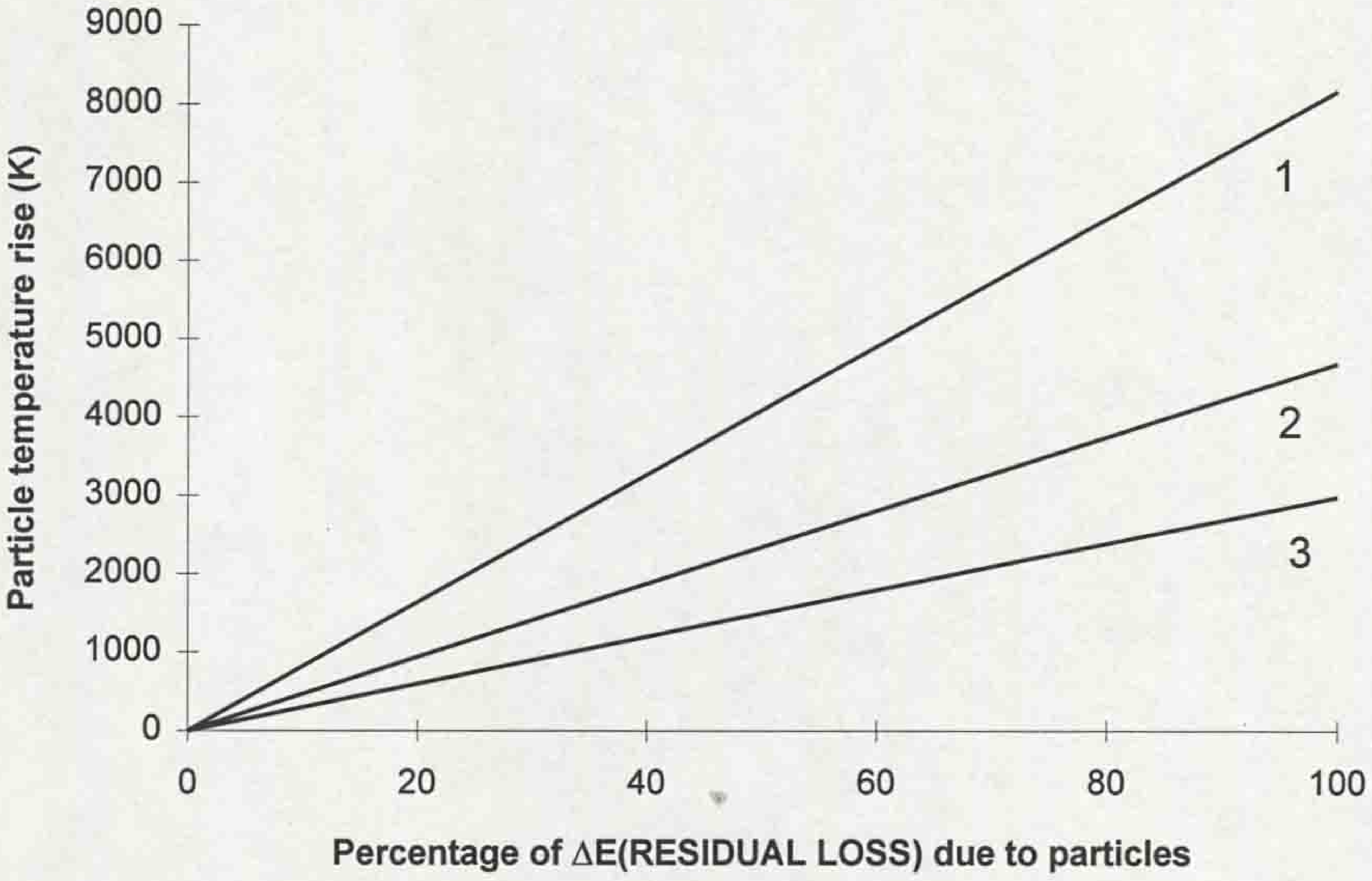

Figure IV.1 - The percentage of $\Delta E_{RESIDUAL\ LOSS}$ which can be attributed to energy absorption by the particles as a function of the mean particle temperature rise

As explained above, curve 1 relates to the particles being composed of equal masses of Tungsten, Copper and Sulphur. If Sulphur were the main particulate component, and the average particle specific heat capacity were 719$Jkg^{-1}K^{-1}$, then curve 2 would be obtained on fig.IV.1. In this case 10% of the residual loss would lead to a temperature rise of approximately 400K

Furthermore, curve 1 is based on $\Delta E_{RESIDUAL\ LOSS}$ being calculated as the energy difference between $\Delta T_{RADIATION\ LOSS}$ and $\Delta T_{PISTON/ARCING/PEAK}$ on fig.11.19. Fig.11.20, however, shows that the piston pressure rise measured after arcing ($\Delta P_{PISTON/POST\text{-}ARC/MEASURED}$ - curve 3 on fig.11.20) indicates lower energy losses than the piston pressure rise measured at its peak (curve 1 on fig.11.20). If the former pressure measurement were used to estimate $\Delta E_{RESIDUAL\ LOSS}$ then 21152J would be obtained. This represents 37% loss, as opposed to the 58% loss when using the peak piston pressure rises. Using this new value for $\Delta E_{RESIDUAL\ LOSS}$, whilst still using Sulphur as the dominant particulate element produces curve 3 on fig.IV.1. This curve suggests that lower temperature changes of the particles would be necessary to account for the residual energy loss eg. ~300K temperature rise in the particles would be necessary to account for 10% of the residual energy loss ($\Delta E_{RESIDUAL\ LOSS}$). Such temperature changes may be feasible, indicating that the particle energy absorption could become a significant energy loss mechanism.

ADDENDUM (References missing from reference list)

Gottleieb, M. and Brandt, G.B. (1983), *Applied optics*, Vol.20, **19**, 3408-3414.
Guild, J. (1931), *Phil. Trans. Roy. Soc.,* **A, 230,** 149-160.
Hallgren, B. and Ofverbeck, P. (1988), *15th Inter-RAM Conf.,* Portland, Oregon.
Henderson, P.J. (1993), *Arc research report*, June, University of Liverpool.
van de Hulst, H.C. (1957), *Light scattering by small particles,* John Wiley & Sons.
Kwan, S.H.T., (1987), *Ph.D thesis,* University of Liverpool.
Mie, G. (1908), *Ann. Physik (4),* **(25)**, 377-445.
Mottschmann, H. (1968), *Z. fur Physik,* **214**, 42-56.
Murphy, M.M. (1992), *Ph.D. thesis*, University of Liverpool.
Ragaller, K. and Reichert, K. (1977), *Current interruption in high voltage networks - Introduction and survey: Physical and network phenomena.*, Plenum press.
Ramirez, R.W. (1985), *The FFT: Fundamentals and Concepts,* Prentice-Hall.
Todorovic, P.S. and Jones, G.R. (1985), *IEEE Trans. Plasma Science,* **PS-13,** 153-162.
Tranter, A.D. (1995), *Ph.D thesis*, University of Liverpool.
Ura, S., Suhara, T. and Nishihara, H. (1989), *J. Lightwave Tech.*, Vol.7, **2**, 270-273.
Wright, W.D. (1929), (fig.233 from) *Researches on normal and defective colour vision,* London 1946.